Woodhead Publishing Series in Composites Science and Engineering

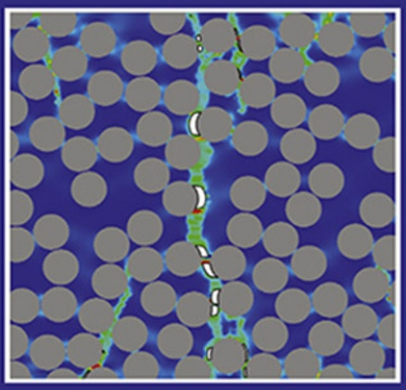

Numerical Modelling of Failure in Advanced Composite Materials

Edited by Pedro P. Camanho and Stephen R. Hallett

WP
Woodhead Publishing

Numerical Modelling of Failure in Advanced Composite Materials

Related titles

Fatigue and fracture of adhesively-bonded composite joints: Behaviour, simulation and modelling
(978-0-85709-806-1)

Residual stresses in composite materials
(978-0-85709-270-0)

Failure mechanisms in polymer matrix composites
(978-1-84569-750-1)

Woodhead Publishing Series in Composites Science and Engineering: Number 62

Numerical Modelling of Failure in Advanced Composite Materials

Edited by

Pedro P. Camanho and Stephen R. Hallett

AMSTERDAM • BOSTON • CAMBRIDGE • HEIDELBERG
LONDON • NEW YORK • OXFORD • PARIS • SAN DIEGO
SAN FRANCISCO • SINGAPORE • SYDNEY • TOKYO
Woodhead Publishing is an imprint of Elsevier

Woodhead Publishing is an imprint of Elsevier
80 High Street, Sawston, Cambridge, CB22 3HJ, UK
225 Wyman Street, Waltham, MA 02451, USA
Langford Lane, Kidlington, OX5 1GB, UK

Copyright © 2015 Elsevier Ltd. All rights reserved.

No part of this publication may be reproduced or transmitted in any form or by any means, electronic or mechanical, including photocopying, recording, or any information storage and retrieval system, without permission in writing from the publisher. Details on how to seek permission, further information about the Publisher's permissions policies and our arrangements with organizations such as the Copyright Clearance Center and the Copyright Licensing Agency, can be found at our website: www.elsevier.com/permissions.

This book and the individual contributions contained in it are protected under copyright by the Publisher (other than as may be noted herein).

Notices

Knowledge and best practice in this field are constantly changing. As new research and experience broaden our understanding, changes in research methods, professional practices, or medical treatment may become necessary.

Practitioners and researchers must always rely on their own experience and knowledge in evaluating and using any information, methods, compounds, or experiments described herein. In using such information or methods they should be mindful of their own safety and the safety of others, including parties for whom they have a professional responsibility.

To the fullest extent of the law, neither the Publisher nor the authors, contributors, or editors, assume any liability for any injury and/or damage to persons or property as a matter of products liability, negligence or otherwise, or from any use or operation of any methods, products, instructions, or ideas contained in the material herein.

ISBN: 978-0-08100-332-9 (print)
ISBN: 978-0-08100-342-8 (online)

British Library Cataloguing-in-Publication Data
A catalogue record for this book is available from the British Library

Library of Congress Control Number: 2015934515

For information on all Woodhead Publishing publications visit our website at http://store.elsevier.com/

Contents

List of contributors xi
Woodhead Publishing Series in Composites Science and Engineering xv
Preface xix

Part One Numerical modelling approaches to interlaminar failure in advanced composite materials 1

1 The virtual crack closure technique for modeling interlaminar failure and delamination in advanced composite materials 3
R. Krueger
1.1 Introduction and outline 3
1.2 Historical overview 4
1.3 Equations for using the VCCT 6
1.4 Modeling and implementation considerations 15
1.5 Mixed-mode fracture criteria for quasi-static delamination propagation and fatigue growth 25
1.6 Analysis benchmarking 34
1.7 New developments and evolving methods 40
1.8 Application example 43
1.9 Resulting recommendations for analysts 45
1.10 Concluding remarks 46
Acknowledgments 46
References 46

2 Modelling delamination with cohesive interface elements 55
S.R. Hallett, P.W. Harper
2.1 Introduction 55
2.2 History and background 55
2.3 Element formulations 58
2.4 Properties and mesh size 62
2.5 Mixed-mode application example 64
2.6 Delamination–matrix crack interaction 68
2.7 Conclusions 69
References 69

3 Interface elements for fatigue-driven delaminations in advanced composite materials **73**
A. Turon, B. Bak, E. Lindgaard, C. Sarrado, E. Lund
3.1 Introduction and motivation **73**
3.2 Extension of CZMs for modeling fatigue loading **75**
3.3 Examples **83**
3.4 Conclusions **88**
References **89**

4 A level set model for delamination in composite materials **93**
F.P. van der Meer
4.1 Introduction **93**
4.2 Cracked laminate model **94**
4.3 Crack growth model **97**
4.4 Solution algorithm **101**
4.5 Numerical example: Double cantilever beam **102**
4.6 Conclusions and outlook **105**
Acknowledgment **106**
References **106**

Part Two Numerical modelling approaches to intralaminar failure in advanced composite materials **109**

5 Three-dimensional invariant-based failure criteria for transversely isotropic fibre-reinforced composites **111**
P.P. Camanho, A. Arteiro, G. Catalanotti, A.R. Melro, M. Vogler
5.1 Introduction **111**
5.2 Invariant-based failure criterion for transverse failure of unidirectional composites **114**
5.3 Failure criteria for longitudinal failure of unidirectional composites **127**
5.4 Validation studies **133**
5.5 Conclusions **146**
References **146**

6 An overview of continuum damage models used to simulate intralaminar failure mechanisms in advanced composite materials **151**
A. Forghani, M. Shahbazi, N. Zobeiry, A. Poursartip, R. Vaziri
6.1 Introduction **151**
6.2 Damage modes in laminated composites **152**
6.3 Size effect in composite structures **153**
6.4 Simulation of damage at various scales **153**
6.5 CDM for simulation of intralaminar damage **157**

6.6 Experimental work for calibration of intralaminar damage models **164**
6.7 Concluding remarks **166**
Acknowledgments **167**
References **167**

7 Numerical modeling of matrix cracking and intralaminar failure in advanced composite materials 175
P. Maimí, H. Rodríguez, N. Blanco, J.A. Mayugo
7.1 Introduction **175**
7.2 First-ply failure **176**
7.3 Evolution of crack density **181**
7.4 Delamination induced by matrix cracking **188**
7.5 Conclusions **189**
References **190**

8 Fibre failure modelling 193
S. Pimenta
8.1 Introduction **193**
8.2 The mechanics of tensile fibre failure in composites **193**
8.3 Modelling the longitudinal tensile strength of UD composites **200**
8.4 Predicting the fracture toughness and modelling progressive failure **212**
8.5 Conclusions and future challenges **219**
References **220**

Part Three Advanced numerical algorithms for modelling and simulation of failure in advanced composite materials 225

9 Mesh-independent matrix cracking and delamination modeling in advanced composite materials 227
E.V. Iarve, D.H. Mollenhauer
9.1 Introduction **227**
9.2 Motivation **232**
9.3 Discrete damage modeling **236**
9.4 Progressive damage modeling **244**
9.5 Application of MIC to a two-crack double cantilever beam **248**
9.6 Application to OCT specimens **249**
9.7 Demonstration of DDM on a plain weave textile **257**
9.8 Conclusions **260**
References **260**

10 A new augmented finite element method (A-FEM) for progressive failure analysis of advanced composite materials 265
Q. Yang, M. Naderi
10.1 Introduction **265**
10.2 Problem statement **270**

10.3 A new 2D A-FEM formulation **275**
10.4 3D A-FEM formulation **289**
10.5 Numerical examples and discussions **292**
10.6 Concluding remarks **303**
Acknowledgment **304**
References **304**

11 Isogeometric analysis for modelling of failure in advanced composite materials 309
J.J.C. Remmers, C.V. Verhoosel, R. de Borst
11.1 Introduction **309**
11.2 Isogeometric finite element discretization **310**
11.3 Kirchhoff–Love Shell element **315**
11.4 Continuum shell formulation **318**
11.5 Concluding remarks **327**
References **328**

12 Peridynamics for analysis of failure in advanced composite materials 331
A. Askari, Y. Azdoud, F. Han, G. Lubineau, S. Silling
12.1 Introduction **331**
12.2 Peridynamic theory **333**
12.3 Peridynamic material models for composites **338**
12.4 Toward a novel treatment of localization **342**
12.5 Summary **347**
Acknowledgments **347**
References **348**

13 Multiscale modeling of the response and life prediction of composite materials 351
C. Oskay
13.1 Introduction **351**
13.2 Multiscale modeling in space–time **354**
13.3 Investigation of CFRP composites **365**
13.4 Conclusions and future trends **370**
References **372**

Part Four Engineering and scientific applications of numerical modelling for analysis of failure in advanced composite materials 377

14 Micromechanical failure analysis of advanced composite materials 379
C. McCarthy, T. Vaughan
14.1 Introduction **379**
14.2 Microstructural characterisation and generation **383**

14.3 Finite element framework **387**
14.4 Prediction of mechanical behaviour **392**
14.5 Applications to failure surfaces and structural load cases **398**
14.6 Micromechanical experimental calibration and validation techniques **402**
14.7 Conclusions and ways forward **405**
14.8 Acknowledgements **407**
References **407**

15 Computational micromechanics strategies for the analysis of failure in unidirectional composites 411
F. Naya, C.S. Lopes, C. González, J. LLorca
15.1 Introduction **411**
15.2 Computational micromechanics strategies for unidirectional plies **412**
15.3 Experimental Micromechanics **418**
15.4 Applications: Matrix-dominated failure **424**
15.5 Conclusions and future developments **429**
Acknowledgements **430**
References **430**

16 Numerical modelling for predicting failure in textile composites 435
M.Y. Matveev, A.C. Long
16.1 Introduction **435**
16.2 Unit cell modelling **436**
16.3 Damage modelling **442**
16.4 Conclusions **451**
16.5 Current trends **452**
References **452**

17 Multi-scale modelling for predicting fracture behaviour in through-thickness reinforced laminates 457
G. Allegri, G. Mohamed, S.R. Hallett
17.1 Introduction **457**
17.2 Modelling single Z-pin behaviour **461**
17.3 Modelling the behaviour of multiple Z-pins **468**
17.4 Conclusions **476**
Acknowledgement **477**
References **477**

18 Numerical modelling of impact and damage tolerance in aerospace composite structures 479
A.F. Johnson, N. Toso-Pentecôte, D. Schueler
18.1 Introduction **479**
18.2 Composites damage and failure models **481**
18.3 Impact damage in composite panel structures **486**

18.4 DT of pre-stressed composite panels under impact loads **491**
18.5 Conclusions and outlook **501**
18.6 Further reading **502**
Acknowledgments **503**
References **503**

19 Strength prediction methods for composite structures: Ensuring aeronautical design office requirements **507**
F. Laurin, N. Carrere, J.-F. Maire
19.1 Introduction **507**
19.2 Presentation of the material progressive failure approach **508**
19.3 FCV method **512**
19.4 The coupled criterion approach **514**
19.5 Comparisons of these strength analysis methods with available test results **519**
19.6 Complementarity between advanced failure approaches and fast calculation methods **525**
19.7 Conclusion/perspectives **528**
Acknowledgment **529**
References **529**

Index **533**

List of contributors

G. Allegri Imperial College London, London, UK

A. Arteiro Instituto de Ciência e Inovação em Engenharia Mecânica e Engenharia Industrial (INEGI), Universidade do Porto, Porto, Portugal

A. Askari Boeing Commercial Airplane, Everett, WA, USA

Y. Azdoud King Abdullah University of Science and Engineering (KAUST), Physical Sciences and Engineering Division, COHMAS Laboratory, Thuwal, Saudi Arabia

B. Bak Aalborg University, Aalborg East, Denmark

N. Blanco Universitat de Girona, Girona, Spain

P.P. Camanho Instituto de Ciência e Inovação em Engenharia Mecânica e Engenharia Industrial (INEGI), Universidade do Porto, Porto, Portugal

N. Carrere ENSTA Bretagne and Laboratoire Brestois de Mécanique et des Systèmes, Brest Cedex, France

G. Catalanotti Instituto de Ciência e Inovação em Engenharia Mecânica e Engenharia Industrial (INEGI), Universidade do Porto, Porto, Portugal

R. de Borst University of Glasgow, Glasgow, UK

A. Forghani The University of British Columbia, Vancouver, BC, Canada

C. González IMDEA Materials Institute, Polytechnic University of Madrid, Madrid, Spain

S.R. Hallett University of Bristol, Bristol, UK

F. Han King Abdullah University of Science and Engineering (KAUST), Physical Sciences and Engineering Division, COHMAS Laboratory, Thuwal, Saudi Arabia

P.W. Harper University of Bristol, Bristol, UK

E.V. Iarve University of Dayton Research Institute, Dayton, OH, USA

A.F. Johnson Consultant, Stuttgart, Germany

R. Krueger National Institute of Aerospace, Hampton, VA, USA

F. Laurin ONERA, Châtillon Cedex, France

E. Lindgaard Aalborg University, Aalborg East, Denmark

J. LLorca IMDEA Materials Institute, Polytechnic University of Madrid, Madrid, Spain

A.C. Long University of Nottingham, Nottingham, UK

C.S. Lopes IMDEA Materials Institute, Madrid, Spain

G. Lubineau King Abdullah University of Science and Engineering (KAUST), Physical Sciences and Engineering Division, COHMAS Laboratory, Thuwal, Saudi Arabia

E. Lund Aalborg University, Aalborg East, Denmark

P. Maimí Universitat de Girona, Girona, Spain

J.-F. Maire ONERA, Châtillon Cedex, France

M.Y. Matveev University of Nottingham, Nottingham, UK

J.A. Mayugo Universitat de Girona, Girona, Spain

C. McCarthy University of Limerick, Ireland

A.R. Melro Instituto de Ciência e Inovação em Engenharia Mecânica e Engenharia Industrial (INEGI), Universidade do Porto, Porto, Portugal; ISVOUGA, Santa Maria da Feira, Portugal

G. Mohamed University of Bristol, Bristol, UK

D.H. Mollenhauer Air Force Research Laboratory, Wright Patterson AFB, OH, USA

M. Naderi University of Miami, Coral Gables, FL, USA

F. Naya IMDEA Materials Institute, Madrid, Spain

C. Oskay Vanderbilt University, Nashville, TN, USA

S. Pimenta Imperial College London, London, UK

A. Poursartip The University of British Columbia, Vancouver, BC, Canada

J.J.C. Remmers Eindhoven University of Technology, Eindhoven, The Netherlands

H. Rodríguez Universitat de Girona, Girona, Spain

C. Sarrado University of Girona, Girona, Spain

D. Schueler Institute of Structures and Design, Stuttgart, Germany

M. Shahbazi The University of British Columbia, Vancouver, BC, Canada

S. Silling Sandia National Laboratories, Albuquerque, NM, USA

N. Toso-Pentecôte German Aerospace Center (DLR), Institute of Structures and Design, Stuttgart, Germany

A. Turon University of Girona, Girona, Spain

F.P. van der Meer Delft University of Technology, Delft, The Netherlands

T. Vaughan National University of Ireland, Galway, Ireland

R. Vaziri The University of British Columbia, Vancouver, BC, Canada

C.V. Verhoosel Eindhoven University of Technology, Eindhoven, The Netherlands

M. Vogler Vogler Engineering & Consulting Services, Hannover, Germany

Q. Yang University of Miami, Coral Gables, FL, USA

N. Zobeiry The University of British Columbia, Vancouver, BC, Canada

This page intentionally left blank

Woodhead Publishing Series in Composites Science and Engineering

1 **Thermoplastic aromatic polymer composites**
F. N. Cogswell
2 **Design and manufacture of composite structures**
G. C. Eckold
3 **Handbook of polymer composites for engineers**
Edited by L. C. Hollaway
4 **Optimisation of composite structures design**
A. Miravete
5 **Short-fibre polymer composites**
Edited by S. K. De and J. R. White
6 **Flow-induced alignment in composite materials**
Edited by T. D. Papthanasiou and D. C. Guell
7 **Thermoset resins for composites**
Compiled by Technolex
8 **Microstructural characterisation of fibre-reinforced composites**
Edited by J. Summerscales
9 **Composite materials**
F. L. Matthews and R. D. Rawlings
10 **3-D textile reinforcements in composite materials**
Edited by A. Miravete
11 **Pultrusion for engineers**
Edited by T. Starr
12 **Impact behaviour of fibre-reinforced composite materials and structures**
Edited by S. R. Reid and G. Zhou
13 **Finite element modelling of composite materials and structures**
F. L. Matthews, G. A. O. Davies, D. Hitchings and C. Soutis
14 **Mechanical testing of advanced fibre composites**
Edited by G. M. Hodgkinson
15 **Integrated design and manufacture using fibre-reinforced polymeric composites**
Edited by M. J. Owen and I. A. Jones
16 **Fatigue in composites**
Edited by B. Harris
17 **Green composites**
Edited by C. Baillie
18 **Multi-scale modelling of composite material systems**
Edited by C. Soutis and P. W. R. Beaumont

19 **Lightweight ballistic composites**
Edited by A. Bhatnagar
20 **Polymer nanocomposites**
Y-W. Mai and Z-Z. Yu
21 **Properties and performance of natural-fibre composite**
Edited by K. Pickering
22 **Ageing of composites**
Edited by R. Martin
23 **Tribology of natural fiber polymer composites**
N. Chand and M. Fahim
24 **Wood-polymer composites**
Edited by K. O. Niska and M. Sain
25 **Delamination behaviour of composites**
Edited by S. Sridharan
26 **Science and engineering of short fibre reinforced polymer composites**
S-Y. Fu, B. Lauke and Y-M. Mai
27 **Failure analysis and fractography of polymer composites**
E. S. Greenhalgh
28 **Management, recycling and reuse of waste composites**
Edited by V. Goodship
29 **Materials, design and manufacturing for lightweight vehicles**
Edited by P. K. Mallick
30 **Fatigue life prediction of composites and composite structures**
Edited by A. P. Vassilopoulos
31 **Physical properties and applications of polymer nanocomposites**
Edited by S. C. Tjong and Y-W. Mai
32 **Creep and fatigue in polymer matrix composites**
Edited by R. M. Guedes
33 **Interface engineering of natural fibre composites for maximum performance**
Edited by N. E. Zafeiropoulos
34 **Polymer-carbon nanotube composites**
Edited by T. McNally and P. Pötschke
35 **Non-crimp fabric composites: Manufacturing, properties and applications**
Edited by S. V. Lomov
36 **Composite reinforcements for optimum performance**
Edited by P. Boisse
37 **Polymer matrix composites and technology**
R. Wang, S. Zeng and Y. Zeng
38 **Composite joints and connections**
Edited by P. Camanho and L. Tong
39 **Machining technology for composite materials**
Edited by H. Hocheng
40 **Failure mechanisms in polymer matrix composites**
Edited by P. Robinson, E. S. Greenhalgh and S. Pinho
41 **Advances in polymer nanocomposites: Types and applications**
Edited by F. Gao
42 **Manufacturing techniques for polymer matrix composites (PMCs)**
Edited by S. Advani and K-T. Hsiao

43 **Non-destructive evaluation (NDE) of polymer matrix composites: Techniques and applications**
Edited by V. M. Karbhari
44 **Environmentally friendly polymer nanocomposites: Types, processing and properties**
S. S. Ray
45 **Advances in ceramic matrix composites**
Edited by I. M. Low
46 **Ceramic nanocomposites**
Edited by R. Banerjee and I. Manna
47 **Natural fibre composites: Materials, processes and properties**
Edited by A. Hodzic and R. Shanks
48 **Residual stresses in composite materials**
Edited by M. Shokrieh
49 **Health and environmental safety of nanomaterials: Polymer nanocomposites and other materials containing nanoparticles**
Edited by J. Njuguna, K. Pielichowski and H. Zhu
50 **Polymer composites in the aerospace industry**
Edited by P. E. Irving and C. Soutis
51 **Biofiber reinforcement in composite materials**
Edited by O. Faruk and M. Sain
52 **Fatigue and fracture of adhesively-bonded composite joints: Behaviour, simulation and modelling**
Edited by A. P. Vassilopoulos
53 **Fatigue of textile composites**
Edited by V. Carvelli and S. V. Lomov
54 **Wood composites**
Edited by M. P. Ansell
55 **Toughening mechanisms in composite materials**
Edited by Q. Qin and J. Ye
56 **Advances in composites manufacturing and process design**
Edited by P. Boisse
57 **Structural Integrity and Durability of Advanced Composites: Innovative modelling methods and intelligent design**
Edited by P.W.R. Beaumont, C. Soutis and A. Hodzic
58 **Recent Advances in Smart Self-healing Polymers and Composites**
Edited by G. Li and H. Meng
59 **Manufacturing of Nanocomposites with Engineering Plastics**
Edited by V. Mittal
60 **Fillers and Reinforcements for Advanced Nanocomposites**
Edited by Y. Dong, R. Umer and A. Kin-Tak Lau
61 **Biocomposites: Design and Mechanical Performance**
Edited by M. Misra, J. K. Pandey and A. K. Mohanty
62 **Numerical Modelling of Failure in Advanced Composite Materials**
Edited by P.P. Camanho and S. R. Hallett

This page intentionally left blank

Preface

Robust predictions of the thermo-mechanical response of polymer composite materials across the length scales are of the utmost importance to improve the efficiency of composite structures and to promote an in-depth understanding of microstructure–property relations.

This book, which addresses state-of-the-art analysis methods for the simulation of inelastic behaviour of polymer composites, is divided into four parts. The first two parts address the modelling of the fundamental failure mechanisms that contribute to overall failure in advance composite materials. Part 1 addresses the interlaminar failure mechanism of delamination. Chapters are presented on the Virtual Crack Closure Technique, cohesive interface elements, fatigue delamination growth modelling and a new level set technique. In Part 2 intra-laminar failure mechanisms are considered. These chapters cover stress-based failure criteria, continuum damage models, matrix cracking and fibre failure. Chapters in these two parts describe many of the numerical modelling techniques that form the building blocks on which more complex formulations and applications are built.

In part 3 we present some of the newer and emerging techniques that are coming to the fore in accurately and efficiently predicting the failure of advanced composite materials. Chapters cover mesh independent crack modelling, isogeometric analysis, peridynamics and multi-scale techniques. As the application of advanced composites becomes more widespread so the requirement for simulation of mechanical performance and failure is growing. Techniques such as those presented here will be more widely used in the future.

The final part 4 focuses on engineering and scientific applications. This cuts across the length scales, from micro-mechanical analysis at the fibre and matrix length scale to the impact of large aerospace structures. Also covered are textile composites, through-thickness reinforcement and using analysis to meet aerospace design requirements.

We are certain that this book will be a valuable source of information for people interested in the mechanics of deformation and fracture of polymer composite materials.

This page intentionally left blank

Part One

Numerical modelling approaches to interlaminar failure in advanced composite materials

This page intentionally left blank

The virtual crack closure technique for modeling interlaminar failure and delamination in advanced composite materials

1

R. Krueger
National Institute of Aerospace, Hampton, VA, USA

1.1 Introduction and outline

One of the most common failure modes for composite structures is interlaminar failure or delamination (Garg, 1988; Bolotin, 1996; Pagano and Schoeppner, 2000; Tay, 2003; Wisnom, 2012). The use of fracture mechanics as a means to characterize the onset and growth of these delaminations has become common practice over the past three decades (O'Brien, 1982; Martin, 1998; Raju and O'Brien, 2008). The total strain energy-release rate, G_T; the mode I component due to interlaminar tension, G_I; the mode II component due to interlaminar sliding shear, G_{II}; and the mode III component due to interlaminar scissoring shear, G_{III} (see Figure 1.1) need to be calculated for a given geometry, material system and loading scheme. To predict delamination onset or growth, these calculated G components are compared to measured interlaminar fracture toughness properties, often given as a function of mixed-mode ratio G_{II}/G_T. Failure is expected when the calculated total energy-release rate, G_T, exceeds the measured interlaminar fracture toughness, G_c. The virtual crack closure technique (VCCT) (Rybicki and Kanninen, 1977; Krueger, 2004) is a widely used method for computing energy-release rates based on results from continuum two-dimensional (2D) and solid three-dimensional (3D) finite element analyses, which allows the calculation of the individual mode components required when using the mixed-mode fracture criterion. Often the application of this fracture mechanics-based approach is referred to as "performing a VCCT analysis" to distinguish it from interface-type approaches discussed in Chapters 2 and 3. Strictly speaking, however, VCCT calculates the mixed-mode energy-release rates based on the computed forces and displacements obtained from a finite element analysis.

The objective of this chapter is to give an overview of the VCCT, summarize the history, and provide the reader with an insight into its application and pitfalls. First, we provide a brief historical overview. Second, we discuss equations for 2D quadrilateral elements as well as 3D solid and plate/shell elements with linear-shape functions. An overview of necessary modifications for the use of the method with geometrically nonlinear finite element analysis and corrections required for elements at the crack

Numerical modelling of failure in advanced composite materials. http://dx.doi.org/10.1016/B978-0-08-100332-9.00001-3
Copyright © 2015 Elsevier Ltd. All rights reserved.

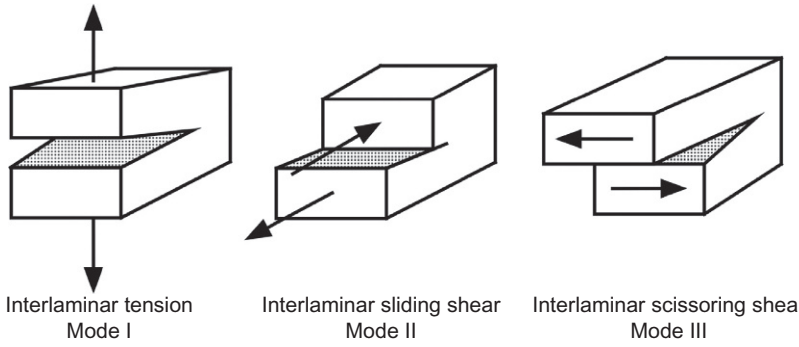

Figure 1.1 Fracture modes.

tip with different lengths and widths are also given. Third, we discuss specific modeling and implementation aspects for curved delamination front contours, including nonconforming meshes at the delamination front, the mode separation at sharp corners, and the approximation of growing delamination fronts. The problems associated with cracks or delaminations propagating between different materials (the so-called bimaterial interface) will also be mentioned briefly, as well as a strategy to minimize these problems. Fourth, mixed-mode fracture criteria will be introduced, together with standardized test methods to obtain fracture toughness data used in quasi-static delamination propagation and fatigue growth analyses. Fifth, the development and application of benchmark examples for the assessment of quasi-static delamination propagation capabilities and analysis verification will be demonstrated. Sixth, the evolving methods and future trends will be introduced where VCCT is used for the analysis of delamination branching, migration, and delamination/matrix interaction. Seventh, an application example will be presented. Finally, recommendations for the use of VCCT will be given to avoid pitfalls, and the chapter will end with some concluding remarks. Throughout the entire chapter, extensive references to key books, reports, journal publications, and standards will be provided to help the reader find the appropriate sources.

1.2 Historical overview

For delaminations in laminated composite materials, where the failure criterion is highly dependent on the mixed-mode ratio and propagation occurs in the laminate plane, the VCCT has been most widely used for computing energy-release rates because fracture-mode separation is determined explicitly. The technique was first used for composites to investigate edge delamination soon after its original publication (Rybicki et al., 1977; O'Brien, 1982). The original journal paper dates back close to four decades now (Rybicki and Kanninen, 1977); however, the implementation of VCCT into the large commercial general-purpose finite element

codes did not start until about 30 years after the method was introduced (Abaqus, 2005). Today the technique is available in a variety of commercial codes in different implementations (Ansys, 2014; Abaqus, 2014b; Marc, 2013; Nastran, 2013; Genoa, 2014; Yarrington et al., 2006).

The modified crack closure integral, as VCCT is called in the original publication, is primarily based on Irwin's crack closure integral (Irwin, 1958; Broek, 1991). Irwin assumed that the energy required to extend a crack by $\triangle a$ is identical to the work required to close it to its original length. This concept is illustrated in Figure 1.2 in the context of finite element analysis where the energy $\triangle E$ released when a crack of length a (as shown in Figure 1.2) is extended by one element from a to $a + \triangle a$ (Figure 1.2b) is identical to the energy required to close the crack between locations k and i. The work $\triangle E$ required to close this crack along one element side can be calculated by multiplying the shear and opening forces calculated at the nodal point i at its closed state (Figure 1.2a) with the respective differences in shear and opening nodal displacements at node i when the crack is open (Figure 1.2b). This analysis requires two steps and is often referred to as "crack closure method," "two-step crack closure technique," or "two-step VCCT" (Krueger, 2004). To avoid these two analyses, Rybicki and Kanninen (1977) additionally assumed self-similar crack growth such that a crack extension of $\triangle a$ from a (node i) to $a + \triangle a$ (node k) does not significantly alter the state at the crack tip (Figure 1.2). Therefore, when the crack tip is located at node k, the displacements behind the crack tip at node i are approximately equal to the displacements behind the crack tip at node ℓ when the crack tip is located at node i. Further, the energy $\triangle E$ released when the crack is extended by $\triangle a$ from $a + \triangle a$ to $a + 2\triangle a$ is identical to the energy required to close the crack between location i and k. Thus, the work $\triangle E$ required to close the crack along one element side can simply be calculated in one step by multiplying the shear and opening forces at nodal point i and with the corresponding shear and opening displacements at node ℓ. The details of calculating the energy-release rate and the separation into the individual mode components will be discussed in the following sections.

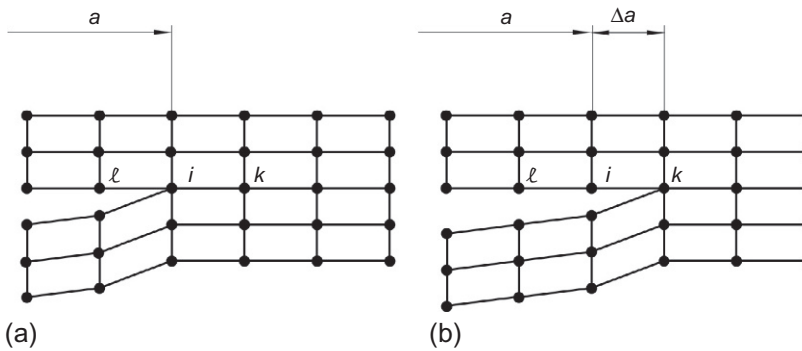

Figure 1.2 Principle of self-similar crack growth. (a) Initial crack of length a and (b) crack extended by $\triangle a$.

1.3 Equations for using the VCCT

In the following paragraphs, equations are presented to calculate mixed-mode strain energy-release rates using 2D finite element models, such as plane stress or plane strain. Different approaches are also discussed for the cases where the crack or delamination is modeled with 3D solids or plate and shell elements. The details presented here are limited to traditional elements with linear-shape functions since these are mainly used in today's software. Although the original paper by Rybicki and Kanninen (1977) is based on heuristic arguments, Raju (1987) proved the validity of the derived equations. Equations and derivations for higher-order and singular elements, further details, and additional references are provided in an earlier overview paper (Krueger, 2004) for further in-depth reading.

1.3.1 Formula for two-dimensional planar elements with four nodes

The mode I and mode II components of the strain energy-release rate, G_{I} and G_{II}, respectively, are calculated for four-node plane stress or plane strain elements (Rybicki and Kanninen, 1977)

$$G_{\mathrm{I}} = -\frac{1}{2\Delta a} F_{zi}(w_{\ell} - w_{\ell^*}). \tag{1.1}$$

$$G_{\mathrm{II}} = -\frac{1}{2\Delta a} F_{xi}(u_{\ell} - u_{\ell^*}). \tag{1.2}$$

where $\triangle a$ is the length of the elements at the crack front and F_{zi} and F_{xi} are the forces at the crack tip (nodal point i), as shown in Figure 1.3a. The relative displacements behind the crack tip are calculated from the nodal displacements at the upper crack face u_{ℓ} and w_{ℓ} (nodal point ℓ), and the nodal displacements u_{ℓ^*} and w_{ℓ^*} at the lower crack face (nodal point ℓ^*), respectively. The crack surface $\triangle A$ created is calculated as $\triangle A = \triangle a \cdot 1$, where it is assumed that the two-dimensional model is of unit thickness.

For problems involving large deformations, a geometric nonlinear analysis may be required for which both forces and displacements obtained in the global coordinate system need to be transformed into a local coordinate system (x', z') which originates at the crack tip, as shown in Figure 1.3b. The transformation is required to correctly compute the mixed-mode energy-release rates G_{I} and G_{II}. The local crack tip system defines the lateral (x', or mode II) and normal (z', or mode I) coordinate directions at the crack tip in the deformed configuration, as shown in Figure 1.3b, for the two-dimensional case. The vector through nodes i and k in the deformed configuration defines the local x' direction, as shown in Figure 1.3b. The local z' direction is perpendicular to the local x' direction. Forces at node row i and displacements at node row ℓ need to be transformed to the local x'–z' system at the tip as shown in

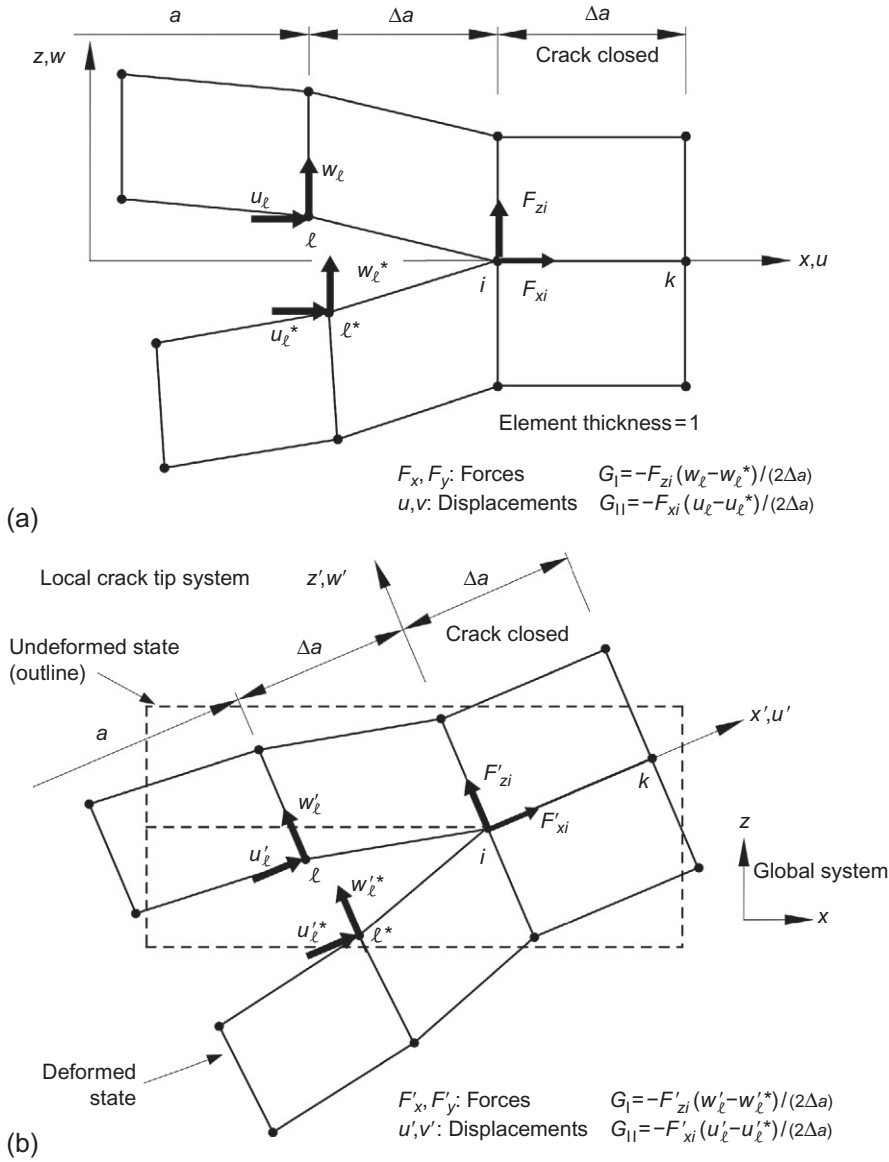

Figure 1.3 VCCT for 2D solid elements. (a) VCCT for 2D solid element with four nodes and (b) VCCT for geometrically nonlinear analysis.

Figure 1.3b. The total energy-release rate remains unaffected by this transformation. The equations to calculate the mixed-mode energy-release rate components remain the same as before, with forces and displacements now expressed in the local system. For the two-dimensional quadrilateral element with linear-shape functions, this yields

$$G_{\mathrm{I}} = -\frac{1}{2\Delta a} F'_{zi}\left(w'_{\ell} - w'_{\ell^*}\right). \tag{1.3}$$

$$G_{\mathrm{II}} = -\frac{1}{2\Delta a} F'_{xi}\left(u'_{\ell} - u'_{\ell^*}\right). \tag{1.4}$$

1.3.2 Correcting for elements with different lengths at the crack tip

All of the aforementioned equations have been derived assuming that the element lengths Δa for the element in front of the crack tip and behind it are identical. Maintaining equal element length may not always be practical, in particular when automatic mesh generators are used to create complex models. In this case, corrections to the previously derived equations are required. In their original paper, Rybicki and Kanninen (1977) used the $1/\sqrt{r}$ singularity of the stress field at the crack tip to derive the corrected equations. A sketch of a crack tip modeled with 2D finite elements of unequal length is shown in Figure 1.4. The forces F_{zi} and F_{xi} at the crack tip (nodal point i) calculated for an element length Δa_2 are known from the finite element analysis. However, the VCCT calculation requires the forces $\bar{F}_{xi}$ and $\bar{F}_{zi}$ that correspond to the relative displacements at node ℓ behind the crack tip, which have been calculated for an element length Δa_1.

The stress field at the crack tip can be expressed as (Broek, 1991)

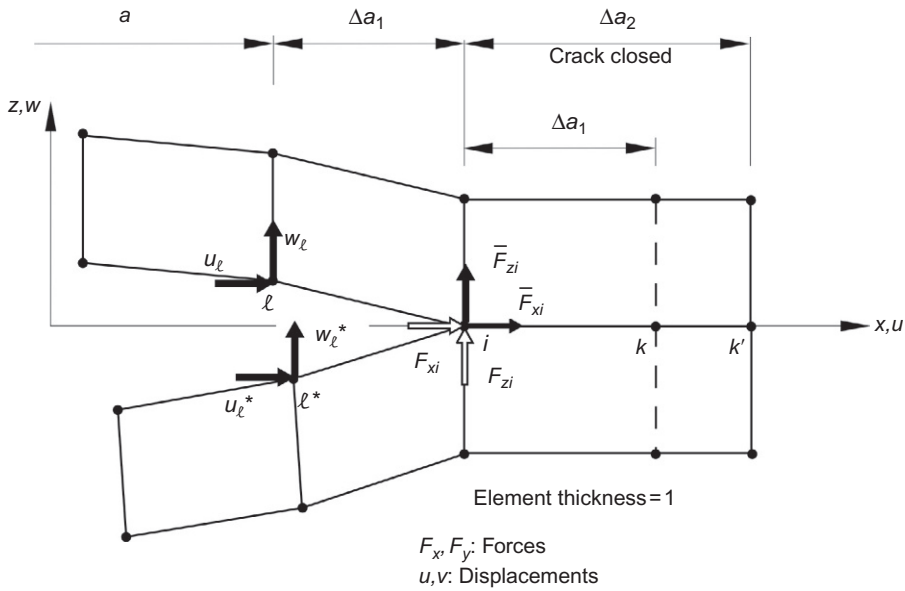

Figure 1.4 Correction for elements with different lengths in front of and behind the crack tip.

$$\sigma(r) = b \cdot \sigma_\infty \cdot \frac{1}{\sqrt{r}} = \frac{\mathrm{d}F_{xi}}{\mathrm{d}A} = \frac{\mathrm{d}F_{xi}}{b \cdot \mathrm{d}r}, \tag{1.5}$$

where b is the element width or thickness, σ_∞ is the undisturbed far field stress, and $\sigma(r)$ is the stress in front of the crack, which is a function of the distance r from the crack tip. The forces at the crack tip for element length $\triangle a_1$ and $\triangle a_2$ are obtained through integration

$$\bar{F}_{xi} = b \cdot \sigma_\infty \int_0^{\Delta a_1} \frac{\mathrm{d}r}{\sqrt{r}} = 2 \cdot b \cdot \sigma_\infty \cdot \sqrt{\Delta a_1}, \tag{1.6}$$

$$F_{xi} = 2 \cdot b \cdot \sigma_\infty \cdot \sqrt{\Delta a_2}. \tag{1.7}$$

A relationship between the forces can be derived which only depends on the length of the elements in front of and behind the crack tip

$$\bar{F}_{xi} = F_{xi} \cdot \sqrt{\frac{\Delta a_1}{\Delta a_2}}. \tag{1.8}$$

The calculation of the crack opening force $\bar{F}_{zi}$ is done accordingly. With the relationship of the forces established, the required forces $\bar{F}_{xi}$ and $\bar{F}_{zi}$ may be substituted for the forces F_{zi} and F_{xi} obtained from the finite element analysis, yielding the corrected equations for the energy-release rate components

$$G_{\mathrm{I}} = -\frac{1}{2\Delta a} F_{zi}(w_\ell - w_{\ell^*}) \sqrt{\left(\frac{\Delta a_1}{\Delta a_2}\right)}, \tag{1.9}$$

$$G_{\mathrm{II}} = -\frac{1}{2\Delta a} F_{xi}(u_\ell - u_{\ell^*}) \sqrt{\left(\frac{\Delta a_1}{\Delta a_2}\right)}. \tag{1.10}$$

1.3.3 Formula for three-dimensional solid, plate, and shell elements

For convenience, only a section of the delaminated area that is modeled with eight-node 3D solid elements is illustrated in Figure 1.5. The mode I, mode II, and mode III components of the strain energy-release rate, G_{I}, G_{II}, and G_{III} are calculated as

$$G_{\mathrm{I}} = -\frac{1}{2\Delta A} F'_{zLi}\left(w'_{L\ell} - w'_{L\ell^*}\right), \tag{1.11}$$

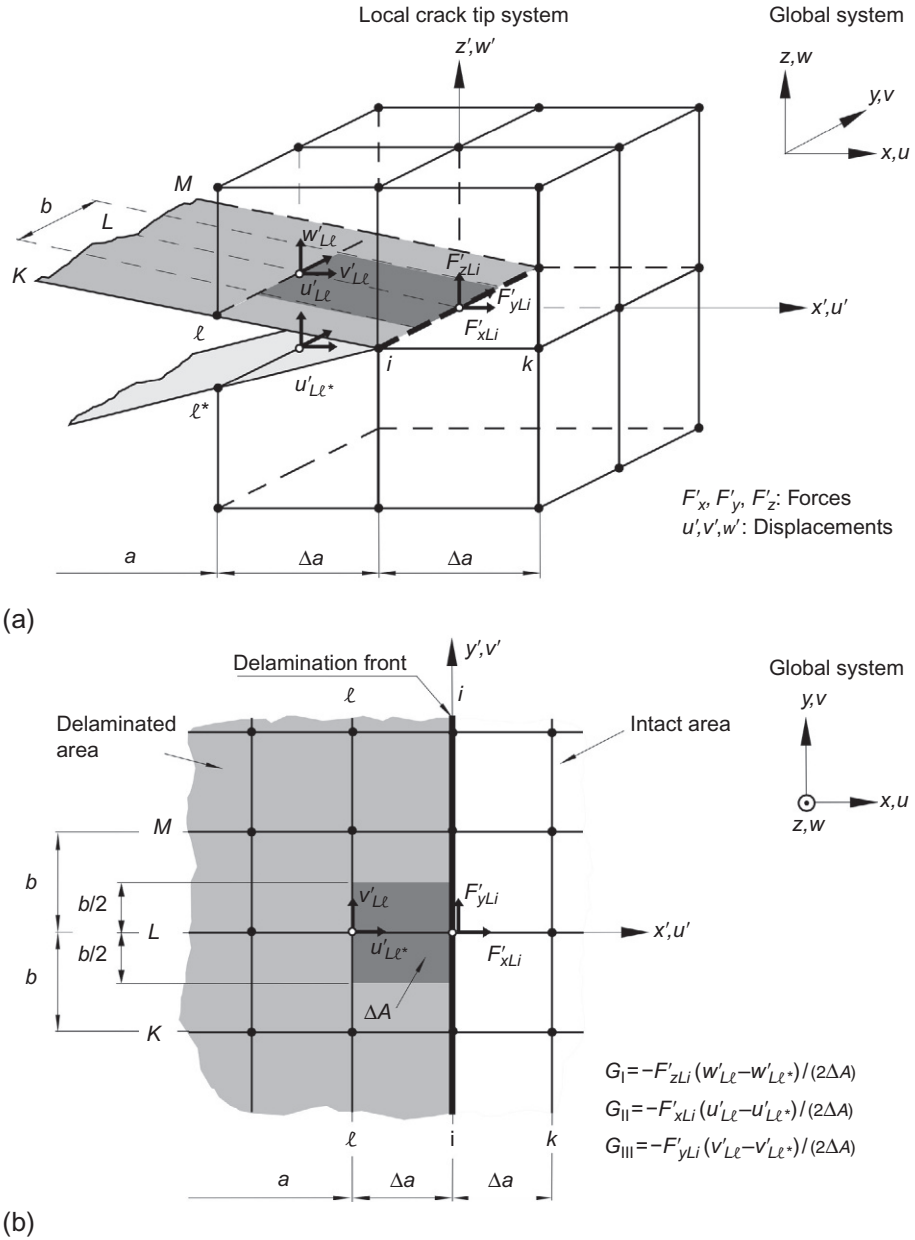

Figure 1.5 VCCT for 3D solid elements. (a) 3D view (lower surface forces have been omitted for clarity) and (b) top view of upper surface (lower surface terms have been omitted for clarity).

$$G_{\mathrm{II}} = -\frac{1}{2\Delta A} F'_{xLi}\left(u'_{L\ell} - u'_{L\ell^*}\right), \tag{1.12}$$

$$G_{\mathrm{III}} = -\frac{1}{2\Delta A} F'_{yLi}\left(v'_{L\ell} - v'_{L\ell^*}\right) \tag{1.13}$$

with $\triangle A = \triangle a \cdot b$ as shown in Figure 1.5b (Shivakumar et al., 1988). Here, $\triangle A$ is the area virtually closed, $\triangle a$ is the length of the elements at the delamination front, and b is the width of the elements. For better identification in this and the following figures, columns are identified by capital letters (L) and rows by lowercase letters (i, k, ℓ) as illustrated in the top view of the upper surface shown in Figure 1.5b. Hence, F'_{xLi}, F'_{yLi}, and F'_{zLi} denote the forces in the local system at the delamination front in column L, row i. The corresponding displacements behind the delamination at the top face node row ℓ are denoted $u_{L\ell}{}'$, $v_{L\ell}{}'$, and $w_{L\ell}{}'$ at the lower face node row ℓ^* are denoted $u'_{L\ell^*}$, $v'_{L\ell^*}$, and $w'_{L\ell^*}$ as shown in Figure 1.5. All forces and displacements are obtained first from the finite element analysis with respect to the global system. The forces and displacements are then transformed with respect to the local crack tip coordinate system (x', y', z') that defines the normal and tangential coordinate directions at the delamination front in the deformed configuration, as discussed earlier for 2D elements. Equations for higher-order elements, further details, and additional references are provided in an overview paper (Krueger, 2004).

The use of four-node plate elements to calculate the total strain energy-release rate was demonstrated by Whitcomb and Shivakumar (1989), who calculated the strain energy-release rate as the work required to change the midplane strains and curvatures in the cracked part of the plate at the crack front so that they are equal to midplane strains and curvatures in the uncracked part of the plate at the crack front. Equations for the use of VCCT in conjunction with four- and nine-node plate elements were derived by Wang and Raju (1996), where two techniques to tie the nodes at the delamination front (row i in Figure 1.6) were also discussed. For nodes of the upper and lower surfaces, which are joined at the crack tip, the first method enforced the compatibility of translational and rotational degrees-of-freedom for nodes with identical coordinates. In the second technique, only the compatibility of the translational degrees-of-freedom were enforced. The second technique allowed the nodes to have independent rotations. For the configurations and loads considered, the second technique appeared to be preferable, yielding accurate strain energy-release rates (Wang and Raju, 1996; Glaessgen et al., 1998, 2002).

The equations to calculate the strain energy-release rate components at the element corner nodes (location Li in Figure 1.6) for this method are identical to Equations (1.11)–(1.13) discussed above for the solid element with eight nodes. Equations for higher-order elements, further details, and additional references are provided in an earlier overview paper (Krueger, 2004).

Very large 3D finite element models may require extensive modeling and computational effort. Therefore, the use of a shell-to-solid submodeling technique offers great potential for saving modeling and computational effort because only a relatively

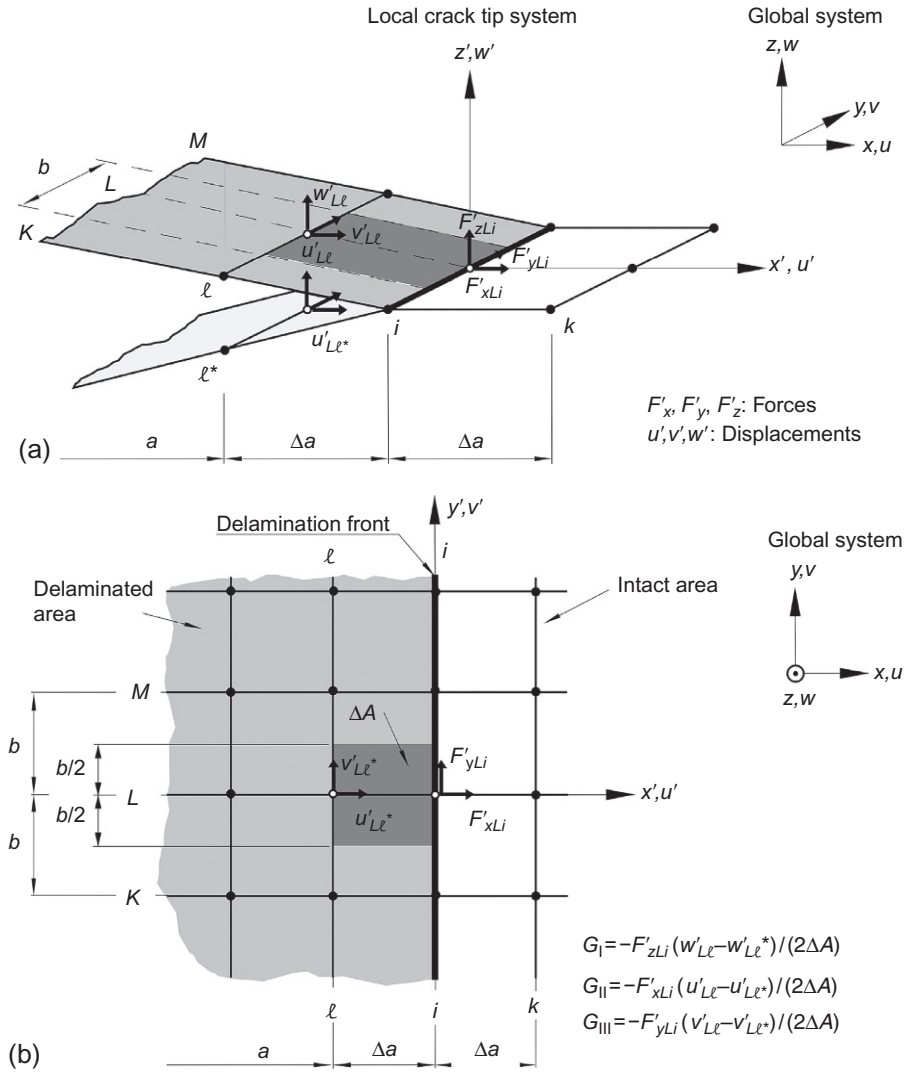

Figure 1.6 VCCT for plate/shell elements with four nodes. (a) 3D view (lower surface forces have been omitted for clarity) and (b) top view of upper surface (lower surface terms have been omitted for clarity).

small section in the vicinity of the delamination front needs to be modeled with solid elements (Krueger and O'Brien, 2001; Pietropaoli and Riccio, 2011).

Large built-up structures such as aircraft fuselage and wing components are traditionally modeled and analyzed using plate or shell finite elements to keep the modeling and computational effort affordable. Often beam elements are used to represent the stiffeners, and shell elements are used to model the skin. Therefore, it may appear

appealing to apply VCCT to cases where the delamination is located at an interface between different element types, as shown in Figure 1.7a and b. A different scenario may be a model where the same elements are used to model the crack or delamination, but the section properties on either side of the interface are different, as shown in Figure 1.7c and d. However, computed mixed-mode strain energy-release rate components depend on many variables such as element order and shear deformation assumptions, kinematic constraints in the neighborhood of the delamination front, and continuity of material properties and section stiffness in the vicinity of the disbond when delaminations or disbonds are modeled with plate or shell finite elements (Wang and Raju, 1996; Glaessgen et al., 2002), in which case VCCT must be used with care. For example, mesh refinement studies showed that computed G_{I}, G_{II}, and G_{III} did not converge when the structure above and below the plane of delamination was modeled with plate elements with different section properties (thickness or layup) (Glaessgen et al., 2002). A comparison of computed mixed-mode strain energy-release rates obtained from plate models with values computed from 3D models showed differences in results near the free edges of the structure where the stress state is three-dimensional (König et al., 2000). This problem seems to be related to the bimaterial interface problem discussed in Section 1.4.5. Currently, however, the community at

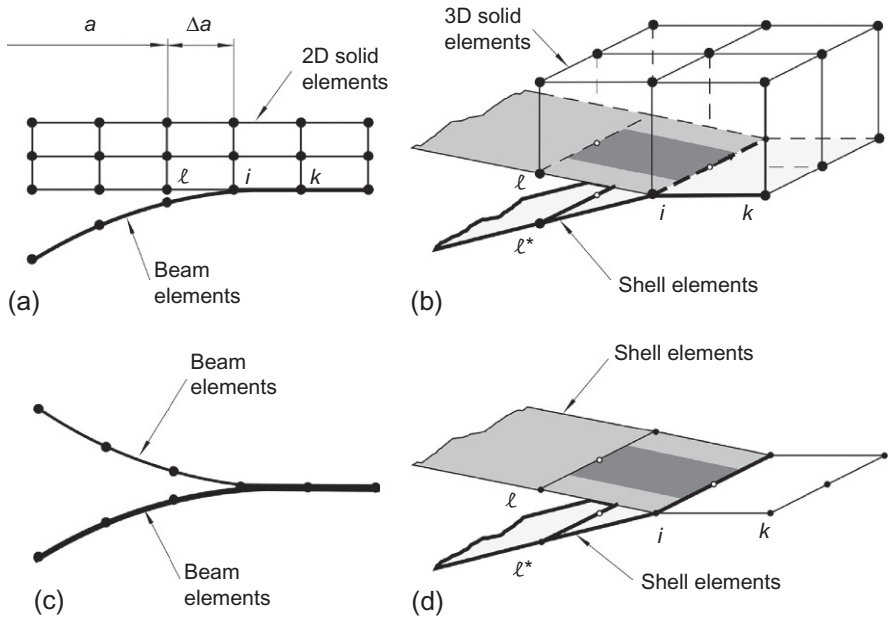

Figure 1.7 Configurations for which accurate mode separation might not be obtained. (a) Interfaces between beam and 2D solid elements; (b) interfaces between shell and 3D solid elements; (c) interfaces between beam elements with different section properties; and (d) interfaces between plate or shell elements with different section properties.

large has not yet reached a consensus on an approach or a set of approaches that provides a practical solution to this problem. New methodologies need to provide analysis tools to determine the mixed-mode fracture parameters along an arbitrarily shaped crack or delamination front located at a bimaterial interface in a 3D solid modeled with any combination of elements (Krueger et al., 2013).

The problem of nonconverged computed mixed-mode strain energy-release rate components, however, may be circumvented by using 3D models. Furthermore, 3D analyses are required when matrix cracks and multiple delaminations need to be modeled at different ply interfaces.

1.3.4 Correcting for elements with different widths along the delamination front

The equations in the previous paragraphs were derived assuming that the delamination front is straight and that element widths b remain constant along the front. Meshing of arbitrarily shaped delamination front contours will, however, cause element length $\triangle a$ and width b to vary along the front. Therefore, the representation of a delamination in a plate/shell or a 3D solid finite element model also requires a correction to account for differences in element widths b along the front. For components modeled with four-node plate/shell-type elements or eight-node solid-brick elements, the correction is straightforward, as shown in Figure 1.8. A variation

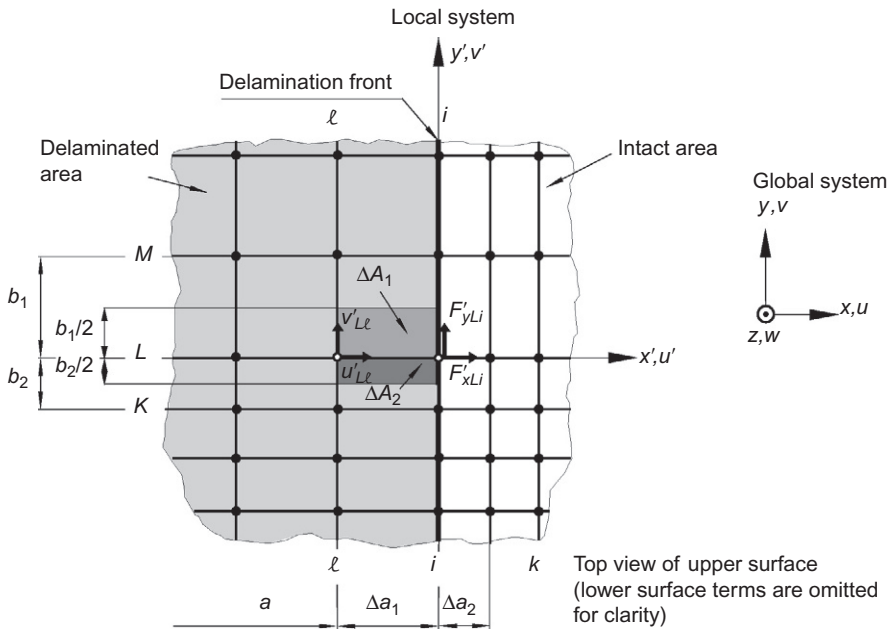

Figure 1.8 VCCT for solid elements with different widths along the front.

of only the element length, $\triangle a$, yields equations equivalent to the 2D case previously discussed. The additional variation of the element width, b, requires the separate calculation of the contributing element surfaces $\triangle A_1 = 1/2 \cdot \triangle a_2 \cdot b_1$ and $\triangle A_2 = 1/2 \cdot \triangle a_2 \cdot b_2$, as shown in Figure 1.8, yielding the corrected equations for the energy-release rate components:

$$G_{\mathrm{I}} = -\frac{1}{2}\frac{1}{\Delta A_1 + \Delta A_2} \cdot F'_{zLi}\left(w'_{L\ell} - w'_{L\ell^*}\right)\sqrt{\left(\frac{\Delta a_1}{\Delta a_2}\right)}, \tag{1.14}$$

$$G_{\mathrm{II}} = -\frac{1}{2}\frac{1}{\Delta A_1 + \Delta A_2} \cdot F'_{xLi}\left(u'_{L\ell} - u'_{L\ell^*}\right)\sqrt{\left(\frac{\Delta a_1}{\Delta a_2}\right)}, \tag{1.15}$$

$$G_{\mathrm{III}} = -\frac{1}{2}\frac{1}{\Delta A_1 + \Delta A_2} \cdot F'_{yLi}\left(v'_{L\ell} - v'_{L\ell^*}\right)\sqrt{\left(\frac{\Delta a_1}{\Delta a_2}\right)}. \tag{1.16}$$

1.4 Modeling and implementation considerations

1.4.1 Modeling

To apply VCCT to a finite element model, a crack or delamination has to be included in the model as a discrete discontinuity. To illustrate this approach, a 2D finite element plane stress, or plane strain model, is shown in Figure 1.9a, where the crack of length a is represented as a one-dimensional discontinuity (thick gray line). Nodes at the top surface and the bottom surface of the discontinuity have identical coordinates, however, and are not connected with each other (open circles) as shown in Figure 1.9a. This lets the elements connected to the top surface of the crack deform independently from those connected to the bottom surface and allows the crack to open. The crack tip and the undamaged section (filled circles) are modeled using single nodes as shown in Figure 1.9a, or two nodes with identical coordinates coupled through multipoint constraints if a crack propagation analysis is desired, as shown in Figure 1.9b. The same logic applies to a finite element model made of plate/shell-type elements or 3D solid elements, where the delamination of length a is represented as a 2D discontinuity by two surfaces.

Commercial codes generally require that the entire plane of delamination is initially split and the intact structure is simulated by using multipoint constraints or surface constraints (Ansys, 2014; Abaqus, 2014b; Marc, 2013; Nastran, 2013). This implementation allows for automated crack or delamination propagation, as shown in Figure 1.9c, where the constraints at crack tip node i are released once the computed mixed-mode energy-release rate exceeds a critical value. The crack is extended by Δa and the nodes at location k now represent the new crack tip.

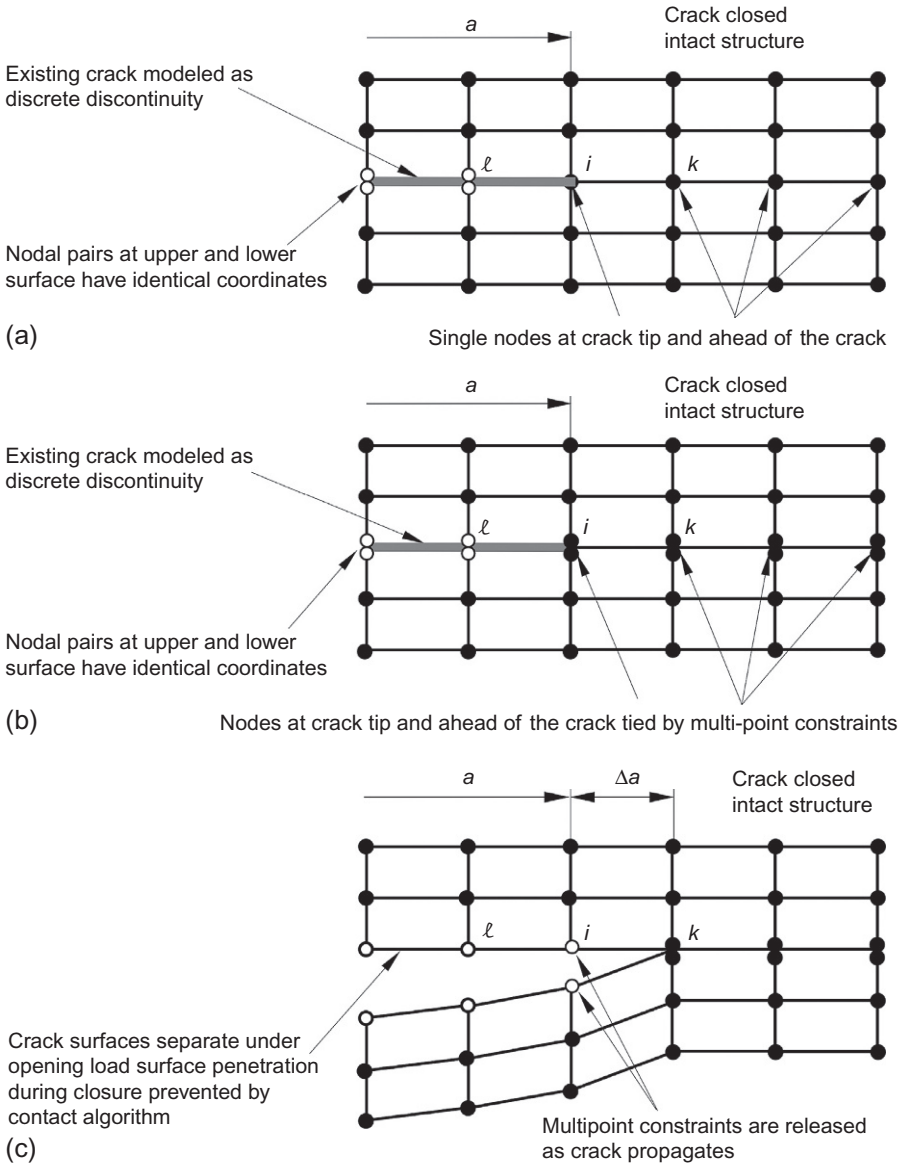

Figure 1.9 Modeling for VCCT analysis and automated crack propagation. (a) Intact region in front of the crack modeled with single nodes; (b) intact region in front of the crack modeled with double nodes tied by multipoint constraints; and (c) crack propagation by automated release of multipoint constraints.

1.4.2 Curved delamination front contours

For a straight front, as shown in Figures 1.5–1.8, the definition of the modes is intuitive and constant for the entire front. However, for an arbitrarily shaped front, the mode definition constantly changes along the contour, as shown in Figure 1.10.

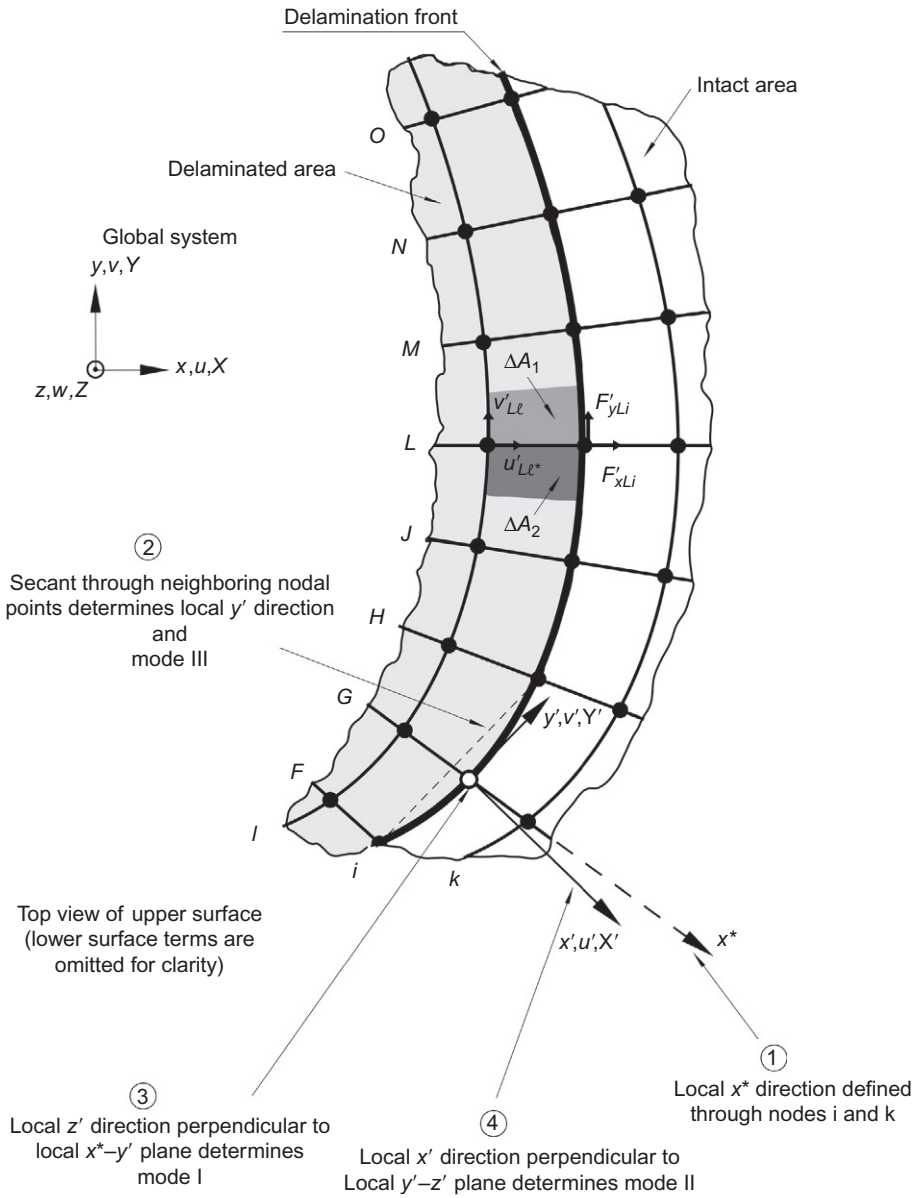

Figure 1.10 VCCT for arbitrarily shaped front.

A local crack tip coordinate system therefore needs to be defined at each nodal point along the front (Whitcomb, 1990). First, the vector through two nodes located in rows i and k in the deformed configuration defines the local x^* direction, as shown for one sample node (column G) in Figure 1.10. Second, the secant through adjacent nodes defines the y' direction and mode III. The local plane of delamination is defined by x^* and y'. Third, the local z' direction, which defines mode I, is perpendicular to the plane of delamination. Fourth, the local x' direction, which defines mode II, is perpendicular to the y' and z′ plane. Forces at node row i and displacements at node row ℓ need to be transformed to the local x'–y'–z′ system at the tip. The transformed forces and displacements are then used in the equations derived previously to calculate the mixed-mode energy-release rates.

Delaminations with sharp corners, as shown in Figure 1.11, pose a problem when computing mixed-mode energy-release rates because the separation into in-plane shear (mode II) and tearing (mode III) is not defined. Ideally sharp corners generally do not exist, so that modeling a rounded corner, as shown in Figure 1.11, may become an acceptable alternative. The mode separation is well defined at the rounded corner and the procedures described in the previous paragraphs may be applied to define the appropriate local crack tip coordinate system. This method was applied successfully to a coupon-type specimen with an embedded, square delamination (Krüger and König, 1995, 1996). The method, however, results in a locally refined model with an increase of nodes and elements and the model may become large. Recently suggested approaches for stair-stepped fronts, which may alleviate this problem and help to avoid an increase in model size, are discussed in Section 1.4.4.

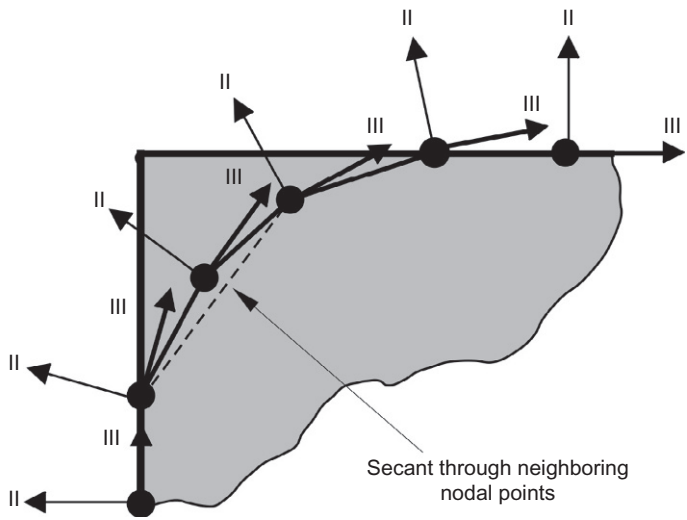

Figure 1.11 Definition of mode separation at sharp corners.

1.4.3 Normality of the mesh at the delamination front

For the aforementioned procedure, it is assumed that the mesh remains normal to the delamination front, as shown in Figure 1.12a. Modern preprocessing software allows the modeling of almost any complex configuration. These programs, however, were not developed to guarantee the normality of the mesh and the delamination front. The effect of a lack of normality at the crack front on the computed energy-release rates was studied in Smith and Raju (1998). It was shown that the standard formulations for VCCT were not able to extract accurate values from models that did not have normality at the crack front, as shown in Figure 1.12b. It was also found that an increased variation from the normal condition yielded a greater discrepancy. The formulation

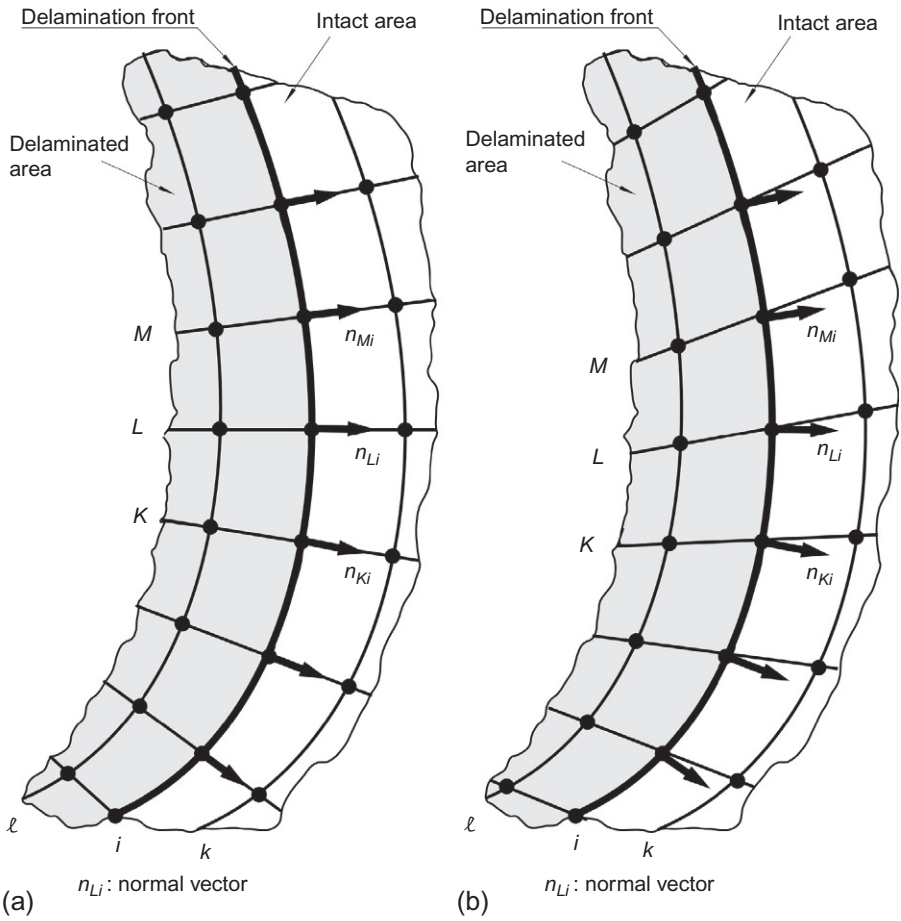

Figure 1.12 Mesh alignment along arbitrarily shaped front. (a) Orthogonal mesh along the delamination front and (b) nonorthogonal (skewed) mesh along the delamination front.

of an extraction method and modified equations for VCCT that yields accurate energy-release rates for models that lack normality is given in Smith and Raju (1998).

1.4.4 Approximation of growing delamination front

Crack advance or delamination propagation is expected when the computed mixed-mode energy-release rate exceeds a critical value (i.e., the experimentally determined fracture toughness), which will be discussed in the following section. In the context of a finite element analysis, this crack tip advance or delamination front propagation can be achieved by

1. Moving the crack tip or front forward at locations where the critical value has been exceeded, as shown in Figure 1.13 (Rinderknecht and Kröplin, 1995), which results in a smooth front. This move is typically performed incrementally along the front until the computed energy-release rate, G_T, is less than or equal to the fracture toughness of the material, G_c, along the entire front. The procedure is then repeated in the following load step.
2. Releasing the nodes at the crack tip or locally along the front and advancing the front one element at a time as shown in Figure 1.14, which may result in a stair-stepped approximation of the actual delamination front contour as shown in Figure 1.14.

Current implementations in commercial finite element codes do not offer the moving mesh option. Adaptive meshing to track the propagation and growth of arbitrarily shaped cracks through a 3D structure is generally handled by specialized codes that interface with commercial finite element codes, which are used to perform the FE analysis (FRANC3D, 2003; Schollmann et al., 2003; Iesulauro, 2009). Therefore, the second method is often used when advancing a front. Hence, algorithms had to be developed that approximate a smooth contour through the stair-stepped front internally and calculate the forces and displacements with respect to that smooth virtual front. Li developed a method to use VCCT in conjunction with a stair-stepped mesh along a delamination front (Li et al., 2008). Liu et al. (2011) proposed a modified

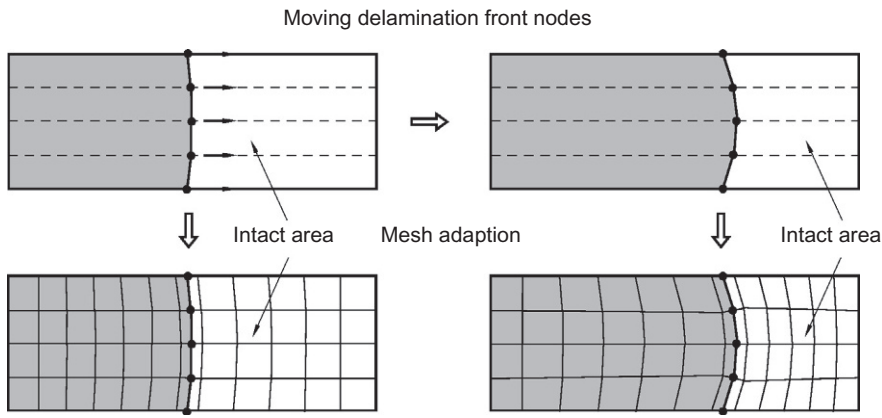

Figure 1.13 Moving mesh technique.

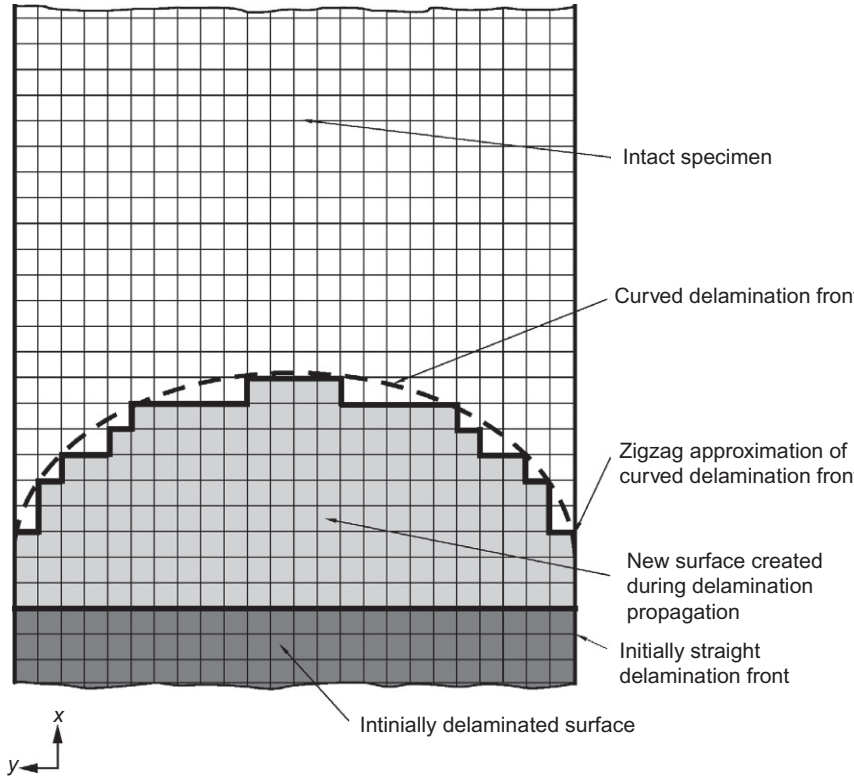

Figure 1.14 Zigzag approximation of curved delamination front.

zigzag approach to approximate a crack front with an arbitrary shape. Xie and Biggers (2006) developed an algorithm to trace a moving delamination front with an arbitrary and changing shape. Using this algorithm, a delamination front can be defined by two vectors that pass through any point on the front. The normal and tangent vector for the local coordinate system can then be obtained based on the two delamination front vectors. This approach allows delamination growth to be analyzed by using stationary meshes, and it does not require the use of meshes where one element edge is orthogonal to the delamination front (Xie and Biggers, 2006).

1.4.5 Fracture mechanics analyses for bimaterial interface crack problems

A crack or delamination located at a bimaterial interface poses an additional concern. Williams showed more than a half a century ago that an oscillatory singularity exists for cracks located at a bimaterial interface, in addition to the classical square root singularity at the crack tip (Williams, 1959). This oscillatory singularity leads to some unsatisfactory consequences. Several investigators over the past three decades showed

that when numerical methods, such as the finite element method, are used to evaluate the total and individual mode strain energy-release rates, the individual modes do not show convergence as the mesh size is refined near the crack tip. The intent of this section is to renew the awareness of the oscillatory singularity at the crack tip of a bimaterial interface and the problems that occur when calculating mode mixity using numerical methods such as VCCT.

1.4.5.1 Background

Raju et al. (1988) showed that for an interface crack between two dissimilar isotropic materials, the individual strain energy-release rates take the form

$$G_{\mathrm{I}} = \lim_{\Delta a \to 0} \mathrm{Re}\left[\boldsymbol{C} + \boldsymbol{D} \cdot (\Delta a)^{\mathrm{i}\gamma}\right], \tag{1.17}$$

$$G_{\mathrm{II}} = \lim_{\Delta a \to 0} \mathrm{Re}\left[\boldsymbol{C} - \boldsymbol{D} \cdot (\Delta a)^{\mathrm{i}\gamma}\right], \tag{1.18}$$

$$G_{\mathrm{T}} = G_{\mathrm{I}} + G_{\mathrm{II}} = \lim_{\Delta a \to 0} \mathrm{Re}[2\boldsymbol{C}], \tag{1.19}$$

where the parameters $\boldsymbol{C}$ and $\boldsymbol{D}$ are complex constants, and Δa is the virtual crack closure length as shown in Figure 1.15 and $\mathrm{i} = \sqrt{-1}$. The parameter

$$\gamma = \frac{1}{2\pi} \ln\left(\frac{1-\beta}{1+\beta}\right) \tag{1.20}$$

is a function of the Dundurs parameter β, which is defined in terms of the shear modulus μ_j and is the Poisson's ratio v_j of materials A and B.

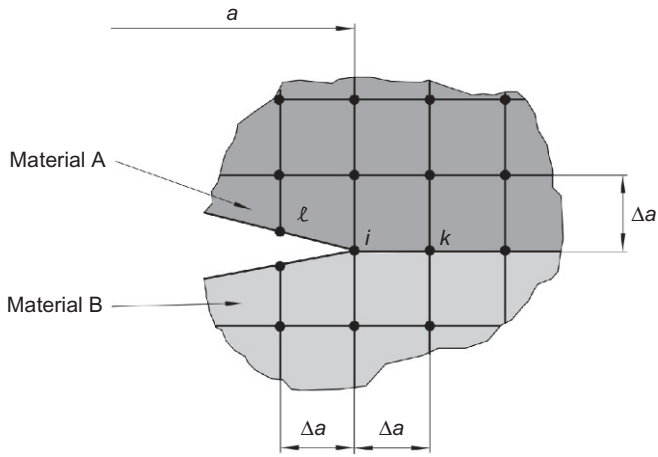

Figure 1.15 Detail of virtual crack closure at bimaterial interface.

$$\beta = \frac{\mu_A(\kappa_B - 1) - \mu_B(\kappa_A - 1)}{\mu_A(\kappa_B + 1) + \mu_B(\kappa_A + 1)}. \tag{1.21}$$

For orthotropic and anisotropic materials, the γ expression is much more complex than the isotropic case; however, the singularity is of similar form. Equations (1.17) and (1.18) demonstrate that the individual strain energy-release rates, G_{I} and G_{II}, depend on Δa and have *no well-defined limits*, whereas the total energy-release rate, G_{T}, in Equation (1.19) is independent of Δa and has *a very well-defined limit* (Raju et al., 1988).

Raju also evaluated the individual mode components and the total energy-release rate values for various bimaterial plates with isotropic, orthotropic, and anisotropic materials and studied the problem of a laminated composite with an edge delamination. A typical FE model used at the crack tip of a bimaterial interface crack is shown in Figure 1.15. The total energy-release rate and individual mode components of the strain energy-release rates for a $[0/35/-35/90]_{\mathrm{S}}$ laminate with two delaminations symmetrically located at the $-35/90$ interfaces were calculated and analyzed. For the interface studied, the individual modes showed Δa dependence whereas the total value of G remained well-defined and independent of Δa. Raju also showed that if the materials were chosen such that the Dundurs parameter, β, equals zero, then the individual, as well as the total G values, are independent of Δa and all have well-defined limits (Raju et al., 1988; He and Hutchinson, 1989).

The independence of the total value of G relative to Δa was also reported by other investigators (Rice, 1988; Dattaguru et al., 1994; Sun and Jih, 1987). Specifically, Sun and Jih (1987) and Dattaguru et al. (1994) observed the nonconvergence of the individual mode strain energy-release rates and showed analytically that if the oscillatory terms are neglected, the mode I and mode II values approach the value $G_{\mathrm{T}}/2$. Additionally, Agrawal and Karlsson (2006) carefully reviewed and extended methods that characterize fracture at a bimaterial interface, with a particular focus on evaluating the mode mixity using VCCT. In a recent overview paper, Krueger provided a summary of the issue and offered possible practical solutions to obtain "satisfactory" mode separation that is acceptable for application in engineering problems (Krueger et al., 2013).

1.4.5.2 *Methods to obtain mode separation acceptable for engineering applications*

Although many new methods and approaches are presented in the literature for the interface crack problem, only a few approaches appear to be of practical use and capable of application to general cases and real-world structural problems. As an approach to eliminate the oscillatory crack tip singularity at the bimaterial interface for a composite laminate, Raju performed analyses using a model where the delamination was located in a thin homogeneous isotropic layer, similar to a resin layer, that existed between the $-35/90$ plies of their edge-delaminated specimen (Raju et al., 1988). For this case, the oscillatory component of the singularity vanished because the delamination was now located in a homogeneous isotropic material. The VCCT was used to calculate the total energy-release rate G_{T} as well as the mode I and mode II

components. Results obtained from the model with a resin layer showed that the individual mode components as well as the total strain energy-release rates remained practically unchanged as the ratio, $\triangle a/h$, of crack tip element length, $\triangle a$, to ply thickness, h, decreased. This observation, however, cannot be generalized. Smith observed that the individual mode components did not converge when a delamination was placed at the center of a thin resin layer of a sandwich facesheet/core interface (Smith, 2001). This configuration has large stiffness differences between the layers on either side of the interface, and other methods to obtain mode separation are required (Krueger et al., 2013).

Raju also reported that the individual mode components obtained from the interface model with the resin layer agreed with those obtained from the models without a resin layer when values of $\triangle a/h$ were either 0.25 or 0.5 (Raju et al., 1988). The maximum difference between the two approaches was reported to be less than 4% for the mode I and 2% for the mode II components. The results suggest that the size of the delamination tip elements, $\triangle a$, should be one-quarter to one-half of the ply thickness, h.

Sun and Jih (1987) also found that the mode components depend on the choice of the crack tip element length $\triangle a$. However, in their analysis the mode mixity worked well with the analytical solutions if the assumed crack extension was larger than the region where stress oscillation was observed. For a calculated bimaterial constant γ (also often referred to as ε) for an AS4/3501-6 composite (where $\gamma = 0.004$, 0.018, and 0.038 for 0/15, 0/45, and 0/90 interfaces, respectively) it was found that the stress-oscillating zone is negligibly small (Sun and Yang, 2001). In particular, for a 90/30 interface, it was shown that the stress will not start oscillating until the distance from the crack tip is on the order of 10^{-12} of the specimen thickness (Sun and Yang, 2001). Outside this zone, the mode I and mode II components were found to be almost constant. Based on these results, it was suggested that for a range of $\triangle a/a$ ratios, these calculated values of G_{I} and G_{II} may be used for practical purposes.

Later, these and similar results were summarized in a comprehensive review of the state-of-the-art of VCCT (Krueger, 2004; Krueger et al., 2013). After a careful study of the published results, Krueger concluded that for certain values of $\Delta a/h$ the variation in the individual mode strain energy-release rates is small, as shown in Figure 1.16a, and a recommended range of $\Delta a/h$ was proposed. A value of $\Delta a/h > 1$ may require smearing ply properties for plies of different orientations, for example, if square elements are used, as shown in Figure 1.16b, which is not acceptable if individual plies need to be modeled. At the other extreme, a value of $\Delta a/h < 1/20$ violates the assumption of a homogeneous continuum as this value is of the same order of magnitude as an individual fiber. As such, the recommended element size range is $1/20 \leq \Delta a/h \leq 1$. Variations in mode mixity between these bounds are typically very small and should prove acceptable for practical applications (Krueger, 2004). Note that the approaches presented are heuristic, based on literature studies and the author's own analyses (Krüger, 1994; Krueger, 2004; Krueger et al., 2007) and may therefore be considered arbitrary. However, a study (Krueger et al., 2013) showed that the approaches found in the literature that have mathematical rigor are very complex and have been applied only to a few simple cases. To date, they have not yet been applied to real-world structural problems.

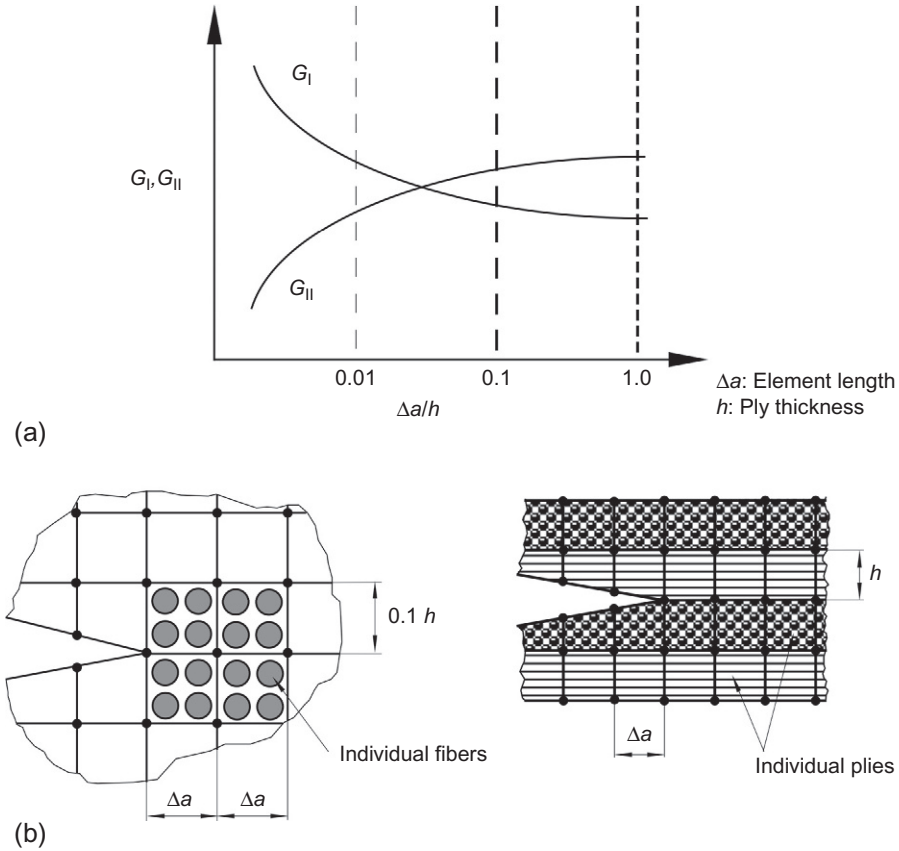

Figure 1.16 Influence of element size on computed mode components. (a) Dependence of computed energy release rate components on element size near the crack tip and (b) upper and lower bounds for element size at crack tip.

1.5 Mixed-mode fracture criteria for quasi-static delamination propagation and fatigue growth

When performing a VCCT analysis in composites, it is assumed that the crack or delamination path remains in the original interface and does not migrate through an adjacent layer into another interface. Further, it is assumed that the effects of fiber bridging can be neglected. Fiber bridging occurs during delamination propagation when fibers get pulled out from the plies on either side of the interface and start bridging the gap, thus increasing the perceived fracture toughness. The fracture toughness then becomes a function of the crack or delamination length (the so-called R-curve effect).

To predict delamination onset, the G components calculated using VCCT are compared to measured interlaminar fracture toughness properties often given as a function of mixed-mode ratio G_{II}/G_T (O'Brien, 1982; Martin, 1998; Raju and O'Brien, 2008).

A failure index, G_T/G_c, is calculated from the computed total energy-release rate, G_T, and the mixed-mode fracture toughness, G_c, of the composite material. It is assumed that the delamination onset occurs when the failure index, G_T/G_c, reaches unity. During an automated delamination propagation analysis, the total strain energy-release rate, G_T, and the mixed-mode ratio G_{II}/G_T are computed internally using VCCT and the crack or delamination is advanced by moving the mesh or releasing nodal constraints as discussed earlier. Test methods to obtain the interlaminar fracture toughness, G_c, are discussed later in Section 1.5.2.

1.5.1 Mixed-mode fracture criteria

Several expressions have been proposed as 2D mixed-mode fracture criteria to account for the observed variation of the fracture toughness with the mixed-mode ratio. The following simple power law expression has been suggested:

$$\left(\frac{G_I}{G_{Ic}}\right)^{\alpha} + \left(\frac{G_{II}}{G_{IIc}}\right)^{\beta} = 1, \tag{1.22}$$

where the exponents α and β are determined by a curve fit to the fracture toughness data (Reeder, 1993). For $\alpha = \beta = 1$, this criterion becomes the linear interaction criterion, where the G_I component of the experimental data is simply plotted versus its G_{II} component. The criterion is illustrated in Figure 1.17 for data obtained for a carbon/epoxy material. Other criteria have been discussed in detail in several overview papers (Reeder, 1993; Marat-Mendes and Freitas, 2010).

Today, the most often used 2D fracture criterion is the so-called B-K criterion proposed by Benzeggagh and Kenane (1996), where a simple mathematical relationship between G_c and G_{II}/G_T is used

$$G_c = G_{Ic} + (G_{IIc} - G_{Ic})\left(\frac{G_{II}}{G_T}\right)^{\eta}. \tag{1.23}$$

The exponent η is determined by a curve fit to the fracture toughness, G_c, data plotted as a function of the mixed-mode ratio, G_{II}/G_T, as illustrated in Figure 1.18 for a typical carbon/epoxy material. The parameters G_{Ic}, G_{IIc}, and η are required input to perform a VCCT analysis in current commercial implementations of the technique (Marc, 2013; Nastran, 2013; Abaqus, 2014b; Ansys, 2014). Bui (2011) developed a modified criterion with two parameters, which can serve as an alternative to the case where the original B-K criterion does not provide a good curve fit to the measured data.

Because the B-K criterion does not incorporate G_{IIIc}, the computed shear components are often combined and the resulting $G_S = G_{II} + G_{III}$ is used to calculate the mixed-mode ratio (G_S/G_T) in Equation (1.23) instead of (G_{II}/G_T).

Because the B-K criterion fit the 2D fracture toughness data well, it became an obvious choice as the basis for a 3D criterion (Reeder, 2006; Bui, 2011). Reeder developed a simple extrapolation into the 3D plane:

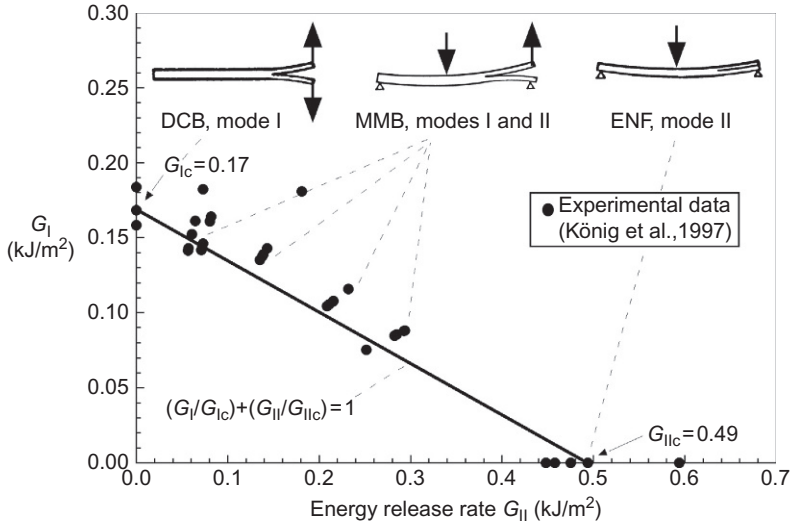

Figure 1.17 Linear mixed-mode fracture criterion for T300/914C.

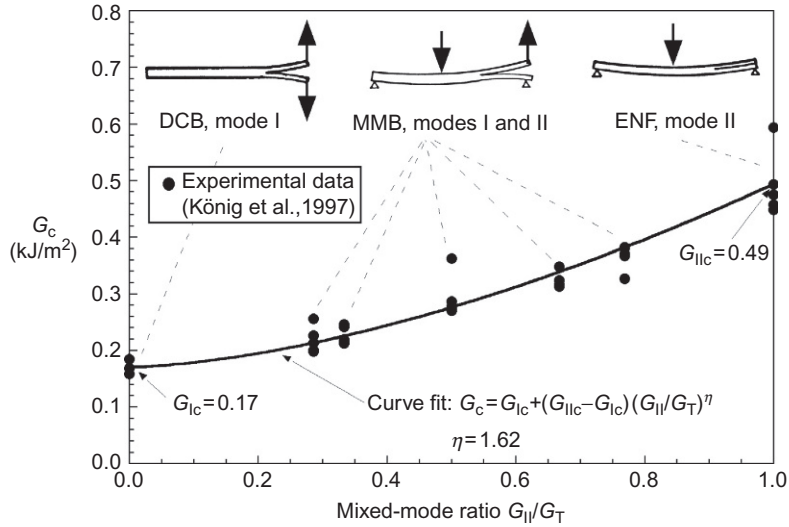

Figure 1.18 B-K mixed-mode fracture criterion for T300/914C.

$$G_c = G_{Ic} + \left[(G_{IIc} - G_{Ic})\frac{G_{II}}{G_T} + (G_{IIIc} - G_{Ic})\frac{G_{III}}{G_T}\right]\left(\frac{G_{II}+G_{III}}{G_T}\right)^{\eta-1} \tag{1.24}$$

based on the observations that measured mode III fracture toughness data are generally higher than the mode II fracture toughness values (Reeder, 2006). In this criterion,

the relationship between mode II and mode III at a given percentage of total shear is linear as shown in Figure 1.19 where a sketch of the criterion is represented on an equilateral triangular base (Reeder, 2006). Reeder (2006) postulated that these assumptions are justified until new tests have been developed to measure mixed-mode fracture toughness with known percentages of mode III. Issues with respect to measuring the mode III fracture toughness and its validity are addressed in Section 1.5.2. This criterion has already been used as part of the VCCT implementation in Abaqus/Standard® (2014b).

1.5.2 Mixed-mode fracture toughness testing

The fracture toughness is determined experimentally using a set of standardized test methods (shown in Figure 1.20) such as the double cantilever beam (DCB) test for pure mode I ($G_{II}/G_T = 0$), the end-notched flexure or calibrated end-loaded split tests for pure mode II ($G_{II}/G_T = 1$), and the mixed-mode bending (MMB) test for varying ratios of G_I and G_{II} (ASTM, 2013a,b, 2014; ISO, 2001, 2014; Brunner et al., 2008). An alternative approach using a single leg bending (SLB) test with a fixed mixed-mode ratio ($G_{II}/G_T = 0.4$) instead of a set of MMB tests was suggested by Davidson (Davidson and Sundararaman, 1996; Davidson and Zhao, 2007).

Several specimens have been suggested for the measurement of the mode III interlaminar fracture toughness property (Lee, 1990, 1993; Martin, 1991; Robinson and

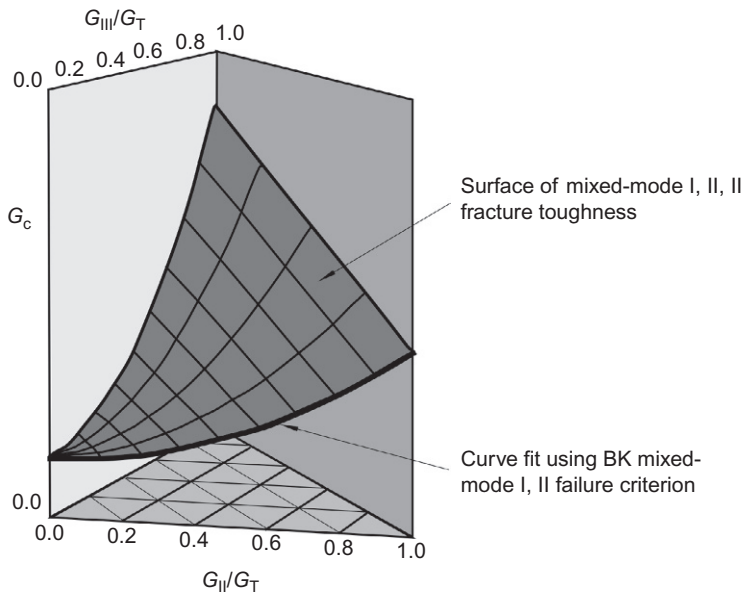

Figure 1.19 3D representation of fracture toughness on equilateral triangular base. Adapted from Reeder (2006).

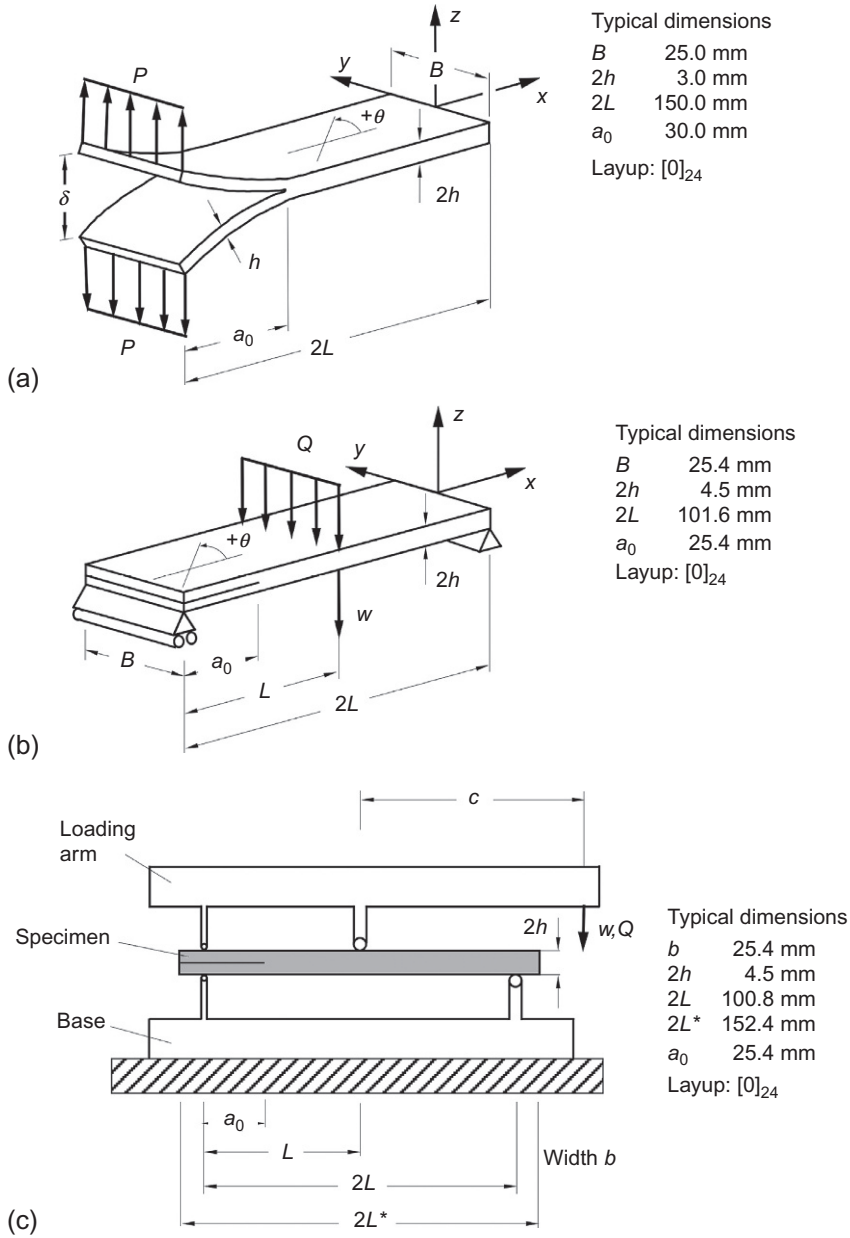

Figure 1.20 Standard test methods for fracture toughness testing. (a) Double cantilever beam (DCB) specimen; (b) end-notched flexure (ENF) specimen; and (c) mixed-mode bending (MMB) specimen.

Song, 1994; Li et al., 1997; Ratcliffe, 2004; Browning et al., 2011; Marat-Mendes and Freitas, 2009, de Morais et al., 2011, Johnston et al., 2014) as well as the mode I/II/III interaction (Davidson and Sediles, 2011). Most recently, Czabaj et al. (2014) discovered that in ECT specimens made of tape-laminates, delamination growth occurs one-ply interface beneath the midplane. They also observed the existence of intralaminar cracking prior to delamination growth. Therefore, the apparent value of mode III toughness that is extracted from the ECT test does not reflect the mechanics or physics of the processes that occur, and there is no reason to expect that the obtained values are valid (Czabaj et al., 2014). Czabaj et al. (2014) therefore concluded that the ECT test, in its current form, is unsuitable for characterizing the onset of mode III delamination growth. These findings might have a significant impact on the shape of the 3D failure surface shown in Figure 1.19 and the subject of formulating a suitable 3D criterion will have to be readdressed.

1.5.3 Delamination onset under cyclic loading

The number of cycles to delamination onset, N_D, can be obtained from a delamination onset curve, as shown in Figure 1.21a (ASTM, 2011; Hansen and Martin, 1999). This onset curve (solid line) is a power law fit

$$G = m_0 \cdot N_D^{m_1} \tag{1.25}$$

of the experimental data (open circles) obtained from a DCB test using the respective ASTM standard for delamination growth onset (ASTM, 2011; Argüelles et al., 2008).

Note that standards for mode II and mixed-mode I/II delamination onset currently do not exist; however, the test methods for static fracture toughness testing have been used to generate onset curves (Hansen and Martin, 1999; O'Brien et al., 2010; Murri, 2014, Ratcliffe and Johnston, 2014). As additional information, an example of a mixed-mode I/II failure surface is provided in Figure 1.21b to guide the analyst who is seeking input data for performing a mixed-mode fatigue onset analysis using commercial codes.

To perform a delamination onset analysis using VCCT, only one quasi-static analysis to determine, G_{max}, and the mixed-mode ratio, G_{II}/G_T, is required. The number of cycles to delamination onset, N_D, can then be determined directly from the experimental data plotted in Figure 1.21. A time-dependent analysis is not required.

1.5.4 Delamination growth under cyclic loading using Paris law

The number of cycles during stable delamination growth, N_G, can be obtained from a fatigue delamination propagation relationship like that shown in Figure 1.22 (König et al., 1997). The delamination growth rate (solid line) can be expressed as a power law function (Paris law)

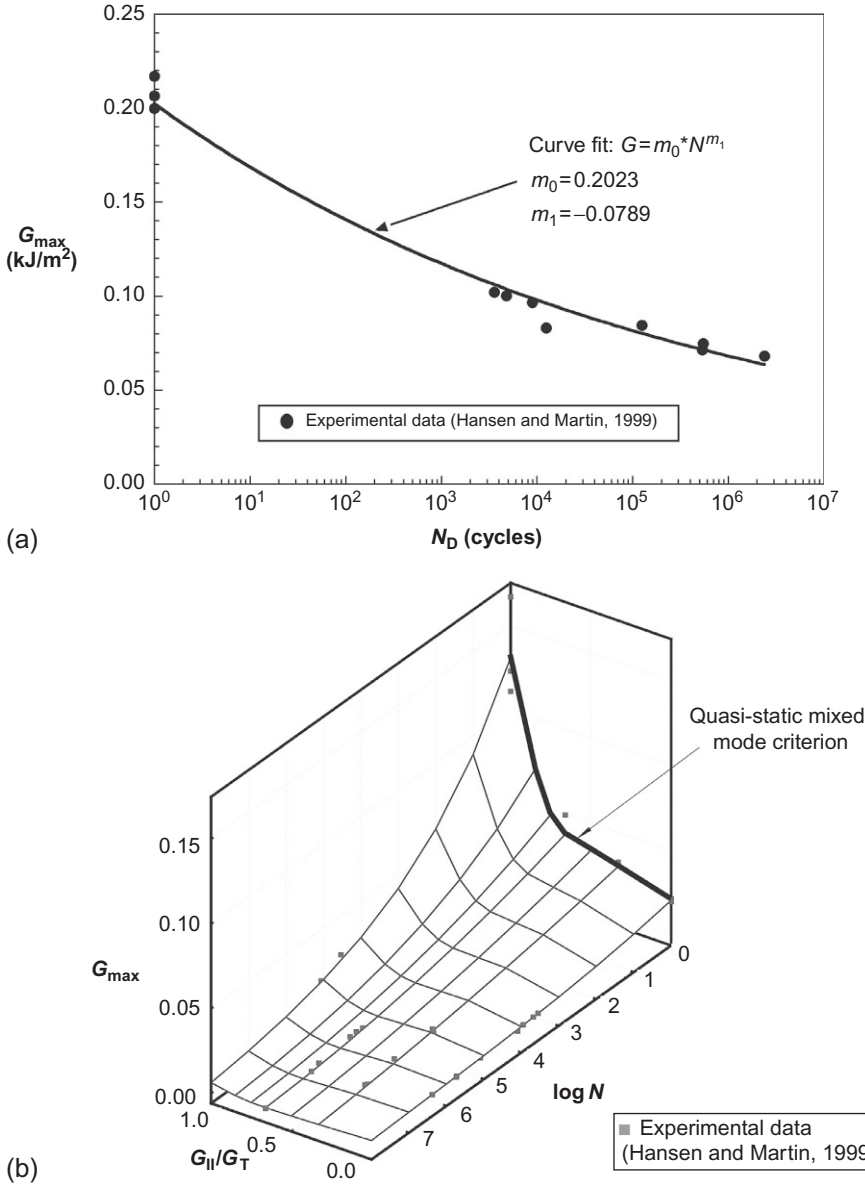

Figure 1.21 Delamination onset under cyclic loading. (a) Mode I delamination growth and (b) mixed-mode I and II delamination growth onset surface.

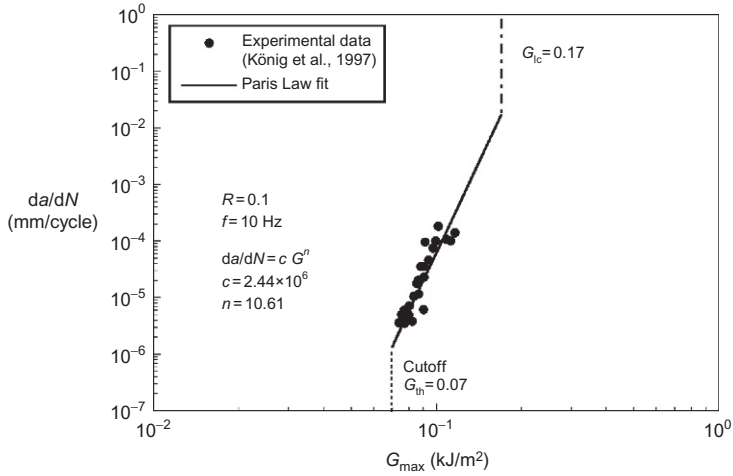

Figure 1.22 Delamination growth rate (Paris Law) for mode I.

$$\frac{da}{dN} = c \cdot G_{\max}^{n}, \tag{1.26}$$

where da/dN is the increase in delamination length, da, per cycles, dN, and $G_{\max}$ is the maximum energy-release rate at the front at peak loading. For the example shown in Figure 1.22, the factor c and exponent n were obtained by fitting the curve to the experimental data (open black circles) obtained from DCB tests (König et al., 1997).

Because composites do not exhibit the same threshold behavior commonly observed in metals, considerable research effort has been spent recently to develop a fatigue delamination threshold criterion (Kenane et al., 2011; Zhang et al., 2012). If not provided, the analyst may need to choose a cutoff value, G_{th}, for analysis input below which delamination growth is assumed to stop (dotted vertical line in Figure 1.22). The critical energy-release rate or fracture toughness, G_{Ic}, was also included in the plot of Figure 1.22 (dashed vertical line).

Note that, currently, except for the draft standard for mode I (ASTM, 2009; Stelzer et al., 2012, 2014), no explicit guidelines for mode II and mixed-mode I/II fatigue delamination growth testing exist. However, the test methods for static fracture toughness testing have been adapted to generate fatigue growth curves (Shivakumar et al., 2006; Brunner et al., 2009; O'Brien et al., 2010; Baere et al., 2012; Murri, 2014; Ratcliffe and Johnston, 2014; Carvalho and Murri, 2014). Attempts have also been made to generate a mixed-mode failure criteria for fatigue (Kenane and Benzeggagh, 1997; Blanco et al., 2004; Peng et al., 2012); however, a universal failure surface (similar to the delamination onset surface in Figure 1.21b) extending from the static case ($N = 1$) to high-cycle fatigue is still missing.

To perform a delamination fatigue growth analysis using VCCT, only a series of quasi-static analyses to determine, $G_{\max}$ (and the mixed-mode ratio, $G_{\text{II}}/G_{\text{T}}$) are

required. The increase in delamination length, da, is determined by the element length at the crack tip $\triangle a$. The number of cycles, dN, can be determined directly from the Paris law plotted in Figure 1.22. The implemented procedure to move the mesh or release nodal constraints to advance the front remain the same as for the static case. As the delamination advances, the number of cycles, dN, for each incremental growth are summarized to obtain the total number of cycles of stable delamination growth, N_G. A time-dependent analysis is not required to perform this type of analysis (Deobald et al., 2007; Mabson et al., 2007; Carvalho et al., 2014). Implementation of algorithms in commercial codes to perform delamination growth analysis under cyclic loading is ongoing and has not yet reached the maturity of automated quasi-static delamination propagation.

1.5.5 Remaining issues related to delamination growth under cyclic loading

Note that the community at large has not yet reached a consensus on an approach for characterizing fatigue-driven delamination growth under mixed-mode conditions and research is ongoing. Pascoe provided a critical overview of methods used for the prediction of fatigue delamination growth in composites (Pascoe et al., 2013, 2014). He found that most models are phenomenological, based on the observed macroscale behavior of test specimens and suggested that a more physics-based approach, focusing on clarifying the mechanisms involved, is required to come to a full understanding of the problem of delamination growth.

Allegri proposed a new semi-empirical law for mode II delamination growth, which only requires two material parameters to represent the fatigue behavior for the entire positive stress ratio range (Allegri et al., 2011; Allegri and Wisnom, 2012). He extended the approach to account for effects of the stress ratio and mode mix on the interlaminar crack propagation simultaneously (Allegri et al., 2013).

The strain energy-release rate range, $\triangle G$, in cyclic loading, defined as the arithmetic difference between maximum and minimum values $\triangle G = G_{max} - G_{min}$ is often used to characterize fatigue delamination growth behavior in a manner analogous to the stress intensity factor $\triangle K$. Rans argued that the basis for similitude for these two parameters, $\triangle G$ and $\triangle K$, is different and can lead to misinterpretations of delamination growth behavior (Rans et al., 2011). He offered a redefinition of $\triangle G$ to avoid potential misinterpretations of fatigue delamination growth. Using $\Delta G = \left(\sqrt{G_{max}} - \sqrt{G_{min}}\right)^2$ he could demonstrate an improved understanding of previously published case studies (Rans et al., 2011). Using a variant of the Hartman–Schijve (Hartman and Schijve, 1970) equation to represent both modes I and II constant amplitude delamination growth in composites, Jones et al. were able to relate the delamination growth rate, da/dN, to $\left(\Delta\sqrt{G} - \Delta\sqrt{G_{th}}\right)^{\alpha}$ here α is approximately 2 and G_{th} is the fatigue threshold value (Jones et al., 2012).

With respect to performing a delamination fatigue growth analysis using VCCT, the formulation of the Paris law as a function of G_{max} only requires one analysis

per growth increment, da, as discussed above. Formulations as a function of ΔG or $\left(\Delta\sqrt{G}-\Delta\sqrt{G_{\text{th}}}\right)^{\alpha}$, however, would require two static analyses.

1.6 Analysis benchmarking

As VCCT and related methods for analyzing composite delamination are incorporated into finite element codes, the need for comparison and benchmarking becomes important, inasmuch as each code requires specific input parameters unique to its implementation. These parameters are unique to the numerical approach chosen and do not reflect real *physical* differences in delamination behavior. An approach for assessing the mode I, II and mixed-mode I/II delamination propagation capabilities in commercial finite element codes under static loading was recently presented and demonstrated for the VCCT implementation in Abaqus/Standard® (Krueger, 2008, 2011, 2012b) as well as MD Nastran™ and Marc™ (Orifici and Krueger, 2012) and Ansys® (Krueger, 2012a). In the following section, the benchmark approach is outlined using the mode I DCB specimen. The same approach can be used for any mixed-mode case (Krueger, 2008, 2011, 2012b). Special attention is given first to the creation of the benchmark case, which is independent of the analysis software. Analysts who are new to delamination onset and growth prediction based on finite element analysis may use the benchmark case as a starting point to gain first-hand experience. In the context of analysis *Verification and Validation* (V&V), these benchmarks may also be used for code and calculation verification (Thacker, 2003) purposes. In a first step, the VCCT implementation would have to be verified, followed by a second step to verify the automated crack or delamination propagation analysis. The benchmarking procedure could be used in this second step and thus serve as a valuable tool for software developers.

1.6.1 Benchmark case for mode I based on the DCB specimen

The procedure is outlined here using the DCB specimen (Figure 1.20a) with a unidirectional layup as an example. This specimen configuration is a well-known case for mode I delamination and was therefore chosen as a benchmark case.

- First, finite element models of the specimen with different delamination lengths, a_0, were created. For the current example, 2D finite element models simulating the DCB specimen (Figure 1.23) with 18 different delamination lengths a_0 were created ($30.5\text{ mm} \le a_0 \le 69.5\text{ mm}$).
- For each delamination length (a_0) modeled, the load (P) and opening displacement (δ) at the load point were plotted as shown in Figure 1.24, where each solid gray line represents a different value of a_0.
- For each delamination length (a_0) modeled, the total strain energy-release rate, G_{T}, and the mixed-mode ratio $G_{\text{II}}/G_{\text{T}}$ were computed using VCCT for applied displacements $\delta = 3.0\text{ mm}$ (for $a_0 < 35.0\text{ mm}$), $\delta = 6\text{ mm}$ (for $40.0\text{ mm} \le a_0 < 50.0\text{ mm}$), and $\delta = 10\text{ mm}$

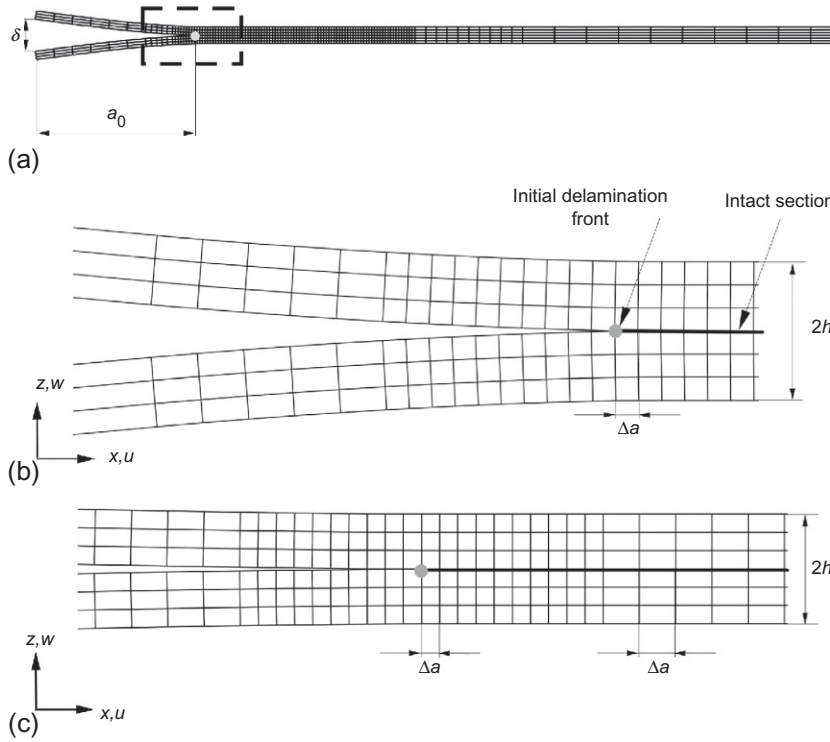

Figure 1.23 Typical 2D FE models of a DCB specimen Krueger (2014). (a) View of full model; (b) detail of crack tip zone for $\triangle a = 0.5$ mm; and (c) detail of crack tip zone for non-uniform $\triangle a$.

(for 55.0 mm $\leq a_0 \leq$ 69.5 mm). The total energy-release rate, G_T, is a function of the delamination length, a_0, and the applied opening displacement, δ, as shown in Figure 1.24, thus $G_T = G_T\ (a_0,\ \delta)$. For the simple case of the mode I DCB specimen shown, the computed values were predominantly mode I as expected.

- For each delamination length (a_0) modeled, a failure index, G_T/G_c, is calculated by comparing the computed total energy-release rate, G_T, with the mixed-mode fracture toughness, G_c, of the material, often computed as a function of the mixed-mode ratio. For the simple case of the DCB specimen shown, the failure index is simply calculated as G_I/G_{Ic}. When obtaining the benchmark, G_c should be determined using the same expression for G_c used in the automated analysis. In the present study, the B-K criterion (Benzeggagh and Kenane, 1996) is used. Details of its definition were provided in Section 1.5.1. It is assumed that the delamination propagates when the failure index reaches unity.
- The critical load, P_{crit}, and critical opening displacement, δ_{crit}, can be calculated—for each delamination length, a_0, modeled—based on the linear fracture mechanics relationship:

$$G = \frac{P^2}{2} \cdot \frac{\partial C_P}{\partial A} \tag{1.27}$$

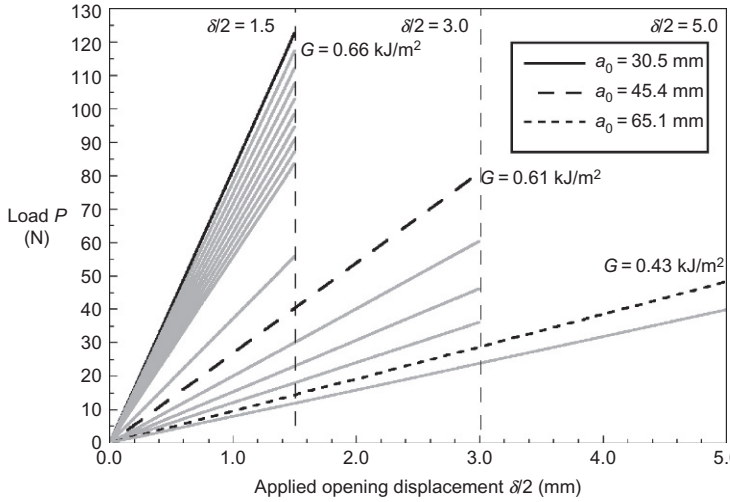

Figure 1.24 Computed load/displacement behavior of a DCB specimen for different delamination lengths a_0.

between load, P, and the energy-release rate, G, where C_P is the compliance of the specimen, and ∂A is the increase in surface area corresponding to an incremental increase in load or displacement at fracture (Broek, 1991). Using Equation (1.27), the critical load, P_{crit}, and critical opening displacement, δ_{crit} can be calculated from

$$\frac{G_{\text{T}}}{G_{\text{c}}}=\frac{P^2}{P_{\text{crit}}^2}\Rightarrow P_{\text{crit}}=P\sqrt{\frac{G_{\text{c}}}{G_{\text{T}}}}\quad\text{and}\quad\frac{\delta_{\text{crit}}}{2}=\frac{\delta}{2}\sqrt{\frac{G_{\text{c}}}{G_{\text{T}}}} \tag{1.28}$$

for each delamination length, a_0, the results are included in the load/displacement plots as shown in Figure 1.25 (solid circles).

- By fitting a curve through these critical load/displacement results (solid circles), a benchmark solution (thick solid line) can be created, as shown in Figure 1.25.

During the automated propagation analysis, the computed load/displacements results should follow the benchmark solution.

To demonstrate the independence of the benchmark procedure from the analysis code used, two benchmark results were created for Ansys® and Abaqus/Standard® using the same model, shown in Figure 1.23. As shown in the plots of Figure 1.26, the computed benchmark results for Ansys® (open circles and thin solid line) compared well with the benchmark results for Abaqus/Standard® (solid black diamond and solid black line) (Krueger, 2014). The benchmark results also agreed with the analytical results (thick sold gray line), as well as the experimental data (solid squares) both published as a NAFEMS benchmark (Davies, 2002). The experiments exhibited only a negligible amount of fiber bridging so that comparison with the analysis appeared justified (Davies, 2002).

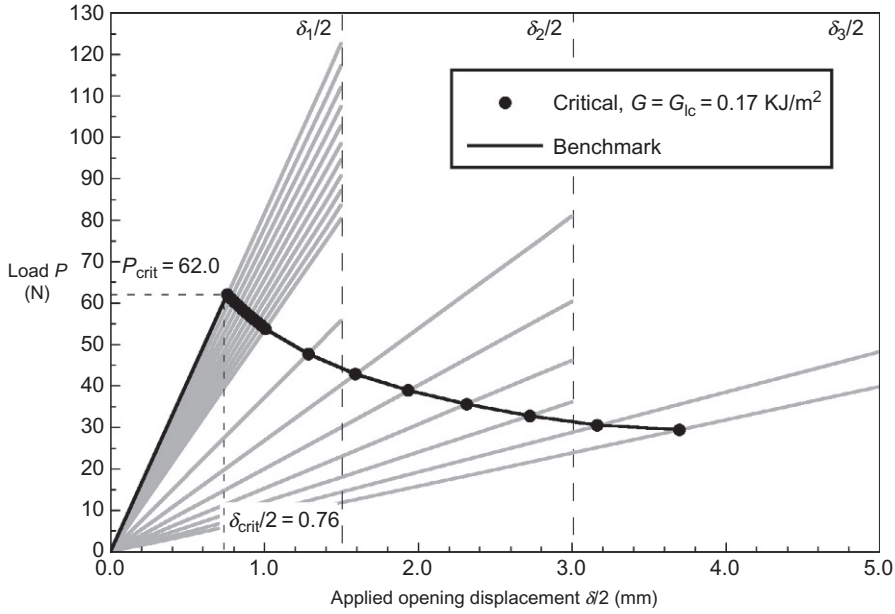

Figure 1.25 Calculated critical behavior and resulting benchmark case for a DCB specimen.

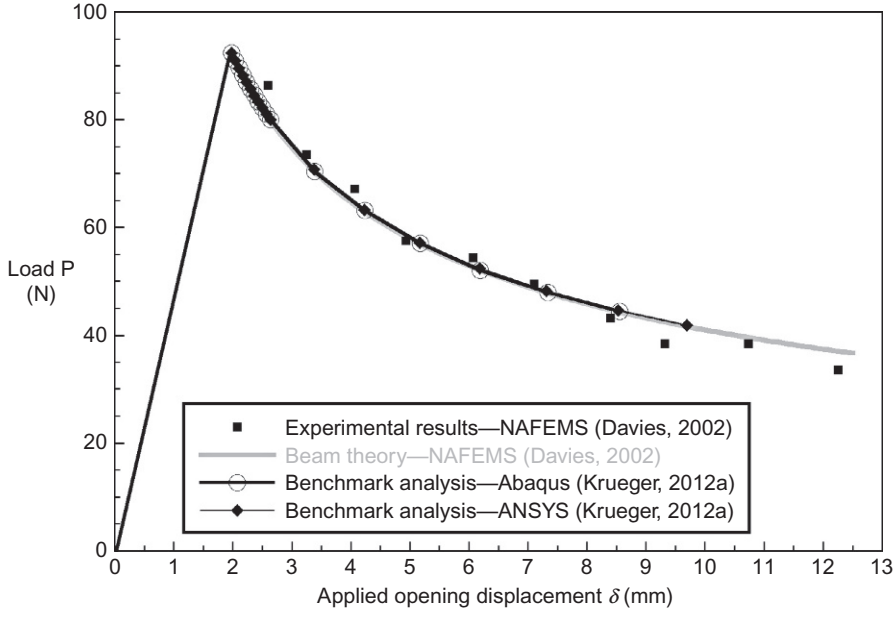

Figure 1.26 Benchmark case for a NAFEMS DCB specimen.

1.6.2 Automated delamination propagation computed for a model of a DCB specimen

A set of example results for automated delamination propagation using a commercial software is shown in Figure 1.27, where the computed load/displacement response of the DCB specimen is plotted for different input parameters (Krueger, 2014). The automated propagation analysis was performed in one step. Starting from an initial delamination length, $a_0 = 30.5$ mm, the delamination was allowed to propagate based on the algorithms implemented into the commercial software (Krueger, 2014). A total crack opening displacement $\delta/2 = 2.0$ mm was applied to each cantilever arm.

For the first propagation analysis with default settings (long dashed line), the stiffness of the specimen remained unchanged once the critical point was reached, and load and displacement kept increasing. Later, the stiffness decreased as the delamination propagated, the load started to drop, and the computed load/displacement path converged to the benchmark result (solid gray circles and solid gray line). To minimize the undesirable overshoot and to closely capture the critical point, additional input parameters for the numerical analysis such as time steps size, release tolerance, and stabilization factor need to be specified depending on the particular FE code used to control the crack propagation analysis. By adjusting default parameters, improved results were obtained (long dashed line). In general, good agreement between the load/displacement relationship obtained from the propagation analysis results and the benchmark results could be achieved by selecting the appropriate input parameter

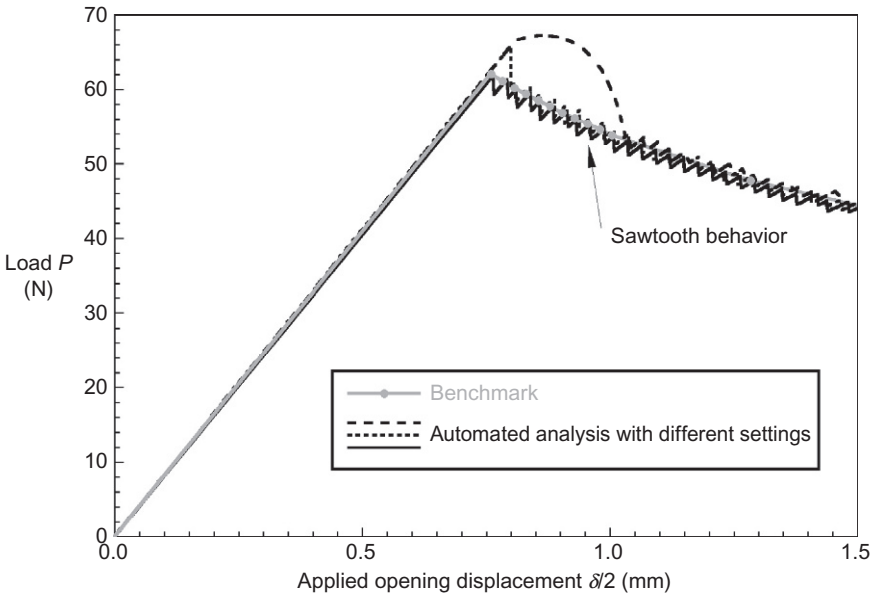

Figure 1.27 Load/displacement behavior for a benchmark case and automated propagation analysis for a DCB specimen.

combination (solid line). Often, a sawtooth pattern was obtained, where the peak values were in good agreement with the benchmark result. The significance of the sawtooth pattern is discussed later. The examples shown highlight the importance of benchmarking to identify critical analysis input parameters (Krueger, 2014).

1.6.3 Origin of observed sawtooth behavior

The sawtooth behavior—evident in the results plotted in Figure 1.27—is an artifact of the VCCT implementation. To illustrate the behavior, the crack tip propagation from an initial crack length, a, to $a+\Delta a$, and finally $a+2\Delta a$ as shown in Figure 1.28a, is discussed step by step. Initially, the computed load, P, increases with applied opening displacement, $\delta/2$, and the analysis (solid black line) follows along the load/displacement curve for crack length a (long dashed line) until the critical energy-release rate is reached (path $1 \rightarrow 2$), as shown in Figure 1.28b. During automated propagation, the crack tip node is released when the critical energy-release rate/fracture toughness, G_c, is reached (point 2). The associated opening of the entire crack tip element length, Δa, causes a load drop while $\delta/2$ remains constant until the load/displacement curve for crack length $a+\Delta a$ (dash dotted line) is reached (path $2 \rightarrow 3$). With increasing applied opening displacement, $\delta/2$, the load, P, increases along the load/displacement curve for crack length $a+\Delta a$ (solid line) until the benchmark curve (solid circles and solid gray line) is reached (path $3 \rightarrow 4$). This cycle is followed by the next node release (path $4 \rightarrow 5$) and the next load increase along the load/displacement curve for crack length $a+2\Delta a$ (short dashed line) until the benchmark curve is reached again (path $5 \rightarrow 6$) and so on. It becomes obvious that longer crack tip elements cause a larger sawtooth behavior. The implementation of a gradual node release and ramp down of the forces at the crack tip is required to avoid this problem.

1.6.4 Influence of crack tip element length and mesh size on computed results

The benchmark case also helps to study what influence a mesh with nonuniform crack tip element length, Δa, along the propagation path may have on the computed results. The finite element model shown in Figure 1.23a and c yielded load/displacement results presented in Figure 1.29. For the fine and coarse mesh, different sawtooth patterns are observed as discussed in the previous section (see Figure 1.29). The peak sawtooth values are always in good agreement with the benchmark results. At the transition between the meshes, however, a sharp increase in computed load occurs, yielding unreliable results. This is an indication that at the time of this writing, the current VCCT implementations in commercial codes do not account for the case where the element in front of the crack tip has a different element length, Δa, compared to the element behind the crack tip (see discussion in Section 1.3.2) (Krueger, 2008, 2011, 2012a,b; Orifici and Krueger, 2012). It is therefore suggested that meshes with uniform crack tip element length, Δa, along the entire length of the anticipated propagation path be used with VCCT analyses in commercial FE codes.

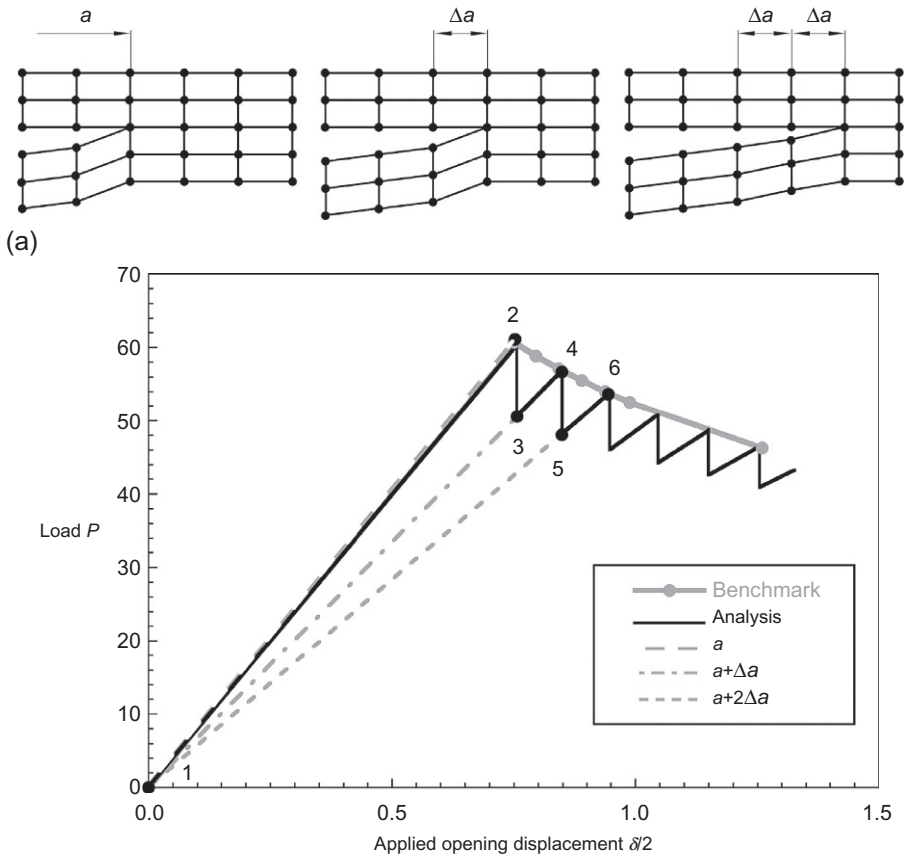

Figure 1.28 Origin of observed sawtooth behavior during automated propagation. (a) Detail of crack propagation from length a to $a+\Delta a$ to $a+2\Delta a$ and (b) computed load/displacement behavior during automated propagation for a DCB specimen.

1.7 New developments and evolving methods

1.7.1 Recent developments and improvements to VCCT

Using an interface element approach, VCCT can be implemented into any open commercial finite element code that allows user-written subroutines. Mabson et al. proposed an interface element to perform either delamination fatigue onset or fatigue growth analysis (Deobald et al., 2007; Mabson et al., 2007). The authors demonstrated

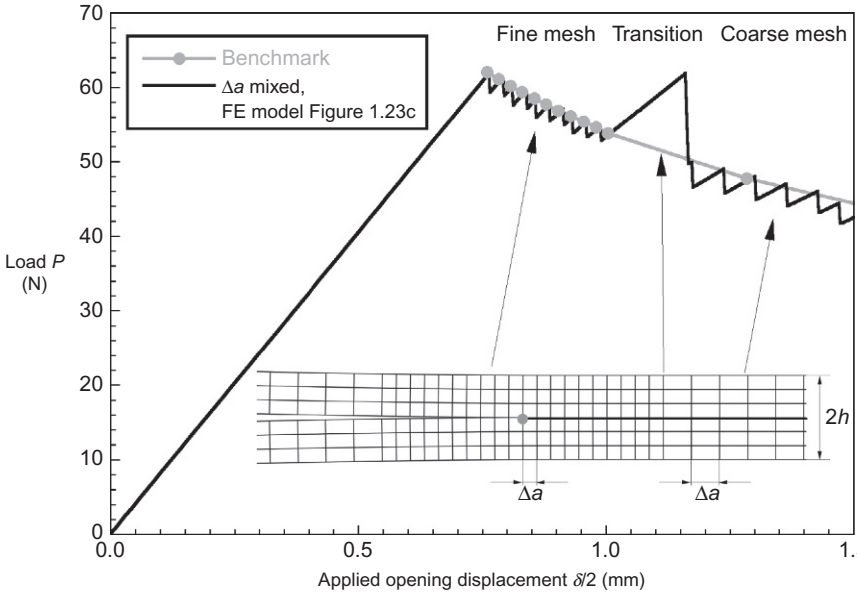

Figure 1.29 Influence of varying crack tip element length, Δa, on computed load/displacement behavior during automated propagation analysis for a DCB specimen.

the capability to fully release one element or more for each time increment and precisely account for the number of cycles needed to cause fatigue growth over that length. A different interface element to study an example of dynamic crack propagation under mixed-mode loading was developed by Qian and Xie and used to study an example of dynamic crack propagation under mixed-mode loading (Qian and Xie, 2007).

Nairn developed a generalized method that allows arbitrary placement of the side nodes for elements with quadratic shape functions (Nairn, 2011). This method included both standard elements, with mid-side nodes, and singularity elements, with quarter-point nodes, as special cases of one general equation (Nairn, 2011). The approach also accounted for traction-loaded cracks.

Valvo (2012) addressed a little known issue, where the standard VCCT calculations can yield small negative values of the individual mode components. This issue is often seen in asymmetric cracks. He found that the origins of these physically inconsistent predictions of the standard VCCT lie in the decomposition of the crack tip forces and displacements. Although crack tip forces and displacements are decomposed into components of a geometrically orthogonal Cartesian coordinate system, a lack of *energetic orthogonality* between these components used to compute the mode components may still exist due to nonzero coupling terms (Valvo, 2012). A revised VCCT was presented, which furnished a physically consistent partitioning of fracture modes that eliminates negative energy-release rate components (Valvo, 2012). The method has recently been extended to 3D problems involving mixed-mode I/II/III fracture (Valvo, 2014).

1.7.2 Crack kinking and delamination/matrix interaction

Traditionally, VCCT has been used to study delamination propagation and growth where the delamination advance is constrained to the original interface plane. Recently, Xie et al. (2004, 2005) proposed a new numerical method based on VCCT, which allows the calculation of strain energy-release rates for cracks that kink, that is, the crack path changes direction and does not remain in the original interface plane. This method allows the evaluation of the mode I and mode II energy-release rate at the tip of a kinking crack using only the nodal forces and displacements near the crack tip (Xie et al., 2004, 2005).

Carvalho recently assessed the performance of VCCT as implemented in combination with the extended finite element method (XFEM) in Abaqus/Standard (Abaqus, 2014a; Carvalho and Krueger, 2014). He further proposed a strategy to model the delamination migration process where a delamination migrates by matrix cracking of the adjacent plies to a new location at another interface. His strategy combines VCCT to model delamination with XFEM or the newly developed floating node method to capture the migration process (Carvalho et al., 2013). Figure 1.30 illustrates the VCCT calculation in combination with the floating node method (Chen et al., 2014). The forces and displacements needed are obtained at the floating degrees-of-freedom (open squares) as the crack develops and Equations (1.3) and (1.4) are used to calculate the mixed-mode energy-release rates. Additionally, floating degrees-of-freedom are also added along a virtual crack plane up to a distance r, named the "enrichment radius."

The aforementioned methods may be of interest for analyzing the interaction of delamination propagation in one interface accompanied by matrix cracking,

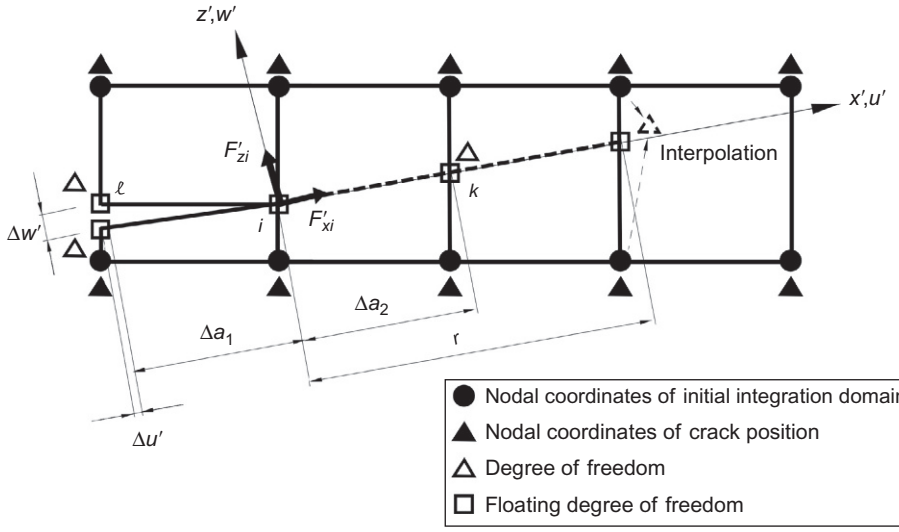

Figure 1.30 VCCT with floating node method.
Adapted from Carvalho et al. (2013).

branching, and subsequent delamination propagation at an adjacent interface, a set of problems that are also independently addressed in Chapters 4, 9, and 10 of this book.

1.8 Application example

In this subsection, we present an example that illustrates the use of a shell-to-solid submodeling technique to circumvent the problem of nonconverged computed mixed-mode strain energy-release rate components when the structure above and below the plane of delamination is modeled with plate elements with different section properties, as discussed in Section 1.3.3. The example also demonstrates the use of elements at the crack tip at a bimaterial interface where the length Δa is larger than the oscillatory zone, as discussed in Section 1.4.5.

A square (1016 mm × 1016 mm) panel made of IM7/8552 carbon/epoxy tape was reinforced with three stiffeners made of IM7/8552 carbon/epoxy plain-weave fabric. During manufacturing, an artificial defect of about 82 mm in length was introduced at the termination of the center stiffener, thus creating a delamination at an interface between a −45° tape layer and a 0° fabric layer. The stiffened panel was bolted to a steel picture frame (see Figure 1.31a) and subjected to shear loading. The shear loading caused the panel to buckle as shown in Figure 1.31a. The resulting out-of-plane deformation caused skin/stiffener separation to initiate at the location of the artificial defect. A finite element model of this panel is shown in Figure 1.31b. A small section of the stiffener foot and the panel skin in the vicinity of the embedded defect were modeled with a local 3D solid model as shown in the enlargement in Figure 1.31b.

One objective of the research was to study the effect of the fidelity of the local 3D finite element model on the computed mode mixity (Krueger et al., 2007). Therefore, the study also included the introduction and modeling of a resin layer at the delaminated interface between the top skin ply (−45° tape) and the bottom of the flange (0° fabric layer). Because the delamination exists in a homogeneous isotropic material (the resin interface layer), the oscillatory singularity at the crack tip of the bimaterial—as mentioned in Section 1.4.5—does not exist. For convenience, the delamination was placed centrally within the resin layer. Therefore, the resin was modeled with two layers of elements with the delamination located between the two layers. Further details are discussed in reference (Krueger et al., 2007). The distribution of the mode mixities (G_I/G_T and G_{II}/G_T) calculated along the delamination front, s, was compared to the distribution calculated from models without a resin layer, as shown in Figure 1.32. For the models without a resin layer, a crack tip element length, $\triangle a$, had been chosen (approximately one-ply thickness, $\triangle a/h \cong 1$) in the range over which the mode mixity exhibits a reduced sensitivity to the value of $\triangle a$, as discussed in Section 1.4.5. The results from both approaches were in good agreement with each other and showed that the approaches yielded nearly equivalent results, confirming the results from reference (Raju et al., 1988). Based on the comparison, local models without the resin layer were used for all subsequent studies to reduce model complexity and analysis time (Krueger et al., 2007).

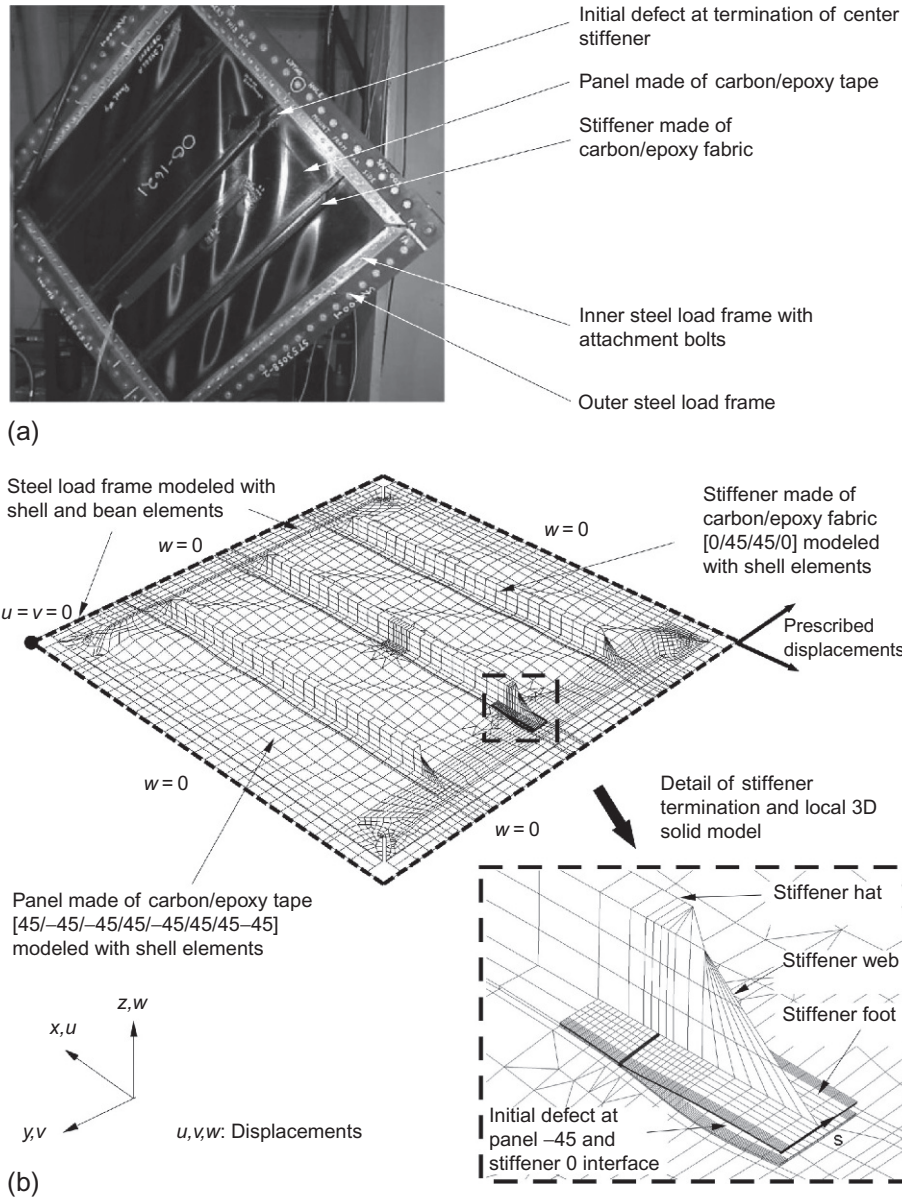

Figure 1.31 Stiffened composite panel (Krueger et al., 2007). (a) Buckled composite panel under shear loading with picture frame and (b) finite element model of stiffened panel and load frame.

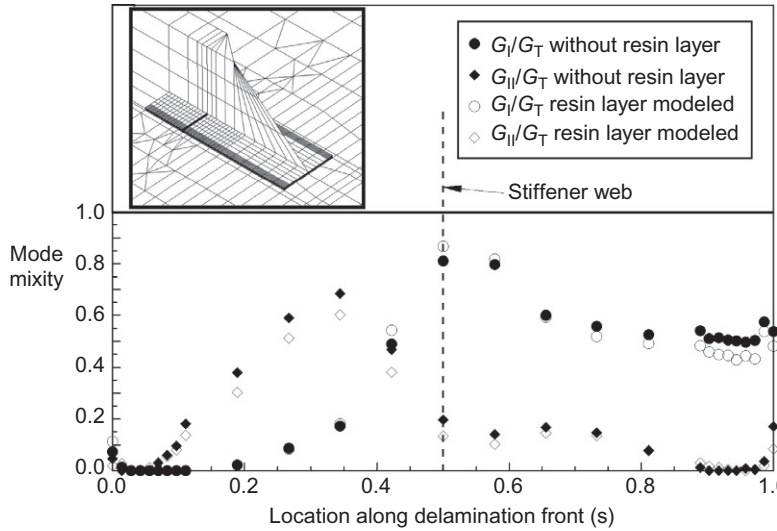

Figure 1.32 Computed mode mix across the width of the stiffener for models with and without a resin layer (Krueger et al., 2007).

1.9 Resulting recommendations for analysts

Based on the detailed discussions in the previous sections, the following recommendations and comments are provided to help the analyst to perform a VCCT analysis successfully:

- The use of standardized or vetted test methods is recommended to obtain accurate fracture toughness data. For fatigue characterization, the user should closely follow the current developments and monitor new publications.
- The recommended element size for composites is $1/20 \leq \Delta a/h \leq 1$. Variations in mode mix between these bounds are typically very small and should prove acceptable for practical applications (Krueger, 2004). For large stiffness differences between the layers on either side of the modeled interface (e.g., for a disbond between the facesheet and the core in a sandwich construction), other methods for mode separation should be considered (Krueger et al., 2013).
- Because the user is most likely unaware if the particular VCCT implementation accounted for varying element length along the path, a uniform mesh is recommended along the path of expected delamination advance, for automated delamination propagation in commercial codes.
- The VCCT implementation in commercial codes is relatively mature and allows the calculation of the energy-release rate components at an arbitrarily shaped, predefined front.
- Implementations today allow a quasi-static propagation analysis; however, the stair-stepped delamination front caused by the simple node release approach remains an issue. The tools to perform a similar growth analysis under cyclic loading are still under development.
- Challenges remain when delaminations are modeled with plate or shell finite elements. Non-converged computed mixed-mode strain energy-release rate components may occur when

the section properties on each side of the interface are different. The problem, however, may be circumvented by using three-dimensional models locally, which was demonstrated in an example where a stiffener separated from the skin of a panel.

1.10 Concluding remarks

The intent of this chapter was to provide an overview of the VCCT, a fracture-mechanics-based approach, which may be used to assess the damage tolerance of composite structures in the design phase and during certification. The technique was described; equations for the use in conjunction with two-dimensional elements and three-dimensional solid elements as well as plate/shell elements were given; insight into modeling issues was provided and potential pitfalls were discussed. Additionally, information for obtaining the proper material input properties was provided, together with an application example and a summary of new developments.

A significant amount of progress has been made in the last decade to make VCCT user friendly and accessible to a wide range of users. In spite of remaining challenges, VCCT appears to be ready for *prime time*.

Acknowledgments

The author gratefully acknowledges Gretchen Murri, Nelson De Carvalho, and James Ratcliffe for the thorough review of this chapter.

References

Abaqus, 2005. VCCT for ABAQUS—User's Manual. Dassault Systèmes Simulia Corporation, Providence, RI, USA.

Abaqus, 2014a. 10.7 Modeling discontinuities as an enriched feature using the extended finite element method. In: Abaqus/Standard 6.14 User's Manual. Dassault Systèmes Simulia Corporation, Providence, RI, USA.

Abaqus, 2014b. 11.4.3 Crack propagation analysis. In: Abaqus/Standard 6.14 User's Manual. Dassault Systèmes Simulia Corporation, Providence, RI, USA.

Agrawal, A., Karlsson, A.M., 2006. Obtaining mode mixity for a bimaterial interface crack using the virtual crack closure technique. Int. J. Fract. 141, 75–98.

Allegri, G., Wisnom, M.R., 2012. A nonlinear damage evolution model for mode II fatigue delamination onset and growth. Int. J. Fatigue 43, 226–234.

Allegri, G., Jones, M.I., Wisnom, M.R., Hallett, S.R., 2011. A new semi-empirical model for stress ratio effect on mode II fatigue delamination growth. Compos. Part A 42, 733–740.

Allegri, G., Wisnom, M.R., Hallett, S.R., 2013. A new semi-empirical law for variable stress-ratio and mixed-mode fatigue delamination growth. Compos. A: Appl. Sci. Manuf. 48, 192–200.

Ansys, 2014. Ansys Structural Analysis, R15.0. Ansys, Inc., Canonsburg, PA.

Argüelles, A., Viña, J., Canteli, A.F., Castrillo, M.A., Bonhomme, J., 2008. Interlaminar crack initiation and growth rate in a carbon-fibre epoxy composite under mode-I fatigue loading. Compos. Sci. Technol. 68, 2325–2331.

ASTM, 2009. Standard test method for mode I fatigue delamination propagation of unidirectional fiber-reinforced polymer matrix composites. In: Draft Standard. ASTM International, West Conshohocken, PA, USA.

ASTM, 2011. ASTM D 6115-97, Standard test method for mode I fatigue delamination growth onset of unidirectional fiber-reinforced polymer matrix composites. In: Annual Book of ASTM Standards. ASTM International, West Conshohocken, PA, USA.

ASTM, 2013a. ASTM D 5528-13, Standard test method for mode I interlaminar fracture toughness of unidirectional fiber-reinforced polymer matrix composites. In: Annual Book of ASTM Standards. ASTM International, West Conshohocken, PA, USA.

ASTM, 2013b. ASTM D 6671/D6671M-13, Standard test method for mixed mode I-mode II interlaminar fracture toughness of unidirectional fiber reinforced polymer matrix composites. In: Annual Book of ASTM Standards. ASTM International, West Conshohocken, PA, USA.

ASTM, 2014. ASTM D 7905-14, Standard test method for determination of the mode II interlaminar fracture toughness of unidirectional fiber-reinforced polymer matrix composites using the end-notched flexure (ENF) test. In: Annual Book of ASTM Standards. ASTM International, West Conshohocken, PA, USA.

Baere, I.D., Jacques, S., Paepegem, W.V., Degrieck, J., 2012. Study of the mode I and mode II interlaminar behaviour of a carbon fabric reinforced thermoplastic. Polym. Test. 31, 322–332.

Benzeggagh, M.L., Kenane, M., 1996. Measurement of mixed-mode delamination fracture toughness of unidirectional glass/epoxy composites with mixed-mode bending apparatus. Compos. Sci. Technol. 56, 439–449.

Blanco, N., Gamstedt, E.K., Asp, L.E., Costa, J., 2004. Mixed-mode delamination growth in carbon-fibre composite laminates under cyclic loading. Int. J. Solids Struct. 41, 4219–4235.

Bolotin, V.V., 1996. Delaminations in composite structures: its origin, buckling, growth and stability. Compos. Part B 27B, 129–145.

Broek, D., 1991. The Practical Use of Fracture Mechanics. Kluwer Academic Publishers, Dordrecht, The Netherlands.

Browning, G., Carlsson, L.A., Ratcliffe, J.G., 2011. Modification of the edge crack torsion specimen for mode III delamination testing. Part II—experimental study. J. Comp. Mater. 45, 2633–2640.

Brunner, A.J., Blackman, B.R.K., Davies, P., 2008. A status report on delamination resistance testing of polymer–matrix composites. Eng. Fract. Mech. 75, 2779–2794.

Brunner, A.J., Murphy, N., Pinter, G., 2009. Development of a standardized procedure for the characterization of interlaminar delamination propagation in advanced composites under fatigue mode I loading conditions. Eng. Fract. Mech. 76, 2678–2689.

Bui, Q.V., 2011. A modified Benzeggagh-Kenane fracture criterion for mixed-mode delamination. J. Compos. Mater. 45, 389–413.

Carvalho, N.V., Krueger, R., 2014. Combining the extended finite element method with virtual crack closure technique and cohesive surface modeling to simulate delamination migration in cross-ply laminates. In: SIMULIA Community Conference, Providence, RI.

Carvalho, N.V., Murri, G., 2014. A novel method for characterizing fatigue delamination growth under Mode I using the Double Cantilever Beam specimen. In: 29th ASC Technical Conference. San Diego, CA.

Carvalho, N.V., Chen, B.Y., Pinho, S.T., Baiz, P.M., Ratcliffe, J.G., Tay, T.E., 2013. Floating node method and virtual crack closure technique for modeling matrix cracking-delamination migration. In: 19th International Conference on Composite Materials (ICCM-19). Montreal, Canada.

Carvalho, N.V., Ratcliffe, J.G., Chen, B.Y., Pinho, S.T., Baiz, P.M., Tay, T.E., 2014. Modeling quasi-static and fatigue-driven delamination migration. In: 29th ASC Technical Conference. San Diego, CA.

Chen, B.Y., Pinho, S.T., Carvalho, N.V., Baiz, P.M., Tay, T.E., 2014. A floating node method for the modeling of multiple discontinuities in composites. Eng. Fract. Mech. 127, 104–134.

Czabaj, M.W., Ratcliffe, J.G., Davidson, B.D., 2014. Observation of intralaminar cracking in the edge crack torsion specimen. Eng. Fract. Mech. 120, 1–14.

Dattaguru, B., Venkatesha, K.S., Ramamurthy, T.S., Buchholz, F.G., 1994. Finite element estimates of strain energy-release rate components at the tip of an interface crack under mode I loading. Eng. Fract. Mech. 49, 451–463.

Davidson, B.D., Sediles, F.O., 2011. Mixed-mode I–II–III delamination toughness determination via a shear–torsion-bending test. Compos. A: Appl. Sci. Manuf. 42, 589–603.

Davidson, B.D., Sundararaman, V., 1996. A single leg bending test for interfacial fracture toughness determination. Int. J. Fract. 78, 193–210.

Davidson, B.D., Zhao, W., 2007. An accurate mixed-mode delamination failure criterion for laminated fibrous composites requiring limited experimental input. J. Compos. Mater. 41, 679–702.

Davies, G.A.O., 2002. Benchmarks for Composite Delamination. NAFEMS, Hamilton, Scotland, UK.

de Morais, A.B., Pereira, A.B., de Moura, M.F.S.F., 2011. Mode III interlaminar fracture of carbon/epoxy laminates using the six-point edge crack torsion (6ECT). Compos. A: Appl. Sci. Manuf. 42, 1793–1799.

Deobald, L., Mabson, G., Dopker, B., Hoyt, D., Baylor, J., Graesser, D., 2007. Interlaminar fatigue elements for crack growth based on virtual crack closure technique. In: 48th AIAA/ASME/ASCE/AHS/ASC Structures, Structural Dynamics, and Materials Conference. Honolulu, Hawaii, AIAA-2007-2091. American Institute of Aeronautics and Astronautics.

FRANC3D, 2003. FRANC3D Concepts and Users Guide—Version 2.6, Cornell Fracture Group, Ithaca, New York.

Garg, A.C., 1988. Delamination—a damage mode in composite structures. Eng. Fract. Mech. 29, 557–584.

Genoa, 2014. GENOA 4.4 Product Fact Sheet, PFA—Virtual Crack Closure Technique (PFA_VCCT). Alpha STAR Corporation.

Glaessgen, E.H., Riddell, W.T., Raju, I.S., 1998. Effect of shear deformation and continuity on delamination modeling with plate elements. In: The 39th AIAA/ASME/ASCE/AHS/ASC Structures, Structural Dynamics and Materials Conference. Long Beach, CA. AIAA-1998-2023. American Institute of Aeronautics and Astronautics.

Glaessgen, E.H., Riddell, W.T., Raju, I.S., 2002. Nodal constraint, shear deformation and continuity effects related to the modeling of debonding of laminates, using plate elements. Comp. Model. Eng. Sci. 3, 103–116.

Hansen, P., Martin, R., 1999. DCB, 4ENF and MMB delamination characterisation of S2/8552 and IM7/8552. Materials Engineering Research Laboratory Ltd. (MERL), Hertford, UK.

Hartman, A., Schijve, J., 1970. The effects of environment and load frequency on the crack propagation law for macro fatigue crack growth in aluminum alloys. Eng. Fract. Mech. 1, 615–631.

He, M.-Y., Hutchinson, J.W., 1989. Kinking of a crack out of an interface. J. Appl. Mech. 56, 270–278.

Iesulauro, E., 2009. FRANC2D/L: A Crack Propagation Simulator for Plane Layered Structures—Version 1.5 User's Guide. Cornell University, Ithaca, New York.

Irwin, G.R., 1958. Fracture I. Handbuch der Physik VI. Springer, Berlin.

ISO, 2001. ISO 15024:2001, Fibre-reinforced plastic composites—determination of mode I interlaminar fracture toughness, GIC, for unidirectionally reinforced materials. ISO (International Organization for Standardization).

ISO, 2014. ISO 15114:2014 Fibre-reinforced plastic composites—determination of the mode II fracture resistance for unidirectionally reinforced materials using the calibrated end-loaded split (C-ELS) test and an effective crack length approach. ISO (International Organization for Standardization).

Johnston, A.L., Davidson, B.D., Simon, K.K., 2014. Assessment of split-beam-type tests for mode III delamination toughness determination. Int. J. Fract. 185, 31–48.

Jones, R., Pitt, S., Bunner, A.J., Hui, D., 2012. Application of the Hartman–Schijve equation to represent mode I and mode II fatigue delamination growth in composites. Compos. Struct. 94, 1343–1351.

Kenane, M., Benzeggagh, M.L., 1997. Mixed-mode delamination fracture toughness of unidirectional glass/epoxy composites under fatigue loading. Compos. Sci. Technol. 57, 597–605.

Kenane, M., Azari, Z., Benmedakhene, S., Benzeggagh, M.L., 2011. Experimental development of fatigue delamination threshold criterion. Compos. Part B 42, 367–375.

König, M., Krüger, R., Kussmaul, K., Von Alberti, M., Gädke, M., 1997. Characterizing static and fatigue interlaminar fracture behaviour of a first generation graphite/epoxy composite. Composite Materials: Testing and Design—13th Volume. American Society for Testing and Materials, ASTM STP 1242.

König, M., Krüger, R., Rinderknecht, S., 2000. Finite element analysis of delamination growth in a multidirectional composite ENF specimen. Composite Materials: Theory and Practice. American Society for Testing and Materials, ASTM STP 1383.

Krueger, R., 2004. Virtual crack closure technique: history, approach and applications. Appl. Mech. Rev. 57, 109–143.

Krueger, R., 2008. An approach to assess delamination propagation simulation capabilities in commercial finite element codes, NASA/TM-2008-215123.

Krueger, R., 2011. Development and application of benchmark examples for mode II static delamination propagation and fatigue growth predictions, NASA/CR-2011-217194.

Krueger, R., 2012a. Application of benchmark examples to assess the single and mixed-mode static delamination propagation capabilities in Ansys, NASA/CR-2012-217588.

Krueger, R., 2012b. Development and application of benchmark examples for mixed-mode I/II quasi-static delamination propagation predictions, NASA/CR-2012-217562.

Krueger, R., 2014. Create your own benchmark examples and learn about delamination propagation prediction capabilities in commercial finite element codes and assess their performance. Benchmark Mag, 10–18.

Krueger, R., O'Brien, T.K., 2001. A shell/3D modeling technique for the analysis of delaminated composite laminates. Compos. A: Appl. Sci. Manuf. 32, 25–44.

Krueger, R., Ratcliffe, J.G., Minguet, P.J., 2007. Analysis of composite panel-stiffener debonding using a shell/3D modeling technique. NASA/CR-2007-214879.

Krueger, R., Shivakumar, K., Raju, I.S., 2013. Fracture mechanics analysis for interface crack problems—a review. In: 54th AIAA/ASME/ASCE/AHS/ASC Structures, Structural Dynamics, and Materials Conference. Boston, MA, AIAA 2013-1476.

Krüger, R., 1994. Three dimensional finite element analysis of multidirectional composite DCB, SLB and ENF specimens. Institute for Statics and Dynamics of Aerospace Structures, University of Stuttgart.

Krüger, R., König, M., 1995. Two- and three-dimensional finite element analysis of a specimen containing a rectangular artificial delamination and additional ply cut. ISD-Report No. 95/11, Institute for Statics and Dynamics of Aerospace Structures, University of Stuttgart.

Krüger, R., König, M., 1996. Investigation of delamination growth between plies of dissimilar orientations. Institute for Statics and Dynamics of Aerospace Structures, University of Stuttgart.

Lee, S.M., 1990. Failure mechanics of edge delamination of composites. J. Composite Mat. 24, 1200–1212.

Lee, S.M., 1993. An edge crack torsion method for mode III delamination fracture testing. J. Compos. Technol. Res. 15, 193–201.

Li, J., Lee, S.M., Lee, E.W., O'Brien, T.K., 1997. Evaluation of the edge crack torsion ECT test for mode III interlaminar fracture toughness of laminated composites. J. Compos. Technol. Res. 19, 174–183.

Li, X., Ferrie, C., Nottorf, E., Portanova, M., 2008. Virtual crack closure technique on stepped crack fronts (VCCT-S). In: AHS 64th Annual Forum.

Liu, Y.-P., Chen, C.-Y., Li, G.-Q., 2011. A modified zigzag approach to approximate moving crack front with arbitrary shape. Eng. Fract. Mech. 78, 234–251.

Mabson, G.E., Deobald, L.R., Dopker, B., Hoyt, D.M., Baylor, J.S., Graesser, D.L., 2007. Fracture interface elements for static and fatigue analysis. In: 16th International Conference on Composite Materials (ICCM-16). Kyoto, Japan.

Marat-Mendes, R., Freitas, M.D., 2009. Characterisation of the edge crack torsion (ECT) test for the measurement of the mode III interlaminar fracture toughness. Eng. Fract. Mech. 76, 2799–2809.

Marat-Mendes, R.M., Freitas, M.M., 2010. Failure criteria for mixed-mode delamination in glass fibre epoxy composites. Compos. Struct. 92, 2292–2298.

Marc, 2013. Marc® 2013.1, Theory and user information. MSC Software Corporation, Newport Beach, CA, USA.

Martin, R.H., 1991. Evaluation of the split cantilever beam for mode III delamination testing. Composite Materials: Fatigue and Fracture (Third Volume). ASTM STP 1110, ASTM International, West Conshohocken, PA, USA.

Martin, R.H., 1998. Incorporating interlaminar fracture mechanics into design. In: International Conference on Designing Cost-Effective Composites. IMechE Conference Transactions, London, U.K.

Murri, G.B., 2014. Effect of data reduction and fiber-bridging on mode I delamination characterization of unidirectional composites. J. Compos. Mater. 48, 2413–2424.

Nairn, J.A., 2011. Generalized crack closure analysis for elements with arbitrarily-placed side nodes and consistent nodal forces. Int. J. Fract. 171, 11–22.

Nastran, 2013. MSC Nastran 2013.1, User's Manual. MSC Software Corporation, Newport Beach, CA, USA.

O'Brien, T.K., 1982. Characterization of delamination onset and growth in a composite laminate. ASTM Spec. Tech. Publ. 775, 140–167.

O'Brien, T.K., Johnston, W.M., Toland, G., 2010. Mode II interlaminar fracture toughness and fatigue characterization of a graphite epoxy composite material. NASA/TM-2010-216838.

Orifici, A., Krueger, R., 2012. Benchmark assessment of automated delamination propagation capabilities in finite element codes for static loading. Finite Elem. Anal. Des. 54, 28–36.
Pagano, N.J., Schoeppner, G.A., 2000. Delamination of polymer matrix composites: problems and assessment. In: Comprehensive Composite Materials. Elsevier Science Ltd.
Pascoe, J.A., Alderliesten, R.C., Benedictus, R., 2013. Methods for the prediction of fatigue delamination growth in composites and adhesive bonds—a critical review. Eng. Fract. Mech. 112–113, 72–96.
Pascoe, J.A., Alderliesten, R.C., Benedictus, R., 2014. Towards understanding fatigue disbond growth via cyclic strain energy. Procedia Mater. Sci. 3, 610–615.
Peng, L., Xu, J., Zhang, J., Zhao, L., 2012. Mixed-mode delamination growth of multidirectional composite laminates under fatigue loading. Eng. Fract. Mech. 96, 676–686.
Pietropaoli, E., Riccio, A., 2011. A global/local finite element approach for predicting interlaminar and intralaminar damage evolution in composite stiffened panels under compressive load. Appl. Compos. Mater. 18, 113–125.
Qian, Q., Xie, D., 2007. Analysis of mixed-mode dynamic crack propagation by interface element based on virtual crack closure technique. Eng. Fract. Mech. 74, 807–814.
Raju, I.S., 1987. Calculation of strain-energy-release rates with higher order and singular finite elements. Eng. Fracture Mech. 28, 251–274.
Raju, I.S., O'Brien, T.K., 2008. Fracture mechanics concepts, stress fields, strain energy-release rates, delamination and growth criteria. In: Sridharan, S. (Ed.), Delamination Behaviour of Composites. Woodhead Publishing in Materials.
Raju, I.S., Crews, J.H., Aminpour, M.A., 1988. Convergence of strain energy-release rate components for edge-delaminated composite laminates. Eng. Fracture Mech. 30, 383–396.
Rans, C., Alderliesten, R., Benedictus, R., 2011. Misinterpreting the results: how similitude can improve our understanding of fatigue delamination growth. Compos. Sci. Technol. 71, 230–238.
Ratcliffe, J.G., 2004. Characterization of the edge crack torsion (ECT) test for mode III fracture toughness measurement of laminated, composites. NASA/TM-2004-213269.
Ratcliffe, J.G., Johnston, W.M., 2014. Influence of mixed mode I-mode II loading on fatigue delamination growth characteristics of a graphite epoxy tape laminate. In: 29th ASC Technical Conference. San Diego, CA.
Reeder, J.R., 1993. A bilinear failure criterion for mixed-mode delamination. Composite Materials: Testing and Design (Eleventh Volume). ASTM International, ASTM STP 1206; pp. 303–322.
Reeder, J.R., 2006. 3D mixed-mode delamination fracture criteria—an experimentalist's perspective. In: 21st Annual Technical Conference, Dearborn, Michigan. American Society for Composites.
Rice, J.R., 1988. Elastic fracture mechanics concepts for interface cracks. J. Appl. Mech. Trans. ASME 55, 98–103.
Rinderknecht, S., Kröplin, B., 1995. A finite element model for the delamination in composite plates. Mech. Compos. Mater. Struct. 2, 19–47.
Robinson, P., Song, D.Q., 1994. Development of an improved mode III delamination test for composites. Compos. Sci. Technol. 52, 217–233.
Rybicki, E.F., Kanninen, M.F., 1977. A finite element calculation of stress intensity factors by a modified crack closure integral. Eng. Fract. Mech. 9, 931–938.
Rybicki, E.F., Schmueser, D.W., Fox, J., 1977. An energy-release rate approach for stable crack growth in the free-edge delamination problem. J. Compos. Mater. 11, 470–487.

Schollmann, M., Fulland, M., Richard, H., 2003. Development of a new software for adaptive crack growth simulations in 3D structures. Eng. Fract. Mech. 70, 249–268.

Shivakumar, K.N., Tan, P.W., Newman, J.C., 1988. A virtual crack closure technique for calculating stress intensity factors for cracked three dimensional bodies. Int. J. Fracture 36, R43–R50.

Shivakumar, K., Chen, H., Abali, F., Le, D., Davis, C., 2006. A total fatigue life model for mode I delaminated composite laminates. Int. J. Fatigue 28, 33–42.

Smith, S.A., 2001. Vacuum assisted resin transfer molding of sandwich structures: material processing, evaluation, fracture testing and analysis (PhD thesis), North Carolina A&T State University.

Smith, S.A., Raju, I.S., 1998. Evaluation of stress-intensity factors using general finite-element models. Fatigue and Fracture Mechanics: 29th Volume. American Society for Testing and Materials, ASTM STP 1321.

Stelzer, S., Brunner, A.J., Argüelles, A., Murphy, N., Pinter, G., 2012. Mode I delamination fatigue crack growth in unidirectional fiber reinforced composites: development of a standardized test procedure. Compos. Sci. Technol. 72, 1102–1107.

Stelzer, S., Pinter, G., Brunner, A.J., 2014. Comparison of quasi-static and cyclic fatigue delamination resistance of carbon fiber reinforced polymer-matrix laminates under different mode loading. Procedia Mater. Sci. 3, 1087–1092.

Sun, C.T., Jih, C.J., 1987. On strain energy-release rates for interfacial cracks in bimaterial media. Eng. Fract. Mech. 28, 13–20.

Sun, C.T., Yang, Z., 2001. K-Dominance in delamination cracks. In: Proceedings of the American Society for Composites. 16th Technical Conference on Composite Materials, Blacksburg, VA.

Tay, T.E., 2003. Characterization and analysis of delamination fracture in composites—an overview of developments from 1990 to 2001. Appl. Mech. Rev. 56, 1–32.

Thacker, B., 2003. The role of nondeterminism in verification and validation of computational solid mechanics models. SAE paper 2003-01-1353.

Valvo, P.S., 2012. A revised virtual crack closure technique for physically consistent fracture-mode partitioning. Int. J. Fract. 173, 101–114.

Valvo, P.S., 2014. A physically consistent virtual crack closure technique for I/II/III mixed-mode fracture problems. Procedia Mater. Sci. 3, 983–1987.

Wang, J.T., Raju, I.S., 1996. Strain energy-release rate formula for skin-stiffener debond modeled with plate elements. Eng. Fract. Mech. 54, 211–228.

Whitcomb, J.D., 1990. Mechanics of instability-related delamination growth. Composite Materials: Testing and Design (Ninth Volume). American Society for Testing and Materials.

Whitcomb, J.D., Shivakumar, K.N., 1989. Strain-energy-release rate analysis of plates with postbuckled delaminations. J. Compos. Mat. 23, 714–734.

Williams, M.L., 1959. The stresses around a fault or crack in dissimilar media. Bull. Seismol. Soc. Am. 49, 199–204.

Wisnom, M.R., 2012. The role of delamination in failure of fibre-reinforced composites. Phil. Trans. R. Soc. A 370, 1850–1890.

Xie, D., Biggers, S.B., 2006. Strain energy-release rate calculation for a moving delamination front of arbitrary shape based on the virtual crack closure technique. Part I: formulation and validation. Eng. Fract. Mech. 73, 771–785.

Xie, D., Waas, A.M., Shahwan, K.W., Schroeder, J.A., Boeman, R.G., 2004. Computation of energy-release rates for kinking cracks based on virtual crack closure technique. Comput. Model. Eng. Sci. 6, 515–524.

Xie, D., Waas, A.M., Shahwan, K.W., Schroeder, J.A., Boeman, R.G., 2005. Fracture criterion for kinking cracks in a tri-material adhesively bonded joint under mixed mode loading. Eng. Fract. Mech. 72, 2487–2504.

Yarrington, P.W., Collier, C.S., Bednarcyk, B.A., 2006. Failure analysis of adhesively bonded composite joints via the virtual crack closure technique. In: 47th AIAA/ASME/ASCE/AHS/ASC Structures, Structural Dynamics, and Materials Conference. Newport, Rhode Island, AIAA-2006-1962. American Institute of Aeronautics and Astronautics.

Zhang, J., Peng, L., Zhao, L., Fei, B., 2012. Fatigue delamination growth rates and thresholds of composite laminates under mixed-mode loading. Int. J. Fatigue 40, 7–15.

This page intentionally left blank

Modelling delamination with cohesive interface elements

2

S.R. Hallett, P.W. Harper
University of Bristol, Bristol, UK

2.1 Introduction

The prediction of failure in composite materials is of great importance in the design of composite structures. However, the prediction of failure in composite materials is not a trivial matter, because modes and mechanisms of failure are complex and varied, occurring at multiple-length scales and often interacting with each other to cause overall failure. Furthermore, the quasi-brittle nature of composites means that crack growth is often extremely sudden, and it is difficult to predict the amount of initial damage necessary before catastrophic failure occurs. That said, after several decades of research into numerical modelling of composites failure, progress is now being made in being able to predict failure using models that accurately capture the physical phenomena, using independently measured input parameters from standard material property tests. This is particularly the case for "high-fidelity" finite element models, where each failure mode is explicitly included in the analysis and their interactions are accounted for by nonlinear progressive failure. Of the different failure modes for laminated composite materials, delamination is widely acknowledged as one of the most important, in that it can occur at relatively low load levels compared to ultimate failure by fibre fracture but still with significant consequences for structural load-bearing capability. It is caused by high interlaminar stress levels, which lead to through-thickness debonding of the individual plies. There is typically no fibre reinforcement in this direction, so the properties are governed by the relatively weak matrix material. Wisnom (2012) identifies a number of loading scenarios that can give rise to delamination failure and highlights its importance in terms of the strength reduction that can occur.

Finite element analysis is becoming an indispensible tool in the design of composite structures. Within this there are now a number of methods for predicting delamination failure; the virtual crack closure technique (VCCT) (Krueger, 2004), continuum damage mechanics (Hou et al., 2001) and cohesive zone models (CZMs). The first two are dealt with in detail in other chapters of this book, and it is the last of these topics that is covered in this chapter.

2.2 History and background

The concept of CZM is based on a presumption of a zone of softening ahead of a sharp crack tip in the material. Within this zone, the opening is resisted by cohesive tractions (see Figure 2.1).

Numerical modelling of failure in advanced composite materials. http://dx.doi.org/10.1016/B978-0-08-100332-9.00002-5
Copyright © 2015 Elsevier Ltd. All rights reserved.

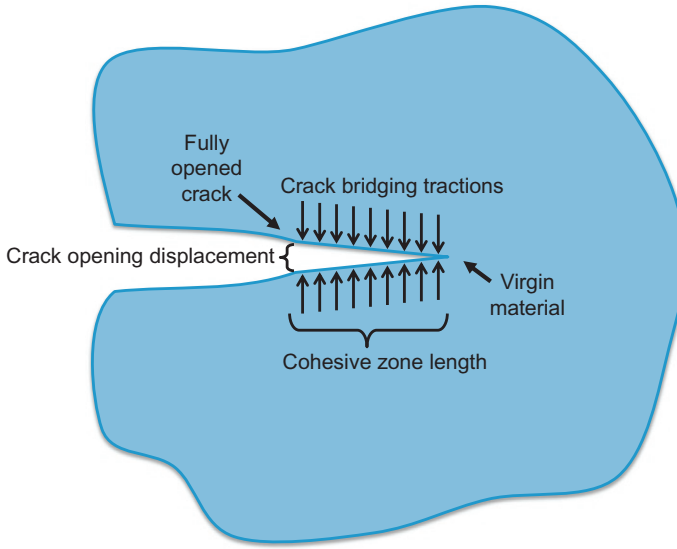

Figure 2.1 Schematic showing crack bridging tractions in cohesive zone.

This concept was first reported by Dugdale (1960), who noted a small zone of plasticity ahead of slits in steel plates subjected to static tension load. Dugdale assumed that within this region, stress is constant and equal to the yield strength of the material. Around the same time, Barrenblatt (1962), in contrast, suggested that stress levels in this softening zone were variable. Despite these minor differences, Dugdale and Barrenblatt are together considered to be the originators of the cohesive zone method, which has since been widely implemented into finite element analyses for a great variety of purposes. The first such implementation was by Hillerborg et al. (1976) who applied the technique to cracking in a concrete beam under bending. Their assumptions were much the same as current formulations – that the material remains linear-elastic until it reaches its tensile strength, $\sigma_{\max}$, after which it degrades linearly to zero at finite displacement (see Figure 2.2a). This is the simplest and numerically most convenient traction–displacement curve to implement because it is monotonic with no discontinuities, but other shapes were also considered and have subsequently been implemented by a range of authors (Figure 2.2b–d) as discussed in Shet and Chandra (2004) and Alfano (2006).

One of the most important features of the traction–displacement curve is the absorbed energy, as calculated by the area under the curve, through integration of stress

$$\int_0^{\delta_f} \sigma \cdot \mathrm{d}u \tag{2.1}$$

where σ is the interfacial stress, u is the crack opening displacement and δ_f is the displacement at failure. For an assumed shape of curve the stress at initiation, $\sigma_{\max}$ and

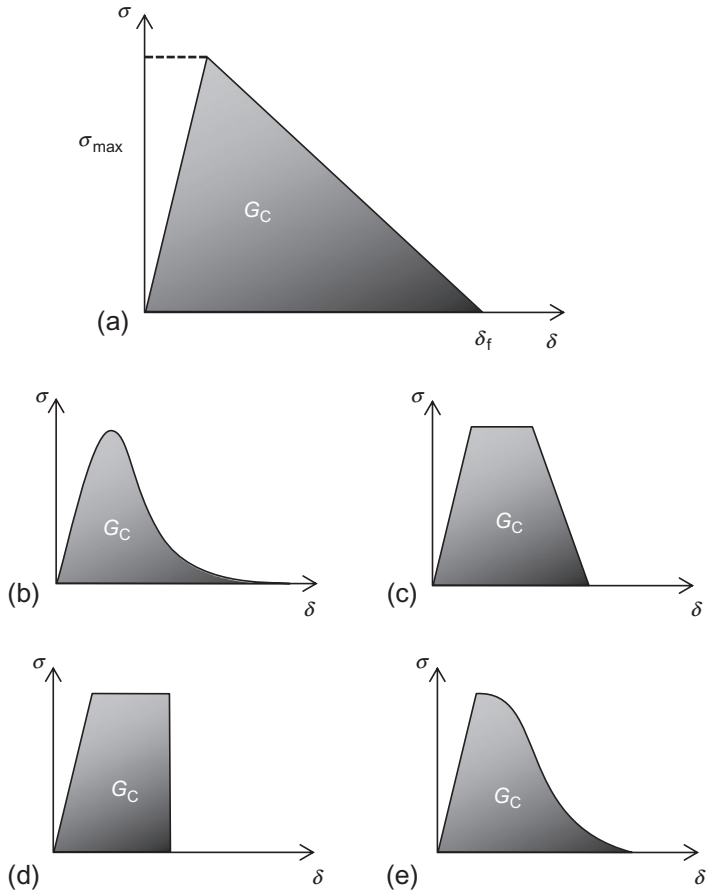

Figure 2.2 Variation of cohesive traction–displacement curves used in the literature. (a) Triangular, (b) exponential, (c) trapezoidal, (d) perfectly plastic and (e) linear/polynomial. From Hallett (2008).

displacement at failure can be set such that the energy absorbed per unit cracked area is equal to the material's critical fracture energy, G_C, thus preserving the Griffith energy balance. The crack thus initiates once the maximum stress criteria is exceeded and has fully propagated once the stress is returned to zero. This gives CZM an advantage over other fracture mechanics-based methods such as VCCT in that it can predict both initiation and propagation of a crack.

In his pioneering implementation of CZM, Hillerborg implemented it directly through corresponding forces at the relevant nodes. More commonly, CZM is implemented through special-purpose interface elements that have the required traction–displacement relationship across the interface, but no other constitutive properties. To implement such elements into a finite element analysis, they are included in the

mesh at the continuum element boundaries. This means that the crack path or multiple potential crack paths need to be known *a priori*. Thus the technique is well suited to modelling of delamination failure in laminated composites, where crack paths are constrained to occur between the plies, but can often develop simultaneously along several different ply interfaces.

There is some experimental evidence of a cohesive or process zone ahead of a crack tip in polymer and composite materials (Datta, 2005; Bradley, 1989), which takes the form of a zone of plasticity or micro-cracking. The size of this region has been found to be smaller than that predicted by closed form solutions or observed in numerical analyses, but it does show that the use of CZM for composites delamination is indeed based on physical reality. Crack bridging effects that occur during large-scale crack propagation may also effectively increase the cohesive zone length, thus accounting for some of the difference between analytical predictions and physical measurements.

2.3 Element formulations

Early implementations of interface elements for composites focused on a single mode of failure, such as mode I free-edge delamination (Schellekens and De Borst, 1993), mode I double cantilever beam (DCB) (Allix and Ladevèze, 1992) and mode II short beam shear and cut ply specimens (Cui and Wisnom, 1993). Implementations of interface elements have largely taken the form of planar two-dimensional elements, which can either be zero thickness with overlapping nodes or have a very small finite thickness, which is said to represent the thin resin-rich layer between plies. Interface elements can also be implemented in a discrete form (Wisnom and Chang, 2000; Xie and Waas, 2006) as a non-linear spring connecting adjacent nodes. Figure 2.3 shows schematically the implementation of such interface elements into a finite element mesh.

Modelling of the individual loading modes provides many useful applications, but for the general case of mixed-mode loading more often encountered in structural applications, the interaction between the modes needs to be taken into account. As for the single-mode cases, an initiation criterion is required for the onset of damage, after which the element continuously softens until the correct mixed-mode fracture

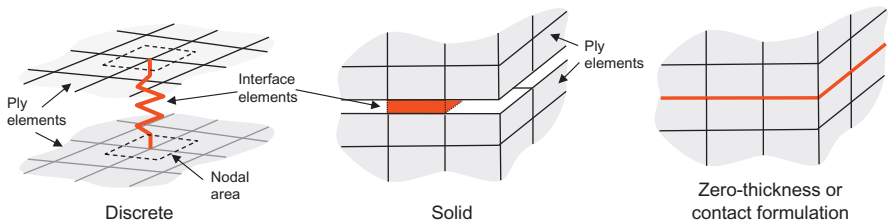

Figure 2.3 Schematic diagrams of the different formulations of interface elements. From Hallett (2008).

energy is absorbed (propagation criterion). Without a knowledge of the orientation of the crack front relative to the loading direction, it is not possible to distinguish between mode II and mode III shear loading at an individual element level. Thus in many implementations, the shear displacement is thereby treated as a resultant shear component in the plane of the interface.

A commonly used criterion for the initiation of damage is the quadratic interaction of stresses, first put forward for matrix failure by Hashin (1980) and applied to delamination by Brewer and Lagace (1988)

$$\sqrt{\left(\frac{\langle\sigma_{\mathrm{I}}\rangle}{\sigma_{\mathrm{I}}^{\max}}\right)^2+\left(\frac{\sigma_{\mathrm{II}}}{\sigma_{\mathrm{II}}^{\max}}\right)^2}=1 \tag{2.2}$$

where $\langle\cdots\rangle$ represents the McCauley brackets operator, σ_{I} the mode I stress, $\sigma_{\mathrm{I}}^{\max}$ the pure mode I initiation stress, σ_{II} the resultant shear stress and $\sigma_{\mathrm{II}}^{\max}$ the pure mode II initiation stress. This criterion has successfully been used in delamination initiation problems by Cui et al. (1992), Davila and Johnson (1993) and Camanho and Matthews (1999). More recent formulations include terms that account for the enhancement effect of through-thickness compression on mode II shear. Li et al. (2008) developed an enhancement term for both initiation and propagation, while Aymerich et al. (2008) used the enhanced initiation criterion of Hou et al. (2001).

In cases where there is a high-stress concentration or singularity, the initiation stress has been shown to be of less importance than the propagation criterion (Mi et al., 1998), but this is limited to cases in which the failure is dominated by the fracture energy absorbed. In cases where there is a relatively high ambient stress level over a larger area, the initiation criterion is also important. This was shown to be the case for overlap joints (Mi et al., 1998) and also short beam shear tests (Cui and Wisnom, 1993).

Once failure has started to initiate, it is controlled by a propagation criterion which ensures that the correct amount of energy is absorbed by each element. Since the mode I and mode II fracture energies are usually quite different for delamination, one must ensure that the propagation criterion correctly predicts the mixed-mode fracture energy throughout the mode mixity range for the material in question. One widely used propagation criterion is the Power law (Mi et al., 1998; Pinho et al., 2006; Jiang et al., 2007)

$$\left(\frac{G_{\mathrm{I}}}{G_{\mathrm{IC}}}\right)^{\alpha}+\left(\frac{G_{\mathrm{II}}}{G_{\mathrm{IIC}}}\right)^{\alpha}=1 \tag{2.3}$$

with α being an empirical parameter derived from a best fit to data from mixed-mode tests. α is generally in the range 1–2, with values of 1 proposed by Hallett and Wisnom (2006b), 1.21 by Pinho et al. (2006) and 1.23 by Borg et al. (2001).

Another popular propagation criterion is that of Benzeggagh and Kenane (1996), known as the B–K criterion:

$$G_{IC} + (G_{IIC} - G_{IC})\left(\frac{G_{II}}{G_I + G_{II}}\right)^{\eta} = G_C \tag{2.4}$$

where η is an empirically derived parameter. This has recently become more commonly used (Camanho et al., 2003; Balzani and Wagner, 2008; Guiamatsia et al., 2009; Van der Meer et al., 2012) as it has been found to fit the mixed-mode data from a greater variety of material systems. Figure 2.4 shows a mixed-mode delamination fracture toughness data set for Hexcel's IM7/8552 carbon–epoxy pre-preg system (Hansen and Martin, 1999) with both the Power law and B–K criterion fitted.

To continuously track the state of an interface element, an irreversible damage variable is usually introduced, which progresses from 0, the undamaged state, to 1, fully failed. Camanho et al. (2003) introduced a damage variable of the form

$$D = \frac{\delta^f\left(\delta - \delta^0\right)}{\delta\left(\delta^f - \delta^0\right)} \tag{2.5}$$

where D is the damage variable, δ is the maximum relative displacement at a given increment, δ^f is the displacement at failure and δ^0 is the displacement at initiation. The damage variable is then used as a multiplier on the element initial stiffness to progressively reduce the stress to zero.

Jiang et al. (2007) introduced a simpler damage variable of the form

$$D = \frac{\delta - \delta^0}{\delta^f - \delta} \tag{2.6}$$

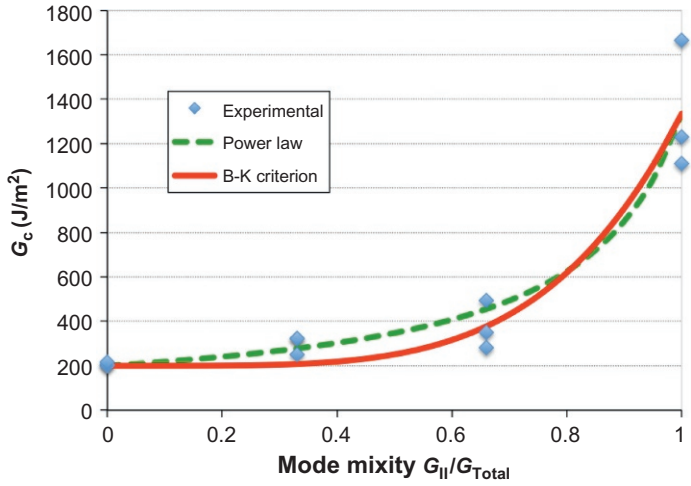

Figure 2.4 B–K and power mixed-mode laws, along with data for IM7/8552. From Hansen and Martin (1999).

which can be used as a direct multiplier on the element maximum stress. This has the advantage of varying linearly over the displacement of the element and not being dependent on initial stiffness.

Figure 2.5 shows how elements initiate failure and progressively soften as damage accumulates in the cohesive zone for a relatively simple double cantilever mode I loading case. This image also helps to illustrate the formation of the cohesive zone and variation of stress within it from zero at the crack tip to the maximum traction at initiation, defining the length of the cohesive zone, L_{CZ}.

The number of implementations of the CZM in interface elements is now quite considerable. Most of the major commercial finite element codes now have in-built cohesive interface capabilities. Perhaps the greatest variation among the different formulations is the shape of the traction–displacement curve (as noted in Figure 2.2) and also the handling of mixed-mode behaviour, which is dealt with in more detail in Section 2.5.

Due to the highly energetic and non-linear nature of failure in composite materials, numerical analyses face a significant challenge to achieve stable and converged solutions. For implicit finite element analysis, a number of different procedures have been proposed such as complex path following algorithms (Alfano and Crisfield, 2001) or viscous regularisation (Hamitouche et al., 2008), with a parameter introduced to aid convergence. Viscous regularisation induces stability in the analysis but care should be taken to ensure that excessively high values do not adversely affect global response. Other authors have adopted the use of explicit solvers to overcome difficulties with convergence in implicit analyses (Hallett and Wisnom, 2006a; Pinho et al., 2006), even though their applications have been predominantly quasi-static. Other authors

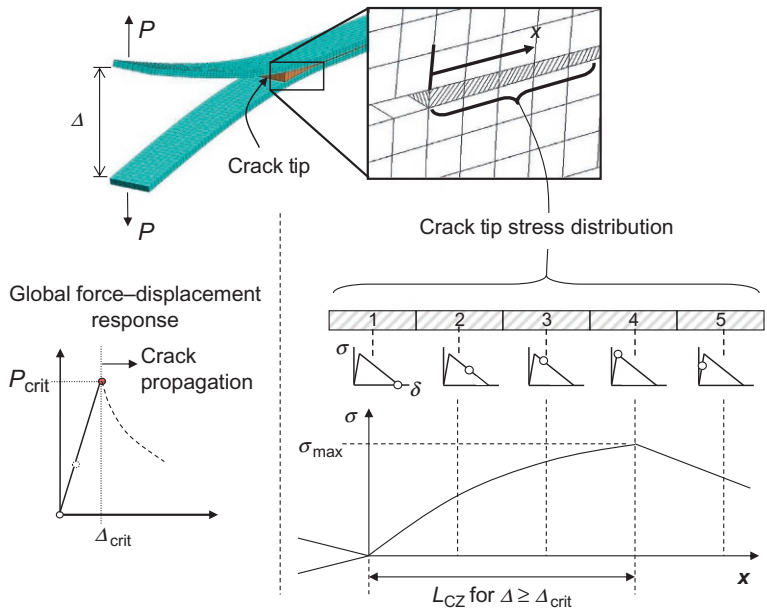

Figure 2.5 Development of the cohesive zone and associated traction–displacement behaviour. From Harper et al. (2012).

have made use of explicit finite element analysis for modelling of delamination failures due to impact or high rate loading (Aymerich et al., 2008; González et al., 2012; Bouvet et al., 2012).

For models at a larger structural scale, it is more efficient to use shell elements. However, for modelling delamination between interfaces, care needs to be taken to properly account for the rotations of the nodes and offsets. Borg et al. (2004) developed an interface element formulation specifically for use between shell elements. Johnson et al. (2001) used layers of stacked shell elements with a cohesive element formulation for delamination. For a 16-ply laminate, it was still not computationally efficient to model every interface so a reduced number of four interfaces were used with each element layer representing the quasi-isotropic sub-laminate. Heimbs et al. (2014) used a similar technique for their pre-loaded 17-ply laminate under impact loading and undertook a systematic study of 0, 2, 6 and 16 interfaces modelled with interface elements. They concluded that six interfaces provided a good compromise between accuracy and computational efficiency.

2.4 Properties and mesh size

Perhaps one of the greatest limitations of the cohesive zone method is the limitation it places on the mesh size that can be used for analysis. It has been found that it is necessary to have between two and three interface elements in the cohesive zone to accurately capture the softening ahead of the crack tip (Mi et al., 1998). Analyses that violate this condition show a characteristic stick–slip behaviour as observed in the double cantilever results shown in Figure 2.6 where the load overshoots that of the accurate solution and then fails more suddenly, resulting in an unstable and incorrect solution.

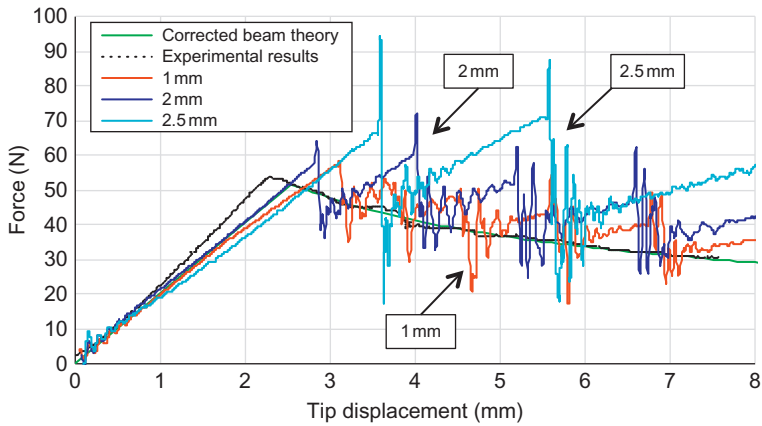

Figure 2.6 Double cantilever beam results from models with insufficiently refined mesh. From Harper and Hallett (2008).

To create a model with the correct mesh size, it is thus necessary to know the size of the cohesive zone in advance. A number of analytical formulae exist such as Equations (2.7a) and (2.7b) (Yang and Cox, 2005; Yang et al., 2006) which build on the original formulation of Hillerborg et al. (1976)

$$l_{\mathrm{ch,I}} = E'_{\mathrm{I}} \frac{G_{\mathrm{IC}}}{(\sigma_{\mathrm{I,max}})^2} \tag{2.7a}$$

$$l_{\mathrm{ch,II}} = E'_{\mathrm{II}} \frac{G_{\mathrm{IIC}}}{(\sigma_{\mathrm{II,max}})^2} \tag{2.7b}$$

where E' is an equivalent elastic modulus for orthotropic materials, whose value depends on the material's longitudinal modulus, transverse modulus, shear modulus, depth and whether plane stress or plane strain conditions exist (Yang et al., 2006). Harper and Hallett (2008) have undertaken a systematic study of the numerical cohesive zone length that occurs in the modelling of mode I, mode II and mixed-mode fracture tests. They showed that the commonly used formulae above consistently overpredict the cohesive zone length that occurs in the finite element models. They found that the modified formulae from Yang and Cox (2005) for slender laminates, which account for specimen thickness, give better results when used with a pre-multiplier of 0.5:

$$l_{\mathrm{ch,\,slender,I}} = 0.5 \left(E'_{\mathrm{I}} \frac{G_{\mathrm{IC}}}{(\sigma_{\mathrm{I,max}})^2} \right)^{1/4} h^{3/4} \tag{2.8a}$$

$$l_{\mathrm{ch,\,slender,II}} = 0.5 \sqrt{\left(E'_{\mathrm{II,\,slender}} \frac{G_{\mathrm{IIC}}}{(\sigma_{\mathrm{II,max}})^2} \right) h} \tag{2.8b}$$

where h is the laminate half-thickness and $E'_{\mathrm{II,\,slender}}$ is a mode II equivalent elastic modulus for a slender body, which takes a different form to that used in Equation (2.7b) (see Harper and Hallett, 2008 for details).

For typical carbon–epoxy composite material properties, these equations give cohesive zone lengths in the order of 1 mm for mode I and 3 mm for mode II. Thus, to have more than two elements in the cohesive zone, one has to resort to sub-millimetre element lengths in the analyses. Since the cohesive zone length is dependent on the material properties used in the analysis, properties that the results are not sensitive to can be artificially adjusted to increase the cohesive zone length and thus allow for coarser meshes. Mi et al. (1998) showed that results for cases where a high-stress concentration exists, such as composite fracture tests, are relatively insensitive to traction-separation law maximum stress. Turon et al. (2007) formalised this to show that maximum stress can be artificially reduced in fracture toughness-dominated failure cases to allow a coarser mesh to be used. This procedure should,

however, be used with care as is shown in Section 2.5, where results are strongly dependent on a variation of interface strength, due to the influence this has on overall mode mixity.

An alternative to the strategy of adjusting input parameters is to enhance the element formulations to allow for enriched shape functions. This approach was adopted by Guiamatsia et al. (2009, 2013) and applied to impact analysis using an explicit finite element formulation, where an increased mesh size will have an advantage in increasing the minimum time step required (Courant condition). It was noted, however, that as implemented in Abaqus/Explicit, it did not yield major computational efficiencies, perhaps due to inefficiencies in the user element interface used or the cost of shape function enrichment.

2.5 Mixed-mode application example

Many of the examples found in the literature available are for cases of pure mode loading. These are usually for relatively simple loading cases such as laboratory scale fracture tests. For more realistic structural applications and loading, it is likely that there will be a component of mixed-mode loading. In cases of mixed-mode loading, a mixed-mode initiation and propagation criterion is used, as shown in Equations (2.2)–(2.4). These define the interpolated traction–displacement relation for the full mixed-mode loading space, as shown in Figure 2.7 for a bilinear law.

It should be noted, however, that variation in interfacial strengths can give variable results in loading scenarios involving mixed mode, even for fracture toughness-

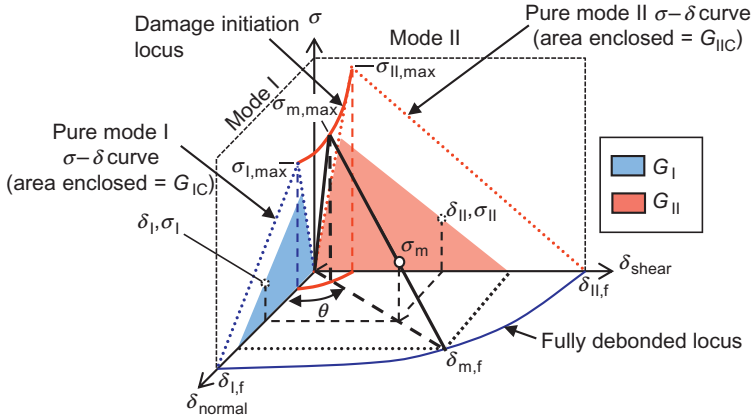

Figure 2.7 Mixed-mode cohesive element traction–displacement behaviour. From Harper and Hallett (2008).

dominated cases. This was shown in Turon et al. (2010) and Sarrado et al. (2012) where for a mixed-mode bending test, different ratios of strength between mode I and mode II gave notable variations in the global load curves. It was found that when the strengths are varied, the ratio between the mode I and mode II values needs to remain constant. The change in global load curve with interface strength is due to the fact that the mode ratio is not constant along the cohesive zone. Therefore, as the crack advances and an element enters the cohesive zone, it has an initial mode mixity, which then varies as the element progresses through the cohesive zone until final failure. This was also studied by Harper et al. (2012), who showed how the traction–displacement curve can vary from the ideal bilinear curve assumed from a constant mode ratio for each element, shown in Figure 2.8. Also shown in Figure 2.9 is the variation of mode ratio along the length of the cohesive zone for a fixed-ratio mixed-mode fracture specimen. It can be seen that as an element enters the cohesive zone from the undamaged part of the laminate, there is a high percentage of mode II. As one then moves along the length of the cohesive zone, the proportion of mode II loading reduces until it is more mode I dominated at the point of full failure. Although the mode ratio varies along the cohesive zone length, and thus also does the instantaneous energy absorption, the global behaviour still captures the correct energy absorption

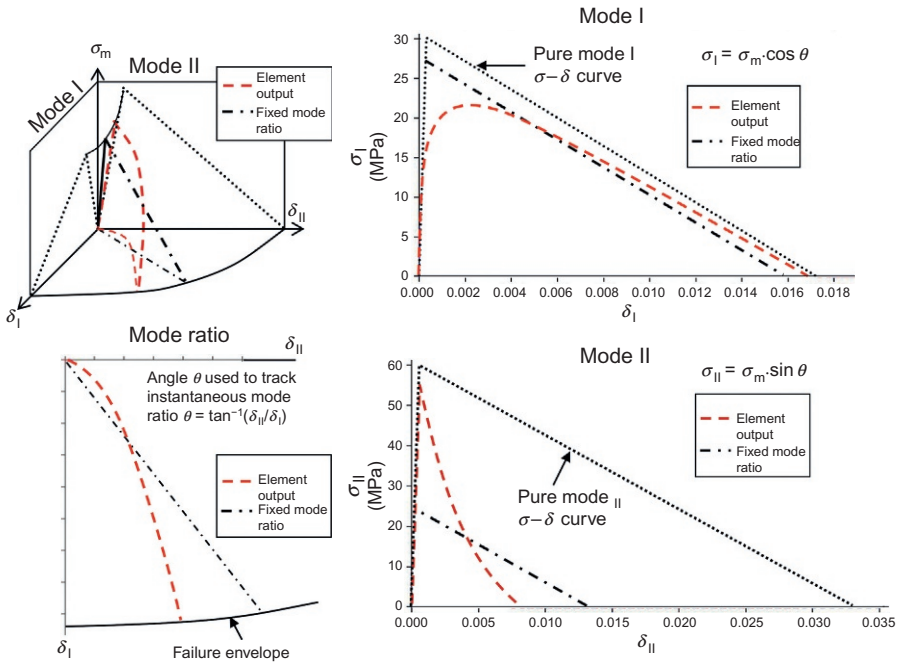

Figure 2.8 Variation from ideal traction–displacement behaviour in mixed-mode loading. From Harper et al. (2012).

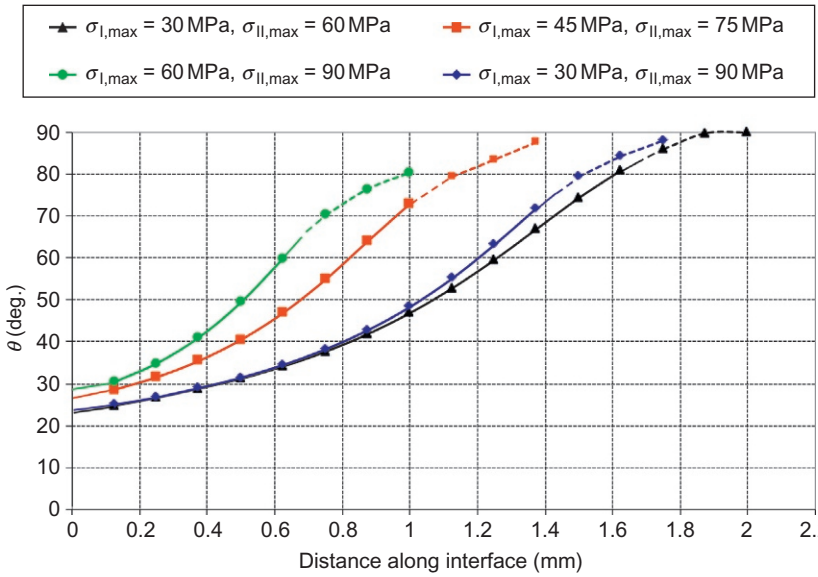

Figure 2.9 Evolution of mode mixity along the cohesive zone length ($\theta = \tan^{-1}(\delta_I/\delta_{II})$). From Harper et al. (2012).

per unit area of new crack formed. This is because it is the integrated area under the traction–displacement curve at full failure that is required to be equal to the correct mixed-mode fracture energy, which controls the propagation of the crack. Thus, although at a given point in the analysis the energy and mode ratio for an individual element might not seem correct, the overall mode ratio and energy absorbed is correct, provided the values of the interfacial strengths are within acceptable limits. A variation in cohesive strengths used affects how this mode ratio variation develops along the cohesive zone, also shown in Figure 2.9 for a variety of strength combinations.

A further example of the effect of cohesive strength on structural performance is given for a specimen made from a series of ply drops to give a tapered laminate (see Figure 2.10), loaded in tension. At each interface between plies, cohesive elements are inserted. Failure occurs by delamination, starting from the last discontinuous ply, nearest the thin end. If one compares the failure load against a reference solution obtained from VCCT, it can be seen that the same range of interfacial strengths that gave good results for a simpler DCB test, here gives a wide variety of predicted strengths (Figure 2.11). This can be explained as resulting from the variation in mode ratio that occurs during loading and failure (Harper et al., 2012), and it is only the highest values, closest to the actual material strength, that give results close to the reference solution.

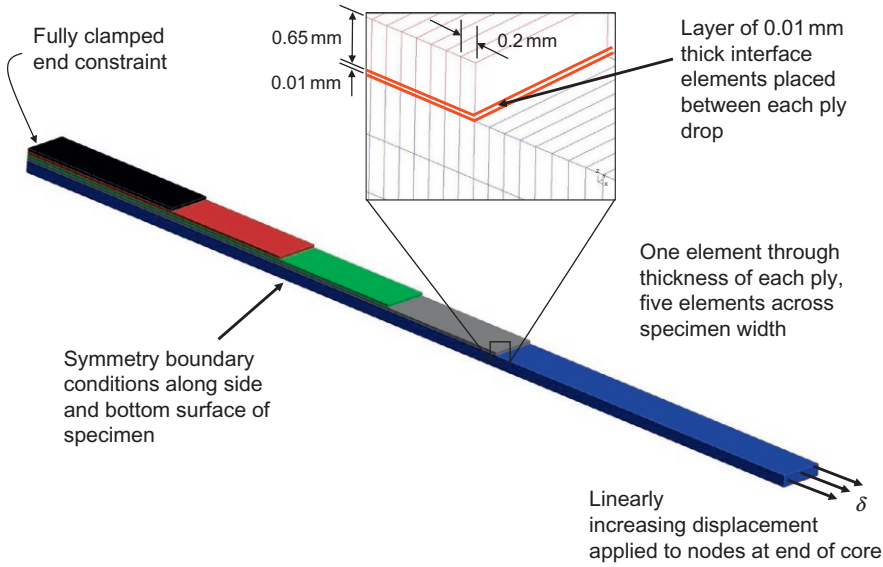

Figure 2.10 Ply drop model with interface elements between plies.
From Harper et al. (2012).

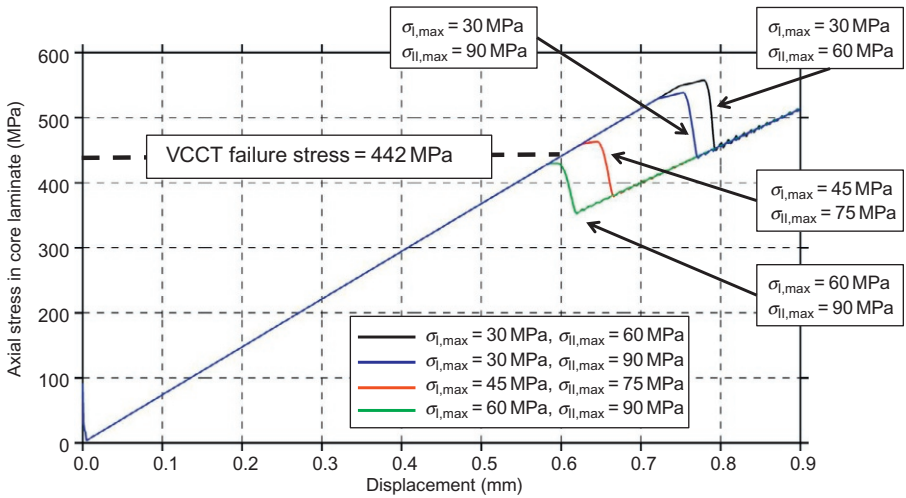

Figure 2.11 Load–displacement analyses for external ply drop model.
From Harper et al. (2012).

2.6 Delamination–matrix crack interaction

With the topic of delamination becoming more widely studied and understood, both through the use of cohesive interface element modelling and the now standardised fracture tests (ASTM, 2013a,b; ISO, 2014), research focus has moved on to more challenging topics. One such area is the interaction of delaminations with matrix cracks. In a number of cases, it has been observed that the propagation of delamination cracks through a multi-directional laminate is influenced by matrix cracks in the adjacent interfaces. This can either occur through delaminations joining up via existing matrix cracks or through a delamination kinking into the adjacent ply as it propagates. The first of these mechanisms has been observed in tensile loading of both unnotched (Wisnom et al., 2008) and notched tensile tests (Green et al., 2007). The second mechanism has been shown in Greenhalgh et al. (2009) and Ratcliffe et al. (2013) and explained to be a result of the changing sign of the shear stress relative to the orientation of the fibres in the adjacent ply.

The phenomenon of delamination migration is important in that it allows delaminations to join up and follow the most energetically favourable path, which can ultimately lead to structural failure. It is, however, relatively complex to model through finite element analysis, since it requires multiple delamination cracks and their interaction with adjacent matrix cracks to be accounted for. Hallett et al. (2008) modelled the unnotched tests of Wisnom et al. (2008) using cohesive interface elements for both delamination and matrix cracks (Figure 2.12). Interface elements were included at each interply interface for delamination and at selected locations for intraply matrix cracks. This technique was able to capture the characteristic delamination patterns, bounded by adjacent matrix cracks observed in experiments. Without the inserted matrix cracks, the predicted delamination stress would not have correlated well with the experimental results. A similar technique was also used for modelling of a comprehensive programme of testing of open hole tensile tests, with very good correlation (Hallett et al., 2009). This work required the pre-insertion of potential matrix cracks along known paths in advance of the analysis. It was shown in Chen et al. (2013) through modelling of the same tests that using a continuum damage model for the matrix cracks does not give very accurate results in the case of strong interaction

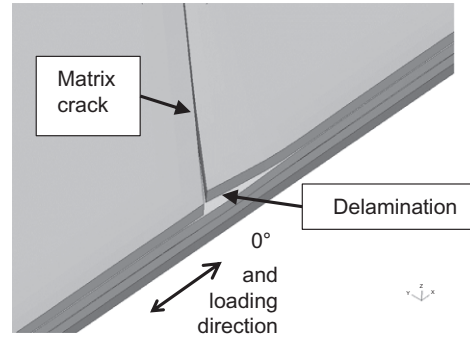

Figure 2.12 Finite element model showing interaction between matrix crack and delamination.
From Hallett et al. (2008).

between matrix cracks and delamination. More advanced techniques for automated modelling of matrix cracks through extended finite element methods have been put forward and shown to give good results (van der Meer and Sluys, 2009; Ling et al., 2009; Iarve et al., 2011; Van der Meer et al., 2012). These are discussed more fully in other chapters of this book.

2.7 Conclusions

Cohesive interface elements are becoming a widely used and powerful tool for modelling delamination failure in composite materials, due to their ease of use and ability to model both initiation and propagation in a single analysis. The use of composites in structural applications is rapidly increasing, and there is a requirement for analysis techniques to predict their failure under a wide range of loading scenarios. Cohesive interface elements can meet this requirement when used with care, taking account of some of the specific points noted in this chapter. In particular, the need for a sufficiently refined mesh is noted and caution should be used in cases where the interface strength is adjusted to allow for larger mesh sizes. The case of mixed-mode loading adds additional complexity. Cohesive interface elements are now available in most commercial finite element software packages, but further development challenges remain, such as applications to large-scale structural analysis (given the mesh size limitations) and interactions with matrix cracks for modelling delamination migration.

References

Alfano, G., 2006. On the influence of the shape of the interface law on the application of cohesive-zone models. Compos. Sci. Technol. 66 (6), 723–730.

Alfano, G., Crisfield, M.A., 2001. Finite element interface models for the delamination analysis of laminated composites: mechanical and computational issues. Int. J. Numer. Methods Eng. 50 (7), 1701–1736.

Allix, O., Ladevèze, P., 1992. Interlaminar interface modelling for the prediction of delamination. Compos. Struct. 22 (4), 235–242.

ASTM, 2013a. Standard test method for mode I interlaminar fracture toughness of unidirectional fiber-reinforced polymer matrix composites1. ASTM Standard D5528.

ASTM, 2013b. Standard test method for mixed mode I mode II interlaminar fracture toughness of unidirectional fiber reinforced polymer matrix composites. D6671 Standard. Available at: http://www.astm.org/Standards/D6671.htm (Accessed January 20, 2015).

Aymerich, F., Dore, F., Priolo, P., 2008. Prediction of impact-induced delamination in cross-ply composite laminates using cohesive interface elements. Compos. Sci. Technol. 68 (12), 2383–2390.

Balzani, C., Wagner, W., 2008. An interface element for the simulation of delamination in unidirectional fiber-reinforced composite laminates. Eng. Fract. Mech. 75 (9), 2597–2615.

Barrenblatt, G.I., 1962. The mathematical theory of equilibrium of cracks in brittle fracture. Adv. Appl. Mech. 7, 55–129.

Benzeggagh, M.L., Kenane, M., 1996. Measurement of mixed-mode delamination fracture toughness of unidirectional glass/epoxy composites with mixed-mode bending apparatus. Compos. Sci. Technol. 56, 439–449.

Borg, R., Nilsson, L., Simonsson, K., 2001. Simulation of delamination in fiber composites with a discrete cohesive failure model. Compos. Sci. Technol. 61 (5), 667–677.

Borg, R., Nilsson, L., Simonsson, K., 2004. Simulating DCB, ENF and MMB experiments using shell elements and a cohesive zone model. Compos. Sci. Technol. 64 (2), 269–278.

Bouvet, C., Rivallant, S., Barrau, J.J., 2012. Low velocity impact modeling in composite laminates capturing permanent indentation. Compos. Sci. Technol. 72 (16), 1977–1988.

Bradley, W.L., 1989. Relationship of matrix toughness to interlaminar fracture toughness. Friedrich, K. (Ed.), Application of Fracture Mechanics to Composite Materials, vol. 6. Composite Materials Series. Elsevier. In: Application of Fracture Mechanics to Composite Materials, pp. 159–187 (Chapter 5).

Brewer, J.C., Lagace, P.A., 1988. Quadratic stress criterion for initiation of delamination. J. Compos. Mater. 22 (12), 1141–1155.

Camanho, P.P., Matthews, F.L., 1999. Delamination onset prediction in mechanically fastened joints in composite laminates. J. Compos. Mater. 33, 906–927.

Camanho, P.P., Davila, C.G., De Moura, M.F., 2003. Numerical simulation of mixed-mode progressive delamination in composite materials. J. Compos. Mater. 37 (16), 1415–1438.

Chen, B.Y., et al., 2013. Numerical analysis of size effects on open-hole tensile composite laminates. Compos. A Appl. Sci. Manufactur. 47, 52–62.

Cui, W.C., Wisnom, M.R., 1993. A combined stress-based and fracture-mechanics-based model for predicting delamination in composites. Composites 24 (6), 467–474.

Cui, W.C., Wisnom, M.R., Jones, M., 1992. A comparison of failure criteria to predict delamination of unidirectional glass epoxy specimens waisted through the thickness. Composites 23 (3), 158–166.

Datta, S., 2005. Investigation of the Micromechanics of Delamination in Fibre Reinforced Composites. Imperial College, London.

Davila, C.G., Johnson, E.R., 1993. Analysis of delamination initiation in postbuckled dropped-Ply laminates. AIAA J. 31 (4), 721–727.

Dugdale, D.S., 1960. Yielding of steel sheets containing slits. J. Mech. Phys. Solids 8 (2), 100–104.

González, E.V., et al., 2012. Simulation of drop-weight impact and compression after impact tests on composite laminates. Compos. Struct. 94 (11), 3364–3378.

Green, B.G., Wisnom, M.R., Hallett, S.R., 2007. An experimental investigation into the tensile strength scaling of notched composites. Compos. A Appl. Sci. Manufactur. 38 (3), 867–878.

Greenhalgh, E.S., Rogers, C., Robinson, P., 2009. Fractographic observations on delamination growth and the subsequent migration through the laminate. Compos. Sci. Technol. 69 (14), 2345–2351.

Guiamatsia, I., et al., 2009. Decohesion finite element with enriched basis functions for delamination. Compos. Sci. Technol. 69 (15–16), 2616–2624.

Guiamatsia, I., et al., 2013. Enriched finite elements for the efficient prediction of impact-induced damage in composite laminates. Compos. Sci. Technol. 79, 87–96.

Hallett, S.R., Wisnom, M.R., 2006a. Experimental investigation of progressive damage and the effect of layup in notched tensile tests. J. Compos. Mater. 40 (2), 119–141.

Hallett, S.R., Wisnom, M.R., 2006b. Numerical investigation of progressive damage and the effect of layup in notched tensile tests. J. Compos. Mater. 40 (14), 1229–1245.

Hallett, S.R., et al., 2008. Modelling the interaction between matrix cracks and delamination damage in scaled quasi-isotropic specimens. Compos. Sci. Technol. 68 (1), 80–89.
Hallett, S.R., et al., 2009. An experimental and numerical investigation into the damage mechanisms in notched composites. Compos. A Appl. Sci. Manufactur. 40 (5), 613–624.
Hamitouche, L., Tarfaoui, M., Vautrin, A., 2008. An interface debonding law subject to viscous regularization for avoiding instability: application to the delamination problems. Eng. Fract. Mech. 75 (10), 3084–3100.
Hansen, P., Martin, R.H., 1999. DCB, 4ENF and MMB delamination characterization of S2/8552 and IM7/8552. MERL Report No. N68171-98-M-5177.
Harper, P.W., Hallett, S.R., 2008. Cohesive zone length in numerical simulations of composite delamination. Eng. Fract. Mech. 75 (16), 4774–4792.
Harper, P.W., Sun, L., Hallett, S.R., 2012. A study on the influence of cohesive zone interface element strength parameters on mixed mode behaviour. Compos. Part A 43 (4), 722–734.
Hashin, Z., 1980. Failure criteria for unidirectional fiber composites. J. Appl. Mech. 47, 329.
Heimbs, S., et al., 2014. High velocity impact on preloaded composite plates. Compos. Struct. 111, 158–168.
Hillerborg, A., Modéer, M., Petersson, P.-E., 1976. Analysis of crack formation and crack growth in concrete by means of fracture mechanics and finite elements. Cement Concrete Res. 6 (6), 773–781.
Hou, J., Petrinic, N., Ruiz, C., 2001. A delamination criterion for laminated composites under low-velocity impact. Compos. Sci. Technol. 61 (14), 2069–2074.
Iarve, E.V., et al., 2011. Mesh-independent matrix cracking and delamination modeling in laminated composites. Int. J. Numer. Methods Eng. 88 (8), 749–773.
ISO, 2014. Fibre-reinforced plastic composites – determination of the mode II fracture resistance for unidirectionally reinforced materials using the calibrated end-loaded split (C-ELS) test and an effective crack length approach. ISO 15114 Standard. Available at: http://www.iso.org/iso/catalogue_detail.htm?csnumber=55357 (Accessed January 20, 2015).
Jiang, W.G., et al., 2007. A concise interface constitutive law for analysis of delamination and splitting in composite materials and its application to scaled notched tensile specimens. Int. J. Numer. Methods Eng. 69 (9), 1982–1995.
Johnson, A., Pickett, A., Rozycki, P., 2001. Computational methods for predicting impact damage in composite structures. Compos. Sci. Technol. 61 (15), 2183–2192.
Krueger, R., 2004. Virtual crack closure technique: history, approach, and applications. Appl. Mech. Rev. 57 (2), 109.
Li, X., Hallett, S.R., Wisnom, M.R., 2008. Predicting the effect of through-thickness compressive stress on delamination using interface elements. Compos. A Appl. Sci. Manufactur. 39 (2), 218–230.
Ling, D.S., Yang, Q.D., Cox, B., 2009. An augmented finite element method for modeling arbitrary discontinuities in composite materials. Int. J. Fract. 156 (1), 53–73.
Mi, Y., et al., 1998. Progressive delamination using interface elements. J. Compos. Mater. 32, 1246–1272.
Pinho, S.T., Iannucci, L., Robinson, P., 2006. Formulation and implementation of decohesion elements in an explicit finite element code. Compos. A Appl. Sci. Manufactur. 37 (5), 778–789.
Ratcliffe, J.G., Czabaj, M.W., Obrien, T.K., 2013. Characterizing delamination migration in carbon/epoxy tape laminates. NASA/TM-2013-218028.

Sarrado, C., et al., 2012. Assessment of energy dissipation during mixed-mode delamination growth using cohesive zone models. Compos. A Appl. Sci. Manufactur. 43 (11), 2128–2136.

Schellekens, J.C.J., De Borst, R., 1993. A non-linear finite element approach for the analysis of mode-I free edge delamination in composites. Int. J. Solids Struct. 30 (9), 1239–1253.

Shet, C., Chandra, N., 2004. Effect of the shape of T-delta cohesive zone curves on the fracture response. Mech. Adv. Mater. Struct. 11 (3), 249–275.

Turon, A., et al., 2007. An engineering solution for mesh size effects in the simulation of delamination using cohesive zone models. Eng. Fract. Mech. 74 (10), 1665–1682.

Turon, A., et al., 2010. Accurate simulation of delamination growth under mixed-mode loading using cohesive elements: definition of interlaminar strengths and elastic stiffness. Compos. Struct. 92 (8), 1857–1864.

Van der Meer, F.P., Sluys, L.J., 2009. A phantom node formulation with mixed mode cohesive law for splitting in laminates. Int. J. Fract. 158 (2), 107–124.

Van der Meer, F.P., et al., 2012. Computational modeling of complex failure mechanisms in laminates. J. Compos. Mater. 46, 603–623.

Wisnom, M.R., 2012. The role of delamination in failure of fibre-reinforced composites. Philos. Trans. A Math. Phys. Eng. Sci. 370 (1965), 1850–1870.

Wisnom, M.R., Chang, F.K., 2000. Modelling of splitting and delamination in notched cross-ply laminates. Compos. Sci. Technol. 60 (15), 2849–2856.

Wisnom, M.R., Khan, B., Hallett, S.R., 2008. Size effects in unnotched tensile strength of unidirectional and quasi-isotropic carbon/epoxy composites. Compos. Struct. 84 (1), 21–28.

Xie, D., Waas, A.M., 2006. Discrete cohesive zone model for mixed-mode fracture using finite element analysis. Eng. Fract. Mech. 73 (13), 1783–1796.

Yang, Q.D., Cox, B., 2005. Cohesive models for damage evolution in laminated composites. Int. J. Fract. 133 (2), 107–137.

Yang, Q.D., et al., 2006. Fracture length scales in human cortical bone: the necessity of nonlinear fracture models. Biomaterials 27 (9), 2095–2113.

Interface elements for fatigue-driven delaminations in advanced composite materials

3

A. Turon*, B. Bak†, E. Lindgaard†, C. Sarrado*, E. Lund†
*University of Girona, Girona, Spain; †Aalborg University, Aalborg East, Denmark

3.1 Introduction and motivation

In laminated composite materials, the fatigue process involves several damage mechanisms that result in the degradation of the structure. However, the simulation of the mechanical response of polymer–matrix fiber-reinforced composites to fatigue loads remains an unsolved challenge. The complex interactions between the various failure mechanisms and the parameters describing the fatigue loads have hindered the advance of robust computational design tools to deal with this case.

One of the most important fatigue damage mechanisms is the interlaminar damage (delamination). To account for delaminations in the safety assessment of an aircraft, reliable computational tools are required to assess the occurrence of static- and fatigue-driven delaminations within the structure and the effect on the structural integrity. The development of such computational methods represents a scientific challenge. While several proposals to account for delamination under static loads have shown their efficiency in the analysis of different load cases, simulation tools for fatigue delamination are limited, and their predictive capabilities are still questionable (Bak et al., 2014; Pascoe et al., 2013).

Fatigue delamination is studied at three different categories (Bak et al., 2014): initiation, onset, and propagation. Initiation is defined as the first occurrence of a new delamination in a pristine material. Onset is defined as the load required to start the growth of an existing crack, and propagation refers to crack growth. Although there are different tests to characterize the three different categories, their level of development is different. For delamination initiation, there is a limited understanding of the physical mechanisms involved and no consolidated experimental tests exist. Delamination onset is addressed through curves that relate load level to the number of cycles for an existing crack to begin to grow. Delamination propagation has deserved more efforts than onset and initiation. The analysis of the experimental data for delamination propagation is widely made using Paris law, such as models for the crack growth rate $\mathrm{d}a/\mathrm{d}N$.

The delamination models available in the literature are divided into the following three categories (Bak et al., 2014): (i) initiation of delamination cracks in undamaged laminates; (ii) no-growth criteria for existing delamination cracks; and (iii) propagation of existing delamination cracks. The models for initiation of delamination describe the start of interface damage or delamination cracks

Numerical modelling of failure in advanced composite materials. http://dx.doi.org/10.1016/B978-0-08-100332-9.00003-7
Copyright © 2015 Elsevier Ltd. All rights reserved.

in areas not connected to any preexisting delamination cracks. The formulations of the models for initiation of delamination are based on damage mechanics, strength of materials, or cohesive zone model (CZM) formulations that mix concepts of damage mechanics and fracture mechanics. No-growth and propagation models describe the behavior of existing delamination cracks. The formulation of the no-growth criteria for delamination cracks is based on linear elastic fracture mechanics (LEFM) approaches, while the formulation of the propagation models is based on either LEFM or CZMs. A recent review of the different existing models can be found in Bak et al. (2014).

The number of models for modeling delamination initiation under fatigue loading is very scarce. This can be related to the fact that initiation of delamination is often governed by material imperfections and/or variations in material properties, which is very difficult to characterize from an experimental point of view. In this topic, the models from May and Hallett (2010, 2011), for example, can be considered.

On the other hand, there exist several CZMs for modeling delamination propagation (Nguyen et al., 2001; Yang et al., 2001, 2004; Roe and Siegmund, 2003; Maiti and Geubelle, 2005; Robinson et al., 2005; Koutsourelakis et al., 2006; Turon et al., 2007b; Tumino and Cappello, 2007; Pirondi and Moroni, 2010; Naghipour et al., 2011; Beaurepaire and Schueller, 2011; Kawashita and Hallett, 2012; Landry and LaPlante, 2012; Bak et al., 2015). Actually, most of these fatigue damage formulations are extensions of the cohesive laws for quasi-static loading. The fatigue models are formulated such that an additional criterion for development of the internal variables, the fatigue model, is added to the quasi-static formulation.

The CZM fatigue models have been grouped in two different families: load envelope methods and loading–unloading hysteresis methods (Bak et al., 2014). The loading–unloading hysteresis methods are characterized by modeling the whole cyclic variation of the applied load to determine the damage per cycle. Hysteresis methods (Nguyen et al., 2001; Yang et al., 2001, 2004; Roe and Siegmund, 2003; Maiti and Geubelle, 2005) are formulated using pointwise information; however, a data reduction scheme to obtain model parameters has not been formulated. On the other side, the load envelope methods are characterized by modeling the maximum load of the cycle only. Load envelope methods (Robinson et al., 2005; Koutsourelakis et al., 2006; Turon et al., 2007b; Tumino and Cappello, 2007; Pirondi and Moroni, 2010; Naghipour et al., 2011; Beaurepaire and Schueller, 2011; Kawashita and Hallett, 2012; Landry and LaPlante, 2012; Bak et al., 2015) are those that have attracted the most attention in the last decade and present a higher degree of consolidation. Load envelope methods are mainly developed to simulate delamination propagation, and almost all of them are calibrated using experimental Paris law curves.

In this chapter, we present an extension of a quasi-static CZM to simulate fatigue loading. The model relates damage accumulation to the number of load cycles while taking into account the loading conditions (load ratio, R, energy release rate, G, and mode ratio). When used in a structural analysis, the model can simulate the dependence of the crack growth rate on these parameters. Moreover, the model is able to

predict fatigue delamination in specimens without initial cracks, provided there are regions with discontinuities or stress concentration regions, such as holes and ply drops. In addition, a procedure to use experimental onset curves for calibrating the model instead of the Paris law data is developed. Finally, the model is used to simulate fatigue loading in different load scenarios.

3.2 Extension of CZMs for modeling fatigue loading

Most of the fatigue damage formulations are extensions of the cohesive laws for quasi-static loading. Although many different cohesive laws for quasi-static loading exist, the fatigue models are all based on either bilinear or exponential cohesive laws for quasi-static loading. The governing properties of both types of laws are the critical energy release rate G_c, the onset point of softening (Δ^o, τ^o) and the critical opening Δ^c for which the cohesive tractions are reduced to zero. To ensure irreversibility, unloading from any point on the cohesive law occurs in a linear elastic manner. Reloading is likewise linear until the cohesive law is once again reached and then follows the cohesive law. Most of the quasi-static formulations, on which the fatigue models are based (Yang et al., 2001; Nguyen et al., 2001; Maiti and Geubelle, 2005; Robinson et al., 2005; Koutsourelakis et al., 2006; Turon et al., 2007b; Tumino and Cappello, 2007; Pirondi and Moroni, 2010; Harper and Hallett, 2010; Naghipour et al., 2011; Beaurepaire and Schueller, 2011; Kawashita and Hallett, 2012; Landry and LaPlante, 2012; Bak et al., 2015), unload linear elastically to $\Delta = 0$ while some (Roe and Siegmund, 2003; Abdul-Baqi et al., 2005) unload to $\Delta > 0$.

To keep track of this irreversibility, the models make use of damage variables or, in a more general understanding, internal variables, which define this unloading and reloading below the cohesive law. Examples of these internal variables used in the quasi-static models, on which the fatigue models are based, are the loading stiffness (Yang et al., 2001; Nguyen et al., 2001; Maiti and Geubelle, 2005; Abdul-Baqi et al., 2005; Beaurepaire and Schueller, 2011) and damage variables that degrade the onset traction (Khoramishad et al., 2010) or the initial stiffness of the cohesive law (Robinson et al., 2005; Turon et al., 2007b; Pirondi and Moroni, 2011; Bak et al., 2015).

All the fatigue models are formulated so that an additional criterion for development of the internal variables, the fatigue model, is added to the quasi-static formulation. Each fatigue CZM formulation works in a different way, but common to them all is that the resulting traction–separation relation in general follows another path than that defined by the quasi-static cohesive law, except for the method proposed by Bak et al. (2015).

In this chapter, an envelope load damage model based on the work of Turon et al. (2006, 2007a,b) is used to simulate fatigue loading in specimens with and without initial cracks.

3.2.1 Quasi-static model

The quasi-static model is built up using a bilinear constitutive equation (see Figure 3.1). An equivalent mixed-mode cohesive law is defined in the form of:

$$\tau = (1 - D)K\lambda \tag{3.1}$$

where K is a penalty stiffness of the interface, λ is a norm of the displacement jumps, and D is a damage variable. Under crack closure during load reversal, the constitutive model prevents interpenetration of the faces of the crack by restoring the normal stiffness of the interface even in the presence of damage.

The model is developed in the framework of the irreversible process of thermodynamics, and the internal variable governing the degradation process of the quasi-static model, r, is defined as

$$r = \frac{\lambda - \Delta^{o}}{\Delta^{c} - \Delta^{o}} \tag{3.2}$$

where Δ^{o} and Δ^{c} are the onset and critical displacement jumps for a given mode mixity. r can be interpreted as the ratio between the energy dissipated during the degradation process and the fracture toughness (Turon et al., 2007b).

The relation between the damage and the internal variable r is

$$D = \frac{\Delta^{c}}{\lambda} r \tag{3.3}$$

The specific details of the kinematics, formulation, and implementation of the quasi-static damage model can be found in Turon et al. (2006).

3.2.2 Load envelope fatigue model

The extension of the quasi-static CZM formulation for fatigue loading is often done by defining an evolution of damage variables of the model with the number of cycles. Most of the models available in the literature divide the damage rate into two terms: a part that is related to fatigue damage, $\dot{D}_{f}$, and a part that is related to quasi-static

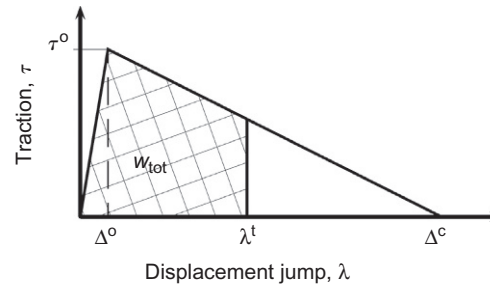

Figure 3.1 Bilinear cohesive law and total specific work, w_{tot}, at a given displacement jump, λ^{t}.

damage, $\dot{D}_s$. The fatigue damage term $\dot{D}_f$ develops according to a fatigue damage rate model, and $\dot{D}_s$ develops according to the quasi-static cohesive law. The total damage rate is the sum of the two (de Andrés et al., 1999):

$$\dot{D} = \dot{D}_s + \dot{D}_f \tag{3.4}$$

In the literature, there are different damage rate models $\dot{D}_f$, some of which are summarized in Table 3.1. The current existing models can be divided into two groups: (i) models that have to be calibrated by fitting the numerical simulations with the experimental data on simple tests and (ii) models with parameters that can be obtained directly from standard tests.

For the first group, the first model to appear specifically for delamination propagation in composite laminates under high-cycle fatigue was proposed by Robinson et al. (2005) and later extended with mode-mixity capability by Tumino and Cappello (2007). Both models are formulated in a pure damage mechanics sense,

Table 3.1 Overview of some of the fatigue damage rate models

Authors	Fatigue damage rate $\frac{dD_f}{dN}$	Nomenclature	Pointwise evaluation
Robinson et al. (2005)	$\frac{C}{1+\beta} e^{\gamma D} \lambda^{1+\beta}$	γ, β, C fitting parameters	✓
Turon et al. (2007a,b)	$\frac{1}{l_{cz}} \frac{[\Delta^c(1-D)+D\Delta^o]^2}{\Delta^c \Delta^o} P(w_{tot})$	l_{cz}: length of the cohesive zone. $P(w_{tot})$: Paris law as a function of the total specific work of each material point	✓
Pirondi and Moroni (2010)	$\frac{1}{l_{cz}} P(G)$	$P(G)$: Paris law as a function of the energy release rate G	✗
Harper and Hallett (2010)	$\frac{1-D_s-D_{f,u}}{a_{fat}} P(w_{tot})$	a_{fat}: length of the fatigue part of the cohesive zone. $D_{f,u}$: fatigue damage correction term for the "quasi-static" part of the cohesive zone	✓
Kawashita and Hallett (2012)	$\frac{1-D}{\Delta N_f}$	ΔN_f: number of cycles to propagate crack through element	✓
Bak et al. (2015)	$(F_\beta \, \partial\beta/\partial\alpha + F_\lambda \, \partial\lambda/\partial\alpha) P(G)$	β: mode-mixity variable. F_β, F_λ: functions related to the rate of change of β and λ, respectively. $P(G)$: Paris law as a function of the energy release rate G	✗

which implies that the damage rate at a given point is dependent only on the displacement at the very same point. Both models are based on the formulation of the strain-based continuum damage mechanics fatigue model proposed by Peerlings et al. (2000). However, the model parameters need to be determined by calibrating the parameters in simulations to match the crack growth rate observed in experiments.

Turon et al. (2007a,b) introduced a model that links the evolution of the damage variable with a Paris law-like model. The evolution of the damage variable is related to a crack growth rate that can be measured experimentally and to the length of the cohesive zone ahead of the crack tip. The estimation of the length of the cohesive zone can be performed numerically or using analytical expressions. In the first model presented by Turon et al. (2007b), the length of the cohesive zone was estimated using Rice's (1980) solution:

$$l_{cz} = \frac{9\pi E_3 G_c}{32(\tau^o)} \tag{3.5}$$

However, it has been demonstrated that this expression is not accurate, especially for slender bodies (Harper and Hallett, 2008; Soto et al., 2014). In a recent work, Soto et al. (2014) obtained a very accurate expression for the cohesive zone length, either for isotropic or orthotropic materials, and valid under mode I and mode II loading. The expression reads:

$$l_{cz} = \left(\frac{1}{l^o_{cz}} + \frac{1}{l^\infty_{cz}}\right)^{-1} \tag{3.6}$$

where l^∞_{cz} is the Hillerborg's constant for infinite bodies:

$$l^\infty_{cz} = \frac{E G_c}{(\tau^o)} \tag{3.7}$$

and l^o_{cz} stands for the length of the cohesive zone for slender bodies. The expressions from Smith (1989) and Massabo and Cox (1999) are used here for mode I and mode II loading:

$$l^o_{czI} = \left(\frac{1}{2}\frac{E_1 G_{Ic}}{(\tau^0_1)}\right)^{1/4} h^{3/4}, \quad l^o_{czII} = \sqrt{\frac{E_{II} G_{IIc}}{(\tau^0_{II})}} h \tag{3.8}$$

Under fatigue loading subcritical crack growth occurs, that is, the cohesive zone is not completely formed once the crack starts to propagate. Therefore, to estimate the length of the cohesive zone under fatigue loading, the fracture toughness G_c is replaced in previous equations by the energy release rate G. The energy release rate can be computed using, for example, the J-integral approach. This has been done in some models available in the literature (Pirondi and Moroni, 2010, Bak et al., 2015). However, in the model presented here, this evaluation is performed pointwise, that is, using the total specific work of each material point w_{tot} instead of the energy release rate G

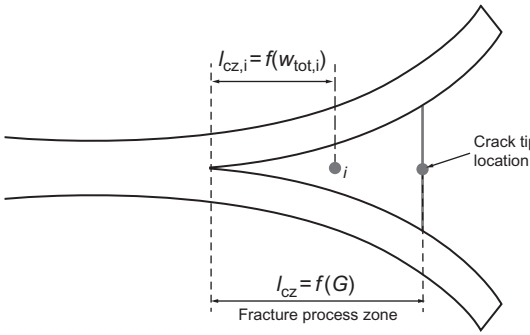

Figure 3.2 Interpretation of the introduced length measure within the cohesive zone computed at a material point "*i*."

(see Figure 3.1). The length of the cohesive zone is computed at each material point within the zone by replacing G_c by w_{tot}. This length measure, which is a field quantity of the cohesive zone, can be interpreted as the distance from each point in the cohesive zone to the crack tip (when assuming self-similar crack growth; see Figure 3.2).

Crack growth rate is then written as:

$$P(w_{tot}) = \begin{cases} C\left(\frac{w_{tot}(1-R^2)}{G_c}\right)^m, & G_{th} < w_{tot} < G_c \\ 0, & \text{otherwise} \end{cases} \tag{3.9}$$

where R is equal to the load ratio (Bak et al., 2014), and G_{th}, C, and m are parameters obtained from experimental results, as described in the next section.

3.2.3 Determination of model parameters

The parameters required to feed the fatigue model (G_{th}, C, and m) have to be linked to experimental data. The most straightforward approach is to obtain them directly from experimental da/dN curves.

The typical pattern of the crack growth rate is shown in Figure 3.3, where three regions can be distinguished. In region I, crack growth is not observed if the maximum energy release rate is smaller than the fatigue threshold of the energy release rate, G_{th}. In region III, the crack growth rate increases because the maximum energy release rate approaches the fracture toughness. Tearing fracture controls the crack growth rate in region III instead of fatigue propagation. In region II, a linear relation in the log–log space is often observed. This linear relation is usually described using a Paris law-like model:

$$\frac{da}{dN} = C\left(\frac{\Delta G}{G_c}\right)^m \tag{3.10}$$

The parameters C and m depend on the mode ratio G_{II}/G and pure mode parameters (C_I, C_{II}, m_I, m_{II}) (Blanco, 2005):

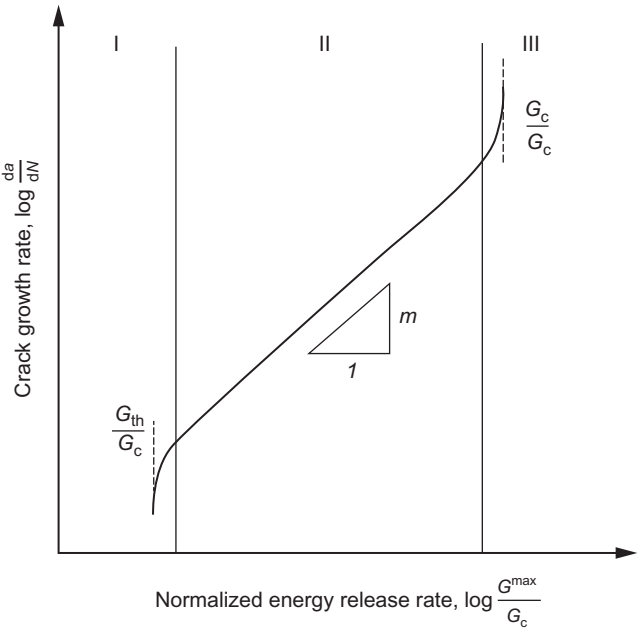

Figure 3.3 Typical crack growth rate regions.

$$\log C = \log C_I + \left(\frac{G_{II}}{G}\right)\log C_m + \left(\frac{G_{II}}{G}\right)^2 \log \frac{C_{II}}{C_m C_I}$$
$$m = m_I + m_m\left(\frac{G_{II}}{G}\right) + (m_{II} - m_I - m_m)\left(\frac{G_{II}}{G}\right)^2 \tag{3.11}$$

where C_m and m_m are fitting parameters that must be determined by curve-fitting experimental data and $G = G_I + G_{II}$.

The energy release rate threshold is also mode ratio dependent, and the following expression is used to describe it (Turon et al., 2007a,b):

$$G_{th} = G_{Ith} + (G_{IIth} - G_{Ith})\left(\frac{G_{II}}{G}\right)^{\eta_2} \tag{3.12}$$

where G_{Ith} and G_{IIth} are pure mode quantities and η_2 is a fitting parameter.

Making the assumption that the local development of the fatigue damage is comparable to the macroscopic crack growth rate, Equations (3.11) and (3.12) can be used to feed the numerical model by replacing G by w_{tot} (e.g., G_{II} by $w_{tot,II}$). This assumption circumvents the need for the more computationally complicated J-integral evaluation of the energy release rate G.

3.2.3.1 Estimation of Paris law parameters from onset curves

The experimental determination of the Paris law curves and the fatigue threshold of the energy release rate G_{th} using propagation tests require monitoring of crack extension with the number of cycles, involving a large workload. In contrast, onset curves are more easily obtained because it is not necessary to monitor crack extension. Actually, the only standard to determine delamination fatigue properties for composite materials is the ASTM Standard D6115 that defines the delamination onset for mode I fatigue loading. The curves relating the number of cycles to delamination onset for different levels of the applied energy release rate can be expressed in the form:

$$\frac{G^{\max}}{G_c} = \varsigma N_o^{-\rho} \tag{3.13}$$

where $G^{\max}$ is the maximum applied energy release rate over the load cycle, N_o are the number of cycles to delamination onset, and ς and ρ are curve-fitting parameters.

The number of cycles to delamination onset, N_o, according to the ASTM Standard D6115, is determined as the cycles needed to increase the compliance of the specimen by 1% or 5%. An increase of the specimen compliance implies an increase of the effective crack length. For the double cantilever beam (DCB) test, the compliance of the specimen is obtained as (Blanco, 2005):

$$S_I = \frac{8a^3}{bE_{11}h^3} \tag{3.14}$$

where a is the effective crack length, E_{11} is the Young's modulus in the fiber direction, b is the width of the specimen, and h is the half-thickness of the specimen. Using Equation (3.14), the increment on the effective crack length after an increase of x% of the compliance reads

$$\Delta a = \left(1 + \frac{x}{100}\right)^{1/3} - 1 \tag{3.15}$$

Therefore, the crack growth rate for the DCB test can be obtained as the ratio between the increase of the effective crack length and the number of cycles obtained using Equations (3.15) and (3.13):

$$\frac{\Delta a}{\Delta N} = a_0 \left[(1+x)^{1/3} - 1\right] \left(\frac{1}{\varsigma}\frac{G^{\max}}{G_c}\right)^{1/\rho} \tag{3.16}$$

By comparing Equation (3.16) and the Paris law equation (3.10), the parameters C and m for mode I loading can be estimated using the expressions:

$$C_{\mathrm{I}} = a_0\left[(1+x)^{1/3}-1\right]\left(\frac{1}{\varsigma}\right)^{1/\rho} \qquad m_{\mathrm{I}} = \frac{1}{\rho} \tag{3.17}$$

Similarly, for mode II loading, the compliance of the end-notched flexure (ENF) test (displacement in the middle of the beam versus load force), for the case that the crack length is smaller than the half length of the specimen, L, is obtained by the following equation (Blanco, 2005):

$$S_{\mathrm{II}} = \frac{2L^3+3a^3}{8bE_{11}h^3} \tag{3.18}$$

Under mode II, the effective crack length increment in an ENF test for an increase of the specimen compliance reads:

$$\Delta a = \left[x\left(\frac{2L^3}{3}\right)+a_0^3(1+x)\right]^{1/3}-a_0 \tag{3.19}$$

and the equivalent Paris law parameters:

$$C_{\mathrm{II}} = \left(\left[x\left(\frac{2L^3}{3}\right)+a_0^3(1+x)\right]^{1/3}-a_0\right)\left(\frac{1}{\varsigma}\right)^{1/\rho} \qquad m_{\mathrm{II}} = \frac{1}{\rho} \tag{3.20}$$

Under mixed-mode loading, the compliance of the system reads (Blanco, 2005)

$$S_{\mathrm{m}} = \frac{a^3}{4bE_{11}h^3}n \tag{3.21}$$

where n depends on the setup of the mixed-mode bending (MMB) test, that is, on the mode ratio (Blanco, 2005).

The increment in the effective crack length at delamination onset for the MMB test is then obtained using Equation (3.16), and the equivalent Paris law parameters for a fixed-mode ratio read:

$$C_{\mathrm{B}} = a_0\left[(1+x)^{1/3}-1\right]\left(\frac{1}{\varsigma}\right)^{1/\rho} \qquad m_{\mathrm{B}} = \frac{1}{\rho} \tag{3.22}$$

3.2.4 Integration scheme for high-cycle fatigue simulation

The extension of the quasi-static CZM for fatigue loading can be incorporated in the formulation of the cohesive element, but the integration of the damage variable over the time deserves some discussion. Despite that the models have been developed for

fatigue, all of them except the model of Bak et al. (2015) rely on evolution of the quasi-static damage term in order to obtain equilibrium in the FE model after each crack propagation increment. Therefore, the damage at a given number of cycles $D(N)$ is determined by integrating the damage rate. Because the problem inherently is non-linear, requiring an incremental solution procedure, the load history is discretized in a number of time/cycle increments, and the damage variable D is updated for each equilibrium substep in the following way:

$$D(N_{\mathrm{n}} + \Delta N) = D(N_{\mathrm{n}}) + \int_{N_{\mathrm{n}}}^{N_{\mathrm{n}} + \Delta N} \frac{\mathrm{d}D}{\mathrm{d}N}\,\mathrm{d}N \tag{3.23}$$

where N is the current number of cycles elapsed and ΔN is the increment in cycles for the next equilibrium substep. Because $\mathrm{d}D/\mathrm{d}N$ is not known *a priori* for all the cycles between equilibrium substeps, the integral in the RHS of Equation (3.23) cannot be determined exactly and is therefore approximated instead. Some damage rate models are implemented using an iteratively applied 2 point Newton–Cotes quadrature to estimate the integral of the damage rate, whereas others use a more simple approach using a 1 point Newton–Cotes quadrature. A discussion on the proper way to proceed with the integration can be found in Bak et al. (2014). In the model of Turon et al. (2007a,b), although it is not the most accurate solution because the quasi-static term is omitted, a 1 point Newton–Cotes quadrature integration of the damage rate is used. Therefore, Equation (3.23) reads

$$D(N_{\mathrm{n}} + \Delta N) = D(N_{\mathrm{n}}) + \left.\frac{\mathrm{d}D_{\mathrm{f}}}{\mathrm{d}N}\right|_{N_{\mathrm{n}}} \Delta N \tag{3.24}$$

3.3 Examples

The model is implemented as a user-written finite element in ABAQUS (Hibbitt et al., 2012) by adding the fatigue damage model to the constitutive behavior of a cohesive element previously developed (Turon et al., 2006). Several analyses of specimens under mode I, mode II, and mixed-mode loading were performed to verify the response of the fatigue damage model and demonstrate that when the constitutive damage model is used in a structural analysis, the analysis can reproduce the response of the test specimens without the use of any model-specific adjustment parameters. Finally, the analysis of a substructure component of an aircraft, a composite skin-stiffener panel, is performed to simulate fatigue delamination onset and growth in a specimen without an initial crack and in a scenario where variable mode ratio may occur.

3.3.1 Mode I, mode II, and mixed-mode delamination propagation

Simulations of mode I, mode II, and mixed-mode delamination tests were conducted to verify the response of the fatigue damage model. The two-dimensional (2D) finite element model was composed of four-noded plane-strain elements for the arms, which

Table 3.2 Material properties for HTA/6376C carbon/epoxy laminate (Asp et al., 2001; Juntti et al., 1999)

E_{11} (GPa)	$E_{22} = E_{33}$ (GPa)	$G_{12} = G_{13}$ (GPa)	G_{23} (GPa)	$\nu_{12} = \nu_{13}$	ν_{23}
120	10.5	5.25	3.48	0.3	0.51
G_{Ic} (kJ/m^2)	G_{IIc} (kJ/m^2)	τ^o_{shear} (MPa)	τ^o_3 (MPa)	η	K (N/mm^3)
0.260	1.002	30	30	1.35	10^6

Table 3.3 Fatigue properties of HTA/637C carbon/epoxy laminates (Asp et al., 2001; Juntti et al., 1999)

C_I (mm/cycle)	0.00308	m_I	5.4	G_{Ith} (kJ/m^2)	0.06
C_{II} (mm/cycle)	0.149	m_{II}	4.5	G_{IIth} (kJ/m^2)	0.10
C_m (mm/cycle)	22,904	m_m	4.94	η_2	2.73

were connected by four-noded cohesive elements representing the interface. Four elements were used through the height of each arm. The length of the element was 0.05 mm. The details of the finite element model and the boundary conditions used in the simulations can be found in Krueger et al. (2002). The material properties used in the simulations are obtained from references (Asp et al., 2001; Juntti et al., 1999) and using Equations (3.11) and (3.12). The data used in the model is summarized in Tables 3.2 and 3.3.

Several benchmarks were conducted to simulate the crack growth rate under mode I, mode II, and mixed-mode 50%. The results obtained for the mode I, mode II, and mixed-mode simulations and the experimental data from Asp et al. (2001) are shown in Figure 3.4. The results show good agreement between the predictions and the experimental data.

3.3.2 Delamination onset simulation under fatigue loading

Delamination onset under fatigue loading can be simulated with the model presented. The prediction of delamination onset in a DCB specimen and a skin-stiffener subcomponent is presented in this section. The material used for the simulations is IM7/8552 carbon epoxy. The elastic and interlaminar fracture properties for this material are given in Tables 3.4 and 3.5, respectively.

Regarding the fatigue properties, Hansen and Martin (1999) obtained the delamination onset curves under mode I, mode II, and mixed-mode loading of IM7/8552. Using these experimental data, the G–N curves fitted by Equation (3.13) are obtained and summarized in Table 3.6. The equivalent C and m parameters required for the model are then obtained using Equations (3.17), (3.20), and (3.22).

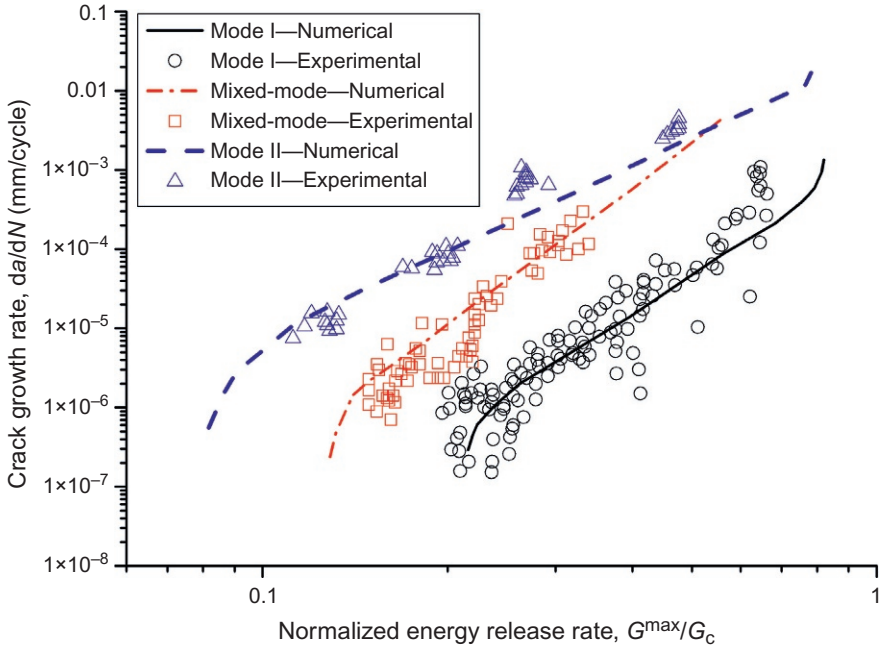

Figure 3.4 Mode I, mixed-mode 50%, and mode II crack growth rate.

Table 3.4 Material properties for IM7/8552 unidirectional and plain-weave fabric graphite/epoxy prepreg (Krueger and Paris, 2001)

UD	E_{11} (GPa)	$E_{22} = E_{33}$ (GPa)	$G_{12} = G_{13}$ (GPa)	G_{23} (GPa)	$\nu_{12} = \nu_{13}$	ν_{23}
	161.0	11.38	5.17	3.92	0.32	0.45
Fabric	$E_{11} = E_{22}$ (GPa)	E_{33} (GPa)	G_{12} (GPa)	$G_{23} = G_{13}$ (GPa)	ν_{12}	$\nu_{23} = \nu_{13}$
	71.7	10.3	4.48	4.14	0.04	0.35

Table 3.5 Properties of the interface for IM7/8552 (Hansen and Martin, 1999)

G_{Ic} (kJ/m^2)	G_{IIc} (kJ/m^2)	τ^o_{shear} (MPa)	τ^o_3 (MPa)	η	K (N/mm^3)
0.200	1.400	61	68	4.356	10^6

The energy release rate threshold was not determined by Hansen and Martin (1999); however, it is estimated from the experimental data reported to be around 0.04 kJ/m^2 for all mode ratios. The complete set of fatigue parameters used in the simulation is summarized in Table 3.7.

Table 3.6 Parameters of the *G–N* curves for DCB, ENF, and MMB tests on IM7/8552 and *C* and *m* parameters estimated using Equations (3.17), (3.20), and (3.22)

	DCB	ENF	MMB 33%	MMB 66%
ς	0.853	0.376	1.962	0.811
ρ	0.064	0.075	0.148	0.112
C (mm/cycle)	13.59	727,940	0.0043	2.68
m	15.59	13.32	6.74	8.95

Table 3.7 Fatigue material properties for IM7/8552 carbon/epoxy used in the simulations

C_{I} (mm/cycle)	13.59	m_{I}	15.59	G_{Ith} (kJ/m^2)	0.04
C_{II} (mm/cycle)	727,940	m_{II}	13.32	G_{IIth} (kJ/m^2)	0.04
C_{m} (mm/cycle)	3.25×10^{-6}	m_{m}	−32.88	η_2	0

Several tension fatigue tests were conducted for different load levels. The load R ratio was 0.1. The simulation is divided into two steps: first is a quasi-static step until the desired displacement is reached and the second step is keeping the displacement constant and introducing fatigue degradation.

The number of cycles required to increase the global compliance of the DCB specimen by 1% is plotted in Figure 3.5 for different load levels. The number of cycles increases exponentially as the load decreases and a good correlation between the numerical and experimental data is obtained.

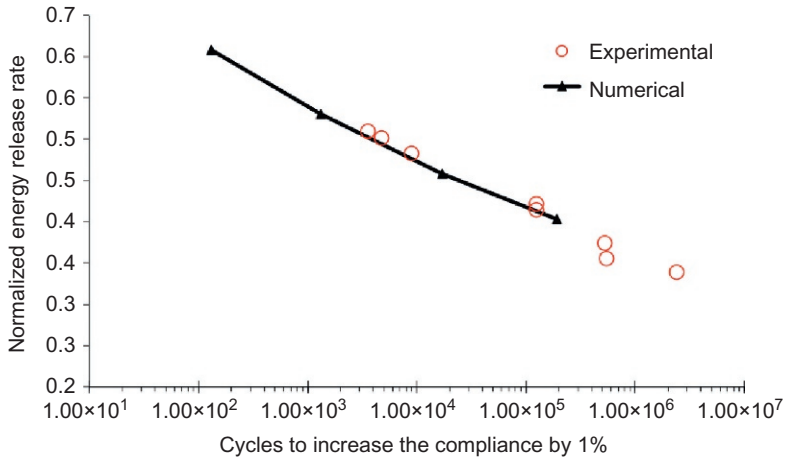

Figure 3.5 Mode I delamination onset curve.

3.3.3 Delamination onset simulation under fatigue loading of a skin-stiffener substructure

Several aerospace composite structures are made of panels with co-cured or adhesively bonded frames and stiffeners. Testing of stiffened panels has shown that bond failure at the tip of the stiffener flange is a common failure mode (Krueger and Paris, 2001). Stiffened panels used in aerospace applications are subjected to fatigue loading, and the prediction of skin-stiffener debonding under cyclic loading is a relevant step in the design of such structures.

The model presented in the previous sections is used in the prediction of skin-stiffener debonding under fatigue loading. This is a challenging problem because in the structure under investigation, the mode ratio can change throughout the analysis and the structure does not have a pre-crack. To further illustrate the capabilities of the model by Turon et al. (2006, 2007a,b), a specimen consisting of a stiffener flange bonded onto a skin previously tested by Krueger and Paris (2001) is considered. The skin is 101.6 mm long, 25.4 mm wide, and the stiffener is 50.8 mm long and 25.4 mm wide. The taper angle of the stiffener edges is 25°.

Both skin and stiffener were made from IM7/8552 graphite/epoxy prepreg tape. A nominal ply thickness of 0.142 mm was used for the skin, and the layup used was [45/−45/0/−45/45/90/90/−45/45/0/45/−45]. The flange consisted of a plain-weave fabric with a 0.208 mm nominal ply thickness and a layup [45/0/45/0/45/0/45/0/45], where 0 represents a 0–90 fabric ply.

A complete analysis of the delamination growth in skin-stiffener structures requires three-dimensional (3D) models with a high degree of complexity. Several alternatives to fully 3D models have been proposed. Krueger et al. (2002) compared 2D finite element modeling assumptions with fully 3D analysis in the simulation of composite skin-stiffener debonding. The results obtained by Krueger et al. (2002) indicate that the 3D generalized plane-strain model most closely agrees with the fully 3D model in terms of the distribution of the energy release rate.

Based on the results reported by Krueger et al. (2002), 3D generalized plane-strain models are used in the analysis of the skin-stiffener specimen. As illustrated in Figure 3.6, the model consists of a plane of eight-noded 3D elements and a row of zero-thickness user-defined eight-noded cohesive elements that connect the upper (stiffener) and lower (skin) parts of the mesh. Two different constraints to impose the generalized plane-strain state are defined: (i) the movement of the nodes located at the back face (represents the *XY* midplane of the structure) is constrained in the *Z*-direction and (ii) the nodes located in the front face are linked by a kinematic constraint that ensures that this surface is always parallel to the *XY* midplane. The specimen is loaded by applying a force at one end of the specimen while keeping the opposite end of the specimen clamped.

Several tension fatigue tests were conducted for different load levels. The load *R* ratio was 0.1. The same procedure as for the DCB simulation presented in previous section has been followed: first, a quasi-static step is taken until the desired displacement is reached; and then, a second step is taken, keeping the displacement constant and introducing fatigue degradation. The number of cycles at delamination onset for different load levels is plotted in Figure 3.7. In the numerical simulations, the number

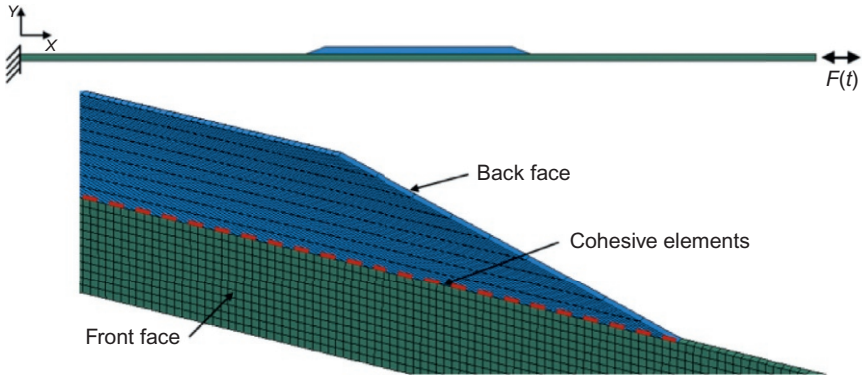

Figure 3.6 Mesh used in the skin-stiffener simulation. The boundary conditions have been defined to impose a generalized plane-strain state (Krueger et al., 2002).

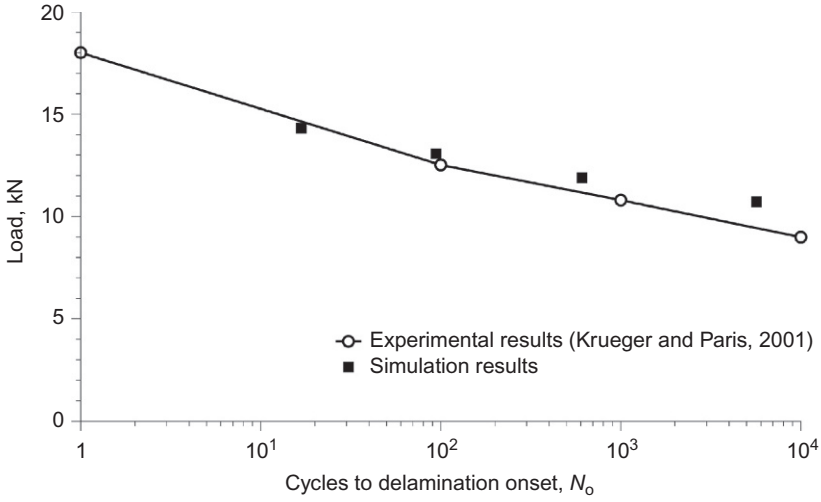

Figure 3.7 Load cycles to increase the global compliance of the subcomponent.

of cycles at delamination onset has been defined as the number of cycles to increase the global compliance of the skin-stiffener subcomponent by 1%. The experimental data reported in Krueger and Paris (2001) is also plotted in Figure 3.7. A good agreement between the numerical and experimental data can be observed.

3.4 Conclusions

The extension of quasi-static CZMs for the simulation of fatigue loading has been presented in this chapter. An envelope load damage model is presented by defining an evolution of internal or damage variables of the quasi-static model with the number of cycles.

The parameters needed to feed the fatigue model can be obtained directly by comparing with experimental data, assuming that the local development of the fatigue damage is comparable to the macroscopic crack growth rate. Using this assumption, the model parameters are directly the coefficient of the Paris law-like curve describing the crack growth rate as a function of the number of cycles. Moreover, a methodology to estimate the model parameters from the onset curves is also presented. Therefore, the model can be used to predict the mechanical response of composite structures using standard data measured in simple test specimens.

The model has been implemented in ABAQUS nonlinear finite element code as a user-defined cohesive element. The accuracy of the model was assessed by comparing its predictions with experimental data obtained in test specimens loaded in pure mode I, pure mode II, and mixed-modes I and II. A good agreement between predictions and experiments was obtained for all loading situations. The model is able to predict the threshold value of the energy release rate below which no delamination propagation is observed.

The model has also been used to simulate fatigue degradation of a specimen without a preexisting crack. The simulations of a mode I specimen and a skin-stiffener substructure component of an aircraft demonstrate that the model by Turon et al. (2006, 2007a,b) is able to predict delamination onset and growth in a specimen without an initial crack under complex loading scenarios.

References

Abdul-Baqi, A., Schreurs, P.J.G., Geers, M.G.D., 2005. Fatigue damage modeling in solder interconnects using a cohesive zone approach. Int. J. Solids Struct. 42 (3–4), 927–942.

Asp, L., Sjögren, A., Greenhalgh, E., 2001. Delamination growth and thresholds in a carbon/epoxy composite under fatigue loading. J. Compos. Technol. Res. 23, 55–68.

ASTM Standard D6115, 2004. Standard test method for mode I fatigue delamination growth onset of unidirectional fiber-reinforced polymer matrix composites.

Bak, B.L.V., Sarrado, C., Turon, A., Costa, J., 2014. Delamination under fatigue loads in composite laminates: a review on the observed phenomenology and computational methods. Appl. Mech. Rev. 66 (6), 1–24.

Bak, B.L.V., Turon, A., Lindgaard, E., Lund, E., 2015. A simulation method for high-cycle fatigue-driven delaminations using a cohesive zone model. Int. J. Numer. Methods Eng., accepted for publication.

Beaurepaire, P., Schueller, G.I., 2011. Modeling of the variability of fatigue crack growth using cohesive zone elements. Eng. Fract. Mech. 78 (12), 2399–2413.

Blanco, N., 2005. Variable Mixed-Mode Delamination in Composite Laminates Under Fatigue Conditions: Testing & Analysis. University of Girona, Spain, ISBN: 84-689-0990-4.

de Andrés, A., Pérez, J.L., Ortiz, M., 1999. Elastoplastic finite element analysis of three-dimensional fatigue crack growth in aluminum shafts subjected to axial loading. Int. J. Solids Struct. 36 (15), 2231–2258.

Hansen, P., Martin, R., 1999. DCB, 4ENF and MMB delamination characterisation of S2/8552 and IM7/8552, United States Army (European Research Office of the US Army), N68171-98-M-5177.

Harper, P.W., Hallett, S.R., 2008. Cohesive zone length in numerical simulations of composite delamination. Eng. Fract. Mech. 75, 4774–4792.

Harper, P.W., Hallett, S.R., 2010. A fatigue degradation law for cohesive interface elements—development and application to composite materials. Int. J. Fatigue 32 (11), 1774–1787.

Hibbitt, Karlsson, Sorensen, 2012. ABAQUS 6.12 Users's Manual. Pawtucket, USA.

Juntti, M., Asp, L., Olsson, R., 1999. Assessment of evaluation methods for the mixed-mode bending test. J. Compos. Technol. Res. 21, 37–48.

Kawashita, L.F., Hallett, S.R., 2012. A crack tip tracking algorithm for cohesive interface element analysis of fatigue delamination propagation in composite materials. Int. J. Solids Struct. 49 (21), 2898–2913.

Khoramishad, H., Crocombe, A.D., Katnam, K.B., Ashcroft, I.A., 2010. Predicting fatigue damage in adhesively bonded joints using a cohesive zone model. Int. J. Fatigue 32 (7), 1146–1158.

Koutsourelakis, P.S., Kuntiyawichai, K., Schueller, G.I., 2006. Effect of material uncertainties on fatigue life calculations of aircraft fuselages: a cohesive element model. Eng. Fract. Mech. 73 (9), 1202–1219.

Krueger, R., Paris, I.L., O'Brien, T.K., Minguet, P.J., 2001. Fatigue life methodology for bonded composite skin/stringer configurations, NASA/TM-2001-210842.

Krueger, R., Paris, I.L., O'Brien, T.K., Minguet, P.J., 2002. Comparison of 2D finite element modeling assumptions with results from 3D analysis for composite skin-stiffener debonding. Compos. Struct. 57, 161–168.

Landry, B., LaPlante, G., 2012. Modeling delamination growth in composites under fatigue loadings of varying amplitudes. Compos. Part B 43 (2), 533–541.

Maiti, S., Geubelle, P.H., 2005. A cohesive model for fatigue failure of polymers. Eng. Fract. Mech. 72 (5), 691–708.

Massabo, R., Cox, B.N., 1999. Concepts for bridged mode II delamination cracks. Int. J. Eng. Sci. 47, 1265–1300.

May, M., Hallett, S.R., 2010. A combined model for initiation and propagation of damage under fatigue loading for cohesive interface elements. Compos. Part A 41 (12), 1787–1796.

May, M., Hallett, S.R., 2011. An advanced model for initiation and propagation of damage under fatigue loading—part I: model formulation. Compos. Struct. 93 (9), 2340–2349.

Naghipour, P., Bartsch, M., Voggenreiter, H., 2011. Simulation and experimental validation of mixed-mode delamination in multidirectional CF/PEEK laminates under fatigue loading. Int. J. Solids Struct. 48 (6), 1070–1081.

Nguyen, O., Repetto, E., Ortiz, M., Radovitzky, R., 2001. A cohesive model for fatigue crack growth. Int. J. Fract. 110, 351–369.

Pascoe, J.A., Alderliesten, R.C., Benedictus, R., 2013. Methods for the prediction of fatigue delamination grow thin composites and adhesive bonds—a critical review. Eng. Fract. Mech. 112–113, 72–96.

Peerlings, R.H.J., Brekelmans, W.A.M., de Borst, R., Geers, M.G.D., 2000. Gradient-enhanced damage modelling of high-cycle fatigue. Int. J. Numer. Methods Eng. 49 (12), 1547–1569.

Pirondi, A., Moroni, F., 2010. A progressive damage model for the prediction of fatigue crack growth in bonded joints. J. Adhes. 86 (5–6), 501–521.

Rice, J.R., 1980. The mechanics of earthquake rupture. In: Fermi, Enrico, Dziewonski, A.M., Boschi, E. (Eds.), Physics of the Earth's Interior. Proceedings of the International School of Physics. North-Holland, Amsterdam, pp. 555–649.

Robinson, P., Galvanetto, U., Tumino, D., Bellucci, G., Violeau, D., 2005. Numerical simulation of fatigue-driven delamination using interface elements. Int. J. Numer. Methods Eng. 63 (13), 1824–1848.

Roe, K., Siegmund, T., 2003. An irreversible cohesive zone model for interface fatigue crack growth simulation. Eng. Fract. Mech. 70, 209–232.

Smith, E., 1989. The size of the fully developed softening zone associated with a crack in a strain-softening material—II. A crack in a double cantilever beam specimen. Int. J. Eng. Sci. 27, 309–314.

Soto, A., González, E.V., Maimí, P., Turon, A., 2014. Length of the cohesive zone in orthotropic materials under pure fracture modes. In: European Conference on Solid Mechanics, 6–10 July 2014, Madrid, Spain.

Tumino, D., Cappello, F., 2007. Simulation of fatigue delamination growth in composites with different mode mixtures. J. Compos. Mater. 41 (20), 2415–2441.

Turon, A., Camanho, P.P., Costa, J., Dávila, C.G., 2006. A damage model for the simulation of delamination in advanced composites under variable-mode loading. Mech. Mater. 38, 1079–1089.

Turon, A., Dávila, C.G., Camanho, P.P., Costa, J., 2007a. An engineering solution for solving mesh size effects in the simulation of delamination with cohesive zone models. Eng. Fract. Mech. 74 (10), 1665–1682.

Turon, A., Costa, J., Camanho, P.P., Dávila, C.G., 2007b. Simulation of delamination in composites under high-cycle fatigue. Compos. Part A 38 (11), 2270–2282.

Yang, B., Mall, S., Ravi-Chandar, K., 2001. A cohesive zone model for fatigue crack growth in quasibrittle materials. Int. J. Solids Struct. 38 (22–23), 3927–3944.

Yang, Q., Shim, D., Spearing, S., 2004. A cohesive zone model for low cycle fatigue life prediction of solder joints. Microelectron. Eng. 75, 85–95.

This page intentionally left blank

A level set model for delamination in composite materials

4

*F.P. van der Meer**
*Delft University of Technology, Delft, The Netherlands

4.1 Introduction

Delamination is one of the main failure processes that occurs in composite laminates. It can develop from the free edge, where stress concentrations exist on the ply interface due to the difference between elastic properties of neighboring plies. Alternatively, delamination can grow from transverse matrix cracks in one of the plies or from ply terminations. As a consequence of delamination, the plies do not work together optimally, which leads to a decreased bending stiffness of the laminate and which makes the structure more prone to buckling.

Different methods exist for the analysis of delamination. The two most popular are the virtual crack closure technique and the cohesive zone method (see Chapters 1 and 2, respectively, for more details). The cohesive zone method is a damage mechanics method, in which crack growth is represented as damage growth in a fracture process zone. For delamination the cohesive zone method is conveniently applied in combination with interface elements: zero-thickness elements which are placed between solid or shell elements representing the neighboring plies. A cohesive damage law is assigned to these elements to gradually reduce the stiffness of the interface from (nearly) rigid to traction free (Allix and Ladevèze, 1992; Schellekens and de Borst, 1994; Yang and Cox, 2005; Turon and Camanho, 2006; Jiang et al., 2007; Van der Meer and Sluys, 2010). The cohesive zone method is relatively straightforward to implement and is supported in most commercial finite element packages.

A limiting factor in using the cohesive zone method is that it comes with an element size requirement. For robustness and accuracy, it is necessary to use elements that are several times smaller than the cohesive zone. For typical engineering composites, this results in a maximum element size of around 0.3 mm. Clearly, such a requirement limits the size of specimens that can be analyzed with this approach within acceptable computation times.

The virtual crack closure technique (Rybicki and Kanninen, 1977; Krueger, 2004) is a fracture mechanics method for which it is assumed that crack growth is energy driven. The technique primarily allows for the computation of energy release rates along a delamination front. The virtual crack closure technique is applied by constructing a mesh in which a delamination crack is present after which energy release rates are computed from looking at nodal forces and displacements. For answering the question whether a given crack grows under a given load, the method can very well be applied, but it is not very well suited for crack growth analysis. The crack front must remain aligned with element boundaries. This means that when the crack grows, either

Numerical modelling of failure in advanced composite materials. http://dx.doi.org/10.1016/B978-0-08-100332-9.00004-9
Copyright © 2015 Elsevier Ltd. All rights reserved.

it has to grow from node to node in a fixed mesh (Shen et al., 2001; Xie and Biggers, 2006), resulting in jagged crack front with inaccurate stresses approximation, or the nodes have to move along with the crack front (Ousset, 1999; Davis et al., 2014), which is cumbersome and only practical for self-similar crack growth.

In this chapter, we present an alternative method that makes use of the level set method to describe the crack front location. Like the virtual crack closure technique, it is a fracture mechanics method. As such, there is no cohesive zone and the method does not suffer from the element size requirement that limits the applicability of the cohesive zone method. In contrast with the virtual crack closure technique, the level set method for delamination is primarily developed for progressive delamination analysis and it can deal very well with non-self-similar crack growth. Moreover, the level set method for delamination can deal with infinitesimally small initial delaminations and, under some conditions, even with initiation (Van der Meer et al., 2012a).

The method consists of two main components. First, there is the kinematic description of a cracked laminate with a given crack front location. Because the crack front can be embedded inside the elements, this requires a special element formulation. Second, there is the crack growth model. Because the crack front does not coincide with the element boundaries, the standard virtual crack closure technique, which relies on nodal quantities, cannot be used to compute energy release rates. Use is made of a modified virtual crack closure technique that was first proposed by Zou et al. (2001) and adapted by Van der Meer et al. (2012c) for higher accuracy with coarse meshes.

In this chapter, the two components of the model will be introduced in Sections 4.2 and 4.3. In Section 4.4, we briefly discuss the solution algorithm. Then, in Section 4.5, the method will be demonstrated with the numerical example of a double cantilever beam in three dimensions. After the first paper on the method that focused on in-plane analysis (Van der Meer et al., 2012a) and a second paper which dealt with the computation and modal partitioning of the energy release rate (Van der Meer et al., 2012c), this chapter summarizes the developed method and demonstrates its applicability to full crack growth analysis with out-of-plane deformations.

4.2 Cracked laminate model

In this section, the model with given crack front location is described. First, the level set method, with which the crack front location is defined, is introduced. Next, the formulation of the kinematically enriched elements that contain the crack front is given.

4.2.1 Level set field

The level set method (see e.g., Sethian, 1999) is a method for implicit description of moving fronts. The basic idea is that the front location is given as the zero level set of an auxiliary field defined over the domain of interest. In this chapter, the level set field is denoted $\phi(\mathbf{x})$. In finite element context, ϕ is defined with nodal values on a given discretization and interpolated with the standard shape functions. The front is then located

inside those elements that have both positive and negative nodal values. Continuity of the front through the domain is ensured by the continuity of the shape functions.

For our current purpose, we let the level set method define the location of a delamination crack front. The level set field is defined on a surface domain Ω_ϕ, which coincides with the plane of the interface. The interface is cracked where $\phi > 0$ and intact where $\phi < 0$. The crack front location is therefore given by the contour line or level set Γ_ϕ at $\phi = 0$. In the model formulation, the boundary Γ_u between the cracked part and the uncracked part of the computational domain Ω_u will play an important role. It will be referred to as the configurational interface as it separates deformations that belong to the cracked configuration from deformations belonging to the uncracked configuration. The surface domain Γ_u is defined as the extension of the front Γ_ϕ through the thickness of the laminate (see Figure 4.1).

A given front defines where ϕ should be equal to zero. In general, this leaves many options for the definition of ϕ away from the front. A practical choice for ϕ is the signed distance function. The signed distance function is positive on one side of the front and negative on the other, and its absolute value at any point is equal to smallest distance from that point to the front. For ϕ to satisfy this property, the following must hold:

$$|\nabla\phi| = 1 \quad \text{on} \quad \Omega_\phi \tag{4.1}$$

$$\phi = 0 \quad \text{on} \quad \Gamma_\phi \tag{4.2}$$

4.2.2 Basic element formulation

The current implementation is based on a laminate representation with stacked shell elements for small displacements.[1] The motivation for the particular element is partially given by the energy release rate computations with the modified virtual crack

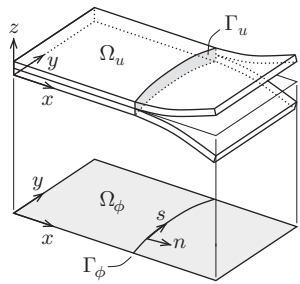

Figure 4.1 Level set domain Ω_ϕ with front Γ_ϕ and laminate domain Ω_u with intersection at the front location Γ_u.

[1] The term *shell elements* is used here to refer to the capability of the element to represent both in-plane and out-of-plane loading.

closure technique by Zou et al. (2001). For stacking of elements, it is convenient if only translational degrees of freedom are used, and no rotational degrees of freedom. An obvious candidate would therefore be the solid-like shell element (Parisch, 1995) with three displacement degrees of freedom on every node and a higher order stretching term, which results in a seven-parameter shell formulation. However, Van der Meer et al. (2012c) have shown that energy release rate computations become inaccurate with partially cracked elements that include through-thickness stretching. The elements must therefore be of the type of a five-parameter shell (two rotations and three translations on every node, no stretch). To be able to stack such elements conveniently, a displacement-only version of the five-parameter shell element has been developed. The mesh is similar to a solid-like shell discretization, with two layers of nodes per element. However, all connected nodes with the same (x,y)-coordinates share a single z-displacement (see Figure 4.2).

Rotations and mid-plane deformations are then computed prior to the evaluation of strains and stresses. These are used to compute the basic generalized strain quantities: in-plane strain $\boldsymbol{\varepsilon} = \{\varepsilon_{xx}, \varepsilon_{yy}, \varepsilon_{xy}\}$, curvature $\boldsymbol{\kappa} = \{\kappa_{xx}, \kappa_{yy}, \kappa_{xy}\}$, and shear strain $\boldsymbol{\gamma} = \{\gamma_{xz}, \gamma_{yz}\}$. The strains are related to in-plane shell force $\mathbf{N} = \{N_{xx}, N_{yy}, N_{xy}\}$, bending moment $\mathbf{M} = \{M_{xx}, M_{yy}, M_{xy}\}$, and shear force $\mathbf{Q} = \{Q_x, Q_y\}$ through the stiffness matrices from first order deformable laminate theory, cf. Alfano et al. (2001):

$$\begin{Bmatrix} \mathbf{N} \\ \mathbf{M} \\ \mathbf{Q} \end{Bmatrix} = \begin{bmatrix} \mathbf{A} & \mathbf{B} & \mathbf{0} \\ \mathbf{B} & \mathbf{D} & \mathbf{0} \\ \mathbf{0} & \mathbf{0} & \mathbf{H} \end{bmatrix} \begin{Bmatrix} \boldsymbol{\varepsilon} \\ \boldsymbol{\kappa} \\ \boldsymbol{\gamma} \end{Bmatrix} \tag{4.3}$$

This element formulation is only applicable to planar structures and small deformations. For curved structures, it is not possible to define displacement-only five-parameter shell elements. Stacking layers of elements then requires the definition of linear constraints between rotational and translational degrees of freedom. For large deformations, these constraints become nonlinear.

4.2.3 Element formulation with embedded crack front

It is central to the level set method that the front is not necessarily located at element edges. The level set front can be embedded inside an element in the level set domain Ω_ϕ. To represent the deformation of the corresponding stack of elements in the physical domain Ω_u, the elements are doubled with the phantom node version of the extended finite element method (Hansbo and Hansbo, 2004; Song, 2006). On the

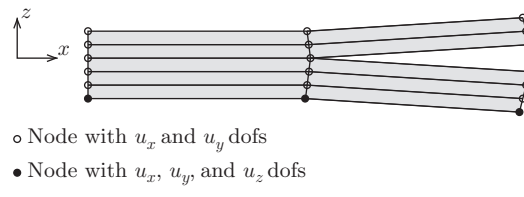

Figure 4.2 Definition of degrees of freedom in stacked laminate where the delamination front coincides with the element boundary (side view).

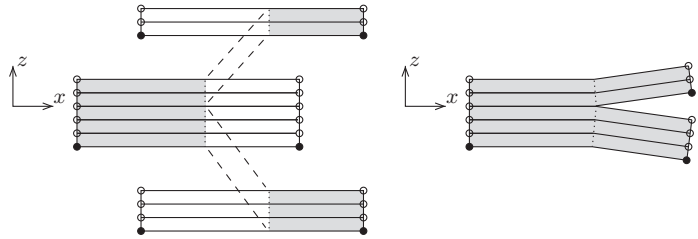

Figure 4.3 Definition of partially active overlapping elements to represent cracked element (side view). The kinematics allow a discontinuity in displacements across the front (dashed lines, left diagram). When this discontinuity is closed, a weak discontinuity remains (dotted line, right diagram).

cracked side, the elements above the delamination crack are not coupled to the elements below the delamination crack. Moreover, there is a discontinuity across the configurational interface Γ_u. However, the displacement jump is enforced to be zero. Van der Meer et al. (2012a) have investigated different methods to achieve this zero displacement jump; in the current implementation a simple penalty method is used. After this, a weak discontinuity across Γ_u remains: displacements are continuous across the front, but stresses and strains are not (see Figure 4.3). The reason behind this procedure, where weak discontinuity is obtained by introducing and closing a strong discontinuity, is that it is impossible to directly enrich the top and bottom parts with a weak discontinuity while keeping compatibility between the top and bottom displacement fields in the uncracked part of the element.

4.3 Crack growth model

Velocities along the front are needed to update the front in the level set method. When normal velocities are computed as a function of coordinate s (see Figure 4.1), they can be used to update the whole level set field with standard operations (Sethian, 1999; Van der Meer et al., 2012a). The level set model for delamination therefore requires the computation of crack growth rates, which is done with the notion from fracture mechanics that a crack grows if the energy release rate G is higher than the fracture energy G_c. The following constitutive law is proposed:

$$v = \frac{1}{\mu}\left\langle \frac{G}{G_c} - 1 \right\rangle \tag{4.4}$$

where v is the crack growth rate or front velocity, $\mu > 0$ is a viscosity parameter to ensure finite velocities are obtained when $G > G_c$ and angle brackets are used to indicate the positivity constraint: $<x>=(x+|x|)/2$ which implies that negative velocities will never occur. In quasi-static simulations, μ does not have physical meaning. For very small μ, the Kuhn–Tucker conditions for fracture mechanics are

approached: $v \geq 0$, $(G - G_c) \leq 0$, $v(G - G_c) = 0$. However, for numerical reasons, a finite value of μ must be used, which results in an actual energy release rate that is higher than the fracture energy.

4.3.1 Energy release rate computation

For the evaluation of the energy release rate G, the jump in strain and stress across the configurational interface Γ_u can be used. It is possible to compute the energy that will be released when the front at a given location s moves in n-direction by integrating the jump in Eshelby tensor over the height of Γ_u (Van der Meer et al., 2012a). However, it is known that for engineering composites, the fracture energy G_c is not a material constant, but rather a function of loading. Its variability is usually expressed in terms of the ratio between contributions from different fundamental fracture modes (see e.g., Benzeggagh and Kenane, 1996). Therefore, it is necessary to compute not only G, but also to decompose it into G_I, G_{II}, and G_{III}. For that reason, the modified virtual crack closure technique by Zou et al. (2001) is adopted, with adaptations for improved accuracy with large elements (Van der Meer et al., 2012c). With this method, the three pure mode energy release rates are computed from the jump in stresses across Γ_u and the crack opening gradient right next to the front.

For any given point along the front Γ_ϕ, the individual contributions are defined with the jump in forces and bending moments on the crack front as illustrated in Figure 4.4. The forces F_i and moments T_i can be seen as line loads and line moments acting from the lower part of the laminate on the upper part of the laminate and vice versa. The values of F_i are computed by taking the difference of the relevant terms of $\mathbf{N}$ and $\mathbf{Q}$, while for the values of T_i, the jump in $\mathbf{M}$ is evaluated along with the eccentricity of the forces $\mathbf{N}$ with respect to the delamination plane. The computation of F_n is spelled out here:

$$F_n(s) = N_{nn}^+(s) - N_{nn}^-(s) \tag{4.5}$$

with

$$N_{nn}^+(s) = \int_{\Gamma_u \cap z<0} \sigma_{nn}(n = 0^+, s, z)\mathrm{d}z \tag{4.6}$$

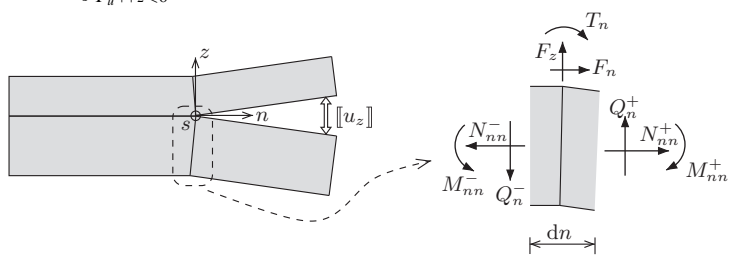

Figure 4.4 Forces F_n and F_z and moment T_n on the crack front, acting between top and bottom sublaminates, balance the jump in stresses across Γ_u (forces and stresses in s and ns direction are not shown in this image).

$$N_{nn}^{-}(s) = \int_{\Gamma_u \cap z<0} \sigma_{nn}(n=0^{-},s,z)\mathrm{d}z \tag{4.7}$$

where $n = 0$ at the front, $n > 0$ on the cracked side, and $z = 0$ at the delamination plane. As N_{nn}^{+} and N_{nn}^{-} are both computed with an integral over the same domain, F_n can be expressed directly as the integral of the jump in stress over the configurational interface.

$$F_n(s) = \int_{\Gamma_u \cap z<0} \sigma_{nn}(n=0^{+},s,z) - \sigma_{nn}(n=0^{-},s,z)\mathrm{d}z \tag{4.8}$$

Similarly, we have for the other components of the force vector:

$$F_s(s) = \int_{\Gamma_u \cap z<0} \sigma_{ns}(n=0^{+},s,z) - \sigma_{ns}(n=0^{-},s,z)\mathrm{d}z \tag{4.9}$$

$$F_z(s) = \int_{\Gamma_u \cap z<0} \sigma_{zn}(n=0^{+},s,z) - \sigma_{zn}(n=0^{-},s,z)\mathrm{d}z \tag{4.10}$$

$$T_n(s) = \int_{\Gamma_u \cap z<0} z\sigma_{nn}(n=0^{+},s,z) - z\sigma_{nn}(n=0^{-},s,z)\mathrm{d}z \tag{4.11}$$

$$T_s(s) = \int_{\Gamma_u \cap z<0} z\sigma_{ns}(n=0^{+},s,z) - z\sigma_{ns}(n=0^{-},s,z)\mathrm{d}z \tag{4.12}$$

These loads are multiplied with the gradient of the crack opening components with respect to n to obtain the pure mode energy release rates:

$$G_{\mathrm{I}} = F_z[\![u_{z,n}]\!] + T_n[\![\kappa_{nn}]\!] + T_s[\![\kappa_{ns}]\!] \tag{4.13}$$

$$G_{\mathrm{II}} = F_n[\![u_{n,n}]\!] \tag{4.14}$$

$$G_{\mathrm{III}} = F_s[\![u_{s,n}]\!] \tag{4.15}$$

where the displacement jump $[\![u_{i,n}]\!]$ is defined as the crack opening gradient evaluated at $n = 0^{+}$

$$[\![u_{i,n}]\!](s) = u_{i,n}(n=0^{+},s,z=0^{+}) - u_{i,n}(n=0^{+},s,z=0^{-}) \tag{4.16}$$

and similarly

$$[\![\kappa_{ij}]\!](s) = \kappa_{ij}(n=0^{+},s,z=0^{+}) - \kappa_{ij}(n=0^{+},s,z=0^{-}) \tag{4.17}$$

Note that the evaluation of the forces involves the jump in stresses over $n = 0$ (the configurational interface), whereas the jump in displacement gradients and curvatures is defined over $z = 0$ (the crack).

The total energy release rate G is simply defined as the sum of the three contributions

$$G = G_{\mathrm{I}} + G_{\mathrm{II}} + G_{\mathrm{III}} \tag{4.18}$$

The fracture energy G_{c} is related to the ratio between shear modes G_{II} and G_{III} through the phenomenological relation proposed by Benzeggagh and Kenane (1996):

$$G_{\mathrm{c}} = G_{\mathrm{Ic}} + (G_{\mathrm{IIc}} - G_{\mathrm{Ic}}) \left(\frac{G_{\mathrm{II}} + G_{\mathrm{III}}}{G_{\mathrm{I}} + G_{\mathrm{II}} + G_{\mathrm{III}}} \right)^{\eta} \tag{4.19}$$

where G_{Ic} is the mode I fracture energy, G_{IIc} the mode II fracture energy, and η is a mode interaction parameter.

In contrast with the original virtual crack closure technique, the computation of the energy release rates is completely expressed in terms of local quantities. All terms on the right-hand side of Equations (4.13)–(4.15) are evaluated on Γ_u (i.e., at $n = 0^-$ and $n = 0^+$). It should be noted that the jumps in stress and displacement used to evaluate G are well defined in terms of first-order shear-deformable shell theory. In continuum mechanics, jumps in stresses do not occur, but with the kinematic assumptions from shell theory, finite values for these jumps exist that will be retrieved in a sufficiently refined discretized model.

4.3.2 Weak form

The energy release rate and velocity computation given above can be performed at any point s along the front. Apart from integration over the thickness of the lower sublaminate (in Equations (4.8)–(4.12)), the procedure for computing the velocity only involves local relationships. However, for the update of the level set method, the velocity will eventually be required on the nodes. Therefore, an approach is adopted that uses nodal degrees of freedom on the nodes of the elements that contain the front.

In discretized form, v is computed on nodes of the elements in Ω_ϕ that contain Γ_ϕ. Equation (4.4) is satisfied in a weak form by solving the linear system of equations:

$$[\mathbf{M} + \mathbf{K}]\mathbf{v} = \mathbf{f} \tag{4.20}$$

where $\mathbf{M}$ is the matrix that represents the viscosity μ, $\mathbf{K}$ is a stabilization term, $\mathbf{v}$ is a vector with nodal velocity values, and $\mathbf{f}$ is the configurational force related to G. The individual terms are defined as:

$$\mathbf{M} = \mu \int_{\Gamma_\phi} \mathbf{N} \otimes \mathbf{N} \, \mathrm{d}s \tag{4.21}$$

$$\mathbf{K} = \kappa h^2 \int_{\Gamma_\phi} (\nabla \mathbf{N} \cdot \mathbf{s}) \otimes (\nabla \mathbf{N} \cdot \mathbf{s}) \mathrm{d}s \tag{4.22}$$

$$\mathbf{f} = \int_{\Gamma_\phi} \mathbf{N}\left(\frac{G}{G_c} - 1\right) \mathrm{d}s \tag{4.23}$$

where κ is a stabilization parameter, the effect of which is scaled with the square of the typical element size h to make it vanish upon mesh-refinement. Integration of $\mathbf{M}$, $\mathbf{K}$ and $\mathbf{f}$ is performed numerically with 2-point Gauss integration over the crack front segment in each element that is cut by the front. Locally, the evaluation of $\mathbf{f}$ involves integration through the thickness to get G and G_c.

A straightforward definition of degrees of freedom on all nodes of the elements that contain the front results in unstable results. The reason for this is that the solution space also includes the possibility of variations in n-direction which are ill-defined because the field equation is a function of s only. This is similar to the issue encountered when applying Dirichlet boundary conditions with Lagrange multipliers on a non-conforming mesh. For this problem, Béchet et al. (2008) proposed a solution that is also adopted here for the reducing the velocity solution space. In this solution, constraints are defined between pairs of degrees of freedom that are on opposite sides of the front until free variation of the field in n-direction is no longer possible. An illustration of the definition of constraints is given in Figure 4.5.

4.4 Solution algorithm

The discretization of a cracked laminate described in Section 4.2 and the crack growth model from Section 4.3 have to be combined in a single solution algorithm to allow for analysis of progressive crack growth. The mechanics problem with given front location is a linear problem. The crack growth model allows for an explicit update of the crack front location. These two tasks are combined in a staggered solution scheme, where first displacements are computed and then velocities are computed with the resulting displacements and stresses. The crack growth step is not finished when

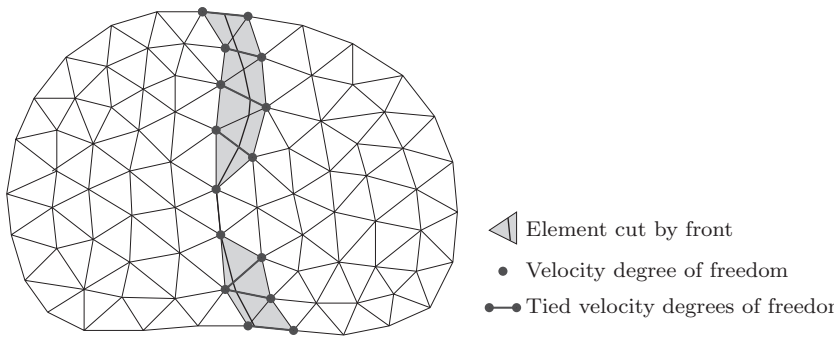

Figure 4.5 Definition of constrained basis for velocity field. Note that when the front is (nearly) located on the element, a special treatment is applied.
Adapted from Van der Meer et al. (2012a), Figure 4.4.

velocities are computed. The velocities are extended with the fast marching method, after which the level set field is updated and possibly reinitialized. The reinitialization is only necessary after every so many time steps, but since the fast marching method with which it is performed is rather cheap, it is done in every time step.

When boundary conditions are a function of time or quasi-time, the time increment is related to the maximum velocity of the front. The increment is adapted such that local front movement in one time step is not larger than half the size of the smallest element in the mesh. In Box 4.1, the global algorithm for a single time step is summarized.

It is emphasized that all operations in the crack growth part are relatively cheap in terms of computational effort. A linear system of equations is solved, but this system is much smaller than the system of equations that is to be solved for the mechanics problem. Taken together, the operations related to crack growth require less computation time than the solution of the global system of equations for computing displacements. Therefore, the algorithm for a single time step is more efficient than that for cohesive methods, where the solution of a linearized global system is repeated several times per time step in an iterative algorithm. This gain in efficiency comes on top of the primary gain due to the possible increase in element size.

4.5 Numerical example: Double cantilever beam

The accuracy and efficiency of the level set method for delamination is demonstrated with the example of a double cantilever beam. Results from level set analysis are compared with results from cohesive zone analysis. A unidirectional beam is modeled with properties and geometry from Davidson (1990). The beam is 127 mm long and 25.4 mm wide and has 24 plies each 0.148 mm thick. The delamination takes place in the mid-plane of the beam and the initial notch, with straight front, has a length of 50.8 mm.

Transversely isotropic material properties are assigned, with $E_1 = 123.4$ GPa, $E_2 = 7.6$ GPa, $G_{12} = 4.4$ GPa, $v_{12} = 0.34$, and $v_{23} = 0.35$. The fracture energy is 1 N/mm.

Box 4.1 Global algorithm for single time step

1. Compute displacements for known crack front location
   - Build discretization with special elements around the front
   - Assemble and solve linear elastic system
2. Grow cracks
   - Assemble and solve linear system for velocity on the front
   - Extend normal velocity with fast marching method
   - Update level set field
   - Reinitialize signed distance function fast marching method
3. Go to next time step
   - Apply load or displacement increment

Numerical parameters for the level set models are $\kappa = 0.5$ s/mm^3, $\mu = 0.012$ s/m, and the penalty stiffness for closing the strong discontinuity across Γ_u is chosen equal to 10^8 N/mm^3.

4.5.1 Results

The evolution of the crack front through the domain is illustrated in Figure 4.6. For readability, the front from even time steps is omitted. The crack grows faster in the specimen center than it does along the boundaries, although the front curvature remains small for this unidirectional specimen, just as reported by Davidson (1990). The front is smooth and symmetric, and it progresses through the domain in regular steps until the fixed boundary is approached.

For comparison, the same specimen has been analyzed with cohesive zone analysis. Interface elements are used with a bilinear cohesive law (cf. Van der Meer et al., 2012b). An additional parameter in the cohesive analysis is the interfacial strength, which is set equal to 80 MPa. To keep the computational cost of the cohesive analysis within acceptable bounds, use is made of symmetry and crack growth is only considered in a subdomain where a fine mesh is applied. In a mesh of six-node prismatic elements, the used in-plane characteristic element length of 0.2 mm was found to be the maximum allowable size for robust analysis.

In Figure 4.7, the global response of the double cantilever beam according to the two different models is compared. The difference between the two curves is very small. The main reason behind the difference in post-peak response is the fact that the level set method presented here is an explicit approach. Because G is allowed to be higher than G_c, the effective fracture energy is higher in the level set analysis. The difference could be further reduced by choosing a lower value for μ.

In Figure 4.8, the shape of the crack front from the level set analysis is compared to the shape of the cohesive zone from cohesive zone analysis. The two are very similar. Altogether, the comparison with cohesive zone analysis gives confidence that the mechanics in the level set model are correct. At the same time, the computational costs are sharply reduced with the new approach.

In Figure 4.9, the computed energy release rate from two different time steps is shown as a function of transverse coordinate y. The value of G_c is indicated with the dotted line. The first data set (the dashed line in Figure 4.9) is from a time step during the early stage of the simulation where the initial straight crack front is

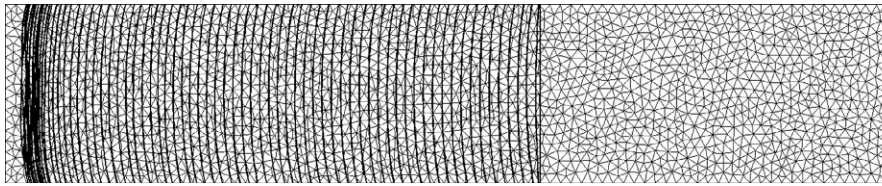

Figure 4.6 Front evolution in level set analysis; plotting the front from every second step.

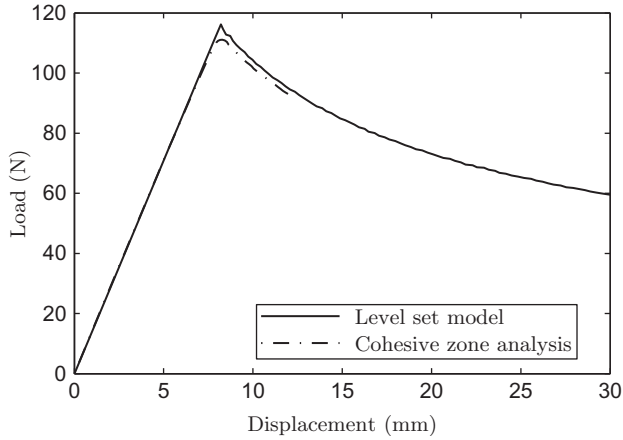

Figure 4.7 Load-displacement response in comparison with cohesive zone analysis.

Figure 4.8 Comparison in shape of level set front and shape of cohesive zone; black lines are consecutive-level set fronts (each time skipping one time step); shading indicates cohesive damage.

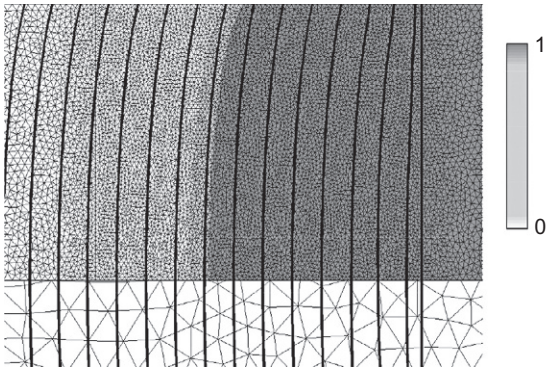

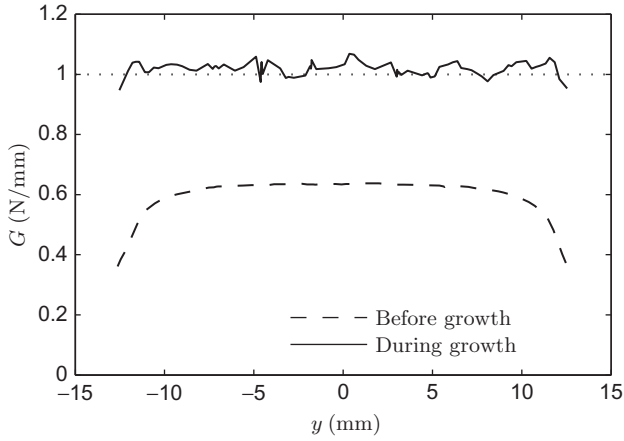

Figure 4.9 Distribution of computed energy release rate G from two different time steps: one during the loading stage before crack growth and one during the stage with stable crack growth.

stationary. Here, the tendency of the crack to grow faster in the middle than along the free edges is already visible. There is a clear drop in energy release rate near the free edge. The computed energy release rate profile is smooth even though the front is not aligned with the element edges in the irregular mesh. The second data set (the solid line in Figure 4.9) shows a typical energy release rate profile from a time step during the stable crack growth process. The curvature of the front has a negative effect on the stability of the computed energy release rate values, which can be observed from the roughness of the curve. The stabilization term in Equation (4.20) smooths the velocity profile that is computed from these energy release rate values. The influence of the viscosity parameter μ in Equation (4.4) is visible through the fact that computed G-values are on average somewhat higher than the fracture energy G_c of 1 N/mm.

4.5.2 Computational costs

The total analysis, where the crack grows from an initial length of 50.8 mm to almost the full specimen length of 127 mm, is performed in 140 time steps. The total number of nodes in the in-plane discretization equals 7713. Using only one layer of elements per arm, this results in a total number of degrees of freedom that ranges from 64,374 for the first time step to 77,346 for the last.

The cohesive analysis, with sufficient mesh-refinement over a small region of 15 by 12.7 mm^2, was performed with 1,31,472 degrees of freedom, about two times as many as in the level set analysis, where crack growth through the full domain of 127 by 25.4 mm^2 was modeled. On top of that, the time steps in the level set analysis are much larger than they can possibly be to obtain convergence with the cohesive zone method. It can be seem from Figure 4.8 that the level set front moves a distance that is more than the cohesive zone width in only two steps, whereas in cohesive zone analysis typically only a few more integration points per step are damaging. Finally, the absence of iterations makes a single time step in the level set analysis computationally cheaper than it is in the iterative cohesive analysis.

In opposition, it should be noted that the level set method requires the solution of a second linear system of equation in each time step. However, the cost of this procedure is negligible in comparison with the cost of the solution of the mechanics problem. In the present analysis, the number of degrees of freedom in the secondary system did not exceed 48.

The increased efficiency comes at the cost of an increased complexity that is mainly felt in terms of implementation: the method with XFEM, level set administration and a staggered solution scheme does not fit readily in conventional finite element packages. Once in place, however, the level set method for delamination allows for enormous gain in efficiency in comparison with the cohesive zone method.

4.6 Conclusions and outlook

The presented level set model for delamination is an efficient and flexible alternative to the cohesive zone method and the virtual crack closure technique. The approach is centered around a level set description of the delamination crack front, which allows

for the modeling of a sharp crack front that does not have to be aligned with the element boundaries. Therefore, crack growth can be analyzed without restrictive meshing requirements.

To compute energy release rates, use is made of through thickness integration of stress quantities in laminated shell theory. The method is therefore only applicable to interply cracks in relatively thin specimens. A generalization of the same approach to other types of damage, such as matrix cracking in laminates, is not straightforward. Under the assumption that matrix cracks develop at subcritical load levels, an approach where brittle stress-based insertion of transverse matrix cracks is combined with the present method for delamination could provide a useful tool for efficient analysis of more complex progressive failure mechanisms in laminates.

For the time being, this is a new approach that is applicable to analysis of crack growth in those load cases, where delamination is the only relevant type of cracking. A study of delamination-buckling with this approach is therefore a logical next step. Although the geometrically nonlinear nature of buckling requires a different element formulation, we foresee no conceptual difficulties.

Another perspective is the modeling of delamination under fatigue conditions. The explicit relation between crack growth rate and energy release rate, Equation (4.4), can be readily replaced by the Paris relation to model crack growth under cyclic loading (Latifi et al., 2015).

Acknowledgment

Financial support by the Dutch Technology Foundation (STW) under grant 12501 is gratefully acknowledged.

References

Alfano, G., Auricchio, F., Rosati, L., Sacco, E., 2001. MITC finite elements for laminated composite plates. Int. J. Numer. Method Eng. 50 (3), 707–738.

Allix, O., Ladevèze, P., 1992. Interlaminar interface modelling for the prediction of delamination. Compos. Struct. 22 (4), 235–242.

Béchet, É., Moës, N., Wohlmuth, B., 2008. A stable Lagrange multiplier space for stiff interface conditions within the extended finite element method. Int. J. Numer. Method Eng. 78 (8), 931–954.

Benzeggagh, M.L., Kenane, M., 1996. Measurement of mixed-mode delamination fracture toughness of unidirectional glass/epoxy composites with mixed mode bending apparatus. Compos. Sci. Technol. 56 (4), 439–449.

Davidson, B.D., 1990. An analytical investigation of delamination front curvature in double cantilever beam specimens. J. Compos. Mater. 24 (11), 1124–1137.

Davis, B., Wawrzynek, P.A., Ingraffea, A.R., 2014. 3-D simulation of arbitrary crack growth using an energy-based formulation—Part I: Planar growth. Eng. Fract. Mech. 115, 204–220.

Hansbo, A., Hansbo, P., 2004. A finite element method for the simulation of strong and weak discontinuities in solid mechanics. Comput. Method Appl. Mech. Eng. 193 (33–35), 3523–3540.

Jiang, W.G., Hallett, S.R., Green, B.G., Wisnom, M.R., 2007. A concise interface constitutive law for analysis of delamination and splitting in composite materials and its application to scaled notched tensile specimens. Int. J. Numer. Method Eng. 69 (9), 1982–1995.

Krueger, R., 2004. Virtual crack closure technique: history, approach, and applications. Appl. Mech. Rev. 57 (2), 109–143.

Latifi, M., Van der Meer, F.P., Sluys, L.J., 2015. A level set model for simulating fatigue-driven delamination in composites. Int. J. Fatigue 80, 434–442.

Ousset, Y., 1999. Numerical simulation of delamination growth in layered composite plates. Eur. J. Mech. Solids 18, 291–312.

Parisch, H., 1995. A continuum-based shell theory for non-linear applications. Int. J. Numer. Method Eng. 38, 1855–1883.

Rybicki, E.F., Kanninen, M.F., 1977. A finite element calculation of stress intensity factors by a modified crack closure integral. Eng. Fract. Mech. 9 (4), 931–938.

Schellekens, J.C.J., De Borst, R., 1994. Free edge delamination in carbon–epoxy laminates: a novel numerical/experimental approach. Compos. Struct. 28 (4), 357–373.

Sethian, J.A., 1999. Level Set, Methods and Fast Marching, Methods, second ed. Cambridge University Press, Cambridge, UK.

Shen, F., Lee, K.H., Tay, T.E., 2001. Modeling delamination growth in laminated composites. Compos. Sci. Technol. 61 (9), 1239–1251.

Song, J., Areias, P.M.A., Belytschko, T., 2006. A method for dynamic crack and shear band propagation with phantom nodes. Int. J. Numer. Method Eng. 67 (6), 868–893.

Turon, A., Camanho, P.P., Costa, J., Dávila, C.G., 2006. A damage model for the simulation of delamination in advanced composites under variable-mode loading. Mech. Mater. 38 (11), 1072–1089.

Van der Meer, F.P., Sluys, L.J., 2010. Mesh-independent modeling of both distributed and discrete matrix cracking in interaction with delamination. Eng. Fract. Mech. 77 (4), 719–735.

Van der Meer, F.P., Moës, N., Sluys, L.J., 2012a. A level set model for delamination—modeling crack growth without cohesive zone or stress singularity. Eng. Fract. Mech. 79, 191–212.

Van der Meer, F.P., Sluys, L.J., Hallett, S.R., Wisnom, M.R., 2012b. Computational modeling of complex failure mechanisms in laminates. J. Compos. Mater. 46 (5), 603–623.

Van der Meer, F.P., Sluys, L.J., Moës, N., 2012c. Toward efficient and robust computation of the energy release rate and mode mix for delamination growth. Compos. Part. A 43, 1101–1112.

Xie, D., Biggers, S.B., 2006. Strain energy release rate calculation for a moving delamination front of arbitrary shape based on the virtual crack closure technique. Part I: Formulation and validation. Eng. Fract. Mech. 73 (6), 771–785.

Yang, Q.D., Cox, B.N., 2005. Cohesive models for damage evolution in laminated composites. Int. J. Fract. 133 (2), 107–137.

Zou, Z., Reid, S.R., Soden, P.D., Li, S., 2001. Mode separation of energy release rate for delamination in composite laminates using sublaminates. Int. J. Solids Struct. 38 (15), 2597–2613.

This page intentionally left blank

Part Two

Numerical modelling approaches to intralaminar failure in advanced composite materials

This page intentionally left blank

Three-dimensional invariant-based failure criteria for transversely isotropic fibre-reinforced composites

5

P.P. Camanho, A. Arteiro*, G. Catalanotti*, A.R. Melro*,†, M. Vogler‡*
*Instituto de Ciência e Inovação em Engenharia Mecânica e Engenharia Industrial (INEGI), Universidade do Porto, Porto, Portugal; †ISVOUGA, Santa Maria da Feira, Portugal; ‡Vogler Engineering & Consulting Services, Hannover, Germany

5.1 Introduction

When composites are used in structural parts, a design development programme is generally implemented during which the performance of the structure is assessed prior to use, in the case of aero-structures, relying on a "*building-block*" approach (MIL-HDBK-17-3F, 2002). The process of validating the structural performance and durability of composite components generally consists of a complex combination of testing and analysis. While testing alone is prohibitively expensive and time consuming, analysis techniques alone are usually not sophisticated enough to adequately predict results under every set of conditions. Therefore, the development of improved, more accurate analytical and numerical tools that are able to predict the response of composites under general loading conditions and geometries is extremely important, whether the interest is to characterise the mechanical response of composite laminates or to assess the structural integrity of composite structures. In the absence of such tools, the design process will rely on mechanical tests based on a large number of specimens and empirical knockdown factors.

The effective use of polymer composite materials in load-carrying structures depends, then, on the ability to obtain reliable predictions of the onset and propagation of the different failure mechanisms. Accordingly, the development of accurate, fully benchmarked failure criteria that predict the onset of ply damage mechanisms in fibre-reinforced polymers (FRPs) is extremely important (Hinton et al., 2004). Indeed, this has been the subject of a great number of research studies in the literature for several years (Puck, 1969; Puck and Schneider, 1969; Tsai and Wu, 1971; Hinton and Soden, 1998; Cuntze and Freund, 2004; Dávila et al., 2005; Catalanotti et al., 2013).

Failure criteria are especially useful to provide failure envelopes from relatively simple experimental data that can be used in the analysis, design and calculation of safety factors of composite structures subjected to complex loading and boundary conditions. Stress- (Christensen, 1997; Liu and Tsai, 1998; Sun and Tao, 1998; Hart-Smith, 1998a; Sun et al., 2002; Kuraishi et al., 2002) and strain-based criteria

Numerical modelling of failure in advanced composite materials. http://dx.doi.org/10.1016/B978-0-08-100332-9.00005-0
Copyright © 2015 Elsevier Ltd. All rights reserved.

(Hart-Smith, 1998b) are generally "*purely empirical*" (Liu and Tsai, 1998), and their replacement by phenomenological failure criteria, with a stronger physical basis, is more and more common (Puck and Schürmann, 1998, 2002; Dávila and Camanho, 2003; Cuntze and Freund, 2004; Dávila et al., 2005; Pinho et al., 2006; Catalanotti et al., 2013). Nevertheless, it should be noted that failure criteria must be simple enough for application in engineering problems while capturing the relevant physics of the problem (Puck and Schürmann, 1998).

To meet the most common design requirements, failure criteria must be applicable at the ply, laminate and structural level. Because failure at these levels is often the consequence of the accumulation of micro-level failure events, an understanding of the micro-mechanical damage mechanisms is crucial to developing accurate and physically based failure theories (Dávila and Camanho, 2003). Regarding the mathematical form of the failure criteria and the shape of the corresponding envelopes, there are some restrictions that must also be taken into account. For example, failure envelopes must be closed, in order to prevent infinite strength, and they must be convex, so that unloading from a stress state will not lead to additional failures (Liu and Tsai, 1998).

Among the phenomenological failure criteria presented in the literature, those proposed by Puck and Schürmann (1998, 2002) for transverse failure are often used by the composites' research and design communities, with several other theories appearing as extensions to these criteria (Dávila and Camanho, 2003; Dávila et al., 2005; Pinho et al., 2005, 2006; Catalanotti et al., 2013). Puck's failure criterion for matrix transverse cracking is based on a modified Mohr/Coloumb theory for brittle transversely isotropic materials. The tractions acting on the fracture plane, which needs to be determined, are used to assess failure under two fundamental regimes: transverse tension (positive normal stress) or transverse compression (negative normal stress). The orientation of the fracture plane is determined when the *plane of maximum stress effort* is found (i.e., the plane that maximises the failure index). This means that a maximisation problem needs to be solved, which is generally done by varying the orientation of the fracture plane, calculating the failure index for every angle and recording the orientation giving the maximum value of the failure index.

In the design and analysis of thick composite laminates, general three-dimensional (3D) stress states should be accounted for, and reliable failure criteria must be formulated for these cases. Improved 3D failure criteria, based on the ideas presented by Puck and Schürmann (1998, 2002), were recently proposed by Catalanotti et al. (2013) to address more general stress states in a consistent way, providing not only the predictions for the onset of ply damage, but also additional information regarding the type of failure and the orientation of the fracture plane.

To obtain a simpler and elegant description of failure of laminated composites, Cuntze and Freund (2004) presented a formulation of different failure criteria based on invariants for each individual failure mode observed in anisotropic, heterogeneous materials. This means that the formulations do not depend on coordinate-system transformations. Therefore, the search for the fracture plane is not necessary. Cuntze and Freund (2004) suggest that the results of the invariant-based failure criteria

can then be used for post-determination of the angle of the fracture plane; for example, Cuntze and Freund (2004) used Mohr/Coloumb theory, but considered only a state of plane stress, without including the shear stresses σ_{12} and σ_{13} (1 corresponds to the fibre direction, and 2–3 to the transverse directions). Cuntze and Freund (2004) claim that, besides not predicting directly the orientation of the fracture plane, the invariant approach's simplicity can result in a certain loss of '*physical correctness*'.

In this work, new 3D failure criteria for fibre-reinforced composite materials based on the transversely isotropic yield function developed by Vogler et al. (2010, 2013) and Camanho et al. (2014) are described. The new 3D failure criteria have an invariant quadratic formulation based on structural tensors that accounts for the preferred directions of the anisotropic material. With this formulation, anisotropy is derived using structural tensors and not symmetry conditions based on a reference coordinate system. The so-called structural tensors represent the material symmetries of the respective anisotropy class as an intrinsic material property, which enables an elegant *coordinate system-free* description of anisotropy using isotropic tensor functions. Note that the 3D invariant-based failure criteria proposed in this work predict failure in a single lamina, requiring the calculation of the strains and stresses of each ply of multidirectional laminates, which is a common procedure in the most recent failure criteria for FRPs (Puck and Schürmann, 1998, 2002; Dávila and Camanho, 2003; Dávila et al., 2005; Catalanotti et al., 2013).

For transverse failure mechanisms, a pragmatic approach is proposed to estimate the orientation of the fracture plane; for failure criteria based on the invariant theory, since a *coordinate system-free* description of failure is considered, there is no means of obtaining the local coordinate system associated with the *maximum effort* directly from the criteria, and the orientation of the fracture plane cannot be determined. With the pragmatic approach proposed here, determining the orientation of the fracture plane of composite laminates under transverse, matrix-dominated failure is made possible, providing a useful evaluation tool, not only for comparison against other failure theories, but also in assessing failure mode types (Christensen and DeTeresa, 2003). It should be noted that the orientation of the fracture plane is essential for the accurate representation of transverse cracking by means of smeared crack formulations (Camanho et al., 2013).

To account for the effect of ply thickness when the laminae are embedded in a multidirectional laminate, proper definitions of the *in situ* properties are derived in the framework of the invariant-based failure criterion for transverse failure mechanisms. This is important for application of the proposed criteria as damage initiation functions in advanced computational models that predict the inelastic and fracture behaviour of composites (Camanho et al., 2007; Maimí et al., 2007a,b; Camanho et al., 2013).

Finally, the proposed 3D failure criteria are validated using several case studies available in the literature based on experimental testing. Moreover, a new validation strategy is explored based on computational micro-mechanics, showing the validity of both approaches for more complex stress states (Camanho et al., 2014).

5.2 Invariant-based failure criterion for transverse failure of unidirectional composites

5.2.1 Failure criterion formulation

The failure criteria for the different failure mechanisms that occur in composite materials reinforced by unidirectional fibres used in this chapter were originally presented in Camanho et al. (2014). The following points summarise the main aspects of the failure criteria.

The proposed 3D invariant-based criterion (Camanho et al., 2014) is formulated directly from the yield function presented by Vogler et al. (2013). According to the invariant formulation of anisotropic constitutive equations (Boehler, 1987a), transversely isotropic materials can be characterised by a preferred direction **a**. For unidirectional (UD) FRPs, this preferred direction **a** is the fibre direction (Spencer, 1987; Vogler et al., 2013). If this direction coincides with the x_1-direction, which is often the case for UD fibre-reinforced laminates, the vector **a** is defined as:

$$\mathbf{a} = [1\ 0\ 0]^{\mathrm{T}} \tag{5.1}$$

The structural tensor **A** of transverse isotropy, which represents the material's intrinsic characteristic direction, is an additional tensor argument to formulate the failure criterion as an isotropic tensor function. It is defined as the dyadic product of the preferred direction **a** (Spencer, 1987; Vogler et al., 2013), that is,

$$\mathbf{A} = \mathrm{a} \otimes \mathrm{a} \tag{5.2}$$

According to the proposed invariant formulation, failure is a function, f_M, of the stress tensor $\boldsymbol{\sigma}$ and of the structural tensor **A**, which are the argument tensors.

The functional basis for transverse isotropy, formed by the argument tensors $\boldsymbol{\sigma}$ and **A**, reads (Boehler, 1987b; Vogler et al., 2013):

$$\mathrm{tr}\,\boldsymbol{\sigma},\quad \mathrm{tr}\,\boldsymbol{\sigma}^2,\quad \mathrm{tr}\,\boldsymbol{\sigma}^3,\quad \mathrm{tr}(\mathbf{A}\boldsymbol{\sigma})\quad \text{and}\quad \mathrm{tr}(\mathbf{A}\boldsymbol{\sigma}^2) \tag{5.3}$$

It should be noted that, according to the invariant theory, an arbitrary linear combination of the stress tensor $\boldsymbol{\sigma}$ can be used in Equation (5.3). Furthermore, a linear combination of the basic invariants given in (5.3) can also be used, without loss of generality (Vogler et al., 2013).

Vogler et al. (2013) reformulated the quadratic ($\mathrm{tr}\,\boldsymbol{\sigma}^2$ and $\mathrm{tr}(\mathbf{A}\boldsymbol{\sigma}^2)$) and the linear ($\mathrm{tr}\,\boldsymbol{\sigma}$) invariants of the functional basis (5.3) to identify particular stress states with the corresponding invariants. The basic invariant $\mathrm{tr}\,\boldsymbol{\sigma}^3$ is neglected; the cubic invariant $\mathrm{tr}\,\boldsymbol{\sigma}^3$ is suitable for modelling metal plasticity, which is obviously not the case. The invariant $\mathrm{tr}(\mathbf{A}\boldsymbol{\sigma})$ can be used to represent yielding in the fibre direction, which is neglected when modelling (conventional) UD fibre-reinforced laminates.

Following Vogler et al. (2013), the quadratic invariants $\mathrm{tr}\,\boldsymbol{\sigma}^2$ and $\mathrm{tr}(\mathbf{A}\boldsymbol{\sigma}^2)$ of the functional basis (5.3) are reformulated using the following decomposition of the stress tensor (Spencer, 1987):

$$\boldsymbol{\sigma} = \boldsymbol{\sigma}^{\mathrm{p}} + \boldsymbol{\sigma}^{\mathrm{r}} \tag{5.4}$$

with:

$$\boldsymbol{\sigma}^{\mathrm{r}} = \frac{1}{2}(\mathrm{tr}\,\boldsymbol{\sigma} - \mathbf{a}\boldsymbol{\sigma}\mathbf{a})\mathbf{1} - \frac{1}{2}(\mathrm{tr}\,\boldsymbol{\sigma} - 3\mathbf{a}\boldsymbol{\sigma}\mathbf{a})\mathbf{A} \tag{5.5a}$$

$$\boldsymbol{\sigma}^{\mathrm{p}} = \boldsymbol{\sigma} - \boldsymbol{\sigma}^{\mathrm{r}} \tag{5.5b}$$

The reaction stress tensor $\boldsymbol{\sigma}^{\mathrm{r}}$ contains the hydrostatic pressure and the projection of the stress tensor onto the preferred direction $\mathbf{a}$. Since the fibre-dominated failure mechanisms are treated separately in the formulation of the failure criteria, the quadratic invariants of the functional basis are reformulated using the plasticity inducing stress tensor $\boldsymbol{\sigma}^{\mathrm{p}}$. This procedure enables the identification of transverse shear loading and in-plane shear loading solely with invariants I_1 and I_2, respectively. The linear invariants tr $\boldsymbol{\sigma}$ and tr($\mathbf{A}\boldsymbol{\sigma}$) of the functional basis (5.3) are used to define the third invariant I_3. The set of transversely isotropic invariants used to formulate the failure surface reads (Vogler et al., 2013):

$$I_1 = \frac{1}{2}\mathrm{tr}(\boldsymbol{\sigma}^{\mathrm{p}})^2 - \mathbf{a}(\boldsymbol{\sigma}^{\mathrm{p}})^2\mathbf{a} \tag{5.6a}$$

$$I_2 = \mathbf{a}(\boldsymbol{\sigma}^{\mathrm{p}})^2\mathbf{a} \tag{5.6b}$$

$$I_3 = \mathrm{tr}\,\boldsymbol{\sigma} - \mathbf{a}\boldsymbol{\sigma}\mathbf{a} \tag{5.6c}$$

The transversely isotropic failure criterion for transverse failure of UD fibre-reinforced laminates reads:

$$f_M = \alpha_1 I_1 + \alpha_2 I_2 + \alpha_3 I_3 + \alpha_{32} I_3^2 \leq 1 \tag{5.7}$$

with:

$$\begin{aligned} &\alpha_3 = \alpha_3^t, \quad \alpha_{32} = \alpha_{32}^t \quad \text{if } I_3 > 0, \quad \text{and} \\ &\alpha_3 = \alpha_3^c, \quad \alpha_{32} = \alpha_{32}^c \quad \text{if } I_3 \leq 0 \end{aligned} \tag{5.8}$$

The distinction between $I_3 > 0$ and $I_3 \leq 0$ enables the representation of failure under biaxial stress states.

The failure criterion represented by Equation (5.7) results in six failure parameters that, together with the respective invariants, are related to certain load states: transverse shear, in-plane shear, uniaxial tension/compression and biaxial tension/compression. These six failure parameters can be calculated imposing simple stress states and applying the failure criterion (Vogler et al., 2013). Taking the x_1-direction as the fibre direction, the six failure parameters read (Vogler et al., 2013):

$$\alpha_1 = \frac{1}{S_{\mathrm{T}}^2} \tag{5.9a}$$

$$\alpha_2 = \frac{1}{S_L^2} \tag{5.9b}$$

$$\alpha_{32}^t = \frac{1 - \dfrac{Y_T}{2Y_{BT}} - \alpha_1 \dfrac{Y_T^2}{4}}{Y_T^2 - 2Y_{BT}Y_T} \tag{5.9c}$$

$$\alpha_3^t = \frac{1}{2Y_{BT}} - 2\alpha_{32}^t Y_{BT} \tag{5.9d}$$

$$\alpha_{32}^c = \frac{1 - \dfrac{Y_C}{2Y_{BC}} - \alpha_1 \dfrac{Y_C^2}{4}}{Y_C^2 - 2Y_{BC}Y_C} \tag{5.9e}$$

$$\alpha_3^c = \frac{1}{2Y_{BC}} - 2\alpha_{32}^c Y_{BC} \tag{5.9f}$$

where S_T and S_L are respectively the transverse and in-plane shear strengths, Y_T and Y_C are respectively the transverse tensile and compressive strengths, and Y_{BT} and Y_{BC} are respectively the biaxial transverse tensile and compressive strengths.

5.2.2 Orientation of the fracture plane: Pragmatic approach

As discussed by Christensen and DeTeresa (2003), determining the orientation of the fracture plane of composite laminates under transverse, matrix-dominated failure is quite important, since it provides a useful evaluation tool, not only in comparing the various failure theories, but also in assessing failure mode types. The knowledge of the orientation of the fracture plane is also essential for the accurate representation of transverse cracking by means of smeared crack formulations (Camanho et al., 2013).

Phenomenological failure theories based on the approach proposed by Puck and Schürmann (1998, 2002) determine the orientation of the fracture plane through a maximisation problem, namely by searching for the *plane of maximum stress effort* (see, e.g., Dávila et al., 2005; Pinho et al., 2005, 2006; Wiegand et al., 2008; Catalanotti et al., 2013). This is, therefore, a direct outcome of the failure criteria. However, for failure criteria based on the invariant theory, since a *coordinate system-free* description of failure is considered, there is no means of obtaining the local coordinate system associated with the *maximum effort* directly from the criteria, and the orientation of the fracture plane cannot be determined. Hence, a pragmatic approach has to be considered to obtain at least an estimate of the orientation of the fracture plane.

According to Thom (1998), for a transverse compression-dominated failure mode, the stress normal to the fracture plane (t_n) remains constant and equal to the transverse shear strength (S_T). Thus, for $\sigma_{22} < 0$ (compression) and $|\sigma_{22}| \geq S_T$, the following relation can be assumed:

$$|t_n| = |\sigma_{22}|\cos^2\alpha = S_T \tag{5.10}$$

and the orientation of the fracture plane, α (see Figure 5.1), can be estimated as:

$$\alpha = \arccos\sqrt{\frac{S_T}{|\sigma_{22}|}} \tag{5.11}$$

However, based on Puck's observations, Thom (1998) suggested the use of a factor R_{23}, instead of the transverse shear strength S_T, derived from Mohr's circle based on transverse compression (see also Dávila et al., 2005):

$$R_{23} = \frac{|Y_C|}{2}\cot\alpha_0 \tag{5.12}$$

where α_0 is the fracture angle for pure transverse compression. The orientation of the fracture angle (α) for a general transverse compression-dominated failure is then:

$$\alpha = \arccos\sqrt{\frac{R_{23}}{|\sigma_{22}|}} \tag{5.13}$$

If Equations (5.12) and (5.13) are used to estimate the orientation of the fracture angle, it is observed, however, that for pure transverse compression, the predicted fracture angle does not coincide with α_0, which is unreasonable. Therefore, instead of Equation (5.12), the following expression should be used to calculate the factor R_{23}:

$$R_{23} = |Y_C|\cos^2\alpha_0 \tag{5.14}$$

which can be obtained manipulating Equation (5.11) and considering $\alpha = \alpha_0$ when $\sigma_{22} = Y_C$ (pure transverse compression).

Koerber et al. (2010) performed off-axis compression tests on IM7/8552 carbon–epoxy and measured the orientation of the fracture plane. Figure 5.2 shows the orientation of the fracture plane as a function of the off-axis angle obtained by Koerber et al.

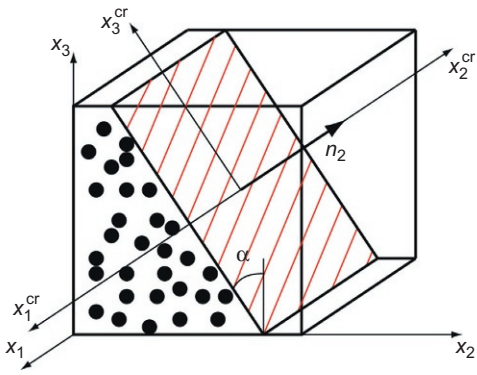

Figure 5.1 Transverse fracture plane.

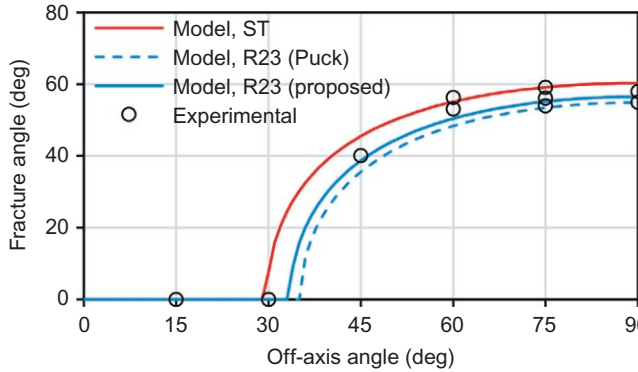

Figure 5.2 Orientation of the fracture plane as a function of the off-axis angle for off-axis compression tests performed by Koerber et al. (2010), and a comparison with the results from the expressions used to estimate the fracture angle.

(2010), and a comparison with the results from the expressions presented before to estimate the orientation of the fracture angle. In Figure 5.2, 'Model, ST' refers to Equation (5.11), whereas 'Model, R23 (Puck)' and 'Model, R23 (proposed)' refer to Equations (5.12) and (5.13) and to Equations (5.13) and (5.14), respectively.

Comparing the estimates shown in Figure 5.2 with the experimental results, it is clear that Equations (5.13) and (5.14) give the best predictions. When using Equations (5.12) and (5.13), the predictions are also very good; however, as already mentioned, in spite of using the angle α_0 to calculate the factor R_{23}, the prediction of the orientation of the fracture plane for pure transverse compression does not coincide with α_0, which is, from a conceptual point of view, not reasonable. Therefore, if the fracture angle α_0 is known *a priori*, the authors suggest the use of Equations (5.13) and (5.14) to estimate the orientation of the fracture plane. Observing the predictions from Equation (5.11), it can be seen that the estimates are reasonable, particularly when taking into account that the fracture angle α_0 is never used to obtain such estimates. Hence, it can be concluded that in case α_0 is not known, Equation (5.11) can be used to estimate the orientation of the fracture plane, without incurring on unrealistic predictions.

From Figure 5.2, it is clear that, in the case of transverse compression-dominated failure for a state of plane stress, the proposed expressions give good predictions of the orientation of the fracture angle, without any kind of maximisation procedure or search for the *plane of maximum stress effort*. But for the general 3D case, other stress states and combinations of them should also be addressed. For example, when subjected to through-the-thickness transverse compression ($\sigma_{33} < 0$), a similar type of expressions to those presented for in-plane transverse compression ($\sigma_{22} < 0$) can be deduced. In this case, assuming a transverse compression-dominated failure mode ($\sigma_{33} < 0$ and $|\sigma_{33}| \geq R_{23}$), the orientation of the fracture plane (α) can be estimated as:

$$\alpha = \arcsin\sqrt{\frac{R_{23}}{|\sigma_{33}|}} \tag{5.15}$$

where R_{23} is given by Equation (5.14); if α_0 is not known *a priori*, $R_{23} = S_T$ can be adopted (as already shown for in-plane transverse compression). Notice that α_0 is the orientation of the fracture plane when pure in-plane transverse compression ($\sigma_{22} = Y_C$, $\sigma_{ij} = 0$) is applied. In the case of biaxial transverse compression, it is assumed that, when $|\sigma_{22}| > |Y_C|$ or $|\sigma_{33}| > |Y_C|$, the orientation of the fracture angle remains constant. Thus, Equations (5.13) and (5.15) can be rewritten, respectively, as:

$$\alpha = \arccos\sqrt{\frac{R_{23}}{\min\{|\sigma_{22}|, |Y_C|\}}} \tag{5.16}$$

and

$$\alpha = \arcsin\sqrt{\frac{R_{23}}{\min\{|\sigma_{33}|, |Y_C|\}}} \tag{5.17}$$

For general transverse compressive failure ($I_3 < 0$), it is assumed that the highest transverse stress (in absolute value) will define the orientation of the fracture plane. In other words, when $I_3 < 0$, $|\sigma_{22}| > |\sigma_{33}|$ and $|\sigma_{22}| \geq S_T$, Equation (5.16) holds; on the other hand, if $I_3 < 0$, $|\sigma_{33}| > |\sigma_{22}|$ and $|\sigma_{33}| \geq S_T$, Equation (5.17) must be used.

When $I_3 < 0$ but $|\sigma_{22}| < S_T$ and $|\sigma_{33}| < S_T$, or when $I_3 > 0$, failure is either dominated by a transverse state of stress or by longitudinal shear. To assess which failure mode is dominating, the contribution of each type of stressing to the failure criterion can be used. Thus, if $\left|\alpha_1 I_1 + \alpha_3 I_3 + \alpha_{32} I_3^2\right| > |\alpha_2 I_2|$, the orientation of the fracture angle can be estimated by the orientation of the plane of the secondary principal stresses:

$$\alpha = \frac{1}{2}\arctan\left(\frac{2\sigma_{23}}{\sigma_{22} - \sigma_{33}}\right) \tag{5.18}$$

otherwise, the orientation of the fracture angle can be estimated by the in-plane shear effort:

$$\alpha = \arctan\left(\frac{\sigma_{13}}{\sigma_{12}}\right) \tag{5.19}$$

Table 5.1 shows the experimental results for the orientation of the fracture plane under transverse tensile and compressive failure given by Christensen and DeTeresa (2003), and a comparison with the predictions of the proposed pragmatic approach. For transverse compression, the relation $R_{23} = S_T$ was adopted. A very good correlation between experiments and predictions can be observed.

Table 5.1 Experimental results for the orientation of the fracture plane under transverse tensile and compressive failure (Christensen and DeTeresa, 2003), and a comparison with the predictions of the proposed pragmatic approach

Material	Transverse strengths (MPa)		Orientation of the fracture plane (°)	
			Measured	*Predicted*
AS4/Ultem[a]	Tension	78.6	90	90
	Compression	191.0	38 (±1.2)[c]	39.9
AS4/3501-6[b]	Tension	64.8	90	90
	Compression	241.3	31 (±4.7)[c]	31.2

[a]AS4 carbon fibre-reinforced thermoplastic (Ultem polyetherimide).
[b]AS4 carbon fibre-reinforced 3501-6 untoughened epoxy.
[c]Standard deviation.

5.2.3 In situ *properties*

When embedded in a multidirectional laminate, the actual strengths of the laminae whose fibre orientation is perpendicular to the loading direction are not only higher than those measured in UD coupons, as they reportedly increase with decreasing ply thickness (Camanho et al., 2006; Saito et al., 2012, 2014). In fact, early research about the strength prediction of multidirectional laminates has shown that using as ply properties those measured directly from UD plies, regardless of ply orientation or laminate thickness, results in very conservative predictions that could differ substantially from the experimental results (Chang and Chen, 1987; Puck and Schürmann, 2002).

This deterministic size effect, known as the *in situ* effect, is typically taken into account by using fracture mechanics models that predict the relation between the ply thickness, its fracture toughness and the *in situ* strengths (Dvorak and Laws, 1987; Camanho et al., 2006), whose accurate determination is necessary for implementation of any physically based failure criteria for transverse fracture in multidirectional laminates (Flaggs, 1985; Chang and Chang, 1987; Chang et al., 1991; Puck and Schürmann, 2002; Dávila et al., 2005; Pinho et al., 2005; Camanho et al., 2006, 2013; Maimí et al., 2006, 2007a; Mayugo et al., 2010). Note that, in the case of in-plane shear, linear elastic fracture mechanics alone is not able to accurately predict the *in situ* strength, and the nonlinear shear response typically observed in laminated composites must be included in the prediction models (Camanho et al., 2006).

Therefore, to account for the effect of ply thickness when the laminae are embedded in a multidirectional laminate, proper definitions of the *in situ* properties must be accounted for in the criterion that predicts transverse fracture. The *in situ* transverse tensile and in-plane shear strengths, Y_T^{is} and S_L^{is} respectively, can be calculated using the analytical models proposed by Camanho et al. (2006). The remaining transverse strength properties, though, should be defined in the framework of the corresponding failure criterion.

The *in situ* transverse shear strength, S_T^{is}, and the *in situ* biaxial transverse tensile strength, Y_{BT}^{is}, are calculated imposing (Catalanotti et al., 2013):

$$\begin{cases} \eta_L^{(+)} = \eta_{L,is}^{(+)} \\ \eta_T^{(+)} = \eta_{T,is}^{(+)} \end{cases} \tag{5.20}$$

where η_L and η_T are, respectively, the slopes in the σ_{22}–σ_{12} and σ_{22}–σ_{23} failure envelopes when $\sigma_{22} = 0$ (Puck and Schürmann, 2002) – see Figure 5.3. They depend on the sign of the stress σ_{22} and, for the tensile case, can be defined as:

$$\eta_L^{(+)} = \left.\frac{\partial \sigma_{12}}{\partial \sigma_{22}^{(+)}}\right|_{\sigma_{22}=0^+} = -\frac{1}{2}\frac{\alpha_3^t}{\sqrt{\alpha_2}} \tag{5.21}$$

$$\eta_T^{(+)} = \left.\frac{\partial \sigma_{23}}{\partial \sigma_{22}^{(+)}}\right|_{\sigma_{22}=0^+} = -\frac{1}{2}\frac{\alpha_3^t}{\sqrt{\alpha_1}} \tag{5.22}$$

The system of Equations (5.20) can be solved for S_T^{is} and Y_{BT}^{is} using, for example, a numerical procedure based on floating-point arithmetics.

In compression, it is assumed that the biaxial transverse compressive strength is not an *in situ* property, that is, $Y_{BC}^{is} = Y_{BC}^{ud}$. This can be justified observing Figure 5.4. Under transverse biaxial compression, the confinement is promoted by the surrounding pressure; therefore, it is assumed that the adjacent plies do not affect such constraining effect.

Assuming that $Y_{BC}^{is} = Y_{BC}^{ud}$, the *in situ* transverse compressive strength, Y_C^{is}, can be determined imposing one of the following relations (both giving the same result):

$$\eta_L^{(-)} = \eta_{L,is}^{(-)} \tag{5.23}$$

$$\eta_T^{(-)} = \eta_{T,is}^{(-)} \tag{5.24}$$

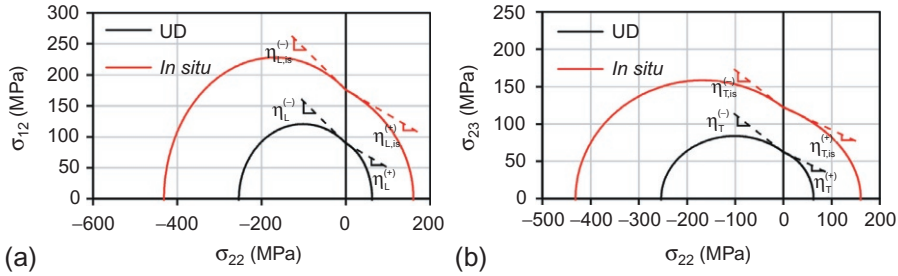

Figure 5.3 Definitions of the parameters η_L and η_T. (a) σ_{22}–σ_{12} failure envelope. (b) σ_{22}–σ_{23} failure envelope.

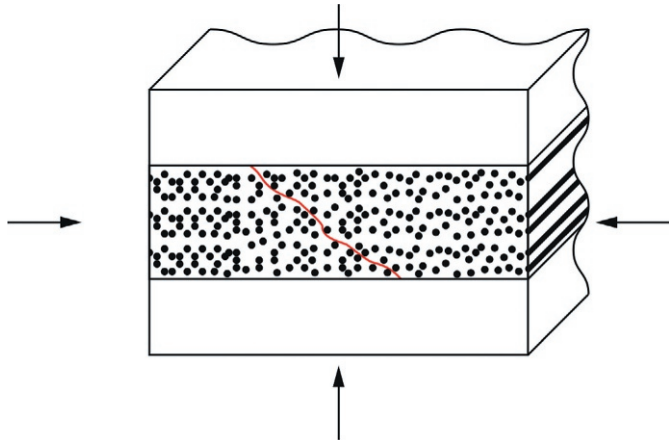

Figure 5.4 Representative volume element of a multidirectional laminate subjected to biaxial transverse compression.

with:

$$\eta_{\mathrm{L}}^{(-)} = \left.\frac{\partial \sigma_{12}}{\partial \sigma_{22}^{(-)}}\right|_{\sigma_{22}=0^{-}} = -\frac{1}{2}\frac{\alpha_3^c}{\sqrt{\alpha_2}} \tag{5.25}$$

$$\eta_{\mathrm{T}}^{(-)} = \left.\frac{\partial \sigma_{23}}{\partial \sigma_{22}^{(-)}}\right|_{\sigma_{22}=0^{-}} = -\frac{1}{2}\frac{\alpha_3^c}{\sqrt{\alpha_1}} \tag{5.26}$$

Equation (5.23) or (5.24) can be solved for $Y_{\mathrm{C}}^{\mathrm{is}}$ using, for example, a numerical procedure based on floating-point arithmetics.

As an example, Table 5.2 shows the UD properties and the *in situ* properties for a 0.125 mm thick IM7/8552 carbon–epoxy inner ply, calculated using the procedure just described. Figure 5.5 shows the relation between the ply thickness and the *in situ* strengths calculated using the same procedure. These values are not far from those obtained using alternative failure criteria (Catalanotti et al., 2013; Camanho et al., 2013).

5.2.4 Preliminary results

Following previous work (Thom, 1998; Cuntze and Freund, 2004), it is assumed that the transverse shear strength, S_{T}, is equal to the transverse tensile strength, Y_{T}. This assumption is based on the observation that under pure transverse shear the fracture angle is roughly 45°. In this case, the first principal stress, σ_1, equals the shear transverse stress σ_{23} – see Figure 5.6; in other words, for pure transverse shear, σ_1 acts as in the case of transverse tension, but in a rotated frame. Therefore, at failure, the critical transverse shear stress, or transverse shear strength, S_{T}, equals the transverse tensile strength, Y_{T}.

Table 5.2 Strength properties of the IM7/8552 carbon–epoxy UD tape and *in situ* properties for a 0.125 mm thick IM7/8552 inner ply embedded in a multidirectional laminate

Properties		Observations
Ply properties (UD tape)		
Y_T (MPa)	62.3	Camanho and Lambert (2006)
Y_{BT} (MPa)	38.7	Vogler et al. (2013)
Y_C (MPa)	−253.7	Koerber et al. (2010)
Y_{BC} (MPa)	−600.0	Vogler et al. (2013)
S_L (MPa)	89.6	Catalanotti et al. (2013)
S_T (MPa)	62.3	Camanho et al. (2014)
In situ *properties*		
Y_T^{is} (MPa)	160.5	Camanho et al. (2006)
Y_{BT}^{is} (MPa)	92.1	Equation (5.20)
Y_C^{is} (MPa)	−575.9	Equation (5.23) (or (5.24))
Y_{BC}^{is} (MPa)	−600.0	$Y_{BC}^{is} = Y_{BC}^{ud}$
S_L^{is} (MPa)	269.8	Camanho et al. (2006)
S_T^{is} (MPa)	187.6	Equation (5.20)

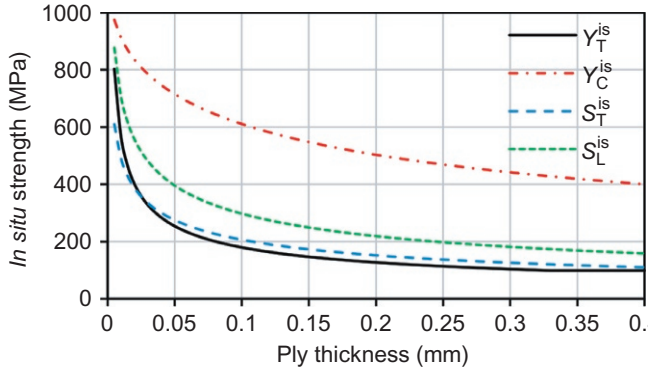

Figure 5.5 Relation between the ply thickness and the *in situ* strengths.

Figure 5.7 shows the failure envelopes of the IM7/8552 CFRP obtained with the invariant-based failure criterion for several stress states involving transverse, matrix-dominated failure mechanisms only. The material properties used to compute the failure envelopes are shown in Table 5.3, where G_{12} is the shear modulus, X_T is the longitudinal tensile strength and X_C is the longitudinal compressive strength of the UD ply (see Section 5.3 for details on the failure criteria for longitudinal failure mechanisms).

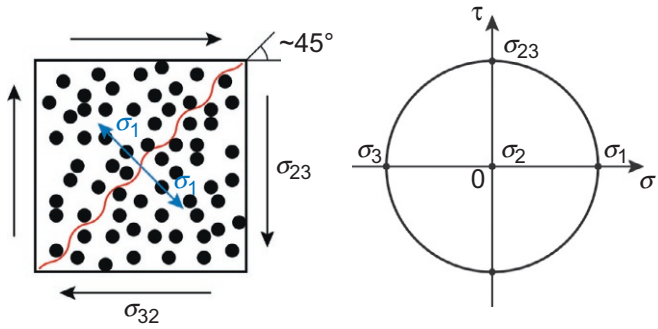

Figure 5.6 Mohr's circle for pure transverse shear.

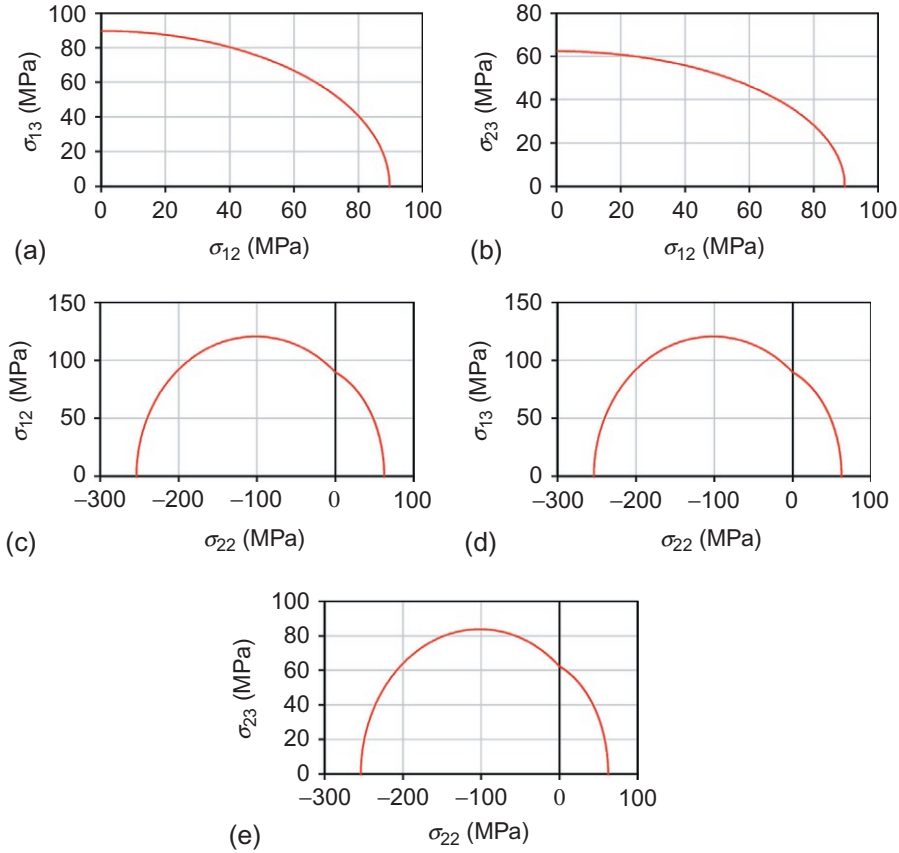

Figure 5.7 Failure envelopes of the IM7/8552 CFRP for several stress states obtained with the invariant-based failure criterion for transverse failure mechanisms. (a) σ_{12}–σ_{13}. (b) σ_{12}–σ_{23}. (c) σ_{22}–σ_{12}. (d) σ_{22}–σ_{13}. (e) σ_{22}–σ_{23}.

Table 5.3 IM7/8552 material properties

Properties		References
G_{12} (MPa)	5290.0	Camanho and Lambert (2006)
X_T (MPa)	2323.5	Catalanotti et al. (2013)
X_C (MPa)	−1017.5	Catalanotti et al. (2013)
Y_T (MPa)	62.3	Camanho and Lambert (2006)
Y_{BT} (MPa)	38.7	Vogler et al. (2013)
Y_C (MPa)	−253.7	Koerber et al. (2010)
Y_{BC} (MPa)	−600.0	Vogler et al. (2013)
S_L (MPa)	89.6	Catalanotti et al. (2013)
β (MPa^{-3})	2.12×10^{-8}	Camanho et al. (2006)

Observing the σ_{22}–σ_{12} stress space (Figure 5.7c), as expected, when the transverse stress σ_{22} becomes compressive, the apparent shear strength increases. Notice, however, that, for transverse failure mechanisms, the transversely isotropic invariant-based failure criterion does not distinguish between the longitudinal shear stresses σ_{12} and σ_{13} (see Equation (5.6b)). Consequently, unlike what is observed in other phenomenological failure criteria (Puck and Schürmann, 1998, 2002; Dávila and Camanho, 2003; Dávila et al., 2005; Pinho et al., 2006; Catalanotti et al., 2013), the failure loci for the σ_{22}–σ_{12} (Figure 5.7c) and σ_{22}–σ_{13} (Figure 5.7d) stress spaces (or σ_{33}–σ_{13} and σ_{33}–σ_{12}) are exactly the same. This does not respect the different interaction of the stress combinations σ_{22}–σ_{12} and σ_{22}–σ_{13} (or σ_{33}–σ_{13} and σ_{33}–σ_{12}), which arises from a typical material asymmetry observed in laminated composites (Cuntze and Freund, 2004); because σ_{22} and σ_{13} (or σ_{33} and σ_{12}) act on different planes, no interaction between them should exist (Catalanotti et al., 2013).

Cuntze and Freund (2004), after "*an intense trial and error search*", proposed an invariant term that respects such different interactions; nevertheless, such term results in mathematical inconsistencies when applied to the proposed failure criterion for longitudinal compressive failure by fibre kinking (Section 5.3.1). Because not accounting for the different interaction between the transverse stresses and longitudinal shear stresses acting on different planes is a side effect of the invariant theory, with negligible influence in the failure predictions for the typical load cases observed in composite structures, it is believed that the advantages of the proposed criteria (namely the ability to predict failure under high values of hydrostatic pressure – Figure 5.8) overcome this limitation.

Figure 5.8 shows the σ_{22}–σ_{33} failure envelopes when nonzero σ_{12} (Figure 5.8a), σ_{13} (Figure 5.8b) or σ_{23} (Figure 5.8c) shear stresses are applied. Unlike other 3D failure criteria (e.g., Pinho et al., 2006; Catalanotti et al., 2013), under biaxial transverse compression the failure envelopes are not open. Thus, the proposed failure criteria is able to predict material failure under high values of hydrostatic pressure, typically seen in the resins used in structural composites (Hoppel et al., 1995; Hine et al., 2005). Under hydrostatic tension, a gradual variation of the failure locus is observed, that is, an

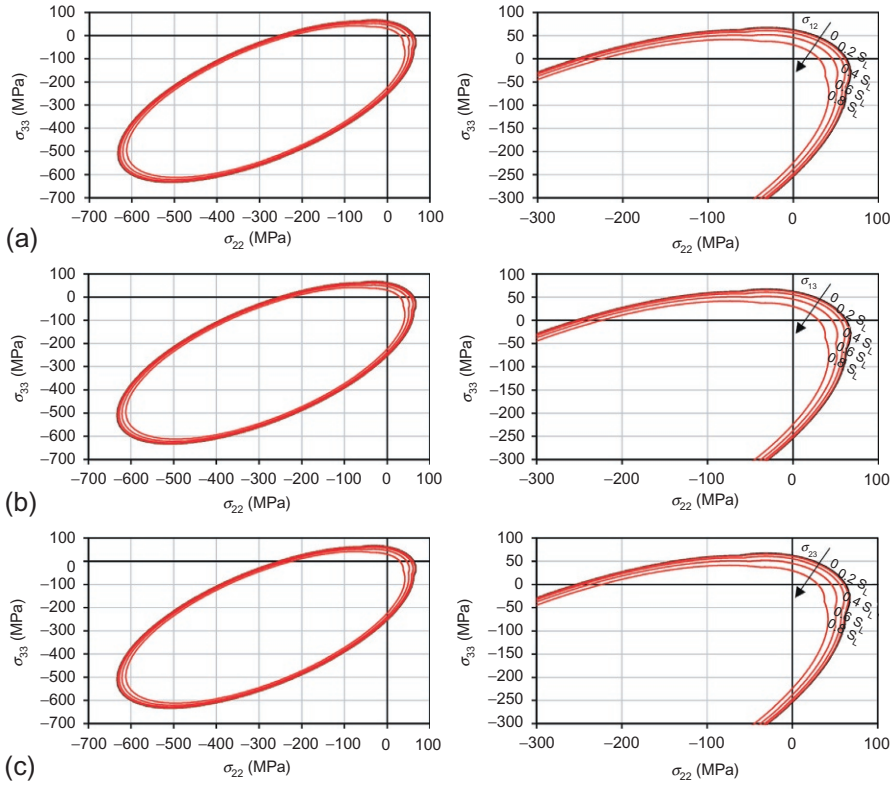

Figure 5.8 IM7/8552 carbon–epoxy's σ_{22}–σ_{33} failure envelopes. (a) Nonzero longitudinal shear stress σ_{12}. (b) Nonzero longitudinal shear stress σ_{13}. (c) Nonzero transverse shear stress σ_{23}.

interaction between $\sigma_{22} > 0$ and $\sigma_{33} > 0$ exists. Also, observing Figure 5.8, it can be seen that, for low values of negative transverse stresses ($\sigma_{22(33)} < 0$), the apparent transverse tensile strength ($\sigma_{33(22)} > 0$) increases slightly. Finally, Figure 5.8 shows that, in relative values, the effect of nonzero shear stresses (σ_{12}, σ_{13} or σ_{23}) in the σ_{22}–σ_{33} failure envelope is exactly the same; increasing the shear stresses, the failure envelope is reduced.

Finally, Figure 5.9 shows the σ_{22}–σ_{12} failure envelopes when a nonzero transverse stress σ_{33} is applied. When $\sigma_{33} > 0$, the failure locus is reduced, either when the transverse stress σ_{22} is positive or negative. This result does not coincide with the one obtained by Catalanotti et al. (2013) when $\sigma_{33} > 0$ and $\sigma_{22} > 0$, who claim that, in this case, the failure envelope must remain constant. According to Catalanotti et al. (2013), there is no interaction between σ_{22} and σ_{33} when they are both positive. However, the invariant-based failure criteria predicts such interaction, as observed in Figure 5.8 (this has been validated using the results from a computational micromechanics framework – see Section 5.4.2). Notice also that, when $\sigma_{33} < 0$, the

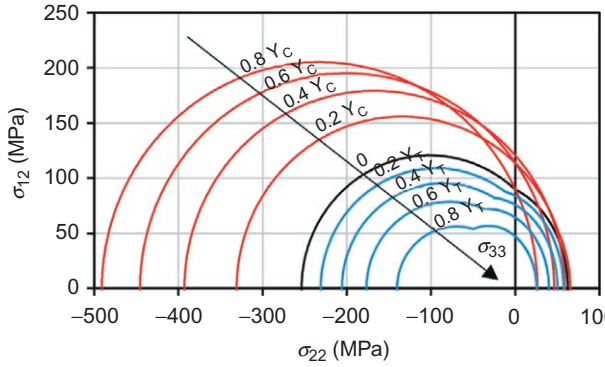

Figure 5.9 IM7/8552 carbon–epoxy's σ_{22}–σ_{12} failure envelopes when a nonzero transverse stress σ_{33} is applied.

longitudinal shear stress σ_{12} increases slightly for low values of σ_{33}, as a result of the interaction predicted by the invariant-based failure criteria for this stress state, as already discussed; for higher values of σ_{33}, however, the longitudinal shear stress σ_{12} decreases considerably. On the other hand, negative values of σ_{33} have a substantial beneficial effect when $\sigma_{22} < 0$, in agreement with the predictions by Catalanotti et al. (2013).

5.3 Failure criteria for longitudinal failure of unidirectional composites

5.3.1 *Invariant-based failure criterion formulation for fibre kinking and definition of the preferred direction $a^{(R)}$ associated with the misaligned fibres in a kink band*

The main hypothesis of the proposed model for fibre kinking is that longitudinal compressive failure of FRPs occurs from the collapse of the fibres as a result of damage of the supporting matrix (Dávila and Camanho, 2003; Dávila et al., 2005). Based on the previous observation, a 3D kinking model relying on the invariant failure criterion previously formulated for transverse fracture is proposed.

The 3D kinking model assumes that fibre kinking is originated by local micro-structural defects that trigger a kink band when local matrix cracking occurs in the vicinity of the misaligned, micro-buckled fibres. These local micro-structural defects are represented in the model as a local initial fibre misalignment (Vogler and Kyriakides, 2001; Dávila and Camanho, 2003; Dávila et al., 2005).

Figure 5.10 shows the kinking plane in the 3D kinking model. The coordinate system $1^0 2^0 3^0$ is aligned with the material axes of the composite, where 1^0 is the fibre direction and 2^0 and 3^0 are the transverse directions. The kinking plane is associated with the coordinate system $1^1 2^1 3^1$, obtained after rotating by an angle ψ (*angle of the*

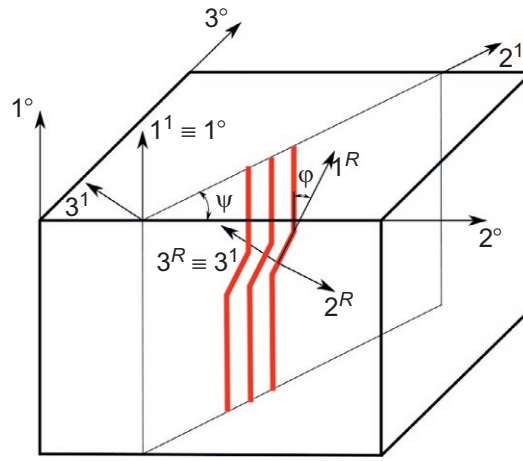

Figure 5.10 3D kinking model.

kinking plane) the $1^0 2^0 3^0$ frame around the 1^0 axis. The misaligned fibres are associated with the rotated $1^R 2^R 3^R$ coordinate system, originated from a rotation of the $1^1 2^1 3^1$ frame by an angle φ around the 3^1 axis. The angle φ is defined as the *kinking angle*.

Based on the previous assumptions, kinking failure is predicted using the invariant-based formulation for transverse failure in the misalignment frame. Here, the preferred direction, $\mathbf{a}^{(R)}$, is the direction of the misaligned fibres, which coincides with the 1^R-direction (see Figure 5.10):

$$\mathbf{a}^{(R)} = [1\ 0\ 0]^{\mathrm{T}} \tag{5.27}$$

To express the preferred direction in the material coordinate system $1^0 2^0 3^0$, two successive transformations are necessary, that is,

$$\mathbf{a}^{(0)} = \mathbf{T}_{10} \cdot \mathbf{a}^1 = \mathbf{T}_{10} \cdot \mathbf{T}_{R1} \cdot \mathbf{a}^{(R)} = \begin{bmatrix} \cos\varphi \\ \cos\psi\ \sin\varphi \\ \sin\psi\ \sin\varphi \end{bmatrix} \tag{5.28}$$

where $\mathbf{T}_{10}$ and $\mathbf{T}_{R1}$ are, respectively, the $1^1 2^1 3^1$–$1^0 2^0 3^0$ and $1^R 2^R 3^R$–$1^1 2^1 3^1$ transformation matrices.

5.3.2 Angle of the kinking plane (ψ)

The angle of the kinking plane, ψ, is the angle that maximises the fibre-kinking failure index. It can be obtained by applying the kinking failure criterion to a range of tentative angles ψ_i in the range $0 \leq \psi_i < \pi$ (Pinho et al., 2006). An alternative expression for ψ is considered, based on the works of Pinho et al. (2006) and Catalanotti et al. (2013).

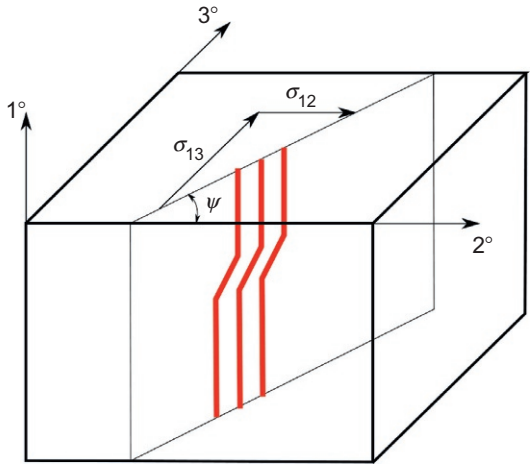

Figure 5.11 Kinking plane and involved shear stresses (after Catalanotti et al. (2013)).

Assuming that the angle of the kinking plane, ψ, is a function of the stress state, in particular of the shear stresses that act on the 2–3 plane (see Figure 5.11), the angle of the kinking plane can be calculated as (Catalanotti et al., 2013):

$$\psi = \arctan \frac{\sigma_{13}}{\sigma_{12}} \tag{5.29}$$

If both σ_{12} and σ_{13} are equal to zero, the angle of the kinking plane can be calculated by the maximum principal stress that acts on the transversely isotropic plane (Catalanotti et al., 2013). Imposing $\sigma_{23}^{(1)} = 0$, and knowing that the stress tensor in the kinking plane, $\boldsymbol{\sigma}^{(1)}$, is given by the transformation $\boldsymbol{\sigma}^{(1)} = \mathbf{T}_{01} \cdot \boldsymbol{\sigma} \cdot \mathbf{T}_{01}^{\mathrm{T}} = \mathbf{T}_{10}^{\mathrm{T}} \cdot \boldsymbol{\sigma} \cdot \mathbf{T}_{10}$, the angle of the kinking plane is obtained as:

$$\psi = \frac{1}{2} \arctan \left(\frac{2\sigma_{23}}{\sigma_{22} - \sigma_{33}} \right) \tag{5.30}$$

5.3.3 Kinking angle (φ)

5.3.3.1 Linear shear response

Figure 5.12 shows the misalignment frame of an UD laminate volume element for generic loading conditions. The kinking angle φ, or total misalignment, can be calculated as the sum of a constant initial misalignment angle φ_0 and, assuming the kinematics of deformation, an angle φ^R that is originated by the applied shear loading, and that depends on the constitutive law. For a material that exhibits linear shear response, the misalignment angle reads:

Figure 5.12 Misalignment frame.

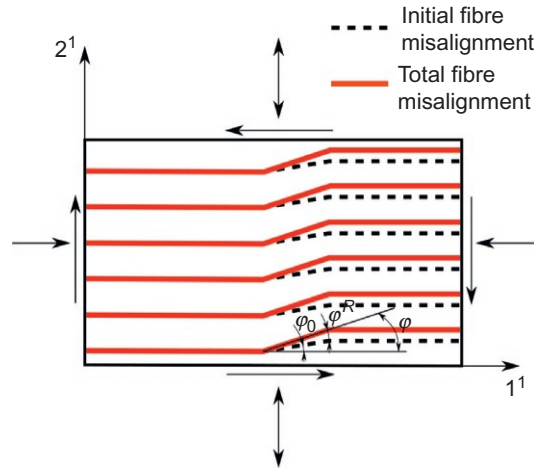

$$\varphi = \operatorname{sgn}\left\{\sigma_{12}^{(R)}(\varphi_0,\psi)\right\}\left(\varphi_0 + \frac{\left|\sigma_{12}^{(R)}(\varphi_0,\psi)\right|}{G_{12}}\right) \tag{5.31}$$

where $\sigma_{12}^{(R)}(\varphi_0,\psi)$ is the applied shear stress in the misalignment frame, which is a function of the initial misalignment angle φ_0 and of the angle of the kinking plane ψ; $\operatorname{sgn}\{x\}$ represents the sign of x (i.e., $\operatorname{sgn}\{x\} = 1$ if $x \geq 0$, and $\operatorname{sgn}\{x\} = -1$ otherwise). In the misalignment frame, the stress state $\boldsymbol{\sigma}^{(R)}$ is given by the transformation of coordinate systems $\boldsymbol{\sigma}^{(R)} = \mathbf{T}_{1R} \cdot \boldsymbol{\sigma}^{(1)} \cdot \mathbf{T}_{1R}^{\mathrm{T}} = \mathbf{T}_{R1}^{\mathrm{T}} \cdot \boldsymbol{\sigma}^{(1)} \cdot \mathbf{T}_{R1}$, with $\boldsymbol{\sigma}^{(1)} = \mathbf{T}_{10}^{\mathrm{T}} \cdot \boldsymbol{\sigma} \cdot \mathbf{T}_{10}$. Rewriting $\mathbf{T}_{R1}$ with $\varphi = \varphi_0$, the applied shear stress in the misalignment frame, $\sigma_{12}^{(R)}(\varphi_0,\psi)$, yields:

$$\begin{aligned}\sigma_{12}^{(R)}(\varphi_0,\psi) = \frac{1}{2}\left[-\sigma_{11} + \sigma_{22}\cos^2\psi + \sigma_{33}\sin^2\psi + \sigma_{23}\sin 2\psi\right]\sin 2\varphi_0 + \\ + (\sigma_{12}\cos\psi + \sigma_{13}\sin\psi)\cos 2\varphi_0\end{aligned} \tag{5.32}$$

The initial misalignment angle, φ_0, can be calculated taking the particular case when the material fails under pure longitudinal compression, that is, when $\sigma_{11} = X_{\mathrm{C}}$ and all the other components of the stress tensor are equal to zero. For this case, recalling Equation (5.31), the total misalignment angle, φ_{C}, reads:

$$\varphi_{\mathrm{C}} = \varphi_0 + \varphi_{\mathrm{C}}^R \tag{5.33}$$

where φ_{C}^R is the angle φ^R when the material fails under pure longitudinal compression. For linear shear behaviour, φ_{C}^R yields:

$$\varphi_{\mathrm{C}}^R = \frac{|X_{\mathrm{C}}\sin 2\varphi_0|}{2G_{12}} \tag{5.34}$$

Combining Equations (5.33) and (5.34), the initial misalignment angle, φ_0, reads:

$$\varphi_0 = \varphi_C - \frac{|X_C \sin 2\varphi_0|}{2G_{12}} \tag{5.35}$$

which is a nonlinear equation in φ_0.

Assuming small initial misalignment angles, Equation (5.35) can be explicitly solved as:

$$\varphi_0 = \varphi_C \left(1 + \frac{|X_C|}{G_{12}}\right)^{-1} \tag{5.36}$$

Finally, it is necessary to determine the misalignment angle at failure when a pure longitudinal compression is applied, φ_C. In this particular case, the stress tensor reads:

$$\boldsymbol{\sigma} = \begin{bmatrix} \sigma_{11} & 0 & 0 \\ 0 & 0 & 0 \\ 0 & 0 & 0 \end{bmatrix} \tag{5.37}$$

and the invariants (Equation 5.6), calculated in the misalignment frame (taking $\mathbf{a}=\mathbf{a}^{(0)}$ – Equation (5.28)), yield:

$$I_1 = \frac{1}{4}\sigma_{11}^2 \sin^4\varphi \tag{5.38a}$$

$$I_2 = \sigma_{11}^2 \sin^2\varphi \cos^2\varphi \tag{5.38b}$$

$$I_3 = \sigma_{11} \sin^2\varphi \tag{5.38c}$$

For a pure longitudinal compressive stress state, $\sigma_{11} < 0$. Therefore, from Equation (5.38c), $I_3 < 0$, and the failure criterion (Equation (5.7)) reads:

$$f = \frac{1}{4}\alpha_1 \sigma_{11}^2 \sin^4\varphi + \alpha_2 \sigma_{11}^2 \sin^2\varphi \cos^2\varphi + \alpha_3^c \sigma_{11} \sin^2\varphi + \alpha_{32}^c \sigma_{11}^2 \sin^4\varphi - 1 \tag{5.39}$$

At failure, under pure longitudinal compression, $\sigma_{11} = X_C$ and $f = 0$, and Equation (5.39) can be solved for $\varphi = \varphi_C$, yielding:

$$\varphi_C = \frac{1}{2}\arccos\left\{\left[4\sqrt{\alpha_1 - 4\alpha_2 + \alpha_2^2 X_C^2 + \left(\alpha_3^c\right)^2 + 2\alpha_2\alpha_3^c X_C + 4\alpha_{32}^c} + \right.\right. \\ \left.\left. + \left(\alpha_1 + 4\alpha_{32}^c\right)X_C + 4\alpha_3^c\right] \cdot \left[\left(\alpha_1 - 4\alpha_2 + 4\alpha_{32}^c\right)X_C\right]^{-1}\right\} \tag{5.40}$$

Having defined φ_0 and φ_C (Equations (5.35) and (5.40), respectively), the kinking angle is calculated using Equation (5.31).

5.3.3.2 Nonlinear shear response

According to Hahn and Tsai (1973), the nonlinear shear response of a composite laminate can be approximated by the following polynomial:

$$\gamma_{12} = \frac{1}{G_{12}}\sigma_{12} + \beta\sigma_{12}^3 \tag{5.41}$$

where β defines the nonlinearity of the shear stress-shear strain relation. Taking into account the nonlinear shear behaviour, the kinking angle, φ, is given as:

$$\begin{aligned}\varphi &= \operatorname{sgn}\left\{\sigma_{12}^{(R)}(\varphi_0,\psi)\right\}(\varphi_0 + \varphi^R) \\ &= \operatorname{sgn}\left\{\sigma_{12}^{(R)}(\varphi_0,\psi)\right\}\left\{\varphi_0 + \left|\frac{\sigma_{12}^{(R)}(\varphi_0,\psi)}{G_{12}} + \beta\left[\sigma_{12}^{(R)}(\varphi_0,\psi)\right]^3\right|\right\}\end{aligned} \tag{5.42}$$

where $\sigma_{12}^{(R)}(\varphi_0,\psi)$ is given by Equation (5.32). The initial misalignment angle, φ_0, is now written as:

$$\varphi_0 = \varphi_C - \varphi_C^R = \varphi_C - \left|\frac{X_C \sin 2\varphi_0}{2G_{12}} + \beta\frac{X_C^3 \sin^3 2\varphi_0}{8}\right| \tag{5.43}$$

where φ_C is given by Equation (5.40). Because Equation (5.43) is a nonlinear equation of φ_0, it has to be solved numerically using, for example, the Newton–Raphson method.

5.3.3.3 Alternative determination of φ

According to Catalanotti et al. (2013), physical incompatibilities may arise when, in the formulation of the failure criterion for fibre kinking, an initial nonzero misalignment angle, φ_0, is considered, as in Dávila et al. (2005), Pinho et al. (2006) and Camanho et al. (2014) and in Sections 5.3.3.1 and 5.3.3.2. Therefore, in the present formulation, an alternative methodology proposed by Catalanotti et al. (2013) is used to determine the kinking angle φ. According to this methodology, the imperfections that trigger fibre kinking (such as local micro-structural defects from manufacture or the intrinsic fibre volume fraction oscillations in the material) are taken into account by a micro-mechanical parameter (χ) associated with the creation of a kink-band:

$$\chi = -\frac{\sin(2\varphi_C)\, X_C}{2\varphi_C} \tag{5.44}$$

The kinking angle, φ, is then obtained imposing the stress equilibrium in a kink band and solving the corresponding nonlinear equation using, for example, the Newton–Raphson method, as suggested by Catalanotti et al. (2013).

5.3.4 Prediction of fibre tensile failure

Based on experimental evidence, and similarly to other failure criteria (Puck and Schürmann, 1998, 2002; Dávila and Camanho, 2003; Dávila et al., 2005; Catalanotti et al., 2013), tensile fracture in the fibre direction ($\sigma_{11} \geq 0$) is predicted using a noninteracting maximum allowable strain criterion:

$$f_F = \frac{\varepsilon_{11}}{\varepsilon_1^T} \leq 1 \tag{5.45}$$

5.4 Validation studies

5.4.1 Experimental data

The criteria outlined in the previous sections of this chapter are validated comparing its predictions with experimental data available in the open literature.

Figures 5.13–5.23 compare the predictions of the failure criteria with experimental data obtained for different material systems under various scenarios of multiaxial loading. The material properties used for each case are given in Tables 5.3 and 5.4, where ϕ_t and ϕ_c and σ_u^t and σ_u^c are respectively the off-axis angles and the mean applied stresses at failure of off-axis tension and compression tests, and $\sigma_{22\,u}^{t/c}$ are the maximum transverse stress and $\sigma_{12\,u}^{t/c}$ the maximum longitudinal shear stress for a specimen subjected to combined transverse tensile (t)/compressive (c) and longitudinal shear loading.

5.4.2 Computational micro-mechanics

The range of stress states that can be imposed by means of experimental tests is limited by the complexity of the load introduction systems. Therefore, a recently proposed approach based on computational micro-mechanics (Totry et al., 2008a,b; Melro et al., 2013b) is used here for generation of failure envelopes corresponding to stress states that either cannot be experimentally imposed to the material or that would require very expensive test setups.

The approach is based on the implementation of thermodynamically consistent constitutive models for each of the constituents of a composite – fibre and matrix. The elastic and strength properties of the UD composite are predicted by the analysis of a representative volume element (RVE) of a composite material under periodic boundary conditions (Melro et al., 2012). This RVE contains a random distribution of reinforcements generated by a specifically developed algorithm for the effect (Melro et al., 2008). Each RVE has a transverse-side measure of 10 times the fibre radius and a thickness of 0.3 times the fibre radius in the longitudinal direction (Melro et al., 2013b).

The material behaviour of the matrix is modelled using an elastic-plastic constitutive model with damage, recently proposed by Melro et al. (2013a). This model is

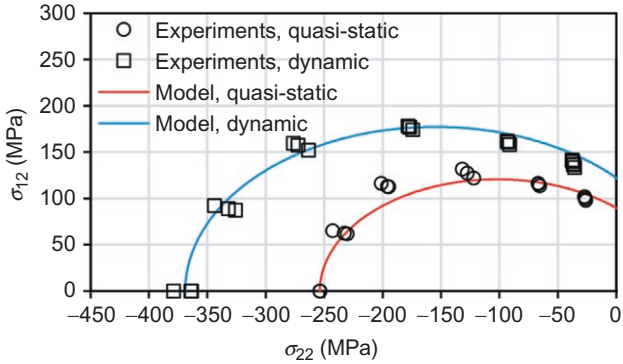

Figure 5.13 Quasi-static and dynamic σ_{22}–σ_{12} failure envelopes for IM7/8552 carbon–epoxy under transverse compression.

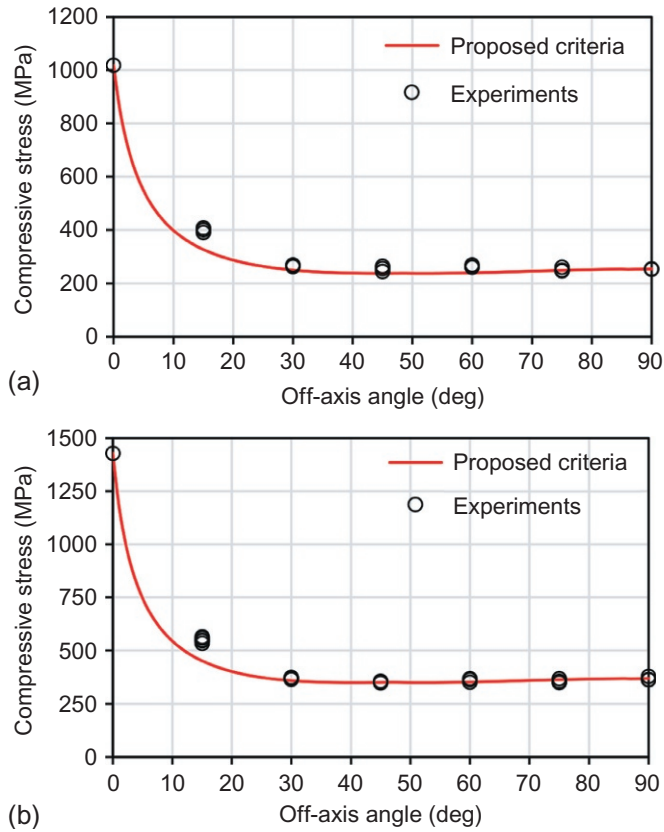

Figure 5.14 Quasi-static and dynamic off-axis compression failure predictions for IM7/8552 carbon–epoxy. (a) Quasi-static loading. (b) Dynamic loading.

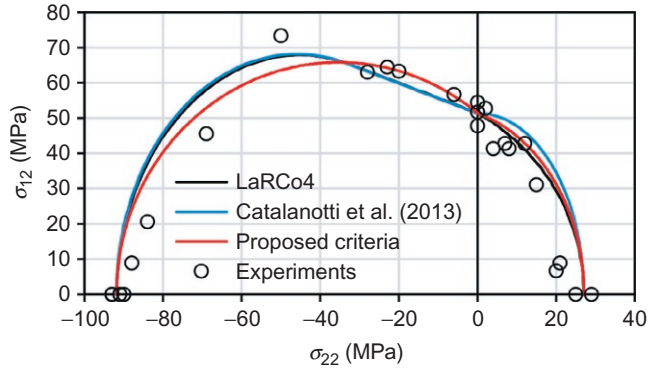

Figure 5.15 σ_{22}–σ_{12} failure envelopes for AS4/55A carbon–epoxy.

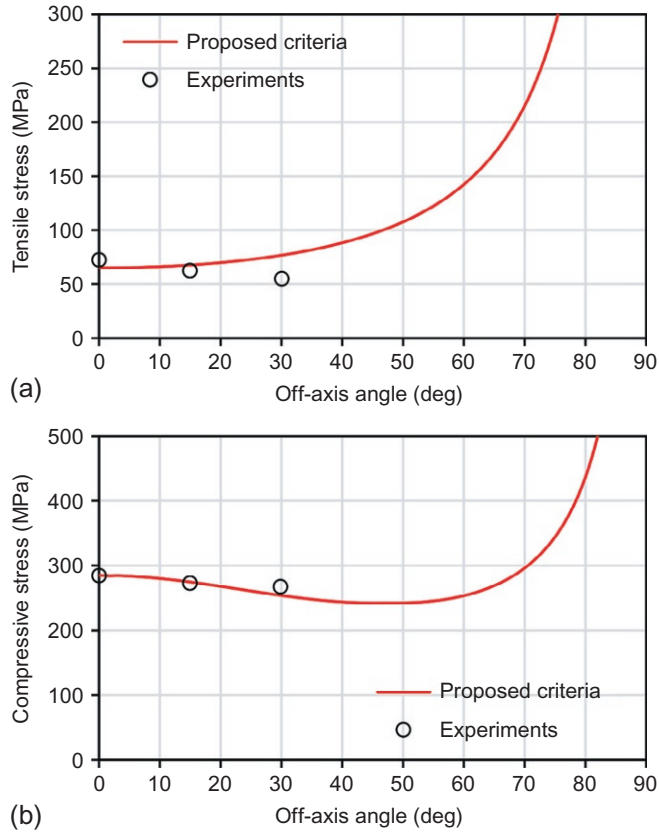

Figure 5.16 Through-the-thickness off-axis failure predictions for AS4/3501-6 carbon–epoxy. (a) Off-axis tension. (b) Off-axis compression.

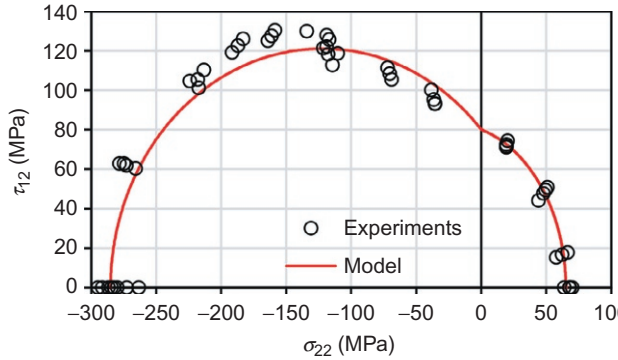

Figure 5.17 σ_{22}–σ_{12} failure envelope for AS4/3501-6 carbon–epoxy.

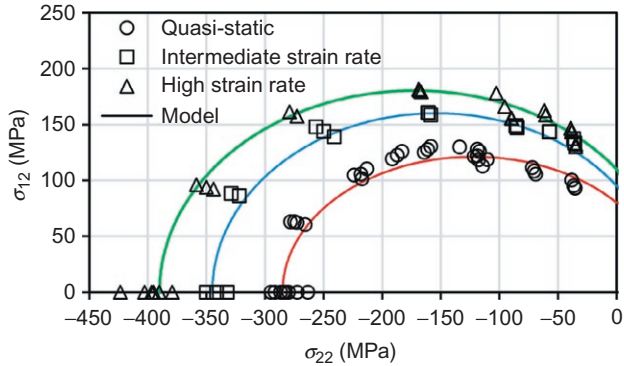

Figure 5.18 σ_{22}–σ_{12} failure envelopes for AS4/3501-6 carbon–epoxy under transverse compressive quasi-static and dynamic (intermediate and high strain rate) loading.

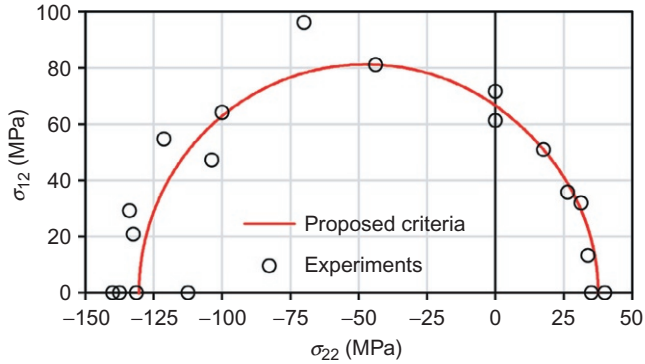

Figure 5.19 σ_{22}–σ_{12} failure envelope for E-Glass/LY556/HT907/DY063 fibreglass–epoxy.

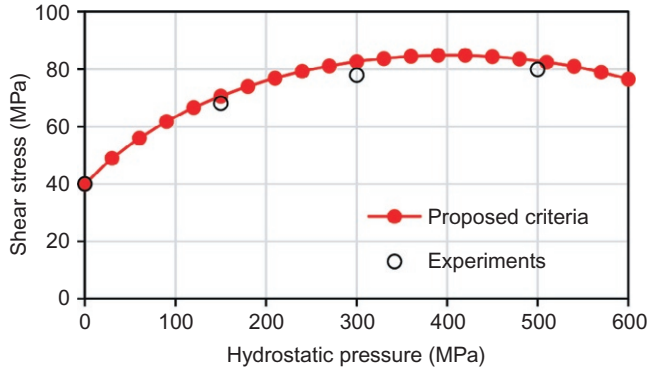

Figure 5.20 Shear response of E-Glass/MY750/HY917/DY063 fibreglass–epoxy subjected to hydrostatic pressure.

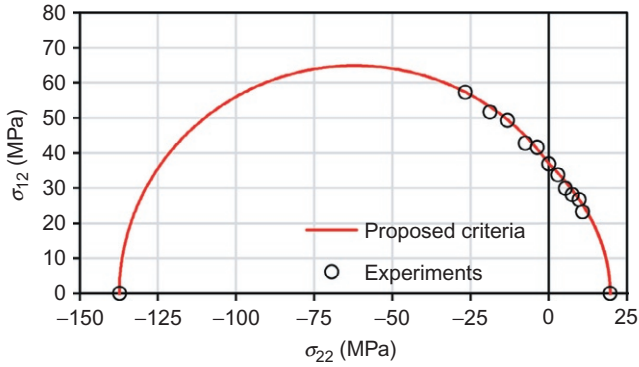

Figure 5.21 σ_{22}–σ_{12} failure envelope for Scotch-ply Type 1002 fibreglass–epoxy.

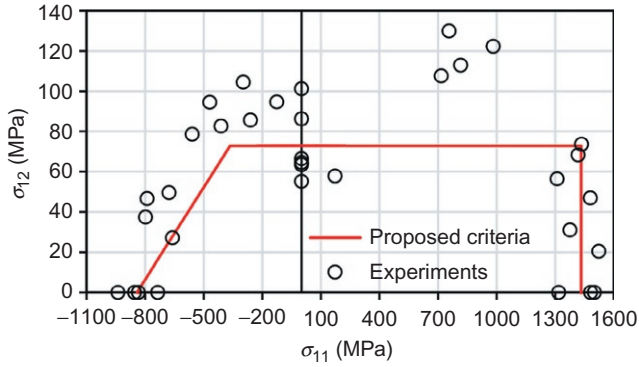

Figure 5.22 σ_{11}–σ_{12} failure envelope for T300/914C carbon–epoxy.

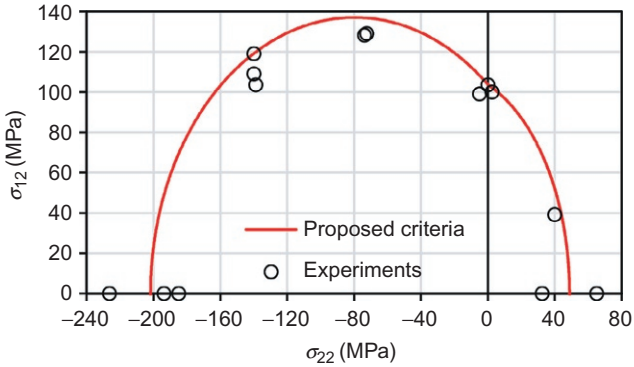

Figure 5.23 σ_{22}–σ_{12} failure envelope for T800/3900-2 carbon–epoxy.

Table 5.4 Material properties

Properties		Observations
IM7/8552 dynamic material properties		
G_{12} (MPa)	6612.5	Koerber et al. (2010)
X_C (MPa)	−1428.0	Catalanotti et al. (2013)
Y_T (MPa)	62.3	Assumed value[a]
ϕ_t (°)	45.0	Assumed value[b]
σ_u^t (MPa)	94.8	Assumed value[b]
Y_C (MPa)	−368.9	Koerber et al. (2010)
S_L (MPa)	122.3	Catalanotti et al. (2013)
ϕ_c (°)	75.0	Koerber et al. (2010)
σ_u^c (MPa)	−363.0	Koerber et al. (2010)
AS4/55A material properties		
Y_T (MPa)	27.0	Swanson et al. (1987)
$\sigma_{22\,u}^t$ (MPa)	12.0	Swanson et al. (1987)
$\sigma_{12\,u}^t$ (MPa)	42.8	Swanson et al. (1987)
Y_C (MPa)	−91.8	Swanson et al. (1987)
$\sigma_{22\,u}^c$ (MPa)	−20.0	Swanson et al. (1987)
$\sigma_{12\,u}^c$ (MPa)	63.3	Swanson et al. (1987)
S_L (MPa)	51.3	Swanson et al. (1987)
AS4/3501-6 material properties		
G_{12} (MPa)	7000.0	Daniel et al. (2011)
X_T (MPa)	2300.0	Daniel et al. (2009)
X_C (MPa)	−1725.0	Daniel et al. (2009)
Y_T (MPa)	65.0	Daniel et al. (2011)
$\sigma_{22\,u}^t$ (MPa)	19.5	Daniel et al. (2011)

Continued

Table 5.4 Continued

Properties		Observations
$\sigma^{t}_{12\,u}$ (MPa)	72.4	Daniel et al. (2011)
Y_C (MPa)	–285.0	Daniel et al. (2011)
$\sigma^{c}_{22\,u}$ (MPa)	−117.0	Daniel et al. (2011)
$\sigma^{c}_{12\,u}$ (MPa)	121.0	Daniel et al. (2011)
S_L (MPa)	80.0	Daniel et al. (2011)
AS4/3501-6 dynamic material properties		
Average strain rate: 1 s^{-1}		
Y_C (MPa)	−345.0	Daniel et al. (2011)
$\sigma^{c}_{22\,u}$ (MPa)	−160.0	Daniel et al. (2011)
$\sigma^{c}_{12\,u}$ (MPa)	159.9	Daniel et al. (2011)
S_L (MPa)	95.0	Daniel et al. (2011)
Average strain rate: 400 s^{-1}		
Y_C (MPa)	390.0	Daniel et al. (2011)
$\sigma^{c}_{22\,u}$ (MPa)	−167.9	Daniel et al. (2011)
$\sigma^{c}_{12\,u}$ (MPa)	180.2	Daniel et al. (2011)
S_L (MPa)	110.0	Daniel et al. (2011)
E-Glass/LY556/HT907/DY063 material properties		
Y_T (MPa)	37.5	Soden et al. (2002)
$\sigma^{t}_{22\,u}$ (MPa)	17.5	Soden et al. (2002)
$\sigma^{t}_{12\,u}$ (MPa)	50.9	Soden et al. (2002)
Y_C (MPa)	−130.3	Soden et al. (2002)
$\sigma^{c}_{22\,u}$ (MPa)	−43.8	Soden et al. (2002)
$\sigma^{c}_{12\,u}$ (MPa)	81.1	Soden et al. (2002)
S_L (MPa)	66.5	Soden et al. (2002)
E-Glass/MY750/HY917/DY063 material properties		
G_{12} (MPa)	5830.0	Soden et al. (1998)
X_T (MPa)	1266.7	Soden et al. (2002)
X_C (MPa)	−783.3	Soden et al. (2002)
Y_T (MPa)	40.0	Soden et al. (2002)
Y_{BT} (MPa)	25.6	Assumed value[c]
Y_C (MPa)	−110.0	Hine et al. (2005)
Y_{BC} (MPa)	−860.0	Assumed value
S_L (MPa)	40.0	Hine et al. (2005)
Scotch-ply Type 1002 material properties		
Y_T (MPa)	19.61	Voloshin and Arcan (1980)
$\sigma^{t}_{22\,u}$ (MPa)	9.72	Voloshin and Arcan (1980)
$\sigma^{t}_{12\,u}$ (MPa)	26.71	Voloshin and Arcan (1980)
Y_C (MPa)	−137.30	Voloshin and Arcan (1980)
$\sigma^{c}_{22\,u}$ (MPa)	−26.73	Voloshin and Arcan (1980)

Continued

Table 5.4 Continued

Properties		Observations
$\sigma^{c}_{12\,u}$ (MPa)	57.33	Voloshin and Arcan (1980)
S_L (MPa)	36.92	Voloshin and Arcan (1980)
T300/914C material properties		
G_{12} (MPa)	5500.0	Soden et al. (1998)
X_T (MPa)	1433.6	Soden et al. (2002)
X_C (MPa)	−841.4	Soden et al. (2002)
Y_T (MPa)	27.0	Soden et al. (1998)
Y_{BT} (MPa)	16.5	Assumed value[d]
Y_C (MPa)	−200.0	Soden et al. (1998)
Y_{BC} (MPa)	−769.8	Assumed value[e]
S_L (MPa)	72.9	Soden et al. (2002)
T800/3900-2 material properties		
Y_T (MPa)	48.8	Swanson and Qian (1992)
Y_{BT} (MPa)	30.3	Assumed value
Y_C (MPa)	−201.7	Swanson and Qian (1992)
$\sigma^{c}_{22\,u}$ (MPa)	−140.0	Swanson and Qian (1992)
$\sigma^{c}_{12\,u}$ (MPa)	119.1	Swanson and Qian (1992)
S_L (MPa)	103.6	Swanson and Qian (1992)

[a]Same value as for quasi-static loading (see Table 5.3).
[b]Same value as for quasi-static loading (Bessa, 2010).
[c]Assumed as equal to E-glass/LY556/HT907/DY063.
[d]Assumed as equal to AS4/55A.
[e]Assumed as equal to T800/3900-2.

capable of accounting for the material nonlinear behaviour of the epoxy matrix under compression or pure shear, and considers the dependency of the material on hydrostatic pressure. The fibres are considered isotropic and linear elastic. Cohesive elements are used to model the interface between matrix and fibres (Melro et al., 2013b).

The elastic and strength properties of the composite under UD loading are estimated using computational micro-mechanics. The failure point is defined as the maximum homogenised stress in the RVE.

The values from the micro-mechanical analyses of the composite under UD loading are used to feed the failure criteria proposed. Two failure envelopes are then generated from both computational micro-mechanics and the failure criteria. Tables 5.5 and 5.6 show the material properties used; E_m is the Young's modulus, ν_m is the Poisson's ratio, ν_p is the plastic Poisson's ratio, G_{fm} is the fracture toughness of the epoxy matrix and E_f and ν_f are respectively the Young's modulus and the Poisson's ratio of the glass fibre. X_T and X_C are respectively the tensile and compressive strengths of the constituents. Table 5.7 shows the material properties predicted by computational micro-mechanics for the UD composite.

Table 5.5 Material properties for epoxy matrix

Properties		References
E_m (MPa)	3760	Fiedler et al. (2001)
ν_m (–)	0.39	Fiedler et al. (2001)
ν_p (–)	0.30	Guild et al. (2001)
G_{fm} (N/mm)	0.09	Assumed value
X_T (MPa)	93	Fiedler et al. (2001)
X_C (MPa)	124	Fiedler et al. (2001)

Table 5.6 Material properties for glass fibre

Properties		References
Fibre diameter (μm)	5	Soden et al. (1998)
Fibre volume (%)	60	Soden et al. (1998)
E_f (GPa)	74	Soden et al. (1998)
ν_f (–)	0.2	Soden et al. (1998)
X_T (MPa)	2150	Soden et al. (1998)
X_C (MPa)	1450	Soden et al. (1998)

Table 5.7 Properties of the UD composite predicted by computational micro-mechanics (Melro et al., 2013a,b)

Properties	
G_{12} (MPa)	5373.0
Y_T (MPa)	48.32
Y_{BT} (MPa)	45.0
Y_C (MPa)	−114.4
Y_{BC} (MPa)	−180.0
S_L (MPa)	40.57

Figures 5.24–5.30 show the comparison between the failure envelopes predicted by computational micro-mechanics and the failure criteria proposed in this work. In general, a good agreement between the two modelling strategies is observed. However, some deviations between the micro-mechanical predictions and the proposed model can be observed in Figures 5.26 and 5.27 for the σ_{22}–σ_{12} and σ_{22}–σ_{13} stress spaces, respectively. One possible reason is related with the random distribution of the reinforcing fibres in the numerical RVE, which results in some scatter of the numerical

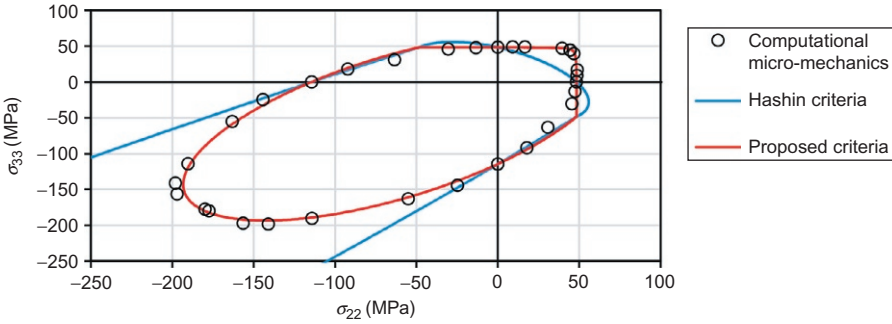

Figure 5.24 σ_{22}–σ_{33} failure envelope – micro-mechanics versus analytical failure criteria.

simulations. Still, the deviations are not large, in particular in Figure 5.26, where the trend of the σ_{22}–σ_{12} failure envelope is well predicted. The deviations observed in Figure 5.27 for the σ_{22}–σ_{13} stress space are also due to the fact that the proposed failure criterion for transverse, matrix-dominated failure, formulated for a homogeneous transversely isotropic material, does not distinguish between the in-plane (σ_{12}) and out-of-plane (σ_{13}) longitudinal shear stresses – observing Figures 5.26 and 5.27, it can be seen that the predictions of the proposed model for the stress combinations σ_{22}–σ_{12} and σ_{22}–σ_{13} are exactly the same. But, due to their morphology, long fibre-reinforced composites show different interaction of the stress combinations σ_{22}–σ_{12} (or σ_{33}–σ_{13}) and σ_{22}–σ_{13} (or σ_{33}–σ_{12}) (Cuntze and Freund, 2004), that is, small compressive values of the normal transverse stress σ_{22} (or σ_{33}) result in an increase of the longitudinal shear strength acting on the same plane, σ_{12} (or σ_{13}), but does not affect the longitudinal shear strength acting on the perpendicular plane, σ_{13} (or σ_{12}). This different interaction is captured by the micro-mechanical analysis, but it is not captured by the proposed model, conducting to the observed deviations. Nevertheless, it is believed that the deviations for this particular stress state shall not affect considerably the prediction capability of the proposed model for general stress states.

Additionally, Figures 5.24 and 5.25 show a comparison between the predictions from computational micro-mechanics and from the proposed invariant-based failure criteria and the predictions from Hashin's failure criteria (Hashin, 1980). The latter have been used, also in recent years, in the analysis of intralaminar failure of composite laminates under complex loading conditions characterised by triaxial stress states, such as damage occurrence at the free edge of blunt notches (McCarthy et al., 2010), bearing or pin loading in mechanically fastened joints (Camanho and Matthews, 1999; McCarthy and McCarthy, 2005; Zhou et al., 2014) or low-velocity impact loading (Palazotto et al., 2000; Foo et al., 2008; Wang et al., 2010; Batra et al., 2012; Maio et al., 2013; Farooq and Myler, 2014). Moreover, their two-dimensional version can be found in commercial finite element codes (ABAQUS, 2012; ANSYS, 2013).

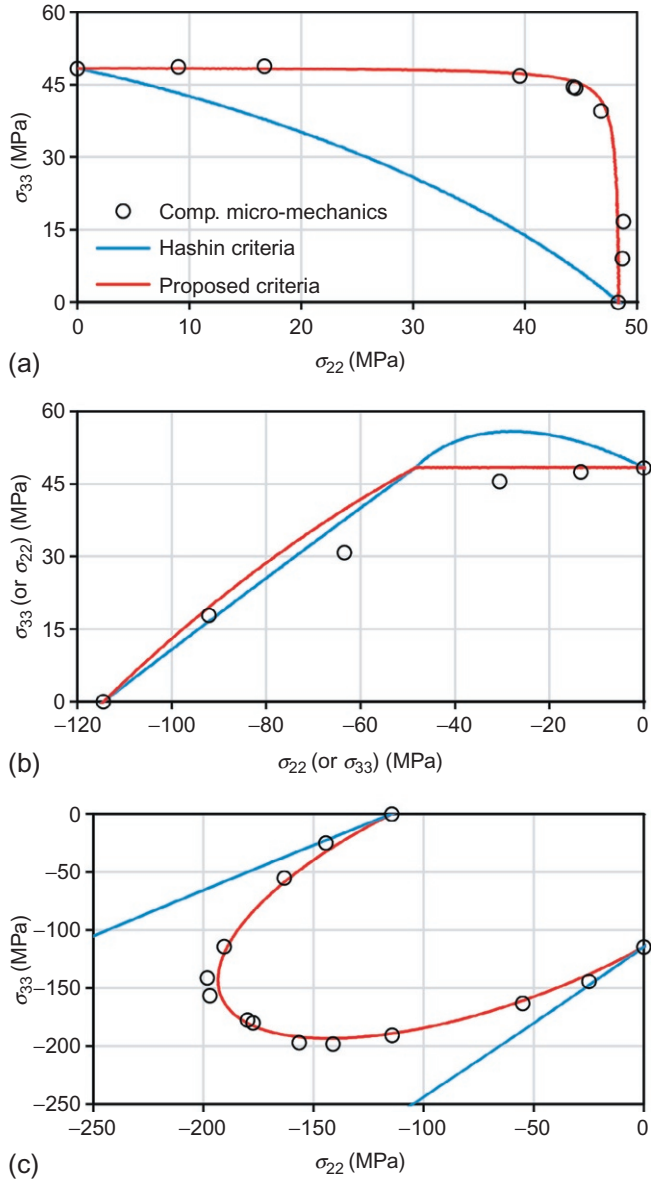

Figure 5.25 Detailed view of the σ_{22}–σ_{33} failure envelope – micro-mechanics versus analytical failure criteria. (a) First quadrant (biaxial transverse tension). (b) Second (fourth) quadrant (transverse tension-transverse compression). (c) Third quadrant (biaxial transverse compression).

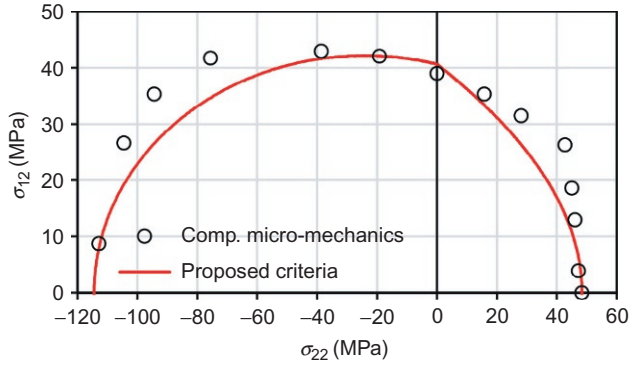

Figure 5.26 σ_{22}–σ_{12} failure envelope – micro-mechanics versus analytical failure criteria.

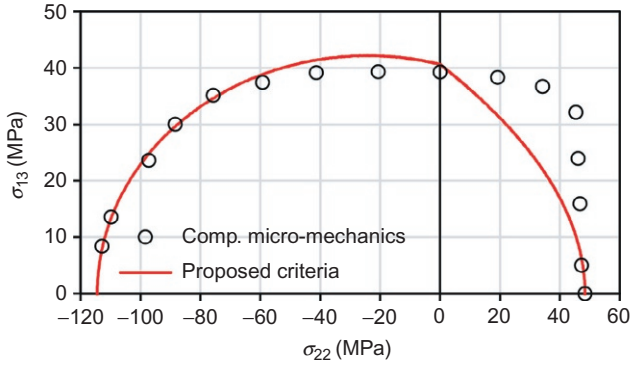

Figure 5.27 σ_{22}–σ_{13} failure envelope – micro-mechanics versus analytical failure criteria.

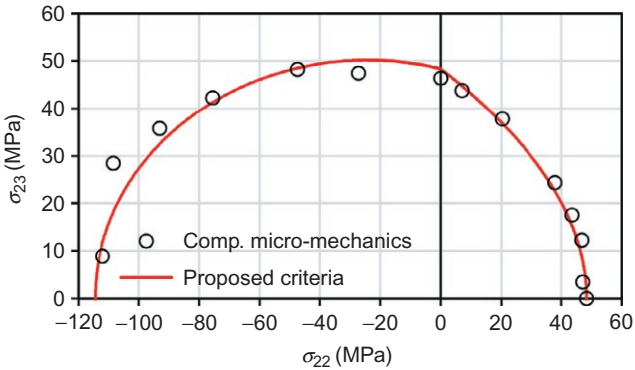

Figure 5.28 σ_{22}–σ_{23} failure envelope – micro-mechanics versus analytical failure criteria.

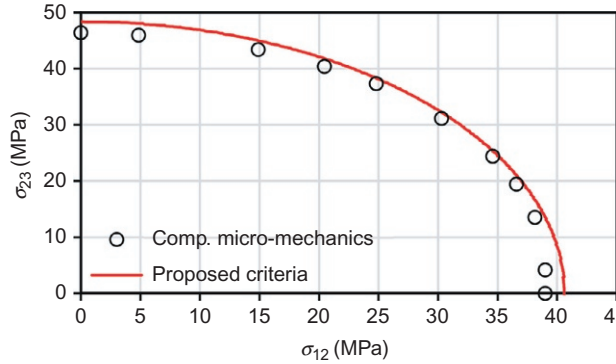

Figure 5.29 σ_{12}–σ_{23} failure envelope – micro-mechanics versus analytical failure criteria.

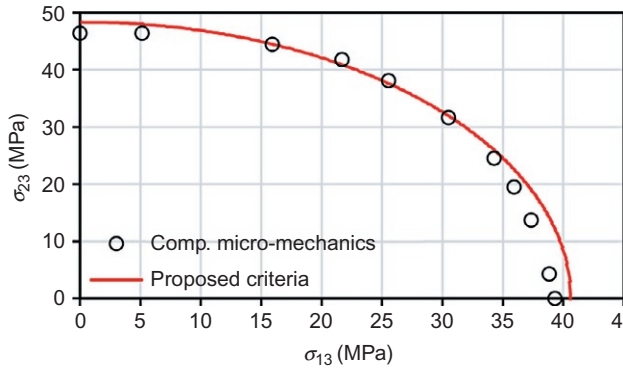

Figure 5.30 σ_{13}–σ_{23} failure envelope – micro-mechanics versus analytical failure criteria.

As can be observed, Hashin's failure criteria are not able to predict the fracture of fibre-reinforced composites subjected to biaxial transverse loading. These failure criteria largely underpredict the biaxial tensile strength of laminated composites. Furthermore, they show an open failure envelope for the biaxial transverse compression quadrant, thus making such failure criteria unsuitable for representing the fracture of composites subjected to hydrostatic pressure. Note that the accurate prediction of fracture under these stress states is crucial to predict the mechanical response of very thick laminates (e.g., for applications in the wind turbine blades and ship industries) or laminates subjected to complex triaxial stress states (e.g., indentation, low-velocity impact, crashworthiness or bearing).

Finally, it is also important to note that, even in those combinations of stress states where there are no experimental values available or the existing ones are scarce or unreliable (e.g., combination of σ_{13} with σ_{23}), computational micro-mechanics is capable of providing predictions.

5.5 Conclusions

The failure criteria described in this chapter include an invariant quadratic formulation based on structural tensors that accounts for the preferred directions of the transversely isotropic material. Failure in a single UD ply is predicted, requiring the analysis of strains and stresses ply-by-ply when analysing multidirectional laminates.

Based on the failure envelopes for fibre kinking obtained for IM7/8552 CFRP, it is concluded that accounting for the nonlinear shear behaviour in the failure criterion has a minor effect on the predicted failure load. In addition, considering small angles approximation for the determination of the initial misalignment angle φ_0 (Equation (5.36)) does not affect the predicted failure envelopes, which means that, for this case, a nonlinear procedure to solve Equation (5.35) does not have to be used, simplifying the implementation of the kinking criterion, and improving its performance when used in computational models.

Because the proposed failure criteria does not use geometrical information to predict failure (due to its invariant-based formulation), a pragmatic approach to estimate the orientation of the fracture plane was proposed. In spite of the simplicity of the approach, it is believed that reliable estimates may be obtained for general 3D stress states. For instance, the ability to determine, in a simple way, the orientation of the fracture angle, can be very useful for future implementations of the invariant-based failure criteria in smeared crack models to predict ply failure mechanisms in composite laminates (see, e.g., Camanho et al., 2013).

To account for the effect of ply thickness when the laminae are embedded in a multidirectional laminate, the *in situ* properties were defined in the framework of the failure criterion for transverse damage mechanisms. Note that an accurate determination of the *in situ* strengths is necessary for the implementation of any physically based failure criteria for transverse fracture in multidirectional laminates (Flaggs, 1985; Chang and Chang, 1987; Chang et al., 1991; Puck and Schürmann, 2002; Dávila et al., 2005; Pinho et al., 2005; Camanho et al., 2006, 2013; Maimí et al., 2006, 2007a; Mayugo et al., 2010).

When compared against experimental data available in the literature, good agreement for transverse failure modes, for failure under off-axis loading and for the effect of superposed hydrostatic pressure on failure behaviour of different FRPs was obtained. For more complex three-dimensional stress states, where the test data available shows large scatter or is not available at all, a computational micro-mechanics framework was used to validate the failure criteria. A good correlation between the predictions of the two modelling strategies was obtained. The computational micro-mechanics framework was shown to be a very useful tool to validate failure criteria under complex three-dimensional stress states.

References

ABAQUS, 2012. ABAQUS 6.12 Documentation. Dassault Systèmes Simulia Corp., Providence, RI, USA.

ANSYS, 2013. ANSYS Release 15.0 Documentation. ANSYS, Inc., Canonsburg, PA, USA.

Batra, R.C., Gopinath, G., Zheng, J.Q., 2012. Damage and failure in low energy impact of fiber-reinforced polymeric composite laminates. Compos. Struct. 94, 540–547.

Bessa, M., 2010. Meso-mechanical model of the structural integrity of advanced composite laminates. Master's thesis, Faculdade de Engenharia, Universidade do Porto, Porto.

Boehler, J.P. (ed.), 1987a. Applications of Tensor Functions in Solid Mechanics, CISM Courses and Lectures No. 292, Springer-Verlag, Wien.

Boehler, J.P., 1987b. Yielding and failure of transversely isotropic solids, Boehler, J.P.(ed.), Applications of Tensor Functions in Solid Mechanics, CISM Courses and Lectures No. 292, Springer-Verlag, Wien, pp. 66–97.

Camanho, P.P., Arteiro, A., Melro, A.R., Catalanotti, G., Vogler, M., 2014. Three-dimensional invariant-based failure criteria for fibre-reinforced composites. Int. J. Solids Struct. doi: http://dx.doi.org/10.1016/j.ijsolstr.2014.03.038.

Camanho, P.P., Bessa, M.A., Catalanotti, G., Vogler, M., Rolfes, R., 2013. Modeling the inelastic deformation and fracture of polymer composites Part II: Smeared crack model. Mech. Mater. 59, 36–49.

Camanho, P.P., Dávila, C.G., Pinho, S.T., Iannucci, L., Robinson, P., 2006. Prediction of in situ strengths and matrix cracking in composites under transverse tension and in-plane shear. Compos. A-Appl. S 37, 165–176.

Camanho, P.P., Lambert, M., 2006. A design methodology for mechanically fastened joints in laminated composite materials. Compos. Sci. Technol. 66, 3004–3020.

Camanho, P.P., Maimí, P., Dávila, C.G., 2007. Prediction of size effects in notched laminates using continuum damage mechanics. Compos. Sci. Technol. 67, 2715–2727.

Camanho, P.P., Matthews, F.L., 1999. A progressive damage model for mechanically fastened joints in composite laminates. J. Compos. Mater. 33 (24), 2248–2280.

Catalanotti, G., Camanho, P.P., Marques, A.T., 2013. Three-dimensional failure criteria for fiber-reinforced laminates. Compos. Struct. 95, 63–79.

Chang, F.K., Chang, K.Y., 1987. Post-failure analysis of bolted composite joints in tension or shear-out mode failure. J. Compos. Mater. 21, 809–833.

Chang, F.K., Chen, M.H., 1987. The in situ ply shear strength distribution in graphite/epoxy laminated composites. J. Compos. Mater. 21, 708–733.

Chang, K.Y., Liu, S., Chang, F.K., 1991. Damage tolerance of laminated composites containing an open hole subjected to tensile loadings. J. Compos. Mater. 25, 274–301.

Christensen, R.M., 1997. Stress based yield/failure criteria for fiber composites. Int. J. Solids Struct. 34 (5), 529–543.

Christensen, R.M., DeTeresa, S.J., 2003. Failure plane orientations for transverse loading of a unidirectional fiber composite. Int. J. Solids Struct. 40, 7055–7062.

Cuntze, R.G., Freund, A., 2004. The predictive capability of failure mode concept-based strength criteria for multidirectional laminates. Compos. Sci. Technol. 64, 343–377.

Daniel, I.M., Luo, J.J., Schubel, P.M., Werner, B.T., 2009. Interfiber/interlaminar failure of composites under multi-axial states of stress. Compos. Sci. Technol. 69, 764–771.

Daniel, I.M., Werner, B.T., Fenner, J.S., 2011. Strain-rate-dependent failure criteria for composites. Compos. Sci. Technol. 71, 357–364.

Dávila, C.G., Camanho, P.P., NASA Langley Research Center, 2003, November. Failure criteria for FRP laminates in plane stress. Hampton, Virginia.

Dávila, C.G., Camanho, P.P., Rose, C.A., 2005. Failure criteria for FRP laminates. J. Compos. Mater. 39 (4), 323–345.

Dvorak, G.J., Laws, N., 1987. Analysis of progressive matrix cracking in composite laminates II. First ply failure. J. Compos. Mater. 21, 309–329.

Farooq, U., Myler, P., 2014. Ply level failure prediction of carbon fibre reinforced laminated composite panels subjected to low velocity drop-weight impact using adaptive meshing techniques. Acta Astronaut. 102, 169–177.

Fiedler, B., Hojo, M., Ochiai, S., Schulte, K., Ando, M., 2001. Failure behavior of an epoxy matrix under different kinds of static loading. Compos. Sci. Technol. 61, 1615–1624.

Flaggs, D.L., 1985. Prediction of tensile matrix failure in composite laminates. J. Compos. Mater. 19, 29–50.

Foo, C.C., Chai, G.B., Seah, L.K., 2008. A model to predict low-velocity impact response and damage in sandwich composites. Compos. Sci. Technol. 68, 1348–1356.

Guild, F.J., Potter, K.D., Heinrich, J., Adams, R.D., Wisnom, M.R., 2001. Understanding and control of adhesive crack propagation in bonded joints between carbon fibre composite adherents II. Finite element analysis. Int. J. Adhes. Adhes. 21, 445–453.

Hahn, H.T., Tsai, S.W., 1973. Nonlinear elastic shear behavior of unidirectional composite laminae. J. Compos. Mater. 7 (1), 102–118.

Hart-Smith, L.J., 1998a. Predictions of a generalized maximum-shear-stress failure criterion for certain fibrous composite laminates. Compos. Sci. Technol. 58, 1179–1208.

Hart-Smith, L.J., 1998b. Predictions of the original and truncated maximum-strain failure models for certain fibrous composite laminates. Compos. Sci. Technol. 58, 1151–1178.

Hashin, Z., 1980. Failure criteria for unidirectional fibre composites. J. Appl. Mech. 47, 329–334.

Hine, P.J., Duckett, R.A., Kaddour, A.S., Hinton, M.J., Wells, G.M., 2005. The effect of hydrostatic pressure on the mechanical properties of glass fibre/epoxy unidirectional composites. Compos. Part A-Appl. S 36, 279–289.

Hinton, M.J., Kaddour, A.S., Soden, P.D., 2004. Evaluation of failure prediction in composite laminates: background to 'part C' of the exercise. Compos. Sci. Technol. 64, 321–327.

Hinton, M.J., Soden, P.D., 1998. Predicting failure in composite laminates: the background to the exercise. Compos. Sci. Technol. 58, 1001–1010.

Hoppel, C.P.R., Bogetti, T.A., Gillespie Jr., J.W., 1995. Literature review – Effects of hydrostatic pressure on the mechanical behavior of composite materials. J. Thermoplast. Compos. 8, 375–409.

Koerber, H., Xavier, J., Camanho, P.P., 2010. High strain rate characterisation of unidirectional carbon-epoxy IM7-8552 in transverse compression and in-plane shear using digital image correlation. Mech. Mater. 42, 1004–1019.

Kuraishi, A., Tsai, S.W., Liu, K.K.S., 2002. A progressive quadratic failure criterion, part B. Compos. Sci. Technol. 62, 1683–1695.

Liu, K.L., Tsai, S.W., 1998. A progressive quadratic failure criterion for a laminate. Compos. Sci. Technol. 58, 1023–1032.

Maimí, P., Camanho, P.P., Mayugo, J.A., Dávila, C.G., NASA Langley Research Center, 2006, March. A thermodynamically consistent damage model for advanced composites. Hampton, Virginia.

Maimí, P., Camanho, P.P., Mayugo, J.A., Dávila, C.G., 2007a. A continuum damage model for composite laminates: Part I – Constitutive model. Mech. Mater. 39, 897–908.

Maimí, P., Camanho, P.P., Mayugo, J.A., Dávila, C.G., 2007b. A continuum damage model for composite laminates: Part II – Computational implementation and validation. Mech. Mater. 39, 909–919.

Maio, L., Monaco, E., Ricci, F., Lecce, L., 2013. Simulation of low velocity impact on composite laminates with progressive failure analysis. Compos. Struct. 103, 75–85.

Mayugo, J.A., Camanho, P.P., Maimí, P., Dávila, C.G., 2010. Analytical modelling of transverse matrix cracking of $\{\pm\theta/90^n\}^s$ composite laminates under multiaxial loading. Mech. Adv. Mater. Struc. 17, 237–245.

McCarthy, C.T., McCarthy, M.A., 2005. Three-dimensional finite element analysis of single-bolt, single-lap composite bolted joints: Part II – Effects of bolt-hole clearance. Compos. Struct. 71, 159–175.

McCarthy, C.T., O'Higgins, R.M., Frizzell, R.M., 2010. A cubic spline implementation of non-linear shear behaviour in three-dimensional progressive damage models for composite laminates. Compos. Struct. 92, 173–181.

Melro, A.R., Camanho, P.P., Pinho, S.T., 2008. Generation of random distribution of fibres in long-fibre reinforced composites. Compos. Sci. Technol. 68, 2092–2102.

Melro, A.R., Camanho, P.P., Pinho, S.T., 2012. Influence of geometrical parameters on the elastic response of unidirectional composite materials. Compos. Struct. 94, 3223–3231.

Melro, A.R., Camanho, P.P., Pires, F.M.A., Pinho, S.T., 2013a. Micromechanical analysis of polymer composites reinforced by unidirectional fibres: Part I – Constitutive modelling. Int. J. Solids Struct. 50, 1897–1905.

Melro, A.R., Camanho, P.P., Pires, F.M.A., Pinho, S.T., 2013b. Micromechanical analysis of polymer composites reinforced by unidirectional fibres: Part II – Micromechanical analyses. Int. J. Solids Struct. 50, 1906–1915.

MIL-HDBK-17-3F, 2002. Composite Materials Handbook, vol. 3: Polymer Matrix Composites Materials Usage, Design and Analysis. Department of Defense Handbook.

Palazotto, A.N., Herup, E.J., Gummadi, L.N.B., 2000. Finite element analysis of low-velocity impact on composite sandwich. Compos. Struct. 49, 209–227.

Pinho, S.T., Dávila, C.G., Camanho, P.P., Iannucci, L., Robinson, P., NASA Langley Research Center, 2005, February. Failure models and criteria for FRP under in-plane or three-dimensional stress states including shear non-linearity. Hampton, Virginia.

Pinho, S.T., Iannucci, L., Robinson, P., 2006. Physically-based failure models and criteria for laminated fibre-reinforced composites with emphasis on fibre kinking: Part I: Development. Compos. Part A-Appl. S 37, 63–73.

Puck, A., 1969. Calculating the strength of glass fibre/plastic laminates under combined load. Kunstst. German Plast. 55, 18–19.

Puck, A., Schneider, W., 1969. On failure mechanism and failure criteria of filament wound glass-fibre/resin composites. Plast. Polym. 37, 33–44.

Puck, A., Schürmann, H., 1998. Failure analysis of FRP laminates by means of physically based phenomenological models. Compos. Sci. Technol. 58, 1045–1067.

Puck, A., Schürmann, H., 2002. Failure analysis of FRP laminates by means of physically based phenomenological models. Compos. Sci. Technol. 62, 1633–1662.

Saito, H., Takeuchi, H., Kimpara, I., 2012. Experimental evaluation of the damage growth restraining in 90° layer of thin-ply CFRP cross-ply laminates. Adv. Compos. Mater. 21, 57–66.

Saito, H., Takeuchi, H., Kimpara, I., 2014. A study of crack suppression mechanism of thin-ply carbon-fiber-reinforced polymer laminate with mesoscopic numerical simulation. J. Compos. Mater. 48 (17), 2085–2096.

Soden, P.D., Hinton, M.J., Kaddour, A.S., 1998. Lamina properties, lay-up configurations and loading conditions for a range of fibre-reinforced composites laminates. Compos. Sci. Technol. 58, 1011–1022.

Soden, P.D., Hinton, M.J., Kaddour, A.S., 2002. Biaxial test results for strength and deformation of a range of E-glass and carbon fibre reinforced composite laminates: failure exercise benchmark data. Compos. Sci. Technol. 62, 1489–1514.

Spencer, A.J.M., 1987. Kinematic constraints, constitutive equations and failure rules for anisotropic materials, Boehler, J.P., (ed.), Applications of Tensor Functions in Solid Mechanics, CISM Courses and Lectures No. 292, Springer-Verlag, Wien, pp. 187–201.

Sun, C.T., Tao, J., 1998. Prediction of failure envelopes and stress/strain behaviour of composite laminates. Compos. Sci. Technol. 58, 1125–1136.
Sun, C.T., Tao, J., Kaddour, A.S., 2002. The prediction of failure envelopes and stress/strain behavior of composite laminates: comparison with experimental results. Compos. Sci. Technol. 62, 1673–1682.
Swanson, S.R., Messick, M.J., Tian, Z., 1987. Failure of carbon/epoxy lamina under combined stress. J. Compos. Mater. 21, 619–630.
Swanson, S.R., Qian, Y., 1992. Multiaxial characterization of T800/3900-2 carbon/epoxy composites. Compos. Sci. Technol. 43, 197–203.
Thom, H., 1998. A review of the biaxial strength of fibre-reinforced plastics. Compos. Part A-Appl. S 29A, 869–886.
Totry, E., González, C., Llorca, J., 2008a. Failure locus of fiber-reinforced composites under transverse compression and out-of-plane shear. Compos. Sci. Technol. 68, 829–839.
Totry, E., González, C., Llorca, J., 2008b. Prediction of the failure locus of C/PEEK composites under transverse compression and longitudinal shear through computational mechanics. Compos. Sci. Technol. 68, 3128–3136.
Tsai, S.W., Wu, E.M., 1971. A general theory of strength for anisotropic materials. J. Compos. Mater. 5 (1), 58–80.
Vogler, M., Ernst, G., Rolfes, R., 2010. Invariant based transversely-isotropic material and failure model for fiber-reinforced polymers. Comput. Mater. Con. 16 (1), 25–49.
Vogler, M., Rolfes, R., Camanho, P.P., 2013. Modeling the inelastic deformation and fracture of polymer composites–Part I: Plasticity model. Mech. Mater. 59, 50–64.
Vogler, T.J., Kyriakides, S., 2001. On the initiation and growth of kink bands in fiber composites: Part I: Experiments. Int. J. Solids Struct. 38, 2639–2651.
Voloshin, A., Arcan, M., 1980. Failure of unidirectional fiber-reinforced materials – New methodology and results. Exp. Mech. 20, 280–284.
Wang, S.X., Wu, L.Z., Ma, L., 2010. Low-velocity impact and residual tensile strength analysis to carbon fiber composite laminates. Mater. Design 31, 118–125.
Wiegand, J., Petrinic, N., Elliott, B., 2008. An algorithm for determination of the fracture angle for the three-dimensional Puck matrix failure criterion for UD composites. Compos. Sci. Technol. 68, 2511–2517.
Zhou, Y., Yazdani-Nezhad, H., McCarthy, M.A., Wan, X., McCarthy, C., 2014. A study of intra-laminar damage in double-lap, multi-bolt, composite joints with variable clearance using continuum damage mechanics. Compos. Struct. 116, 441–452.

An overview of continuum damage models used to simulate intralaminar failure mechanisms in advanced composite materials

6

A. Forghani, M. Shahbazi, N. Zobeiry, A. Poursartip, R. Vaziri
The University of British Columbia, Vancouver, BC, Canada

6.1 Introduction

Fracture mechanics and progressive damage analysis are integral components of analysis tools used for damage-tolerant design, which requires that structures continue to carry the required service loads in the presence of damage. Recent advances in computational damage/fracture mechanics, combined with experimental full-field image analysis techniques to capture the intricate details of damage and failure mechanisms in a nondestructive manner, have paved the way for more realistic modelling of the nonlinear behaviour of structural composites.

Among the various approaches to model fracture and damage in solids, methods of continuum damage mechanics (CDM) have gained the most attention. This is mainly due to the convenience of their implementation in general purpose finite element software. In continuum approaches, the effect of material degradation due to fracture and damage in the fracture process zone (FPZ) is modelled in a smeared manner and by reducing the apparent stiffness of the material (strain-softening) inside the FPZ.

Although strain-softening is not a real physical phenomenon at the microscale of the material, it provides an appealing framework to simulate the effect of damage on the macroscopic structural response.

Before the emergence of CDM and strain-softening-based models, the linear elastic fracture mechanics (LEFM) was the basis for predicting the fracture strength of brittle materials. LEFM, however, ignores the existence of a FPZ in front of the crack tip. In many of the modern engineered materials, such as concrete and laminated composites known as quasi-brittle materials, the size of the FPZ becomes significant and the underlying assumptions of the LEFM break down leading to erroneous predictions of strength that, in some cases, can be non-conservative. Furthermore, LEFM can be applied only to structures with preexisting sharp notches and is unable to predict the initiation of fracture and damage.

Experimental evidence shows that the FPZ in laminated composites can grow into a relatively large area. This is due to the formation of delamination cracks and splits in front of the notch tip that leads to a blunting effect and significant reduction in the level of strain gradients.

Numerical modelling of failure in advanced composite materials. http://dx.doi.org/10.1016/B978-0-08-100332-9.00006-2
Copyright © 2015 Elsevier Ltd. All rights reserved.

CDM is able to provide a framework for a smeared or distributed description of the effect of the process zone on the mechanical properties of quasi-brittle materials and their behaviour beyond the maximum strength point. The effective degradation of the material stiffness in CDM can be defined by strain-softening-based formulations.

First successful application of strain-softening models was in concrete structures to capture the global load redistribution as a result of the formation of the damage zone, without the need for rigorous modelling of detailed progressive damage mechanisms in that zone (Bazant and Oh, 1983; Belytschko and Bazant, 1984; Bazant and Pijaudier-Cabot, 1988).

In the early to mid-1990s, strain-softening approaches for simulation of damage in composite structures gained notable attention. The NASA/Boeing-lead programme for Advanced Technology Composite Aircraft Structure (ATCAS) in collaboration with the Composites Group at the University of British Columbia that included testing of notched laminated composite panels with various materials and geometric configurations, provided the first comprehensive experimental and strain-softening based modelling framework to simulate damage and failure in laminated composites (see Dopker et al., 1994; Ilcewicz et al., 1993, 1996; Kongshavn and Poursartip, 1999; Williams and Vaziri, 1995, 2001).

6.2 Damage modes in laminated composites

One can categorize damage modes in laminated composites into two groups; namely, intralaminar and interlaminar damage. Intralaminar modes are formed in the plane of the plies that include fibre-dominated damage modes: fibre breakage, fibre pullout and fibre buckling as well as matrix-dominated modes such as matrix cracking and fibre–matrix splitting. Interlaminar damage, on the other hand, is separation of two adjacent layers in the laminate also known as disbonding or delamination.

Initiation and progression of damage in laminated composite materials depends on characteristics of the constituents and laminate design as well as the loading scenario. There are some major differences between the damage mechanisms under in-plane tension and compression loading conditions. Tensile damage leading to failure is most commonly due to matrix cracking and fibre breakage. However, depending on the laminate layup, failure can also involve delamination. Under compressive loading, the primary failure mechanism is kink-band formation, which is a consequence of matrix cracking or yielding and fibre rotation in plies that are oriented in the loading direction. This mechanism, along with delamination and off-axis matrix cracking, is most prevalent in failure of composites under compression.

In practical laminate configurations, damage does not occur in isolated modes. Matrix damage and splitting are typically accompanied by delamination. Engagement of various damage modes usually leads to further energy absorption during a progressive damage growth and results in a more superior behaviour of the laminate when subjected to severe loading conditions.

Although damage modes in laminated composites are interactive, due to the complex nature of damage initiation and growth in such structures, the majority of modelling approaches tend to simulate interlaminar and intralaminar damage modes separately.

6.3 Size effect in composite structures

In the design of composite components, it is usually desirable to use the material parameters obtained from the small-scale tests to save time and cost. Therefore, it is necessary to have a good understanding of the effects of scaling from a test (coupon) model to a full scale (structure) model.

Experimental studies show the strong effect of size scaling in composite structures with various configurations and under different loading scenarios (see Wisnom et al., 2008, 2010; Lavoie et al., 2000, among others).

The early studies have shown that quasi-brittle materials exhibit size effects that cannot be adequately represented by strength-based theories (for which there is no size effect) and LEFMs (for which the size effect is the strongest). This intermediate size effect is an indication of the presence of a certain nonnegligible characteristic size of the FPZ (see Bazant et al., 1996; Bazant and Planas, 1998).

Both LEFMs and statistical models (e.g., based on the Weibull distribution) predict strength reduction with increasing size of the structure. However, experimental evidence shows that neither of these approaches can accurately predict the size effect in quasi-brittle materials. This is due to the inability of such approaches to account for the FPZ and its effect on the response of structures made up of these materials (Sutherland et al., 1999).

Cohesive crack models and properly regularized CDM-based formulations, on the other hand, are shown to be capable of capturing the effect of FPZ on the structural response leading to a better prediction of size effect in structures made from quasi-brittle materials (see Hillerborg et al., 1976; Jiang et al., 2007; Turon et al., 2010; Soutis et al., 1991).

A comprehensive summary of various techniques used to study size effects can be found in a number of articles including Bazant (1999), Sutherland et al. (1999) and Wisnom et al. (2010), among others.

6.4 Simulation of damage at various scales

Formation and propagation of damage in composite structures is a multiscale event in nature. It usually initiates with microscale cracking in the matrix typically accompanied by small-scale delamination at the layer interfaces. Further increase of the load results in growth of matrix cracks to mesoscale cracks and delamination, which eventually leads to macroscale cracks and fibre breakage.

The existing damage models typically target one of these scales and study the damage behaviour of the material/structure at that scale. Depending on the target scale of

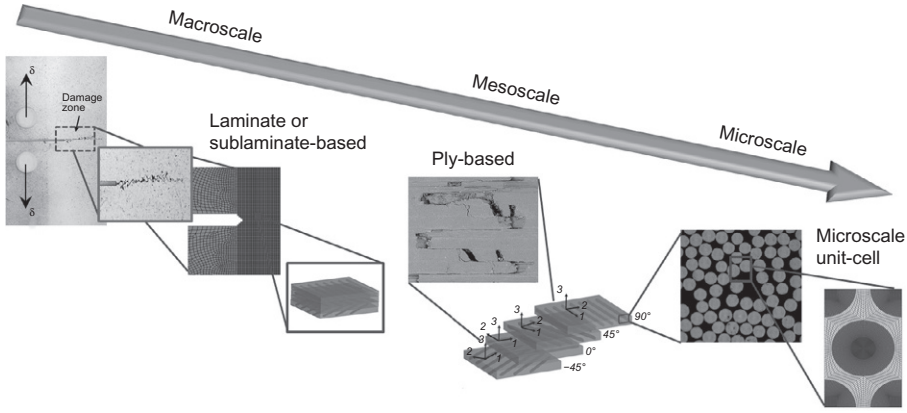

Figure 6.1 A schematic representation of the various scales involved in modelling the damage behaviour of composites.

interest, models are designed to capture the behaviour of the material (and the structure) at different levels of details (see Figure 6.1).

6.4.1 Microscale modelling

The microscale models, such as those described in more detail in Chapters 13 and 14, study the details of the interaction between the fibre and matrix at scales up to a few hundred microns. These models aim to predict the behaviour of the laminae based on the behaviour of its constituents (fibre and matrix) under various loading combinations (see Xia et al., 2000; Zhang et al., 2005; Grufman and Ellyin, 2008; Melro et al., 2013, among others).

Microscale models have been successfully used to predict the mechanical properties of undamaged laminae such as the elasticity moduli and coefficients of thermal expansion, and the like. When it comes to modelling damage at the microscale, two major approaches have been employed. In the first approach, that is most popular, a periodic distribution of the reinforcements is assumed. In this approach, the building block of the model is a repeated unit-cell that consists of a fibre at its centre surrounded by the matrix material. Analytical, closed-form solutions or finite element simulations are employed to predict the behaviour of the unit-cell under various loading scenarios. Fibre, matrix and the fibre–matrix interface are the constituents of a micromechanical unit-cell model (see Xia et al., 2000; Zhang et al., 2004, for instance).

In the second approach, the morphology and distribution of the fibres in the laminae are taken into account. The size of the RVE in this approach depends primarily on the distribution of the fibres and can be up to a few hundred microns (see Grufman and Ellyin, 2007; Grufman and Ellyin, 2008; Melro et al., 2013, for instance).

Although the microscale models have been shown to be very successful in predicting the properties of the undamaged material and also in predicting the onset of damage, they are unable to predict damage evolution. This is due to the fact that the representative volume assumed for predicting the behaviour of the virgin material in a microscale model cannot be used as a representative volume for the extensively damaged material. In other words, in a damaged material, smearing and homogenization cannot be performed at the same scale that is performed in the undamaged material.

6.4.2 Mesoscale (ply-based) models

At the next scale, the mesomechanical models study the behaviour of the composite laminate at the ply-level (e.g., Williams and Vaziri, 1995, 2001; Talreja, 1985; Ladeveze et al., 2000; Kashtalyan and Soutis, 2005; Maimi et al., 2007a; van der Meer et al., 2012; Pinho et al., 2013). At this scale, plies are the building blocks of the model. If the intention is to simulate delamination, cohesive interfaces are placed between the neighbouring layers to connect them (Li et al., 2012; Shi et al., 2012, for instance). In those cases where delamination is not explicitly modelled, the layers are assumed to be perfectly bonded together.

Quantities related to the behaviour of individual plies, and the interface between them, are required as inputs to the ply-based models and the response of the laminate is predicted based on such information. The damage behaviour of the individual plies is either extracted from tests performed on unidirectional laminates or from an underlying micromechanical theory. By using the properties extracted from tests on unidirectional laminates, or extracted from micromechanical simulation of individual plies, the ply-based models implicitly assume that the damage behaviour of a ply in a laminate is independent of its neighbours with the consequential implication that the interaction of damage mechanisms between the neighbouring plies does not influence the inelastic damage response of the laminate. It is generally accepted that the orientation of the neighbouring plies play a major role in the response of a lamina particularly in the inelastic regime where damage initiation and evolution in the lamina strongly depend on the level of confinement provided by the adjacent plies in the laminate.

Considering the fact that the standard test methods suggested for characterization of unidirectional laminates often exhibit instability (or catastrophic failure), the behaviour observed in such a test would not represent the behaviour of a ply in a multidirectional laminate. In a multidirectional laminate, neighbouring plies provide structural support to the damaged layers and introduce alternative load paths to the structure. Therefore the individual plies exhibit a different effective behaviour when placed in a multidirectional laminate (see Camanho et al., 2006).

The other problem associated with the ply-based models is their computational cost. Because each and every layer of the laminate is simulated, the excessive computational cost (and time) makes the ply-based models impractical for simulation of real size structures.

6.4.3 Macroscale models

Macroscale models are the only models that can be used practically for simulation of large-scale structures. These models are designed to simulate the overall response of the laminate. The macroscale models are typically not capable of predicting the details of the damage events in the layers. Numerical efficiency and also accurately predicting the behaviour of the structure in terms of macroscale parameters are the main objectives of the macroscale models.

As we have discussed, the ply-based approach encounters two problems: high computational cost and the assumption of the independent behaviour of layers. The sublaminate-based approach, which was first introduced by Williams et al. (2003), takes the sublaminate as the building block of the laminated composite structure. This approach considers the sublaminates as the representative volume and as the base level for constructing the damage model. Given that the response of a single lamina in a stack is governed by its *in situ* characteristics, only a model constructed at the scale of a block of layers or sublaminate has the potential to incorporate the interactions of damage mechanisms between layers caused by the stacking sequence.

The goal of the sublaminate approach is to predict, in a smeared manner, the essence of the overall nonlinear response of a laminated composite structure (e.g., its stiffness, load-carrying capacity, stability and post-peak behaviour) due to progressive damage caused by a given loading condition rather than capturing the details of the damage in each and every layer of the laminate. In this approach, in contrast with the ply-based approach, an element in the numerical simulation represents a sublaminate.

As the damage behaviour of the sublaminate depends on orientation, sequence and thickness of its constituent layers, each variant of the stacking sequence must be regarded as a distinct material for which the material model assigned to the sublaminate needs to be recalibrated.

6.4.4 Multiscale models

The multiscale nature of damage and failure in composite structures has been the motivation for recently proposed multiscale models. A multiscale simulation consists of modelling the behaviour of the material/structure at different scales. One can categorize the multiscale models into two groups: *hierarchical* and *concurrent*.

Hierarchical models are the first generation of multiscale approaches. In this approach, homogenization is employed to transfer the predicted behaviour of the material from a lower scale (e.g., micromechanical RVE) to a higher scale (see Chamis et al., 2000; Fish and Yu, 2001; Ladeveze, 2004; Mayes and Hansen, 2004; Gonzalez and LLorca, 2006; Wu et al., 2012, for instance). In its most common form, an underlying numerical micromechanical model governs the stress–strain behaviour at an integration point of a macroscale model (e.g., Mayes and Hansen, 2004).

The desire to predict the behaviour of composites with complex fibre architectures has made hierarchical multiscale models popular. Models based on this approach have

been implemented in commercial finite element packages (or add-ons) such as *MSC Digimat* (MSC Software Corporation) and *Autodesk Simulation Composite Analysis* (formerly *Firehole Helius:MCT*) (Autodesk Inc.), and *MDS-C* (Multiscale Design Systems).

While hierarchical multiscale models are typically capable of predicting the elastic response of materials with complex architectures at the microscale, when it comes to prediction of damage and failure, they face a fundamental problem stemming from the fact that in the presence of damage, homogenization ceases to be valid due to localization of strain. As a result, hierarchical multiscale models are unable to predict fracture energy, size of FPZ and thus size effect objectively. The characteristic material length, which is linked to the constitutive model at the macroscale, cannot be built up from the lower scales in a hierarchical manner.

In concurrent multiscale models, on the other hand, instead of applying homogenization to bridge the scales, both scales are concurrently present in the model. In undamaged areas, a macromodel with effective homogenized behaviour is employed, while in damaged areas, the model resolution is increased and mesomicro features are explicitly accounted for.

As one of the earlier concurrent multiscale models, Ghosh and co-workers (Raghavan et al., 2004; Ghosh et al., 2007) proposed an adaptive multilevel computational model for prediction of damage due to matrix cracking in a composite lamina. Waas and co-workers have recently extended the concurrent modelling framework to simulation of damage growth in 3D braided composites (Smilauer et al., 2011).

Among the shortcomings of the concurrent multiscale models are their immense computational costs along with the difficulties in characterization of small-scale (microscale) models.

Table 6.1 presents an overview of the ongoing research on simulation of damage in composites at various research centres around the world. It is not intended to provide a historically complete and exhaustive survey of all the contributions that have been made but rather a comparative overview.

6.5 CDM for simulation of intralaminar damage

From a computational standpoint, there are various approaches that can be employed to simulate the progression of damage and fracture in composites. A taxonomy of these approaches is shown in Figure 6.2. Although, due to its discrete nature, delamination is simulated using the cohesive crack concept, CDM approaches are often employed to simulate intralaminar damage. In multidirectional laminates, intralaminar damage usually forms in a more widely spread and diffused pattern. Therefore, the continuum approach offers a better physical representation of intralaminar damage compared to the discrete approach.

In CDM, the secant stiffness matrix of the damaged material is written in terms of a set of damage parameters. A strain-based evolution law usually governs the damage

Table 6.1 An overview of the ongoing research on simulation of damage in composites at various research institutes around the world including sample articles and model scales as well as their applications

Research group	Sample references	Scales			Application (composite topology)
		Micro	Meso	Macro	
University of Liege, Computational and Multiscale Mechanics of Materials	Wu et al. (2012, 2013)	x		x	Two-phase composites with moderate fibre volume fraction (unidirectional)
Polytechnic University of Madrid	Llorca et al. (2011)	x		x	Two-phase unidirectional composites
Northwestern University Michigan University	Smilauer et al. (2011)		x	x	Two-phase braided composites
Ohio State University	Ghosh et al. (2007) and Raghavan et al. (2004)	x	x	x	Matrix with particle reinforcements
Luisiana State University	Voyiadjis et al. (2001)	x		x	Transverse matrix cracking
LMT-Cachan	Lemaitre et al. (2000), Ladeveze (2004) and Ladeveze and Nouy (2003)		x		Examples shown for unidirectional and woven materials but applicable to various architectures
University of Illinois at Urbana-Champaign	Inglis et al. (2008)	x		x	Transverse crack in matrix
Delft University of Technology	Nguyen et al. (2012) and van der Meer et al. (2012)	x	x	x	Can be applied to transverse matrix cracking, mixed cohesive-X-FEM for laminates
Columbia University	Fish and Yu (2001)	x	x	x	Transverse matrix cracking
Texas A&M University	Singh and Talreja (2009)	x	x		Matrix cracking in multidirectional laminate
University of Girona University of Porto	Maimi et al. (2007a,b)		x	x	Ply-based (unidirectional lamina), sublaminate

NASA Lewis Research Centre NASA Glenn Research Centre	Chamis et al. (1996)	x	x	x	Multiscale framework, part of the WWFE I
University of California, Berkeley	Matzenmiller et al. (1995)		x		Unidirectional lamina
Technical University of Denmark Georgia Institute of Technology	Talreja (1985, 1989) Lacy et al. (1997)		x		Unidirectional lamina Short fibre composites
University of Illinois at Chicago	Krajcinovic (1985)	x	x		Unidirectional lamina
NPL Materials Centre, UK	McCartney (2005)		x		Unidirectional laminate
Louisiana State University	Voyiadjis and Deliktas (2000)		x	x	Composite laminates
RPI and Northwestern	Cusatis et al. (2008)		x		Microplane-based damage model for unidirectional lamina
US Air Force Materials Lab Hercules Materials Technology Dept.	Tan and Nuismer (1989)			x	Matrix cracking in laminates
University of Bristol	Hallett (2005) and Hallett et al. (2009)		x	x	Ply-based simulation of laminates
University of Alberta	Karihaloo and Xiao (2003) Grufman and Ellyin (2007)	x			Micromechanical models for matrix cracking and fibre–matrix interface failure in unidirectional laminates
University of British Columbia	Williams et al. (2003) and Forghani et al. (2011, 2013)			x	Macroscale modelling of laminated composites using sublaminate approach

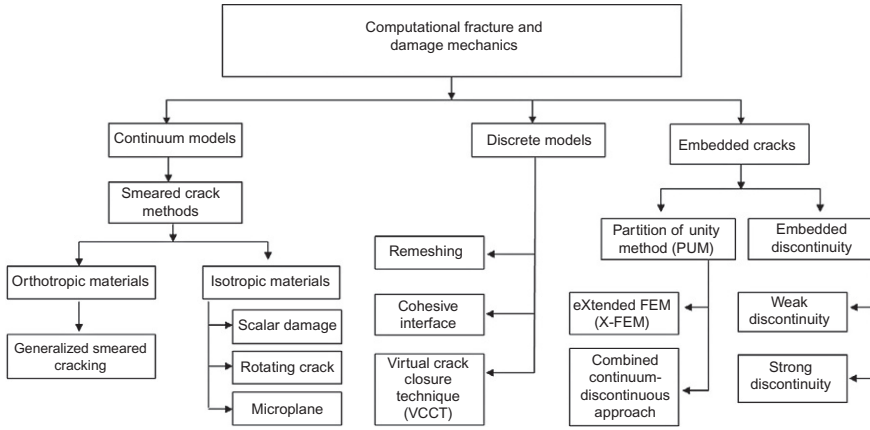

Figure 6.2 A taxonomy of computational fracture and damage mechanics approaches.

growth in these models (see Talreja, 1985, 1989; Ladeveze, 1995; Lemaitre et al., 2000; Maimi et al., 2007a, for instance).

6.5.1 Determining the stiffness of a damaged material

In establishing a damage model for laminated composites, the first challenge is to describe the stiffness of the damaged material in terms of the damage parameters. Extending the concepts developed for isotropic damage theories to an orthotropic material is not straightforward. As an example, employing the concept of strain equivalence for an orthotropic material leads to an asymmetric secant stiffness matrix. The secant stiffness describes the elastic behaviour of the damaged material and an asymmetric secant stiffness does not comply with the Betti–Maxwell's reciprocity law for elastic systems (see Matzenmiller et al., 1995; Jirasek, 2007, for instance). Matzenmiller and co-workers (1995) modified the asymmetric material compliance matrix by applying reduction factors to the Poisson's ratios to come up with a symmetric compliance matrix. An alternative method to derive the stiffness matrix of the damaged material is to employ the so-called principle of energy equivalence that leads to a symmetric matrix (see Chow and Wang, 1987; Kennedy and Nahan, 1996, for instance).

Some researchers start by expressing the Helmholtz free energy function of the damaged material in terms of its elastic properties, strain state and damage parameters. This approach leads to an energetically consistent and symmetric secant stiffness matrix (see Maimi et al., 2007a; Lemaitre et al., 2000; Voyiadjis and Deliktas, 2000, for instance).

Inspired by micromechanics of defects in solids, some researchers have defined damage parameters based on the size and orientation of the microscale cracks distributed over an RVE. See Krajcinovic (1985) for the formulation proposed for initially isotropic materials and Talreja (1985, 1989) and Lacy et al. (1997) for laminated composites. Micromechanical calculations are employed in this approach to determine the

effect of distributed microcracks on the characteristics of the RVE such as its stiffness. This approach typically assumes that noninteractive microcracks are uniformly spread over the RVE in the damaged material. Such an assumption is valid only during the early stages of damage development. At the later stages of damage development, when microcracks start to interact, coalesce and form meso or macrocracks, the assumptions are invalid and the approach would not be applicable (Lacy et al., 1997).

In another attempt, Cusatis and co-workers have generalized Bazant's microplane theory to simulate damage within the laminae (Cusatis et al., 2008; Beghini et al., 2008).

6.5.2 Damage evolution laws

The second challenge in the continuum damage approach is writing the evolution law for the multiple damage parameters. Evolution laws that govern the condition for initiation and growth of damage parameters are usually written in terms of the strain state in the layer. In composites, owing to the existence of various damage modes and their potential interactions, defining the damage evolution laws for continuum damage models becomes challenging.

A popular approach to formulate the evolution law is based on the hypothesis of maximum damage dissipation that is analogous with the associated flow rule of plasticity. In this approach, the evolution of each damage parameter is governed by its work conjugate, the so-called energy release rate density parameters. Ladeveze and co-workers have employed this hypothesis to derive the evolution law for intralaminar damage (Ladeveze et al., 2000; Ladeveze, 1995). Although the hypothesis of maximum damage dissipation offers a straightforward framework for formulating the evolution law, it is a pure mathematical hypothesis that does not necessarily represent the underlying physics involved in damage evolution. For instance, models based on maximum damage dissipation leads to path-independent energy dissipation. In other words, according to this hypothesis, the energy dissipated during the course of a damage process becomes independent of the load path taken to reach a particular damage state.

A more general approach motivated by the nonassociated flow rule of plasticity defines a dissipation potential function (which is different from the free energy function) and the damage evolution law is written in terms of the derivatives of that potential function with respect to each damage parameter. The choice of the dissipation potential function depends on the available test data and the purpose of the damage model (see Krajcinovic, 1985; Lemaitre et al., 2000; Lemaitre and Desmorat, 2005, for instance). The hypothesis of maximum damage dissipation can be reckoned as a special case where the Helmholtz free energy is taken to be the dissipation potential function.

6.5.3 Other approaches to simulate intralaminar damage

Although CDM is the most common approach to simulation of intralaminar damage in laminated composites, some researchers have chosen alternative approaches to simulate this damage mode. Wisnom, Hallett and co-workers have employed a discrete cohesive crack approach to simulate the matrix splitting cracks (e.g., Jiang et al., 2007;

Li et al., 2012). The eXtended Finite Element Method (X-FEM) and similar enriched finite element-based approaches have also been employed to simulate intralaminar damage (see van der Meer et al., 2012; Fang et al., 2011, for instance).

6.5.4 UBC composite damage model

The UBC composite damage model (CODAM) introduced by Williams et al. (2003) is a macroscale model that uses a repeating unit of the laminate or sublaminate as its building block. This macroscopic scale of resolution is required to account for the damage interactions among the various layers. The goal of this modelling approach is to predict the effective nonlinear behaviour of large-scale laminated composite structures undergoing progressive damage development. When dealing with large structures, a simple model that captures the behaviour of the material in terms of macroscale entities, such as the overall dissipation of energy due to damage and crack patterns, would be able to predict the behaviour of the structure fairly well.

It has been shown that a model as simple as a scalar damage model can be used to accurately predict the load–displacement response of a notched specimen made of laminated CFRP (see McClennan, 2004, among others). Although the formation of microcracks, matrix cracking, fibre breakage and delamination, all contribute to the behaviour of the laminate in a structure, it is not necessary to model all such details in order to be able to predict the load–displacement response accurately. Because in this case the load–displacement behaviour mainly depends on the peak stress carried by the laminate and the energy that it absorbs due to damage formation, these two parameters dictate the overall behaviour of the laminate.

The first generation of CODAM (Williams et al., 2003) was introduced in the late 1990s. This damage model accounts for the effects of matrix cracking and fibre breakage on the degradation of the laminate's stiffness. The loss of the laminate's stiffness is written in terms of three damage parameters that represent the degradation of effective modulus in two perpendicular directions (in-plane principal directions) and the shear modulus in the same coordinate system (plane). The damage parameters in this model are explicitly written in terms of equivalent strain functions also known as damage driving forces (see Williams et al., 2003, for further details).

The original formulation of CODAM shows an unrealistic dependence on the choice of the coordinate system used to formulate it and is not capable of predicting the damage-induced orthotropy. CODAM2 is the second generation of the UBC CODAM, which aims to address the material objectivity issue of the original CODAM formulation.

Owing to the mismatch between the individual layer properties in laminated composites, the local stress–strain state in the laminate is very complex. The complexity increases when damage is introduced to the system as damage modes interact at smaller scales. The interaction between the layers and existence of various damage mechanisms affects the behaviour of a layer within the laminate significantly. Therefore, the behaviour observed in the tests performed on unidirectional coupons does not represent the effective behaviour of a layer in a laminated system.

CODAM2 acknowledges the fact that orientations of the layers play an important role in damage behaviour of the laminate. In CODAM2, the response of the laminate is based on the effective behaviour of the layers in the laminate. Two reduction coefficients that represent the reduction of stiffness in the longitudinal (fibre) and transverse (matrix) directions have been employed. Evolution of damage parameters is written in terms of equivalent strain functions (see Forghani et al., 2013, for further details on the model).

6.5.5 Localization problem in strain-softening materials

It is widely acknowledged that the continuum damage models resulting in strain-softening constitutive behaviour lead to *localization* phenomenon. The solution for a structure made of a progressively damaging elastic solid predicts localization of damage over a surface of zero thickness resulting in zero energy dissipation. This would happen regardless of the shape of the softening part of the stress–strain curve. The causes and effects of localization have been discussed in detail in several articles published on this subject (e.g., Belytschko and Bazant, 1984; Bazant and Oh, 1983; Bazant and Oh, 1985).

From a mathematical point of view, when damage initiates in a strain-softening material, the partial differential equation governing the equilibrium of the quasi-static system loses its ellipticity and the boundary value problem ceases to have a unique solution. In dynamic problems, the initial value problem of stress wave propagation loses its hyperbolicity when the material starts to soften. This implies that the stress waves cannot be transferred through the damaged zone. Furthermore, within the damaged zone, the solution to the dynamic problem becomes an exponential function leading to unbounded velocity of the material points in this region (see Sluys, 1992, among others).

This problem manifests itself as spurious mesh-size dependency in the finite element solution. In such cases, damage and/or crack patterns tend to localize to the smallest length scale of the model that is the height of one element. Therefore, with successive mesh refinement, damage localizes into a zone of zero volume and the numerical predictions fail to converge to a unique solution. Consequently, the global response of the system shows dependence on the spatial discretization (see, e.g., Bazant and Oh, 1983; Belytschko and Lasry, 1989; Lasry and Belytschko, 1988).

To address the localization issue, various remedies have been proposed. Some of the remedies such as the crack band method (Bazant and Oh, 1983) offer a technique that can be used in the finite element solution to avoid the mesh-size dependency of the numerical solution, but they do not solve the underlying mathematical problem. The crack band scaling has been previously used to reduce the mesh-size dependency in modelling the in-plane damage in laminated composites (e.g., Maimi et al., 2007a,b; Williams et al., 2003; McClennan, 2004; Prabhakar and Waas, 2013; Floyd et al., 2003; Floyd, 2004; McGregor et al., 2007; McGregor, 2005; Xiao et al., 2009).

Other remedies, such as the family of nonlocal methods, offer a more fundamental solution that addresses the localization issue by introducing a length scale into the governing equations. These so-called localization limiters (Belytschko and Lasry, 1989; Lasry and Belytschko, 1988) force the damage to grow in a zone with a finite

width that is independent of the spatial finite element discretization. Among the localization limiters are the nonlocal averaging schemes based on the explicit and implicit strain gradient theories (Peerlings et al., 1996, 1998) as well as rate-dependent damage models (e.g., Sluys, 1992).

The nonlocal averaging approach is one of the well-established localization limiters in which, unlike the local approach, the state of stress at a material point depends on the state of strain and history parameters in a finite neighbourhood of that point (see Bazant and Planas, 1998; Bazant and Pijaudier-Cabot, 1988, among others). The effect of nonlocal averaging on improving the predicted damage pattern and addressing the localization issue is not limited to quasi-static loading conditions. It was shown in Forghani and Vaziri (2009) that employing a nonlocal averaging scheme improves the predicted damage pattern under severe dynamic loading conditions such as blast and lateral impact on composite laminates.

The choice of the parameter that is subjected to nonlocal averaging plays a very important role in the predictions of a nonlocal model and employing an inappropriate parameter for averaging can lead to unrealistic predictions. It has been shown that equivalent strains are suitable parameters for nonlocal averaging (Jirásek, 1998). The nonlocal equivalent strain, $\overline{\varepsilon}^{\mathrm{eq}}$, is calculated by averaging the local equivalent strain, $\varepsilon^{\mathrm{eq}}$, over a finite neighbourhood, $\Omega_{\mathbf{X}}$:

$$\overline{\varepsilon}^{\mathrm{eq}} = \int_{\Omega_{\mathbf{X}}} \varepsilon^{\mathrm{eq}}(\mathbf{x}) w(\mathbf{X}-\mathbf{x}) \mathrm{d}\Omega \tag{6.1}$$

where $\mathbf{X}$ represents the position vector of the original point of interest; $\mathbf{x}$ denotes the position vector of all other points in the averaging zone; and w is the function used to perform the weighted averaging.

The nonlocal method was originally proposed for isotropic materials like concrete and also applied to composites with random distribution of short fibres (e.g., Geers et al., 1999). In this approach, the averaging zone around a material point is a circle (or sphere in 3D) and the weight function (w) has an isotropic spatial distribution which only depends on the distance between the two points ($|\mathbf{X}-\mathbf{x}|$). In laminated composites that are made of strongly orthotropic constituents (e.g., unidirectional layers), an isotropic averaging scheme would not be appropriate.

Forghani (2011) introduced an orthotropic nonlocal averaging technique where the direction of the fibres and its effect on crack growth is taken into account. In this work, it was shown that employing an orthotropic averaging scheme significantly improves the predicted crack pattern both in terms of its size and growth path.

6.6 Experimental work for calibration of intralaminar damage models

One of the practical challenges in applying CDM-based models to simulation of intralaminar damage in composites is the calibration of the model constants based on physical experiments. This requires a good understanding of the physics of the damage

mechanisms and devising specialized laboratory experiments that can link these mechanisms to the effective model parameters in a quantitative manner. As discussed before, a strain-softening based damage model is one of the most practical approaches to describe the progressive intralaminar damage behaviour in composites. In general, strain-softening laws that are associated with low total fracture energy, but high values of peak stress can predict high-strength, low-toughness responses. Whereas material laws with high total fracture energy but low values of peak stress lead to low-strength and high-toughness behaviours. In this regard, the two key parameters for characterization of a strain-softening law are the peak stress and the area under the stress–strain curve. The latter is dependent on a length scale and the amount of energy release rate (fracture energy) associated with a particular damage mode. The quantification of this energy is challenging as there is no standard technique for its determination because of its strong dependency on the laminate layup, loading and test configurations. It is also important to have a testing configuration or methodology that promotes a stable growth of damage in a given composite laminate to establish a relationship between the crack growth and the energy release rate. Many ply-based progressive damage models, for instance, must have an estimation of the fracture toughness of the layers in each of the failure modes (i.e., fibre-dominated and matrix-dominated failures both in tension and compression).

The compact tension (CT) test is one of the techniques used to obtain the fracture toughness for the tensile fibre failure mode of laminated composites. Typically, a cross-ply laminate layup is used in such tests (see Jose et al., 2001; Pinho et al., 2006).

The compact compression (CC) test, which is similar to CT, is another technique used to measure the fracture toughness associated with kink-band failure for a carbon epoxy system. An example of the use of this technique for calculation of the fracture energy associated with the 0°-plies in a cross-ply laminate can be found in Pinho et al. (2006). The authors obtained a normalized fracture energy function from linear finite element simulations using the J-integral technique. The energy release rate was then directly determined from the maximum load obtained from the test.

In the application of CT and CC tests using a cross-ply layup, it is assumed that the calculated energy release rate is the sum of those for fibre fracture in the 0° layers and matrix cracking in the 90° layers with the interaction between them being neglected. Therefore, the use of unidirectional laminates is more appealing in application. Some examples of using unidirectional laminates for measuring intralaminar fracture toughness in tension can be found in various test methods including the three-point bending (Garg, 1986), the four-point bending (Pinho et al., 2009) and the CT (Garg, 1986) tests.

Other simplified methods using centre-notched specimens under compression loading that consider the kink-band formation were introduced by Soutis et al. (1991, 1993) and Soutis and Curtis (2000).

There have been fewer studies devoted to the extraction of softening laws for calibration of macroscale damage models. The simplest approach is to use a trial-and-error procedure to calibrate the softening law that leads to a reasonably good prediction of the strength for a range of small-notch specimens. In Boeing's programme for ATCAS reported in Walker et al. (1991, 1992, 1993), various test configurations

with different notch lengths and specimen widths, both for tension and compression, were conducted to back-calculate the strain-softening law. These softening laws were then used successfully for larger structures.

Kongshavn and Poursartip (1999) developed an over-height compact tension (OCT) specimen to predict the notch behaviour and to extract the softening properties (associated with tensile loading) for a laminate directly from a fewer number of test data. In this type of specimen configuration, which allows for a reasonably stable damage growth in front of the notch, the displacement of the inscribed surface lines in a zone close to the notch gives an indication of the progression of damage across the specimen width throughout the test. More recently, full-field measurement techniques have been applied to measure the displacement vectors and the surface strains of the specimen at each point within the damage zone. As a result, and owing to the advent of high-resolution cameras and image-processing techniques, a more accurate identification of damage properties can be achieved. Employing the results of full-field measurement techniques with the digital image correlation technique, Zobeiry (2010) and Zobeiry et al. (2015) have developed a two-step method to directly extract the key parameters for characterizing the strain-softening law as well as its shape for a specific layup and material system. This method can be applied for determination of the strain-softening law for both tension and compression with the use of the OCT and CC test data, respectively.

6.7 Concluding remarks

Several approaches can be employed for modelling the progression of damage in composite materials, which can be classified broadly as the smeared and discrete cracking models. Some of these approaches as they apply to simulation of intralaminar failure of composite laminates have been reviewed here. The particular choice of the model depends on the purpose of the analysis. In general, if determination of the overall response (or load-deflection behaviour) is desired, without regard to completely realistic crack patterns and local stresses, then the smeared crack model is probably the best choice and one that lends itself to a more efficient analysis of large-scale composite structures. If, on the other hand, detailed local behaviour is of interest, the use of the discrete crack model may prove necessary. For most structural engineering applications, the smeared cracking model is generally adopted. Such representation assumes that the cracked composite remains a continuum, that is, cracks are treated out in a smeared fashion. The effects of such cracks on the behaviour of the damaged layer, sublaminate or laminate is the reduction of stiffness and/or strength in certain directions leading to a strain-softening behaviour.

CDM has emerged as a popular and theoretically sound framework for describing the smeared effect of damage and fracture processes in composite materials. Specifically, intralaminar damage mechanisms involving fibre breakage and matrix cracking within a single layer can be well represented by CDM formulations. However, for a damaged layer within a multilayer laminate, the crack opening displacements will be

constrained by the adjacent layers. The extent of softening, marked by the slope of the descending part of the stress–strain curve, is in such cases dependent on the orientation of the adjacent plies in a laminate. This leads to considerable complications in the development and calibration of CDM-based constitutive models for laminated structures as these models cannot be built up from the constitutive models at the lower levels (e.g., ply-level) in a hierarchical manner. Therefore, each variant of stacking sequence must be regarded as a distinct material that needs to be characterized experimentally to quantify the damage model. The physical tests required are often nonstandard and require special configurations of geometry and loading that result in a self-similar progression of damage in the laminate. To create crack growths that are energetically stable may in some cases (depending on the characteristics of the particular laminate being tested) require large specimen geometries. The link between the model and real experimental testing is central to the development of CDM models to capture the correct physics.

In addition to the experimental challenges in characterizing them, CDM models and the strain-softening material behaviour that results from their application lead to a few numerical issues that need to be considered (e.g., mesh size and orientation objectivity of numerical results; stability of iterative methods required for nonlinear solution convergence when such models are implemented in implicit codes). In some cases, mesh-size requirements may lead to prohibitive computational costs when modelling practical and configured structures with dimensions that greatly exceed the small coupon sizes for which these models are generally validated.

Continuum approaches alone cannot realistically simulate laminate responses that are dominated by delamination and splitting mechanisms that are discrete in nature and are sensitive to the local stress fields and boundary conditions. A more effective computational approach in such cases would have to include a concurrent combination of smeared and discrete models to capture the interaction between the material and structural (or local and global) behaviour. This calls for availability of robust, integrated, multiscale computational tools that are capable of predicting the progressive damage behaviour of realistic, large-scale composite structures with algorithmic and computational efficiencies that enable their practical usage in damage tolerant or crashworthy design applications.

Acknowledgements

The authors would like to acknowledge the financial support provided by the Natural Sciences and Engineering Research Council (NSERC) of Canada. The contributions made to this work by many of the past members of the Composites Group at UBC are also gratefully acknowledged.

References

Autodesk Inc., Autodesk simulation composite analysis. Available: http://www.autodesk.com/products/autodesk-simulation-family/features/simulation-composite-design/all/list-view.

Bazant, Z.P., 1999. Size effect on structural strength: a review. Arch. Appl. Mech. 69 (9–10), 703–725.

Bazant, Z.P., Oh, B.H., 1983. Crack band theory for fracture of concrete. Mater. Construct. 16 (93), 155–177.

Bazant, Z.P., Oh, B.H., 1985. Microplane model for progressive fracture of concrete and rock. J. Eng. Mech. 111 (4), 559–582.

Bazant, Z.P., Pijaudier-Cabot, G., 1988. Nonlocal continuum damage, localization instability and convergence. Preprint. Am. Soc. Mech. Eng. 1988,18–7.

Bazant, Z.P., Planas, J., 1998. Fracture and Size Effect in Concrete and Other Quasibrittle Materials. CRC Press, Boca Raton.

Bazant, Z.P., Daniel, I.M., Li, Z., 1996. Size effect and fracture characteristics of composite laminates. J. Eng. Mater. Technol. 118 (3), 317–324.

Beghini, A., Cusatis, G., Bazant, Z.P., 2008. Spectral stiffness microplane model for quasibrittle composite laminates – part II: calibration and validation. J. Appl. Mech. Trans. ASME 75 (2), 0210101–0210106.

Belytschko, T., Bazant, Z.P., 1984. Strain-softening materials and finite element solutions. In: Constitutive Equations: Macro and Computational Aspects. Presented at the Winter Annual Meeting of the American Society of Mechanical Engineers. ASME, pp. 253–272.

Belytschko, T., Lasry, D., 1989. Study of localization limiters for strain-softening in statics and dynamics. Comput. Struct. 33 (3), 707–715.

Camanho, P.P., Dávila, C.G., Pinho, S.T., Iannucci, L., Robinson, P., 2006. Prediction of in situ strengths and matrix cracking in composites under transverse tension and in-plane shear. Compos. A: Appl. Sci. Manuf. 37 (2), 165–176.

Chamis, C.C., Murthy, P.L.N., Minnetyan, L., 1996. Progressive fracture of polymer matrix composite structures. Theor. Appl. Fract. Mech. 25 (1), 1–15.

Chamis, C.C., Murthy, P.L.N., Gotsis, P.K., Mital, S.K., 2000. Telescoping composite mechanics for composite behavior simulation. Comput. Methods Appl. Mech. Eng. 185 (2–4), 399–411.

Chow, C.L., Wang, J., 1987. Anisotropic theory of elasticity for continuum damage mechanics. Int. J. Fract. 33 (1), 3–16.

Cusatis, G., Beghini, A., Bazant, Z.P., 2008. Spectral stiffness microplane model for quasibrittle composite laminates – part I: theory. J. Appl. Mech. Trans. ASME 75 (2), 0210091–0210099.

Dopker, B., Murphy, D., Ilcewicz, L., and Walker, T., 1994. Damage tolerance analysis of composite transport fuselage structure. American Institute of Aeronautics and Astronautics, AIAA-94-1406-CP, pp. 803–810.

Fang, X.J., Zhou, Z.Q., Cox, B.N., Yang, Q.D., 2011. High-fidelity simulations of multiple fracture processes in a laminated composite in tension. J. Mech. Phys. Solids 59 (7), 1355–1373.

Fish, J., Yu, Q., 2001. Multiscale damage modelling for composite materials: theory and computational framework. Int. J. Numer. Methods Eng. 52, 161–191.

Floyd, A., 2004. An engineering approach to the simulation of gross damage development in composite laminates (Ph.D. thesis), The University of British Columbia, Vancouver, Canada.

Floyd, A., Vaziri, R., Poursartip, A., 2003. A numerically objective continuum damage model to accurately simulate damage growth in composites. In: 4th Canadian International Composites Conference (CANCOM 2003).

Forghani, A., 2011. A nonlocal approach to simulation of damage in composite structures. (Ph.D. thesis), The University of British Columbia, Vancouver, Canada.

Forghani, A., Vaziri, R., 2009. Computational modeling of damage development in composite laminates subjected to transverse dynamic loading. J. Appl. Mech. Trans. ASME 76 (5), 051304.

Forghani, A., Zobeiry, N., Vaziri, R., Poursartip, A., Ellyin, F., 2011. A nonlocal approach to simulation of damage in laminated composites. In: ASC/CANCOM Conference.

Forghani, A., Zobeiry, N., Poursartip, A., Vaziri, R., 2013. A structural modelling framework for prediction of damage development and failure of composite laminates. J. Compos. Mater. 47 (20–21), 2553–2573.

Garg, A.C., 1986. Intralaminar and interlaminar fracture in graphite/epoxy laminates. Eng. Fract. Mech. 23 (4), 719–733.

Geers, M.G.D., De Borst, R., Peijs, T., 1999. Mixed numerical-experimental identification of nonlocal characteristics of random-fibre-reinforced composites. Compos. Sci. Technol. 59 (10), 1569–1578.

Ghosh, S., Bai, J., Raghavan, P., 2007. Concurrent multilevel model for damage evolution in microstructurally debonding composites. Mech. Mater. 39 (3), 241–266.

Gonzalez, C., Llorca, J., 2006. Multiscale modeling of fracture in fiber-reinforced composites. Acta Mater. 54 (16), 4171–4181.

Grufman, C., Ellyin, F., 2007. Determining a representative volume element capturing the morphology of fibre reinforced polymer composites. Compos. Sci. Technol. 67 (3–4), 766–775.

Grufman, C., Ellyin, F., 2008. Numerical modelling of damage susceptibility of an inhomogeneous representative material volume element of polymer composites. Compos. Sci. Technol. 68 (3–4), 650–657.

Hallett, S.R., 2005. Numerical investigation of progressive damage and the effect of layup in notched tensile tests. J. Compos. Mater. 40 (14), 1229–1245.

Hallett, S.R., Green, B.G., Jiang, W.G., Wisnom, M.R., 2009. An experimental and numerical investigation into the damage mechanisms in notched composites. Compos. A: Appl. Sci. Manuf. 40 (5), 613–624.

Hillerborg, A., Modéer, M., Petersson, P., 1976. Analysis of crack formation and crack growth in concrete by means of fracture mechanics and finite elements. Cem. Concr. Res. 6 (6), 773–781.

Ilcewicz, L.B., Walker, T.H., Murphy, D.P., Dopker, B., Scholz, D.B., Cairns, D.S., Poe, C.C., 1993. Tension fracture of laminates for transport fuselage – part 4: damage tolerance analysis. In: Fourth NASA/DoD Advanced Composite Technology Conference, NASA CP-3229, pp. 265–298.

Ilcewicz, L.B., Smith, P.J., Hanson, C.T., Walker, T.H., Metschan, S.L., Mabson, G.E., Wilden, K.S., Flynn, B.W., Scholz, D.B., Polland, D.R., Fredrikson, H.G., Olson, J.T., Backman, B.F., 1996. Advanced technology composite fuselage – program overview. NASA CR-4734.

Inglis, H.M., Geubelle, P.H., Matous, K., 2008. Boundary condition effects on multiscale analysis of damage localization. Philos. Mag. 88 (16), 2373–2397.

Jiang, W., Hallett, S.R., Green, B.G., Wisnom, M.R., 2007. A concise interface constitutive law for analysis of delamination and splitting in composite materials and its application to scaled notched tensile specimens. Int. J. Numer. Methods Eng. 69 (9), 1982–1995.

Jirásek, M., 1998. Nonlocal models for damage and fracture: comparison of approaches. Int. J. Solids Struct. 35 (31–32), 4133–4145.

Jirasek, M., 2007. Course Notes on Modeling of Localized Elastic Deformation, first ed. John Wiley and Sons, New York.

Jose, S., Ramesh Kumar, R., Jana, M.K., Venkateswara Rao, G., 2001. Intralaminar fracture toughness of a cross-ply laminate and its constituent sublaminates. Compos. Sci. Technol. 61 (8), 1115–1122.

Karihaloo, B.L., Xiao, Q.Z., 2003. Modelling of stationary and growing cracks in FE framework without remeshing: a state-of-the-art review. Comput. Struct. 81 (3), 119–129.

Kashtalyan, M., Soutis, C., 2005. Analysis of composite laminates with intra and interlaminar damage. Prog. Aerosp. Sci. 41 (2), 152–173.

Kennedy, T.C., Nahan, M.F., 1996. Simple nonlocal damage model for predicting failure of notched laminates. Compos. Struct. 35 (2), 229–236.

Kongshavn, I., Poursartip, A., 1999. Experimental investigation of a strain-softening approach to predicting failure in notched fibre-reinforced composite laminates. Compos. Sci. Technol. 59 (1), 29–40.

Krajcinovic, D., 1985. Continuous damage mechanics revisited: basic concepts and definitions. In: Winter Annual Meeting – American Society of Mechanical Engineers. ASME, New York, NY, USA.

Lacy, T.E., McDowell, D.L., Willice, P.A., Talreja, R., 1997. On representation of damage evolution in continuum damage mechanics. Int. J. Damage Mech. 6 (1), 62–95.

Ladeveze, P., 1995. Damage computational approach for composites: basic aspects and micromechanical relations. Comput. Mech. 17 (1–2), 142–150.

Ladeveze, P., 2004. Multiscale modeling and computational strategies for composites. Int. J. Numer. Meth. Eng. 60, 233–253.

Ladeveze, P., Nouy, A., 2003. On a multiscale computational strategy with time and space homogenization for structural mechanics. Comput. Methods Appl. Mech. Eng. 192 (28–30), 3061–3087.

Ladeveze, P., Allix, O., Deu, J., Leveque, D., 2000. Mesomodel for localisation and damage computation in laminates. Comput. Methods Appl. Mech. Eng. 183 (1), 105–122.

Lasry, D., Belytschko, T., 1988. Localization limiters in transient problems. Int. J. Solids Struct. 24 (6), 581–597.

Lavoie, J.A., Soutis, C., Morton, J., 2000. Apparent strength scaling in continuous fiber composite laminates. Compos. Sci. Technol. 60 (2), 283–299.

Lemaitre, J., Desmorat, R., 2005. Engineering Damage Mechanics: Ductile, Creep, Fatigue and Brittle Failures. Springer-Verlag, Heidelberg, DEU.

Lemaitre, J., Desmorat, R., Sauzay, M., 2000. Anisotropic damage law of evolution. Eur. J. Mech. A Solids 19 (2), 187–208.

Li, X., Hallett, S.R., Wisnom, M.R., 2012. Numerical investigation of progressive damage and the effect of layup in overheight compact tension tests. Comp A: Appl. Sci. Manuf. 43, 2137–2150.

Llorca, J., Gonzalez, C., Molina-Aldareguia, J., Segurado, J., Seltzer, R., Sket, F., Rodriguez, M., Sadaba, S., Munoz, R., Canal, L.P., 2011. Multiscale modeling of composite materials: a roadmap towards virtual testing. Adv. Mater. 23 (44), 5130–5147.

Maimi, P., Camanho, P.P., Mayugo, J.A., Davila, C.G., 2007a. A continuum damage model for composite laminates: part I – constitutive model. Mech. Mater. 39 (10), 897–908.

Maimi, P., Camanho, P.P., Mayugo, J.A., Davila, C.G., 2007b. A continuum damage model for composite laminates: part II – computational implementation and validation. Mech. Mater. 39 (10), 909–919.

Matzenmiller, A., Lubliner, J., Taylor, R.L., 1995. A constitutive model for anisotropic damage in fiber-composites. Mech. Mater. 20 (2), 125–152.

Mayes, J.S., Hansen, A.C., 2004. Composite laminate failure analysis using multicontinuum theory. Compos. Sci. Technol. 64 (3–4), 379–394.

McCartney, L.N., 2005. Energy-based prediction of progressive ply cracking and strength of general symmetric laminates using a homogenisation method. Compos. A: Appl. Sci. Manuf. 36 (2), 119–128.

McClennan, S.A., 2004. Crack growth and damage modeling of fibre reinforced polymer composites (M.A.Sc. thesis), The University of British Columbia, Vancouver, Canada.

McGregor, C.J., 2005. Simulation of progressive damage development in braided composite tubes under axial compression (M.A.Sc. thesis), The University of British Columbia, Vancouver, Canada.

McGregor, C.J., Vaziri, R., Poursartip, A., Xiao, X., 2007. Simulation of progressive damage development in braided composite tubes under axial compression. Compos. A: Appl. Sci. Manuf. 38 (11), 2247–2259.

Melro, A.R., Camanho, P.P., Andrade Pires, F.M., Pinho, S.T., 2013. Micromechanical analysis of polymer composites reinforced by unidirectional fibres: part I – constitutive modelling. Int. J. Solids Struct. 50 (11–12), 1897–1905.

MSC Software Corporation, The nonlinear multiscale material and structure modeling platform. Available: http://www.mscsoftware.com/product/digimat.

Multiscale Design Systems, LLC, Multiscale design system for continuum scales. Available: http://multiscale.biz/index.html.

Nguyen, V.P., Stroeven, M., Sluys, L.J., 2012. Multiscale failure modeling of concrete: micromechanical modeling, discontinuous homogenization and parallel computations. Comput. Methods Appl. Mech. Eng. 201–204, 139–156.

Peerlings, R.H.J., De Borst, R., Brekelmans, W.A.M., De Vree, J.H.P., 1996. Gradient enhanced damage for quasi-brittle materials. Int. J. Numer. Methods Eng. 39 (19), 3391–3403.

Peerlings, R.H.J., De Borst, R., Brekelmans, W.A.M., Geers, M.G.D., 1998. Wave propagation and localisation in nonlocal and gradient-enhanced damage models. J. Phys. IV 8 (8), 293–300.

Pinho, S.T., Robinson, P., Iannucci, L., 2006. Fracture toughness of the tensile and compressive fibre failure modes in laminated composites. Compos. Sci. Technol. 66 (13), 2069–2079.

Pinho, S.T., Robinson, P., Iannucci, L., 2009. Developing a four point bend specimen to measure the mode I intralaminar fracture toughness of unidirectional laminated composites. Compos. Sci. Technol. 69 (7–8), 1303–1309.

Pinho, S.T., Vyas, G.M., Robinson, P., 2013. Response and damage propagation of polymer-matrix fibre-reinforced composites: predictions for WWFE-III Part A. J. Compos. Mater. 47 (20–21), 2595–2612.

Prabhakar, P., Waas, A.M., 2013. A novel continuum-decohesive finite element for modeling in-plane fracture in fiber reinforced composites. Compos. Sci. Technol. 83, 1–10.

Raghavan, P., Li, S., Ghosh, S., 2004. Two scale response and damage modeling of composite materials. Finite Elements Anal. Des. 40, 1619–1640.

Shi, Y., Swait, T., Soutis, C., 2012. Modelling damage evolution in composite laminates subjected to low velocity impact. Compos. Struct. 94 (9), 2902–2913.

Singh, C.V., Talreja, R., 2009. A synergistic damage mechanics approach for composite laminates with matrix cracks in multiple orientations. Mech. Mater. 41 (8), 954–968.

Sluys, L.J., 1992. Wave propagation, localization and dispersion in softening solids (Ph.D. edn), Delft University of Technology, Netherlands.

Smilauer, V., Hoover, C.G., Bazant, Z.P., Caner, F.C., Waas, A.M., Shahwan, K.W., 2011. Multiscale simulation of fracture of braided composites via repetitive unit cells. Eng. Fract. Mech. 78 (6), 901–918.

Soutis, C., Curtis, P.T., 2000. A method for predicting the fracture toughness of CFRP laminates failing by fibre microbuckling. Compos. A: Appl. Sci. Manuf. 31 (7), 733–740.

Soutis, C., Fleck, N.A., Smith, P.A., 1991. Failure prediction technique for compression loaded carbon fibre-epoxy laminate with open holes. J. Compos. Mater. 25 (11), 1476–1498.

Soutis, C., Curtis, P.T., Fleck, N.A., 1993. Compressive failure of notched carbon fibre composites. Proc. R. Soc. Lond. Ser. A: Math. Phys. Sci. 440 (1909), 241–256.

Sutherland, L.S., Shenoi, R.A., Lewis, S.M., 1999. Size and scale effects in composites: I. Literature review. Compos. Sci. Technol. 59 (2), 209–220.

Talreja, R., 1985. Continuum mechanics characterization of damage in composite materials. Proc. R. Soc. Lond. Ser. A: Math. Phys. Sci. 399 (1817), 195–216.

Talreja, R., 1989. Damage development in composites: mechanisms and modelling. J. Strain Anal. Eng. Des. 24 (4), 215–222.

Tan, S.C., Nuismer, R.J., 1989. A theory for progressive matrix cracking in composite laminates. J. Compos. Mater. 23 (10), 1029–1047.

Turon, A., Camanho, P.P., Costa, J., Renart, J., 2010. Accurate simulation of delamination growth under mixed-mode loading using cohesive elements: definition of interlaminar strengths and elastic stiffness. Compos. Struct. 92 (8), 1857–1864.

Van Der Meer, F.P., Moës, N., Sluys, L.J., 2012. A level set model for delamination – modeling crack growth without cohesive zone or stress singularity. Eng. Fract. Mech. 79, 191–212.

Voyiadjis, G.Z., Deliktas, B., 2000. A coupled anisotropic damage model for the inelastic response of composite materials. Comput. Methods Appl. Mech. Eng. 183 (3–4), 159–199.

Voyiadjis, G.Z., Deliktas, B., Aifantis, E.C., 2001. Multiscale analysis of multiple damage mechanisms coupled with inelastic behavior of composite materials. J. Eng. Mech. 127 (7), 636–645.

Walker, T.H., Avery, W.B., Ilcewicz, L.I., Poe, C.C.J., Harris, C.E., 1991. Tension fracture of laminates for transport fuselage – part I: material screening. In: Second NASA Advanced Technology Conference, NASA CP 3154, pp. 197–238.

Walker, T.H., Ilcewicz, L.B., Polland, D.R., Poe, C.C.J., 1992. Tension fracture of laminates for transport fuselage – part II: large notches. In: Third NASA Advanced Technology Conference, NASA CP 3178 1992, pp. 727–758.

Walker, T.H., Ilcewicz, L.B., Polland, D.R., Bodine, J.B., Poe, C.C.J., 1993. Tension fracture of laminates for transport fuselage – part III: structural configurations. In: Fourth NASA Advanced Technology Conference, NASA CP3229, pp. 243–264.

Williams, K., Vaziri, R., 1995. Finite element analysis of the impact response of CFRP composite plates. In: Tenth International Conference on Composite Materials (ICCM/10).

Williams, K.V., Vaziri, R., 2001. Application of a damage mechanics model for predicting the impact response of composite materials. Comput. Struct. 79 (10), 997–1011.

Williams, K.V., Vaziri, R., Poursartip, A., 2003. A physically based continuum damage mechanics model for thin laminated composite structures. Int. J. Solids Struct. 40 (9), 2267–2300.

Wisnom, M.R., Khan, B., Hallett, S.R., 2008. Size effects in unnotched tensile strength of unidirectional and quasi-isotropic carbon/epoxy composites. Compos. Struct. 84 (1), 21–28.

Wisnom, M.R., Hallett, S.R., Soutis, C., 2010. Scaling effects in notched composites. J. Compos. Mater. 44 (2), 195–210.

Wu, L., Noels, L., Adam, L., Doghri, I., 2012. A multiscale mean-field homogenization method for fiber-reinforced composites with gradient-enhanced damage models. Comput. Methods Appl. Mech. Eng. 233–236, 164–179.

Wu, L., Noels, L., Adam, L., Doghri, I., 2013. Nonlocal multiscale analyzes of composite laminates based on a damage-enhanced mean-field homogenization formulation. 17th International Conference on Composite Structure.

Xia, Z., Chen, Y., Ellyin, F., 2000. Meso/micromechanical model for damage progression in glass-fiber/epoxy cross-ply laminates by finite-element analysis. Compos. Sci. Technol. 60 (8), 1171–1179.

Xiao, X., McGregor, C., Vaziri, R., Poursartip, A., 2009. Progress in braided composite tube crush simulation. Int. J. Impact Eng. 36 (5), 711–719.

Zhang, Y., Xia, Z., Ellyin, F., 2004. Evolution and influence of residual stresses/strains of fiber reinforced laminates. Compos. Sci. Technol. 64 (10–11), 1613–1621.

Zhang, Y., Xia, Z., Ellyin, F., 2005. Viscoelastic and damage analyses of fibrous polymer laminates by micro/mesomechanical modeling. J. Compos. Mater. 39 (22), 2001–2022.

Zobeiry, N., 2010. Extracting the strain softening response of composites using full-field displacement measurement (Ph.D. thesis), The University of British Columbia, Vancouver, Canada.

Zobeiry, N., Vaziri, R., Poursartip, A., 2015. Characterization of strain-softening behaviour and failure mechanisms of composites under tension and compression. Compos. A: Appl. Sci. Manuf. 68, 29–41.

This page intentionally left blank

Numerical modeling of matrix cracking and intralaminar failure in advanced composite materials

7

P. Maimí, H. Rodríguez, N. Blanco, J.A. Mayugo
Universitat de Girona, Girona, Spain

7.1 Introduction

A common damage mechanism of layered composite materials with unidirectional reinforcement is the formation and growth of subcritical matrix cracks (Beuth, 1992; Hutchinson and Suo, 1992; Xia and Hutchinson, 2000). In general, these cracks are confined in the thickness of the layer because they are arrested by the tougher fibers of the adjacent plies with a different orientation. Mechanical loads and the mismatch of thermal coefficients of fibers and matrix and/or different layers are the main driving forces that trigger these cracks.

Transverse cracks are formed within the matrix and in the interface between fiber and matrix with a normal direction perpendicular to the fibers and the laminate thickness. Then, these cracks grow in the brittler direction, without breaking the fibers. In laminated composites, this damage usually is the first to appear and is usually caused by normal transverse and in-plane shear stresses. Matrix cracking is a noncatastrophic damage mechanism; the laminate is able to sustain larger loads with the presence of cracks. For this reason matrix cracking is accepted in some applications, while in others, such as pressure vessels, are not allowed.

As a noncatastrophic damage mechanism, the appearance of the first crack is followed by the formation of new cracks while external loads continue increasing, see Figure 7.1a. For multiple cracked plies, the cracks usually appear staggered, as shown in Figure 7.1b (Nairn, 2000). Finally, for very thick plies oblique cracks appear just beside the main transverse cracks (Figure 7.1c; Nairn, 2000; Parvizi et al., 1978).

Although they are not considered a catastrophic damage mechanism, matrix cracks can trigger different damage mechanisms such as matrix microdamage and delaminations (Figure 7.1d and e). Delaminations are a dangerous damage mechanism because they reduce the flexural and compressive strength of the laminate. Furthermore, matrix cracks act as stress raisers that can promote the failure of adjacent plies if the interface is tough enough to avoid crack kinking (see Figure 7.1f).

Numerical modelling of failure in advanced composite materials. http://dx.doi.org/10.1016/B978-0-08-100332-9.00007-4
Copyright © 2015 Elsevier Ltd. All rights reserved.

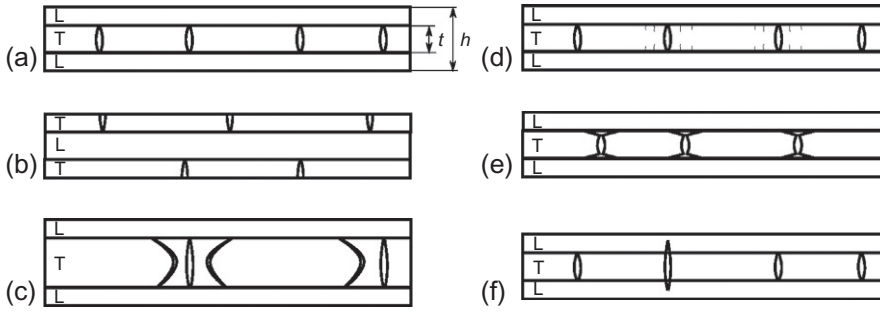

Figure 7.1 Different crack patterns in cross-ply laminates (a–c) and other damage mechanisms triggered by matrix cracks (d–f) (L stands for longitudinal and T for transversal).

7.2 First-ply failure

7.2.1 In situ *strength. Thin and thick plies*

Transverse and shear strengths of a ply embedded in a laminate are larger than the corresponding strengths of a unidirectional ply. This effect is known as *in situ* strength (Camanho et al., 2006; Dvorak and Laws, 1987; Maimí et al., 2014). The most remarkable effect of the *in situ* strength is the increase of the nominal strength by reducing the ply thickness or the number of clustered plies with the same orientation. The ply strength when a ply is embedded is defined as the load required to propagate a crack and, as a consequence, is analyzed by means of fracture mechanics theory.

The transversal strength of a unidirectional ply (Y_T^{UD}) can be experimentally characterized by means of a traction test as the ASTM Standard (2010). This unidirectional strength is always smaller than the strength of the ply embedded in a laminate. The results found by Wang (1984) and Crossman and Wang (1982) are summarized in Figure 7.2 and show a decrease of the *in situ* strength when increasing the number of transverse plies clustered together.

For thin plies the ply strength is defined by the mean stress at ply level required to propagate a crack in the direction of the fibers, or crack tunneling (Figure 7.3). Because of linear elastic fracture mechanics (LEFM), the energy release rate (ERR) required to propagate a crack longitudinally is expressed as

$$G = \frac{\sigma_{\mathrm{T}}^2}{4\bar{E}_{\mathrm{T}}} t\kappa \tag{7.1}$$

where σ_{T} is the stress of the ply, $\bar{E}_{\mathrm{T}}$ the plane strain Young modulus, t the ply thickness, and κ is a constant that depends on the elastic properties of the outer plies, the relative thickness of each ply, the laminate stacking sequence, and the position of the considered ply in the laminate.

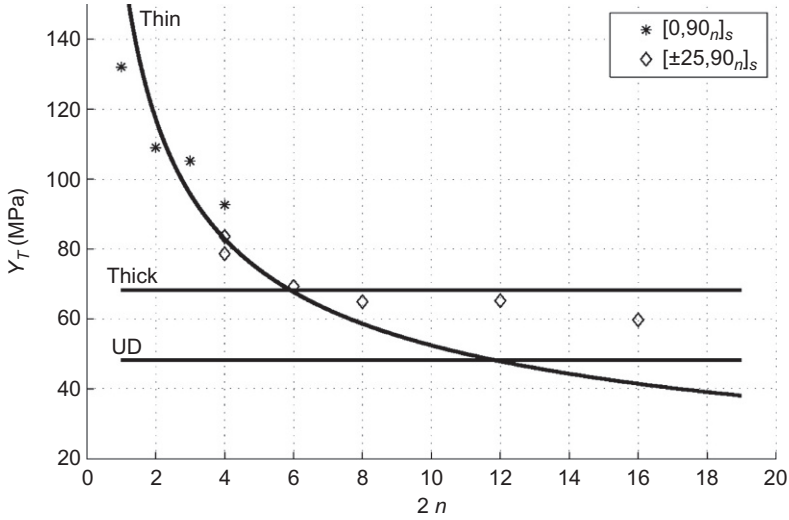

Figure 7.2 *In situ* strength with respect to ply clustering (n). Adapted from Wang (1984) and Crossman and Wang (1982).

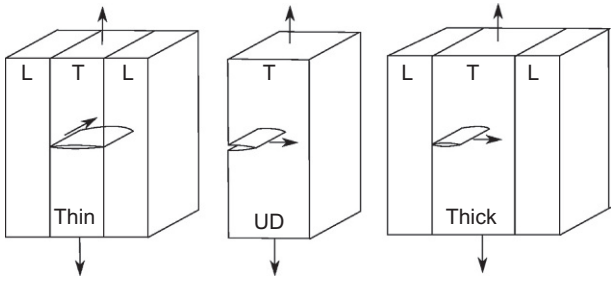

Figure 7.3 Modes of crack growth in a thin embedded layer, unidirectional ply, and thick embedded layer.

Then, the *in situ* strength of a thin ply can be expressed as a function of the critical ERR G_C as

$$Y_T^{Thin} = 2\sqrt{\frac{\bar{E}_T G_C}{t\kappa}} \tag{7.2}$$

which is represented in Figure 7.2 by the thin line. According to this, by increasing the ply thickness, the ply strength will decrease until it reaches the thick plies *in situ* strength.

A common explanation (Camanho et al., 2006; Dvorak and Laws, 1987; Maimí et al., 2011a) for the strength of thick plies is the presence of a characteristic defect as shown in Figure 7.3. By means of LEFM, the mean stress required to propagate the crack is larger in the embedded ply than in the unidirectional ply (UD) due to the free-

edge effect. Obviously, this effect is not present in the outer plies. The thick ply strength can be expressed as

$$Y_T^{Thick} = \kappa_T Y_T^{UD} \tag{7.3}$$

where κ_T is a constant that depends on the elastic properties of the outer plies, the relative thickness of each ply, the laminate stacking sequence, and the position of the ply in the laminate. Usually κ_T is taken as $1.12\sqrt{2}$ (Camanho et al., 2006; Dvorak and Laws, 1987), which is rigorously true for two isotropic materials (one for the longitudinal or L plies and the other for the transversal or T plies) with the same elastic properties (Tada et al., 2000).

The ply thickness that defines the boundary between thin and thick plies can be computed with the combination of Equations (7.1) and (7.2):

$$t_{Lim} = \frac{\bar{E}_T G_C}{\kappa\left(\kappa_T Y_T^{UD}\right)^2} \tag{7.4}$$

When the material is loaded under shear stress, the same type of transverse cracks appear but they grow in mode II instead of in mode I. Moreover, the material exhibits an important nonlinear response before cracking that must be taken into account for realistic predictions (Camanho et al., 2006; Maimí et al., 2011a). Typical plies sustain a combination of normal and shear stress and cracks typically propagate under mixed-mode ratios.

Transverse cracks initiate at the free edges (FEs) (Berthelot et al., 1996b; Berthelot et al., 2001; Maimí et al., 2008), and after they reach some critical length they grow to the laminate centerline (tunneling) at the stress defined by Equation (7.2). However, in thick plies the crack grows first in the transverse direction and when it spans all along the ply thickness it grows in the longitudinal direction. Since the stress required for transverse growth of the crack is larger than the one required for longitudinal growth, the propagation of transverse cracks in thick plies is unstable (Maimí et al., 2011a,b). As a consequence, the cracking process in thick plies is defect sensitive and is influenced by the free-edge effect. Therefore, the use of thick plies is not recommended in structural applications (MIL-HDBK-17-3E, 1997). On the contrary, the thin ply *in situ* strength is a safe measure of ply strength to use because it is insensitive to defect and it is also insensitive to any material discontinuity or stress raiser.

7.2.2 ERR for crack tunneling

The ERR required for crack tunneling can be obtained by computing the elastic stress field of a two-dimensional problem with and without a completely generated matrix crack, as illustrated in Figure 7.4, and can be expressed as

$$G = \frac{U_U - U_C}{t} = \frac{\sigma_T}{2t}\int \delta_{COD}(x)\mathrm{d}x \tag{7.5}$$

where U_U is the elastic energy per unit length stored in the uncracked region, and U_C is the elastic energy in the cracked plane subjected to the same displacement (it must be

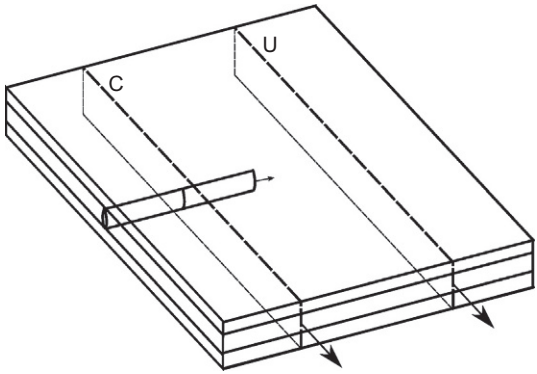

Figure 7.4 Schema of the computation of energy release rate by means of a two-dimensional stress analysis, at planes C and U.

pointed out that both planes share the same displacement but not the same load because both sections work in parallel). The ERR can also be computed by means of the σ_T of the transverse ply in the uncracked plane and the mean crack opening displacement of the cracked one, δ_{COD}.

The most significant parameter that defines the *in situ* strength is the ply thickness although the elastic mismatch between different plies is also of importance. For the simple case of the cross-ply laminate shown in Figure 7.3, the parameter κ in Equation (7.2) depends on

$$\kappa(\lambda_T, \rho_T, \lambda_L, \rho_L, \alpha, \beta, \bar{t}) \tag{7.6}$$

where $\bar{t}$ is the relative thickness of the ply with respect to the total thickness of the laminate

$$\bar{t} = \frac{t}{h} \tag{7.7}$$

λ and ρ (Lekhnitskii, 1963) depend on the elastic coefficients of the transverse and longitudinal plies and for plane stress conditions can be defined as

$$\lambda = \frac{s_{11}}{s_{22}} \text{ and } \rho = \frac{2s_{12} + s_{66}}{2\sqrt{s_{11}s_{22}}} \tag{7.8}$$

where s_{ij} are the components of the compliance tensor. For plane strain, it is necessary to use the terms $s_{ij} \equiv s_{ij} - s_{i3}s_{j3}/s_{33}$ where 1 is the direction of the applied load and 2 the direction normal to the laminate plane. If the laminate is transversely isotropic, then parameters $\lambda_T = \rho_T = 1$ and κ can expressed as $\kappa(\lambda_L, \rho_L, \alpha, \beta, \bar{t})$. α and β are the generalized Dundurs parameters that define the mismatch of the elastic properties of the plies. For two orthotropic materials (Suo, 1990; Ting, 1995)

$$\alpha = \frac{s_{11}^T - s_{11}^L}{s_{11}^T + s_{11}^L} \text{ and } \beta = \frac{\left[\sqrt{s_{11}s_{22}} + s_{12}\right]_T - \left[\sqrt{s_{11}s_{22}} + s_{12}\right]_L}{H_{11}H_{22}} \tag{7.9}$$

where

$$H_{11} = \left[2n\lambda^{1/4}\sqrt{s_{11}s_{22}}\right]_{\mathrm{T}} + \left[2n\lambda^{1/4}\sqrt{s_{11}s_{22}}\right]_{\mathrm{L}}$$
$$H_{22} = \left[2n\lambda^{-1/4}\sqrt{s_{11}s_{22}}\right]_{\mathrm{T}} + \left[2n\lambda^{-1/4}\sqrt{s_{11}s_{22}}\right]_{\mathrm{L}}$$
$$n = \sqrt{\frac{1}{2}(1+\rho)}$$

Again, it is necessary to use the terms $s_{ij} \equiv s_{ij} - s_{i3}s_{j3}/s_{33}$ for plane strain.

Hutchinson and Suo (1992) presented some solutions of κ for isotropic materials which are summarized in Figure 7.5. According to these results, the mismatch of elastic parameters, α, has the most important effect on the parameter κ of Equation (7.2). For example, according to the results obtained by Hutchinson and Suo for isotropic materials, the parameter κ is equal to 2 for a ply embedded in an infinitely stiff layer and increases up to π if the stiffness of the outer and inner plies is the same. In case the outer ply was more compliant than the cracked one, the parameter κ would quickly increase. However, this is not the case of composite laminates in which transverse cracks are arrested by the stiffer adjacent plies.

The relative thickness of the ply ($\bar{t}$) is important only in the case of thin and compliant adjacent plies. The value of κ decreases by decreasing the relative stiffness of the cracked ply to a constant value corresponding to the case of a layer embedded in an infinite medium. In the case of isotropic materials with the same stiffness, the limit is π, as the well-known solution of a crack in an infinite sheet (Tada et al., 2000). For the same case but for external plies $\kappa = 1.12^2 2\pi$. The increase of κ with respect

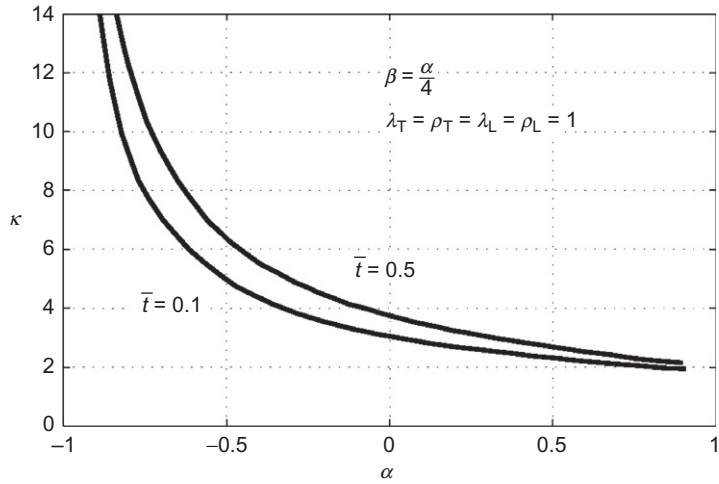

Figure 7.5 Variation of the parameter κ with respect to the main Dundur parameter (α) for two different relative thicknesses of the inner ply and isotropic materials.

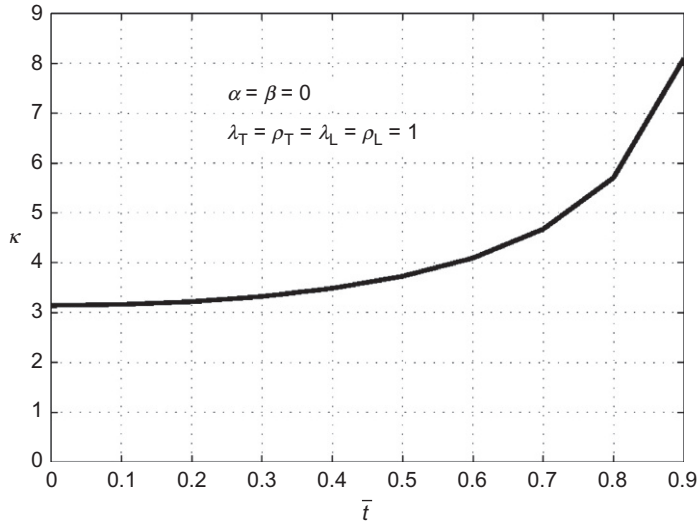

Figure 7.6 Variation of the parameter κ with respect to the relative thickness of the ply for equal isotropic materials.

to the relative thickness is presented in Figure 7.6 for isotropic materials with $\alpha = \beta = 0$. If the outer plies are stiffer than the cracked plies (i.e., the value of α increases), the slope of the function in Figure 7.6 is lower. As a consequence, for very stiff outer layers, a very thin adjacent ply is enough to increase the *in situ* strength to its infinitely thick adjacent plies limit, $\bar{t} = 0$. This can be seen in Figure 7.5 where the difference of κ between $\bar{t} = 0.1$ and 0.5 decrease by increasing α.

7.3 Evolution of crack density

Once the process of cracking is initiated, as the process is stable, the number of cracks increases when the external load is applied. The distribution of cracks inside the material is usually assumed to be uniformly distributed, as sketched in Figure 7.7. Under this assumption, a single scalar variable can be used to objectively describe the number of cracks in the ply. In general, the variable used is the crack density defined as the inverse of the distance between two consecutive cracks

$$\varrho = \frac{1}{\ell} \tag{7.10}$$

A nondimensional measure of the crack density can be defined by multiplying the crack density by the ply thickness

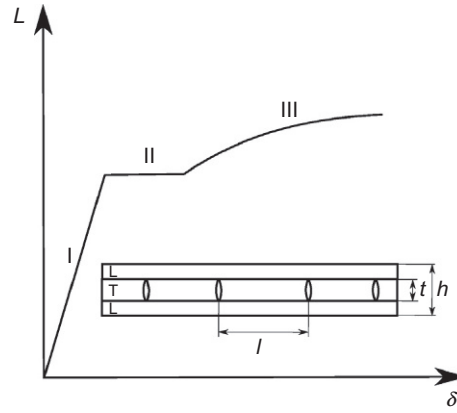

Figure 7.7 Load–displacement response of a laminate: I, elastic region; II, low crack density; and III, high crack density.

$$\overline{\varrho} = \frac{t}{\ell} \tag{7.11}$$

As shown in Figure 7.7, three main regions can be distinguished in the load–displacement curve of a composite laminate. The first region is elastic and no cracks are present in the laminate. When the stress in the transverse ply reaches the *in situ* strength the cracking process starts. This region is defined as II in the figure and corresponds to a low crack density. In this case, the global load required to increase the crack density is almost constant (rigorously constant if no defects are assumed in the laminate) (Hashin, 1996; Maimí et al., 2011b).

The justification for the first stage of cracking (region II) that occurs at constant load if the material has no flaws is the following. The first cracking in the ply occurs when the level of ERR at a certain point of the ply reaches its critical value, causing a perturbation of the stress distribution in the laminate. By the Saint Venant's principle, the effect of this perturbation disappears at a certain distance. Then, the second crack in the same layer must appear at a certain distance larger than twice the critical distance where the ERR reaches, at constant load, the critical value. As a consequence, region II in Figure 7.7 must be horizontal if no flaws are present in the ply.

The third phase (region III) corresponds to a high crack density. In this case, the ERR decreases with crack density and the external load to produce cracking must be increased. In this region, the perturbation of the stress field produced by a crack influences the growth of the closer cracks.

For thin plies, the ERR is expressed as in Equation (7.1) but a new variable is introduced in κ related with the crack density ($\overline{\varrho}$)

$$\kappa(\overline{\varrho}, \lambda_T, \rho_T, \lambda_L, \rho_L, \alpha, \beta, \bar{t}) \tag{7.12}$$

The crack density at the intersection point between regions II and III depends on the same parameters as κ, but according to Hashin (1996) and as shown in the next sections, for composite laminates it can be approximated as $\overline{\varrho}_{\mathrm{II-III}} \approx 0.45$.

7.3.1 ERR and laminate stiffness

The stress field and the corresponding ERR in a cracked specimen can be determined using different analytical methods (McCartney, 2000) based on a shear lag analysis (Parvizi et al., 1978; Krasnikovs and Varna, 1997; Varna and Krasnikovs, 1998; Berthelot et al., 1996a; Nairn and Mendels, 2001; Mayugo et al., 2010) or variational methods (Hashin, 1985, 1996; Vinogradov and Hashin, 2010; Nairn and Hu, 1992; Nairn, 2000) or using finite element methods (Xia et al., 1993; Leblond et al., 1996; Berthelot et al., 2001; Ladevèze and Lubineau, 2002). By using these approaches, it is possible to determine the required conditions for crack tunneling and, as a consequence, the *in situ* strength of thin plies. The results presented here have been obtained by means of the finite elements method using the procedure explained in Xia et al. (1993). With the finite element method, the ERR can be obtained by means of Equation (7.5) but taking into account that the ply stress before crack growth is not necessarily constant:

$$G = \frac{1}{2t}\int \sigma(x)\delta_{\mathrm{COD}}(x)\mathrm{d}x \tag{7.13}$$

where σ is the stress normal to the crack surface prior to cracking and δ_{COD} the crack opening displacement. The mean Young modulus of the cracked laminate can be defined as $\bar{E}_{\mathrm{C}} = \sigma_O/\varepsilon$. Then, the loss of stiffness of the laminate can be quantified by normalizing $\bar{E}_{\mathrm{C}}$ with respect to the initial Young modulus as

$$e_{\mathrm{C}} = \frac{\bar{E}_{\mathrm{C}}}{\bar{E}_{\mathrm{O}}} \tag{7.14}$$

where the Young modulus of the uncracked laminate is defined as

$$\bar{E}_{\mathrm{O}} = \bar{E}_{\mathrm{T}}\bar{t} + \bar{E}_{\mathrm{L}}(1-\bar{t}) \tag{7.15}$$

According to Xia et al. (1993) and by means of the reciprocal theorem of elasticity, the following relation keeps:

$$e_{\mathrm{C}}^{-1} = 1 + \frac{\overline{\varrho}}{2\bar{t}}\kappa_{\mathrm{O}} = 1 + \frac{\bar{E}_{\mathrm{T}}\overline{\varrho}}{2\bar{E}_{\mathrm{O}}\bar{t}}\kappa \tag{7.16}$$

where κ_{O} is equivalent to κ and is obtained by defining the ERR with the global laminate stress and stiffness as

$$G = \frac{\sigma_O^2}{4\bar{E}_O} t\kappa_O \tag{7.17}$$

Therefore, the relation between κ_O and κ is defined as

$$\bar{E}_O \kappa_O = \bar{E}_T \kappa \tag{7.18}$$

The parameter κ is defined at ply level and is related to the *in situ* strength of the ply, while κ_O is defined at the laminate level and is related to the global laminate stress–strain response.

The variation of the laminate stiffness loss, defined by Equation (7.14), and κ for a laminate with isotropic materials with the same elastic properties ($\alpha = \beta = 0$) with respect to the nondimensional crack density and relative thickness of the inner ply is shown in Figure 7.8. It must be pointed out that the values of κ in Figure 7.8 coincide with those shown in Figure 7.6 for the onset of crack density ($\overline{\varrho} = 0$).

As it is difficult to obtain a general solution for the parameter κ due to the large number of variables involved, it is necessary to solve numerically the elastic stress field for each laminate system. In this case, two typical cross-ply laminates with carbon and glass fibers, respectively, are considered. The elastic properties of the unidirectional plies of the laminates are summarized in Table 7.1. The values of the nondimensional parameters for the determination of κ for both types of cross-ply laminates are reported in Table 7.2.

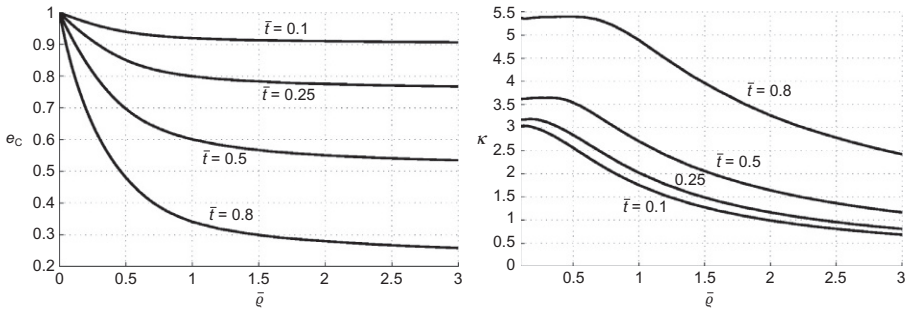

Figure 7.8 Variation of e_C (left) and κ (right) for isotropic materials $\alpha = \beta = 0$ with respect to the nondimensional crack density and relative ply thickness.

Table 7.1 Elastic properties of the unidirectional plies

Material	E_{LL} (GPa)	E_{TT} (GPa)	G_{LT} (GPa)	ν_{LT}	ν_{TT}
Carbon fiber	132	10.8	5.65	0.24	0.59
Glass fiber	43.5	11.5	3.45	0.27	0.4

Table 7.2 Nondimensional properties of the cross-ply laminates

Material	λ_L	ρ_L	λ_T	ρ_T	α	β
Carbon fiber laminate	0.125	4.013	1	1	0.849	0.072
Glass fiber laminate	0.309	3.357	1	1	0.582	0.058

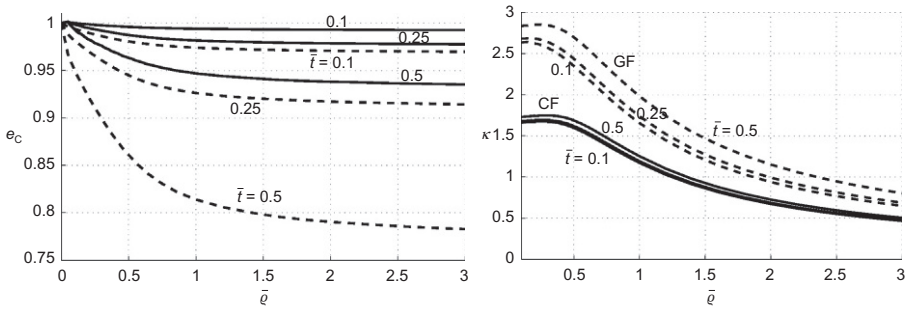

Figure 7.9 Variation of e_C (left) and κ (right) for glass fiber (dotted lines) and carbon fiber (solid lines) cross-ply laminates with respect to the nondimensional crack density and relative ply thickness.

Figure 7.9 shows the variation of the stiffness loss in laminates and κ with respect to crack density as well as the relative thickness of the inner ply for the two typical glass and carbon cross-ply laminates.

In the figure, one can observe a constant region in the variation of κ until an approximate crack density of $\bar{\varrho}_{II-III} \approx 0.45$. This corresponds to a low crack density and a constant load–displacement region as previously sketched in Figure 7.7. After this point, κ decreases and an increase of external load is required to increase the crack density.

It can also be seen in Figure 7.9 that the variation of κ with respect to the relative ply thickness ($\bar{t}$) is smaller for carbon fiber than for glass fiber laminates. This is a consequence of the larger stiffness of the carbon fibers that produce a better confinement of the laminate and is expressed by a larger value of the parameter α in Table 7.2. The relative thickness of the ply is only important for laminates with small values of α. From these computations, it can be concluded that the *in situ* strength of the central ply of a laminate $[0_{GF}, 0_{CF}, 90]_S$ is larger than the one of a $[0_{CF}, 0_{GF}, 90]_S$ laminate. Even though the overall laminate stiffness is the same, the adjacent ply to the 90 layer is stiffer in the former case.

7.3.2 Crack distribution

The distribution of matrix cracks in the transversal ply of a laminate is not uniform as it is usually considered to be for practical solutions. There are two main reasons for this nonuniform crack distribution: the presence of defects in the material

(Lebon et al., 1998; Berthelot et al., 1996b; Manders et al., 1983; Vinogradov and Hashin, 2005) and the process of cracking in region II (see Figure 7.7; Maimí et al., 2011b). In this region, the distance between two consecutive cracks is $\ell > \overline{\varrho}_{\text{II-III}}^{-1}$. This means that new cracks appear and grow away enough from the pre-existing cracks so as not to perturb or interact with their stress field. If the variation of the ERR with respect to the distance between existing cracks is plotted, the resultant function has the form sketched in Figure 7.10. Just beside the existing cracks, the ERR is null and it increases until reaching a constant value if the next crack is far enough. Then, it decreases until zero when reaching the next crack. In this case, there is a certain length (**x** in Figure 7.10) with the same probability for crack onset and tunneling. As a consequence, a new crack will not necessarily appear in the middle of two preexisting cracks even for the case of a material without defects.

When the crack density is large enough, the short distance between existing cracks does not allow reaching a constant value of ERR with its maximum located in the middle of two existing cracks. This corresponds to region III in Figure 7.7 and no new cracks can appear until the applied load is increased and the pic level of ERR between cracks reaches the critical value. Under these circumstances, if the material has no defects, the next crack will grow just in the middle of two preexisting cracks and the nonuniformity of crack distribution is the resultant of the preceding process of cracking, region II.

From a mathematical point of view, the consideration of nonuniform crack distribution requires the introduction of a vector of densities $\overline{\varrho}_i$ with as many terms as the number of cracks existing in the laminate ($i = 1 \ldots N_{\text{Cracks}}$) (Vinogradov and Hashin, 2005; Maimí et al., 2011b) or the definition of a distribution function describing the distribution of cracks in the ply.

Since in region II the formation of a new crack requires a distance between two consecutive cracks larger than $\overline{\varrho}_{\text{II-III}}^{-1}$, in the border of regions II and III all the lengths between cracks ($\overline{\varrho}_i^{-1}$.) must be in the range defined by

$$\overline{\varrho}_{\text{II-III}}^{-1}/2 \leq \overline{\varrho}_i^{-1} < \overline{\varrho}_{\text{II-III}}^{-1} \tag{7.19}$$

This means that the value of the constant crack density under constant loading is a little larger than $\overline{\varrho}_{\text{II-III}}^{-1} = 0.45$ if statistical considerations are taken into account. Cho et al. (1992) carried out an outstanding analysis of the form of the cumulative distribution of distances between cracks. By considering that the cracks grow in the middle of two preexisting cracks and that the spacing distribution preserves

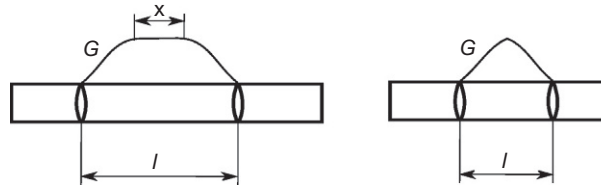

Figure 7.10 Representation of the variation of the energy release rate with respect to the distance between existing cracks: (left) low crack density and (right) high crack density.

its form while increasing the crack density, the normalized cumulative distribution function is

$$\Phi\left(\overline{\varrho}^{-1}\right) = 2 - \frac{\overline{\varrho}_{\mathrm{M}}^{-1}}{\ln(2)\overline{\varrho}^{-1}} \tag{7.20}$$

where ϱ_{M} is the mean crack density. The standard deviation of crack spacing is $0.2017\overline{\varrho}_{\mathrm{M}}^{-1}$ (Cho et al., 1992). Finally, the statistical crack density that defines the onset of region III is $\overline{\varrho}^{S}_{\mathrm{II-III}} = \overline{\varrho}_{\mathrm{II-III}}/\ln(2)$.

7.3.3 Laminate load–displacement response

The normalized laminate load–displacement response can be expressed with respect to crack density by the following expressions:

$$\sigma_{\mathrm{O}}\sqrt{\frac{t}{4\bar{E}_{\mathrm{O}}G_{\mathrm{C}}}} = \frac{1}{\sqrt{\overline{\kappa}_{\mathrm{O}}}} \text{ and } \varepsilon\sqrt{\frac{t\bar{E}_{\mathrm{O}}}{4G_{\mathrm{C}}}} = \frac{1}{e_{\mathrm{C}}\sqrt{\overline{\kappa}_{\mathrm{O}}}} \tag{7.21}$$

where $\overline{\kappa}_{\mathrm{O}}$ depends on the crack distribution considered. For example, if $\overline{\kappa}_{\mathrm{O}} = \kappa_{\mathrm{O}}$ it is assumed a continuum crack-density function. In other words, it considers that the number of cracks increases continuously and, as a consequence, each time a crack appears the existing cracks move to keep all cracks equally spaced. Another possibility, more common, is to consider that each time that a crack grows, the crack density is doubled because each next crack appears at the middle of the preexisting cracks under the consideration $\overline{\kappa}_{\mathrm{O}} = 2\kappa_{\mathrm{O}}(\overline{\varrho}) - \kappa_{\mathrm{O}}(\overline{\varrho}/2)$.

If a nonuniform crack distribution is considered, the internal variable describing the crack density is expressed as an array of crack densities as large as the number of cracks in the ply: $\overline{\varrho}_i$ for $i = 1 \ldots N_{\mathrm{Cracks}}$. In this case, the load required to increase the crack density is obtained by considering that the maximum distance between two consecutive cracks: $\overline{\kappa}_{\mathrm{O}}(\min \overline{\varrho}_i)$ (where $\min \overline{\varrho}_i = \overline{\varrho}_{\mathrm{M}}/\ln(2)$). The stiffness of the global laminate in Equation (7.21) can be determined as (McCartney and Schoeppner, 2002):

$$\frac{1}{e_{\mathrm{C}}} = \frac{1}{L}\sum_{i=1}^{N_{\mathrm{Cracks}}} \frac{1}{\overline{\varrho}_i e_{\mathrm{C}}(\overline{\varrho}_i)} \tag{7.22}$$

where $L = \sum_{i=1}^{N_{\mathrm{Cracks}}} \overline{\varrho}_i^{-1}$ is the total length of the laminate considered.

From a practical point of view, the global load–displacement is quite similar and the differences are practically imperceptible. In Figure 7.11, different normalized load–displacement curves are presented considering a continuum distribution of crack density for several material systems.

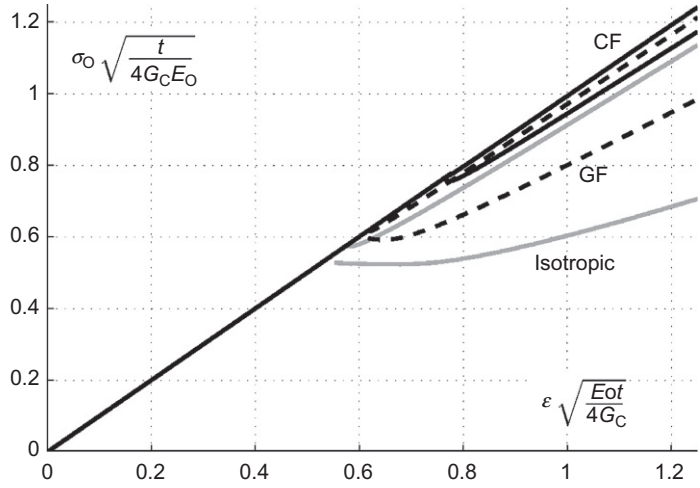

Figure 7.11 Normalized global stress–strain curves for isotropic, glass fiber and carbon fiber laminates with $\bar{t}=0.1$ (upper curves) and $\bar{t}=0.5$ (bottom curves).

7.4 Delamination induced by matrix cracking

One of the consequences of the presence of cracks is that they act as stress raisers which can induce delaminations. These delaminations are usually triggered by a combination of cracks and FE, except for very thin plies in which delaminations grow from the FE before the ply is cracked due to the mismatch of Poisson coefficients (O'Brien, 1985).

Contrarily to matrix cracking, the ERR that promotes delamination from matrix cracks depends on the whole laminate stiffness rather than that of the adjacent plies to the transverse ply. The ERR can be expressed as (O'Brien, 1985; Zubillaga et al., 2014):

$$G_{DC}=\frac{1}{4}N^{T}aN \tag{7.23}$$

where $a=A_{LD}^{-1}-A^{-1}$. A is the elastic stiffness of the laminate and A_{LD} is the stiffness of the laminate after delamination.

For cross-ply laminates with constant $\bar{t}$, the laminate stiffness is proportional to t, and the external load N is proportional to $t\sigma_T$. Therefore, the stress required to form a delamination from an existing crack is also proportional to $\sigma_T \propto 1/\sqrt{t}$, as in the case of the *in situ* strength of thin plies expressed in Equation (7.2). Usually the delamination strength is larger than the matrix cracking one for thin plies. On the other hand, for thick plies matrix cracking can generate unstable delaminations. Indeed, for plies thicker than a critical thickness value, which depends on the laminate

stacking sequence, the appearance of a first matrix crack produces an unstable delamination.

The ERR for free-edge delamination due to the difference between Poisson coefficients is defined as (O'Brien, 1985; Sebaey et al., 2014)

$$G_{\mathrm{FE}} = \frac{h\varepsilon^2}{2m}(E_{\mathrm{O}} - E_{\mathrm{D}}) \tag{7.24}$$

where the Young modulus of a laminate with m delaminations E_{D} can be determined as

$$E_{\mathrm{D}} = \frac{1}{h}\sum_{i=1}^{m+1} E_i t_i \tag{7.25}$$

where E_i and t_i are the Young modulus and the thickness of the sublaminates between delaminations, respectively.

For a cross-ply laminate with constant $\bar{t}$, the stress required for free-edge delamination is also proportional to $1/\sqrt{t}$. On the other hand, if the thickness of the outer plies is kept as constant (i.e., constant $h-t$), the different damage mechanisms decrease with a proportionality smaller than $1/\sqrt{t}$. This variation is small in the *in situ* strength, defined by the dependence of κ on $\bar{t}$ as shown in Figure 7.6, is more pronounced in the delamination due to matrix cracking (Zubillaga et al., 2014), and is especially important in free-edge delamination. The stress required to delaminate from an FE, from an existing crack (DC) and the corresponding *in situ* strength for thin and thick plies of a carbon fiber laminate with stacking sequence $[\pm 45, 90_n]_S$ with a ply thickness of 0.182 mm (Sebaey et al., 2014) is shown in Figure 7.12. For n smaller than 1.3 free-edge delamination appears before matrix cracking. For thicknesses between $n = 1.3$ and 3, matrix cracking appears before free-edge delamination and the crack density increases if the external load is also increased. For n larger than 3, the growth of the first matrix crack causes an unstable delamination.

7.5 Conclusions

The process of matrix cracking has been analyzed and several important conclusions have been reached. The main results have focused on cross-ply laminates under mode I.

The effect on the onset and evolution of matrix cracking of the ply thickness, the relative thickness of the laminate and elastic properties has been studied. It has been shown that the most important parameter is the ply thickness. Regarding the effect of the mismatch between the elastic properties, the stiffer the outer plies, the more difficult is the growth of ply cracks. The thickness of the outer plies is an important parameter for compliant plies, but its influence decreases for stiffer outer plies.

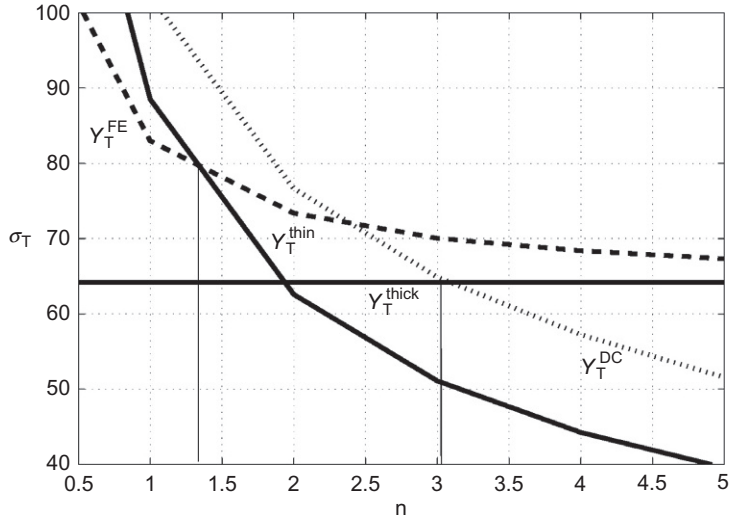

Figure 7.12 Variation of the *in situ* strength for thin and thick plies, matrix cracking delamination (DC), and free-edge delamination (FE) for a $[\pm 45, 90_n]_S$ carbon fiber composite for different values of n.

The evolution of crack density has been studied. Two regions are defined: low- and high-crack densities. For the low-crack density, the cracks do not interact. The global load–displacement is constant and a random distribution of cracks emerges without considering material inhomogeneity. On the other hand, under high crack density, cracks are closer enough to interact. In this case, to increase crack density it is necessary to increase the external load applied and, if no flaws are assumed in the material, the randomness of crack distribution is inherit from the previous, low-density, process of cracking.

Delamination is a critical damage mechanism that can be triggered by matrix cracking. For very thin plies, delamination is triggered by the mismatch of Poisson coefficients between plies and grows from FE before matrix cracks appears. Increasing the ply thickness, matrix cracking appears and its density increases before delamination. Beyond a critical ply thickness, the appearance of the first matrix crack induces unstable delamination and arrests the appearance of more matrix cracks.

References

ASTM Standard, 2010. Standard Test Method for Tensile Properties of Polymer Matrix Composite Materials. American Society for Testing and Materials, PA, USA.

Berthelot, J.-M., Leblond, P., El Mahi, A., Le Corre, J.-F., 1996a. Transverse cracking of cross-ply laminates: Part 1. Analysis. Compos. A: Appl. Sci. Manuf. 27 (10), 989–1001.

Berthelot, J.-M., El Mahi, A., Leblond, P., 1996b. Transverse cracking of cross-ply laminates: Part 2. Progressive widthwise cracking. Compos. A: Appl. Sci. Manuf. 27 (10), 1003–1010.
Berthelot, J.-M., El Mahi, A., Le Corre, J.-F., 2001. Development of transverse cracking in cross-ply laminates during fatigue tests. Compos. Sci. Technol. 61 (12), 1711–1721.
Beuth, J.L., 1992. Cracking of thin bonded films in residual tension. Int. J. Solids Struct. 29 (13), 1657–1675.
Camanho, P.P., Dávila, C.G., Pinho, S.T., Iannucci, L., Robinson, P., 2006. Prediction of in situ strengths and matrix cracking in composites under transverse tension and in-plane shear. Compos. A: Appl. Sci. Manuf. 37 (2), 165–176.
Cho, C., Holmes, J.W., Barber, J.R., 1992. Distribution of matrix cracks in a uniaxial ceramic composite. J. Am. Ceram. Soc. 75 (2), 316–324.
Crossman, F.W., Wang, A.S.D., 1982. The dependence of transverse cracking and delamination on ply thickness in graphite/epoxy laminates. In: Reifsnider, K. L. (Ed.), Damage in Composite Materials. American Society for Testing and Materials, PA, USA, pp. 118–139, ASTM STP 775.
Dvorak, G.J., Laws, N., 1987. Analysis of progressive matrix cracking in composite laminates II. First ply failure. J. Compos. Mater. 21, 309–329.
Hashin, Z., 1985. Analysis of cracked laminates: a variational approach. Mech. Mater. 4, 121–136.
Hashin, Z., 1996. Finite thermoelastic fracture criterion with application to laminate cracking analysis. J. Mech. Phys. Solids 44 (7), 1129–1145.
Hutchinson, J.W., Suo, Z., 1992. Mixed mode cracking in layered materials. Adv. Appl. Mech. 29, 63–164.
Krasnikovs, A., Varna, J., 1997. Transverse cracks in crossply laminates. 1. Stress analysis. Mech. Compos. Mater. 33 (6), 565–582.
Ladevèze, P., Lubineau, G., 2002. An enhanced mesomodel for laminates based on micromechanics. Compos. Sci. Technol. 62 (4), 533–541.
Leblond, P., El Mahi, A., Berthelot, J.-M., 1996. 2D and 3D numerical models of transverse cracking in cross-ply laminates. Compos. Sci. Technol. 56 (7), 793–796.
Lebon, B., Baxevanakis, C., Jeulin, D., Renard, J., 1998. Fracture statistics of a composite laminate. Compos. Sci. Technol. 58 (5), 765–771.
Lekhnitskii, S.G., 1963. Theory of Elasticity of an Anisotropic Body. MIR Publishers, Moscow.
Maimí, P., Mayugo, J.A., Camanho, P.P., 2008. A three dimensional damage model for transversely isotropic composite laminates. J. Compos. Mater. 42 (25), 2717–2745.
Maimí, P., Camanho, P.P., Mayugo, J.A., Turon, A., 2011a. Matrix cracking and delamination in laminated composites. Part I: ply constitutive law, first ply failure and onset of delamination. Mech. Mater. 43 (4), 169–185.
Maimí, P., Camanho, P.P., Mayugo, J.A., Turon, A., 2011b. Matrix cracking and delamination in laminated composites. Part II: evolution of crack density and delamination. Mech. Mater. 43 (4), 194–211.
Maimí, P., Gonzalez, E.V., Camanho, P.P., 2014. Comment to the paper 'Analysis of progressive matrix cracking in composite laminates II. First ply failure' by George J Dvorak and Norman Laws. J. Compos. Mater. 48 (9), 1139–1141.
Manders, P.W., Chou, T.-W., Jones, F.R., Rock, J.W., 1983. Statistical analysis of multiple fracture in 0/90/0 glass fibre/epoxy resin laminates. J. Mater. Sci. 18, 2876–2889.
Mayugo, J.A., Camanho, P.P., Maimí, P., Dávila, C.G., 2010. Analytical modelling of transverse matrix cracking of $[\pm\theta/90_n]_s$ composite laminates under multiaxial loading. Mech. Adv. Mater. Struct. 17 (4), 237–245.
McCartney, L.N., 2000. Model to predict effects of triaxial loading on ply cracking in general symmetric laminates. Compos. Sci. Technol. 60 (12–13), 2255–2279.

McCartney, L.N., Schoeppner, G.A., 2002. Predicting the effect of nonuniform ply cracking on the thermoelastic properties of cross-ply laminates. Compos. Sci. Technol. 62 (14), 1841–1856.

MIL-HDBK-17-3E, 1997. Handbook Polymer Matrix Composites, Vol. 3. Materials Usage, Design, and Analysis. Department of Defense.

Nairn, J.A., 2000. Exact and variational theorems for fracture mechanics of composites with residual stresses, traction-loaded cracks, and imperfect Interfaces. Int. J. Fract. 105, 243–271.

Nairn, J.A., 2004. Finite fracture mechanics of matrix microcracking in composites. In: Moore, D. R. (Ed.), The Application of Fracture Mechanics to Polymers, Adhesives, and Composites. Elsevier, Oxford, UK, pp. 207–212, ISBN: 0-08-044205-6.

Nairn, J.A., Hu, S., 1992. Formation and effect of outer-ply microcracks in cross-ply laminates. A variational approach. Eng. Fract. Mech. 41 (2), 203–221.

Nairn, J.A., Mendels, D., 2001. On the use of planar shear-lag methods for stress-transfer analysis of multilayered composites. Mech. Mater. 33 (6), 335–362.

O'Brien, T.K., 1985. Analysis of local delaminations and their influence on composite laminate behavior. In: Johnson, W.S. (Ed.), Delamination and Debonding of Materials. American Society for Testing and Materials, PA, USA, pp. 282–297, ASTM STP 876.

Parvizi, A., Garrett, K.W., Bailey, J.E., 1978. Constrained cracking in glass fibre-reinforced epoxy cross-ply laminates. J. Mater. Sci. 13, 195–201.

Sebaey, T.A., Costa, J., Maimí, P., Batista, Y., Blanco, N., Mayugo, J.A., 2014. Measurement of the in situ transverse tensile strength of composite plies by means of the real time monitoring of microcracking. Compos. Part B Eng. 65, 40–46.

Suo, Z., 1990. Singularities, interfaces and cracks in dissimilar anisotropic media. Proc. R. Soc. A: Math. Phys. Eng. Sci. A427, 331–358.

Tada, H., Paris, P.C., Irwin, G.R., 2000. The Stress Analysis of Cracks Handbook. American Society of Mechanical Engineers, New York.

Ting, T.C.T., 1995. Generalized dundurs constants for anisotropic bimaterials. Int. J. Solids Struct. 32 (3/4), 483–500.

Varna, J., Krasnikovs, A., 1998. Transverse cracks in crossply laminates, 2. Stiffness degradation. Mech. Compos. Mater. 34 (2), 153–170.

Vinogradov, V., Hashin, Z., 2005. Probabilistic energy based model for prediction of transverse cracking in cross-ply laminates. Int. J. Solids Struct. 42 (2), 365–392.

Vinogradov, V., Hashin, Z., 2010. Variational analysis of cracked angle-ply Laminates. Compos. Sci. Technol. 70 (4), 638–646.

Wang, A.S.D., 1984. Fracture mechanics of sublaminate cracks in composite materials. J. Compos. Technol. Res. 6 (2), 45.

Xia, Z.C., Hutchinson, J.W., 2000. Crack patterns in thin films. J. Mech. Phys. Solids 48 (6–7), 1107–1131.

Xia, Z.C., Carr, R.R., Hutchinson, J.W., 1993. Transverse cracking in fiber-reinforced brittle matrix, cross-ply laminates. Acta Metall. Mater. 41 (8), 2365–2376.

Zubillaga, L., Turon, A., Maimí, P., Costa, J., Mahdi, S., Linde, P., 2014. An energy based failure criterion for matrix crack induced delamination in laminated composite structures. Compos. Struct. 112, 339–344.

Fibre failure modelling

8

S. Pimenta
Imperial College London, London, UK

8.1 Introduction

Fibre-dominated tensile failure in fibre-reinforced polymers (FRPs) is a complex phenomenon characterised by failure of load-aligned plies across the section of the individual fibres; this failure mode is also denominated as *longitudinal tensile failure* and *translaminar failure* in the literature, and therefore the three denominations will be used interchangeably. Because the stiffness of an FRP laminate is controlled to a great extent by the fibres in the load-aligned plies, fibre-dominated tensile failure leads to a significant drop in local stiffness and can therefore trigger catastrophic failure of an entire composite structure.

A unidirectional (UD) FRP ply is composed of typically millions of individual fibres all aligned in the same direction; hence fibre-dominated tensile failure actually results from the accumulation of individual fibre breaks. The process is therefore controlled by two main features: (i) the statistics of defects in individual fibres, and (ii) the stress redistribution around broken fibres. Consequently, modelling translaminar failure accurately at the macroscale requires the ability to take into account not only the stochastic nature of fibre strength, but also the micromechanical stress field in each phase and the nonlinearity due to damage. This is a phenomenal task, yet to be mastered in the literature.

This chapter provides an overview of the modelling approaches available to predict and simulate fibre-dominated tensile failure in UD FRP plies (with continuous fibres), ranging from the classical models to recent developments in the literature. Section 8.2 will summarise the background literature focused on the physical mechanisms for tensile fibre failure in composites. Section 8.3 describes models for predicting the strength of UD FRPs under longitudinal tension, starting with classical models (both deterministic and stochastic) and followed by recent developments of stochastic models. Section 8.4 focuses on predicting fracture toughness and simulating damage accumulation in fibre-dominated tensile failure. Finally, Section 8.5 draws the main conclusions and highlights the current challenges in modelling fibre-dominated tensile failure in composites.

8.2 The mechanics of tensile fibre failure in composites

8.2.1 The strength of high-performance fibres

High-performance synthetic fibres typically used in fibre-reinforced composites (e.g. glass- and carbon-fibres) are characterised by microscale diameters (4–7 μm), high tensile stiffness (200–600 GPa), and high tensile strength (3–7 GPa) (Toray Industries Inc.,

Numerical modelling of failure in advanced composite materials. http://dx.doi.org/10.1016/B978-0-08-100332-9.00008-6
Copyright © 2015 Elsevier Ltd. All rights reserved.

2005; Hexcel Corporation, 2015). However, technical fibres (especially glass- and carbon-fibres) are usually very brittle (with maximum elongation typically below 3%), and their failure is governed by defects.

The strength of these fibres is stochastic and prone to statistical size effects. Leonardo da Vinci (da Vinci, 1493–1494; Pedretti, 1979) was the first to note that longer wires are weaker than shorter ones. This is explained by the weakest link theory (WLT) (Pierce, 1926), which states that a chain (length l_n) of n elements survives the remote applied stress σ^∞ only if each of its elements (length $l_0 = l_n/n$) survives the applied stress. This can be mathematically represented by:

$$\begin{aligned} F_n(\sigma^\infty) = 1 - [1 - F_0(\sigma^\infty)]^n \Leftrightarrow S_n(\sigma^\infty) = [S_0(\sigma^\infty)]^n \Rightarrow \\ \ln[S_n(\sigma^\infty)] = \frac{l_n}{l_0} \cdot \ln[S_0(\sigma^\infty)], \end{aligned} \tag{8.1}$$

where $F_0(\sigma^\infty)$ and $F_n(\sigma^\infty)$ are the failure probability or strength cumulative distribution functions (CDFs) of the elements and of the chain, respectively, and $S(\sigma^\infty) = 1 - F(\sigma^\infty)$ is the survival probability or complementary-CDF (cCDF).

The Weibull distribution (Weibull, 1951) is one of the few statistical distributions that verifies Equation (8.1) and has been widely used to represent the strength of brittle materials. The Weibull distribution ($F_0^{\mathrm{f}}(\sigma^\infty)$ in Equation 8.2) is characterised by a shape parameter (or Weibull modulus) m and a scale parameter σ_0^{f} measured at the length l_0. This can be scaled to a different length according to the WLT (Equation 8.1), hence:

$$\begin{aligned} F_0^{\mathrm{f}}(\sigma^\infty) = 1 - \exp\left[-\left(\frac{\sigma^\infty}{\sigma_0^{\mathrm{f}}}\right)^m\right] \Rightarrow F_n^{\mathrm{f}}(\sigma^\infty) = 1 - \exp\left[-\frac{l_n}{l_0} \cdot \left(\frac{\sigma^\infty}{\sigma_0^{\mathrm{f}}}\right)^m\right] \\ = 1 - \exp\left[-\left(\frac{\sigma^\infty}{\sigma_n^{\mathrm{f}}}\right)^m\right], \end{aligned} \tag{8.2}$$

where $\sigma_n^{\mathrm{f}} = \sigma_0^{\mathrm{f}} \cdot (l_n/l_0)^{-1/m}$.

As shown by Equation (8.2), the WLT applied to Weibull distributions predicts that (see Figure 8.1):

- **(i)** fibre strength distributions fit a straight line with slope equal to m in a Weibull plot (with horizontal axis $\ln(\sigma^\infty)$, and the vertical axis $\ln[-\ln(1 - F(\sigma^\infty))]$);
- **(ii)** all strength distributions for a given fibre type have the same shape parameter (m) irrespective of the gauge length;
- **(iii)** the average stresses measured at different fibre lengths fit a straight line with slope m in a log–log plot.

The agreement between these expected trends and experimental data (obtained with single-fibre tensile tests at different gauge lengths) has been judged positively by most researchers, and Equation (8.2) is widely used to model size effects in the strength of technical fibres.

However, some authors claim that the true strength distribution of individual fibres is not fully captured by a simple Weibull distribution. For instance, Figure 8.1 (Pickering and Murray, 1999) shows that fibre strength distributions may present a concave-down

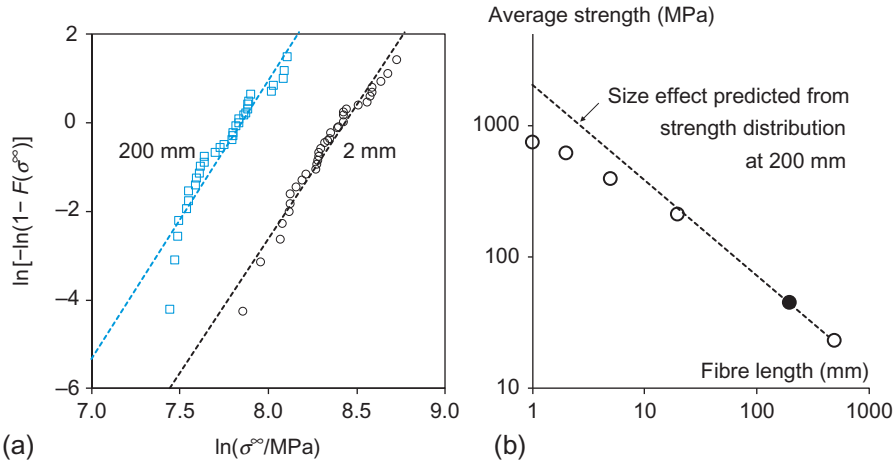

Figure 8.1 Single-fibre strength distributions (Pickering and Murray, 1999). Datapoints were obtained with a plot digitizer. (a) Fibre strength distributions at different gauge lengths in Weibull plots. (b) Average fibre strength vs. gauge length in a log–log plot.

curvature in a Weibull plot, and that the length dependence of the average strength becomes less pronounced for shorter fibres. This is commonly attributed to the presence of two independent populations of defects in the fibres (Watanabe et al., 2014), one operating at longer gauge lengths and characterised by large variability (with parameters m_1 and σ_1^{f}), and another operating at shorter gauge lengths and associated with smaller strength variability (with parameters $m_2 > m_1$ and σ_2^{f}); this would lead to a bi-modal Weibull strength distribution defined as

$$F_n(\sigma^{\infty}) = 1 - \exp\left[-\frac{l_n}{l_0}\cdot\left(\frac{\sigma^{\infty}}{\sigma_1^{\mathrm{f}}}\right)^{m_1} - \frac{l_n}{l_0}\cdot\left(\frac{\sigma^{\infty}}{\sigma_2^{\mathrm{f}}}\right)^{m_2}\right]. \tag{8.3}$$

Alternatively, other researchers have proposed using a power-law accelerated Weibull model (Padgett et al., 1995) or the Weibull of Weibulls model (Curtin, 2000), although there is no solid physical foundation associated with these types of distribution.

Although the bi-modal Weibull distribution suggested in Equation (8.3) can explain the deviations of experimental data from the expected Weibull behaviour, several researchers have shown that testing artefacts can also account for this mismatch. Stoner et al. (1994) proposed that stress concentrations at the grips could lead to premature failure of shorter fibres, thus justifying the reduction of size effects for reducing gauge lengths (Figure 8.1b). Moreover, Thomason (2013) showed that biased sampling – in which fibres below a strength threshold do not survive sample preparation – can generate concave-down fibre strength distributions (as seen in Figure 8.1a), especially at large gauge lengths.

Altogether, whether the intrinsic strength of individual fibres follows a Weibull distribution and the WLT remains an open question in the literature. In the absence of clear evidence supporting more complex strength distributions, most models consider the classical approach as defined in Equation (8.2).

8.2.2 Size effects on the tensile strength of composites

Size effects influence not only the strength of individual fibres, but also the longitudinal tensile strength and failure process of composite specimens and structures (Wisnom, 1999; Bazant, 1999). Most authors agree that the statistics of fibre strength are essential for establishing the relationship between composite longitudinal tensile strength and size; in addition, other sources of size effects (e.g. energetic, Bazant et al., 1996; fractal, Carpinteri, 1994; change in failure modes, Hallett et al., 2009; and manufacturing or testing artefacts, Wisnom, 1999) are often considered as well. Size effects pose a challenge for the design of large composite structures based on experimental data measured in small coupons, and predictive models are therefore of upmost importance. This section reviews the experimental evidence of size effects in longitudinal tensile failure of composites, briefly addressing the potential sources identified above.

The longitudinal tensile failure of FRPs is governed by fibre failure. Consequently, a larger composite structure – with more and/or longer fibres than a smaller one – will be more likely to have a severe defect, which will cause a reduction in composite strength with size. Figure 8.2 shows two examples of size effect on the longitudinal tensile failure of UD carbon-epoxy specimens (Okabe and Takeda, 2002; Wisnom et al., 2008). Models to predict or simulate these size effects will be presented in Section 8.3.

Deterministic size effects can also be present in composites, for instance, due to the finite size of the damage process zone. Bazant has shown that final failure of a composite structure is governed by the composite's strength for small-scale components, and by the composite's fracture toughness for large-scale components (Bazant et al.,

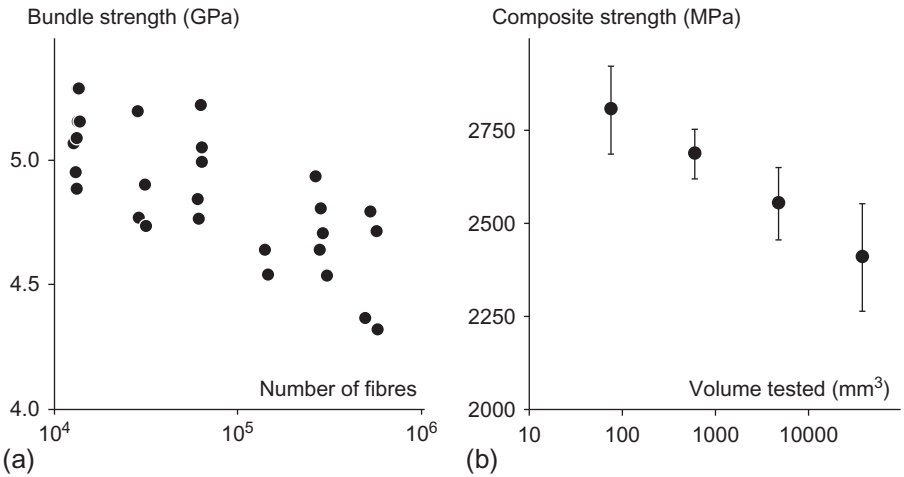

Figure 8.2 Size effects in the longitudinal tensile strength of UD carbon-epoxy composites. (a) Size effect in the strength of composite bundles of constant length but different filament counts (Okabe and Takeda, 2002). (b) Size effect in the strength of scaled UD composites measured in tapered specimens especially designed to fail in the gauge section and avoid gripping effects (Wisnom et al., 2008).

1996). Deterministic size effects associated with the translaminar fracture toughness of UD composites will be addressed in detail in Section 8.4.

Delamination between composite plies of different orientations is extremely common in composites, and it is strongly promoted by layups with thick plies (Hallett et al., 2009; Sihn et al., 2007). This size effect can be directly explained by linear-elastic fracture mechanics and is therefore fully deterministic. Although delamination is not directly related to fibre failure, it may significantly affect stress concentrations in the fibre-dominated plies, leading to changes in the strength and even in the failure mode of the composite structure (Hallett et al., 2009). This will be further explored in Section 8.3.

Although most researchers agree that size effects in composites are due to the intrinsic properties and failure mechanisms of the material, it has also been highlighted that manufacturing and testing artefacts may influence the results and interfere with measured size effects (Wisnom, 1999). For instance, thick composites typically present larger waviness and higher void content than thin laminates, which could lead to a reduction of strength in the former; in addition, thick composites require higher loads to be transferred at the gripping region, which makes them more prone to failure at the grips. These problems could contribute to a further reduction of the tensile strength in thicker laminates even in the absence of stochastic or deterministic size effects, thus leading to their overestimation.

8.2.3 The role of the matrix on tensile failure in UD composites

Although the longitudinal tensile response of UD composites is governed by the properties of the fibres, there is some evidence that the matrix also plays an important role. Figure 8.3 shows the influence of two different matrices on the tensile properties of composites with the same fibre type (Baron et al., 1987). It is clearly shown that the composites manufactured with the stronger and more ductile matrix led to stronger composites, with an increase of over 10% in the composite failure strain.

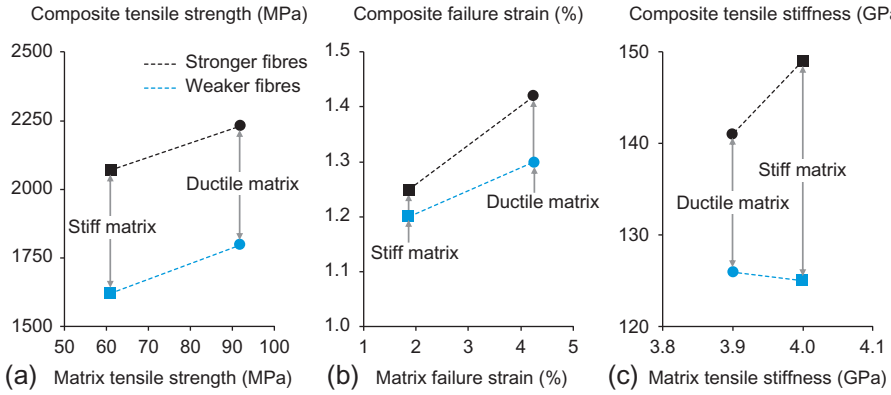

Figure 8.3 Influence of different matrix properties on the longitudinal tensile properties of carbon-epoxy UD composite (Baron et al., 1987). (a) Tensile strength. (b) Tensile failure strain. (c) Tensile stiffness.

Similar studies – with UD composite specimens made of the same fibre type and different matrices, manufactured and tested exactly in the same conditions – are surprisingly scarce in the literature, which makes it difficult to understand which matrix properties (such as stiffness, strength or failure strain) are the main contributors to the longitudinal tensile strength of the composite. Nevertheless, several micromechanical models (Swolfs et al., 2013; Pimenta and Pinho, 2013; Thionnet et al., 2014) suggest that stronger and/or stiffer matrices lead to a more effective recovery of remote stresses along the axis of a broken fibre, and also shield its neighbours from stress concentrations at intermediate distances (see Section 8.3); both effects contribute positively to delay final failure of the UD composite, which supports the experimental data presented in Figure 8.3.

8.2.4 Micromechanical features of longitudinal tensile failure in UD composites

At a macroscopic level, the tensile failure of UD composites appears to occur in a fully brittle manner, with no previous warning and no signs of damage accumulation in the overall stress–strain curve of the composite. However, detailed experiments (Scott et al., 2011; Aroush et al., 2006) demonstrate that a UD composite may sustain a significant amount of microscopic damage under tension before failing catastrophically.

Recent improvements in the resolution of synchrotron-computed tomography now allow for individual fibre breaks to be tracked *in situ* during tensile loading. Scott et al. have analysed the kinetics of fibre breakage in carbon-epoxy composites (Scott et al., 2011), and reported that fibre breaks start forming at low applied stresses in seemingly random locations. However, as the remote stress approached the strength of the material, clusters of broken fibres started forming and growing, until the largest cluster reached a critical size that triggered catastrophic failure of the entire specimen (Figure 8.4).

Similar techniques applied to quartz-epoxy UD composites have revealed similar kinetics of fibre breakage and clustering (Aroush et al., 2006). The experimental observations of Aroush et al. and Scott et al. suggest that the critical broken cluster in a UD composite under longitudinal tension can contain approximately 16–32 broken fibres. Once such a large failed cluster is formed, the high-stress concentrations generated overcome the damage tolerance provided by the variability in fibre strength, therefore precipitating final failure.

The variability of fibre strength in composites also leads to the formation of fibre and bundle pullouts in fracture surfaces (Figures 8.5 and 8.6). Laffan et al. (2010) demonstrated that the translaminar fracture surfaces of the 0° layers in cross-ply laminates increases as the ply becomes thicker, due to the formation of larger pullout features as shown in Figure 8.5. Pimenta et al. (2010) suggested that the translaminar fracture surfaces of composites present pulled-out individual fibres and bundles in a statistically self-similar fashion (Figure 8.6).

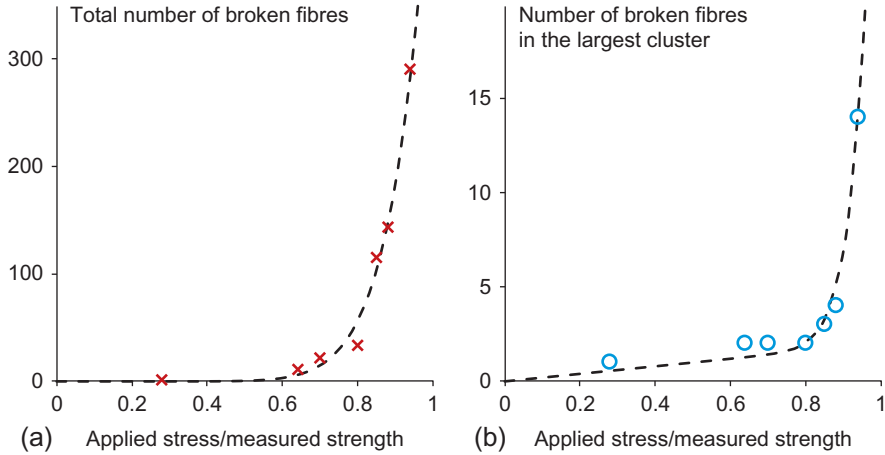

Figure 8.4 Accumulation of fibre damage in UD composites (Scott et al., 2011). (a) Accumulation of fibre breaks with increasing applied stress. (b) Progressive growth of the largest cluster of broken fibres with increasing applied stress.

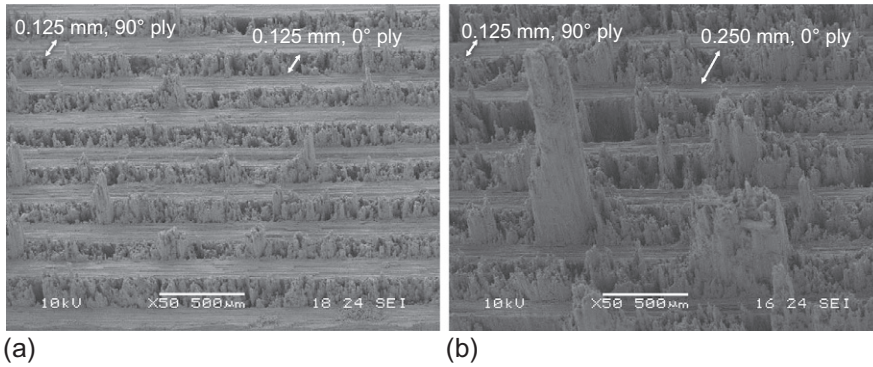

Figure 8.5 Size effects of translaminar fracture of UD carbon–epoxy plies (Laffan et al., 2010; Pimenta and Pinho, 2014). (a) Fracture surface with 0.125 mm thick layers and a fracture toughness of 65 kJ/m^2. (b) Fracture surface with 0.250 mm thick layers and a fracture toughness of 132 kJ/m^2.

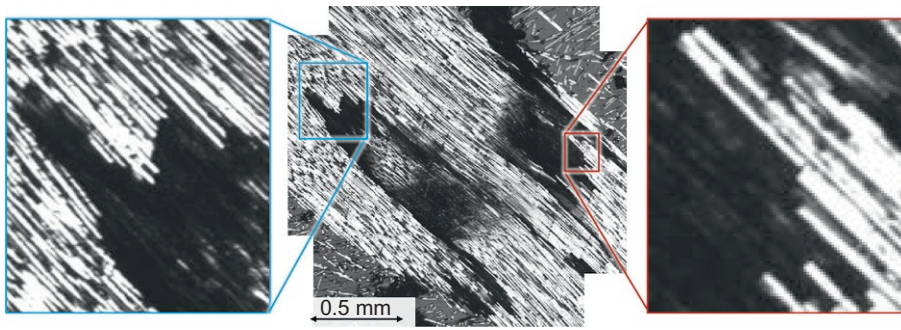

Figure 8.6 Self-similar pullout features formed during tensile failure of fibre bundles (Pimenta et al., 2010).

8.3 Modelling the longitudinal tensile strength of UD composites

8.3.1 Deterministic rule of mixtures

The simplest model for predicting the tensile strength of UD composites makes use of the rule of mixtures. For the typical technical fibres (e.g. glass or carbon) and polymers (e.g. epoxy) used in high-performance FRPs, the failure strain of the fibres (e^{f}) is lower than that of the matrix (e^{m}), and under remote tension the fibres will fail first. For composites with high fibre volume fractions (V^{f}), the matrix is unable to withstand the remote stresses once the fibres fail, and therefore the failure strain of the composite (e^{C}) will be dictated by the failure strain of the fibres (Aveston et al., 1971). The tensile strength of the composite (X^{C}) can therefore be calculated as

$$e^{\mathrm{C}} = e^{\mathrm{f}} \Rightarrow X^{\mathrm{C}} = V^{\mathrm{f}} \cdot X^{\mathrm{f}} + \left(1 - V^{\mathrm{f}}\right) \cdot \sigma^{\mathrm{m}}\left(e^{\mathrm{C}}\right) \approx V^{\mathrm{f}} \cdot X^{\mathrm{f}}\,, \tag{8.4}$$

where E^{f} and X^{f} are, respectively, the fibre stiffness and strength, $\sigma^{\mathrm{m}}(e^{\mathrm{C}})$ is the stress in the matrix at the fibre failure strain ($\sigma^{\mathrm{m}}(e^{\mathrm{C}}) = E^{\mathrm{m}} \cdot X^{\mathrm{f}}/E^{\mathrm{f}}$ for a linear-elastic matrix), and X^{C} is the strength of the composite; the final approximation is valid if $\sigma^{\mathrm{m}}(e^{\mathrm{C}}) \ll X^{\mathrm{f}}$.

Although widely used for rough estimations of the tensile strength of composites, Equation (8.4) raises two main problems: first, the tensile strength of most technical fibres is stochastic (see Section 8.2.1) and has a significant length dependence, which makes it difficult to select the input X^{f}; second, Equation (8.4) predicts a negligible effect of the matrix on the tensile strength of the composite, as there is experimental evidence suggesting otherwise (see Section 8.2.3). More refined models are therefore required, and the remaining part of this section will focus on classical models (Section 8.3.2) and current trends (Sections 8.3.3 and 8.3.4) for modelling tensile failure of UD composites, taking into account the stochastic nature of fibre strength, the influence of the matrix and size effects.

8.3.2 Classical fibre-bundle models

Fibre bundle models (FBMs, Figure 8.7) comprise the classical approach to predict longitudinal tensile failure in UD composites. FBMs consider a parallel array of fibres with stochastic strength, loaded remotely under tension (bundle stress σ^{∞} and strain ε^{∞}); once the weakest fibre fails, this generates a stress concentration in the neighbouring fibres, potentially leading to their failure. Remote tensile stresses or strains are progressively increased until all fibres are broken, or until the composite cannot withstand further load increments.

This section focuses on classical analytical approaches to FBMs, in which probability distributions and average outcomes are calculated analytically rather than through Monte Carlo simulations (the latter will be the topic of Section 8.3.3). FBMs have been developed for dry (with no matrix) and for composite bundles; in the latter,

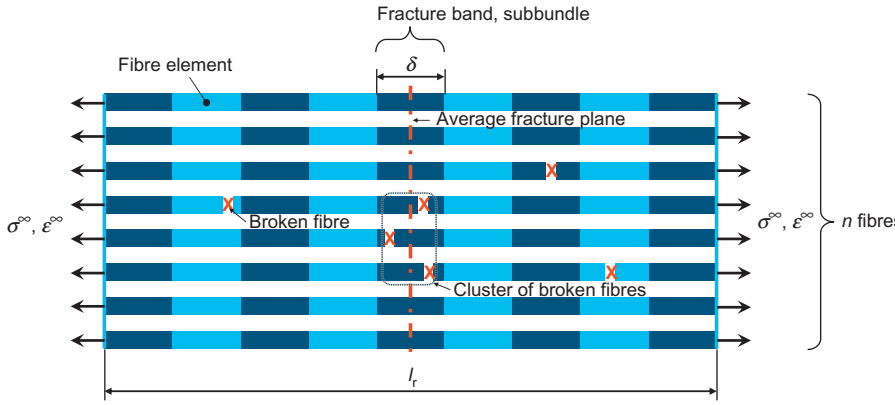

Figure 8.7 Diagram of a typical fibre-bundle model (Rosen, 1964; Curtin, 1991).

the matrix influences the *ineffective length* (defined as the distance from a fibre break at which remote stresses are recovered) and the development of stress concentrations in fibres neighbouring a break. Depending on the load sharing in the neighbourhood of a fibre break, models are qualified as global (or equal) load sharing (GLS or ELS, where all nonbroken fibres see the same stress concentration) or local load sharing (LLS, where the closest neighbours to the broken fibre undergo higher stress concentrations than the more distant ones).

8.3.2.1 Global load-sharing models

Daniels (1945) developed the first FBM by considering a dry bundle of length l_r under GLS. The expected tensile constitutive law (expressed as remote bundle stresses, σ^∞, vs. remote applied strain, ε^∞) of a bundle with an asymptotically large number of fibres is predicted as

$$\sigma^\infty(\varepsilon^\infty) = \left[E^f \cdot \varepsilon^\infty\right] \cdot \left[S_r^f\left(E^f \cdot \varepsilon^\infty\right)\right], \tag{8.5}$$

where the first term ($E^f \cdot \varepsilon^\infty = \sigma^f$) represents the tensile stress seen by the surviving fibres, and $S_r^f(\sigma^f)$ is the fibre survival probability under the remote stresses σ^f measured at length l_r (see Section 8.2.1 and Equations 8.1 and 8.2).

Daniels then showed that the strength of a large bundle will follow a normal distribution with expected value $E[X_r^b]$ and standard deviation SDev$[X_r^b]$ defined as

$$E\left[X_r^b\right] = \sigma_{crit}^f \cdot S_r^f\left(\sigma_{crit}^f\right) \quad \text{and} \quad \text{SDev}\left[X_r^b\right] = \sigma_{crit}^f \cdot \sqrt{\frac{F_r^f\left(\sigma_{crit}^f\right) \cdot S_r^f\left(\sigma_{crit}^f\right)}{n}}, \tag{8.6}$$

where σ_{crit}^f is the fibre stress that maximises the bundle stress in Equation (8.5), and $F_r^f(\sigma^\infty) = 1 - S_r^f(\sigma^\infty)$ is the fibre strength distribution. If the strength of the fibres

follows a Weibull distribution (with parameters m and σ_0^{f}measured at length l_0, see Equation 8.2), then the expected value for the strength of a large bundle becomes:

$$X_{\mathrm{r}}^{\mathrm{b}} = \frac{\sigma_{\mathrm{r}}^{\mathrm{f}}}{m^{1/m} \cdot \exp(1/m)}, \quad \text{where} \quad \sigma_{\mathrm{r}}^{\mathrm{f}} = \sigma_0^{\mathrm{f}} \cdot \left(\frac{l_{\mathrm{r}}}{l_0}\right)^{-1/m}. \tag{8.7}$$

Daniels's model considers dry bundles and is therefore rarely used for predicting the tensile strength of FRPs. Nevertheless, this model lays the foundation for most of the subsequently developed FBMs.

Rosen (1964) improved Daniel's model by considering the presence of the matrix through a shear-lag model (Figure 8.8): near a fibre break, the matrix would transfer shear stresses to the broken fibre, which would therefore recover tensile stresses along the longitudinal direction. Assuming a linear-elastic (with shear modulus G^{m}) matrix, Rosen defined the ineffective length δ as the distance from the break where the fibre had recovered a large percentage ξ (e.g. 90%) of the remote stress σ^{∞}:

$$\delta = \frac{\phi^{\mathrm{f}}}{2} \cdot \sqrt{\frac{1-\sqrt{V^{\mathrm{f}}}}{\sqrt{V^{\mathrm{f}}}} \cdot \frac{E^{\mathrm{f}}}{G^{\mathrm{m}}}} \cdot \ln\left[\frac{1}{1-\xi}\right], \quad \text{where } \phi^{\mathrm{f}} \text{ is the fibre diameter.} \tag{8.8}$$

Rosen then assumed that a composite bundle of length l_{r} is equivalent to a chain of l_{r}/δ subbundles with length δ (Figure 8.7), and will therefore fail once all fibres break within a subbundle. The strength of a subbundle (of length δ) with n fibres is given by Daniels's analysis, and therefore follows a normal distribution $F_{\delta}^{\mathrm{b}}(\sigma^{\infty})$ with parameters $E[X_{\delta}^{b}]$ and $\mathrm{SDev}[X_{\delta}^{\mathrm{b}}]$ (see Equation 8.6). The strength distribution of a bundle of length l_{r} – defined by $F_{\mathrm{r}}^{\mathrm{b}}(\sigma^{\infty})$ and $f_{\mathrm{r}}^{\mathrm{b}}(\sigma^{\infty}) = \mathrm{d}F_{\mathrm{r}}^{\mathrm{b}}(\sigma^{\infty})/\mathrm{d}\sigma^{\infty}$ – can be calculated according to the WLT (Equation 8.1) as

$$F_{\mathrm{r}}^{\mathrm{b}}(\sigma^{\infty}) = 1 - \left[1 - F_{\delta}^{\mathrm{b}}(\sigma^{\infty})\right]^{l_{\mathrm{r}}/\delta} \Rightarrow f_{\mathrm{r}}^{\mathrm{b}}(\sigma^{\infty}) = \frac{l_{\mathrm{r}}}{\delta} \cdot f_{\delta}^{\mathrm{b}}(\sigma^{\infty}) \cdot \left[1 - F_{\delta}^{\mathrm{b}}(\sigma^{\infty})\right]^{(l_{\mathrm{r}}/\delta)-1}. \tag{8.9}$$

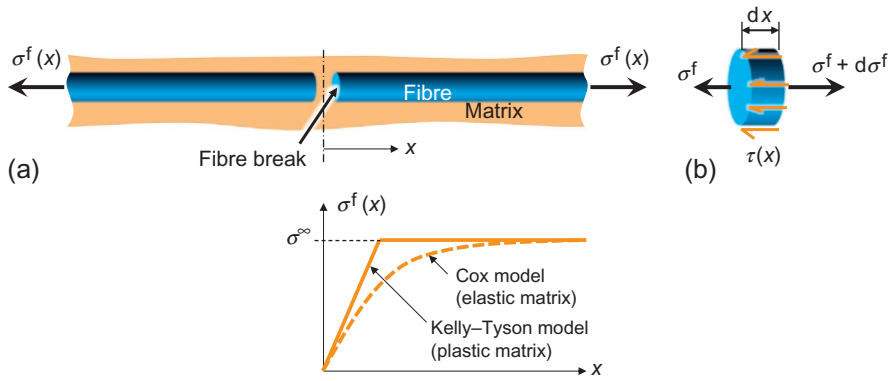

Figure 8.8 Representation of the shear-lag model. (a) Stress transfer near a fibre break. (b) Equilibrium of fibre element.

Finally, the most likely bundle strength X_r^b is calculated by imposing $df_r^b\left(X_r^b\right)/dX_r^b = 0$ in Equation (8.9). For the particular case of a bundle with $n \to \infty$ (and $\mathrm{SDev}\left[X_r^b\right] \to 0$) and Weibull fibre strength distribution (where the scale parameter σ_0^f was determined at the length l_0, see Equation 8.2), the most likely strength of the bundle becomes:

$$X_r^b = \frac{\sigma_\delta^f}{m^{1/m} \cdot \exp(1/m)}, \quad \text{where} \quad \sigma_\delta^f = \sigma_0^f \cdot \left(\frac{\delta}{l_0}\right)^{-1/m}. \tag{8.10}$$

Equations (8.7) and (8.10) are formally identical, apart from the length correction in the Weibull scale parameter. Rosen's model is therefore equivalent to Daniels's, except for considering the ineffective length of the composite rather than the full length of the bundle. Also and although Rosen's full model (Equation 8.9) takes into account the stochastic variation of bundle strengths and can therefore represent size effects, the simplified equation does not; Equation (8.10) represents a deterministic model based on the average of stochastic fibre strength distributions, hence captures no size effects.

Curtin (1991) developed a GLS model primarily aimed at ceramic–matrix composites, which defines a fracture band (of length δ) centred at the average fracture plane of the bundle (Figure 8.7). For a given remote stress σ^∞, a fraction χ of the fibres in the fracture band is broken, with each break located at a random distance l_{po} from the average fracture plane. Fibre stresses are recovered linearly from the break, according to shear lag with constant shear stresses τ_{SL} (Figure 8.8); Kelly–Tyson's model (Kelly and Tyson, 1965) is then used to define the length of the fracture band δ (i.e. the length required to recover the undisturbed fibre stress σ^f) and the stress of a broken fibre at the average fracture plane σ_{po} as

$$\delta = \frac{\sigma^f \cdot \phi^f}{2 \cdot \tau_{SL}} \quad \text{and} \quad \sigma_{po} = \frac{4 \cdot l_{po} \cdot \tau_{SL}}{\phi^f} \Rightarrow \frac{\sigma_{po}}{\sigma^f} = \frac{2 \cdot l_{po}}{\delta}. \tag{8.11}$$

Assuming a random location of fibre breaks, the average pullout length within the fracture band will be $\overline{l_{po}} = \delta/4$; consequently, $\overline{\sigma_{po}} = \sigma^f/2$. Imposing equilibrium between the remote stress σ^∞ and the stresses at the fracture surface (with contribution from both surviving and failed fibres),

$$\sigma^\infty = (1-\chi) \cdot \sigma^f + \chi \cdot \frac{\overline{\sigma_{po}}}{2} \Rightarrow \sigma^\infty = (1 - \chi/2) \cdot \sigma^f. \tag{8.12}$$

Curtin then assumes that fibre breakage is limited; the fraction of broken fibres χ can then be approximated by the Weibull stress ratio scaled to the length δ (as in Equation 8.2):

$$\chi = \frac{\delta}{l_0} \cdot \left(\frac{\sigma^f}{\sigma_0^f}\right)^m \Rightarrow \chi = \left(\frac{\sigma^f}{\sigma_\delta^f}\right)^{m+1} \text{where } \sigma_\delta^f = \left[\frac{2 \cdot \left(\sigma_0^f\right)^m \cdot \tau_{SL} \cdot l_0}{\phi^f}\right]^{1/(m+1)}, \tag{8.13}$$

The parameter $\sigma_{\delta}^{\mathrm{f}}$ defines the characteristic strength of the material. The overall composite strength is calculated by finding the maximum of $\sigma^{\infty}\left(\sigma^{\mathrm{f}}\right)$ in Equation (8.12) after replacing χ, i.e.:

$$X_{\mathrm{r}}^{\mathrm{b}} = \sigma^{\infty}\left(\sigma_{\mathrm{crit}}^{\mathrm{f}}\right) \text{ with } \frac{\mathrm{d}\sigma^{\infty}}{\mathrm{d}\sigma_{\mathrm{crit}}^{\mathrm{f}}}\left(\sigma_{\mathrm{crit}}^{\mathrm{f}}\right) = 0 \Rightarrow X_{\mathrm{r}}^{\mathrm{b}} = \sigma_{\delta}^{\mathrm{f}} \cdot \frac{m+1}{m+2} \cdot \left(\frac{2}{m+2}\right)^{1/(m+1)}. \tag{8.14}$$

Curtin's model differs conceptually from Rosen's in two main aspects: (i) it accounts for the stress contribution of fibres broken before final failure ($\overline{\sigma_{\mathrm{po}}}$), and (ii) it considers a characteristic length δ which increases with the applied stress level. However, both models consider a GLS scheme, which is a limitation that several other researchers tried to overcome.

8.3.2.2 Local load-sharing models

Hedgepeth (1961) first analysed the problem of local stress concentrations using shear lag of stiff layers in a linear-elastic matrix, and calculated the stress concentration factor in a fibre neighbouring a cluster of b broken fibres as

$$k_b = \frac{4 \cdot 6 \cdot 8 \cdot \ldots \cdot (2b+2)}{3 \cdot 5 \cdot 7 \cdot \ldots \cdot (2b+1)}. \tag{8.15}$$

This problem was revisited by a large number of researchers using different techniques (e.g. shear lag, Landis and McMeeking, 1999; de Morais, 2001; Beyerlein and Phoenix, 1996; finite elements, Swolfs et al., 2013; Nedele and Wisnom, 1994; Accorsi et al., 1996; variational mechanics, Nairn, 1992; fracture mechanics, Beyerlein et al., 1996). However, there is still no universally accepted LLS model, and many effects – e.g. interaction between fibre breaks, dynamic effects, nonlinearity of the matrix and fibre–matrix interface, fibre packing – are still being investigated (this is further discussed in Section 8.3.3). Also, combining the complexity of fibre strength distributions and detailed stress fields is impractical; consequently, most analytical LLS models adopt very simplified formulations for the latter.

Harlow and Phoenix (1978a,b) developed one of the most influential LLS fibre-bundle analyses in the literature. They considered a bundle of n fibres (with Weibull strength distribution $F^{\mathrm{f}}(\sigma^{\infty})$) of length δ, in which a cluster of b broken fibres would generate stress concentrations $k_{\mathrm{b}} = 1 + b/2$ in the immediate surviving neighbours (fibres were arranged in a ring to eliminate boundary effects). Bundle failure probabilities ($F^{[n]}(\sigma^{\infty})$) were derived considering all possible different sequences of fibre break events leading to overall bundle failure; because the number of possible failure sequences was 2^n, calculations were made only for $n \leq 9$. The main conclusions from this study were:

- At high loads, $F^{[n]}(\sigma^{\infty}) \to 1 - \left[1 - F^{\mathrm{f}}(\sigma^{\infty})\right]^n$ (i.e. the right tail asymptote of bundle strength follows the WLT and leads to a Weibull distribution with same shape parameter as that of the individual fibres);

- At low loads (at the left tail asymptote), $F^{[n]}(\sigma^{\infty})$ tends to a Weibull distribution with a shape parameter $n \cdot m$, thus with reducing variability;
- As n increases, the asymptotic Weibull behaviours just mentioned start governing the strength distributions for more extreme probabilities (especially extreme for the LTA);
- The magnitude of size effects (i.e. decreasing strength with increasing bundle length or cross section) becomes less pronounced as n increases;
- Within reasonable probabilities (e.g. $1\% \leq F^{[n]}(\sigma^{\infty}) \leq 99\%$), the strength distribution of large bundles resembles a Weibull distribution (i.e. it is linear on a Weibull plot);
- There is a function $F^{\mathrm{WLT}}(\sigma^{\infty})$ such that:

$$F^{\mathrm{WLT}}(\sigma^{\infty}) \stackrel{\mathrm{def}}{=} \lim_{n\to\infty}\left(1-\left[1-F^{[n]}(\sigma^{\infty})\right]^{1/n}\right) \quad \text{and}$$
$$F^{[n]}(\sigma^{\infty}) \approx 1-\left[1-F^{\mathrm{WLT}}(\sigma^{\infty})\right]^{n}, \quad \forall n \geq n^{\mathrm{WLT}}. \tag{8.16}$$

Following its definition in Equation (8.16), $F^{\mathrm{WLT}}(\sigma^{\infty})$ is the equivalent single-fibre strength distribution calculated through the WLT based on the strength distribution of a bundle with an asymptotically large number of fibres. Harlow and Phoenix used this definition to plot equivalent single-fibre strength distributions based on bundles with a finite number of fibres, and verified that the equivalent distributions actually converged for $n \geq 7$ (which defines n^{WLT} in Equation 8.16). Consequently, once the converged characteristic function $F^{\mathrm{WLT}}(\sigma^{\infty})$ is calculated, it is possible to estimate the strength distribution of any large bundle (with $n \geq n^{\mathrm{WLT}}$) using the WLT (Equation 8.16).

Despite extensive further developments since 1978, Harlow and Phoenix's conclusions are remarkably accurate, as shown by recent experimental investigations (Scott et al., 2011; Aroush et al., 2006) on the kinetics of fibre breakage in UD composites (see Section 8.2.4). These conclusions are also supported by much more sophisticated and computationally expensive models, which will be described in the next section.

8.3.3 Monte Carlo simulations of micromechanical models

Most of the recent efforts in modelling the tensile failure process of UD composites employ Monte Carlo simulations of micromechanical models. These models represent explicitly a large number of fibres (each fibre split into elements with a realisation of the stochastic fibre strength), and simulate the accumulation of fibre breaks and stress redistribution with progressive loading; this analysis is repeated a large number of times with a new realisation of fibre strengths (usually derived from a Weibull distribution scaled to the element's length through the WLT, Equation 8.2), until there is a sufficient number of results to characterise the response of the material.

The main challenges of Monte Carlo simulations are (i) calculating stress fields in the neighbourhood of fibre breaks, and (ii) performing a Monte Carlo progressive failure analysis for the accumulation of fibre breaks. The methods proposed in the literature can be broadly classified into three categories:

- *Single-step spring-based models*, which address both challenges above by stochastic modelling of fibres and matrix under simplified shear-lag assumptions (see Section 8.3.3.1);

- *Combined field-superposition and fibre-bundle simulations,* which calculate deterministic stress fields near single fibre breaks at a first stage, and then use a superposition method to include those fields in Monte Carlo simulations of fibre bundles (see Section 8.3.3.2);
- *Two-scales finite element (FE) models*, which use FE to calculate the deterministic response of unit cells (UCs) with different numbers of fibre breaks, and then use those responses in Monte Carlo FE simulations of UD composites (see Section 8.3.3.3).

8.3.3.1 Single-step spring-based models

Single-step spring-based models (Zhou and Curtin, 1995; Okabe and Takeda, 2001; Okabe et al., 2005) represent a lattice of nodes (with degrees of freedom restricted to longitudinal displacements) connected longitudinally by fibre springs with stochastic strengths, and transversely by matrix shear springs. This method combines the presence of the matrix with stochastic fibre strengths, thus allowing for calculating stress fields and analysing progressive failure in a single model.

One of the most sophisticated models in recent literature is Okabe et al.'s (Okabe and Takeda, 2001; Okabe et al., 2005) spring element model (SEM, Figure 8.9). The SEM considers a hexagonal lattice of nodes with longitudinal displacements **u**, connected by N^{f} longitudinal fibre springs (of length l and modulus E^{f}), associated with a random strength X_l^{f} and with a linear-elastic stiffness matrix $\mathbf{K}^{\mathrm{f}}$ (calculated as a function of A^{f}, E^{f} and l). The N^{m} transverse shear matrix springs are also linear-elastic, with stiffness matrix $\mathbf{K}^{\mathrm{m}}$ calculated as a function of C^{f}, l, G^{m} and t^{m} (matrix thickness).

Under remote applied strain ε^{∞}, a fibre element fails once its tensile stress reaches the strength. In a broken fibre, longitudinal stresses are recovered by shear lag within a length x_{SL}. Assuming a perfectly plastic matrix with strength τ_{SL}, the stress $\sigma_{\mathrm{SL}}(x)$ in an element at a distance $x \le x_{\mathrm{SL}}$ from the break is

$$\sigma_{\mathrm{SL}}^{\mathrm{f}}(x) = \frac{4 \cdot \tau_{\mathrm{SL}} \cdot x}{\phi^{\mathrm{f}}} \text{ with } x \le x_{\mathrm{SL}} = \frac{E^{\mathrm{f}} \cdot \varepsilon^{\infty} \cdot \phi^{\mathrm{f}}}{4 \cdot \tau_{\mathrm{SL}}}. \tag{8.17}$$

At a given applied strain ε^{∞}, $N_{\mathrm{b}}^{\mathrm{f}}$ is the number of broken fibre elements in the model (with zero stress), and $N_{\mathrm{SL}}^{\mathrm{f}}$ is the number of fibre elements whose stress is governed by

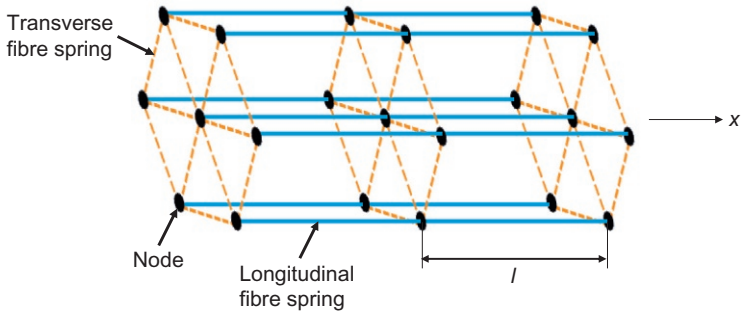

Figure 8.9 Schematics of the spring element model of Okabe and Takeda (2001).

Equation (8.17) (independent of the applied strain). The overall equilibrium of the assembled model is imposed as:

$$\left(\sum_{N^{\mathrm{f}}-N_{\mathrm{b}}^{\mathrm{f}}-N_{\mathrm{SL}}^{\mathrm{f}}}\mathbf{K}^{\mathrm{f}}+\sum_{N^{\mathrm{m}}}\mathbf{K}^{\mathrm{m}}\right)\cdot\mathbf{u}+\sum_{N_{\mathrm{SL}}}A^{\mathrm{f}}\cdot\int_{x_i}^{x_i+l}\mathbf{B}^{\mathrm{f}^{\mathrm{T}}}\cdot\sigma_{SL}(x)\,\mathrm{d}x=\mathbf{f}, \tag{8.18}$$

where $\mathbf{B}^{\mathrm{f}}$ is the deformation matrix of the fibre elements, and $\mathbf{u}$ and $\mathbf{f}$ are nodal displacements and forces (respectively). Equation (8.18) is fully linear (the second term on the left-hand side is calculated analytically using Equation 8.17), hence can be solved efficiently for incremental remote strains. At each increment, the model calculates the stresses in the fibres as $\boldsymbol{\sigma}^{\mathrm{f}}=E^{\mathrm{f}}\cdot\mathbf{B}^{\mathrm{f}}\cdot\mathbf{u}$, removes each fibre element where $\sigma^{\mathrm{f}}\geq X_l^{\mathrm{f}}$, and iterates the calculation.

The SEM has been extensively used in the literature (Okabe and Takeda, 2002; Xia et al., 2002; Okabe et al., 2006, 2010, 2014), and it has been shown to predict accurately the response of FRPs with up to a few thousand fibres.

8.3.3.2 Combined field-superposition and fibre-bundle simulations

Combined field-superposition and fibre-bundle simulations build up on classical FBMs (see Section 8.3.2), but consider more realistic – and, consequently, more complex – load-sharing rules. This requires three model components: (i) a deterministic model for stress fields in the neighbourhood of fibre breaks, (ii) a superposition model to determine how fibre breaks interact, and (iii) a Monte Carlo simulation of FBMs (as the added complexity makes purely analytical treatments impossible).

The literature on this type of simulation is extensive, and most of the earlier models (Beyerlein and Phoenix, 1996, 1997; Landis et al., 2000; Curtin and Takeda, 1998; Ibnabdeljalil and Curtin, 1997) considered analytical solutions for stress fields. More recently, Swolfs et al. (2013, 2015) used FE simulations of UD composites (with realistic fibre packings) to provide detailed stress fields to a FBM.

The FE simulations developed by Swolfs et al. model a representative volume element (RVE) with approximately 80 fibres ($V^{\mathrm{f}}=50\%$) and 0.140 mm long, considering orthotropic linear-elastic fibres and a linear-elastic or elasto-plastic matrix. Random fibre packings were assumed (hence the model was geometrically stochastic), and the central fibre was assumed to be broken at the beginning of the analysis. It was shown that, for given material properties, stress concentrations in fibres neighbouring the break depended only on their distance to the break, and were relatively insensitive to the realisation of packing geometry and to the presence of transverse matrix cracks.

Trend lines for full stress concentration profiles determined from the FE analyses were then used in a FBM (with approximately 10,000 fibres and 10 mm long, modelled with 3.6 μm long elements), considering a bi-modal Weibull fibre strength distribution and realistic (i.e. random) fibre packing. Stress concentrations near single-fibre breaks were directly taken from the FE trend lines; for multiple broken

fibres, a modified linear superposition method (which conserves equilibrium of stresses in each 3.5 μm long layer of fibre elements) was used. Following Rosen (1964)'s assumption (see Section 8.3.2.1), the bundle was assumed to fail once 10% of the fibres failed within a subbundle of length δ=35 μm.

Swolfs et al. (2015) have used this model to predict the failure strain of UD composites under longitudinal tension, as well as the formation and evolution of clusters of broken fibres. This predicted that a critical cluster (which leads to catastrophic failure of the entire bundle) contains 21–24 broken fibres, which correlates well with experimental data (see Section 8.2.4 and Figure 8.4).

8.3.3.3 Two-scales FE models

FE analyses have been extensively used to model the micromechanical response of composites under longitudinal tension (Thionnet et al., 2014; Nedele and Wisnom, 1994; González and Llorca, 2006; Mishnaevsky and Brøndsted, 2009). However, a very fine mesh is required to accurately account for stress concentrations near fibre breaks, meaning that most FE models consider very small RVEs only. Nevertheless, Blassiau et al. (2009) and Thionnet et al. (2014) recently developed a coupled *two-scales (micro–macro) FE model* to predict the longitudinal failure process in UD composites, which is able to simulate composite specimens with millions of fibres.

The microscale FE analysis is deterministic and considers a 4 mm long UC with 32 linear-elastic isotropic fibres in a square arrangement, embedded in a visco-elastic matrix. Different damage states (with 2, 4, 8, 16 or 32 co-planar fibre breaks in the UC, uniformly dispersed in the cross section) were simulated, assuming a 35 μm fibre–matrix debond at each fibre break. The microscale model generates a library with the stiffness of the UC and stress concentrations in fibres neighbouring the break for the different damage states.

The macroscale FE analysis modelled each UC with one integration point and five realisations of single-fibre strength (assumed to follow a Weibull distribution scaled to the UC length according to Equation 8.2). This, combined with the stress concentrations calculated in the microscale model, allows the number of broken fibres at each integration point to evolve from an undamaged state to sequential damage states with 2, 4, 8, 16 and 32 broken fibres. The longitudinal stiffness associated with each integration point was degraded to the corresponding value calculated by the microscale model.

Failure was assumed to occur at the onset of a numerical instability, characterised by a rapid increase in remote strain under nearly constant remote stress; the critical damage state (after which failure is catastrophic) in a UD composite corresponds to the formation of clusters with 32 broken fibres (Thionnet et al., 2014). This model has been used to predict longitudinal tensile failure in UD composites, in laminates and in pressure vessels. Also, by considering a visco-elastic matrix, the model predicts that tensile strength should increase with higher strain rates (due to stiffening of the matrix), and that failure can occur under constant remote stress (due to relaxation of the matrix and progressive damage accumulation) (Thionnet et al., 2014); these predictions are qualitatively supported by experiments.

8.3.4 Hierarchical scaling law for the strength of composite fibre bundles

A main drawback with Monte Carlo simulations of micromechanical models (Section 8.3.3) is computational efficiency, as a very fine mesh of fibre elements and a large number of simulations are required to achieve representative results. Pimenta and Pinho (2013) recently proposed a hierarchical scaling law for the strength of composite fibre bundles, which has been extensively validated against experimental results, and predicts full strength distributions of bundles with millions of fibres in less than 1 second.

The model assumes that fibre bundles are generated hierarchically (see Figure 8.10, following Newman and Gabrielov, 1991) by pairing two individual fibres (of level-[0]) into a level-[1] bundle, and then sequentially grouping two level-$[i-1]$ bundles into a level-$[i]$ bundle (which therefore contains $n^{[i]} = 2^i$ fibres).

The model considers a level-[1] bundle of length l_r (composed by two embedded level-[0] fibres) under the remote tensile stress σ^∞ (expressed as fibre stress); in the absence of any fibre break (Figure 8.11a), both fibres are loaded uniformly such that $\sigma^{\mathcal{A}}(x) = \sigma^{\mathcal{B}}(x) = \sigma^\infty$. It is then assumed that fibre $\mathcal{A}$ fails at $x = 0$ (Figure 8.11b); following a perfectly plastic shear-lag formulation for the matrix or fibre–matrix interface (with shear-lag strength τ_{SL}), fibre $\mathcal{A}$ will linearly recover the remote stress σ^∞ within the level-[0] *effective recovery length* ($l_e^{[0]}$, similar to δ in Equation 8.13). Conversely, fibre $\mathcal{B}$ experiences linear stress concentrations within the length $l_e^{[0]}$, with a maximum stress $k \cdot \sigma^\infty$ at $x = 0$ (equilibrium dictates $k = 2$).

Bundle failure requires that both fibres $\mathcal{A}$ and $\mathcal{B}$ break in nearby locations, in order to promote complete yielding of the matrix (or fibre–matrix interface) between the two fibre breaks (Figure 8.11c). Assuming that fibre $\mathcal{A}$ fails at $x = 0$, the level-[1] *control region* (subscript c, with length $l_c^{[1]} = 2 \cdot l_e^{[0]}$) defines the region within which a break in fibre $\mathcal{B}$ leads to bundle failure.

Statistically, a level-[1] bundle survives the remote stress σ^∞ in the control length $l_c^{[1]}$ in one of the following two cases:

(i) If both level-[0] fibres survive the uniform stress σ^∞. The control region is composed of four fibre elements with length $l_e^{[0]}$; consequently, taking $S_{U,e}^{[0]}$ as the element's survival probability in $l_e^{[0]}$ under constant stress, the probability of this event is $[S_{U,e}^{[0]}]^4$;

(ii) If the weakest fibre fails under σ^∞, and the strongest fibre survives the resulting stress field (i.e. half-length under uniform stresses σ^∞, and the other half-length under linear stress

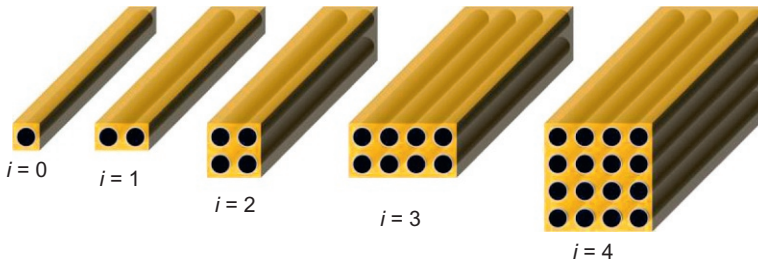

Figure 8.10 Hierarchical fibre bundles defined by Pimenta and Pinho (2013).

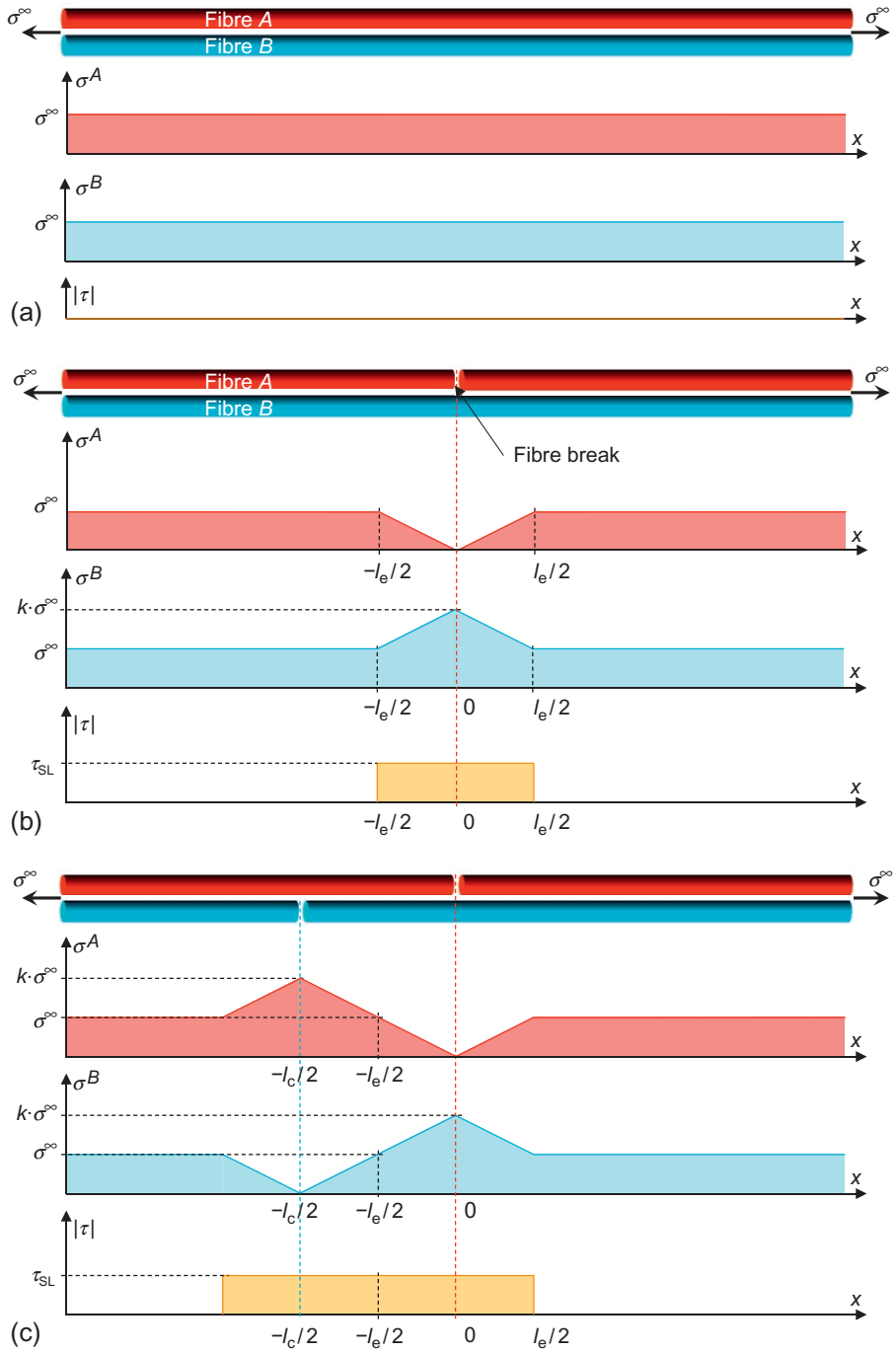

Figure 8.11 Stress fields and length scales during failure of a level-[1] fibre bundle (Pimenta and Pinho, 2013). (a) Stress fields before the first fibre failure, (b) stress fields before the first fibre failure, defining the effective recovery length $l_e^{[0]}$, and (c) definition of control distance $l_e^{[1]}$ the bundle fails only if fibre $\mathcal{B}$ breaks at a distance smaller than $l_c^{[1]}/2$ from the break in fibre $\mathcal{A}$.

concentrations). Taking $S_{\mathrm{K,e}}^{[0]}$ as the as the element's survival probability in $l_{\mathrm{e}}^{[0]}$ under linear stress concentrations, the probability of this event is $2 \cdot \left[1 - \left(S_{\mathrm{U,e}}^{[0]}\right)^2\right] \cdot S_{\mathrm{U,e}}^{[0]} \cdot S_{\mathrm{K,e}}^{[0]}$.

Assuming a self-similar hierarchical failure process as suggested by the statistically self-similar features in Figure 8.6, the statistical events just defined can be generalised for hierarchical bundles of any level. The survival distributions of a level-$[i+1]$ bundle can therefore be calculated recursively from that of level-$[i]$ bundle according to the following hierarchical scaling law:

$$S_{\mathrm{U,c}}^{[i+1]} = \left[S_{\mathrm{U,e}}^{[i]}\right]^4 + 2 \cdot \left[1 - \left(S_{\mathrm{U,e}}^{[i]}\right)^2\right] \cdot S_{\mathrm{U,e}}^{[i]} \cdot S_{\mathrm{K,e}}^{[i]}\,, \tag{8.19}$$

where

- $S_{\mathrm{U,e}}^{[i]}$ is the survival probability of a level-$[i]$ bundle under uniform stresses σ^{∞} within the effective recovery length $l_{\mathrm{e}}^{[i]}$;
- $S_{\mathrm{K,e}}^{[i]}$ is the survival probability of a level-$[i]$ bundle under linear stress concentrations (with factor k) within the effective recovery length $l_{\mathrm{e}}^{[i]}$;
- $S_{\mathrm{U,c}}^{[i+1]}$ is the survival probability of the level-$[i+1]$ bundle (with 2^{i+1} fibres) under uniform stresses σ^{∞} within the control length $l_{\mathrm{c}}^{[i+1]}$.

The distributions $S_{\mathrm{U,e}}^{[i]}$ and $S_{\mathrm{K,e}}^{[i]}$ can be analytically calculated from $S_{\mathrm{U,c}}^{[i]}$ using the extended WLT (Equation 8.1, Pimenta and Pinho, 2013) and the definitions of $l_{\mathrm{e}}^{[i]}$ and $l_{\mathrm{c}}^{[i]}$:

$$l_{\mathrm{e}}^{[i]} = 2 \cdot \frac{n^{[i]} \cdot A^{\mathrm{f}}}{C^{[i]} \cdot \tau_{\mathrm{SL}}} \cdot \sigma^{\infty} \quad \text{and} \quad l_{\mathrm{c}}^{[i]} = 2 \cdot l_{\mathrm{e}}^{[i-1]}\,, \tag{8.20}$$

where $C^{[i]}$ is the shear-lag perimeter of the level-$[i]$ bundle. Equation (8.20) predicts that the length of the damage process zone (i.e. $l_{\mathrm{c}}^{[i]}$) increases not only with applied stress σ^{∞}, but also with the size of the cluster of broken fibres; this implies that clusters of broken fibres can interact from farther away than individual fibre breaks, which are deemed to be more realistic than fixing the process zone (or ineffective) length (as in Sections 8.3.2 and 8.3.3).

Figure 8.12 shows that the hierarchical scaling law can accurately predict not only size effects on the average strength of UD composites (Figure 8.12a), but also full strength distributions for composites with different matrices (Figure 8.12b). Moreover, the model predicts that there is a critical bundle size n^{WLT} which verifies

$$S^{[n_i]}(\sigma^{\infty}) \approx \left[S^{[n^{\mathrm{WLT}}]}(\sigma^{\infty})\right]^{n_i/n^{\mathrm{WLT}}}, \quad \forall n_i \geq n^{\mathrm{WLT}}\,, \tag{8.21}$$

meaning that a bundle with a large number of fibres n^i fails as soon as the weakest bundle with n^{WLT} fibres breaks. This is analogous to Equation (8.16) proposed by Harlow and Phoenix (1978b).

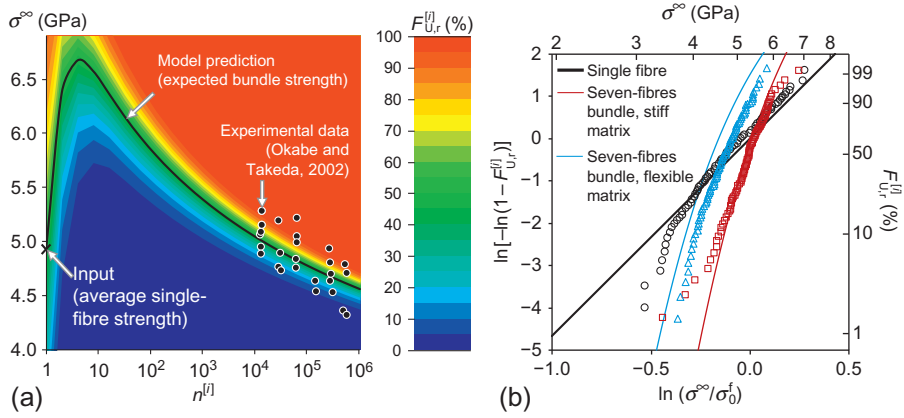

Figure 8.12 Validation of Pimenta and Pinho's hierarchical scaling law (modelling predictions represented as lines) against experimental results (represented as datapoints, from Kazanci (2004)) (Pimenta and Pinho, 2013). (a) Probability map for the strength of UD carbon-epoxy bundles of different sizes. Experiments from Okabe and Takeda (2002). (b) Full strength distributions for UD carbon-epoxy micro-bundles. Experiments from Kazanci (2004).

8.4 Predicting the fracture toughness and modelling progressive failure

8.4.1 Toughening mechanisms and analytical models

Even though most technical fibres and matrices are relatively brittle (the fracture toughness of carbon-fibres is lower than 0.010 kJ/m^2, Watanabe et al., 2014; Honjo, 2003; and most epoxy matrices present a mode I toughness bellow 1.0 kJ/m^2, Pearson and Yee, 1991; Johnsen et al., 2007), FRPs dissipate a large amount of energy during fibre-dominated tensile failure (translaminar fracture toughness above 100 kJ/m^2 are common for UD composites, Laffan et al., 2012). This toughness magnification is usually attributed to the formation of intricate 3D fracture surfaces, as shown in Figure 8.5, which promote energy dissipation by fibre–matrix debonding (or matrix mode II failure) and by pullout (Kim and Mai, 1991).

Translaminar toughening mechanisms in composites have been extensively investigated in the literature. Kim and Mai (1991)'s review of energy-dissipation mechanisms in different types of composites suggested that, for UD materials with relatively brittle fibres and matrices, debonding (subscript deb) and pullout (subscript po) are the main toughening mechanisms. The corresponding work of fracture R due to each contribution can be estimated as

$$R_{\text{deb}} = \frac{4 \cdot V^{\text{f}} \cdot \mathcal{G}_{\text{SL}} \cdot l_{\text{deb}}}{\phi^{\text{f}}} \quad \text{and} \quad R_{\text{po}} = \frac{2 \cdot V^{\text{f}} \cdot \tau_{\mu} \cdot l_{\text{po}}^2}{\phi^{\text{f}}}, \tag{8.22}$$

where $\mathcal{G}_{\text{SL}}$ is the shear-lag fracture toughness (i.e. mode II toughness of the matrix or fibre–matrix interface), τ_{μ} is the pullout frictional shear stress, and l_{deb} and l_{po} are lengths of debonding and pullout (respectively).

The physics expressed in Equation (8.22) are simplistic (it considers only the mode II component of energy release rate during fibre–matrix debonding, as well as constant interfacial friction during the pullout process), and improvements have been proposed (Gao et al., 1988; Wells and Beaumont, 1985a). Still, a main issue in using Equation (8.22) or its refinements to predict the fracture toughness of UD composites is accounting for the stochastic nature of debonding and pullout lengths, which arises directly from the statistical variability in fibre strength. Some of the FBMs mentioned in Section 8.3 have been extended to predict the translaminar fracture toughness of UD composites (Beyerlein and Phoenix, 1997; Curtin, 1993).

However, most models have not captured an important characteristic of the fracture surfaces of UD composites: the presence of bundle – in addition to fibre – pullouts. Until very recently, this feature had only been included in the multiscale analytical model proposed by Wells and Beaumont (1985a,b); it considered the contributions from debonding, elastic energy, and pullout (correcting Equation 8.22 to account for Poisson's contraction, Gao et al., 1988), both in individual fibres and in bundles with known (measured) diameter. However, Wells and Beaumont's model did not account for the continuous range of sizes of pulled-out features shown in Figure 8.5, nor predicted a size effect associated with the translaminar toughness of composites (Laffan et al., 2010).

As recently proposed by Pimenta and Pinho (2014), the nature of size effects in the fracture toughness of UD composites (Laffan et al., 2010; Figure 8.5), as well as the observation of statistically self-similar features in the fracture surfaces (Pimenta et al., 2010; Figure 8.6), suggest that the analogy between invasive fractals and the fracture surfaces of heterogeneous materials introduced by Carpinteri (1994) might be useful (this is true even if the mathematical formalisms of fractal theory, criticised by Bazant (1997), are not used). This is the foundation for the model presented in Section 8.4.2, which represents the translaminar fracture surface as a stochastic fractal and combines micromechanics, fracture mechanics and statistics to predict the fracture toughness of composites and the associated size effect.

8.4.2 Modelling the fracture toughness of stochastic quasi-fractal fracture surfaces

Pimenta and Pinho (2014)'s model for the translaminar (fibre-dominated) tensile toughness of UD composites considers debonding and pullout of individual fibres and bundles of different sizes. The pulled-out features protrude from the fracture surfaces, which are modelled as stochastic variations of quasi-fractal fracture surfaces (see Figure 8.13).

The fracture surfaces are characterised by the coordination number c, representing the number of level-$[i-1]$ bundles in a level-$[i]$ bundle. Level $[i]$ has $n^{[i]} = c^i$ fibres, and is characterised by the total fibre cross section $A^{[i]}$, and bundle perimeter $C^{[i]}$. For a given coordination number (e.g. $c = 7$ as in Figure 8.13), the only unknowns defining the fracture surface are the pullout and debonding lengths of each level-$[i]$ bundle, respectively $\mathcal{L}_{\text{po}}^{[i]}$ and $\mathcal{L}_{\text{deb}}^{[i]}$. These are treated as stochastic variables, with CFDs and cCDFs represented as

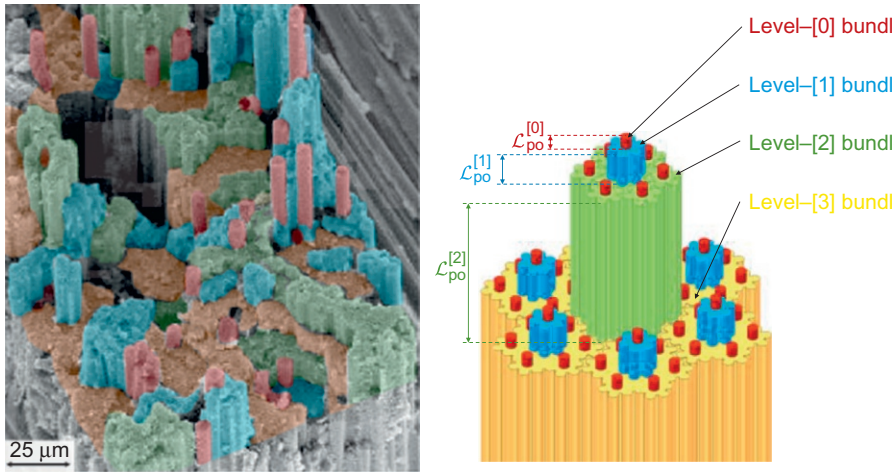

Figure 8.13 Translaminar fracture surfaces in Pimenta and Pinho's model (Pimenta and Pinho, 2014). (a) Real translaminar fracture surface in a carbon-epoxy ply. (b) Idealised quasi-fractal fracture surface ($c=7$, hexagonal packing).

$$\mathcal{F}_{\text{po}}^{[i]}\left(l_{\text{po}}^{[i]}\right)=\Pr\left(\mathcal{L}_{\text{po}}^{[i]}\le l_{\text{po}}^{[i]}\right)\ \text{ and }\ \mathcal{S}_{\text{po}}^{[i]}\left(l_{\text{po}}^{[i]}\right)=\Pr\left(\mathcal{L}_{\text{po}}^{[i]}> l_{\text{po}}^{[i]}\right)=1-\mathcal{F}_{\text{po}}^{[i]}\left(l_{\text{po}}^{[i]}\right),$$
$$\mathcal{F}_{\text{deb}}^{[i]}\left(l_{\text{deb}}^{[i]}\right)=\Pr\left(\mathcal{L}_{\text{deb}}^{[i]}\le l_{\text{deb}}^{[i]}\right)\ \text{ and }\ \mathcal{S}_{\text{deb}}^{[i]}\left(l_{\text{deb}}^{[i]}\right)=\Pr\left(\mathcal{L}_{\text{deb}}^{[i]}> l_{\text{deb}}^{[i]}\right)=1-\mathcal{F}_{\text{deb}}^{[i]}\left(l_{\text{deb}}^{[i]}\right). \tag{8.23}$$

It is assumed that the fracture surface is formed hierarchically, hence the failure process associated with each level-[i] bundle is analysed independently. Figure 8.14a illustrates this for $c=7$ and $i=1$: all level-[2] fibres are assumed broken, and the fracture surface is bridged by the intact level-[1] central bundle and the level-[0] fibres; this creates a stress concentration factor seen by the central level-[i] bundle which can be calculated generically as

$$k^{[i]}=\frac{1}{1-(1-1/c)^{i+1}}. \tag{8.24}$$

The distribution of debond lengths in a given level [i] is calculated through an axisymmetric linear-elastic fracture mechanics model, represented in Figure 8.14b for $c=7$ and $i=1$. At the fracture plane of the level-(Hexcel Corporation, 2015) fibres ($x=0$), the bridging level-(Toray Industries Inc, 2005) bundle sees a stress $\sigma_0^{\mathcal{A}}=k\cdot\sigma^{\infty}$, and the partially broken level-(Hexcel Corporation, 2015) bundle sees a stress $\sigma_{\mathcal{B}}\ge 0$ (transferred by the level-[0] bridging fibres). This stress mismatch may propagate a debond (or matrix shear crack) at the level-(Toray Industries Inc, 2005) bundle along the distance $a^{[1]}$; constant frictional stresses τ_{μ} are transferred to the partially broken level-(Hexcel Corporation, 2015) bundle, resulting in the stress fields represented in Figure 8.14b. For a generic i and c, linear-elastic fracture mechanics leads to

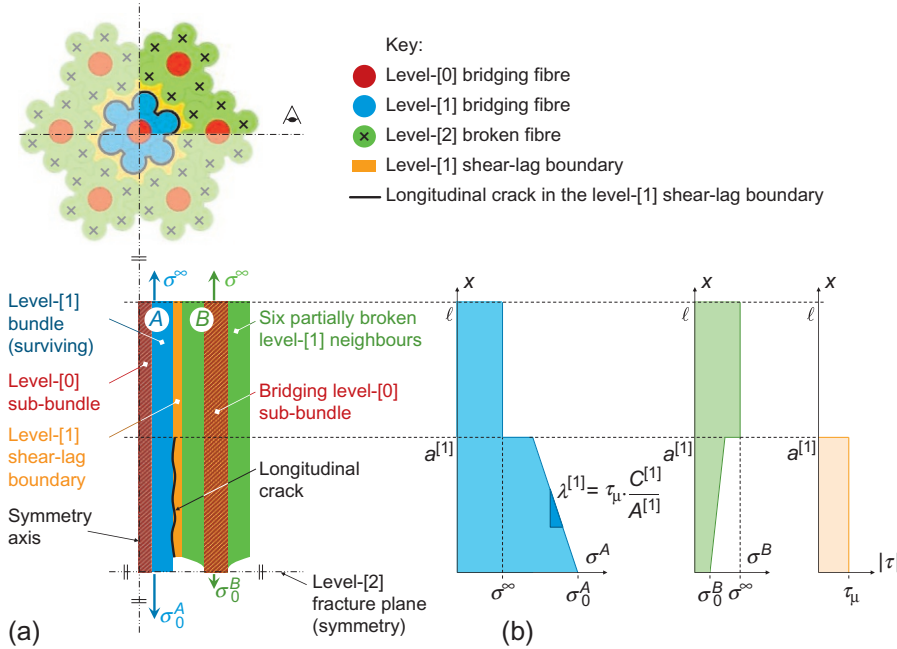

Figure 8.14 Hierarchical axisymmetric model for predicting debonding and pullout lengths, considering $c = 7$ and imminent failure of level $i = 1$ (Pimenta and Pinho, 2014). (a) Geometry. (b) Stress fields.

$$a^{[i]}(\sigma^{\infty}) = \begin{cases} 0, & \sigma^{\infty} \leq \sqrt{\psi^{[i]}/\kappa^{[i]}} \\ \dfrac{(c-1)\cdot\sigma^{\infty} - \sqrt{\left[(c-k^{[i]})\cdot\sigma^{\infty}\right]^2 + \psi^{[i]}}}{\lambda^{[i]}}, & \sigma^{\infty} > \sqrt{\psi^{[i]}/\kappa^{[i]}} \end{cases}, \tag{8.25}$$

where $\lambda^{[i]} = \tau_{\mu}\cdot C^{[i]}/A^{[i]}$, $\psi^{[i]}$ is a function of E^{f}, c, $A^{[i]}$ and $C^{[i]}$, and $\kappa^{[i]}$ is a function of $k^{[i]}$ and c.

Equation (8.25) shows an unequivocal relationship between the debonded distance $a^{[i]}$ and the applied remote stress σ^{∞}. Consider now the following stochastic variables:

- $X^{[i]}_{\mathrm{deb}}$ is the realisation of the strength of a level-$[i]$ bundle within the debonded length, such that the bundle survives if and only if $X^{[i]}_{\mathrm{deb}} > \sigma^{\infty}$;
- $L^{[i]}_{\mathrm{deb}}$ is the realisation of the debond length of the same level-$[i]$ bundle.

Because the bundle fails at $\sigma^{\infty} = X^{[i]}_{\mathrm{deb}}$, and defining the debond length as twice the debonded distance $a^{[i]}$ at the moment of bundle failure, then $L^{[i]}_{\mathrm{deb}} = 2\cdot a^{[i]}\left(X^{[i]}_{\mathrm{deb}}\right)$. Consequently,

$$S^{[i]}_{\mathrm{deb}}\left(l^{[i]}_{\mathrm{deb}}\right) = \Pr\left(L^{[i]}_{\mathrm{deb}} > l^{[i]}_{\mathrm{deb}}\right) = \Pr\left(X^{[i]}_{\mathrm{deb}} > \sigma^{\infty}\right), \quad \text{with } l^{[i]}_{\mathrm{deb}} = 2\cdot a^{[i]}(\sigma^{\infty}). \tag{8.26}$$

The debond length distribution is the same as the bundle strength distribution under the linear stress field represented in Figure 8.14b, within $x \in \left[-a^{[i]}, a^{[i]}\right]$. Using the WLT, this can be calculated from the strength distribution of the level-[i] bundle of length l_r under uniform stresses (with survival probability $S^{[i]}_{\mathrm{U},\mathrm{r}}(\sigma)$, obtained for instance with the strength model presented in Section 8.3.4) as

$$\ln\left[S^{[i]}_{\mathrm{deb}}\left(l^{[i]}_{\mathrm{deb}}\right)\right] = \frac{2}{\lambda^{[i]} \cdot l_\mathrm{r}} \cdot \int_{\sigma=\sigma^{[i]}_a}^{\sigma^{[i]}_0} \ln\left[S^{[i]}_{U,r}(\sigma)\right] \mathrm{d}\sigma, \quad \text{with} \quad \begin{cases} \sigma^{[i]}_0 = k^{[i]} \cdot \sigma^\infty \\ \sigma^{[i]}_a = \sigma^{[i]}_0 - \lambda^{[i]} \cdot a^{[i]}(\sigma^\infty) \end{cases} \tag{8.27}$$

Once the bundle fails within the debonded length when $\sigma^\infty = X^{[i]}_{\mathrm{deb}}$, the exact location of failure – i.e. the realisation of the pullout length $L^{[i]}_{\mathrm{po}}$ – is a stochastic variable with possible values $0 \le L^{[i]}_{\mathrm{po}} \le a^{[i]}\left(X^{[i]}_{\mathrm{deb}}\right)$. The distribution of pullout lengths is defined as

$$S^{[i]}_{\mathrm{po}}\left(l^{[i]}_{\mathrm{po}}\right) = \Pr\left(L^{[i]}_{\mathrm{po}} > l^{[i]}_{\mathrm{po}}\right) = \int_{a^{[i]}(\sigma^\infty)=l^{[i]}_{\mathrm{po}}}^{\infty} \Pr\left(X^{[i]}_{\mathrm{deb}} = \sigma^\infty \wedge L^{[i]}_{\mathrm{po}} > l^{[i]}_{\mathrm{po}}\right) \tag{8.28}$$

Calculating the full expression is cumbersome (Pimenta and Pinho, 2014), but it fully defines $S^{[i]}_{\mathrm{po}}(l^{[i]}_{\mathrm{po}})$ as a function of $S^{[i]}_{\mathrm{U},\mathrm{r}}(\sigma)$ and of the geometric and mechanical properties of the composite.

In the fracture surface represented in Figure 8.13, only one out of c bundles actually debonds and pulls out. Consequently, debonding and pullout length distributions are better represented by *extreme value distributions* (i.e. the maximum length $L^{[i]}$ out of the c bundles, represented in cursive font), which can be calculated from the *expected distributions* (defined in Roman font in Equations 8.27 and 8.28) as

$$\mathcal{F}^{[i]}_{\mathrm{deb}}\left(l^{[i]}_{\mathrm{deb}}\right) = \left[1 - S^{[i]}_{\mathrm{deb}}\left(l^{[i]}_{\mathrm{deb}}\right)\right]^c \quad \text{and} \quad \mathcal{F}^{[i]}_{\mathrm{po}}\left(l^{[i]}_{\mathrm{po}}\right) = \left[1 - S^{[i]}_{\mathrm{po}}\left(l^{[i]}_{\mathrm{po}}\right)\right]^c \tag{8.29}$$

The model considers that for each hierarchical level defined in the fracture surface $i \in \{0, \ldots, i^{\max}\}$, energy is dissipated through debonding and pullout. Following Equation (8.22), the expected value of the fracture toughness is thus:

$$\mathcal{G}^{[i^{\max}]} = \sum_{i=0}^{i^{\max}} \frac{C^{[i]} \cdot \mathcal{G}_{\mathrm{SL}} \cdot \left[\mathcal{L}^{[i]}_{\mathrm{deb}}\right]_\mathrm{m}}{c \cdot A^{[i]}/V^\mathrm{f}} + \frac{{}^1\!/_2 \cdot C^{[i]} \cdot \tau_\mu \cdot \left[\left(\mathcal{L}^{[i]}_{\mathrm{po}}\right)^2\right]_\mathrm{m}}{c \cdot A^{[i]}/V^\mathrm{f}}, \tag{8.30}$$

where the subscript m indicates the expected value of the length distributions in Equation (8.29).

Equation (8.30) shows that the fracture toughness increases with the number of hierarchical levels $i^{\max}$ defined within the fracture surface (e.g. $i^{\max} = 3$ in Figure 8.13). For a laminate with n^f fibres across the thickness of each 0° ply (or 0° ply block), $i^{\max} = \log_c\left[\left(n^\mathrm{f}\right)^2\right]$.

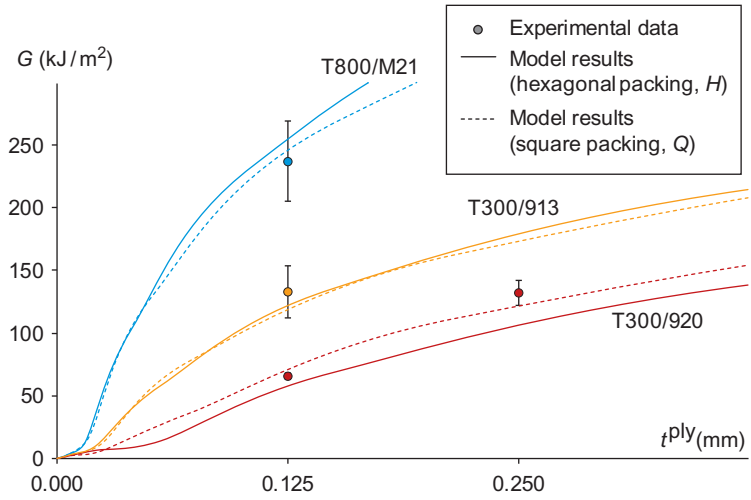

Figure 8.15 Validation of Pimenta and Pinho's fracture toughness model (Pimenta and Pinho, 2014) against experimental results obtained with CT tests (averages and standard deviations) of carbon-epoxy materials (T300/913, Pinho et al., 2006a; T300/920, Laffan et al., 2010; and T800/M21, Teixeira et al., 2011).

Figure 8.15 compares the overall fracture toughness predicted by the model to experimentally measured fracture toughness of 0° plies in compact tension specimens manufactured with different carbon-epoxy composites. This shows that the model has the ability to capture the effect of different fibres (T800/M21 vs. T300/913 and T300/920), different matrices (T300/913 vs. T300/920), and different ply thicknesses (T300/920 at 0.125 mm vs. 0.250 mm).

8.4.3 Modelling progressive failure in macroscopic notched specimens

Hallett et al. (2009) obtained experimentally a complete dataset showing size effects in composite (carbon-epoxy) specimens, which can be used to demonstrate how the models presented in Sections 8.3 and 8.4.2 can be applied to real composite structures. Open-hole specimens with quasi-isotropic layups and sublaminate scaling (i.e. changing n in the layup $[+45,90,-45,0]_{ns}$) were tested under tension and showed a progressive decrease in notched strength with the increasing number of sublaminate repetitions (see Figure 8.16).

Classic strength-of-materials approaches would predict the same strength for any value of n in sublaminate scaling. For instance, in numerical simulations of macroscopic composite structures, tensile failure of a 0° ply is usually represented by a maximum-stress or maximum-strain failure initiation criterion:

$$\sigma_1 = X_{T1} \text{ or } \varepsilon_1 = e_{T1}\,, \quad \text{with } e_{T1} = X_{T1}/E_{T1}\,, \tag{8.31}$$

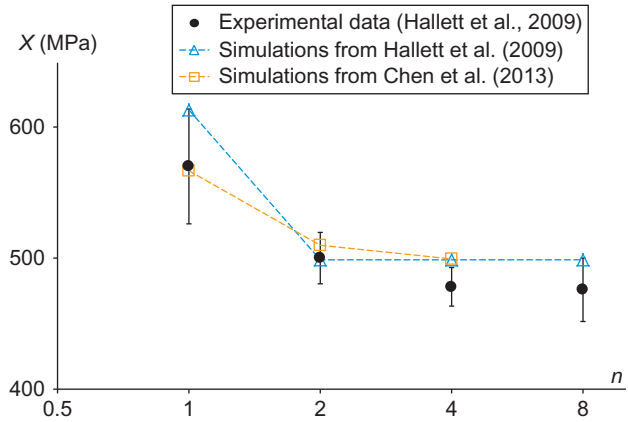

Figure 8.16 Size effects in the strength of quasi-isotropic open-hole specimens under tension: experimental data and FE predictions (Hallett et al., 2009; Chen et al., 2013).

where X_{T1} and E_{T1} are, respectively, the longitudinal tensile strength and longitudinal tensile modulus of the 0° ply. Alternatively, progressive damage can be analysed using cohesive zone models (Elices et al., 2002), smeared approaches (Bazant and Oh, 1983), or partition of unity (Moes et al., 1999), where the degradation of stiffness properties and strain localisation after onset of failure are governed by the fracture toughness of the material (Pinho et al., 2006b; Systèmes, 2013). In either case, neglecting size effects on the fibre-dominate tensile strength and fracture toughness leads to size-independent predictions (van der Meer et al., 2012), contrary to experimental results.

To conciliate simulations with experimental data, Hallett et al. (2009) considered statistical size effects for fibre-dominated tensile strength in the 0° plies. The fibre-dominated longitudinal tensile strength was characterised by a Weibull distribution with parameters m_{T1} and $\sigma_{T1,\,V_0}$ (associated with the volume V_0), determined through the experimentally measured size effect in unnotched UD composites shown in Figure 8.2b. Using detailed FE simulations of the open-hole specimens, Hallett et al. assumed that fibre-dominated failure would occur once the following criterion (corresponding to the Weibull-based WLT in Equation 8.2) was verified.

$$\int \left(\frac{\sigma_{\mathrm{FE}}}{\sigma_{T1,\,V_0}}\right)^{m_{T1}} \frac{\mathrm{d}V}{V_0} = 1, \quad \text{where } \sigma_{T1,V0} = X_{T1} \cdot \left(\frac{V_0}{V_{T1}}\right)^{-1/m_{T1}} \tag{8.32}$$

Following Equation (8.32), fibre damage occurred earlier in the thicker specimens ($n = 8$) than in the thinner ones ($n = 1$), in good agreement with experimental data (see Figure 8.16).

Chen et al. (2013) neglected statistical effects on the strength, and instead considered the deterministic size effect on translaminar fracture toughness ($\mathcal{G}_{T1}$). Progressive failure in the plies (near the notch) was modelled through a smeared crack model, with

the toughness for fibre-dominated tensile failure assumed to increase with the thickness of the 0° ply block. The specimens had a double 0° ply block in the centre of the layup (with higher translaminar toughness), and single 0° plies elsewhere (with lower translaminar toughness). The higher toughness of the central double-ply block increased the damage tolerance of the 1-mm thin specimens (with layup $[+45,90,-45,0]_{1s}$ and all 0° plies blocked together), thus strengthening the thin specimen. However, the effect of the central double-ply block on the 4-mm thick specimens (with layup $[+45,90,-45,0]_{4s}$ and six unblocked 0° plies) was less pronounced, leading to a reduction in the overall damage tolerance and, therefore, in strength, accurately reproducing the experimentally observed size effect (see Figure 8.16).

The work of Hallett et al. (2009) and Chen et al. (2013) clearly demonstrates that fibre-dominated tensile failure is size dependent and cannot be fully described with deterministic and size-independent models. It also shows that both statistical- and toughness-based approaches (explored in Sections 8.3 and 8.4.2, respectively) can be used to model size effects in the strength of composite structures with notched geometries and complex layups.

8.5 Conclusions and future challenges

This chapter has reviewed classical and state-of-the-art models for the fibre-dominated tensile failure of UD composites. Most literature agrees that failure is characterised by progressive accumulation and clustering of fibre breaks until a critical damage state is reached, after which failure becomes catastrophic. This process, which can be (maybe surprisingly) accurately predicted by a range of different models, is governed by fibre strength statistics and by the micromechanics of stress-redistribution near fibre breaks. Although there has been renewed interest on the micromechanics of longitudinal tensile failure in UD composites in the last 5–10 years, there are still several challenges ahead.

At the microscale, a fundamental question is whether the strength of single fibres can be represented by a standard Weibull distribution (Section 8.2.1). Recent data (Watanabe et al., 2014) suggest that there might be two populations of defects, although this requires further investigation. A main parameter in all statistical micromechanical models is the Weibull modulus of single-fibre strength distributions, which can vary significantly (for the same fibre type) in the literature. Reliable and more representative methods to measure single-fibre strength distributions (e.g. relying on composite-level tests rather than at single-fibre tests) would therefore be of great interest.

Another challenge is to understand and characterise the response of the matrix *in situ*, which is likely to be different to that in bulk specimens due to very small volumes (Hobbiebrunken et al., 2007), potentially modified molecular structure and presence of the fibres. Smaller-scale models of the *in situ* matrix and fibre–matrix interface should be developed, for instance, using molecular dynamics.

At a slightly larger scale, the interaction between fibre breaks also requires further research. Extremely detailed models exist for the stress fields near a single-fibre break (Beyerlein and Phoenix, 1996; Swolfs et al., 2015), but most assume very simple

interactions of stress fields in the presence of multiple fibre breaks. Because all experimental evidence suggests that final failure of UD composites under longitudinal tension is governed by formation of clusters with 10–30 broken fibres, more effort should go into modelling stress concentrations near clusters of intermediate sizes. Also, most models do not consider that broken clusters can interact at larger distances than individual fibre breaks, although this is supported by experimental evidence (Figures 8.5 and 8.6, Pimenta and Pinho, 2013).

As the number of distinct models for predicting longitudinal tensile strength in composites increases, it becomes vital to run benchmarking exercises to understand which features are critical and what are the trade-offs between accuracy and computational efficiency. It is also interesting to notice that, despite the developments described, longitudinal tensile failure is still considered by most researchers as the simplest failure mode in composites. In the third WWFE (Kaddour et al., 2013a), only 2 out of 13 loading cases were dominated by fibre tensile failure, and no statistical strength distributions nor fracture toughness values were provided. Moreover, most of the models included in the exercise (Kaddour et al., 2013b) neglect the statistics and micromechanics of the longitudinal tensile failure process, as well as the associated size effects.

There is a clear challenge in linking the micromechanisms of longitudinal tensile failure to the macroscopic response of composites, primarily due to the statistical and multiscale nature of the problem. High-fidelity models may be advantageous in explaining the kinetics of fibre breakage and stress-transfer in the neighbourhood of fibre breaks, but simpler and computationally inexpensive analytical approaches (Pimenta and Pinho, 2013, 2014) are required if size effects are to be modelled at the structural level.

References

Accorsi, M.L., Pegoretti, A., Dibenedetto, A.T., 1996. Dynamic analysis of fibre breakage in single- and multiple-fibre composites. J. Mater. Sci. 31 (16), 4181–4187.

Aroush, D.R.-B., et al., 2006. A study of fracture of unidirectional composites using in situ high-resolution synchrotron X-ray microtomography. Compos. Sci. Technol. 66 (10), 1348–1353.

Aveston, J., Cooper, G.A., Kelly, A., 1971. Single and multiple fracture. In: The Properties of Fibre Composites. National Physical Laboratory, UK.

Baron, C., Schulte, K., Harig, H., 1987. Influence of fibre and matrix failure strain on static and fatigue properties of carbon fibre-reinforced plastics. Compos. Sci. Technol. 29 (4), 257–272.

Bazant, Z.P., 1997. Scaling of quasibrittle fracture: hypotheses of invasive and lacunar fractality, their critique and Weibull connection. Int. J. Fract. 83 (1), 41–65.

Bazant, Z.P., 1999. Size effect on structural strength: a review. Arch. Appl. Mech. 69 (9–10), 703–725.

Bazant, Z.P., Oh, B., 1983. Crack band theory for fracture of concrete. Matériaux et Construction (Materials and Structures) 16 (93), 155–177.

Bazant, Z.P., Daniel, I.M., Li, X., 1996. Size effect and fracture characteristics of composite laminates. J. Eng. Mater. Technol. 118 (3), 317–324.

Beyerlein, I.J., Phoenix, S.L., 1996. Stress concentrations around multiple fiber breaks in an elastic matrix with local yielding or debonding using quadratic influence superposition. J. Mech. Phys. Solids 44 (12), 1997–2039.
Beyerlein, I.J., Phoenix, S.L., 1997. Statistics of fracture for an elastic notched composite lamina containing Weibull fibers - Part I. Features from Monte-Carlo Simulation. Eng. Fract. Mech. 57 (2–3), 241–265.
Beyerlein, I.J., Phoenix, S.L., Sastry, A.M., 1996. Comparison of shear-lag theory and continuum fracture mechanics for modeling fiber and matrix stresses in an elastic cracked composite lamina. Int. J. Solids Struct. 33 (18), 2543–2574.
Blassiau, S., Thionnet, A., Bunsell, A.R., 2009. Three-dimensional analysis of load transfer micro-mechanisms in fibre/matrix composites. Compos. Sci. Technol. 69 (1), 33–39.
Carpinteri, A., 1994. Scaling laws and renormalization-groups for strength and toughness of disordered materials. Int. J. Solids Struct. 31 (3), 291–302.
Chen, B.Y., et al., 2013. Numerical analysis of size effects on open-hole tensile composite laminates. Compos. A: Appl. Sci. Manuf. 47 (4), 52–62.
Curtin, W.A., 1991. Theory of mechanical properties of ceramic-matrix composites. J. Am. Ceram. Soc. 74 (11), 2837–2845.
Curtin, W.A., 1993. The tough to brittle transition in brittle matrix composites. J. Mech. Phys. Solids 41 (2), 217–245.
Curtin, W.A., 2000. Tensile strength of fiber-reinforced composites: III. Beyond the traditional Weibull model for fiber strengths. J. Compos. Mater. 34 (15), 1301–1332.
Curtin, W.A., Takeda, N., 1998. Tensile strength of fiber-reinforced composites: I. Model and effects of local fiber geometry. J. Compos. Mater. 32 (22), 2042–2059.
da Vinci, L., 1493–1494. Diagram of how to determine the breaking strength of iron wires of various lengths, in Codex Atlanticus. p. 82 recto-b.
Daniels, H.E., 1945. The statistical theory of the strength of bundles of threads. I. Proc. R. Soc. A Math. Phys. Eng. Sci. 183, 405–435.
de Morais, A.B., 2001. Stress distribution along broken fibres in polymer-matrix composites. Compos. Sci. Technol. 61 (11), 1571–1580.
Elices, M., et al., 2002. The cohesive zone model: advantages, limitations and challenges. Eng. Fract. Mech. 69 (2), 137–163.
Gao, Y.C., Mai, Y.W., Cotterell, B., 1988. Fracture of fiber-reinforced materials. J. App. Math. Phys. 39 (4), 550–572.
González, C., Llorca, J., 2006. Multiscale modeling of fracture in fiber-reinforced composites. Acta Mater. 54 (16), 4171–4181.
Hallett, S.R., et al., 2009. An experimental and numerical investigation into the damage mechanisms in notched composites. Compos. A: Appl. Sci. Manuf. 40 (5), 613–624.
Harlow, D.G., Phoenix, S.L., 1978a. The chain-of-bundles probability model for the strength of fibrous materials. I: analysis and conjectures. J. Compos. Mater. 12 (2), 195–214.
Harlow, D.G., Phoenix, S.L., 1978b. The chain-of-bundles probability model for the strength of fibrous materials. II: a numerical study of convergence. J. Compos. Mater. 12 (3), 314–334.
Hedgepeth, J.M., 1961. Stress Concentrations in Filamentary Structures. NASA, Washington, DC, USA.
Hexcel Corporation, 2015. cited 2015 9 February, HexTow Continuous Carbon Fiber Products. Available from: http://www.hexcel.com/Resources/Cont-Carbon-Fiber-Data-Sheets.
Hobbiebrunken, T., et al., 2007. Experimental determination of the true epoxy resin strength using microscaled specimens. Compos. A: Appl. Sci. Manuf. 38 (3), 814–818.
Honjo, K., 2003. Fracture toughness of PAN-based carbon fibers estimated from strength-mirror size relation. Carbon 41 (5), 979–984.

Ibnabdeljalil, M., Curtin, W.A., 1997. Strength and reliability of fiber-reinforced composites: localized load-sharing and associated size effects. Int. J. Solids Struct. 34 (21), 2649–2668.
Johnsen, B.B., et al., 2007. Toughening mechanisms of nanoparticle-modified epoxy polymers. Polymer 48 (2), 530–541.
Kaddour, A.S., et al., 2013a. Mechanical properties and details of composite laminates for the test cases used in the third world-wide failure exercise. J. Compos. Mater. 47 (20–21), 2427–2442.
Kaddour, A.S., et al., 2013b. A comparison between the predictive capability of matrix cracking, damage and failure criteria for fibre reinforced composite laminates: Part A of the third world-wide failure exercise. J. Compos. Mater. 47 (20–21), 2749, U147.
Kazanci, M., 2004. Carbon fiber reinforced microcomposites in two different epoxies. Polym. Test. 23 (7), 747–753.
Kelly, A., Tyson, W.R., 1965. Tensile properties of fibre-reinforced metals: copper/tungsten and copper/molybdenum. J. Mech. Phys. Solids 13 (6), 329–338.
Kim, J.-K., Mai, Y.-W., 1991. High strength, high fracture toughness fibre composites with interface control—a review. Compos. Sci. Technol. 41 (4), 333–378.
Laffan, M.J., et al., 2010. Measurement of the in situ ply fracture toughness associated with mode I fibre tensile failure in FRP. Part II: size and layup effects. Compos. Sci. Technol. 70 (4), 614–621.
Laffan, M.J., et al., 2012. Translaminar fracture toughness testing of composites: a review. Polym. Test. 31 (3), 481–489.
Landis, C.M., McMeeking, R.M., 1999. A shear-lag model for a broken fiber embedded in a composite with a ductile matrix. Compos. Sci. Technol. 59 (3), 447–457.
Landis, C.M., Beyerlein, I.J., McMeeking, R.M., 2000. Micromechanical simulation of the failure of fiber reinforced composites. J. Mech. Phys. Solids 48 (3), 621–648.
Mishnaevsky Jr., L., Brøndsted, P., 2009. Micromechanisms of damage in unidirectional fiber reinforced composites: 3D computational analysis. Compos. Sci. Technol. 69 (7–8), 1036–1044.
Moes, N., Dolbow, J., Belytschko, T., 1999. A finite element method for crack growth without remeshing. Int. J. Numer. Methods Eng. 46 (1), 131–150.
Nairn, J.A., 1992. A variational mechanics analysis of the stresses around breaks in embedded fibers. Mech. Mater. 13 (2), 131–154.
Nedele, M.R., Wisnom, M.R., 1994. 3-dimensional finite-element analysis of the stress-concentration at a single-fiber break. Compos. Sci. Technol. 51 (4), 517–524.
Newman, W.I., Gabrielov, A.M., 1991. Failure of hierarchical distributions of fiber-bundles. 1. Int. J. Fract. 50 (1), 1–14.
Okabe, T., Takeda, N., 2001. A 3D shear-lag model considering micro-damage and statistical strength prediction of unidirectional fiber-reinforced composites. Compos. Sci. Technol. 61 (12), 1773–1787.
Okabe, T., Takeda, N., 2002. Size effect on tensile strength of unidirectional CFRP composites – experiment and simulation. Compos. Sci. Technol. 62 (15), 2053–2064.
Okabe, T., et al., 2005. Numerical method for failure simulation of unidirectional fiber-reinforced composites with spring element model. Compos. Sci. Technol. 65 (6), 921–933.
Okabe, T., et al., 2006. Effect of matrix hardening on the tensile strength of alumina fiber-reinforced aluminum matrix composites. Acta Mater. 54 (9), 2557–2566.
Okabe, T., et al., 2010. Prediction of tensile strength of unidirectional CFRP composites. Adv. Compos. Mater. 19 (3), 229–241.
Okabe, T., Sasayama, T., Koyanagi, J., 2014. Micromechanical simulation of tensile failure of discontinuous fiber-reinforced polymer matrix composites using Spring Element Model. Compos. A: Appl. Sci. Manuf. 56, 64–71.

Padgett, W.J., Durham, S.D., Mason, A.M., 1995. Weibull analysis of the strength of carbon fibers using linear and power law models for the length effect. J. Compos. Mater. 29 (14), 1873–1884.
Pearson, R.A., Yee, A.F., 1991. Influence of particle-size and particle-size distribution on toughening mechanisms in rubber-modified epoxies. J. Mater. Sci. 26 (14), 3828–3844.
Pedretti, C., 1979. The Codex Atlanticus of Leonardo da Vinci: A catalogue of its newly restored sheets. Johnson Reprint, Italy, Pt. 1.
Pickering, K.L., Murray, T.L., 1999. Weak link scaling analysis of high-strength carbon fibre. Compos. A: Appl. Sci. Manuf. 30 (8), 1017–1021.
Pierce, F.T., 1926. Tensile tests for cotton yarns, V. "The weakest link" theorems on the strength of long and short composite specimens. J. Text. Inst. Trans 17 (7), 355–368.
Pimenta, S., Pinho, S.T., 2013. Hierarchical scaling law for the strength of composite fibre bundles. J. Mech. Phys. Solids 61, 1337–1356.
Pimenta, S., Pinho, S.T., 2014. An analytical model for the translaminar tensile toughness of fibre composites with stochastic quasi-fractal fracture surfaces. J. Mech. Phys. Solids 66 (5), 78–102.
Pimenta, S., et al., 2010. Mechanical analysis and toughening mechanisms of a multiphase recycled CFRP. Compos. Sci. Technol. 70 (12), 1713–1725.
Pinho, S.T., Robinson, P., Iannucci, L., 2006a. Fracture toughness of the tensile and compressive fibre failure modes in laminated composites. Compos. Sci. Technol. 66 (13), 2069–2079.
Pinho, S.T., Robinson, P., Iannucci, L., 2006b. Physically based failure models and criteria for laminated fibre-reinforced composites with emphasis on fibre kinking. Part II: FE implementation. Compos. A: Appl. Sci. Manuf. 37 (5), 766–777.
Rosen, B.W., 1964. Tensile failure of fibrous composites. AIAA J. 2 (11), 1985–1991.
Scott, A.E., et al., 2011. In situ fibre fracture measurement in carbon-epoxy laminates using high resolution computed tomography. Compos. Sci. Technol. 71 (12), 1471–1477.
Sihn, S., et al., 2007. Experimental studies of thin-ply laminated composites. Compos. Sci. Technol. 67 (6), 996–1008.
Stoner, E.G., Edie, D.D., Durham, S.D., 1994. An end-effect model for the single-filament tensile test. J. Mater. Sci. 29 (24), 6561–6574.
Swolfs, Y., et al., 2013. Stress concentrations in an impregnated fibre bundle with random fibre packing. Compos. Sci. Technol. 74 (1), 113–120.
Swolfs, Y., et al., 2015. Matrix cracks around fibre breaks and their effect on stress redistribution and failure development in unidirectional composites. Compos. Sci. Technol. 108, 16–22.
Dassault Systèmes, ABAQUS 6.13 analysis user's manual. 2013.
Teixeira, R., Pinho, S.T., Robinson, P., 2011. Translaminar ply fracture toughness of advanced composites. In: 18th International Conference on Composite Materials. Jeju Island, South Korea: ICCM.
Thionnet, A., Chou, H.Y., Bunsell, A., 2014. Fibre break processes in unidirectional composites. Compos. A: Appl. Sci. Manuf. 65, 148–160.
Thomason, J.L., 2013. On the application of Weibull analysis to experimentally determined single fibre strength distributions. Compos. Sci. Technol. 77, 74–80.
Toray Industries Inc, 2005. cited 2015 9 February, Torayca. Available from: http://www.torayca.com/en/.
van der Meer, F.P., et al., 2012. Computational modeling of complex failure mechanisms in laminates. J. Compos. Mater. 46 (5), 603–623.
Watanabe, J., et al., 2014. Tensile strength distribution of carbon fibers at short gauge lengths. Adv. Compos. Mater. 23 (5–6), 535–550.

Weibull, G.W., 1951. A statistical distribution function of wide applicability. J. Appl. Math. 18, 293–297.
Wells, J.K., Beaumont, P.W.R., 1985a. Debonding and pullout processes in fibrous composites. J. Mater. Sci. 20 (4), 1275–1284.
Wells, J.K., Beaumont, P.W.R., 1985b. Crack-tip energy-absorption processes in fiber composites. J. Mater. Sci. 20 (4), 2735–2749.
Wisnom, M.R., 1999. Size effects in the testing of fibre-composite materials. Compos. Sci. Technol. 59 (13), 1937–1957.
Wisnom, M.R., Khan, B., Hallett, S.R., 2008. Size effects in unnotched tensile strength of unidirectional and quasi-isotropic carbon/epoxy composites. Compos. Struct. 84 (1), 21–28.
Xia, Z., Curtin, W.A., Okabe, T., 2002. Green's function vs. shear-lag models of damage and failure in fiber composites. Compos. Sci. Technol. 62 (10–11), 1279–1288.
Zhou, S.J., Curtin, W.A., 1995. Failure of fiber composites: a lattice green function model. Acta Metall. Mater. 43 (8), 3093–3104.

Part Three

Advanced numerical algorithms for modelling and simulation of failure in advanced composite materials

This page intentionally left blank

Mesh-independent matrix cracking and delamination modeling in advanced composite materials

9

E.V. Iarve[*], *D.H. Mollenhauer*[†]
*University of Dayton Research Institute, Dayton, OH, USA; †Air Force Research Laboratory, Wright Patterson AFB, OH, USA

9.1 Introduction

Rapid increases in the utilization of composite materials in aviation and other lightweight applications have revitalized interest in manufacturing, performance, and cost characteristics of these materials. The cost associated with such advanced structures, however, is determined less by the cost of the materials than by design and qualification expense. Detailed modeling of the deformation and fracture of composites materials is widely considered a vital step towards a new design and qualification paradigm where significant volumes of conventional testing are replaced by computational simulation. Development of high-fidelity mechanism-based simulation tools also provides a level of understanding of the structural and material behavior required for advancement of future products and designs. However, strength prediction, even in composite laminates under uniform in-plane loading, has presented formidable problems as reflected in the results of the World Wide Exercise (Hinton and Soden, 1998). The complexity of the problem lies in the interaction of various modes of damage such as matrix cracking, delamination, and fiber failure, which cooperatively lead to a loss of load-carrying capacity and/or loss of integrity. In some situations, these damage modes can be isolated, at least approximately, and have been studied exhaustively, for example, transverse cracking in cross-ply laminates (Varna and Berglund, 1991, 1993; Berthelot et al., 1996; Li and Wisnom, 1997; Anderssen et al., 1998; Sun et al., 2003); delaminations and free-edge delaminations (Pagano and Schoeppner, 2000; Tay, 2003), and fiber failure (Rosen, 1964). However, even in these situations, specific failure modes can be isolated only at certain load levels. Transverse cracking will lead to delamination, and delamination propagation in unidirectional composites is accompanied by fiber bridging. Free-edge delaminations in most cases are precipitated and/or closely followed by matrix cracking. Thus the goal of the present chapter is to develop analysis methods capable of simulating such interactions for arbitrary composite laminates.

Continuum damage mechanics (CDM) methodology is the most common and widely used approach for progressive damage modeling in laminated composites. The ease of implementation of this methodology in conventional finite element (FE) frameworks has greatly proliferated its application. FE implementation of CDM methodology results in representing all forms of damage as local stiffness reduction in individual elements,

Numerical modelling of failure in advanced composite materials. http://dx.doi.org/10.1016/B978-0-08-100332-9.00009-8
Copyright © 2015 Elsevier Ltd. All rights reserved.

that is, the effects of matrix and fiber damage are described by directionally reducing the stiffness properties of affected elements. Several reviews of this methodology have been presented (Tang, 1991; Tay et al., 2008; Camanho and Matthews, 1999), including ply-level three-dimensional (3D) formulations (Iarve et al., 2005). Early implementations of the methodology (Tang, 1991) used rule-based degradation algorithms, that is, if the matrix failure in the element is detected, then the transverse stiffness of this element is zeroed out, or the like. Such an approach leads to strong mesh size dependence of the solution. To address this difficulty, energy-based property degradation has been introduced along with consistent thermodynamic damaged, variable-based derivation of constitutive equations (Maimí et al., 2007a,b). The degree of stiffness reduction in this approach is dependent on both the fracture toughness of the composite and the mesh size. A different type of mesh dependence, namely the mesh directionality dependence, is also a concern in CDM-based models. This issue has been investigated in detail by Iarve et al. (2005), where a property degradation CDM is applied to modeling longitudinal splits in plies with fibers aligned with the tensile loading direction. Experimental evaluation of the effect of splitting on stress redistribution in the vicinity of the hole has been performed by Mollenhauer et al. (2006). The splitting showed a quantifiable relaxation on the fiber direction strain. However, attempts to reproduce that behavior using a property degradation technique to model splitting have been unsuccessful (Iarve et al., 2005).

Directional degradation of the transverse properties of the unidirectional ply in the locations associated with splitting resulted in a qualitatively incorrect effect on the stress/strain distribution in the vicinity of the hole edge and the splits. Within the CDM framework, recent advances such as aligned mesh methods (Nikishov et al., 2009, 2010; Song et al., 2011) have been made to improve the damage propagation directionality, which may also improve the fidelity of damage interaction characteristics in the model. In these methods, ply-level analysis is performed so that the mesh in each ply is aligned with the fiber direction and the plies are interconnected by multipoint constraints.

Interlaminar failure simulation in conjunction with CDM intra-ply failure simulation has also been addressed and represents another area where modifications are needed to describe the interaction between delamination and matrix cracking. Matrix cracks practically always precede delaminations and create local interlaminar stress concentrations, which initiate interlaminar failure. If, on the other hand, the matrix cracking is described as local stiffness reduction, it will actually result in lower interlaminar stress, thus having an effect opposite to that seen in experiment. To address these difficulties within the CDM framework, several solutions have been proposed. A phenomenological mesoscopic model composed of stacks of alternating homogenized plies and damageable interfaces was proposed by Allix et al. (2000) for modeling impact damage in laminated composites. The kinematic interaction between the intralaminar CDM and the interfaces was represented using empirical coupling parameters. The coupled analysis method was shown to reproduce correctly the "double-helix" damage cone observed in the experiments. Transverse cracking and delamination interaction has been studied by Ladevèze and coworkers using a nonlocal mesomodel where the coupling between intralaminar and interlaminar damage variables is defined by an energy equivalence between a

meso- and a micromodel in which the cracks are introduced explicitly (Ladevèze et al., 2006; Lubineau and Ladevèze, 2008). With such a coupling, the prediction of delamination induced by transverse cracking was quite accurate.

The CDM methodology has enabled progressive failure modeling in various types of composite materials under complex loading conditions; however, as described above, it has significant difficulties in predicting local effects of damage and interaction of different modes of damage. These difficulties transpire from the nature of CDM where the damage, namely, the local displacement discontinuity, which it introduces in the material, is not modeled explicitly and is instead replaced by its effect on stiffness in the homogenized sense.

Discrete damage modeling (DDM) represents an approach to progressive failure modeling in composites when multiple individual damage events such as matrix cracks and delamination are explicitly introduced into the model via the displacement discontinuities, which they create. In the context of the present chapter, we will emphasize the multiplicity and interaction of failure modes when referring to DDM progressive damage modeling as opposed to progressive damage modeling involving one specific damage mode such as delamination, albeit it was modeled explicitly. In a series of works (Spearing and Beaumont, 1992; Kortschot and Beaumont, 1989), Beaumont and colleagues pioneered parametric DDM in double- and single-notched cross-ply laminates. They explicitly meshed delamination and matrix splits of various lengths to parameterize the energy release rate (ERR) of the laminate with damage as well as the fiber direction stress blunting due to damage. The damage progression was then simulated in a separate computation based on this parametric information and showed good correlation with experimental data and more importantly provided insight on the nonintuitive effects of matrix cracking and delamination interaction leading to higher apparent strength of notched laminates.

Increased computational power as well as development of progressive failure simulation technology and specifically cohesive zone modeling techniques led to a series of works (Wisnom and Hallett, 2009; Hallett et al., 2007, 2009) devoted to simulation of scale effects in notched and unnotched quasi-isotropic composites. The simulation was carried out in explicit FE analysis by modeling each ply with one layer of solid elements and premeshing several matrix cracks in the vicinity of the hole. The location of the cracks was selected based on experimental observations and included matrix splits in 0° plies. Identical meshes were used in all plies requiring a complex mesh to accommodate all crack surfaces with different orientation at the same time. Cohesive zone models were used between plies and at the crack surface allowing for initiation and propagation of damage inside the ply and at the ply interfaces. A broad spectrum of experimental results for varying ply thicknesses and hole sizes were accurately predicted by DDM with fixed and relatively small amount of predefined matrix cracking from within a single model based on independently measured ply-level input data.

A natural evolution of the approaches described above is lifting the limitation of preconceived damage distribution. To achieve this goal, a departure from the conventional FE platform was required. Recent developments of DDM are based on mesh-independent approaches such as x-FEM (Moes et al., 1999). In these methods, the

displacement discontinuity associated with cracking is modeled by changing the FE kinematics and adding additional degrees of freedom in the displacement approximation to represent local displacement discontinuity, rather than reducing the stiffness properties as in CDM. Such a formulation adds significant mathematical complexity compared to property degradation-based damage simulation. The integration path into commercial FE software is much less straightforward than CDM, since the damage effect is not contained entirely within the constitutive equations. However, these formulations overcome some of the most significant problems associated with the CDM approach. In the original x-FEM formulation, degrees of freedom are added to elements along the crack surface to describe the displacement discontinuity. This surface essentially partitions the element into two regions, in which integration must be performed separately to compute the stiffness matrix, residual forces, and consistent distributed loads. An especially advantageous approach to introducing the additional degrees of freedom, the so-called phantom node method, was first proposed by Hansbo and Hansbo (2002). The cracked element has double the number of degrees of freedom of the uncracked initial element, providing independent displacement approximations on each of the partitioned regions.

The shape functions in both regions are the same as in the original element; the node is called real if its degrees of freedom are used in the region to which it belongs and phantom otherwise. This approach provides displacement continuity on both sides of a crack by simply connecting the real nodes to each other, and the phantom nodes to each other. Since the phantom and real nodes coincide in space, the connection between plies can be established by appropriate connections of nodes and cohesive springs tying them together. This methodology was applied to DDM in composite laminates by Van der Meer and Sluys (2009), Van der Meer et al. (2010, 2012), Van der Meer (2012) and Yang and coworkers (Ling et al., 2009; Zhou et al., 2010; Fang et al., 2011). The latter implementation was termed augmented FEM (A-FEM). One of the differences in implementation concerns the connection between plies with different crack orientation. Van der Meer et al. (2012) established that Simpson's surface integration provides accurate delamination shapes in the vicinity of matrix cracks, whereas Fang et al. (2011) concluded that a special interfacial element integrating the double-crack partitioning at the interface is required. In addition, Van der Meer's approach included fiber failure modeling by introducing a global damage variable responsible for element stiffness degradation due to fiber failure. A notable A-FEM development was reported in Li et al. (2013) in which the phantom degrees of freedom were condensed out of the element formulation thus allowing maintenance of the original degrees of freedom and robust integration in commercial FE packages.

Several x-FEM variants different from Hansbo and Hansbo formulation (Hansbo and Hansbo, 2002) have been recently proposed. Kawashita et al. (2012) proposed a method where extra nodes are introduced on the element edges at the locations where they are intersected by a crack. Cohesive zone model formulation was used for crack opening. Uniquely with respect to other implementations, an explicit formulation was used in Kawashita et al. (2012). Segmentation was used in the enriched elements for purposes of integration and visualization. The fracture process in tensile-loaded open hole $[+45/-45]_s$ laminates was successfully modeled.

de Carvalho and coworkers (Chen et al., 2014; de Carvalho et al., 2013) proposed a technique termed the *floating node method*. The introduction of enrichment degrees of freedom is similar to Kawashita et al. (2012) at the specimen edges at the locations in which they are intercepted by the crack. However, they proposed a different approach to crack propagation. The floating node formulation allowed for implementation of the virtual crack closure techniques (VCCTs) (Krueger, 2002) for crack extension. The floating node method was successfully applied to delamination migration propagation prediction in single cantilever beam specimens (de Carvalho et al., 2014). The distinctive feature of this formulation is modeling both the matrix cracking and delamination through element enrichment.

The regularized extended finite element method (Rx-FEM) (Iarve, 2003; Patzak and Jirásek, 2003; Benvenuti, 2008; Oliver et al., 2006; Benvenuti et al., 2008) is another direction in which the x-FEM has been recently developed. In Rx-FEM, the step function used in x-FEM to describe the crack surface is replaced by a continuous function. Different types (for example, exponential or power law-based approximation) were considered in Benvenuti (2008) and Benvenuti et al. (2008). Iarve (2003) proposed the use of displacement approximation shape functions to approximate the step function and thus maintain the Gauss integration schema for element stiffness matrix computation, without regard to cracking orientation. In this case, the Gauss integration points of the initial approximation may be used for integration of the enriched functions, providing a framework for connecting plies where the matrix cracks can propagate in arbitrary directions. The elements are not partitioned since the crack surface is not encapsulated inside an element, but spread over several neighboring elements. One can consider the Rx-FEM as an element duplication method. This arrangement can, in some cases, increase the minimum crack spacing to more than an element between the cracked elements as is the case with the conventional phantom node x-FEM formulation. In both approaches to x-FEM, the crack spacing can be reduced by increasing the phantom node multiplicity, but current practical implementations, including the one presented below, are limited to creating one phantom node per real node. An advantage of Rx-FEM is in maintaining a fixed Gauss integration schema throughout the analysis without regard to location and direction of the cracks created during the analysis, which allows for a straightforward 3D implementation.

In the early works (Iarve, 2003; Mollenhauer et al., 2006), Rx-FEM was applied to stress analysis in open hole composites and showed good correlation of the surface strains in cracked and uncracked plies with moiré interferometry results. In these references, Rx-FEM was used to insert cracks and delaminations in laminates without progressive damage analysis. The latter was accomplished in Iarve et al. (2011) and Swindeman et al. (2013) for matrix damage modes and in Mollenhauer et al. (2012) in combination with the fiber failure mode.

We begin by discussing experimental and numerical results, which led to DDM development. Next, the DDM framework and algorithm will be presented, followed by Rx-FEM formulation and theoretical foundation. A verification example and application to laminated composite failure modeling will follow. Finally, an application of DDM to textile composites will be demonstrated.

9.2 Motivation

Damage evolution in laminated composites consists of a complex array of matrix damage leading to fiber failure. Matrix damage often occurs far below the ultimate failure load, but is believed to have a large influence on the nature of fiber failure. An example of fiber fracture associated with subcritical matrix damage is shown in Figure 9.1. In this figure, the tensile loading is aligned with the 0° ply on the top surface of the laminate. The fibers in this ply carry the majority of the load and are seen to have failed in association with transverse matrix cracks in the neighboring 45° ply. This and other observations led to an experimental effort to understand the influence of subcritical matrix damage in adjacent plies on the main, load-bearing 0° plies (Iarve et al., 2005; Mollenhauer et al., 2006).

An open-hole IM7/5250-4 tensile specimen with a ply stacking sequence of $[0/45/90/-45]_s$ was examined using the full-field displacement measuring technique known as moiré interferometry. This technique is an optical interferometry method capable of measuring in-plane displacements with high sensitivity. The technique yields a displacement fringe pattern that is a contour map of in-plane displacements in a given direction on the face of the specimen. A rigorous explanation of the physics and principles of moiré interferometry can be found in Post et al. (1994).

The test specimen, measuring 300 mm by 38 mm, was loaded in tension to a minimal load of 2225 N. Displacement data was gathered using moiré in a region around one side of the 6.35 mm open hole, as shown in Figure 9.2. The loading was then incrementally increased. After each loading increment, the load was reduced to the original 2225 N and displacement data was again gathered. In this fashion, the distribution of displacements on the surface 0° ply could be monitored for changes as matrix damage evolved. Figure 9.2 also contains a planar X-ray image of the extent of matrix cracking in all plies resulting from the final load increment of 17,125 N.

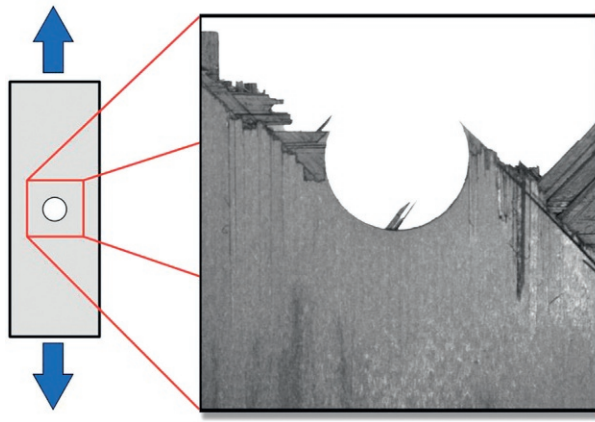

Figure 9.1 Extensive transverse ply cracking and delamination accompany final specimen failure.

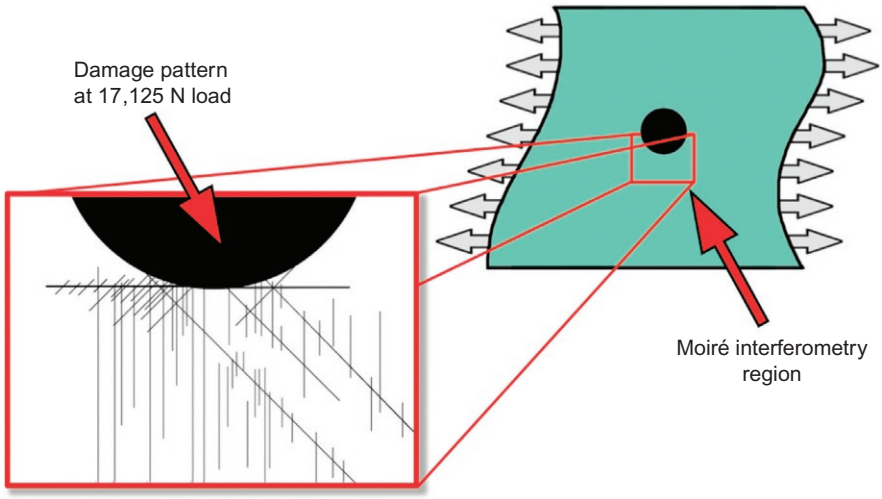

Figure 9.2 Configuration of test specimen examined using moiré interferometry showing the final extent of matrix cracking determined via X-ray imaging.

Axial surface strains obtained before matrix damage and at the maximum extent of matrix damage are compared in Figure 9.3. This comparison shows that the generally smooth variation of strain in the undamaged state becomes highly localized in the specimen when matrix damage is present. The axial strain concentrations appear to be associated with the subsurface matrix cracking, specifically the adjacent 45° ply cracks.

Another illustration of the importance of considering subcritical matrix damage is shown in Figure 9.4. In this figure, axial surface strains are compared along a line through the center of the hole and along a line 1 mm to the right of centerline. These plots show both undamaged and damaged response. Behavior for the undamaged state is as expected. The highest strain concentration occurs at the hole edge along

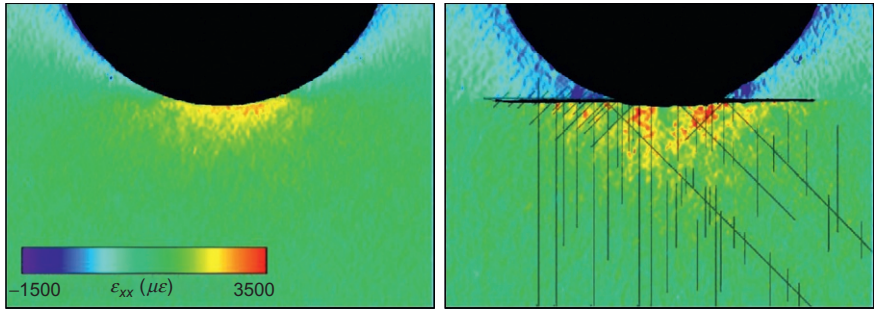

Figure 9.3 Load direction strains resulting from a 2225 N load for the specimen preloaded to 4448 and 17,125 N with superimposed matrix damage pattern.

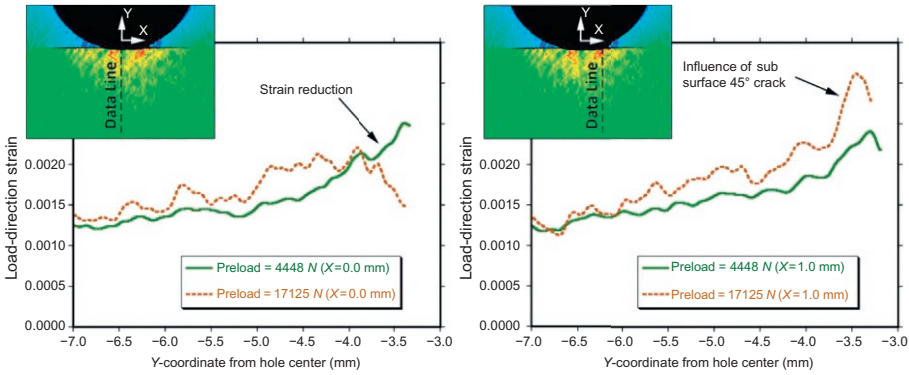

Figure 9.4 Load direction strains resulting from a 2225 N load for the specimen preloaded to 4448 and 17,125 N along $X = 0.0$ mm and $X = 1.0$ mm.

the centerline. However, as subcritical matrix damage evolves, the location and magnitude of the maximum strain concentration shifts away from the centerline and away from the hole edge as seen in Figure 9.4.

To further examine the importance of matrix cracking on ultimate failure in notched laminates, a modeling effort was used to examine the property degradation-based damage modeling methods available at the time (Iarve et al., 2005). A 0° tensile specimen with an open hole was examined experimentally and modeled. The specimen was an AS4/3501-6 material, 300 mm × 38 mm with a 6.35 mm hole. Experimentally, the specimen develops matrix splits at the hole edge, effectively shielding the remaining 0° fibers from the open-hole. It was hoped that the numerical model would capture this effect as well. The FE model determined matrix and/or fiber failure using a simple maximum stress criteria. When the matrix criteria was exceeded, the transverse stiffness of the particular element was completely degraded. In this manner, the specimen was incrementally loaded until the maximum stress of the fiber was exceeded, indicating complete failure. Figure 9.5 shows a comparison between experiment and simulation. Clearly, the simulation underpredicts the strength of the specimen.

Figure 9.6 shows a detailed examination of the stresses approaching the hole edge for an undamaged 0° specimen compared with predictions from two differing representations of matrix damage. First, cracking in the matrix was again represented by property degradation as described previously. Alternatively, it was represented by a complete elimination, or discounting, of the damaged element. The resulting stress profiles clearly show that the degradation of transverse properties within an element do not reduce the stress concentration of the hole significantly, resulting in an early failure. However, complete element discounting serves to reduce the axial stress concentration dramatically.

This observation and the moiré interferometry experimental observations led to the conclusion that a new method for modeling matrix damage needed to be explored. The new method must have, at a minimum, been able to capture the reduction in

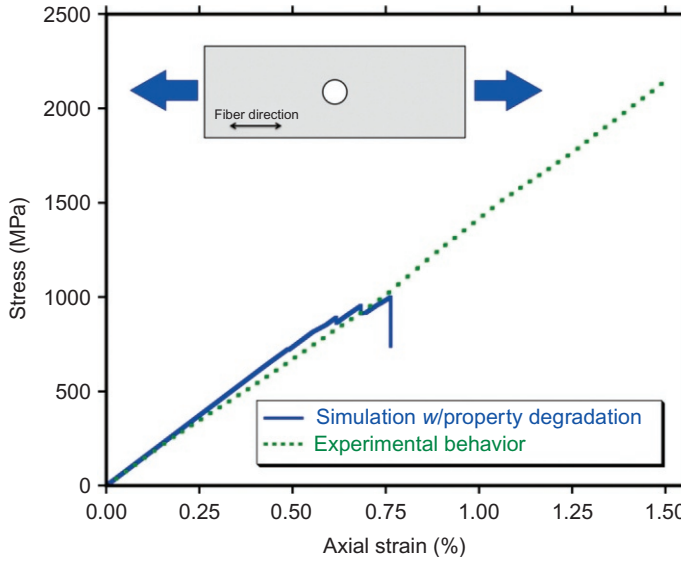

Figure 9.5 Comparison of experimental and simulated stress–strain behavior of a 0° open-hole lamina. The simulation was an FE model with maximum stress criteria and an element-based transverse stiffness property degradation scheme.

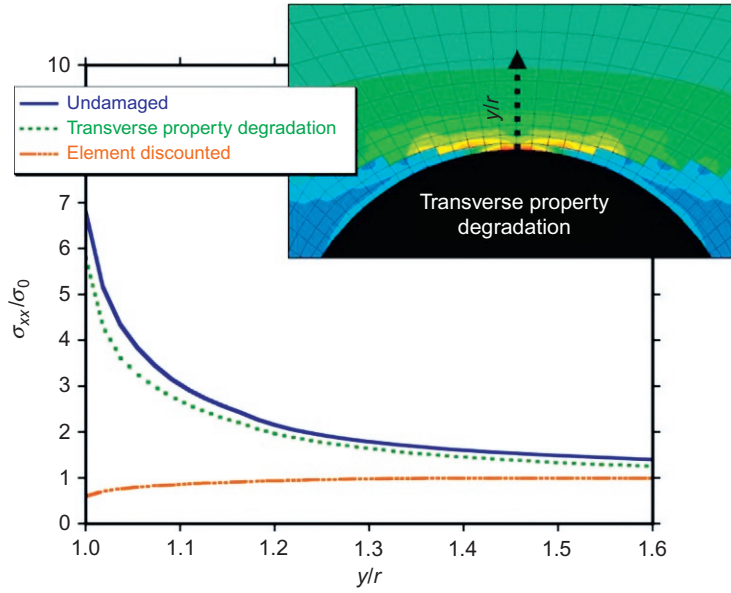

Figure 9.6 Normalized stress versus position away from the hole edge for a 0° open-hole lamina. Simulation results are undamaged, with matrix failure degrading only transverse properties, and with matrix failure completely discounting the element.

fiber-direction stress concentration associated with the presence of a split in the 0° ply. Additionally, it must have been able to show localization of strains in the 0° ply associated with matrix damage in adjacent plies.

9.3 Discrete damage modeling

A simplified damage progression sequence of coupled transverse matrix cracking and interlaminar delamination is shown in Figure 9.7a–d for the case of a laminated plate subjected to a tensile load. Initially, the laminate is undamaged, Figure 9.7a. As a result of the load application, transverse matrix cracks form in different plies of the laminate, as shown in Figure 9.7b. In the absence of a stress concentration, the locations of the initial matrix cracks are random, and cannot be known *a priori*. As the load increases, new cracks appear and the spacing between them becomes increasingly deterministic. At some value of the applied load, delaminations initiate from the matrix cracks (Figure 9.7c). These delaminations can connect matrix cracks in adjacent plies, which can cause the disintegration of the laminate. The aforementioned failure scenario is intended for illustration purposes only, and simplifies the actual damage progression and failure process in which there is no separation of the transverse matrix cracking and delamination phases. Finally, fiber failure occurs and the laminate separates in two parts.

The DDM approach proposed herein for modeling networks of multiple parallel transverse matrix cracks within individual plies of a laminate and delaminations between plies couples a regularized mesh independent crack (MIC) modeling technique (Iarve et al., 2011; Swindeman et al., 2013) for arbitrary transverse matrix cracks and a cohesive model for the delamination between plies. In the regularized

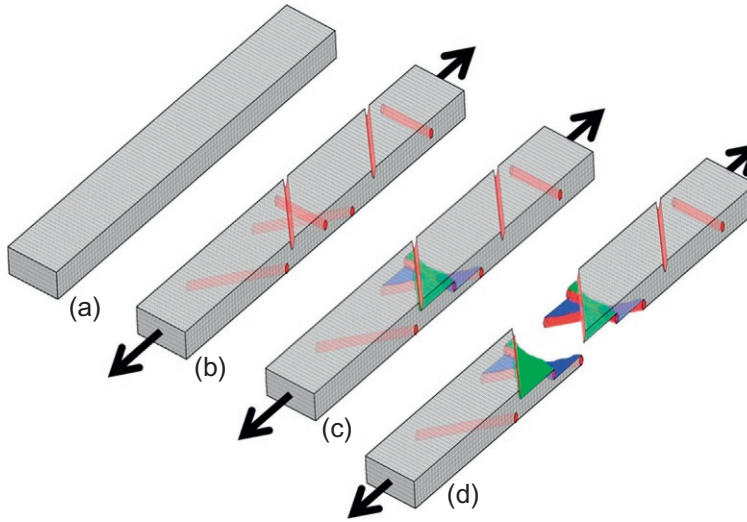

Figure 9.7 Schematic of the damage evolution process in a laminated composite. Pristine (a), matrix cracks(b), delaminations (c), failure (d).

MIC formulation proposed in Iarve et al. (2011) and Swindeman et al. (2013), the step function used in traditional x-FEM approaches to construct local enrichment for a crack discontinuity is replaced with a continuous function that is approximated by the same shape functions as those used for the initial displacement approximation. The surface of each crack is replaced with a gradient zone (a volume where the gradient of the approximate step function is nonzero) and the surface fracture energy is replaced with the cohesive energy in the gradient zone.

A flowchart of a typical simulation is shown in Figure 9.8. A simulation begins without any initial matrix cracks. As the loading is increased, matrix cracks are inserted according to a failure criterion. In the present paper, the LaRC03 in-plane stress-based failure criterion (Dávila et al., 2005) as well as the 3D LaRC04 criterion (Pinho et al., 2005) are used. The criterion is evaluated at each integration point and, if the criterion is exceeded, a matrix crack oriented in the fiber direction is added. LaRC04 predicts the crack angle with respect to ply surface, which is 90° under tensile normal stresses whereas in shear and compression-dominated loading states can significantly differ from 90°. The crack is inserted using the displacement enrichment necessary to model the displacement jump. The magnitude of the jump is initially zero and is controlled by an interface cohesive law (Turon et al., 2006). The same cohesive law is used at the ply interfaces to represent potential delamination surfaces.

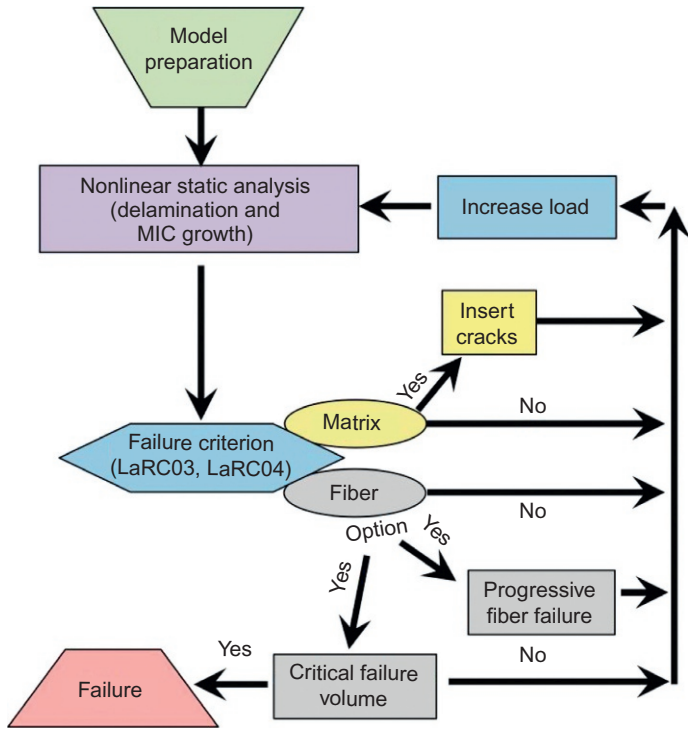

Figure 9.8 Flowchart of a typical DDM simulation.

Fiber failure is handled by using two techniques. A statistical failure criteria called the critical failure volume (CFV) method (Iarve et al., 2006) is used in problems where the fiber failure has a catastrophic character (e.g., open hole tension problems). The CFV approach effectively adds no burden associated with the fiber failure mode and is therefore more efficient and preferable where applicable. When the CFV criterion is satisfied the simulation stops, as seen on Figure 9.8. The second approach represents progressive fiber failure (PFF) methodology and is used in problems where fiber failure progression is important (e.g., saw-cut composite panel problems and/or overheight compact tension [OCT] specimens (Mollenhauer et al., 2012)). This method, conceptually similar to Van der Meer et al. (2012), is based on uniform degradation of the element stiffness when the fiber failure mode is detected. In our work, the methodology by Maimí et al. (2007a,b) is used for this purpose. The PFF method continuously degrades stiffness in a given integration point as a function of normal strain in the fiber direction. The degradation begins after a threshold value corresponding to tensile strength of unidirectional coupons is reached. In this chapter, we focus on the latter method suitable for the OCT specimen simulations considered below. A Newton–Raphson procedure is applied to find the equilibrium solution at each load step of the implicit incremental solution combining softening mechanisms from cohesive interface matrix damage models and stiffness degradation from fiber failure models.

9.3.1 Regularized x-FEM development and validation

The goal of the present study is to model networks of transverse matrix cracks and delaminations in a composite laminate. A single ply containing $s=1,\ldots,S$ cracks parallel to the fiber direction defined by the angle θ is discussed first. Consider a partition of unity set of continuous 3D basis functions $X_i(\mathbf{x})$ and a displacement approximation on the domain of interest V corresponding to one ply in the laminate,

$$\mathbf{u}(\mathbf{x}) = \sum_{i\in\Omega} X_i(\mathbf{x})\mathbf{U}_i \tag{9.1}$$

where $\mathbf{U}_i$ are displacement approximation coefficients, not necessarily associated with nodal displacements, and Ω is the set of all index values. Next consider a crack appearing in this volume, with a surface Γ_α defined by means of the signed distance function defined as

$$f_\alpha(\mathbf{x}) = \text{sign}(\mathbf{n}(\bar{\mathbf{x}})(\mathbf{x}-\bar{\mathbf{x}})) \min_{\bar{\mathbf{x}}\in\Gamma_\alpha} ||\mathbf{x}-\bar{\mathbf{x}}|| \tag{9.2}$$

where $\mathbf{n}(\bar{\mathbf{x}})$ is the normal to the crack surface Γ_α at the point $\bar{\mathbf{x}}$. The traditional x-FEM strong discontinuity formulation is based on element enrichment with displacement modes discontinuous over the crack surface. The discontinuity is obtained by multiplying the shape functions by the Heaviside step function $H(f_\alpha(\mathbf{x}))$. In the regularized

formulation (Iarve et al., 2011), the Heaviside step function is replaced with a continuous function $\widetilde{H}(\mathbf{x})$

$$\widetilde{H}(\mathbf{x}) = \sum_{i \in \Omega} X_i(\mathbf{x}) h_i \tag{9.3}$$

where $X_i(\mathbf{x})$ are the same shape functions as in Equation (9.1). This function is equal to 0 or 1 everywhere, except in the vicinity of the crack surface. The coefficients h_i are calculated as follows:

$$h_i = \frac{1}{2}\left(1 + \frac{\int_V X_i(\mathbf{x}) f_\alpha(\mathbf{x}) \mathrm{d}V}{\int_V X_i(\mathbf{x}) |f_\alpha(\mathbf{x})| \mathrm{d}V}\right) \tag{9.4}$$

This definition involves only continuous functions so the integrals can be calculated by using standard Gauss quadratures. The coefficients h_i are equal to 0 or 1 if the signed distance function does not change sign in the support domain of the shape function $X_i(\mathbf{x})$. On the other hand, when the crack crosses the support domain of the shape function, then $0 < h_i < 1$. Denoting the set of such index values (for which h_i is not equal to 0 or 1) by Ω_α, the enriched approximation for the domain V with an arbitrary crack is defined in the following form:

$$\mathbf{u} = \widetilde{H}\mathbf{u}^{(1)} + \left(1 - \widetilde{H}\right)\mathbf{u}^{(2)} + \mathbf{u}^{(3)} \tag{9.5}$$

$$\mathbf{u}^{(1)} = \sum_{i \in \Omega_\alpha} X_i \mathbf{U}_i^{(1)}, \quad \mathbf{u}^{(2)} = \sum_{i \in \Omega_\alpha} X_i \mathbf{U}_i^{(2)} \tag{9.6}$$

and

$$\mathbf{u}^{(3)} = \sum_{i \in \Omega\, \Omega_\alpha} X_i \mathbf{U}_i^{(3)} \tag{9.7}$$

where the spatial argument has been omitted for conciseness. The displacement approximation given in Equation (9.5) contains the enrichment in the crack region via displacement fields $\mathbf{u}^{(1)}$ and $\mathbf{u}^{(2)}$ as well as the unchanged displacement field, $\mathbf{u}^{(3)}$, away from the crack. Equations (9.5)–(9.7) define the enriched displacement approximation by replacing each original shape function X_i influenced by the crack, $i \in \Omega_\alpha$, with two shape functions, $\widetilde{H}X_i$ and $\left(1 - \widetilde{H}\right)X_i$. This approximation was applied in Iarve (2003) in conjunction with a higher order C^0 displacement approximation (p-elements), as well as with a B-spline approximation of displacements, where the coefficients $\mathbf{U}_i$ do not correspond to nodal displacements. The bookkeeping of the

connectivity is transparent, and the two copies, $\widetilde{H}$ and $\left(1-\widetilde{H}\right)$, of the shape function do not interact. They are only connected to alike $\widetilde{H}$ or $\left(1-\widetilde{H}\right)$ multiple copies of other enriched shape functions if their supports overlap.

For multiple cracks in a single ply, the function F is used in Equation (9.4) instead of f_α to define the set Ω_α of enriched shape functions.

$$F=\prod_{s=1}^{S} f_s \tag{9.8}$$

The product function F maintains some key features of the signed distance function for each of the s cracks in the ply under consideration. This function changes sign over the surface of each crack, and its gradient ∇F is perpendicular to the face of each crack. As follows from Equation (9.4), the enrichment is triggered by the change of sign of f_α, and thus replacing Equation (9.2) with Equation (9.8) extends the previous discussion to multiple parallel MICs in each ply. However, when a single signed distance function is used to represent multiple physical cracks, the crack spacing is limited by the size of the mesh and exceeds the span of a shape function.

The limitation on minimum cracking distance for a given mesh size can be reduced by using individual step functions for individual cracks. Iarve et al. (2005) and Mollenhauer et al. (2006) used this approach to investigate the effect of matrix cracks and delaminations around open holes in composite laminates on stress redistribution in the fiber direction. Damage progression was not modeled and the mesh independent technique was used to place predefined matrix cracks and delaminations. To represent such damage networks with displacement discontinuity surfaces crossing each other, the displacement shape functions have to be quadrupled for two crossing cracks, and reproduced 2^n times for n crossing cracks. Such a representation is useful in the case of parallel cracking networks as well, because it allows the minimum crack spacing distance for given mesh size to be significantly reduced. This development will be pursued in the future.

The strain energy in the volume V with displacement approximation given by Equation (9.5) is written as

$$\begin{aligned} W=&\frac{1}{2}\int_V\left\{\widetilde{H}\left(\boldsymbol{\varepsilon}^{(1)}-\mathbf{e}\right)^{\mathrm{T}}\boldsymbol{\sigma}^{(1)}+\left(1-\widetilde{H}\right)\left(\boldsymbol{\varepsilon}^{(2)}-\mathbf{e}\right)^{\mathrm{T}}\boldsymbol{\sigma}^{(2)}\right\}\mathrm{d}V\\ &+\int_V\left\{\widetilde{H}\left(\boldsymbol{\varepsilon}^{(1)}-\mathbf{e}\right)^{\mathrm{T}}\boldsymbol{\sigma}^{(3)}+\left(1-\widetilde{H}\right)\left(\boldsymbol{\varepsilon}^{(2)}-\mathbf{e}\right)^{\mathrm{T}}\boldsymbol{\sigma}^{(3)}\right\}\mathrm{d}V\\ &+\frac{1}{2}\int_V\left\{\left(\boldsymbol{\varepsilon}^{(3)}-\mathbf{e}\right)^{\mathrm{T}}\boldsymbol{\sigma}^{(3)}\right\}\mathrm{d}V \end{aligned} \tag{9.9}$$

where superscript T denotes the transpose operation, $\boldsymbol{\sigma}^{(k)}$ are elastic stress tensors, and $\boldsymbol{\varepsilon}^{(k)}$ and $\mathbf{e}$ are the total and the nonmechanical strain tensors, respectively. In the global xyz coordinate system, Hooke's law reads

$$\boldsymbol{\sigma}^{(k)}=\mathbf{C}\left(\boldsymbol{\varepsilon}^{(k)}-\mathbf{e}\right) \tag{9.10}$$

where $\mathbf{C}$ is the elastic orthotropic stiffness tensor (see Whitney, 1987 for engineering constant and ply coordinate transformation expressions). The nonmechanical strain is required to account for the residual stress state arising in a composite laminate from the curing process, and in the present study is $\mathbf{e} = (T - T_0)\boldsymbol{\alpha}$. Here, $T - T_0$ is the difference between the cure temperature and room temperature, and $\boldsymbol{\alpha}$ is the tensor of thermal expansion coefficients in the global coordinate system. The strain tensors $\boldsymbol{\varepsilon}^{(k)}$ are computed from displacement fields $\mathbf{u}^{(k)}$ in Equation (9.5) for $k = 1, 2, 3$, so that

$$\varepsilon_{ij}^{(k)} = u_{i,j}^{(k)} + u_{j,i}^{(k)} \tag{9.11}$$

The strain energy given in Equation (9.9) does not include the energy associated with the propagation of transverse cracks.

9.3.2 Transverse splitting in unidirectional composite plate with an open hole

Consider the example of a unidirectional composite material with an open hole under tensile loading. As previously discussed, such specimen develops matrix cracks in the form of longitudinal splitting, which shield the fiber direction stress concentration. We also illustrated difficulties in predicting this effect by using directional property degradation methodology. In the present section, Rx-FEM will be applied in a similar setting. We will verify the accuracy of fiber direction stress prediction in the $x = 0$ cross section in unidirectional composites with a short split (Figure 9.9) by using the higher order approximation-based MIC modeling method. This simplified problem can be readily modeled by commercial FEM, thus providing a basis for comparison. Solution details, material properties, and convergence studies can be found in Iarve (2003). A unidirectional eight-ply IM7/5250-4 composite with a quarter-inch central hole

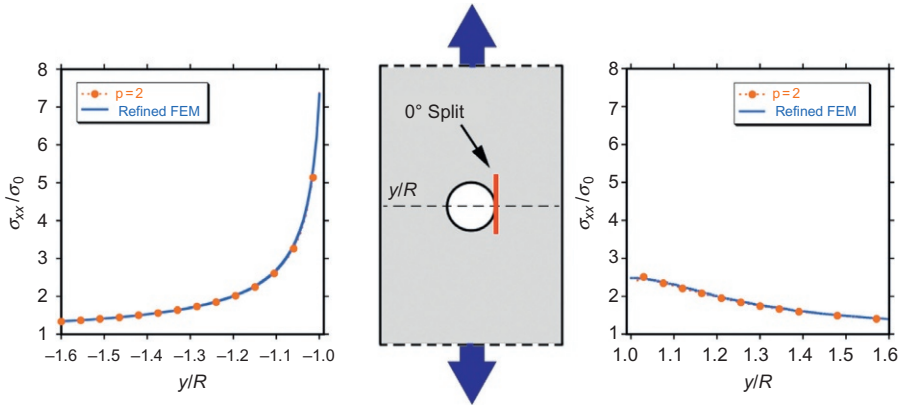

Figure 9.9 Rx-FEM cracking demonstrated on an open-hole 0° lamina, modeled using second order p-elements. The refined FEM explicitly meshed the crack.

and $W/D = 8$ was considered. The length of the vertical split is taken to be equal to the hole diameter. A total of 864 three-dimensional brick FE mesh, typical for stress concentration analysis near the hole edge, was used. To verify the accuracy of the stress prediction by the mesh-independent crack modeling technique, standard FE analysis by meshing the surface of the split and the hole edge was performed by using the ANSYS FE software. The hoop stress $\sigma_{\theta\theta}$ along the symmetry line (dashed line) near the hole normalized by the average applied stress is shown on the left and right side of Figure 9.9. The distance from the hole edge is normalized by hole radius and the stress distributions correspond to the sides of the hole with and without split as shown by schematics in the middle. The Rx-FEM solution was obtained by using quadratic elements and can be seen to accurately capture the stress concentration reduction due to splitting. The relatively small split is responsible for reducing the stress concentration approximately three times. The Rx-FEM solution practically coincides with the directly meshed ANSYS analysis.

9.3.3 Rx-FEM formulation

The formulation described in the previous section is fully applicable to an individual FE. Such methodology may be required in geometrically large elements, such as p-elements or B-spline based elements of early formulation (Iarve, 2003). However, the development to date has evolved in the direction of lower order elements with small support, which are more suitable for analysis of problems with evolving networks of discontinuities. In this case, the relatively small element size allows us to make two simplifications, namely (i) only one crack per element will be allowed, and (ii) the crack cannot terminate inside the element, and the transition from uncracked region to cracked region will be facilitated through connection of nodal degrees of freedom. The latter assumption simplifies Equations (9.5)–(9.7) and (9.9) by eliminating the displacement field $\mathbf{u}^{(3)}$, and all associated terms as well as the element not containing cracks will have only one displacement field. Resorting to conventional notations, we write the displacement field in uncracked elements as

$$\mathbf{u}(\boldsymbol{\xi}) = \sum_{a=1}^{n_a} N_a(\boldsymbol{\xi})\mathbf{u}_a \tag{9.12}$$

where $N_a(\boldsymbol{\xi})$ is the element shape functions, $\boldsymbol{\xi}$ is the local coordinate, $\mathbf{u}_a$ is the nodal displacements, and n_a is the number of nodes. The strains (9.12) are computed as

$$\boldsymbol{\varepsilon}(\boldsymbol{\xi}) = \mathbf{B}(\boldsymbol{\xi})\mathbf{u} \tag{9.13}$$

by using well-known nonsquare differentiation matrices $\mathbf{B}$. The strain energy can be written by combining (9.13) with constitutive relationship (9.10)

$$W^e = \frac{1}{2}\int_{\Omega_e} \left(\mathbf{u}^{\mathrm{T}}\mathbf{B}^{\mathrm{T}} - \mathbf{e}^{\mathrm{T}}\right)\boldsymbol{C}(\mathbf{B}\mathbf{u} - \mathbf{e})\mathrm{d}\Omega \tag{9.14}$$

In the element containing a crack, we first introduce the step function approximation within an element

$$\widetilde{H}(\boldsymbol{\xi}) = \sum_{a=1}^{n} N_a(\boldsymbol{\xi})\widetilde{H}_a \tag{9.15}$$

Nodal $\widetilde{H}_a$ values are computed according to Equation (9.4) with the understanding that the basis function X_a corresponding to a FE node consists of all corresponding shape functions of elements sharing this node. The two-field displacement approximation can then be written as

$$\mathbf{u} = \left(1 - \widetilde{H}(\boldsymbol{\xi})\right)\mathbf{u}^{(1)} + \widetilde{H}(\boldsymbol{\xi})\mathbf{u}^{(2)} \tag{9.16}$$

and the strain energy becomes

$$\begin{aligned} W^e = \frac{1}{2}\Bigg\{ \int_{\Omega_e} & \widetilde{H}(\boldsymbol{\xi})\left(\mathbf{u}^{(1)\mathrm{T}}\mathbf{B}^{\mathrm{T}} - \mathbf{e}^{\mathrm{T}}\right)\boldsymbol{C}\left(\mathbf{B}\mathbf{u}^{(1)} - \mathbf{e}\right) \\ & + \left(1 - \widetilde{H}(\boldsymbol{\xi})\right)\left(\mathbf{u}^{(2)\mathrm{T}}\mathbf{B}^{\mathrm{T}} - \mathbf{e}^{\mathrm{T}}\right)\boldsymbol{C}\left(\mathbf{B}\mathbf{u}^{(2)} - \mathbf{e}\right)\Bigg\}\mathrm{d}\Omega \end{aligned} \tag{9.17}$$

Nodes are classified by the zone number, namely 1 if $f_\alpha(\mathbf{x}_a) > 0$ and 2 if $f_\alpha(\mathbf{x}_a) < 0$. When a node in region 1 or 2 is duplicated, the duplicate node is labeled as belonging to the opposite zone. The continuity of displacements on each side of the crack surface is achieved by connecting nodes within each zone.

The displacement fields in the zones 1 and 2 are kinematically independent and are tied together through the cohesive fracture energy formulation. Within each cracked element, one can define the displacement jump as $\Delta\mathbf{u} = \mathbf{u}^{(1)} - \mathbf{u}^{(2)}$. In the original x-FEM formulation, this jump is concentrated at the crack surface Γ_α, whereas in the regularized formulation zones 1 and 2 overlap over the entire element volume.

The central idea of the regularized formulation is the equivalence of the true surface area of the crack and effective "area" of the crack surface described by an approximate step function. Consider an arbitrary volume v, which contains a crack surface defined by a signed distance function $f_\alpha(\mathbf{x})$. Then the surface area of this crack S_v inside the volume v can be computed according to (Iarve, 2003)

$$S_v = \int_v \delta_{\mathrm{D}}(f_\alpha)\mathrm{d}V = \int_v \nabla H|\mathrm{d}V \approx \int_v \nabla\widetilde{H}|\mathrm{d}V \tag{9.18}$$

where δ_{D} is the Dirac delta function, H is the Heaviside step function, and $\widetilde{H}$ is its regularized approximation (9.3). Note that the volume v must be larger than a single element volume. However, the surface area of the crack can now be calculated without discretizing the crack surface, but performing volume-based integration of the right-hand side of Equation (9.18) using the original Gauss integration points. The caveat is that this integral includes all elements for which the nodal values $\widetilde{H}_a$ are not identically 1 or 0 in all nodes. This set includes not just the elements traversed by the crack, but

those that share a node with the cracked elements. This narrow volume surrounding the crack surface is called a gradient zone because in this region $|\nabla\widetilde{H}| > 0$. Thus, in the Rx-FEM, more elements will be enriched to model the same crack than in the x-FEM. Whereas this feature is a disadvantage of the current approach, the additional computational work is compensated by the preservation of the original Gaussian quadrature scheme in each Rx-FEM element. Rx-FEM is ideally suited for 3D formulation and higher-order element formulation.

9.4 Progressive damage modeling

We begin by discussing the mixed-mode cohesive zone interface fracture model proposed by Turon et al. (2006). The brief description below is given for completeness of the present formulation and the reader is referred to Turon et al. (2006) for full details. We consider an arbitrary point at the crack interface with a normal vector $\mathbf{n}$ and a displacement jump vector $\Delta\mathbf{u}$. Our goal is to define the fracture energy of separation of an arbitrary interface point, which then will be used in deriving the governing equations from the minimum potential energy principle. This discussion will directly pertain to the delamination propagation between plies and will be later used for matrix crack propagation as well.

The cohesive energy can be written in the invariant form as a function of the norm of the displacement jump $\lambda = ||\Delta\mathbf{u}||$ and a mode mixity parameter B

$$B = 1 - \frac{\langle \Delta u_n \rangle^2}{\lambda^2} \tag{9.19}$$

where $\Delta u_n = (\Delta\mathbf{u} \cdot \mathbf{n})$ is the normal, mode I component of the displacement jump, and the brackets $\langle x \rangle = \frac{1}{2}(x + |x|)$ represent the McAuley operator. The parameter B is equal to 0 for mode I propagation, and is equal to 1 for mode II propagation. The functional shape of the fracture energy as a function of the displacement gap is defined by the relationship between the cohesive tractions and the displacement jump, which is assumed to have the form

$$\boldsymbol{\tau} = (1 - d)K\Delta\mathbf{u} + \mathrm{d}K\langle \Delta u_n \rangle \mathbf{n} \tag{9.20}$$

where K is a high initial penalty stiffness and d is the damage parameter. The first term in Equation (9.20) represents the crack cohesive force, and the second term prevents interpenetration of the crack surfaces. A bilinear relationship is assumed for the magnitude $\tau(\lambda) = |\boldsymbol{\tau}|$ of the cohesive traction vector, defined in (9.20) such that $d = 0$ if $\lambda < \Delta_0$ and $d = 1$ if $\lambda > \Delta_f$. The initial value of the displacement jump, beyond which the interface failure begins, is defined as

$$\Delta_0 = \tau_0 / K \tag{9.21}$$

where τ_0 is the cohesive strength. The cohesive strength depends on the mode mixity parameter B as

$$(\tau_0)^2 = Y^2 + \left(S^2 - Y^2\right)B^{\eta} \tag{9.22}$$

where Y and S are the interfacial normal and shear strengths, respectively, and η is an experimentally determined influence parameter (Turon et al., 2006). The fracture energy density $g(\lambda,B)$ is the area under the $\tau(\lambda)$ curve, so that

$$g(\lambda, B) = \int_{q=0}^{\lambda} \tau(q, B)\mathrm{d}q \tag{9.23}$$

To ensure the correct crack propagation characteristics, the final value of the displacement jump, Δ_f, is defined so that the following condition is satisfied:

$$g(\Delta_f, B) = G_c(B) \tag{9.24}$$

where the ERR, G_c, or fracture toughness, is assumed to be a function of the mode mixity

$$G_c = G_{Ic} + (G_{IIc} - G_{Ic})B^{\eta} \tag{9.25}$$

and G_{Ic} and G_{IIc} are experimentally measured fracture toughness values. In the case of a bilinear $\tau(\lambda)$ relationship, the final value of the displacement jump is determined by the initial value of the displacement jump and the fracture toughness as

$$\Delta_f = 2G_c/(K\Delta_0) \tag{9.26}$$

All parameters entering the analysis, such as the fracture toughness and strength values, are material properties that can be measured by using standard test methods.

9.4.1 MIC propagation

The critical aspect of the cohesive zone crack propagation model, which makes it suitable for extension to the regularized MIC formulation, is the fact that the crack tip ERR concept of classical fracture mechanics is replaced by a surface fracture energy at a given point. Although the discussion of this fundamental topic is beyond the scope of this chapter, it can be seen that development of a unit length open crack surface where $\lambda \geq \Delta_f$ requires an ERR G_c according to Equation (9.24), which is consistent with the Griffith definition of G_c. A similar argument is used to calculate the fracture energy of a MIC in the regularized formulation. First, using Equation (9.23), we calculate fracture energy at each integration point of the gradient zone. The only parameters needed are the displacement jump vector $\Delta\mathbf{u} = \mathbf{u}^{(1)} - \mathbf{u}^{(2)}$ and the normal vector to the crack surface, which we calculate by using the sign distance function. Next, the relationship between the fracture energies $g(\lambda,B)$ computed in the volume of the gradient zone and the surface energy of the crack needs to be determined. The expression of the surface area by means of the volume integration (9.18) can be generalized (Iarve et al., 2011) and used to compute surface integrals of continuous functions as follows:

$$\int_v g(\mathbf{x})\delta_{\mathrm{D}}(f_\alpha)\mathrm{d}V = \int_v g(\mathbf{x})|\nabla H|\mathrm{d}V \approx \int_v g(\mathbf{x})|\nabla \widetilde{H}|\mathrm{d}V \tag{9.27}$$

where $\delta_{\mathrm{D}}(f_\alpha)$ is the Dirac delta function of the signed distance function.

Substituting $g(\mathbf{x})$ with the surface energy (9.23), we can obtain the surface energy of a crack by computing the volume integral on the right-hand side of Equation (9.27), which on the single element level will be

$$M^e \approx \sum_{l=1}^{n_{\mathrm{int}}} g(\lambda, B)|\nabla \widetilde{H}|\big|_{\boldsymbol{\xi}_l} W_l \tag{9.28}$$

where summation is carried over integration points ξ_l, $l=1,\ldots,n_{\mathrm{int}}$ and W_l are weight coefficient including Gauss weights and Jacobean.

To compute the fracture energy of the crack, the contributions for all elements where $|\nabla \widetilde{H}| > 0$ must be combined. Thus, the fracture energy (9.23) is a function of the displacement jump $\Delta\mathbf{u} = \mathbf{u}^{(1)} - \mathbf{u}^{(2)}$, and ties together the otherwise independent displacement approximations in the cracked zones.

9.4.2 Delaminations and their interaction with MIC

The delamination between two plies in a laminate is modeled using the previously outlined cohesive zone method (Turon et al., 2006) outlined in the previous section. Let us consider the interface between plies n and $n+1$, where the enriched displacement approximation (9.9) is used. The displacement jump between the two plies is then computed as

$$\Delta\mathbf{u} = \widetilde{H}_{n+1}\mathbf{u}_{n+1}^{(1)} + \left(1-\widetilde{H}_{n+1}\right)\mathbf{u}_{n+1}^{(2)} - \widetilde{H}_n\mathbf{u}_n^{(1)} - \left(1-\widetilde{H}_n\right)\mathbf{u}_n^{(2)} \tag{9.29}$$

which can be evaluated at an arbitrary point on the surface between the two plies (subscript denotes the ply number). The fracture energy of a delamination between the two plies is computed by integrating the pointwise fracture energy (9.22) over the area of the interface between the plies

$$\Phi_n = \iint_{z=z_n} g(\lambda, B)\mathrm{d}S \tag{9.30}$$

We can now write the minimum potential energy principle for deriving the equilibrium equations for an N-layer laminate, which contains cohesive zones between the plies and MIC in each ply

$$\delta\left(\sum_{n=1}^{N}\left(\sum_{e=1}^{E_n}(W^e + M^e)\right) + \sum_{n=1}^{N-1}\Phi_n - A\right) = 0 \tag{9.31}$$

The summation includes the strain energy, W^e, and fracture energy, M^e, of each element $e=1,\ldots,E_n$ of each ply $n=1,\ldots,N$ and the delamination fracture energy between plies. As outlined previously, the regularized formulation allows the computation of all quantities in Equation (9.31) by Gauss integration over the element domain. As a result, a system of equations for computing the enriched displacement approximations in each ply can be obtained without introducing any special partitions or integration rules and without regard to the mesh orientation in the plies.

The Rx-FEM has been implemented using an in-house FE code BSAM (BSAM Users Manual, 2014). This code uses fully integrated, three-dimensional, eight-node, isoparametric brick elements, but may be extended to incorporate other element types.

9.4.3 Fiber failure

In the DDM framework presented here, a property degradation approach was used to address fiber failure in composite laminates and textile composite tows. The stiffness tensor at a given stress level is defined as $C=(1-d)C_0$, where C_0 is the initial stiffness. The damage variable, d, is defined based on the stress strain relationship proposed in Maimí et al. (2007a,b), and is shown in Figure 9.10. Determination of the numerical values of the parameters defining the cohesive curve in Figure 9.10 for IM7/8552 in tension, for example, include the fracture toughness, $G_X=81.5$ N/mm and coefficients $f_X=0.2, f_G=0.4$ as well as the characteristic length, which has been addressed in Camanho et al. (2007). The initiation stress value, X, represents the fiber direction strength measured on standard unidirectional coupon type tests. According to the experimental data obtained by Wisnom et al. (2008), this value depends on the volume of the coupon and for IM7/8552 follows the Weibull distribution with the modulus of $\alpha=40$. Thus, the specific value used for simulation with property degradation is not entirely defined. In our simulations, we will use two values of the failure initiation strength: (i) $X=2400$ N/mm^2 obtained for a typical eight-ply unidirectional coupon with total volume of $V_0=34{,}300$ mm^3 and $X=3116$ N/mm^2 scaled strength for a 1 mm^3 of stressed volume.

An example application of the property degradation approach combined with delamination propagation and MIC insertion and propagation is shown in Figure 9.11. This figure shows the fiber damage evolution resulting from tensile loading in a 100 mm long

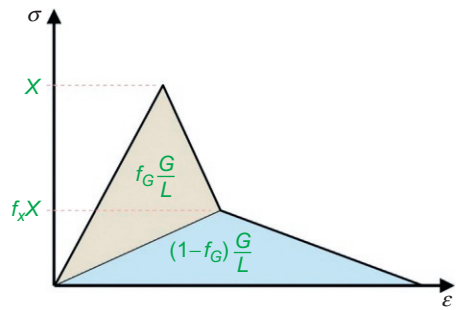

Figure 9.10 Property degradation approach to fiber fracture.

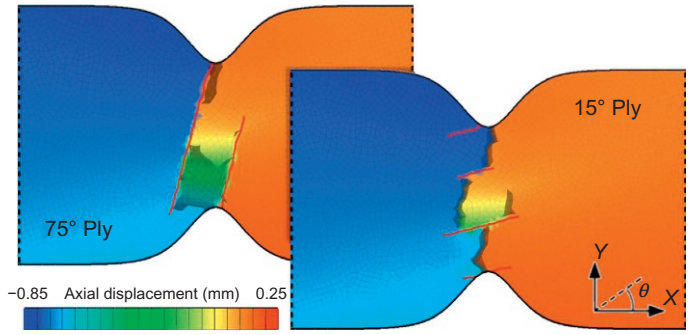

Figure 9.11 Demonstration of the property degradation approach for fiber fracture combined with MIC matrix damage and delamination on a $[15/75]_s$ notched laminate. MIC cracks in red, gray patches are either delamination between plies or fiber damage in the 15° ply.

by 30 mm wide $[15/75]_s$ IM7/8552 specimen with a smooth notch section of 15 mm wide. The figure shows axial displacement distribution in each ply, MIC cracking in each ply, delamination between plies, and fiber damage in the 15° ply at an advanced state of damage evolution.

9.5 Application of MIC to a two-crack double cantilever beam

Before proceeding with examples illustrating the interaction of multiple failure modes in composite laminate, we focus on verification of the Rx-FEM MIC propagation modeling. We chose a two-crack double cantilever beam (DCB) experiment conducted in Robinson et al. (1999) for this purpose. This example has been considered by several authors for verification of cohesive zone models (Alfano and Crisfield, 2001) and automated VCCT (Mabson et al., 2007). The Rx-FEM technique has been applied to the same example, and results of analysis compared to experiment and other predictions. Figure 9.12 shows the specimen geometry. Two initial cracks are placed in the beam, offset in the ply stack-up direction by two layers. The meshes around the crack tips are shown in Figure 9.12. The meshes in the vicinity of the cracks are unstructured; however, due to the high aspect ratio of the sample, the mesh is aligned with the crack direction over most of the length. MICs, initially closed, are placed at the tip of each of the cracks. For each crack, the signed distance function has been predefined and the respective elements enriched by Rx-FEM. The cohesive model described earlier assures displacement continuity along the crack face prior to loading.

Vertical displacements of equal magnitude and opposite direction are applied to the left-hand side arms of the double cantilever specimen. Figure 9.13 illustrates the simulated damage progression, with elements containing fully opened cracks shown in orange. The load displacement curve predicted by Rx-FEM and the experimental data (Robinson et al., 1999) are shown in Figure 9.14. Both the cracking sequence and the

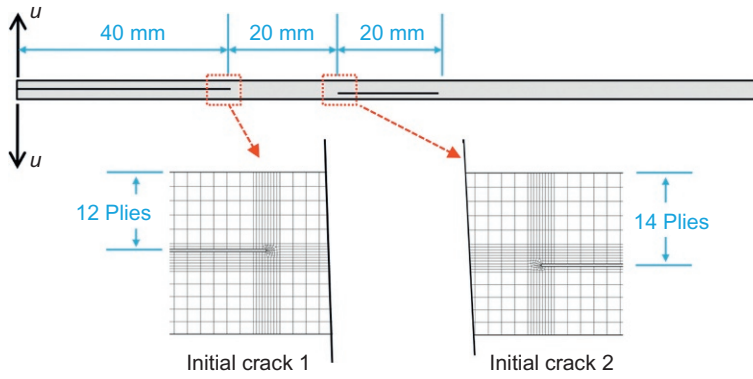

Figure 9.12 The two-crack problem schematic and crack tip mesh details.

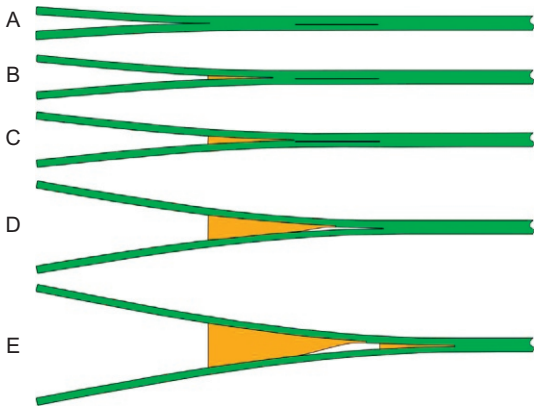

Figure 9.13 The two-crack model failure progression.

load–displacement response predicted by Rx-FEM match the experimental data well. A double peak load drop associated with the second crack propagation initiation is not observed in the experiment; however, it has been predicted both by conventional cohesive zone models (Alfano and Crisfield, 2001) as well as VCCT (Mabson et al., 2007). It is therefore concluded that the MIC modeling capability within Rx-FEM allows for simulation of multiple-crack propagation scenarios at the level of accuracy of the conventional techniques where the cracks are meshed explicitly.

9.6 Application to OCT specimens

Often matrix damage occurs well before ultimate failure and tends to cause redistribution of stress in the failing composite. With most notched composite test specimens, as soon as 0° fiber fracture begins to occur, final specimen failure is rapid and

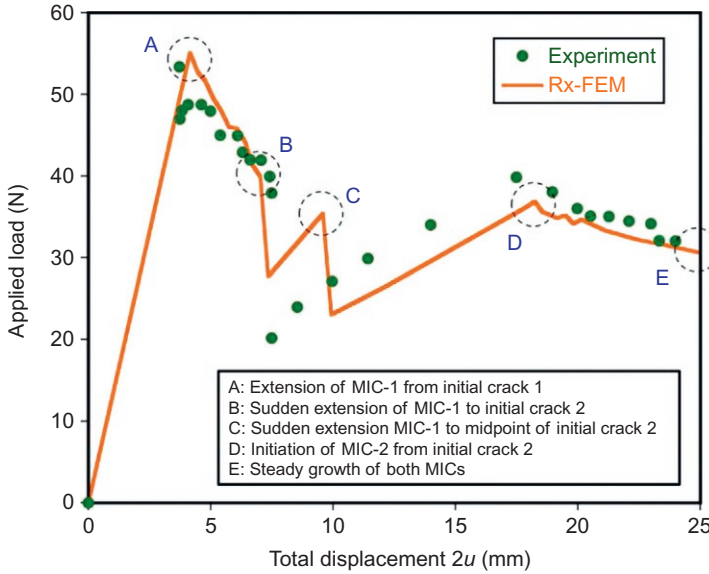

Figure 9.14 Load–displacement relationship for the two-crack problem.

catastrophic, providing the researcher with no means of investigating the effects of sub-critical damage on the progression of fiber failure.

To overcome this experimental dilemma, the OCT specimen was conceived at the University of British Columbia (Kongshavn and Poursartip, 1999). It was designed to represent laminate behavior of large aircraft structures. It has the advantage, depending on stacking sequence, of allowing stable formation of matrix damage and delamination ahead of the notch tip in the presence of 0° fiber fracture. This allows the examination of laminate failure in the context of evolving subcritical matrix damage in association with fiber breakage. The Rx-FEM DDM framework described was applied to this type of specimen in conjunction with an extensive experimental program conducted by Li et al. (2009) and additional experimental examination by Mollenhauer et al. (2012). The analysis was applied first to specimens dominated by delamination and transverse ply cracking and then to specimens exhibiting fiber damage in addition to matrix damage.

9.6.1 Experimental program

The material used to manufacture the specimens in this work was IM7/8552 carbon-epoxy pre-preg with a nominal cured ply thickness of 0.125 mm. Li et al. (2009) examined eight different layups, four with blocked plies and four with dispersed plies. All specimens were laid up as large panels, cured according to the manufacturer's recommendations, and cut to dimensions shown in Figure 9.15. Six specimens were obtained from each panel. Pin loading holes were drilled using tungsten carbide drills

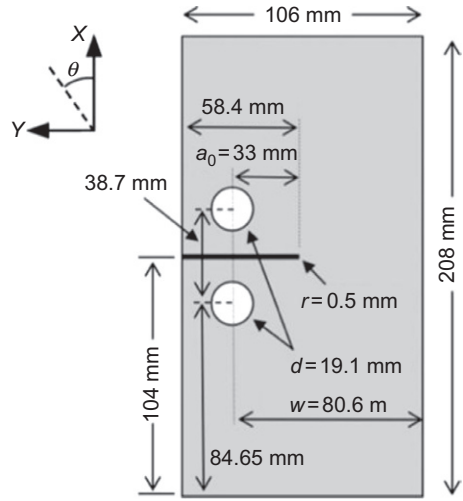

Figure 9.15 Dimensioned schematic of an overheight compact tension specimen.

Table 9.1 Stacking sequences of OCT specimens examined in Li et al.

Blocked-plies: exhibiting primarily matrix damage	Dispersed-plies: exhibiting fiber and matrix damage
$[0_2/90_2]_{2s}$	$[0/90]_{4s}$
$[0_4/90_4]_{2s}$	$[0/90]_{8s}$
$[45_2/90_2/-45_2/0_2]_s$	$[45/90/-45/0]_{2s}$
$[45_4/90_4/45_4/0_4]_s$	$[45/90/45/0]_{4s}$

and the notch was cut using a diamond-sintered cutting wheel with a 1 mm blade thickness. Table 9.1 contains a listing of the ply stacking sequences examined in the experimental effort of Li et al. (2009), of which the $[45_2/90_2/45_2/0_2]_s$, $[0_4/90_4]_{2s}$, and the $[45/90/-45/0]_{2s}$ specimens were examined experimentally and numerically in detail in the present work.

A screw-driven universal testing machine was used to load the OCT specimens through 19 mm diameter steel pins inserted through the holes shown in Figure 9.15. Pin opening displacement (POD) was obtained through an extensometer fixed to the ends of the loading pins. A set of five or six tests was conducted for each of the eight specimen types. In each of these sets, some were fully loaded until the specimen was damaged such that the load dropped to below half the peak load value. The other tests were interrupted at various load levels below the peak value.

Several of the specimens from Li et al. (2009) were examined in a 3D X-ray micro-computed tomography (μCT) unit by Mollenhauer et al. (2012). The advantage of this

type of system is that the resulting 3D array of intensity data (voxels) is a map of density in three dimensions through the specimen. To maximize the spatial resolution for this study, all specimens examined in the CT unit were initially cut using a diamond-sintered cutting wheel along the x-axis (see Figure 9.15) just to the left of the notch tip, resulting in 50 mm-wide specimens ready for CT examination. Final voxel spatial resolution was approximately 0.059 mm. Additionally, the dispersed-ply specimen was sectioned further by removing the undamaged free-edge region. CT scans of this specimen resulted in a voxel spatial resolution of 0.022 mm and allowed for better imaging of fiber breakage. Prior to μCT examination, all specimens examined were soaked in an X-ray enhancement solution as described in Mollenhauer et al. (2012).

The resulting images show cracks as bright lines against a dark gray background. A typical image is shown in Figure 9.16a. In this image, only cracking in one 0° ply is visible. In Figure 9.16b, delamination as well as ply cracking is visible. The delamination appears as a general lightening of the gray with a brighter outline at the delamination front. An important point regarding Figure 9.16b is that cracks appear to be running in two directions, which is contrary to expectations for a given ply. This is a result of the 0.059 mm deep voxel straddling the interface between two plies and averaging the density results from the portions of each ply embedded within the voxel. Recall that the nominal ply thickness is 0.125 mm, only slightly bigger than twice a 0.059 mm voxel dimension. Figure 9.16c shows both matrix cracking and fiber breakage.

9.6.2 Numerical modeling

Rx-FEM-based DDM framework implemented in BSAM (BSAM Users Manual, 2014) was used for analysis. Figure 9.17 shows an example of an analysis mesh generated within BSAM, in this case for the examination of matrix cracking in the $[45_2/90_2/45_2/0_2]_s$, the $[0_4/90_4]_{2s}$, and the $[45/90/-45/0]_{2s}$ specimens. Specimen geometry was matched as closely as possible to the actual test specimens. The only difference is that the actual specimen had a nearly square notch tip and the model contained a rounded blunt notch tip. Important to note is that the mesh used in all of the analyses

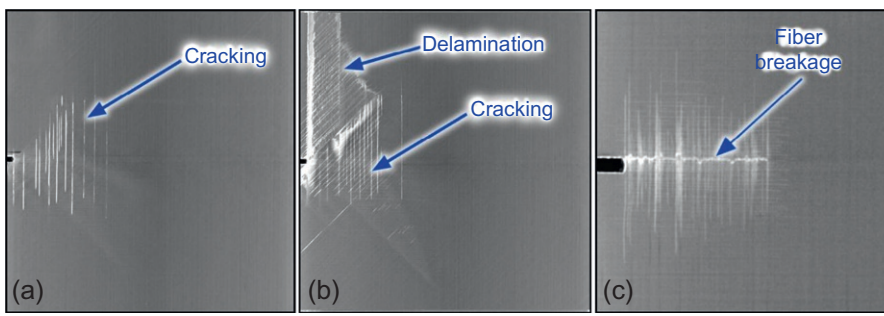

Figure 9.16 Example X-ray CT image slices containing ply cracking (a), cracking and delamination (b), and cracking and fiber breakage (c), respectively.

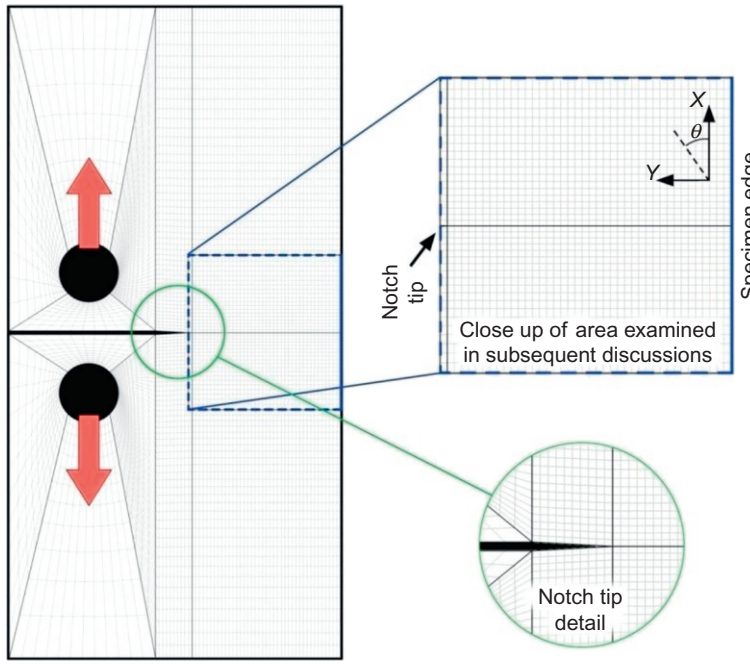

Figure 9.17 Representative OCT mesh used in analyses.

in this work contained one element through each ply thickness. This is consistent with the previous efforts of Jiang et al. (2007), who examined the effects of pre-implanted matrix cracks in laminated composites with open holes. The primary limitation imposed on the simulations by a mesh such as that shown in Figure 9.17 is that the crack density cannot exceed the mesh density. That is, a crack adjacent to another crack in a given ply must be located at least one full mesh line away, thus limiting the overall density of cracking.

The specimen thicknesses were matched by modeling half the specimen thickness and employing symmetry conditions about the specimen midplane. Material properties of the IM7/8552 pre-preg are shown in Table 9.2 and were obtained from Hallett et al. (2009) where specified, and by this chapter's authors otherwise. The simulations conducted in this work contain no calibrations, only experimentally obtained values. In addition, to obtain more realistic initial crack insertion patterns and mimic statistical material variability, quasi-random strength properties were generated across the coupon volume, following Gurvich (1999). Distributions of random transverse strength properties Y_t (tensile), Y_c (compressive), and shear strength, S, were assumed to follow a classical two-parameter Weibull law. The random distribution of strength was used only for crack initiation purposes. There was no variability introduced in the cohesive law.

Load was applied via specified x-displacements at the edges of the loading holes shown in Figure 9.17. Specifically, a positive x-displacement was applied along the

Table 9.2 Properties for an IM7/8552 lamina

Material property	Value
E_{11} (GPa) (Hinton and Soden, 1998)	161.0
E_{22}, E_{33} (GPa) (Hinton and Soden, 1998)	11.38
G_{12}, G_{13} (GPa) (Hinton and Soden, 1998)	5.17
G_{23} (GPa) (Hinton and Soden, 1998)	3.98
ν_{12}, ν_{13} (Hinton and Soden, 1998)	0.32
ν_{23} (Hinton and Soden, 1998)	0.44
α_1 (1/°C)	0.00
α_2 (1/°C)	3.00e−05
G_{Ic} (N/mm) (Hinton and Soden, 1998)	0.2
G_{IIc} (N/mm) (Hinton and Soden, 1998)	1.0
Y_t (MPa)	60.0
Y_c (MPa)	275.0
S (MPa)	90.0

top quadrant of the top loading hole and similarly, a negative x-displacement was applied along the bottom quadrant of the bottom loading hole. Symmetry conditions were applied on the plane $z = 0$. Finally, a single point in each hole was restricted in the y-direction to fully constrain rigid body motion of the numerical model. In addition to applied displacements, the OCT models were subjected to thermal loading of −150 °C consistent with a specimen cool-down from the curing process.

During a typical simulation, the OCT specimen is subjected to ever-increasing POD. At each displacement step, the crack initiation criterion is checked. As discussed previously, if the criterion is exceeded, then a MIC crack surface is inserted in the proper ply and at the proper location. It is important to note that this crack surface is *not* an open crack but allows the cohesive formulation of Turon et al. (2006) to guide the opening of the crack. After the crack surface(s) are inserted, an iterative approach is used to advance the opening of the crack according to Turon et al. (2006). Once convergence is attained, the next displacement step is applied and the process is repeated. At each displacement step, cohesive layers between plies are allowed to advance delaminations, also according to Turon et al. (2006). After each displacement step, data output files are written that contain a complete map of displacements, strains, stresses, the crack damage variable, and the delamination damage variable. Also recorded are the applied loads to the "pin" surfaces. In this work, each displacement step corresponded to an increase in POD of 0.076 mm.

9.6.3 Results comparison

Figure 9.18 shows damage extent comparisons for the $[45_2/90_2/45_2/0_2]_s$ blocked-ply specimen. In this figure, the delaminations are colored according to their respective interfaces whereas the cracking is either black (model results) or white (X-ray μCT

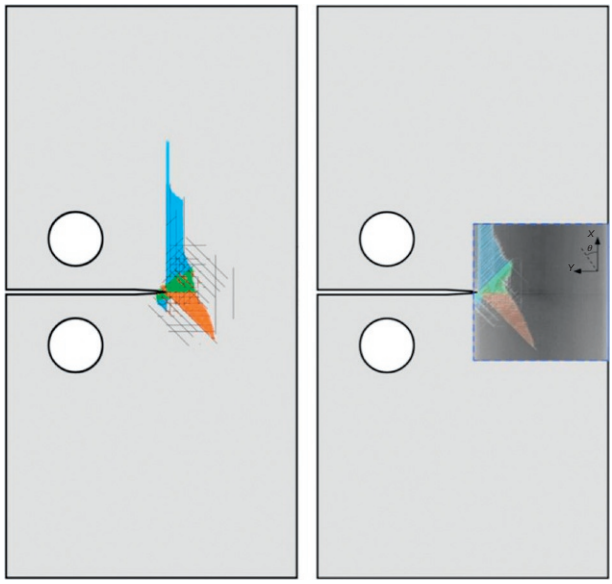

Figure 9.18 Superimposed comparison view of cracking and matrix damage for a $[45_2/90_2/45_2/0_2]_s$ specimen obtained through experiment (μCT) and modeling.

results). The results in Figure 9.18 show all damage throughout the specimen superimposed on the specimen outline. X-ray μCT slice images were extracted and stacked together for comparison. The numerical modeling effort produces damage distributions that are quite similar to those resulting from experiment.

Close-ups of the simulated and μCT imaged damage extent are shown in Figure 9.19. In these images, both for simulation and μCT, the delaminations are shown at their respective interfaces. The cracks, indicated by black lines (model) or white lines (μCT), have been superimposed through the thickness of the two plies adjacent to the interface where the delamination is shown. Immediately obvious from these image comparisons is the similarity between the simulated damage patterns and the experimental images. The simulated delaminations share the same characteristics that are seen in the μCT images. Some of the delamination edges are bounded by crack edges, and others appear bounded by crack terminations, exactly as observed in the X-ray images. Some small features in the CT images are present in the simulations. An example of this is seen in Figure 9.19c, where the bottom edge of the CT delamination has a protrusion down away from a generally −45° straight edge. This protrusion is represented in the simulated pattern as by two protrusions in similar locations. A comparison of crack spacing and extent indicates a reasonably close match between simulation and experiment. Due to limitations on the simulated crack spacing, as mentioned previously, the simulated cracks are spaced more coarsely than shown in experiment; however, their extent and locations are close to the X-ray images.

A comparison of POD versus applied load for the $[0_4/90_4]_{2s}$ and $[45_2/90_2/45_2/0_2]_s$ specimens are shown in Figure 9.20a and b, respectively. Figure 9.20a shows that the cross-ply simulation results track very closely with the experiment, including the

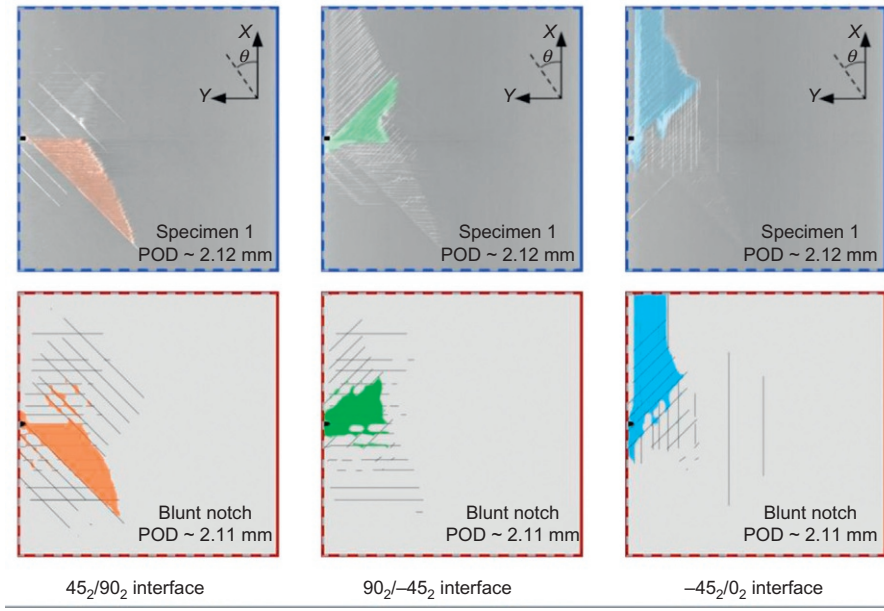

Figure 9.19 Magnified comparison view of cracking and matrix damage for $[45_2/90_2/45_2/0_2]_s$ specimen obtained through experiment (μCT) and modeling.

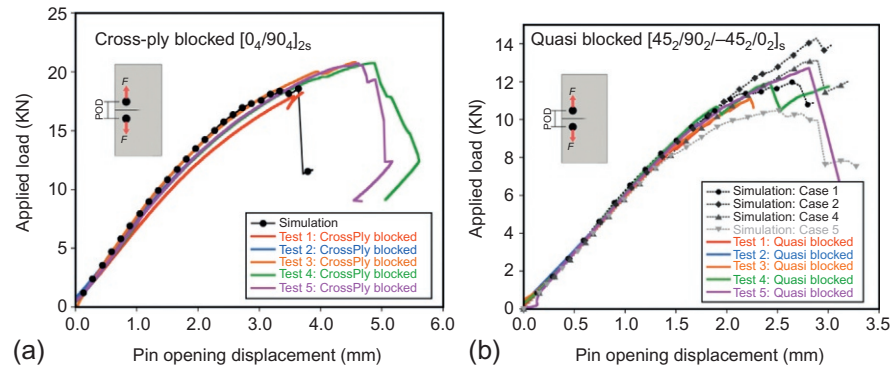

Figure 9.20 Simulated and experimental load–displacement curves for (a) the $[0_4/90_4/45_2/0_2]_{2s}$ specimen and (b) the $[45_2/90_2/45_2/0_2]_s$ specimen with simulations from multiple realizations of statistical strength distribution.

softening beginning around 14 kN. The simulation results from the quasi-isotropic specimen, Figure 9.20b, are from four instantiations of the Weibull distribution of matrix strength parameters, as discussed above. Six instantiations were simulated, but for clarity only four are shown. These are superimposed on the experimental

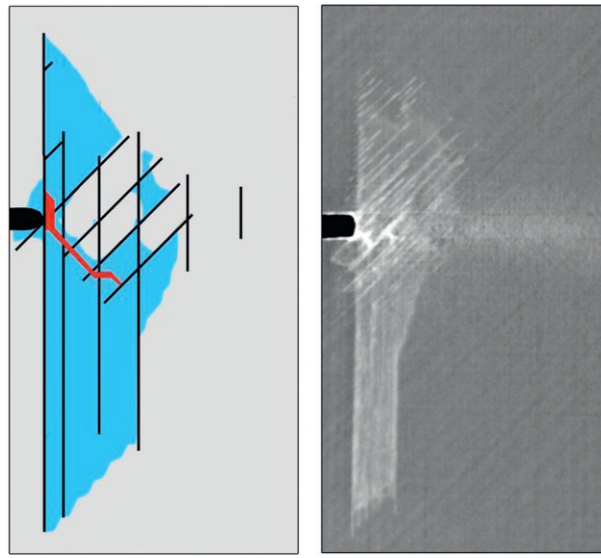

Figure 9.21 Comparison of simulated and μCT damage extent from the $[45/90/-45/0]_{2s}$ specimen at the middle −45/0 interface. Note: simulated fiber damage in red, matrix cracking in black, and delamination in blue.

results and show generally good agreement. The distribution of behavior resulting from the simulations of this specimen appears to be wider spread than what is found in the experimental results. One thing to note concerning the experimental results in Figure 9.20 are that three specimens from each set were removed from loading for examination with X-ray CT. The set of curves, therefore, does not show the complete spread of behavior.

Simulation results for the $[45/90/-45/0]_{2s}$ specimen are shown in Figures 9.21 and 9.22. Damage extent at the −45/0 interface closest to the midplane is compared in Figure 9.21. This specimen exhibited significant fiber failure as indicated by the red line in Figure 9.21 and modeled with the property degradation method described previously. Transverse cracking is represented by black lines and delaminations are colored light blue in the simulation results. Generally, the shape of the damage is quite similar, although the simulated damage covers a slightly greater area than the experimentally observed damage. The POD versus load results are compared with experimental results in Figure 9.22, showing excellent agreement.

9.7 Demonstration of DDM on a plain weave textile

Damage development in textile composite materials is quite complex, even when compared with the complex damage seen in laminated composites. A given tow will exhibit all of the damage modes generally seen in a laminate including transverse

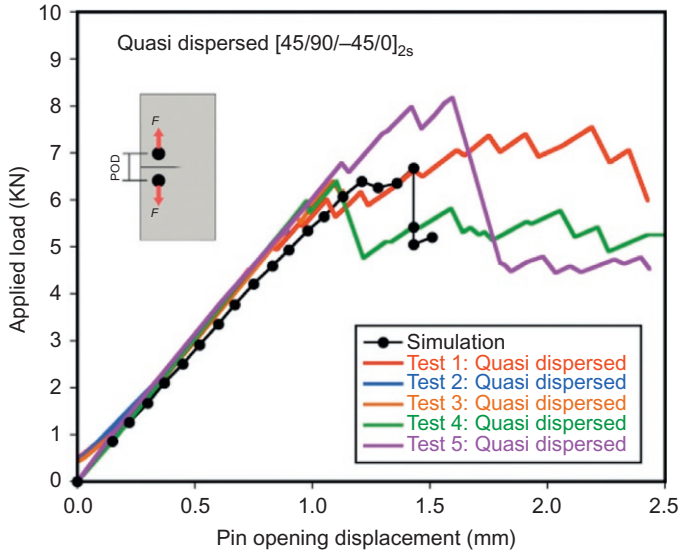

Figure 9.22 Simulated load–displacement curves from the $[45/90/-45/0]_{2s}$ specimen compared with the experimentally obtained load–displacement curves.

matrix cracking and fiber damage. Additionally, the tow could experience delamination between neighboring tows and matrix pockets, analogous to delamination between lamina. However, these inter-tow delamination surfaces will no longer be planar and may be suppressed as tows undulate through the textile. As with laminates, transverse matrix cracking in one tow will affect the nature of the delaminations between tows. Tow cracking must also account for the variation in fiber direction along the length of the tow. Finally, cracking in matrix pockets is both affected by and will affect damage in neighboring tows. This extremely complex system of damage in textiles is, therefore, an ideal candidate for simulation with a DDM approach, a demonstration of which is presented here.

A compacted virtual fiber preform was generated using the multichain digital element method described in Zhou et al. (2004). This was used to generate a plain-weave textile PMC numerical model. The MIC cracking framework was combined with delamination and property degradation fiber failure to model damage evolution in this textile model. Additionally, damage in matrix pockets between tows was accounted for through use of the property degradation method described above. The axial displacement and schematic of boundary conditions are shown in Figure 9.23 with the matrix removed for clarity. The specimen measured 7 mm in the warp direction, 3 mm in the weft direction, and was 0.375 mm thick. Material properties used for modeling were the same as shown in Table 9.2. The specimen was loaded via an axial (warp direction) tensile load with a small transverse (weft direction) shearing load as indicated in Figure 9.23.

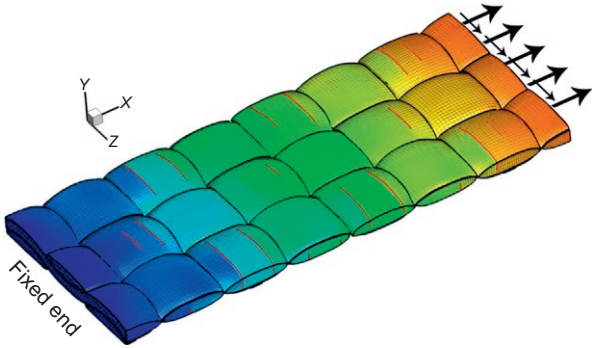

Figure 9.23 Axial displacements with transverse matrix cracks in red at one load step before failure.

All modes of damage were present in the modeled specimen at failure. Transverse matrix cracking in the weft tows is clearly visible as displacement discontinuities in Figure 9.23 with the cracks highlighted in red. Failure in the matrix, although for brevity not shown here, was clearly visible. Delamination damage and fiber fracture were also present. Figure 9.24a shows delamination damage on the surface of the warp tows

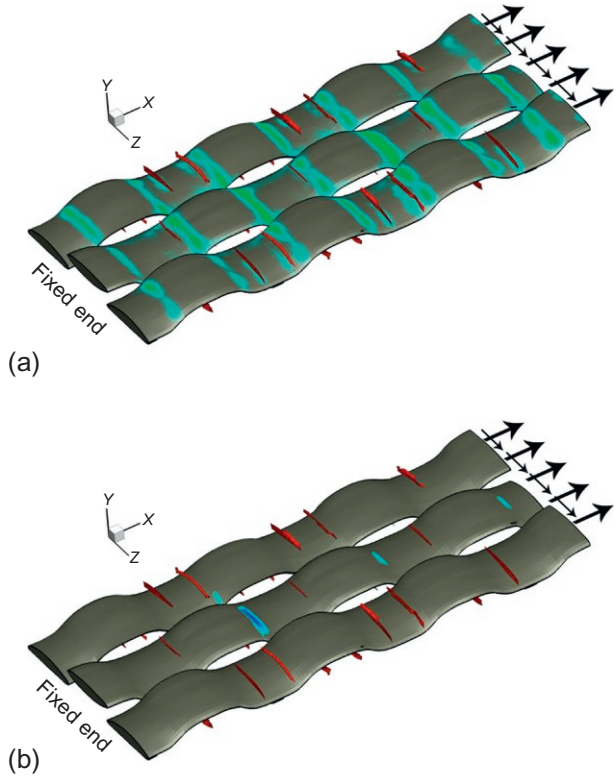

Figure 9.24 Warp tows of plain weave specimen showing transverse matrix cracking in red with (a) delamination damage in green or (b) fiber damage in blue.

with the associated weft-tow matrix cracks floating above and below the tows. Evidence of the weft-tow crack influence on delamination is clearly seen. Similarly, Figure 9.24b shows the initial fiber damage. The specimen failed completely on the next load step with the failure emanating from the largest region of fiber damage in the middle tow, visible in Figure 9.24b.

9.8 Conclusions

A Rx-FEM has been developed and implemented, allowing the modeling of complex interactive networks of matrix cracks and delaminations in a DDM framework. The regularized formulation preserves the element Gauss integration schema for arbitrary cracking direction and allows straightforward connections between neighboring plies with different orientations of properties and cracks. A cohesive zone method is used in conjunction with Rx-FEM to predict the damage associated with matrix cracking and delamination evolution. Ply level stiffness, along with strength and fracture toughness properties measured in independent experiments, are the only properties required for analysis.

Experimental observation was used extensively to guide development and validate the DDM framework described here. Initial observations of strain redistribution, localization, and concentration reduction in laminates with advancing matrix damage led to the development of the Rx-FEM capability. Investigation of a two-crack DCB specimen validated the predictive capability when compared with DCB load–displacement curves. Finally, application of the DDM framework for simulation of a variety of OCT specimen stacking sequences proved useful in examining the effectiveness of the simulation method. Comparison with matrix-dominated damage experimental results showed favorable predictions of both load–displacement behavior as well as matrix damage extent and location. The same proved true for application of the DDM to an OCT specimen with extensive fiber failure as well as matrix damage.

The DDM methodology appears to be well suited to a large number of complicated damage evolution problems in composite materials. It has been applied to unidirectional lamina, multidirectional laminates, notched laminates, and now textile composites. Experimental efforts to validate textile simulation results are currently underway. The DDM methodology is being extended to include other, important aspects of damage simulation in composite materials. These include addressing fatigue damage evolution, microscale geometric specimens, realistic stochastic considerations, and thermal-oxidative damage growth. The DDM framework presented herein provides a predictive tool for modeling complex composite material damage evolution.

References

Alfano, G., Crisfield, M.A., 2001. Finite element interface models for the delamination analysis of laminated composites: mechanical and computational issues. Int. J. Numer. Methods Eng. 50 (7), 1701–1736.

Allix, O., Guedra-Degeorges, D., Guinard, S., Vinet, A., 2000. Analyse de la tenue aux impacts à faible vitesse et faible énergie des stratifiés composites par la mécanique de l'Endommagement. Méc. Ind. 1 (1), 27–35.

Anderssen, R., Gradin, P.A., Gustafson, C.G., 1998. Prediction of the stiffness degradation in cross-ply laminates due to transverse matrix-cracking: an energy method approach. Adv. Compos. Mater. 7 (4), 325–346.

Benvenuti, E., 2008. A regularized X-FEM framework for embedded cohesive interfaces. Comput. Methods Appl. Mech. Eng. 197, 4367–4378.

Benvenuti, E., Tralli, A., Ventura, G., 2008. A regularized XFEM model for the transition from continuous to discontinuous displacements. Int. J. Numer. Methods Eng. 74, 911–944.

Berthelot, J.M., Leblond, P., El Mahi, A., Le Corre, J.F., 1996. Transverse cracking of cross-ply laminates. 1. Anal. Compos. A: Appl. Sci. Manuf. 27A (10), 989–1001.

BSAM Users Manual, 2014, University of Dayton Research Institute, Dayton, Ohio, USA.

Camanho, P.P., Matthews, F.L., 1999. Stress analysis and strength prediction of mechanically fastened joints in FRP: a review. Compos. Part A 28A, 529–547.

Camanho, P.P., Maimi, P., Davila, C.G., 2007. Prediction of size effects in notched laminates using continuum damage mechanics. Compos. Sci. Technol. 67, 2715–2727.

Chen, B.Y., Pinho, S.T., de Carvalho, N.V., Baiz, P.M., Tay, T.E., 2014. A floating node method for modeling of discontinuities in composites. Eng. Fract. Mech. 127, 104–134. http://dx.doi.org/10.1016/j.fracmech.2014.06.018.

Dávila, C.G., Camanho, P.P., Rose, C.A., 2005. Failure criteria for FRP laminates. J. Compos. Mater. 39 (4), 323–345.

de Carvalho, N.V., Chen, B.Y., Pinho, S.T., Baiz, P.M., Tay, T.E., 2013. Floating node method and virtual crack closure technique for modeling matrix cracking—delamination migration. NASA/CR-2013-218022.

de Carvalho, N.V., Ratcliffe, J.G., Chen, B.Y., Pinho, S.T., Baiz, P.M., Tay, T.E., 2014. Modeling quasi-static and fatigue-driven delamination migration. In: American Society for Composites 29th Technical Conference, San Diego, CA, September 8–10. (Paper 661).

Fang, X.J., Zhou, Z.Q., Cox, B.N., Yang, Q.D., 2011. High-fidelity simulations of multiple fracture processes in laminated composites. J. Mech. Phys. Solids 59, 1355–1373.

Gurvich, M.R., 1999. Strength size effect for anisotropic brittle materials under random stress state. Compos. Sci. Technol. 59 (11), 1701–1711.

Hallett, S.R., Green, B.G., Wisnom, M.R., 2007. An experimental investigation into the tensile strength scaling of unnotched composites. Compos. Part A 38 (3), 867–878.

Hallett, S.R., Green, B.G., Jiang, W.J., Wisnom, M.R., 2009. An experimental and numerical investigation into the damage mechanisms in notched composites. Compos. Part A 40 (5), 613–624.

Hansbo, A., Hansbo, P., 2002. An unfitted finite element method for the simulation of strong and weak discontinuities in solid mechanics. Comput. Methods Appl. Mech. Eng. 193 (47–48), 5537–5552.

Hinton, M.J., Soden, P.D., 1998. Predicting failure in composite laminates: the background to the exercise. Compos. Sci. Technol. 58 (7), 1001–1010.

Iarve, E.V., 2003. Mesh independent modeling of cracks by using higher order shape functions. Int. J. Numer. Methods Eng. 56, 869–882.

Iarve, E.V., Mollenhauer, D.H., Kim, R., 2005. Theoretical and experimental investigation of stress redistribution in open hole composite laminates due to damage accumulation. Compos. Part A 36 (2), 163–171.

Iarve, E.V., Mollenhauer, D.H., Whitney, T.J., Kim, R., 2006. Strength prediction in composites with stress concentrations: classical Weibull and critical failure volume methods with micromechanical considerations. J. Mater. Sci. 41 (20), 6610–6622.

Iarve, E.V., Gurvich, M.R., Mollenhauer, D.H., Rose, C.A., Dávila, C.G., 2011. Mesh-independent matrix cracking and delamination modeling in laminated composites. Int. J. Numer. Methods Eng. 88 (8), 749–773.

Jiang, W.G., Hallett, S.R., Green, B.G., Wisnom, M.R., 2007. A concise interface constitutive law for analysis of delamination and splitting in composite materials and its application to scaled notched tensile specimens. Int. J. Numer. Methods Eng. 69, 1982–1995.

Kawashita, L.F., Bedos, A., Hallett, S., 2012. Modelling mesh independent transverse cracks in laminated composites with a simplified cohesive segment method. CMC 32 (2), 133–158.

Kongshavn, I., Poursartip, A., 1999. Experimental investigation of a strain-softening approach to predicting failure in notched fibre-reinforced composite laminates. Compos. Sci. Technol. 59 (1), 29–40.

Kortschot, M.T., Beaumont, P.W.R., 1989. Damaged-based notched strength modeling: summary. In: Proceedings of the ASTM Conference on Fracture and Fatigue of Composites, Orlando, USA, pp. 596–616.

Krueger, R., 2002. The virtual crack closure technique: history, approach and applications. NASA/CR-2002-211628.

Ladevèze, P., Lubineau, G., Marsal, D., 2006. Towards a bridge between the micro- and mesomechanics of delamination for laminated composites. Compos. Sci. Technol. 66, 698–712.

Li, D.S., Wisnom, M.R., 1997. Evaluating Weibull parameters for transverse cracking in cross-ply laminates. J. Compos. Mater. 31 (9), 935–951.

Li, X., Hallett, S.R., Wisnom, M.R., Zobeiry, N., Vaziri, R., Poursartip, A., 2009. Experimental study of damage propagation in over-height compact tension tests. Compos. Part A 40, 1891–1899.

Li, W., Yang, Q.D., Su, Y.U., Ling, D.S., 2013. An accurate and efficient augmented finite element method for arbitrary crack interactions. J. Appl. Mech. 80 (4), 041033.

Ling, D., Yang, Q.D., Cox, B.N., 2009. An augmented finite element method for modeling arbitrary discontinuities in composite materials. Int. J. Fract. 156 (1), 53–73.

Lubineau, G., Ladevèze, P., 2008. Construction of a micromechanics-based intralaminar mesomodel, and illustrations in ABAQUS/standard computational. Mater. Sci. 43, 137–145.

Mabson, G., Deobald, L.R., Dopker, B., Hoyt, D.M., Baylor, J.S., Graesser, D.L., 2007. Fracture interface elements for static and fatigue analysis. In: Proceedings of the ICCM-16, July 8–13, Kyoto, Japan.

Maimí, P., Camanho, P.P., Mayugo, J.A., Dávila, C.G., 2007a. A continuum damage model for composite laminates: part I—constitutive model. Mech. Mater. 39 (10), 897–908.

Maimí, P., Camanho, P.P., Mayugo, J.A., Dávila, C.G., 2007b. A continuum damage model for composite laminates: part II—computational implementation and validation. Mech. Mater. 39 (10), 909–919.

Moes, N., Dolbow, J., Belytschko, T., 1999. A finite element method for crack growth without remeshing. Int. J. Numer. Methods Eng. 46 (1), 131–150.

Mollenhauer, D.H., Iarve, E.V., Kim, R., Langley, B., 2006. Examination of ply cracking in composite laminates with open-holes: a moiré interferometric and numerical study. Compos. Part A 37 (2), 282–294.

Mollenhauer, D., Ward, L., Iarve, E., Putthanarat, S., Hoos, K., Hallett, S., Li, X., 2012. Simulation of discrete damage in composite overheight compact tension specimens. Compos. Part A 43 (10), 1667–1679.

Nikishov, Y., Makeev, A., Seon, G., 2009. Finite element-based simulations of damage in composites. Presented at the American Helicopter Society 65th Annual Forum, Grapevine, Texas, May 27–29.

Nikishov, Y., Makeev, A., Seon, G., 2010. Simulation of damage in composites based on solid finite elements. J. Am. Helicopter Soc. 55 (4), 42009.

Oliver, J., Huespe, A.E., Sánchez, P.J., 2006. A comparative study on finite elements for capturing strong discontinuities: E-FEM vs X-FEM. Comput. Methods Appl. Mech. Eng. 195, 4732–4752.

Pagano, N.J., Schoeppner, G.A., 2000. Delamination of polymer matrix composites: problems and assessment. Compr. Compos. Mater. 2, 433–528.

Patzak, B., Jirásek, M., 2003. Process zone resolution by extended finite elements. Eng. Fract. Mech. 70, 957–977.

Pinho, S.T., Dávila, C.G., Camanho, P.P., Iannuci, L., Robinson, P., 2005. Failure modes and criteria for FRP under in-plane or three-dimensional stress states including shear nonlinearity. NASA/TM-2005-213530.

Post, D., Han, B., Ifju, P., 1994. High Sensitivity Moiré: Experimental Analysis for Mechanics and Materials. Springer-Verlag Inc., New York.

Robinson, P., Besant, T., Hitchings, D., 1999. Delamination growth prediction using a finite element approach. In: 2nd ESIS TC4 Conference on Polymers and Composites, Les Diablerets, Switzerland.

Rosen, B.W., 1964. Tensile failure of fibrous composites. AIAA J. 2, 1985–1991.

Song, K., Li, Y., Rose, C., 2011. Continuum damage mechanics models for the analysis of progressive failure in open-hole tension laminates. In: 52nd AIAA Structures Structural Dynamics and Materials Conference, Denver, Colorado.

Spearing, S.M., Beaumont, P.W.R., 1992. Fatigue damage mechanics of composite materials. I: experimental measurement of damage and post-fatigue properties. Compos. Sci. Technol. 44 (2), 159–168.

Sun, Z., Daniel, I.M., Luo, J.J., 2003. Statistical damage analysis of transverse cracking in high temperature composite laminates. Mater. Sci. Eng. A: Struct. Mater. Prop. Microstruct. Process. A341 (1–2), 49–56.

Swindeman, M.J., Iarve, E.I., Brockman, R.A., 2013. Strength prediction in open hole composite laminates by using discrete damage modeling. AIAA J. 51 (4), 936–945.

Tang, S.C., 1991. A progressive failure model for composite laminates containing openings. J. Compos. Mater. 25, 556–577.

Tay, T.E., 2003. Characterization and analysis of delamination fracture in composites: an overview of developments from 1990 to 2001. Appl. Mech. Rev. 56 (1), 1–32.

Tay, T.E., Liu, G., Tan, V.B.C., Sun, X.S., Pham, D.C., 2008. Progressive failure analysis of composites. J. Compos. Mater. 42 (18), 1921–1966.

Turon, A., Camanho, P.P., Costa, J., Dávila, C.G., 2006. A damage model for the simulation of delamination in advanced composites under variable-mode loading. Mech. Mater. 38 (11), 1072–1089.

Van der Meer, F.P., 2012. Mesolevel modeling of failure in composite laminates: constitutive, kinematic and algorithmic aspects. Arch. Comput. Methods Eng. 19 (3), 381–425.

Van der Meer, F.P., Sluys, L.J., 2009. A phantom node formulation with mixed mode cohesive law for splitting in laminates. Int. J. Fract. 158 (2), 107–124.

Van der Meer, F.P., Oliver, C., Sluys, L.J., 2010. Computational analysis of progressive failure in a notched laminate including shear nonlinearity and fiber failure. Compos. Sci. Technol. 70 (4), 692–700.

Van der Meer, F.P., Sluys, L.J., Hallett, S.R., Wisnom, M.R., 2012. Computational modeling of complex failure mechanisms in laminates. J. Compos. Mater. 46 (5), 603–623.

Varna, J., Berglund, L., 1991. Multiple transverse cracking and stiffness reduction in cross-ply laminates. J. Compos. Technol. Res. 13 (2), 97–106.

Varna, J., Berglund, L., 1993. Two-dimensional transverse cracking in $[0_m/90_n]_s$ cross-ply laminates. Eur. J. Mech. A Solids 12 (5), 699–723.

Whitney, J.M., 1987. Structural Analysis of Laminated Anisotropic Plates. Technomic Publishing, Lancaster, PA.

Wisnom, M.R., Hallett, S.R., 2009. The role of delamination in strength, failure mechanism and hole size effect in open hole tensile tests on quasi-isotropic laminates. Compos. Part A 40 (4), 335–342.

Wisnom, M.R., Khan, B., Hallett, S.R., 2008. Size effects in unnotched tensile strength of unidirectional and quasi-isotropic carbon/epoxy composites. Compos. Struct. 84, 21–28.

Zhou, G., Sun, X., Wang, Y., 2004. Multi-chain digital element analysis in textile mechanics. Compos. Sci. Technol. 64, 239–244.

Zhou, Z.Q., Fang, X.J., Cox, B.N., Yang, Q.D., 2010. The evolution of a transverse intra-ply crack coupled to delamination cracks. Int. J. Fract. 165 (1), 77–92.

A new augmented finite element method (A-FEM) for progressive failure analysis of advanced composite materials

10

Q. Yang, M. Naderi
University of Miami, Coral Gables, FL, USA

10.1 Introduction

Composite materials are now widely used in many key areas such as aerospace, defense, renewable energy, and offshore pipelines. Recent high-profile examples include the Boeing 787 Dreamliners, ultra-lightweight composite blades for windmills, and multi-layered FRPC-steel pipelines for deep-sea oil transportation. Multiscale hierarchical microstructures are usually integrated into such structures to achieve multifunctional purposes and/or to further gain the weight savings. Key advantages of composites over the traditional structural metal and metal alloys include significant weight savings, better reliability and durability, and lower manufacturing and maintenance costs. In particular, composite engineering offers the exciting possibility to design the hierarchical features in micro- or mesoscale to achieve the desired structural performance through the optimization process (Cox and Yang, 2006; LLorca et al., 2011; Yang et al., 2011).

However, due to the relatively short history of composite usage as primary load-bearing structural components, the current knowledge base remains inadequate for the confident design of safe and durable composite structures. The uncertainty of composite structures remains high, and damage-tolerance analysis must be considered as an integral part in the design process. However, unlike structural metals, which are homogeneous and isotropic, composites are inherently inhomogeneous and anisotropic. Microscopic flaws and imperfections are inevitably present in these materials due to manufacturing processes. Currently the damage tolerance and durability design relies heavily on large experimental test programs that are extremely costly and time consuming. High-fidelity estimation/prediction of composite strength at structural scale remains elusive despite decades of intensive research (Kaddour et al., 2013; Soden et al., 1998; Fawcett et al., 1997). High-fidelity simulation capabilities that can offer efficient and accurate strength and durability predictions based on constituent materials properties can greatly reduce the costly experimental inputs.

It proves very changing to faithfully predict the ultimate strength of composites due to the fact that almost all composites exhibit complex progressive damage evolution phenomena before complete failure. For example, a composite laminate will typically develop noncritical intraply cracks (transverse cracks in off-axial plies and

Numerical modelling of failure in advanced composite materials. http://dx.doi.org/10.1016/B978-0-08-100332-9.00010-4
Copyright © 2015 Elsevier Ltd. All rights reserved.

longitudinal splits in 0^0-plies) far below the ultimate load, which facilitates local delaminations between neighboring plies. These damage processes continuously evolve in a nonlinearly coupled manner and eventually lead to the formation of large delaminations, which in turn cause significant fiber breakage in primary load-bearing plies and lead to ultimate structural failure (Hallett and Wisnom, 2006a; Pierron et al., 2007). Whereas it is desired from a damage-tolerance point of view, predicting such progressive damage evolution up to ultimate failure proves to be very challenging.

Owing to recent developments in numerical modeling methods and high-resolution experimental characterization, significant advances in composite strength prediction, especially in continuous fiber-reinforced composite laminates, have been made in the past decade (Cox and Yang, 2006; LLorca et al., 2011; Van de Meer, 2012; Cox et al., 2014). This was enabled by (1) the development of advanced finite element methods (FEMs), including the extended finite element method (X-FEM, e.g., Huynh and Belytschko, 2009; Dolbow et al., 2001; Iarve et al., 2011; Iarve et al., 2005), Phantom node method (PNM) (e.g., Van de Meer et al., 2010; Van de Meer and Sluys, 2009; de Borst et al., 2006), and the PNM-based augmented FEM (PNM-based A-FEM, e.g., Ling et al., 2009; Yang et al., 2010a; Fang et al., 2011a; Liu et al., 2014); and (2) the nonlinear cohesive zone models (CZMs) for discrete fracture events in composites (e.g., Yang et al., 1999; Yang and Cox, 2005; Turon et al., 2006; Wisnom and Chang, 2000; Hallett and Wisnom, 2006b; Xu and Needleman, 1994; Hutchinson and Evans, 2000). The key is to embed CZM descriptions for major damage modes into the advanced FEM formulations so that the discrete cracking events can be initiated and propagated at the locations determined by local stresses in response to external loads. For a more comprehensive review of the recent advances and the remaining outstanding numerical and material issues associated with such progressive damage modeling in composite laminates, the readers are referred to the recent review article by Van de Meer (2012).

Figure 10.1 gives a recent example of successful analysis coupled ply-cracking and delamination in a double-notched tension specimen using the PNM-based A-FEM. To achieve such a high-fidelity prediction, several key elements have to be considered simultaneously in the numerical framework: (1) the numerical model should allow for crack/discontinuity initiation from a pristine continuum at locations determined by local stress environments; (2) carefully calibrated cohesive laws for crack/discontinuity evolution and propagation; (3) crack/discontinuity initiation criteria that account for the constraining effects from neighboring plies (*in situ* strength, e.g., Davila et al., 2005; Camanho et al., 2006); and (4) correct representation of the shear nonlinearity at ply level (Fang et al., 2011a; Wisnom and Chang, 2000; Chang et al., 1991). In addition, special numerical treatment is needed to correctly account for the coupling between the cracked ply elements and the interfacial cohesive elements. Otherwise, correct stress transfer is not always guaranteed and numerical stress locking may occur (Fang et al., 2011b; Ling et al., 2011; Yang et al., 2010b).

Compared to the multidirectional laminates, the material heterogeneity in textile composites makes it far more challenging in strength prediction. Unlike in laminates where the individual plies can be homogenized using orthotropic continuum theory (before cracking) and there are well-defined interlaminar interfaces that facilitate the meshing and modeling with explicit cohesive zone elements, textile composites

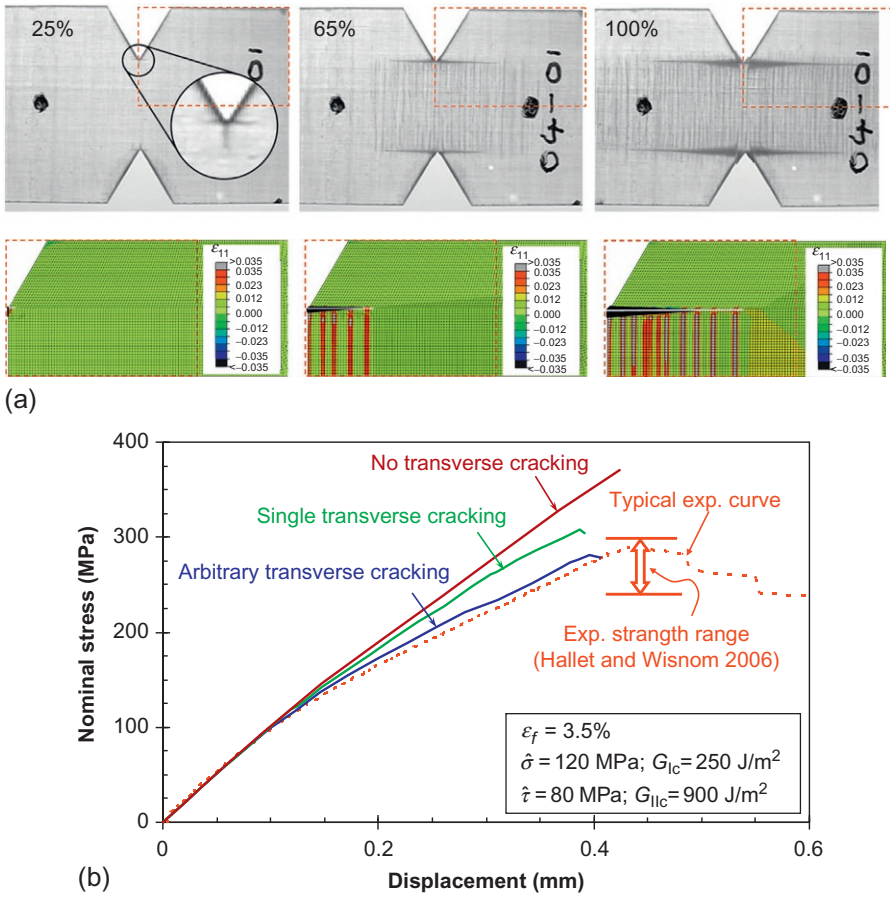

Figure 10.1 (a) Comparison of experimentally observed and the simulated nonlinearly coupled, multiple cracking systems in a DNT specimen. (b) Direct comparison of stress–displacement curves showing enabling arbitrary cracking gives much superior results. The predicted transverse crack density, split-crack growth rate, delamination shape and area, are all part of excellent if experimental results (Fang et al., 2011a). All damages are generated automatically with the cohesive model parameters (in the inset of panel b) calibrated from literature data. Fang et al. (2011a).

contain complex material heterogeneity highly dependent on the spatial reinforcement architectures of fiber tows. In such materials, heterogeneity poses special problems with the accurate prediction of local stress and strain fields, which can vary strongly with local material features; and with predicting cracks and localized damage bands, which can appear during damage evolution not only on the material boundaries, but also on other surfaces that cannot be specified *a priori*.

The material heterogeneity issue of textile composites cannot be resolved adequately by mainstream formulations of conventional materials/structures modeling,

owing to the complex interaction between fiber tow architecture and constituent material heterogeneity, which are on the same scale as that of the features of the structures. This negates the common strategy of homogenizing the material properties in simulations. The heterogeneity arises from the distinct fiber tows in the textile, which are strongly anisotropic and their shapes may be significantly distorted due to manufacturing process (Figure 10.2). The tows are typically $\sim$0.1–1 mm in lateral dimension, which is of the same order of the panel thickness ($1 \sim 10$ mm). Furthermore, the interlacing pattern of an integral textile structure, which has profound impact on the elastic properties and failure strength (Morris et al., 1989; Cox et al., 1994, 1996), can be quite complex, involving many hundreds of geometrically dissimilar tow segments or local tow arrangements. The structure will generally be subject to nonperiodic mechanical and thermal loads, including spatial and temporal peaks. In a piece of structure of relevant size, it is so far an unresolved challenge to develop a mesh that deals with the interlacing architecture, the heterogeneity of the tows, and general loads, while maintaining computational tractability. The challenging in strength prediction can be seen from Figure 10.2. The randomly distributed matrix-rich pockets have to be explicitly considered because they are susceptible to microcrack formation at relatively small loads. The complex coupling of all the nonlinear processes associated with crack nucleation, bifurcation, and deflection must be adequately captured.

The above challenges require the establishment of numerical modeling platforms that can deal with not only the arbitrary cracking issue, but also the issue of arbitrary crack interaction such as crack merging and crack bifurcation, again, without any *a priori* knowledge of the locations and load levels at which such events should happen. Unfortunately, the aforementioned advanced numerical methods (X-FEM, PNM-based A-FEM) are all very inflexible in dealing with multiple-crack merging

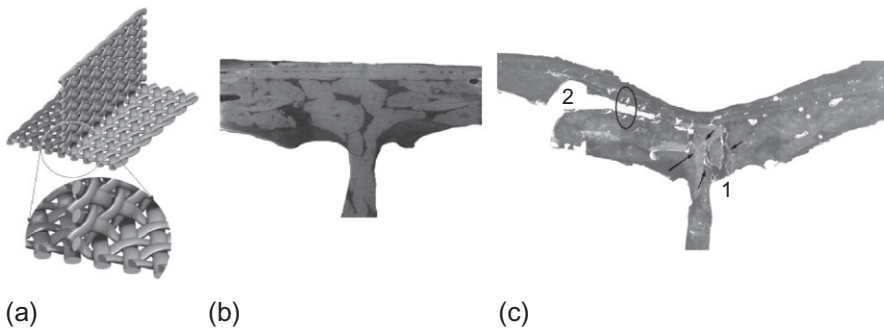

Figure 10.2 (a) An integrally woven T-stiffener perform with idealized tow architecture; (b) cross section of the final product after draping, tooling, and matrix infiltration; and (c) the postmortem micrograph after being subjected to failure load in a pull-off test (Yang et al., 2003). During the pull-off test, a crack was initiated at location 1 but was quickly deflected and diffused into multiple cracks, as shown by the arrows, due to fiber tow interlacing. At a later stage, a second crack initiated at location 2 and this crack moved into the interface between the skin and the stiffener, which led to final failure.
Yang et al. (2003).

or bifurcation. This is because, in these methods each individual crack requires its own additional copy of degree of freedoms (DoFs) (X-FEM) or extra-node copies (PNM-based A-FEM) to describe the discontinuous displacement field associated with it. Tracing the evolution of complex fracture surfaces of multiple cracks quickly becomes extremely tedious and numerically burdensome because, in such cases, there are no effective tracking algorithms that can judiciously assign different copies of DoFs or nodes to different cracks for complex crack configurations.

Therefore it is beneficial to seek numerical methods that can account for arbitrary discontinuities and their nonlinear interactions with less numerical burden for tracing complex crack surfaces. In this regard, there are mainly two methods to reduce or eliminate the need for additional DoFs or nodes. One method is the phase field method (Borden et al., 2011; Miehe et al., 2010; Bourdin et al., 2008). This method introduces an additional nodal DoF to approximate a fracture surface with a highly concentrated yet continuous phase field, which smooths the boundary of the crack over a small region. The major advantage is that the evolution of the fracture surfaces follows from the solution of a coupled system of partial differential equations. Thus, it does not require the fracture surfaces to be tracked algorithmically. However, this method is mesh-dependent and it requires an extremely fine mesh to resolve the sharp discontinuity associated with an interface or a crack surface. The computational cost remains extremely high. There are also serious ambiguities regarding the nonzero stresses at crack wake surfaces.

Another approach is the embedded discontinuity method. This method follows the earlier work in smeared localization models and enhanced strain methods (Belytschko et al., 1988; Dvorkin et al., 1990; Ortiz et al., 1987; Simo and Rifai, 1990; Wriggers and Korelc, 1996; Simo and Hughes, 1986) and it has been extended to account for discrete discontinuities by several research groups (Alfaiate et al., 2002; Ibrahimbegovic and Melnyk, 2007; Sluys and Berends, 1998; Linder and Armero, 2007, 2009; Dias-da-Costa et al., 2009; Rudraraju et al., 2010; Jirásek, 2000) following Simo and colleagues' seminal approach in treating plastic strain localizations with discrete discontinuous descriptions (Simo et al., 1993; Armero and Garikipati, 1996). Special (or regularized) shape functions are used to account for the discontinuous crack displacements within an element (Linder and Armero, 2007, 2009; Rudraraju et al., 2010; Armero and Garikipati, 1996). However, the special shape functions have to be carefully constructed so that the orthogonal principle is satisfied. Otherwise, spurious deformation modes or serious stress locking may occur (Jirásek, 2000; Simo et al., 1993). Furthermore, the ability of this approach in handling interactive cracks is limited—Thus far there is no report on regularized shape functions that can describe multiple discontinuities within a single element.

It is therefore highly desired to develop new finite element methods that can deal with discrete cracks without the need to introduce additional DoFs or nodes, so that the numerical burden for tracing crack surfaces can be minimized. In this paper, we present a new A-FEM formulation that can treat multiple intra-element cohesive cracks in homogeneous or heterogeneous solids, without the need to introduce any extra DoFs. In the new A-FEM formulation, four internal nodes with regular displacement DoFs were introduced to account for a cohesive crack, so that the crack displacements are natural outcomes from element equilibrium consideration. Thus, it does not need to

assume the deformation modes *a priori* for crack displacements as in the enhanced strain method or in many of the embedded discontinuity methods. More importantly, we will see that the new A-FEM can account for (1) intra-element material heterogeneity, which involves a natural evolution from a weak discontinuity to a strong one, and (2) repeated elemental augmentation to enable multiple, interactive intra-element discontinuities to account for crack merging (from a bulk material domain into a material interface) or crack bifurcation away from the interface. These capabilities are crucial to high-fidelity simulations of heterogeneous materials such as textile composites, but they have yet to be addressed adequately. In addition, we report a novel and efficient solving algorithm for elemental condensation that provides analytical solutions to the local equilibrium equations with embedded piecewise linear cohesive crack-like discontinuities. It will be demonstrated that the new A-FEM with the help of the new condensation algorithm can provide orders of magnitude improvement in numerical efficiency, accuracy, and robustness. Another attractive feature of the new A-FEM is that it is completely compatible with any standard FE programs (Liu et al., 2013, 2014).

10.2 Problem statement

10.2.1 Strong and weak form

Consider a discontinuous physical domain Ω as shown in Figure 10.3. The domain is composed of two subdomains of the same or different materials, that is, $\Omega = \Omega^+ \cup \Omega^-$. The two domains are connected by a discontinuity that could be a cohesive crack or a material boundary, $\Gamma_c = \Gamma_c{}^+ \cup \Gamma_c{}^-$.[1] The prescribed tractions $\mathbf{f}$ are imposed on

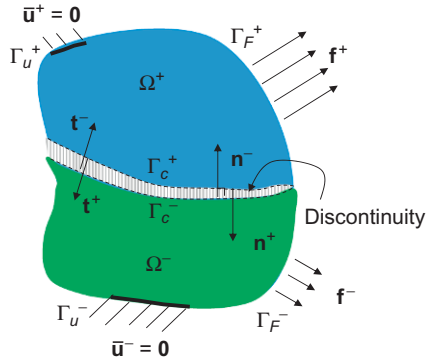

Figure 10.3 Notation for an elastic body with a discontinuity.
Liu et al. (2014).

[1] For a weak discontinuity $\Gamma_c{}^+ = \Gamma_c{}^-$, but for a strong discontinuity $\Gamma_c{}^+$ and $\Gamma_c{}^-$ are separated.

boundary Γ_F and the prescribed displacements $\bar{\mathbf{u}}$ on boundary Γ_u. The stress field inside the domain, $\boldsymbol{\sigma}$, is related to the external loading $\mathbf{f}$. The strong form of the equilibrium equations and boundary conditions are

$$\begin{aligned}
&\nabla\cdot\boldsymbol{\sigma}^+=0 \ \ (\text{in}\,\Omega^+) && \nabla\cdot\boldsymbol{\sigma}^-=0 \ \ (\text{in}\,\Omega^-)\\
&\boldsymbol{\sigma}^+\cdot\mathbf{n}^+=\mathbf{f}^+ \ \ \left(\text{on}\,\Gamma_F^+\right) && \boldsymbol{\sigma}^-\cdot\mathbf{n}^-=\mathbf{f}^- \ \ \left(\text{on}\,\Gamma_F^-\right)\\
&\mathbf{u}^+=\bar{\mathbf{u}}^+ \ \ \left(\text{on}\,\Gamma_u^+\right) && \mathbf{u}^-=\bar{\mathbf{u}}^- \ \ \left(\text{on}\,\Gamma_u^-\right)\\
&\mathbf{t}^+=\boldsymbol{\sigma}^+\cdot\mathbf{n}^+=-\mathbf{t} \ \ \left(\text{on}\,\Gamma_c^+\right) && \mathbf{t}^-=\boldsymbol{\sigma}^-\cdot\mathbf{n}^-=\mathbf{t} \ \ \left(\text{on}\,\Gamma_c^-\right)
\end{aligned} \tag{10.1}$$

where $\boldsymbol{\sigma}^+$ and $\boldsymbol{\sigma}^-$ are the stresses in the subdomains Ω^+ and Ω^-, respectively; $\mathbf{t}^+$ and $\mathbf{t}^-$ are the tractions along the discontinuity surfaces Γ_c^+ and Γ_c^-, respectively; $\mathbf{n}^+$ and $\mathbf{n}^-$ are the outward normal of Γ_c^+ and Γ_c^-, respectively. The last two expressions in Equations (10.1) come from the stress continuity across the discontinuity. The traction, $\mathbf{t}$, is a function of the relative displacements, $\boldsymbol{\Delta}\mathbf{u}$, between Γ_c^+ and Γ_c^-, that is,

$$\begin{aligned}
&\mathbf{t}=\mathbf{t}(\boldsymbol{\Delta}\mathbf{u}) && (\text{on}\,\Gamma_c)\\
&\boldsymbol{\Delta}\mathbf{u}=\mathbf{u}^+-\mathbf{u}^- && (\text{on}\,\Gamma_c)
\end{aligned} \tag{10.2}$$

where $\mathbf{u}^+$ and $\mathbf{u}^-$ are the displacement fields in Ω^+ and Ω^-, respectively. Equation (10.2) serves as the constitutive law and kinematic equation of the discontinuity. In this study, cohesive zone models with piecewise linear traction-separation laws are used to describe strong discontinuities.

The domain surrounding the discontinuity is assumed to be elastic. We further assume small strains and displacements condition. Thus, the constitutive law and kinematic equations for the two domains can be written as

$$\begin{aligned}
&\boldsymbol{\sigma}^+=\mathbf{C}^+:\boldsymbol{\varepsilon}^+ \ \ (\text{in}\,\Omega^+); && \boldsymbol{\sigma}^-=\mathbf{C}^-:\boldsymbol{\varepsilon}^- \ \ (\text{in}\,\Omega^-)\\
&\boldsymbol{\varepsilon}^+=\left[\nabla\mathbf{u}^+ + (\nabla\mathbf{u}^+)^{\mathbf{T}}\right]/2 \ \ (\text{in}\,\Omega^+); && \boldsymbol{\varepsilon}^-=\left[\nabla\mathbf{u}^- + (\nabla\mathbf{u}^-)^{\mathbf{T}}\right]/2 \ \ (\text{in}\,\Omega^-)
\end{aligned} \tag{10.3}$$

where $\mathbf{C}^+$ and $\mathbf{C}^-$ are the material stiffness tensors of the two subdomains traversed by the discontinuity, respectively. They can be of identical (for homogeneous materials) or different materials (for heterogeneous materials). The superscript $(\cdot)^{\mathbf{T}}$ denotes transposition.

The above strong form of the problem can be converted into a weak form using the principle of virtual work. The displacement fields ($\mathbf{u}^+$ and $\mathbf{u}^-$) must be subsets of the kinematically admissible displacement fields, u:

$$\mathbf{u}^+\in\mathsf{u}=\left\{\mathbf{v}^+\in\mathsf{v}:\mathbf{v}^+=\bar{\mathbf{u}}^+\ \text{on}\,\Gamma_u^+\right\};\ \ \mathbf{u}^-\in\mathsf{u}=\left\{\mathbf{v}^-\in\mathsf{v}:\mathbf{v}^-=\bar{\mathbf{u}}^-\ \text{on}\,\Gamma_u^-\right\} \tag{10.4}$$

Applying the principle of virtual work separately to the subdomains, the weak forms can be written as

$$\begin{cases} \int_{\Omega^+} \boldsymbol{\sigma}^+ : \boldsymbol{\varepsilon}^+(\mathbf{v}^+)\mathrm{d}\Omega = \int_{\Gamma_F{}^+} \mathbf{F}^+ \cdot \mathbf{v}^+ \mathrm{d}\Gamma - \int_{\Gamma_c} \mathbf{t}(\Delta\mathbf{v}) \cdot \mathbf{v}^+ \mathrm{d}\Gamma \\ \int_{\Omega^-} \boldsymbol{\sigma}^- : \boldsymbol{\varepsilon}^-(\mathbf{v}^-)\mathrm{d}\Omega = \int_{\Gamma_F{}^-} \mathbf{F}^- \cdot \mathbf{v}^- \mathrm{d}\Gamma + \int_{\Gamma_c} \mathbf{t}(\Delta\mathbf{v}) \cdot \mathbf{v}^- \mathrm{d}\Gamma \end{cases} \quad \forall(\mathbf{v}^+, \mathbf{v}^-) \in \mathsf{u} \tag{10.5}$$

where $\boldsymbol{\Delta}\mathbf{v} = \mathbf{v}^+ - \mathbf{v}^-(\text{on}\,\Gamma_c)$. The left-hand sides are the internal virtual work and the right-hand sides are the virtual work done by the external forces and the tractions along the crack surfaces. Note that if one of the subdomains (say Ω^-) further cracks, the principle of virtual work can be applied to all three subdomains without any further modifications.

10.2.2 Piecewise linear cohesive laws

The discontinuity in Section 10.2.1 is often modeled by cohesive laws that provide explicit traction-separation relations. Any nonlinear cohesive laws can be approximated with piecewise linear laws as shown in Figure 10.4. The cohesive law employs separate mode I and mode II traction-separation relations, which was first proposed by Yang, Thouless, and colleagues (Yang et al., 1999; Kafkalidis et al., 2000; Thouless and Yang, 2008; Ling et al., 2014). For those cohesive laws employing coupled mode I and mode II relation as in Turon et al. (2006) and Hallett and Wisnom (2006b), the piecewise linear form of the traction-separation laws can be obtained with an incremental form.

For the piecewise linearized models, it is advantageous to index the traction-separation laws by cohesive segment numbers as labeled in Figure 10.4 by the circled numbers. Each segment is characterized by a critical stress ($\hat{\tau}^{(i)}$ or $\hat{\sigma}^{(j)}$), a

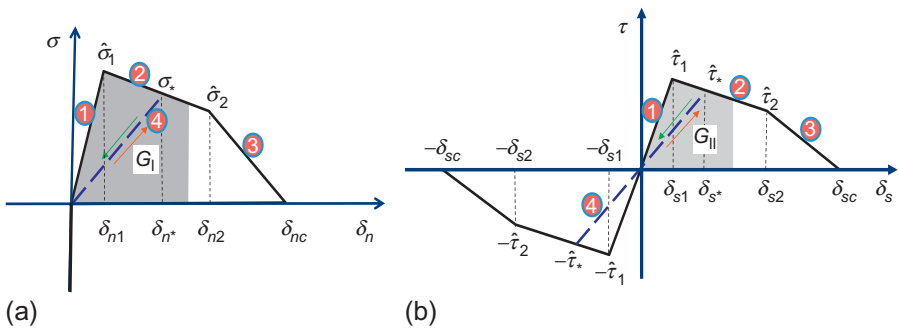

Figure 10.4 A mixed-mode piecewise linear cohesive law with (a) mode I and (b) mode II traction-separation relations.
Liu et al. (2014).

corresponding local crack displacement ($\delta_s^{(i)}$ or $\delta_n^{(j)}$), and a constant stiffness ($\alpha_s^{(i)}$ or $\alpha_n^{(j)}$). Here the superscripts (i) and (j) ($i, j = 1, 2$, and 3) are free indices for the cohesive segments with constant stiffness. For the cohesive model shown in Figure 10.4,

$$\hat{\sigma}^{(1)} = \hat{\sigma}_1;\ \ \hat{\sigma}^{(2)} = \hat{\sigma}_2;\ \ \hat{\sigma}^{(3)} = 0;\ \ \hat{\tau}^{(1)} = \hat{\tau}_1;\ \ \hat{\tau}^{(2)} = \hat{\tau}_2;\ \ \hat{\tau}^{(3)} = 0 \tag{10.6}$$

$$\delta_n^{(1)} = \delta_{n1};\ \ \delta_n^{(2)} = \delta_{n2};\ \ \delta_n^{(3)} = \delta_{nc};\ \ \delta_s^{(1)} = \delta_{s1};\ \ \delta_s{}^{(2)} = \delta_{s2};\ \ \delta_s^{(3)} = \delta_{sc} \tag{10.7}$$

And the constant cohesive slopes for any segments are

$$\begin{aligned} \alpha_s^{(i)} &= \left(\hat{\tau}^{(i)} - \hat{\tau}^{(i-1)}\right) / \left(\delta_s^{(i)} - \delta_s^{(i-1)}\right); \\ \alpha_n^{(j)} &= \left(\hat{\sigma}^{(j)} - \hat{\sigma}^{(j-1)}\right) / \left(\delta_n^{(j)} - \delta_n^{(j-1)}\right) \quad (i, j = 1,2,3), \end{aligned} \tag{10.8}$$

where $\hat{\sigma}^{(0)} = \hat{\tau}^{(0)} = 0$ and $\delta_n^{(0)} = \delta_s^{(0)} = 0$. Further, the crack displacement ranges consistent with the cohesive segments are indexed with

$$\overset{\leftrightarrow}{\delta}{}_s^{(i)} = \left(\delta_s^{(i-1)}, \delta_s^{(i)}\right];\ \ \overset{\leftrightarrow}{\delta}{}_n^{(j)} = \left(\delta_n^{(j-1)}, \delta_n^{(j)}\right] \quad (i, j = 1,2,3) \tag{10.9}$$

Thus, the linearized relation between the cohesive stresses, $\sigma(\delta_n)$ and $\tau(\delta_s)$, and the crack displacements, δ_n and δ_s, for any segments may be written as

$$\begin{aligned} \tau(\delta_s) &= \mathrm{sgn}(\delta_s)\left[\hat{\tau}^{(i-1)} + \alpha_s^{(i)}\left(|\delta_s| - \delta_s^{(i-1)}\right)\right] \quad \left(\text{for } |\delta_s| \in \overset{\leftrightarrow}{\delta}{}_s^{(i)} \,\&\&\, |\delta_s| \geq \delta_{s*}\right) \\ \sigma(\delta_n) &= \hat{\sigma}^{(j-1)} + \alpha_n{}^{(j)}\left(\delta_n - \delta_n{}^{(j-1)}\right) \quad \left(\text{for } \delta_n \in \overset{\leftrightarrow}{\delta}{}_n^{(j)} \,\&\&\, \delta_n \geq \delta_{n*}\right) \end{aligned} \tag{10.10}$$

where the sign function sgn(•) is defined as $\mathrm{sgn}(\bullet) = \begin{Bmatrix} 1 & \text{if} \bullet > 0 \\ 0 & \text{if} \bullet = 0 \\ -1 & \text{if} \bullet < 0 \end{Bmatrix}$. $|\bullet|$ denotes taking the absolute value of the argument. δ_{s*} and δ_{n*} are two solution-dependent variables related to the irreversibility of the cohesive model, as discussed below.

The irreversibility of the cohesive model is explicitly considered by an additional unloading segment in each traction-separation law (segment 4 in Figure 10.4). In this paper, the maximum crack displacements ever reached, δ_{n*} for mode I and δ_{s*} for mode II as shown in Figure 10.4, are used as the historical (or, solution-dependent) variables to facilitate distinguishing between loading and unloading path, that is, unloading occurs when the current crack displacements are smaller than the respective historical displacements. The corresponding historical cohesive stresses, $\hat{\sigma}_*$ and $\hat{\tau}_*$, are computed from these historical crack displacements using Equation (10.10). Thus, for segment i or $j = 4$, the cohesive stress–crack displacement relation is

$$\begin{aligned}\tau(\delta_s) &= \mathrm{sgn}(\delta_s)\alpha_s^{(4)}|\delta_s| \quad \left(\text{for } |\delta_s| \in \overset{\leftrightarrow}{\delta}{}_s^{(4)} \,\&\&\, |\delta_s| < \delta_{s*}\right) \\ \sigma(\delta_n) &= \alpha_n^{(4)}\delta_n \quad \left(\text{for } \delta_n \in \overset{\leftrightarrow}{\delta}{}_n^{(4)} \,\&\&\, \delta_n < \delta_{n*}\right)\end{aligned} \tag{10.11}$$

The corresponding ranges for the cohesive stiffness and the displacement are

$$\alpha_s^{(4)} = (\hat{\tau}_*/\delta_{s*}); \;\; \alpha_n^{(4)} = (\hat{\sigma}_*/\delta_{n*}) \tag{10.12}$$

$$\overset{\leftrightarrow}{\delta}{}_s^{(4)} = [0, \delta_{s*}]; \;\; \overset{\leftrightarrow}{\delta}{}_n^{(4)} = [-\infty, \delta_{n*}]$$

For other cohesive laws, such cohesive segments may be constructed similarly after piecewise linearization.

Based on the individual modes, a mixed-mode cohesive model can be constructed by recognizing that the total traction-separation work absorbed during fracture, $\mathcal{G}$, can be separated into the mode I and mode II components, $\mathcal{G}_I$ and $\mathcal{G}_{II}$, so that,

$$\mathcal{G} = \mathcal{G}_I + \mathcal{G}_{II} \tag{10.13}$$

The two separate components can be calculated by integration of the mode I and mode II traction-separation curves (Fig. 10.4):

$$\begin{aligned}\mathcal{G}_I &= \int_0^{\delta_n} \sigma(\delta)\mathrm{d}\delta \\ \mathcal{G}_{II} &= \int_0^{\delta_s} \tau(\delta)\mathrm{d}\delta\end{aligned} \tag{10.14}$$

Note that δ_n and δ_s are not independent parameters; they evolve together as a natural result of the interplay between the deformation of two joined domains and the details of the two pure-mode traction-separation laws. A failure criterion is required to determine the critical values of the two components of $\mathcal{G}$, $\mathcal{G}_I^*$, and $\mathcal{G}_{II}^*$ (shaded areas in Figure 10.4), at which point complete fracture of the cohesive zone occurs. The criterion used in this study is a simple one from Wang and Suo (1990)

$$\mathcal{G}_I^*/\Gamma_I + \mathcal{G}_{II}^*/\Gamma_{II} = 1 \tag{10.15}$$

where Γ_I and Γ_{II} are the *total* areas under the pure-mode I and pure-mode II cohesive laws. They are the mode I and mode II fracture toughnesses in the linear-elastic fracture-mechanics (LEFM) context.

A more detailed account of this mixed-mode cohesive zone model can be found in Yang and Cox (2005), Thouless and Yang (2008), and Ling et al. (2014). The major advantage of this cohesive law is that there is no need to specify the mode mixedness *a priori*. The mode mixedness and the mixed-mode toughness evolve as numerical

outcomes of the local equilibrium of stresses. More importantly, this law guarantees correct mode mixedness when LEFM conditions are satisfied (Yang et al., 2010b; Parmigiani and Thouless, 2007; Goutianos and Sorensen, 2012).

10.3 A new 2D A-FEM formulation

10.3.1 A-FEM formulation with single intra-elemental crack

Without the loss of generality, the four-node, quadrilateral plane element is used here to illustrate the augmented finite element scheme. The physical element with regular or external nodes 1, 2, 3, and 4 is severed by a cohesive crack or a bimaterial interface as shown in Figure 10.5. We take a common approach that assumes: (1) during crack growth, a crack tip always resides at an element boundary during its propagation as in the phantom node method and the like (Ling et al., 2009; Fang et al., 2011a; Remmers, 2006; de Borst, 2003), and (2) the existence of a cohesive zone eliminates the crack tip singularity (Yang et al., 1999, 2006; Yang and Cox, 2005; Moës and Belytschko, 2002; Yang and Thouless, 2001). Thus, the method proposed here cannot treat cracks with crack tip singularities as can be conveniently done in the X-FEM framework. However, for many engineering materials that fail by the development of finite damage process zones (i.e., polymers, concretes, ductile metals, fiber-reinforced polymeric composites, etc.), such a treatment is appropriate (Yang and Cox, 2005; Hutchinson and Evans, 2000; de Borst, 2003; Cavalli et al., 2004, 2005).

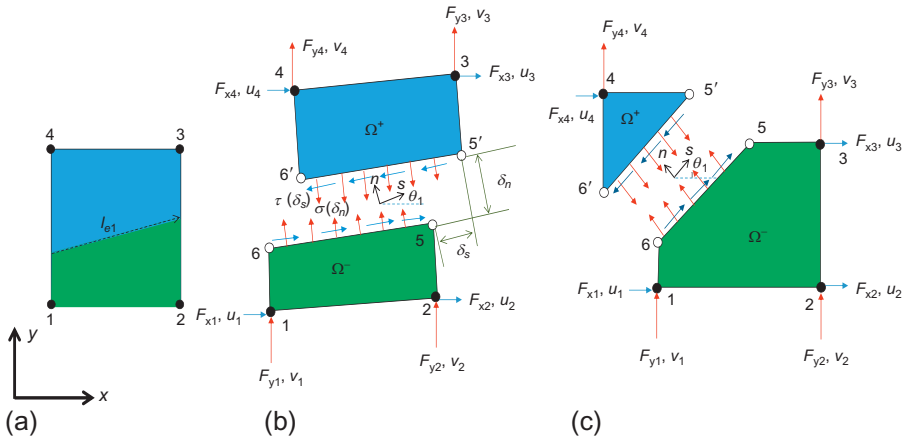

Figure 10.5 The element augmentation from (a) a regular element with possible different material domains, to (b) an A-FE with two quadrilateral subdomains, or to (c) an A-FE with one triangular subdomain and one pentagonal subdomain.
Liu et al. (2014).

If the element is cut by a single crack, there are two basic crack configurations: (1) two quadrilateral subdomains as shown in Figure 10.5b; and (2) one triangular subdomain and one pentagonal subdomain as shown in Figure 10.5c. For each crack, a local coordinate system is defined by the directions along (**s**) and perpendicular to (**n**) the crack path, from which the normal (δ_n) and shear (δ_s) crack displacements can be defined as shown in Figure 10.5b. These local crack displacements are related to the global crack displacements, Δu and Δv, by $\{\delta_s, \delta_n\}^T = [\mathbf{R}_1]\{\Delta u, \Delta v\}^T$, where $[\mathbf{R}_1] = \begin{bmatrix} \cos\theta_1 & \sin\theta_1 \\ -\sin\theta_1 & \cos\theta_1 \end{bmatrix}$ is the rotational matrix between the global and local coordinates and θ_1 is the angle between global **x**-axis and local **s**-axis (Figure 10.5).

We introduce four internal nodes (nodes 5, 6, 6′, and 5′ in Figure 10.5b and c) with regular displacement DoFs so that the displacement jumps across the crack are simply the differences in displacements between the respective node pairs 5–5′ and 6–6′.

With the help of these internal nodes, the displacement field in each subdomain, $\mathbf{u}^\alpha$ ($\alpha = +$ or $-$), can be obtained through standard FE shape function interpolation as below:

$$\mathbf{u}^\alpha = \mathbf{N}^\alpha \cdot \mathbf{d}^\alpha \tag{10.16}$$

where $\mathbf{d}^\alpha$ is the nodal displacement array of the subdomain α ($\alpha = +$ or $-$). If the element is cut into two quadrilateral subdomains as shown in Figure 10.5b, $\mathbf{d}^+ = \{u_3, v_3, u_4, v_4, |u_{6'}, v_{6'}, u_{5'}, v_{5'}\}^T$ and $\mathbf{d}^- = \{u_1, v_1, u_2, v_2, |u_6, v_6, u_5, v_5\}^T$. $\mathbf{N}^\alpha$ is the interpolation matrix composed of standard bilinear isoparametric shape functions. The symbol "|" indicates that the displacements ahead of it are external nodal displacements that are denoted with $\mathbf{d}^+_{ext} = \{u_3, v_3, u_4, v_4\}^T$, and those behind it are the internal nodal displacements that are denoted with $\mathbf{d}^+_{int} = \{u_{6'}, v_{6'}, u_{5'}, v_{5'}\}^T$. Similarly, $\mathbf{d}^-_{ext} = \{u_1, v_1, u_2, v_2\}^T$ and $\mathbf{d}^-_{int} = \{u_6, v_6, u_5, v_5\}^T$.

If the element is cut into a triangular and a pentagonal subdomain as in Figure 10.5c, then $\mathbf{d}^+ = \begin{Bmatrix} \mathbf{d}^+_{ext} \\ \mathbf{d}^+_{int} \end{Bmatrix} = \{u_4, v_4, |u_{6'}, v_{6'}, u_{5'}, v_{5'}\}^T$ and $\mathbf{d}^- = \begin{Bmatrix} \mathbf{d}^-_{ext} \\ \mathbf{d}^-_{int} \end{Bmatrix} = \{u_1, v_1, u_2, v_2, u_3, v_3, |u_6, v_6, u_5, v_5\}^T$. The shape functions in the interpolation matrix $\mathbf{N}^\alpha$ are from the polygon FEM with optimized quadrature rules recently developed by Sukumar and colleagues (Mousavi et al., 2010; Sukumar et al., 1998). The strain field in each subdomain is

$$\boldsymbol{\varepsilon}^\alpha = \left(\partial_L^T \mathbf{N}^\alpha\right) \cdot \mathbf{d}^\alpha = \mathbf{B}^\alpha \cdot \mathbf{d}^\alpha \tag{10.17}$$

where ∂_L is the differentiation operator, that is, $\partial_L = \begin{bmatrix} \partial/\partial x & 0 & \partial/\partial y \\ 0 & \partial/\partial y & \partial/\partial x \end{bmatrix}$, and $\mathbf{B}^\alpha$ is the so-called strain matrix.

Substituting Equations (10.16) and (10.17) into Equation (10.5) and using the principle of virtual work, one obtains the weak form of the equilibrium equation for standard elements

$$\begin{cases} \mathbf{L}^+ \cdot \mathbf{d}^+ = \mathbf{F}^+_{ext} + \mathbf{F}^+_{int} \\ \mathbf{L}^- \cdot \mathbf{d}^- = \mathbf{F}^-_{ext} + \mathbf{F}^-_{int} \end{cases} \tag{10.18}$$

where

$\mathbf{L}^{\alpha} = \int_{\Omega_e^{\alpha}} (\mathbf{B}^{\alpha})^{\mathrm{T}} \mathbf{D}^{\alpha} \mathbf{B}^{\alpha} \mathrm{d}\Omega$ is the stiffness matrix corresponding to subdomain α;

$\mathbf{F}_{\mathrm{ext}}^{\alpha} = \int_{\Gamma_F^{\alpha}} (\mathbf{N}^{\alpha})^{\mathrm{T}} \mathbf{f}^{\alpha} \mathrm{d}\Gamma$ is the equivalent external force array on subdomain α;

$\mathbf{F}_{\mathrm{int}}^{\alpha} = \int_{\Gamma_c^{\alpha}} \left(\mathbf{N}_{\mathrm{coh}}^{\alpha}\right)^{\mathrm{T}} \mathbf{t}^{a} \, \mathrm{d}\Gamma$ is the equivalent internal force array integrated from the cohesive stresses along the intra-element cohesive crack; and

$\mathbf{D}^{\alpha} = \dfrac{E^{\alpha}}{1-(\nu^{\alpha})^2} \begin{bmatrix} 1 & \nu^{\alpha} & 0 \\ \nu^{\alpha} & 1 & 0 \\ 0 & 0 & (1-\nu^{\alpha})/2 \end{bmatrix}$ is the material stiffness matrix of subdomain α.

In the interest of developing an efficient A-FE that can deal with multiple interactive intra-elemental cracks, here we adopt the nonconforming approach, which basically assumes that the interelement continuity is enforced only through the regular (or external) nodes and their nodal DoFs ($\mathbf{d}_{\mathrm{ext}}^{+}$ and $\mathbf{d}_{\mathrm{ext}}^{-}$); whereas the conformity of the internal DoFs associated with the internal nodes ($\mathbf{d}_{\mathrm{int}}^{+}$ and $\mathbf{d}_{\mathrm{int}}^{-}$) are not enforced. This simplification leads to the conclusion that $\mathbf{F}_{\mathrm{ext}}^{\alpha}$ is a function of regular nodal DoFs ($\mathbf{d}_{\mathrm{ext}}^{+}$ and $\mathbf{d}_{\mathrm{ext}}^{-}$) only, and $\mathbf{F}_{\mathrm{int}}^{\alpha}$ is a function of internal DoFs ($\mathbf{d}_{\mathrm{int}}^{+}$ and $\mathbf{d}_{\mathrm{int}}^{-}$) only, which allow us to rewrite Equation (10.8) as follows:

$$\begin{cases} \begin{bmatrix} \mathbf{L}_{11}^{+} & \mathbf{L}_{12}^{+} \\ \mathbf{L}_{21}^{+} & \mathbf{L}_{22}^{+} \end{bmatrix} \begin{Bmatrix} \mathbf{d}_{\mathrm{ext}}^{+} \\ \mathbf{d}_{\mathrm{int}}^{+} \end{Bmatrix} = \begin{Bmatrix} \mathbf{F}_{\mathrm{ext}}^{+} \\ \mathbf{F}_{\mathrm{int}}^{+} \end{Bmatrix} \\ \begin{bmatrix} \mathbf{L}_{11}^{-} & \mathbf{L}_{12}^{-} \\ \mathbf{L}_{21}^{-} & \mathbf{L}_{22}^{-} \end{bmatrix} \begin{Bmatrix} \mathbf{d}_{\mathrm{ext}}^{-} \\ \mathbf{d}_{\mathrm{int}}^{-} \end{Bmatrix} = \begin{Bmatrix} \mathbf{F}_{\mathrm{ext}}^{-} \\ \mathbf{F}_{\mathrm{int}}^{-} \end{Bmatrix} \end{cases} \tag{10.19}$$

where $\mathbf{L}_{ij}^{\alpha}(i,j=1,2;\alpha=+,-)$ are the submatrices of $\mathbf{L}^{\alpha}$, that is, $\mathbf{L}^{\alpha} = \begin{bmatrix} \mathbf{L}_{11}^{\alpha} & \mathbf{L}_{12}^{\alpha} \\ \mathbf{L}_{21}^{\alpha} & \mathbf{L}_{22}^{\alpha} \end{bmatrix}$. We note that $\mathbf{L}_{22}^{\alpha}$ is the sub-stiffness matrix related to the two internal nodes of the subdomain α.

Next we derive the condensed elemental equilibrium equation for both of the configurations in Figure 10.5b and Figure 10.5c in a unified formulation. It is noted that for both-configurations, the internal DoF and equivalent force arrays are the same, that is,

$$\begin{aligned} \mathbf{d}_{\mathrm{int}}^{+} &= \mathbf{d}_{6'5'} = \{u_{6'}, v_{6'}, u_{5'}, v_{5'}\}^{\mathrm{T}}; \quad \mathbf{F}_{\mathrm{int}}^{+} = \mathbf{F}_{6'5'} = \left\{F_{x6'}, F_{y6'}, F_{x5'}, F_{y5'}\right\}^{\mathrm{T}} \\ \mathbf{d}_{\mathrm{int}}^{-} &= \mathbf{d}_{65} = \{u_6, v_6, u_5, v_5\}^{\mathrm{T}}; \qquad \mathbf{F}_{\mathrm{int}}^{-} = \mathbf{F}_{65} = \left\{F_{x6}, F_{y6}, F_{x5}, F_{y5}\right\}^{\mathrm{T}} \end{aligned} \tag{10.20a}$$

The external DoF and force arrays are specific to a particular crack configuration. For the two quadrilateral subdomain configurations (Figure 10.5b),

$$\begin{aligned} \mathbf{d}_{\mathrm{ext}}^{+} &= \mathbf{d}_{34} = \{u_3, v_3, u_4, v_4\}^{\mathrm{T}}; \quad \mathbf{F}_{\mathrm{ext}}^{+} = \mathbf{F}_{34} = \left\{F_{x3}, F_{y3}, F_{x4}, F_{y4}\right\}^{\mathrm{T}} \\ \mathbf{d}_{\mathrm{ext}}^{-} &= \mathbf{d}_{12} = \{u_1, v_1, u_2, v_2\}^{\mathrm{T}}; \quad \mathbf{F}_{\mathrm{ext}}^{-} = \mathbf{F}_{12} = \left\{F_{x1}, F_{y1}, F_{x2}, F_{y2}\right\}^{\mathrm{T}} \end{aligned} \tag{10.20b}$$

For the triangular–pentagonal subdomain configuration of Figure 10.5c,

$$\mathbf{d}_{\text{ext}}^{+} = \mathbf{d}_4 = \{u_4, v_4\}^{\text{T}};\ \ \mathbf{F}_{\text{ext}}^{+} = \mathbf{F}_4 = \{F_{x4}, F_{y4}\}^{\text{T}}$$
$$\mathbf{d}_{\text{ext}}^{-} = \mathbf{d}_{123} = \{u_1, v_1, u_2, v_2, u_3, v_3\}^{\text{T}};\ \ \mathbf{F}_{\text{ext}}^{-} = \mathbf{F}_{123} = \{F_{x1}, F_{y1}, F_{x2}, F_{y2}, F_{x3}, F_{y3}\}^{\text{T}} \tag{10.20c}$$

However, for both configurations, the equilibrium can be written as

$$\begin{bmatrix} \mathbf{L}_{11}^{+} & \mathbf{L}_{12}^{+} \\ \mathbf{L}_{21}^{+} & \mathbf{L}_{22}^{+} \end{bmatrix} \begin{Bmatrix} \mathbf{d}_{\text{ext}}^{+} \\ \mathbf{d}_{6'5'} \end{Bmatrix} = \begin{Bmatrix} \mathbf{F}_{\text{ext}}^{+} \\ \mathbf{F}_{6'5'} \end{Bmatrix} \begin{matrix} \text{(a)} \\ \text{(b)} \end{matrix} \quad (\text{for } \Omega^{+})$$
$$\begin{bmatrix} \mathbf{L}_{11}^{-} & \mathbf{L}_{12}^{-} \\ \mathbf{L}_{21}^{-} & \mathbf{L}_{22}^{-} \end{bmatrix} \begin{Bmatrix} \mathbf{d}_{\text{ext}}^{-} \\ \mathbf{d}_{65} \end{Bmatrix} = \begin{Bmatrix} \mathbf{F}_{\text{ext}}^{-} \\ \mathbf{F}_{65} \end{Bmatrix} \begin{matrix} \text{(c)} \\ \text{(d)} \end{matrix} \quad (\text{for } \Omega^{-}) \tag{10.21}$$

Also, due to stress continuity across the cohesive crack, $\mathbf{F}_{65} = -\mathbf{F}_{6'5'} = \int_{\Gamma_c^{\alpha}} \mathbf{N}_{\text{coh}}^{\text{T}} \mathbf{t} \, \text{d}\Gamma$. Equation (10.21) is valid for both weak and strong discontinuous problems.

10.3.1.1 Weak discontinuity

For weak discontinuity problems, $\mathbf{d}_{6'5'} = \mathbf{d}_{65}$. Together with the condition of $\mathbf{F}_{65} = -\mathbf{F}_{6'5'}$, Equation (10.21) further simplifies to

$$\begin{Bmatrix} \mathbf{F}_{\text{ext}}^{-} \\ \mathbf{F}_{\text{ext}}^{+} \end{Bmatrix} = \begin{bmatrix} \mathbf{L}_{11}^{-} - \mathbf{L}_{12}^{-}\boldsymbol{\Lambda}^{-1}\mathbf{L}_{21}^{-} & -\mathbf{L}_{12}^{-}\boldsymbol{\Lambda}^{-1}\mathbf{L}_{21}^{+} \\ -\mathbf{L}_{12}^{+}\boldsymbol{\Lambda}^{-1}\mathbf{L}_{21}^{-} & \mathbf{L}_{11}^{+} - \mathbf{L}_{12}^{+}\boldsymbol{\Lambda}^{-1}\mathbf{L}_{21}^{+} \end{bmatrix} \begin{Bmatrix} \mathbf{d}_{\text{ext}}^{-} \\ \mathbf{d}_{\text{ext}}^{+} \end{Bmatrix}, \tag{10.22}$$

where $\boldsymbol{\Lambda} = \mathbf{L}_{22}^{-} + \mathbf{L}_{22}^{+}$. Furthermore, the internal forces are determined as

$$\mathbf{F}_{65} = \left\{ \left(\mathbf{I} - \mathbf{L}_{22}^{-}\boldsymbol{\Lambda}^{-1}\right)\mathbf{L}_{21}^{-}, \ \ -\mathbf{L}_{22}^{-}\boldsymbol{\Lambda}^{-1}\mathbf{L}_{21}^{+} \right\} \begin{Bmatrix} \mathbf{d}_{\text{ext}}^{-} \\ \mathbf{d}_{\text{ext}}^{+} \end{Bmatrix} \tag{10.23}$$

Thus, for an element containing two material domains with a perfectly bonded interface, once the external nodal displacements are given (which is the case for displacement-based FEs), the resultant forces acting along the interface are immediately known. This solution is mathematically rigorous in the FEM sense.

With $\mathbf{F}_{65}$ known, the current tractions acting on the interface are known. For example, the normal and shear stresses averaged along the interface, in local coordinates, are $\begin{Bmatrix} \overline{\tau}_{\text{int}} \\ \overline{\sigma}_{\text{int}} \end{Bmatrix} = [\mathbf{R}_1]^{\mathbf{T}} \begin{Bmatrix} (F_{x5} + F_{x6})/l_{e1} \\ (F_{y5} + F_{y6})/l_{e1} \end{Bmatrix}$, where l_{e1} is the interface length (Figure 10.5a). These stresses can then be used to determine the initiation of interface debonding, which is the turning point from a weak discontinuity to a strong one. A common initiation criterion used in this paper is

$$\left(\langle \overline{\sigma}_{\text{int}} \rangle / \hat{\sigma}_1\right)^2 + \left(\overline{\tau}_{\text{int}} / \hat{\tau}_1\right)^2 = 1 \tag{10.24}$$

where the MacAuley bracket $\langle\bullet\rangle$, defined as $\langle\bullet\rangle = (\bullet + |\bullet|)/2$, is used to reflect the physical observation that compressive normal stresses do not contribute to crack initiation.

If this criterion of Equation (10.24) is met, the discontinuity becomes a strong one, that is, $\mathbf{d}_{6'5'} \neq \mathbf{d}_{65}$, which is addressed next.

10.3.1.2 Strong discontinuity

For strong discontinuities, we consider cohesive cracks with mixed-mode piecewise linear traction-separation laws as detailed in Figure 10.4, where the linear segments of each traction-separation laws are properly indexed. The indexing scheme is closely related to the new condensation solver that will be described shortly.

Following the notation established in Section 10.2.2, the cohesive stresses between the two pairs of internal nodes 5–5′ and 6–6′ can be expressed in its local coordinates as

$$\left\{\tau_{6'6}{}^{(i)}, \sigma_{6'6}{}^{(j)}, \tau_{5'5}{}^{(k)}, \sigma_{5'5}{}^{(l)}\right\}^{\mathrm{T}} = \boldsymbol{\sigma}_0 + \boldsymbol{\alpha}_0\{\delta_{\mathrm{s}6'6}, \delta_{\mathrm{n}6'6}, \delta_{\mathrm{s}5'5}, \delta_{\mathrm{n}5'5}\}^{\mathrm{T}} \quad (i,j,k,l = 1,2,\ldots,4) \tag{10.25a}$$

where

$$\boldsymbol{\sigma_0} = \left\{\hat{\tau}^{(i-1)} - \alpha_{\mathrm{s}}^{(i)}\delta_{\mathrm{s}}^{(i-1)}, \hat{\sigma}^{(j-1)} - \alpha_{\mathrm{n}}^{(j)}\delta_{\mathrm{n}}^{(j-1)}, \hat{\tau}^{(k-1)} - \alpha_{\mathrm{s}}^{(k)}\delta_{\mathrm{s}}^{(k-1)}, \hat{\sigma}^{(l-1)} - \alpha_{\mathrm{n}}^{(l)}\delta_{\mathrm{n}}^{(l-1)}\right\}^{\mathrm{T}} \tag{10.25b}$$

is the characteristic stress matrix. The critical stresses, $\hat{\tau}^{(i)}$ and $\hat{\sigma}^{(j)}$ $(i,j = 1,\ldots,4)$ have been defined in Section 10.2.2 (Equations 10.10 and 10.11 and Figure 10.4).

$$\boldsymbol{\alpha}_0 = \mathrm{Diag}\left[\alpha_{\mathrm{s}}^{(i)}; \alpha_{\mathrm{n}}^{(j)}; \alpha_{\mathrm{s}}^{(k)}; \alpha_{\mathrm{n}}^{(l)}\right] \tag{10.25c}$$

is the cohesive stiffness matrix. Here, Diag[a; b; c; d] means a diagonal matrix with nonzero arguments a, b, c, and d at the corresponding diagonal places. This notation will be used in the rest of this paper. $\{\delta_{\mathrm{s}6'6}, \delta_{\mathrm{n}6'6}, \delta_{\mathrm{s}5'5}, \delta_{\mathrm{n}5'5}\}^{\mathrm{T}}$ is the crack displacement array at internal node-pairs 6′–6 and 5′–5 measured in the local coordinate system.

Each of the free indices (i, j, k, l) can range from 1 to the maximum cohesive segment number, indicating in which segments of the cohesive laws the current cohesive stresses are located (Section 10.2.2). Note that the characteristic stress ($\boldsymbol{\sigma_0}$) and stiffness matrices ($\boldsymbol{\alpha_0}$) are determined if any particular combination of (i, j, k, l) is chosen.

$\mathbf{F}_{65}$ and $\mathbf{F}_{6'5'}$ are obtained by integrating the cohesive stresses in Equation (10.25a) over the crack plane and then converted into global coordinates using the rotation matrix $\mathbf{R_1}$, which gives:

$$\mathbf{F}_{65} = -\mathbf{F}_{6'5'} = l_{e1}(\mathbf{S_0} + \boldsymbol{\alpha} \cdot \Delta\mathbf{d}_{\mathrm{int}}) \tag{10.26a}$$

where $\Delta\mathbf{d}_{\text{int}} = \mathbf{d}_{6'5'} - \mathbf{d}_{65} = \{(\mathbf{d}_{6'} - \mathbf{d}_{6}), (\mathbf{d}_{5'} - \mathbf{d}_{5})\}^{\text{T}}$ are the crack displacements at node pairs 6′–6 and 5′–5 in global coordinates, that is,

$$\Delta\mathbf{d}_{\text{int}} = \mathbf{d}_{6'5'} - \mathbf{d}_{65} = \text{Diag}[\mathbf{R}_1; \mathbf{R}_1]\{\delta_{\text{s}6'6}, \delta_{\text{n}6'6}, \delta_{\text{s}5'5}, \delta_{\text{n}5'5}\}^{\text{T}} \tag{10.26b}$$

$\{\mathbf{S_0}\}$ and $[\boldsymbol{\alpha}]$ are related to the characteristic cohesive stress and stiffness matrices in Equation (10.25a)–(10.25c):

$$\begin{aligned} \mathbf{S}_0 &= \text{Diag}\left[\mathbf{R}_1^{\text{T}}; \mathbf{R}_1^{\text{T}}\right] (\mathbf{T}_{\text{coh}})^{\text{T}} \boldsymbol{\sigma}_0 \\ \boldsymbol{\alpha} &= \text{Diag}\left[\mathbf{R}_1^{\text{T}}; \mathbf{R}_1^{\text{T}}\right] (\mathbf{T}_{\text{coh}})^{\text{T}} \boldsymbol{\alpha}_0 \mathbf{N}_{\text{coh}} \text{Diag}[\mathbf{R}_1; \mathbf{R}_1] \end{aligned} \tag{10.26c}$$

Here, $\mathbf{T}_{\text{coh}}$ and $\mathbf{N}_{\text{coh}}$ are the integration and interpolation matrices associated with the cohesive stress integration and the displacement interpolation along the crack plane, respectively. For the single crack case, we used the standard Gaussian interpolation and integration scheme with two integration points, that is,

$$\mathbf{N}_{\text{coh}} = \begin{bmatrix} \text{Diag}[\xi_{\text{B}}; \xi_{\text{B}}] & \text{Diag}[\xi_{\text{A}}; \xi_{\text{A}}] \\ \text{Diag}[\xi_{\text{A}}; \xi_{\text{A}}] & \text{Diag}[\xi_{\text{B}}; \xi_{\text{B}}] \end{bmatrix}; \quad \mathbf{T}_{\text{coh}} = \frac{1}{2}\begin{bmatrix} \text{Diag}[\xi_{\text{B}}; \xi_{\text{B}}] & \text{Diag}[\xi_{\text{A}}; \xi_{\text{A}}] \\ \text{Diag}[\xi_{\text{A}}; \xi_{\text{A}}] & \text{Diag}[\xi_{\text{B}}; \xi_{\text{B}}] \end{bmatrix} = \frac{1}{2}(\mathbf{N}_{\text{coh}})^{\text{T}}$$

where $\xi_{\text{A}} = \left(1 - 1/\sqrt{3}\right)/2$ and $\xi_{\text{B}} = \left(1 + 1/\sqrt{3}\right)/2$. (The matrices for several other popular interpolation and integration schemes have been summarized and evaluated in Liu et al., 2013; Do et al., 2013.)

Substituting Equation (10.26a)–(10.26c) into expressions (b) and (d) in Equation (10.21), the following equation is derived:

$$\begin{cases} \left(\mathbf{L}_{22}^{+} + l_{e1}\boldsymbol{\alpha}\right)\mathbf{d}_{6'5'} - (l_{e1}\boldsymbol{\alpha})\mathbf{d}_{65} = -l_{e1}\mathbf{S_0} - \mathbf{L}_{21}^{+}\mathbf{d}_{\text{ext}}^{+} \\ -(l_{e1}\boldsymbol{\alpha})\mathbf{d}_{6'5'} + \left(\mathbf{L}_{22}^{-} + l_{e1}\boldsymbol{\alpha}\right)\mathbf{d}_{65} = l_{e1}\mathbf{S_0} - \mathbf{L}_{21}^{-}\mathbf{d}_{\text{ext}}^{-} \end{cases} \tag{10.27}$$

For a given cohesive segment combination (i, j, k, l) this is a linear equation, from which the crack displacements at the internal node pairs, $\Delta\mathbf{d}_{\text{int}} = \mathbf{d}_{6'5'} - \mathbf{d}_{65}$, is solved explicitly:

$$\begin{aligned} \Delta\mathbf{d}_{\text{int}} = &-l_{e1}\left(\mathbf{A}^{-1} + \mathbf{B}^{-1} - l_{e1}\mathbf{A}^{-1}\boldsymbol{\alpha}\left(\boldsymbol{\Psi}_{22}^{-}\right)^{-1} + l_{e1}\mathbf{B}^{-1}\boldsymbol{\alpha}\left(\boldsymbol{\Psi}_{22}^{+}\right)^{-1}\right)\mathbf{S}_0 \\ &+ \left(\mathbf{B}^{-1} - l_{e1}\mathbf{A}^{-1}\boldsymbol{\alpha}\left(\boldsymbol{\Psi}_{22}^{-}\right)^{-1}\right)\mathbf{L}_{21}^{-}\mathbf{d}_{\text{ext}}^{-} + \left(l_{e1}\mathbf{B}^{-1}\boldsymbol{\alpha}\left(\boldsymbol{\Psi}_{22}^{+}\right)^{-1} - \mathbf{A}^{-1}\right)\mathbf{L}_{21}^{+}\mathbf{d}_{\text{ext}}^{+} \end{aligned} \tag{10.28a}$$

where

$$\begin{aligned} &\boldsymbol{\Psi}_{22}^{+} = \mathbf{L}_{22}^{+} + l_{e1}\boldsymbol{\alpha}; \quad \boldsymbol{\Psi}_{22}^{-} = \mathbf{L}_{22}^{-} + l_{e1}\boldsymbol{\alpha}; \quad \mathbf{A} = \boldsymbol{\Psi}_{22}^{+} - {l_{e1}}^{2}\boldsymbol{\alpha}\left(\boldsymbol{\Psi}_{22}^{-}\right)^{-1}\boldsymbol{\alpha}; \\ &\mathbf{B} = \boldsymbol{\Psi}_{22}^{-} - {l_{e1}}^{2}\boldsymbol{\alpha}\left(\boldsymbol{\Psi}_{22}^{+}\right)^{-1}\boldsymbol{\alpha} \end{aligned} \tag{10.28b}$$

The explicit solution to the crack displacements can also be solved as

$$\begin{Bmatrix} \mathbf{d}_{6'5'} \\ \mathbf{d}_{65} \end{Bmatrix} = \begin{bmatrix} -l_{e1}\mathbf{A}^{-1}\left(\mathbf{I} - l_{e1}\boldsymbol{\alpha}\left(\boldsymbol{\Psi}_{22}^{-}\right)^{-1}\right) & \mathbf{0} \\ \mathbf{0} & l_{e1}\mathbf{B}^{-1}\left(\mathbf{I} - l_{e1}\boldsymbol{\alpha}\left(\boldsymbol{\Psi}_{22}^{+}\right)^{-1}\right) \end{bmatrix} \begin{Bmatrix} \mathbf{S}_0 \\ \mathbf{S}_0 \end{Bmatrix} + \begin{bmatrix} -l_{e1}\mathbf{A}^{-1}\boldsymbol{\alpha}\left(\boldsymbol{\Psi}_{22}^{-}\right)^{-1}\mathbf{L}_{21}^{-} & -\mathbf{A}^{-1}\mathbf{L}_{21}^{+} \\ -\mathbf{B}^{-1}\mathbf{L}_{21}^{-} & -l_{e1}\mathbf{B}^{-1}\boldsymbol{\alpha}\left(\boldsymbol{\Psi}_{22}^{+}\right)^{-1}\mathbf{L}_{21}^{+} \end{bmatrix} \begin{Bmatrix} \mathbf{d}_{\text{ext}}^{-} \\ \mathbf{d}_{\text{ext}}^{+} \end{Bmatrix} \tag{10.28c}$$

The fully condensed equilibrium equation without any internal forces and displacements can be obtained by substituting Equation (10.28c) into expressions (a) and (c) in Equation (10.21) and eliminating $\mathbf{F}_{65}$ and $\mathbf{F}_{6'5'}$, that is,

$$\begin{bmatrix} \mathbf{L}_{11}^{-} - \mathbf{L}_{12}^{-}\mathbf{B}^{-1}\mathbf{L}_{21}^{-} & -l_{e1}\mathbf{L}_{12}^{-}\mathbf{B}^{-1}\boldsymbol{\alpha}\left(\boldsymbol{\Psi}_{22}^{+}\right)^{-1}\mathbf{L}_{21}^{+} \\ -l_{e1}\mathbf{L}_{12}^{+}\mathbf{A}^{-1}\boldsymbol{\alpha}\left(\boldsymbol{\Psi}_{22}^{-}\right)^{-1}\mathbf{L}_{21}^{-} & \mathbf{L}_{11}^{+} - \mathbf{L}_{12}^{+}\mathbf{A}^{-1}\mathbf{L}_{21}^{+} \end{bmatrix} \begin{Bmatrix} \mathbf{d}_{\text{ext}}^{-} \\ \mathbf{d}_{\text{ext}}^{+} \end{Bmatrix} = \begin{Bmatrix} \mathbf{F}_{\text{ext}}^{-} \\ \mathbf{F}_{\text{ext}}^{+} \end{Bmatrix}$$
$$- \begin{bmatrix} l_{e1}\mathbf{L}_{12}^{-}\mathbf{B}^{-1}\left(\mathbf{I} - l_{e1}\boldsymbol{\alpha}\left(\boldsymbol{\Psi}_{22}^{+}\right)^{-1}\right) & 0 \\ 0 & -l_{e1}\mathbf{L}_{12}^{+}\mathbf{A}^{-1}\left(\mathbf{I} - l_{e1}\boldsymbol{\alpha}\left(\boldsymbol{\Psi}_{22}^{-}\right)^{-1}\right) \end{bmatrix} \begin{Bmatrix} \mathbf{S}_0 \\ \mathbf{S}_0 \end{Bmatrix} \tag{10.29}$$

Equation (10.29) is highly nonlinear because the matrices $\mathbf{S}_0, \mathbf{A}, \mathbf{B}, \boldsymbol{\Psi}_{22}^{+}$, and $\boldsymbol{\Psi}_{22}^{-}$ are all nonlinear functions of the crack displacements $\Delta\mathbf{d}_{\text{int}}$ (through $\boldsymbol{\alpha}_0$ and $\boldsymbol{\sigma}_0$ – see Equations 10.26c and 10.28b), which are not known because at this point the only information is the external displacements $\mathbf{d}_{\text{ext}}^{-}$ and $\mathbf{d}_{\text{ext}}^{+}$. We shall defer the discussion of solution procedure until Section 10.3.3.

10.3.2 A-FE formulation with two interactive cracks

The internal DoFs associated with the four internal nodes, together with the regular nodal DoFs, allow for stress evaluations at each subdomain, making it possible for further augmentation of the element for hosting more than one cohesive crack. A second crack can be introduced to a subdomain as long as it has more than one regular (external) node. In such a case, there are altogether three basic cracking configurations as shown in Figure 10.6a1–a3, where l_{e1} is the first crack length and l_{e2} is the second crack length. The second crack intersects and cuts the first crack into two segments with length γl_{e1} (left) and $(1-\gamma)l_{e1}$ (right). The three subdomains are noted with Ω^{+}, Ω^{l-}, and Ω^{r-} as shown in Figure 10.6b.

The deformed configurations corresponding to the three cases in Figure 10.6a1–a3 are shown in Figure 10.6b1–b3. To describe the discontinuity induced by the second crack, four more internal nodes, 7, 8, 7′, and 8′ are introduced and a local coordinate system is defined by the angle between its tangential direction ($\mathbf{s}_2$) and global x-direction, θ_2. The rotation matrix associated with this crack is $[\mathbf{R}_2] = \begin{bmatrix} \cos\theta_2 & \sin\theta_2 \\ -\sin\theta_2 & \cos\theta_2 \end{bmatrix}$. With the eight

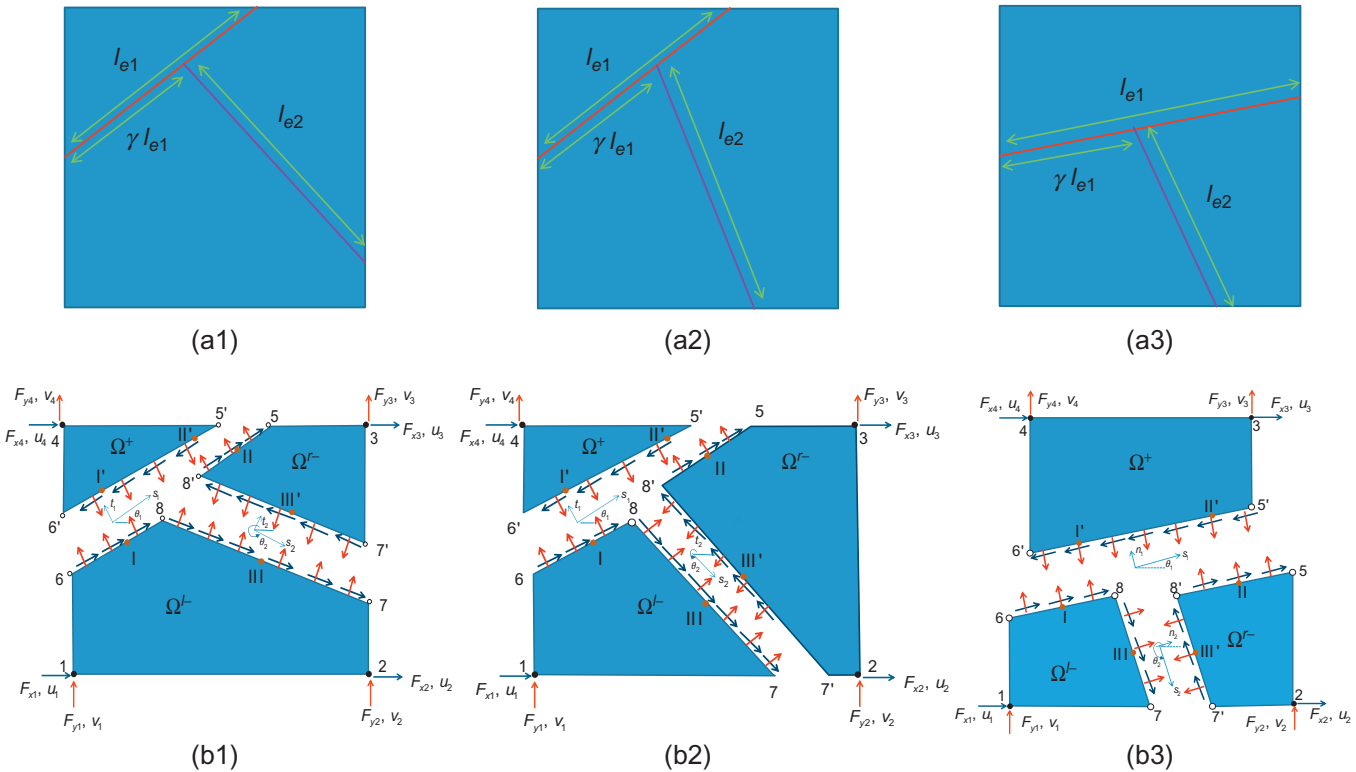

Figure 10.6 Illustration of a 2D A-FE with two intra-elemental cracks (three subdomains). Liu et al. (2014).

internal nodes, it is possible to integrate the subdomain stiffness matrix for each subdomain. In the following, we show that a unified elemental equilibrium equation can be derived for all the three configurations.

Despite the different crack configurations in Figure 10.6, the internal DoF and force arrays can be arranged in a unified way as shown below:

$$\begin{aligned}&\mathbf{d}_{\text{int}}^{+}=\mathbf{d}_{6'5'};\ \ \mathbf{d}_{\text{int}}^{r-}=\mathbf{d}_{58'7'};\ \ \mathbf{d}_{\text{int}}^{l-}=\mathbf{d}_{786}\\&\mathbf{F}_{\text{int}}^{+}=\mathbf{F}_{6'5'};\ \ \mathbf{F}_{\text{int}}^{r-}=\mathbf{F}_{58'7'};\ \ \mathbf{F}_{\text{int}}^{l-}=\mathbf{F}_{786}\end{aligned} \tag{10.30}$$

This enables a unified expression for the equilibrium of all three subdomains as follows:

$$\begin{cases}\begin{bmatrix}\mathbf{L}_{11}^{+} & \mathbf{L}_{12}^{+}\\ \mathbf{L}_{21}^{+} & \mathbf{L}_{22}^{+}\end{bmatrix}\begin{Bmatrix}\mathbf{d}_{\text{ext}}^{+}\\ \mathbf{d}_{6'5'}\end{Bmatrix}=\begin{Bmatrix}\mathbf{F}_{\text{ext}}^{+}\\ \mathbf{F}_{6'5'}\end{Bmatrix} & \begin{matrix}\text{(a)}\\ \text{(b)}\end{matrix}\quad(\text{for }\Omega^{+})\\ \begin{bmatrix}\mathbf{L}_{11}^{r-} & \mathbf{L}_{12}^{r-}\\ \mathbf{L}_{21}^{r-} & \mathbf{L}_{22}^{r-}\end{bmatrix}\begin{Bmatrix}\mathbf{d}_{\text{ext}}^{r-}\\ \mathbf{d}_{58'7'}\end{Bmatrix}=\begin{Bmatrix}\mathbf{F}_{\text{ext}}^{r-}\\ \mathbf{F}_{58'7'}\end{Bmatrix} & \begin{matrix}\text{(c)}\\ \text{(d)}\end{matrix}\quad(\text{for }\Omega^{r-})\\ \begin{bmatrix}\mathbf{L}_{11}^{l-} & \mathbf{L}_{12}^{l-}\\ \mathbf{L}_{21}^{l-} & \mathbf{L}_{22}^{l-}\end{bmatrix}\begin{Bmatrix}\mathbf{d}_{\text{ext}}^{l-}\\ \mathbf{d}_{786}\end{Bmatrix}=\begin{Bmatrix}\mathbf{F}_{\text{ext}}^{l-}\\ \mathbf{F}_{786}\end{Bmatrix} & \begin{matrix}\text{(e)}\\ \text{(f)}\end{matrix}\quad(\text{for }\Omega^{l-})\end{cases} \tag{10.31}$$

Here, the submatrices ($\mathbf{L}_{ij}^{l-}$, $\mathbf{L}_{ij}^{r-}$, and $\mathbf{L}_{ij}^{+}$ $(i,j=1,2)$) are the stiffness matrices of the subdomains Ω^{+}, Ω^{r-}, and Ω^{l-}, respectively. They can be computed, according to the respective crack configurations in Figure 10.6b1–b3, with the subdomain integration scheme discussed in Section 10.3.1.

To integrate the cohesive stress along the three cohesive crack segments into respective internal nodal forces, the first-order Gaussian integration scheme with one integration points were used on each of the three cracked segments (i.e., assuming uniform cohesive stresses along each crack segment). The integration points are at the center of each crack segment as indicated in Figure 10.6b by the solid dots labeled by I, II, and III.

Denote the cohesive stresses at these points as $(\sigma_{\text{I}}{}^{(i)}, \tau_{\text{I}}{}^{(j)})$, $(\sigma_{\text{II}}{}^{(k)}, \tau_{\text{II}}{}^{(l)})$, and $(\sigma_{\text{III}}{}^{(m)}, \tau_{\text{III}}{}^{(n)})$. The superscripts (i, j, k, l, m, n) are the free indices of the assumed cohesive segment numbers. The relation between these cohesive stresses and the internal nodal displacements is

$$\begin{cases}\left\{\tau_{\text{I}}{}^{(i)}, \sigma_{\text{I}}{}^{(j)}\right\}^{\text{T}}=\boldsymbol{\sigma}_{0\text{I}}+\boldsymbol{\alpha}_{0\text{I}}\mathbf{R}_1((1-\gamma/2)\mathbf{d}_{6'}+(\gamma/2)\mathbf{d}_{5'})-\boldsymbol{\alpha}_{0\text{I}}\mathbf{R}_1(\mathbf{d}_6+\mathbf{d}_8)/2\\ \left\{\tau_{\text{II}}{}^{(k)}, \sigma_{\text{II}}{}^{(l)}\right\}^{\text{T}}=\boldsymbol{\sigma}_{0\text{II}}+\boldsymbol{\alpha}_{0\text{II}}\mathbf{R}_1((1-\gamma/2)\mathbf{d}_{6'}+(1+\gamma/2)\mathbf{d}_{5'})-\boldsymbol{\alpha}_{0\text{II}}\mathbf{R}_1(\mathbf{d}_5+\mathbf{d}_{8'})/2\\ \left\{\tau_{\text{III}}{}^{(m)}, \sigma_{\text{III}}{}^{(n)}\right\}^{\text{T}}=\boldsymbol{\sigma}_{0\text{III}}+\boldsymbol{\alpha}_{0\text{III}}\mathbf{R}_2(\mathbf{d}_{7'}+\mathbf{d}_{8'})/2-\boldsymbol{\alpha}_{0\text{III}}\mathbf{R}_2(\mathbf{d}_7+\mathbf{d}_8)/2\end{cases} \tag{10.32a}$$

where

$$\boldsymbol{\sigma}_{0\text{I}}=\begin{Bmatrix}\hat{\tau}^{(i)}-\alpha_{\text{s}}^{(i)}\delta_{\text{s}}^{(i)}\\ \hat{\sigma}^{(j)}-\alpha_{\text{n}}^{(j)}\delta_{\text{n}}^{(j)}\end{Bmatrix};\ \ \boldsymbol{\sigma}_{0\text{II}}=\begin{Bmatrix}\hat{\tau}^{(k)}-\alpha_{\text{s}}^{(k)}\delta_{\text{s}}^{(k)}\\ \hat{\sigma}^{(l)}-\alpha_{\text{n}}^{(l)}\delta_{\text{n}}^{(l)}\end{Bmatrix};\ \ \boldsymbol{\sigma}_{0\text{III}}=\begin{Bmatrix}\hat{\tau}^{(m)}-\alpha_{\text{s}}^{(m)}\delta_{\text{s}}^{(m)}\\ \hat{\sigma}^{(n)}-\alpha_{\text{n}}^{(n)}\delta_{\text{n}}^{(n)}\end{Bmatrix} \tag{10.32b}$$

$$\boldsymbol{\alpha}_{0\mathrm{I}}=\mathrm{Diag}\left[\alpha_{\mathrm{s}}^{(i)};\alpha_{\mathrm{n}}^{(j)}\right];\quad \boldsymbol{\alpha}_{0\mathrm{II}}=\mathrm{Diag}\left[\alpha_{\mathrm{s}}^{(k)};\alpha_{\mathrm{n}}^{(l)}\right];\quad \boldsymbol{\alpha}_{0\mathrm{III}}=\mathrm{Diag}\left[\alpha_{\mathrm{s}}^{(m)};\alpha_{\mathrm{n}}^{(n)}\right];\tag{10.32c}$$

The internal forces, $\{\mathbf{F}_{6'5'}\}$, $\{\mathbf{F}_{58'7'}\}$, and $\{\mathbf{F}_{786}\}$, integrated from the cohesive stresses along the respective crack lengths are

$$\begin{cases}\mathbf{F}_{6'5'}=\mathbf{T}_{\mathbf{R}}^{+}\left\{\tau_{\mathrm{I}}^{(i)},\ \sigma_{\mathrm{I}}^{(j)},\ \tau_{\mathrm{II}}^{(k)},\ \sigma_{\mathrm{II}}^{(l)}\right\}^{\mathrm{T}}\\ \mathbf{F}_{786}=\mathbf{T}_{\mathbf{R}}^{l-}\left\{\tau_{\mathrm{I}}^{(i)},\ \sigma_{\mathrm{I}}^{(j)},\ \tau_{\mathrm{III}}^{(m)},\ \sigma_{\mathrm{III}}^{(n)}\right\}^{\mathrm{T}}\\ \mathbf{F}_{58'7'}=\mathbf{T}_{\mathbf{R}}^{r-}\left\{\tau_{\mathrm{I}}^{(k)},\ \sigma_{\mathrm{I}}^{(l)},\ \tau_{\mathrm{III}}^{(m)},\ \sigma_{\mathrm{III}}^{(n)}\right\}^{\mathrm{T}}\end{cases}\tag{10.33a}$$

where $\mathbf{T}_{\mathbf{R}}^{+}$, $\mathbf{T}_{\mathbf{R}}^{l-}$, and $\mathbf{T}_{\mathbf{R}}^{r-}$ are the respective integration matrices as shown below:

$$\mathbf{T}_{\mathbf{R}}^{+}=-\frac{1}{2}\begin{bmatrix}\gamma(2-\gamma)l_{e1}\mathbf{R}_1^{\mathrm{T}} & (1-\gamma)^2 l_{e1}\mathbf{R}_1^{\mathrm{T}}\\ \gamma^2 l_{e1}\mathbf{R}_1{}^{\mathbf{T}} & (1-\gamma^2)l_{e1}\mathbf{R}_1^{\mathrm{T}}\end{bmatrix};$$

$$\mathbf{T}_{\mathbf{R}}^{l-}=\frac{1}{2}\begin{bmatrix}\mathbf{0} & l_{e2}\mathbf{R}_2^{\mathrm{T}}\\ \gamma l_{e1}\mathbf{R}_1^{\mathrm{T}} & l_{e2}\mathbf{R}_2^{\mathrm{T}}\\ \gamma l_{e1}\mathbf{R}_1^{\mathrm{T}} & \mathbf{0}\end{bmatrix};\quad \mathbf{T}_{\mathbf{R}}^{r-}=\frac{1}{2}\begin{bmatrix}(1-\gamma)l_{e1}\mathbf{R}_1^{\mathrm{T}} & \mathbf{0}\\ (1-\gamma)l_{e1}\mathbf{R}_1^{\mathrm{T}} & -l_{e2}\mathbf{R}_2^{\mathrm{T}}\\ \mathbf{0} & -l_{e2}\mathbf{R}_2^{\mathrm{T}}\end{bmatrix}\tag{10.33b}$$

Substituting Equations (10.32a)–(10.32c) into (10.33a) and (10.33b) and reorganizing terms, the internal forces become

$$\begin{Bmatrix}\mathbf{F}_{6'5'}\\ \mathbf{F}_{786}\\ \mathbf{F}_{58'7'}\end{Bmatrix}=\begin{Bmatrix}\mathbf{S}_1\\ \mathbf{S}_2\\ \mathbf{S}_3\end{Bmatrix}+\begin{bmatrix}\boldsymbol{\alpha}_{11} & \boldsymbol{\alpha}_{12} & \boldsymbol{\alpha}_{13}\\ \boldsymbol{\alpha}_{21} & \boldsymbol{\alpha}_{22} & \boldsymbol{\alpha}_{23}\\ \boldsymbol{\alpha}_{31} & \boldsymbol{\alpha}_{32} & \boldsymbol{\alpha}_{33}\end{bmatrix}\begin{Bmatrix}\mathbf{d}_{6'5'}\\ \mathbf{d}_{786}\\ \mathbf{d}_{58'7'}\end{Bmatrix}\tag{10.34a}$$

where

$$\mathbf{S}_1=\mathbf{T}_{\mathbf{R}}^{+}\begin{Bmatrix}\boldsymbol{\sigma}_{0\mathrm{I}}\\ \boldsymbol{\sigma}_{0\mathrm{II}}\end{Bmatrix},\quad \mathbf{S}_2=\mathbf{T}_{\mathbf{R}}^{l-}\begin{Bmatrix}\boldsymbol{\sigma}_{0\mathrm{I}}\\ \boldsymbol{\sigma}_{0\mathrm{III}}\end{Bmatrix},\quad \mathbf{S}_3=\mathbf{T}_{\mathbf{R}}^{r-}\begin{Bmatrix}\boldsymbol{\sigma}_{0\mathrm{II}}\\ \boldsymbol{\sigma}_{0\mathrm{III}}\end{Bmatrix};\tag{10.34b}$$

$$\boldsymbol{\alpha}_{11}=\frac{1}{2}\mathbf{T}_{\mathbf{R}}^{+}\begin{bmatrix}(2-\gamma)\boldsymbol{\alpha}_{0\mathrm{I}}\mathbf{R}_1 & \gamma\boldsymbol{\alpha}_{0\mathrm{I}}\mathbf{R}_1\\ (1-\gamma)\boldsymbol{\alpha}_{0\mathrm{II}}\mathbf{R}_1 & (1+\gamma)\boldsymbol{\alpha}_{0\mathrm{II}}\mathbf{R}_1\end{bmatrix};\quad \boldsymbol{\alpha}_{12}=\frac{1}{2}\mathbf{T}_{\mathbf{R}}^{+}\begin{bmatrix}\mathbf{0} & -\boldsymbol{\alpha}_{0\mathrm{I}}\mathbf{R}_1 & -\boldsymbol{\alpha}_{0\mathrm{I}}\mathbf{R}_1\\ \mathbf{0} & \mathbf{0} & \mathbf{0}\end{bmatrix};$$

$$\boldsymbol{\alpha}_{13}=\frac{1}{2}\mathbf{T}_{\mathbf{R}}^{+}\begin{bmatrix}\mathbf{0} & \mathbf{0} & \mathbf{0}\\ -\boldsymbol{\alpha}_{0\mathrm{II}}\mathbf{R}_1 & -\boldsymbol{\alpha}_{0\mathrm{II}}\mathbf{R}_1 & \mathbf{0}\end{bmatrix};\quad \boldsymbol{\alpha}_{21}=\frac{1}{2}\mathbf{T}_{\mathbf{R}}^{l-}\begin{bmatrix}(2-\gamma)\boldsymbol{\alpha}_{0\mathrm{I}}\mathbf{R}_1 & \gamma\boldsymbol{\alpha}_{0\mathrm{I}}\mathbf{R}_1\\ \mathbf{0} & \mathbf{0}\end{bmatrix};$$

$$\boldsymbol{\alpha}_{22}=\frac{1}{2}\mathbf{T}_{\mathbf{R}}^{l-}\begin{bmatrix}\mathbf{0} & -\boldsymbol{\alpha}_{0\mathrm{I}}\mathbf{R}_1 & -\boldsymbol{\alpha}_{0\mathrm{I}}\mathbf{R}_1\\ -\boldsymbol{\alpha}_{0\mathrm{III}}\mathbf{R}_2 & -\boldsymbol{\alpha}_{0\mathrm{III}}\mathbf{R}_2 & \mathbf{0}\end{bmatrix};\quad \boldsymbol{\alpha}_{23}=\frac{1}{2}\mathbf{T}_{\mathbf{R}}^{l-}\begin{bmatrix}\mathbf{0} & \mathbf{0} & \mathbf{0}\\ \mathbf{0} & \boldsymbol{\alpha}_{0\mathrm{III}}\mathbf{R}_2 & \boldsymbol{\alpha}_{0\mathrm{III}}\mathbf{R}_2\end{bmatrix};$$

$$\boldsymbol{\alpha}_{31}=\frac{1}{2}\mathbf{T}_{\mathbf{R}}^{r-}\begin{bmatrix}(1-\gamma)\boldsymbol{\alpha}_{0\mathrm{II}}\mathbf{R}_1 & (1+\gamma)\boldsymbol{\alpha}_{0\mathrm{II}}\mathbf{R}_1\\ \mathbf{0} & \mathbf{0}\end{bmatrix};\quad \boldsymbol{\alpha}_{32}=\frac{1}{2}\mathbf{T}_{\mathbf{R}}^{r-}\begin{bmatrix}\mathbf{0} & \mathbf{0} & \mathbf{0}\\ -\boldsymbol{\alpha}_{0\mathrm{III}}\mathbf{R}_2 & -\boldsymbol{\alpha}_{0\mathrm{III}}\mathbf{R}_2 & \mathbf{0}\end{bmatrix};$$

$$\boldsymbol{\alpha}_{33}=\frac{1}{2}\mathbf{T}_{\mathbf{R}}^{r-}\begin{bmatrix}-\boldsymbol{\alpha}_{0\mathrm{II}}\mathbf{R}_1 & -\boldsymbol{\alpha}_{0\mathrm{II}}\mathbf{R}_1 & \mathbf{0}\\ \mathbf{0} & \boldsymbol{\alpha}_{0\mathrm{III}}\mathbf{R}_2 & \boldsymbol{\alpha}_{0\mathrm{III}}\mathbf{R}_2\end{bmatrix}$$

(10.34c)

Substituting Equation (10.34a) into expressions (b, d, and f) in Equation (10.31) and solving the internal displacements as functions of the regular (external) nodal displacements, we get

$$\begin{bmatrix} \mathbf{L}_{22}^{+}-\boldsymbol{\alpha}_{11} & -\boldsymbol{\alpha}_{12} & -\boldsymbol{\alpha}_{13} \\ -\boldsymbol{\alpha}_{21} & \mathbf{L}_{22}^{l-}-\boldsymbol{\alpha}_{22} & -\boldsymbol{\alpha}_{23} \\ -\boldsymbol{\alpha}_{31} & -\boldsymbol{\alpha}_{32} & \mathbf{L}_{22}^{r-}-\boldsymbol{\alpha}_{33} \end{bmatrix} \begin{Bmatrix} \mathbf{d}_{6'5'} \\ \mathbf{d}_{786} \\ \mathbf{d}_{58'7'} \end{Bmatrix}$$

$$= \begin{Bmatrix} \mathbf{S}_1 \\ \mathbf{S}_2 \\ \mathbf{S}_3 \end{Bmatrix} + \begin{bmatrix} \mathbf{0} & \mathbf{0} & -\mathbf{L}_{21}^{+} \\ -\mathbf{L}_{21}^{l-} & \mathbf{0} & \mathbf{0} \\ \mathbf{0} & -\mathbf{L}_{21}^{r-} & \mathbf{0} \end{bmatrix} \begin{Bmatrix} \mathbf{d}_{\text{ext}}^{l-} \\ \mathbf{d}_{\text{ext}}^{r-} \\ \mathbf{d}_{\text{ext}}^{+} \end{Bmatrix} \tag{10.35}$$

The internal nodal displacements can be further expressed explicitly as functions of external nodal displacements as below:

$$\begin{Bmatrix} \mathbf{d}_{6'5'} \\ \mathbf{d}_{786} \\ \mathbf{d}_{58'7'} \end{Bmatrix} = \begin{bmatrix} \mathbf{Y}_7 & \mathbf{Y}_8 & \mathbf{Y}_9 \\ \mathbf{Y}_4 & \mathbf{Y}_5 & \mathbf{Y}_6 \\ \mathbf{Y}_1 & \mathbf{Y}_2 & \mathbf{Y}_3 \end{bmatrix} \begin{Bmatrix} \mathbf{S}_1 \\ \mathbf{S}_2 \\ \mathbf{S}_3 \end{Bmatrix} + \begin{bmatrix} \mathbf{X}_{13} & \mathbf{X}_{14} & \mathbf{X}_{15} \\ \mathbf{X}_{10} & \mathbf{X}_{11} & \mathbf{X}_{12} \\ \mathbf{X}_7 & \mathbf{X}_8 & \mathbf{X}_9 \end{bmatrix} \begin{Bmatrix} \mathbf{d}_{\text{ext}}^{l-} \\ \mathbf{d}_{\text{ext}}^{r-} \\ \mathbf{d}_{\text{ext}}^{+} \end{Bmatrix} \tag{10.36}$$

where the matrices $\mathbf{X}_p$ ($p=1, 2, \ldots, 15$) and $\mathbf{Y}_q$ ($q=1, 2, \ldots, 9$) can be found in Liu et al. (2014).

Finally, by substituting Equation (10.36) into Equation (10.31a, c, and e) to eliminate the internal nodal displacements, the fully condensed elemental equilibrium equation is obtained as

$$\begin{bmatrix} \mathbf{L}_{11}^{l-}+\mathbf{L}_{12}^{l-}\mathbf{X}_{10} & \mathbf{L}_{12}^{l-}\mathbf{X}_{11} & \mathbf{L}_{12}^{l-}\mathbf{X}_{12} \\ \mathbf{L}_{12}^{r-}\mathbf{X}_7 & \mathbf{L}_{11}^{r-}+\mathbf{L}_{12}^{r-}\mathbf{X}_8 & \mathbf{L}_{12}^{r-}\mathbf{X}_9 \\ \mathbf{L}_{12}^{+}\mathbf{X}_{13} & \mathbf{L}_{12}^{+}\mathbf{X}_{14} & \mathbf{L}_{11}^{+}+\mathbf{L}_{12}^{+}\mathbf{X}_{15} \end{bmatrix} \begin{Bmatrix} \mathbf{d}_{\text{ext}}^{l-} \\ \mathbf{d}_{\text{ext}}^{r-} \\ \mathbf{d}_{\text{ext}}^{+} \end{Bmatrix}$$

$$= \begin{Bmatrix} \mathbf{F}_{\text{ext}}^{l-} \\ \mathbf{F}_{\text{ext}}^{r-} \\ \mathbf{F}_{\text{ext}}^{+} \end{Bmatrix} - \begin{bmatrix} \mathbf{L}_{12}^{l-}\mathbf{Y}_4 & \mathbf{L}_{12}^{l-}\mathbf{Y}_5 & \mathbf{L}_{12}^{l-}\mathbf{Y}_6 \\ \mathbf{L}_{12}^{r-}\mathbf{Y}_1 & \mathbf{L}_{12}^{r-}\mathbf{Y}_2 & \mathbf{L}_{12}^{r-}\mathbf{Y}_3 \\ \mathbf{L}_{12}^{+}\mathbf{Y}_7 & \mathbf{L}_{12}^{+}\mathbf{Y}_8 & \mathbf{L}_{12}^{+}\mathbf{Y}_9 \end{bmatrix} \begin{Bmatrix} \mathbf{S}_1 \\ \mathbf{S}_2 \\ \mathbf{S}3 \end{Bmatrix} \tag{10.37}$$

Note that Equations (10.36) and (10.37) share the same matrices $\mathbf{X}_p$ ($p=1, 2, \ldots, 15$), $\mathbf{Y}_q$ ($q=1, 2, \ldots, 9$), and $\boldsymbol{S}_r$ ($r=1, 2, 3$), which are all functions of the characteristic cohesive stresses ($\boldsymbol{\sigma}_{0\text{I}}, \boldsymbol{\sigma}_{0\text{II}}$, and $\boldsymbol{\sigma}_{0\text{III}}$)$^{(i,j,k,l,m,n)}$ (10.32b) and the cohesive stiffnesses ($\boldsymbol{\alpha}_{0\text{I}}, \boldsymbol{\alpha}_{0\text{II}}$, and $\boldsymbol{\alpha}_{0\text{III}}$)$^{(i,j,k,l,m,n)}$ (10.32c). They are not known at this point because the crack displacements are not known yet. The solving procedure for these equations will be discussed in Section 10.3.3.

10.3.3 Elemental condensation algorithm

In Sections 10.3.1 and 10.3.2, the elemental equilibrium equations for a single crack (10.29) and for two interactive cracks (10.37) have been derived. However, these

nonlinear equations have yet to be solved. In the literature, Equation (10.29) or (10.37) is typically reformulated into an incremental form and then solved with either the direct matrix inversion technique (Linder and Armero, 2007, 2009; Rudraraju et al., 2010) or a Newton–Raphson type of iterative solver (Sluys and Berends, 1998; Dias-da-Costa et al., 2013; De Borst et al., 2012). This is known as the static condensation process.

In this chapter, the explicit nature of the solutions enables a very efficient elemental condensation process that is completely different from what has been used in the literature. Instead of solving the incremental form of the elemental equilibrium of Equation (10.29) or (10.37), in this chapter we first solve the internal nodal displacements (10.28c or 10.36) analytically through a simple consistency checking procedure. It will be shown that once these equations are solved, the equilibrium equations (10.29 or 10.37) are satisfied with mathematical exactness by substituting the related matrices into them.

10.3.3.1 Single intra-elemental crack

In this case, the internal crack displacements have been given in Equation (10.28a). It is noted that, once Equation (10.28a) is solved, that is, $\mathbf{S}_0, \mathbf{A}, \mathbf{B}, \boldsymbol{\Psi}_{22}^{+}$, and $\boldsymbol{\Psi}_{22}^{-}$ are established, simply substituting these matrices into Equation (10.29) will guarantee the elemental equilibrium. We first convert the global crack displacements in Equation (10.28a) into local crack displacements using Equation (10.26b), which gives

$$\begin{Bmatrix} \delta_{s6'6} \\ \delta_{n6'6} \\ \delta_{s5'5} \\ \delta_{n5'5} \end{Bmatrix} = \mathrm{Diag}\left[\mathbf{R}_1^{\mathrm{T}}; \mathbf{R}_1^{\mathrm{T}}\right]$$

$$\begin{pmatrix} -l_{e1}\left(\mathbf{A}^{-1} + \mathbf{B}^{-1} - l_{e1}\mathbf{A}^{-1}\boldsymbol{\alpha}\left(\boldsymbol{\Psi}_{22}^{-}\right)^{-1} + l_{e1}\mathbf{B}^{-1}\boldsymbol{\alpha}\left(\boldsymbol{\Psi}_{22}^{+}\right)^{-1}\right)\mathbf{S}_0 \\ + \left(\mathbf{B}^{-1} - l_{e1}\mathbf{A}^{-1}\boldsymbol{\alpha}\left(\boldsymbol{\Psi}_{22}^{-}\right)^{-1}\right)\mathbf{L}_{21}^{-}\mathbf{d}_{\mathrm{ext}}^{-} + \left(l_{e1}\mathbf{B}^{-1}\boldsymbol{\alpha}\left(\boldsymbol{\Psi}_{22}^{+}\right)^{-1} - \mathbf{A}^{-1}\right)\mathbf{L}_{21}^{+}\mathbf{d}_{\mathrm{ext}}^{+} \end{pmatrix}^{(i,j,k,l)} \tag{10.38}$$

In Equation (10.38), the superscripts (i, j, k, l) in the right-hand side are included to emphasize that the matrices $\mathbf{S}_0, \mathbf{A}, \mathbf{B}, \boldsymbol{\Psi}_{22}^{+}$, and $\boldsymbol{\Psi}_{22}^{-}$ are all functions of the cohesive slope matrix $\boldsymbol{\alpha}_0{}^{(i,j,k,l)}$ and characteristic stress matrix $\boldsymbol{\sigma}_0{}^{(i,j,k,l)}$ (10.26c and 10.28b). Thus, for any trial cohesive segment combination (i, j, k, l), a set of local crack displacements is immediately solved from Equation (10.38). The solved local crack displacements are then subjected to a consistency check, and *the true solution is found if the following statement is true:*

$$\left(\delta_{s6'6} \in \overleftrightarrow{\delta}_{s}^{(i)} \text{ is true}\right) \&\& \left(\delta_{n6'6} \in \overleftrightarrow{\delta}_{n}^{(j)} \text{ is true}\right) \&\& \left(\delta_{s5'5} \in \overleftrightarrow{\delta}_{s}^{(k)} \text{ is true}\right) \&\& \left(\delta_{n5'5} \in \overleftrightarrow{\delta}_{n}^{(l)} \text{ is true}\right)$$

where $\overleftrightarrow{\delta}_{\mathrm{s}}^{(i)}$, $\overleftrightarrow{\delta}_{\mathrm{n}}^{(j)}$, $\overleftrightarrow{\delta}_{\mathrm{s}}^{(k)}$, and $\overleftrightarrow{\delta}_{\mathrm{n}}^{(l)}$ are the respective crack displacement ranges of the assumed segments (i, j, k, l) (Section 10.2.2).

This is the core idea behind the solving algorithm used in this chapter. The mathematical exactness (in piecewise linear sense) of the solution is guaranteed by the solution uniqueness of the local problem (the solution uniqueness for linear material with nonlinear discontinuities has been discussed in Cervera et al., 2010). The detailed algorithm formulation and extended discussions on its numerical performance in solving fracture problems can be found in Liu et al. (2015).

10.3.3.2 Two intra-elemental cracks

In this case, the crack displacements as explicit functions of external displacements (e.g., Equation 10.38 for the single crack case) are not readily available. However, the solving procedure presented above remains applicable in solving the internal displacement equation of Equation (10.36). The equation is repeated below with superscripts added to emphasize the dependence of $\mathbf{X}_p$ ($p=1, 2, \ldots, 15$), $\mathbf{Y}_q$ ($q=1, 2, \ldots, 9$), and $\mathbf{S}_r$ ($r=1, \ldots,3$) on the cohesive segment combination (i,j,k,l,m,n).

$$\begin{Bmatrix} \mathbf{d}_{6'5'} \\ \mathbf{d}_{786} \\ \mathbf{d}_{58'7'} \end{Bmatrix} = \left(\begin{bmatrix} \mathbf{Y}_7 & \mathbf{Y}_8 & \mathbf{Y}_9 \\ \mathbf{Y}_4 & \mathbf{Y}_5 & \mathbf{Y}_6 \\ \mathbf{Y}_1 & \mathbf{Y}_2 & \mathbf{Y}_3 \end{bmatrix} \begin{Bmatrix} \mathbf{S}_1 \\ \mathbf{S}_2 \\ \mathbf{S}_3 \end{Bmatrix} \right)^{(i,j,k,l,m,n)} + \begin{bmatrix} \mathbf{X}_{13} & \mathbf{X}_{14} & \mathbf{X}_{15} \\ \mathbf{X}_{10} & \mathbf{X}_{11} & \mathbf{X}_{12} \\ \mathbf{X}_7 & \mathbf{X}_8 & \mathbf{X}_9 \end{bmatrix}^{(i,j,k,l,m,n)} \begin{Bmatrix} \mathbf{d}_{\mathrm{ext}}^{l-} \\ \mathbf{d}_{\mathrm{ext}}^{r-} \\ \mathbf{d}_{\mathrm{ext}}^{+} \end{Bmatrix} \tag{10.39}$$

For a trial cohesive segment combination (i,j,k,l,m,n) and given external nodal displacements, a set of solution to the internal nodal displacements, $\mathbf{d}_{6'5'} = \{\mathbf{d}_{6'}, \mathbf{d}_{5'}\}^{\mathrm{T}}$, $\mathbf{d}_{786} = \{\mathbf{d}_7, \mathbf{d}_8, \mathbf{d}_6\}^{\mathrm{T}}$, and $\mathbf{d}_{58'7'} = \{\mathbf{d}_5, \mathbf{d}_{8'}, \mathbf{d}_{7'}\}^{\mathrm{T}}$, is immediately solved from Equation (10.39). Then, the crack displacements at the integration point of each segment (points I, II, and III in Figure 10.6) are computed and converted to local coordinates, that is,

$$\begin{cases} \{\delta_{\mathrm{sI}}, \delta_{\mathrm{nI}}\}^{\mathrm{T}} = \mathbf{R}_1^{\mathrm{T}}((1-\gamma/2)\mathbf{d}_{6'} + (\gamma/2)\mathbf{d}_{5'} - (\mathbf{d}_6 + \mathbf{d}_8)/2)^{(i,j,k,l,m,n)} \\ \{\delta_{\mathrm{sII}}, \delta_{\mathrm{nII}}\}^{\mathrm{T}} = \mathbf{R}_1^{\mathrm{T}}((1-\gamma/2)\mathbf{d}_{6'} + (1+\gamma)/2\mathbf{d}_{5'} - (\mathbf{d}_5 + \mathbf{d}_{8'})/2)^{(i,j,k,l,m,n)} \\ \{\delta_{\mathrm{sIII}}, \delta_{\mathrm{nIII}}\}^{\mathrm{T}} = \mathbf{R}_2^{\mathrm{T}}((\mathbf{d}_{7'} + \mathbf{d}_{8'})/2 - (\mathbf{d}_7 + \mathbf{d}_8)/2)^{(i,j,k,l,m,n)} \end{cases} \tag{10.40}$$

The local crack displacements are then subjected to a consistency check similar to the single crack case and the exact solution is found when the following statement is true.

$$\left(\delta_{\mathrm{sI}} \in \overset{\leftrightarrow}{\delta}{}_{\mathrm{s}}^{(i)} \text{ true}\right) \&\& \left(\delta_{\mathrm{nI}} \in \overset{\leftrightarrow}{\delta}{}_{\mathrm{n}}^{(j)} \text{ true}\right) \&\& \left(\delta_{\mathrm{sII}} \in \overset{\leftrightarrow}{\delta}{}_{\mathrm{s}}^{(k)} \text{ true}\right) \&\&$$
$$\left(\delta_{\mathrm{nII}} \in \overset{\leftrightarrow}{\delta}{}_{\mathrm{n}}^{(l)} \text{ true}\right) \&\& \left(\delta_{\mathrm{sIII}} \in \overset{\leftrightarrow}{\delta}{}_{\mathrm{s}}^{(m)} \text{ true}\right) \&\& \left(\delta_{\mathrm{nIII}} \in \overset{\leftrightarrow}{\delta}{}_{\mathrm{n}}^{(n)} \text{ true}\right)$$

Once the solution is found, $\mathbf{X}_p$ ($p = 1, 2, \ldots, 15$), $\mathbf{Y}_q$ ($q = 1, 2, \ldots, 9$), and $\mathbf{S}_r$ ($r = 1, 2, 3$) are all established with the determined (i, j, k, l, m, n). Substituting them into Equation (10.29), the fully condensed elemental equilibrium is then satisfied with mathematical exactness (in piecewise linear sense and within the limit of FE discretization accuracy).

10.3.4 Numerical implementation

The new A-FEM and the solving procedure above can be integrated into any standard FE programs as a general-purposed element because the elemental locality is completely retained. Here, we briefly describe how to implement it into an existing FE program as an element.

For any displacement-based FEM programs, the external nodal displacements are passed into the element to establish: (1) instantaneous element stiffness matrix or Jacobian matrix and (2) the external force array (also called right-hand side or RHS). Both matrices have been derived and solved explicitly in Section 10.3.1 for the single crack case (10.29) and in Section 10.3.2 for the case of two intra-elemental cracks (10.37).

The local crack displacements are saved as solution-dependent variables (or state variables) and subjected to constant updates so that their maximum values, if ever experienced, are always available for assessing loading or unloading condition (for consistency check). Another minor issue is to guarantee the deformation continuity across the element edge that is shared by a crack tip element and the element immediately ahead of it, which is a standard continuous element. This is done in this paper by enforcing the internal nodal displacements at the edge to be $\mathbf{d}_5 = \mathbf{d}_{5'} = N_A\mathbf{d}_A + N_B\mathbf{d}_B$, where 5 and 5′ are the internal nodes at the crack tip; A and B are the two external nodes of the element edge hosting the crack tip; and N_A and N_B are the standard line shape functions associated with nodes A and B.

One of the advantages of this method is that it does not need a sophisticated global tracking algorithm such as the level-set functions in the X-FEM for a propagating crack, which requires heavy calculations when implemented in a narrowband manner. However, it is beneficial to record the crack path so that the interelement continuity of a crack is reinforced. This was done with a common block accessible to all user elements, within which the geometric information of a crack is constantly updated as it propagates. A detailed data structure and propagation rules regarding multiple crack interaction have been given in detail in Liu et al. (2014).

We note that the new A-FEM only needs to record the cracks developed in response to the local stress conditions. There is no need to actively assign an incremental crack

length for crack extension. The crack initiation in an element is purely determined by the local stresses in the crack front element accordingly to a specified initiation criterion (such as the maximum principal stress criterion used in the following numerical examples in Section 10.4). The propagation is purely determined by the cohesive crack propagation rule of Equation (10.15).

10.4 3D A-FEM formulation

Extension of the two-dimensional (2D) A-FEM formulation to three-dimensional (3D) is relatively straightforward. Here, we briefly present the 3D A-FEM for the four-node tetrahedron element as shown in Figure 10.7a (Naderi et al., 2015). There are two possible configurations if the element is cut by a crack surface: (1) the element is cut into one tetrahedron subdomain and one wedge subdomain as shown in Figure 10.7b; and (2) the element is cut into two wedge subdomains as shown in Figure 10.7c.

The tetrahedron-wedge configuration with the triangular crack plane (Figure 10.7b) has six internal nods as 5, 6, 7, 5′, 6′, and 7′ whereas the wedge–wedge configuration with quadrilateral crack plane has eight internal nodes 5, 6, 7, 8, 5′, 6′,7′, and 8′. Displacement jumps across the cohesive crack are simply the difference in displacements between node-pair 5–5′, 6–6′, 7–7′, and 8–8′. Defining a local coordinate system as shown in Figure 10.7d with the surface out-normal ($\vec{\mathbf{N}}$) as the local z-axis, the rotation matrix can be obtained as

$$\mathbf{R} = \begin{bmatrix} l_1 & m_1 & n_1 \\ l_2 & m_2 & n_2 \\ l_3 & m_3 & n_3 \end{bmatrix} \tag{10.41a}$$

where l_i, m_j, and n_k $(i, j, k = 1,2,3)$ are the direction cosines of the crack plane with $\vec{\mathbf{N}} = l_1\,\vec{i} + m_1\,\vec{j} + n_1\,\vec{k}$ as the out-normal direction, $\vec{\mathbf{T}} = l_2\,\vec{i} + m_2\,\vec{j} + n_2\,\vec{k}$ and $\vec{\mathbf{S}} = n_1\,\vec{i} + n_2\,\vec{j} + n_3\,\vec{k}$ as the two orthogonal in-plane shear directions, and

$$l_i = \mathrm{Cos}\alpha_i, \quad m_i = \mathrm{Cos}\beta_i, \quad n_i = \mathrm{Cos}\gamma_i \quad (i = 1,2,3) \tag{10.41b}$$

α_i, β_i, and γ_i are the angles between the local axes and global axes as illustrated in Figure 10.7d.

Following the similar procedure of 2D A-FEM in Section 10.3.1, the local equilibrium equation can be written as the identical form of Equation (10.19):

$$\begin{cases} \begin{bmatrix} \mathbf{L}_{11}^{+} & \mathbf{L}_{12}^{+} \\ \mathbf{L}_{21}^{+} & \mathbf{L}_{22}^{+} \end{bmatrix} \begin{Bmatrix} \mathbf{d}_{\mathrm{ext}}^{+} \\ \mathbf{d}_{\mathrm{int}}^{+} \end{Bmatrix} = \begin{Bmatrix} \mathbf{F}_{\mathrm{ext}}^{+} \\ \mathbf{F}_{\mathrm{int}}^{+} \end{Bmatrix} \\ \begin{bmatrix} \mathbf{L}_{11}^{-} & \mathbf{L}_{12}^{-} \\ \mathbf{L}_{21}^{-} & \mathbf{L}_{22}^{-} \end{bmatrix} \begin{Bmatrix} \mathbf{d}_{\mathrm{ext}}^{-} \\ \mathbf{d}_{\mathrm{int}}^{-} \end{Bmatrix} = \begin{Bmatrix} \mathbf{F}_{\mathrm{ext}}^{-} \\ \mathbf{F}_{\mathrm{int}}^{-} \end{Bmatrix} \end{cases} \tag{10.42}$$

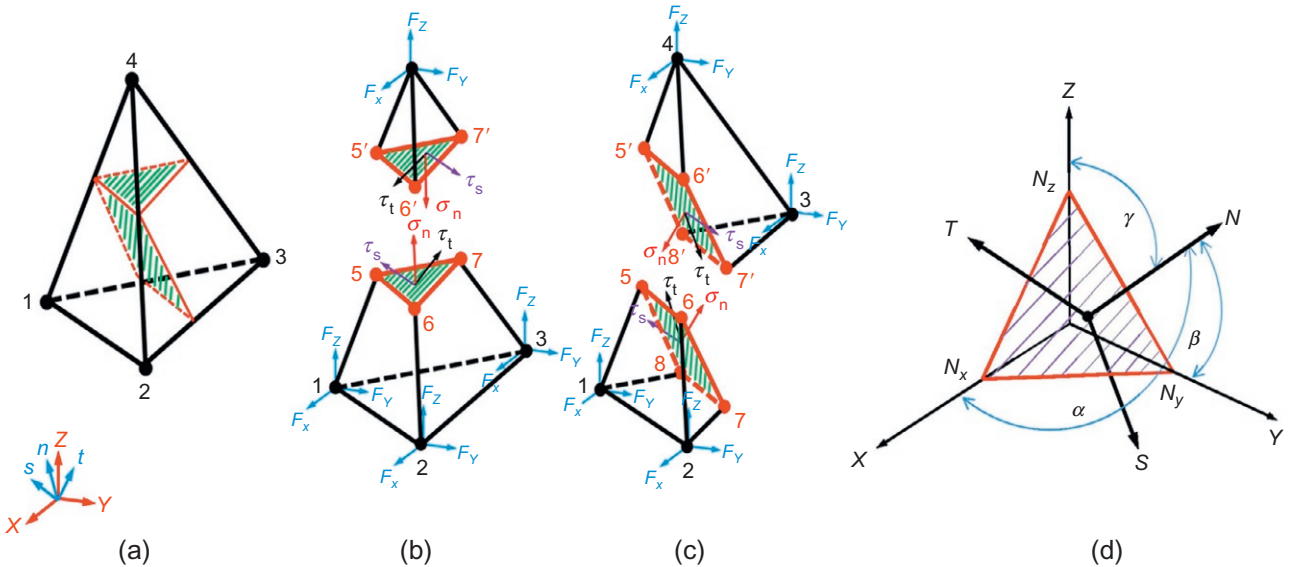

Figure 10.7 Element illustration for (a) a regular four-node tetrahedron element with two possible cut configurations by a crack plane, (b) the A-FE with tetrahedron-wedge configuration, (c) the A-FE with wedge–wedge configuration, and (d) the definition of local coordinates for the crack plane.

The only differences between Equations (10.19) and (10.42) are the dimension of the submatrices and the definition of external and internal DoFs and forces. For the tetrahedron wedge cut configuration (Figure 10.7a),

$$\mathbf{F}_{\text{ext}}^{+}=\mathbf{F}_{4};\ \ \mathbf{F}_{\text{ext}}^{-}=\mathbf{F}_{123};\ \ \mathbf{d}_{\text{ext}}^{+}=\mathbf{d}_{4};\ \ \mathbf{d}_{\text{ext}}^{-}=\mathbf{d}_{123}$$
$$\mathbf{F}_{\text{int}}^{+}=\mathbf{F}_{5'6'7'};\ \ \mathbf{F}_{\text{int}}^{-}=\mathbf{F}_{567};\ \ \mathbf{d}_{\text{int}}^{+}=\mathbf{d}_{5'6'7'};\ \ \mathbf{d}_{\text{int}}^{-}=\mathbf{d}_{567}$$

and for the wedge–wedge cut configuration (Figure 10.7b),

$$\mathbf{F}_{\text{ext}}^{+}=\mathbf{F}_{34};\quad \mathbf{F}_{\text{ext}}^{-}=\mathbf{F}_{12};\quad \mathbf{d}_{\text{ext}}^{+}=\mathbf{d}_{34};\quad \mathbf{d}_{\text{ext}}^{-}=\mathbf{d}_{12}$$
$$\mathbf{F}_{\text{int}}^{+}=\mathbf{F}_{5'6'7'8'};\ \ \mathbf{F}_{\text{int}}^{-}=\mathbf{F}_{5678};\ \ \mathbf{d}_{\text{int}}^{+}=\mathbf{d}_{5'6'7'8'};\ \ \mathbf{d}_{\text{int}}^{-}=\mathbf{d}_{5678}$$

The internal force array integrated from cohesive stresses between the cohesive crack surfaces can be written as

$$\mathbf{F}_{\text{int}}^{-}=-\mathbf{F}_{\text{int}}^{+}=A_e(\mathbf{S_0}+\boldsymbol{\alpha}\cdot\Delta\mathbf{d}_{\text{int}}),\tag{10.43a}$$

where A_e is the area of the crack surface. $\mathbf{S_0}$ and $\boldsymbol{\alpha}$ are the characteristic stress and cohesive stiffness matrix similar to those in Equation (10.26a)–(10.26c). For the tetrahedron wedge cut configuration,

$$\begin{aligned}
&\mathbf{S_0}=\text{Diag}\left[\mathbf{R}^{\text{T}};\mathbf{R}^{\text{T}};\mathbf{R}^{\text{T}}\right](\mathbf{T}_{\text{coh}})^{\text{T}}\boldsymbol{\sigma_0}\\
&\boldsymbol{\alpha}=\text{Diag}\left[\mathbf{R}^{\text{T}};\mathbf{R}^{\text{T}};\mathbf{R}^{\text{T}}\right](\mathbf{T}_{\text{coh}})^{\text{T}}\boldsymbol{\alpha}_0\mathbf{N}_{\text{coh}}\text{Diag}[\mathbf{R};\mathbf{R};\mathbf{R}]\\
&\boldsymbol{\sigma_0}=\left\{\hat{\tau}_{\text{s}}^{(i)}-\alpha_{\text{s}}^{(i)}\delta_{\text{s}}^{(i)};\hat{\tau}_{\text{t}}^{(j)}-\alpha_{\text{t}}^{(j)}\delta_{\text{t}}^{(j)};\hat{\sigma}^{(k)}-\alpha_{\text{n}}^{(k)}\delta_{\text{n}}^{(k)};\cdots;\hat{\sigma}^{(q)}-\alpha_{\text{n}}^{(q)}\delta_{\text{n}}^{(q)}\right\}^{\text{T}};\\
&\boldsymbol{\alpha}_0=\text{Diag}\left[\alpha_{\text{s}}^{(i)};\alpha_{\text{t}}^{(j)};\alpha_{\text{n}}^{(k)};\alpha_{\text{s}}^{(l)};\alpha_{\text{t}}^{(m)};\alpha_{\text{n}}^{(n)}\alpha_{\text{s}}^{(o)};\alpha_{\text{t}}^{(p)};\alpha_{\text{n}}^{(q)}\right]
\end{aligned}\tag{10.43b}$$

where $\mathbf{T}_{\text{coh}}$ and $\mathbf{N}_{\text{coh}}$ are the respective integration and interpolation matrix for the three-node cohesive crack surface. Each of the free indices (i,j,k,l,m,n,o,p,q) can range from one to four for the cohesive law shown in Figure 10.4.

For the wedge–wedge cut configuration,

$$\begin{aligned}
&\mathbf{S_0}=\text{Diag}\left[\mathbf{R}^{\text{T}};\mathbf{R}^{\text{T}};\mathbf{R}^{\text{T}};\mathbf{R}^{\text{T}}\right](\mathbf{T}_{\text{coh}})^{\text{T}}\boldsymbol{\sigma_0}\\
&\boldsymbol{\alpha}=\text{Diag}\left[\mathbf{R}^{\text{T}};\mathbf{R}^{\text{T}};\mathbf{R}^{\text{T}};\mathbf{R}^{\text{T}}\right](\mathbf{T}_{\text{coh}})^{\text{T}}\boldsymbol{\alpha}_0\mathbf{N}_{\text{coh}}\text{Diag}[\mathbf{R};\mathbf{R};\mathbf{R};\mathbf{R}]\\
&\boldsymbol{\sigma_0}=\left\{\hat{\tau}_{\text{s}}^{(i)}-\alpha_{\text{s}}^{(i)}\delta_{\text{s}}^{(i)};\hat{\tau}_{\text{t}}^{(j)}-\alpha_{\text{t}}^{(j)}\delta_{\text{t}}^{(j)};\hat{\sigma}^{(k)}-\alpha_{\text{n}}^{(k)}\delta_{\text{n}}^{(k)};\cdots;\hat{\sigma}^{(t)}-\alpha_{\text{n}}^{(t)}\delta_{\text{n}}^{(t)}\right\}^{\text{T}};\\
&\boldsymbol{\alpha}_0=\text{Diag}\left[\alpha_{\text{s}}^{(i)};\alpha_{\text{t}}^{(j)};\alpha_{\text{n}}^{(k)};\alpha_{\text{s}}^{(l)};\alpha_{\text{t}}^{(m)};\alpha_{\text{n}}^{(n)};\alpha_{\text{s}}^{(o)};\alpha_{\text{t}}^{(p)};\alpha_{\text{n}}^{(q)};\alpha_{\text{s}}^{(\text{r})};\alpha_{\text{t}}^{(\text{s})};\alpha_{\text{n}}^{(\text{t})}\right]
\end{aligned}\tag{10.43c}$$

In this case, $\mathbf{T}_{\text{coh}}$ and $\mathbf{N}_{\text{coh}}$ are the respective integration and interpolation matrix for the four-node cohesive surface. Each of the free indices (i,j,k,l,m,n,o,p,q,r,s,t) can range from one to four for the cohesive law shown in Figure 10.4.

With the characteristic stress, cohesive stiffness, interpolation, and integration matrices fully defined, the equation that relates internal displacements to the

external displacements, and the equation of elemental equilibrium are found to be in exactly the same matrix form of Equations (10.28a)–(10.28c) and (10.29), respectively. Thus, the consistency check-based procedure for elemental condensation as described in Section 10.3.3 can be readily applied to solve the element equilibrium.

One of the biggest challenges in 3D fracture modeling is to maintain the conformity of the evolving crack surface. A crack surface tracking scheme is absolutely necessary, and proper numerical treatments have to be done to guarantee that the crack surface, which may cut multiple elements before they merge at some point, maintains a relatively smooth planar configuration without too much out-of-plane oscillation. Several crack-tracking schemes, such as local and global tracking algorithms, have been developed in the literature (Areias and Belytschko, 2005; Gasser and Holzapfel, 2006; Oliver and Huespe, 2002; Oliver et al., 2004). Here, we adopt the local tracking algorithm first proposed by Areias and Belytschko (2005). The detailed algorithm will not be given in this chapter, but interested readers are referred to Areias and Belytschko (2005).

10.5 Numerical examples and discussions

10.5.1 Four-point shear beam test

In this section, we test the new A-FEM's capability in simulating the crack propagation in a four-point shear beam test reported by Carpinteri et al. (1993). The problem has been simulated successfully using extended finite element method (X-FEM) by Moës and Belytschko (2002). Here, we adopt the numerical model setup used in Moës and Belytschko (2002), which is reproduced in Figure 10.8. The geometry dimensions are $b=200$ mm; $l=4b$; $a=0.2b$; $c/b=0.4$; $l_1=l_2=20$ mm; $t=100$ mm.

Maximum principal stress criterion was used for crack initiation. That is, crack initiation from a pristine elastic element occurs when the maximum principal stress averaged within the element ($\overline{\sigma}_{\max}$) reaches the mode I cohesive strength ($\hat{\sigma}$). The crack path is perpendicular to the maximum principal stress direction. The concrete material properties are $E=28{,}000\,\mathrm{N/mm^2}$; $\nu=0.1$; $\Gamma_{\mathrm{I}}=0.145\,\mathrm{N/mm}$; $\hat{\sigma}=2.4\,\mathrm{N/mm^2}$. The cohesive law used is a triangular type with an initial slope of $\alpha_{n1}=2.0\times10^4\,\mathrm{N/mm^3}$ and a softening slope of $\alpha_{n2}=-20\,\mathrm{N/mm^3}$.

To investigate the mesh sensitivity of the new A-FEM, the problem was analyzed by five different structured meshes with characteristic mesh size of $h=2$, 4, 8, 13, and 20 mm (the total elements are 10,760, 2849, 1094, 640, and 410, in the same order), and three unstructured meshes with $h\sim4$, 8, and 15 mm (total elements 4062, 1333, and 463, respectively). The two finer meshes, $h=2$ and 4 mm, are typical of those used in the literature (Linder and Armero, 2007; Dias-da-Costa et al., 2009, 2013; Moës and Belytschko, 2002), whereas the larger meshes (8, 13.3, and 20 mm) are used in this study to explore the mesh limit of the new A-FEM. The unstructured meshes of ~4, 8, and 13 mm were intended to check the mesh sensitivity and the robustness of the new A-FEM. Five of the discretized models (structured $h=2$, 8, and 20 mm

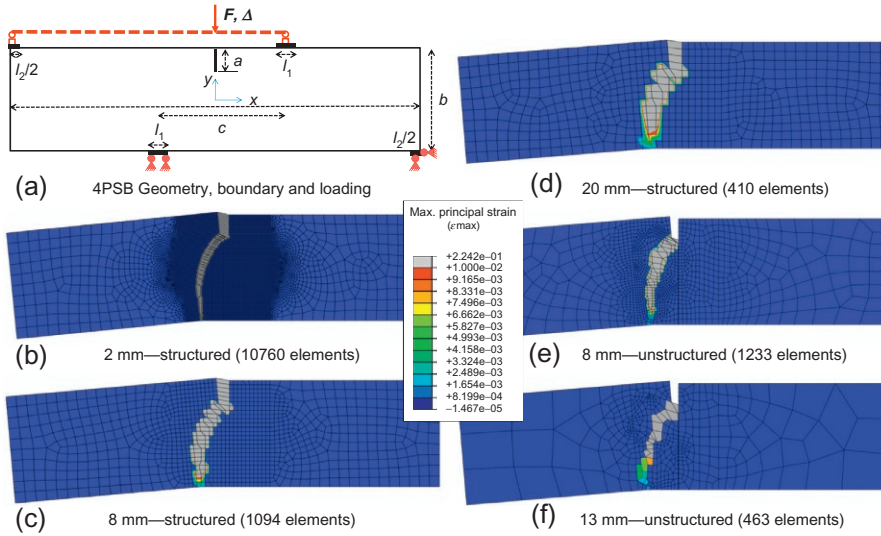

Figure 10.8 (a) Numerical models and simulated crack paths for structured (b) 2 mm mesh, (c) 8 mm mesh, (d) and 20 mm mesh, and unstructured (e) 8 mm and (f) 13 mm meshes. Liu et al. (2014).

meshes and unstructured $h \sim 8$ and 13 mm meshes) under deformed states are shown in Figure 10.8b–f with the crack trajectories roughly following the center lines of the white bands.

The loading parameters were set to be identical for all the cases, with a maximum prescribed displacement of 1.0 mm, a suggested initial incremental size of 0.001 mm, and a maximum incremental size of 0.01 mm. The actual size of each increment was determined by the automatic incrementation scheme in ABAQUS, which depends on the convergence rate.

All simulations were run on a Dell precision M4600 ($\times$64 bit) mobile workstation with Intel Core i7-2860 QM CPU at 2.5 GHz and with 8 GB of RAM. Simulations were terminated when the load-point displacement reached 0.1 mm (after snapback). RIKS option (arc-length method) was invoked in an attempt to capture the snapback behavior.

10.5.1.1 Numerical accuracy and mesh sensitivity

The simulated load–displacement curves are plotted in Figure 10.9a. The X-FEM prediction obtained by Moës and Belytschko (2002), which used a triangular mesh of $h \sim 3$ mm, was superimposed on this plot for comparison. For each case, the load linearly increases with the applied displacement until crack initiation from the precrack tip, which occurs at an applied displacement of $\sim$0.04 mm. After the initiation, the load–displacement curve becomes increasingly nonlinear due to continuous crack growth. The peak load is reached at the displacement of about $\sim$0.09 mm. After

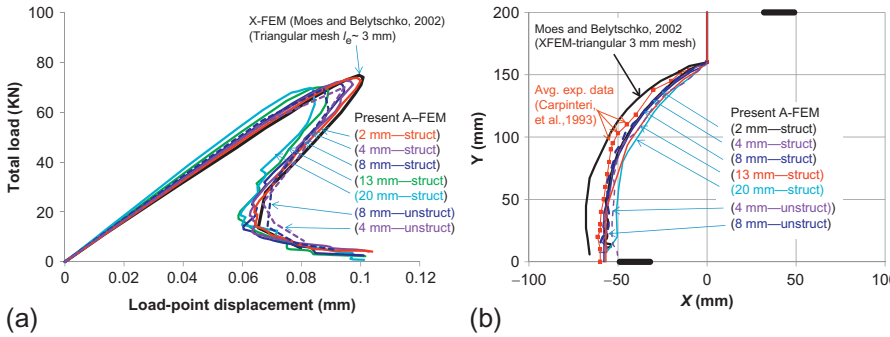

Figure 10.9 A-FEM simulated (a) load–displacement curves and (b) crack trajectories the X-FEM results of Moës and Belytschko (2002) and experimental results of Carpinteri et al. (1993).
Liu et al. (2014).

the peak load, all curves exhibit a strong snapback behavior. In this study, the strong snapback behavior was captured using the arc-length method available in ABAQUS (Option RIKS).

The A-FEM computed load–displacement results are very consistent with the X-FEM result obtained in Moës and Belytschko (2002). In particular, the load–displacement curves obtained with smaller mesh sizes (i.e., $h = 2$, 4, and 8 mm) are almost identical with the X-FEM results. For the larger meshes, that is, $h = 13$ and 20 mm, the curves deviate mildly from the finer mesh curves due to increases in initial stiffness. The systematic increase of initial stiffness with the increase of mesh sizes is largely due to the inherent numerical inaccuracy associated with the four-node plane elements (it is well known that larger FE elements lead to an overestimation of elemental stiffness). If the deviation of initial slope is discounted, the load–displacement curves obtained with larger meshes ($h = 13$ and 20 mm) remain very consistent with the X-FEM curve and the finer mesh results. This clearly demonstrates the mesh insensitivity of the new A-FEM.

The mesh insensitivity of the new A-FEM is further demonstrated by the fact that the load–displacement curves obtained from unstructured meshes are also very consistent with the results of the structured meshes with similar mesh sizes. Two of the load–displacement curves obtained from the unstructured meshes, $h = 4$ and 8 mm, as shown in Figure 10.9a by the dashed lines, are basically indistinguishable from the results of the respective structured meshes.

Figure 10.9b summarizes the crack trajectories predicted by the new A-FEM simulations with the structured (solid lines) and unstructured (dashed lines) meshes. The crack paths are all very consistent and close to the experimental curve, even though they were obtained with vastly different mesh sizes and structures. The mild difference in crack paths with larger meshes is largely attributed to the maximum kinking angle limit of $\pm 45°$ permitted by our numerical program. This is a standard numerical treatment to avoid a possible crack curve back. It is seen that even with this artificial

limit, it takes no more than two to three sequential kinks for the trajectories to establish a path that is very close to the experimental curve.

It should be mentioned that the mesh insensitivity in this example is expected because all the mesh sizes are considerably smaller than the cohesive zone size (or fracture process zone size). The cohesive zone size, estimated by $l_{coh} = E\Gamma_I/2\hat{\sigma}^2$ (Yang and Cox, 2005; Turon et al., 2007), is about $l_{coh} = 350$ mm. This is about twice the beam depth and more than 15 times the largest mesh size (20 mm). In this example, the mesh size is limited by the spacing between the notch and the nearest loading zone, which is merely 40 mm (Figure 10.8a). With the largest 20 mm mesh, there are only two columns of elements between the notch and the nearest loading zone. The fact that the new A-FEM simulation can still correctly capture the crack trajectory is rather encouraging. Elsewhere, it has been demonstrated through other examples that the new A-FEM remains fairly accurate with mesh sizes up to 70% of the cohesive zone size, in which cases the X-FEM exhibited serious (unacceptable) mesh dependency (Liu et al., 2013).

10.5.1.2 *Numerical efficiency and stability as compared to phantom-node-based A-FEM*

In this section, we compare the numerical accuracy, efficiency, and stability of the new A-FEM against the phantom-node-based A-FEM. The meshes and boundary conditions are exactly the same as those used in the previous section. It is noted that both the new A-FEM and the PNM-based A-FEM have been implemented in the ABAQUS package (v6.11) as user-defined elements, and they employ the same crack-tracking algorithm (Ling et al., 2009; Liu et al., 2014) (the tracking algorithm of the new A-FEM was directly inherited from the previous PNM-based A-FEM). Thus, the numerical performance comparison should be objective.

For all simulations, the loading parameters were set to be identical with a maximum prescribed displacement of 0.1 mm, and a suggested maximum incremental size of 0.002 mm. The minimum increment size is 10^{-8} mm and the largest suggested incremental size is 10^{-3} mm. The RIKS option (arc-length method) was invoked in an attempt to capture the snapback behavior.

Comparisons of the predicted load–displacement curves using the new A-FEM and the PNM-based A-FEM are given in Figure 10.10a. The X-FEM result reported in Moës and Belytschko (2002) is also included in this plot for comparison. Both the new A-FEM and the PNM-based A-FEM completed the simulations without much numerical difficulty. The new A-FEM results agree very well with the X-FEM result of Moës and Belytschko (2002). The PNM-based A-FEM also did a good job except that the snapbacks are slightly sharper than those predicted by the new A-FEM and the X-FEM.

The new A-FEM empowered by the consistency-check-based condensation algorithm, however, is much more efficient than the PNM-based A-FEM. Figure 10.10b compares the CPU time (in seconds) required by the two methods in completing the simulations. For an identical mesh, the CPU time required by the new A-FEM is, on average, merely 1/50 of that required by the PNM-based A-FEM (i.e., an increase of

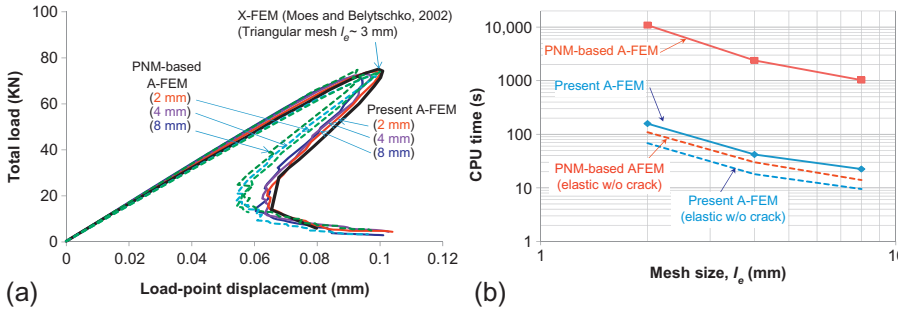

Figure 10.10 (a) Comparison of predicted load–displacement curves using the PNM-based A-FEM and the new A-FEM. (b) Comparison of the CPU time as a function of mesh sizes.

numerical efficiency by 5000%). The ~50 times increase of CPU time by the PNM-based A-FEM is *not* due to the use of double nodes (recall that the total DoFs of a PNM-based A-FEM model is two times the DoFs of the corresponding model of the new A-FEM). The two dashed lines in Figure 10.10b represent the CPU times required by both methods to complete the elastic problems with the same mesh and the same load incremental numbers, but with crack initiation and propagation prohibited. In such crack-free, elastic simulations, the CPU time required by the PNM-based A-FEM is about 60% more than that required by the new A-FEM, which is consistent with what reported in Ling et al. (2009). Thus, for the PNM-based A-FEM, the ~100 times (10,000%) increase of CPU time from a crack-free elastic simulation to the respective crack propagation simulation is directly due to the additional computational cost in treating the propagating crack. The CPU times of the new A-FEM simulations are on average about twice that of the respective elastic calculations (~100% increase).

A close examination of the two methods shows that the significant increase of CPU time by the PNM-based A-FEM is associated with (1) the ever-increasing active DoFs as a crack propagates and (2) the numerical procedure to judicially determine the crack configuration and to properly assign the ghost and real nodes to cracked subdomains. These two elements are critical to many advanced numerical methods that employ additional external DoFs to account for propagating cracks (e.g., X-FEM,[2] PNM, and G-FEM). However, the new A-FEM does not need either of them (see Liu et al., 2014 for the detailed A-FEM formulation). It is obvious that the consistency-check-based algorithm of the new A-FEM contributes significantly to the improvement in numerical efficiency and accuracy.

[2] We also compared the numerical efficiency with the X-FEM in ABAQUS (v6.11) and found that the present A-FEM is two to three orders of magnitude more efficient (see (Mohammadizadeh, 2013) Mohammadizadeh, S., *A Novel Augmented Finite Element Method for Modeling Arbitrary Cracking in 2D Solids*, in Dept. of Mechanical and Aerospace Engineering University of Miami, PhD thesis, 2013).

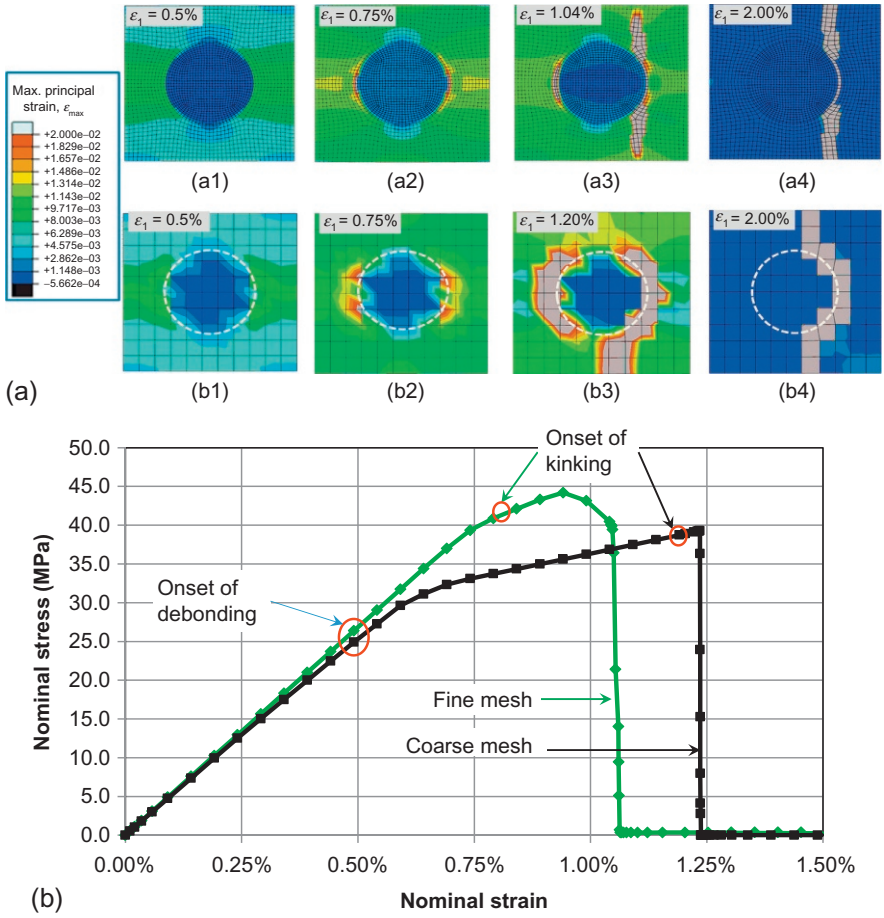

Figure 10.11 (a) The new A-FEM simulated crack development for a single fiber–matrix domain under uniaxial tension. The entire progressive damage processes, including the initial fiber–matrix interface (dashed line), debonding crack, and final kinking cracks in matrix, are indicated in the top and bottom contour plots for the two meshes, (b) the predicted nominal stress–strain curve with characteristic points indicated.

10.5.2 Coupled fiber–matrix interface debonding and kinking

We next demonstrate the capability of the new A-FEM in dealing with multiple crack interaction. We chose to model a single fiber/matrix domain as shown in Figure 10.11. The entire domain is 1 mm × 1 mm and the fiber diameter is 0.5 mm (i.e., fiber volume fraction 19.6%). Two sets of meshes were used to simulate the problem: (a) a fine mesh as shown in Figure 10.11a with 2244 elements, and (b) a coarse mesh as shown in Figure 10.11b with 110 elements. In the fine mesh (a) the elements are arranged to conform to the circular fiber/matrix interface. The ring of elements that host the bimaterial interface are initially augmented with a weak discontinuity and are allowed for

secondary crack kinking into the matrix subdomain if the subdomain stresses meet the maximum stress criterion. The coarse mesh (b) is a structured one and does not conform to the fiber/matrix interface (shown by the dashed circle in Figure 10.11b). That is, the fiber–matrix interface is deliberately set to bisect the structured elements. The elements traversed by the interface are initially augmented to account for intra-element material difference, possible interface debonding, and crack kinking into the matrix.

The modulus and Poisson's ratio for the fiber and matrix, respectively, are $E_f = 40$ GPa; $v_f = 0.33$; and $E_m = 4$ GPa; $v_m = 0.4$. A cohesive model with triangular traction-separation laws were used for interface debonding and matrix cracking. The cohesive parameters for matrix cracking and interface debonding are set to be identical: $\hat{\sigma} = \hat{\tau} = 50\,\text{MPa}$; $\delta_{\text{nc}} = \delta_{\text{sc}} = 1 \times 10^{-2}\text{mm}$; and $\delta_{\text{n1}} = \delta_{\text{s1}} = 1 \times 10^{-6}\text{mm}$. Therefore, the fracture toughnesses for modes I and II are $\Gamma_{\text{I}} = \Gamma_{\text{II}} = 0.25\,\text{N/mm}$. For the kinking crack initiation and propagation in the matrix, the maximum principal stress criterion is assumed.

Symmetric, displacement-controlled loading is imposed on both the left and right edges, whereas the top and bottom edges are stress free. For both cases, the prescribed maximum nominal strain is 2% and the maximum nominal strain increment is 0.05%. Under this loading scheme, the CPU time needed to complete the simulations is 140 s (58 increments) for the fine-conforming mesh, and 20 s (58 increments) for the coarse-nonconforming mesh.

The maximum strain distributions at four loading stages for the two cases are shown in Figure 10.11a and b. The predicted curves of nominal stress versus nominal strain are shown in Figure 10.11c. In both cases, the nominal stress–strain curves can be roughly categorized into three stages. The first stage is the elastic stage ($\varepsilon_1 < 0.5\%$), wherein the interface remains well bonded and the response is linear, which can be seen from Figure 10.11a1 and b1.[3] At a nominal strain of 0.5%, debonding cracks start to initiate at (R, 0) and (−R, 0), and they propagates both upward and downward along the interface. These interface cracks propagate in a symmetric fashion in both horizontal and vertical directions (Figure 10.11a2 and b2). As the debonding length increases, the composite stiffness is gradually reduced, but the stress continues to rise due to further stretching in matrix. This stage is eventually followed by a kinking initiation. For the fine mesh, kinking occurs at a nominal strain of ~0.84% and for the coarse mesh, it happens at a strain of 1.2% (Figure 10.11a3 and b3). Shortly after the kinking initiation, the kinking cracks propagate quickly toward the top and bottom specimen boundaries, completely separating the entire domain (Figure 10.11a4 and b4). This process is characterized by a sudden drop of load in the load–displacement curves.

It is seen that, despite the vast difference in mesh size and interface conformity, the predicted stress–strain curves remain very similar to each other. The differences in

[3] The apparent strange strain distributions in Figure 10.11(b) are due to ABAQUS graphics output. Since ABAQUS does not support graphic depicting of UELs, we had to superimpose a layer of ABAQUS CPS4 elements with near zero stiffness to display the strain distribution. In this way, any displacements are interpolated continuously within an element.

predicted composite elastic modulus and energy dissipation are well within 5% (the predicted modulus values, 5.2 GPa for mesh (a) or 5.37 GPa for mesh (b), are moderately greater than the lower-bound estimation of 4.86 GPa based on the rule-of-mixture, which is a quick proof that the current predictions are reasonable). Finally, the 10% and 14% difference in predicted composite strengths and ultimate strains, respectively, by the two meshes are at least acceptable given the large difference in mesh size and interface conformity.

It is emphasized here that in the above simulations, the tightly coupled cracking development processes, especially the formation of the kinking crack from the active interface debonding crack tip zone, is purely determined by the program from the computed local stresses in the matrix subdomain according to the prescribed maximum principal stress criterion (for initiation). Although this complex, coupled fracture process can be captured with relative ease by the present A-FEM with subdomain (secondary) cracking capability, few other existing methods can handle this with explicit consideration of the interactive stresses at the two active fracture process zones.

10.5.3 2D textile composite simulation

In this example, we demonstrate the proposed 2D A-FEM's capability in predicting the coupled crack evolution in a highly heterogeneous 3D textile composites. Figure 10.12 shows a cross section of a 3D interlock textile composite. The geometries and allocations of weft tows, warp tows, and matrix pockets were replicated using a geometric generator based on data from μCT characterization. Thus, statistics of material heterogeneities are built in. The material properties for matrix, tows, and matrix/tow interfaces are typical of textile ceramic matrix composites (CMCs). In this simulation, the matrix is assumed to be elastic with $E_m = 16$ GPa; $\nu_m = 0.4$. The fiber tow is assumed to be transversely isotropic with $E_1 = 130$GPa, $E_2 = E_3 = 25$ GPa, $G_{12} = G_{13} = 16$ GPa, $\nu_{12} = \nu_{13} = 0.3$; $\nu_{23} = 0.3$. These parameters were from Yang et al. (2005). The interface and tow cohesive fracture parameters were calibrated by Sudre and Yang (unpublished work, 2005).

The 2D A-FEM was used to analyze this cross section. For this 2D problem, the tow-matrix and tow-tow interfaces were all modeled explicitly with cohesive zone elements. The left edge was fixed while the right edge was subjected to a displacement controlled loading.

The 2D A-FEM simulated damage evolution as compared to the experimental observations is shown in Figure 10.12a and b. Although the simulation is 2D, the actual specimen is 3D, and the A-FEM is able to capture all the major damage modes (see legend in Figure 10.12c). The crack locations are also well predicted. The nominal stress–strain curve follows the experimental data closely up to the point of the first major cracking events (cracks 2 and 4 in Figure 10.12a and b). After that the curves are different because the 2D model cannot realistically account for the 3D interlock effects in 3D textiles. This illustrates the urgent need for 3D A-FEM development, but also clearly demonstrates the great potential of our A-FEM.

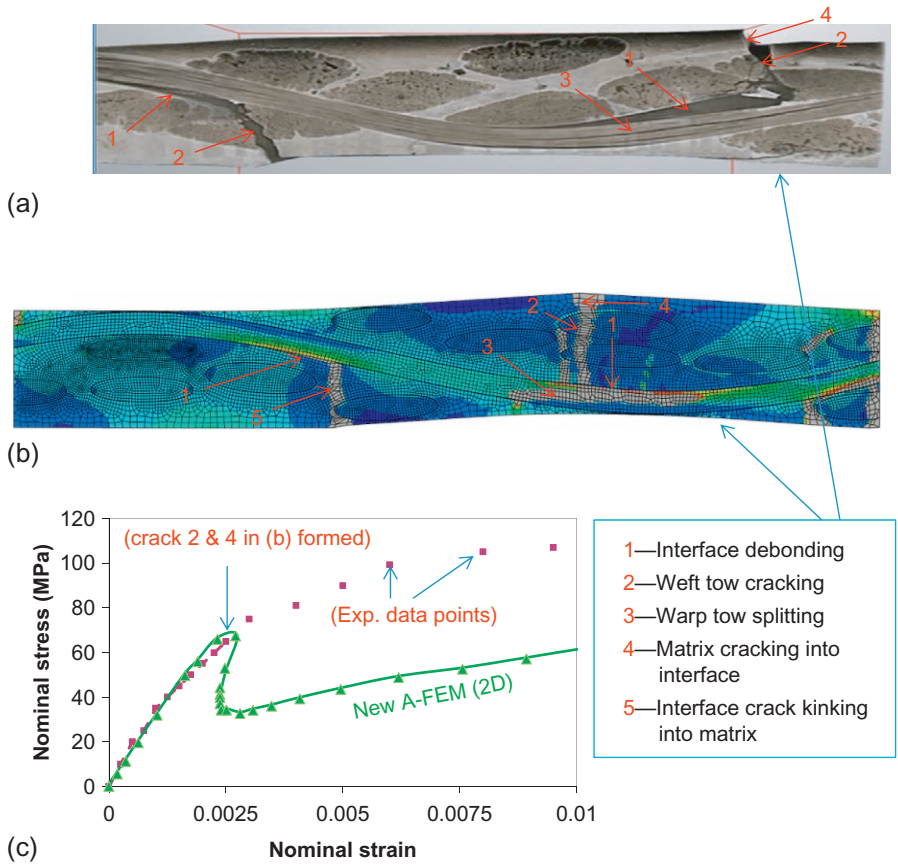

Figure 10.12 (a) Experimentally observed damages (2D cross-sectional view), (b) the 2D A-FEM predicted damages capturing all the damage modes observed in the experiments, and (c) predicted nominal stress–strain curve showing the 2D A-FEM in excellent agreement with measured curve up to first major cracking events.

10.5.4 Simulations of complex damage evolution in a 3D textile composite

In this example, the 3D A-FEM is used to simulate the multiple crack initiation in a C/SiC angle interlock weave shown in Figure 10.13a, which is a 3D reconstruction from a high-resolution μCT measurement reported in Bale et al. (2011). A virtual specimen was generated with stochastic tow geometry using Monte Carlo methods in which the geometrical model resulting from application of the Markov chain algorithm was converted into a mesh of solid computational elements suited to the A-FEM formulation as shown in Figure 10.13b (Cox et al., 2014; Rinaldi et al., 2012). The calibrated tow elasticity is numerically similar to the elasticity deduced for a similar carbon/SiC material, reported in Yang et al. (2005). Nonlinear fracture laws were

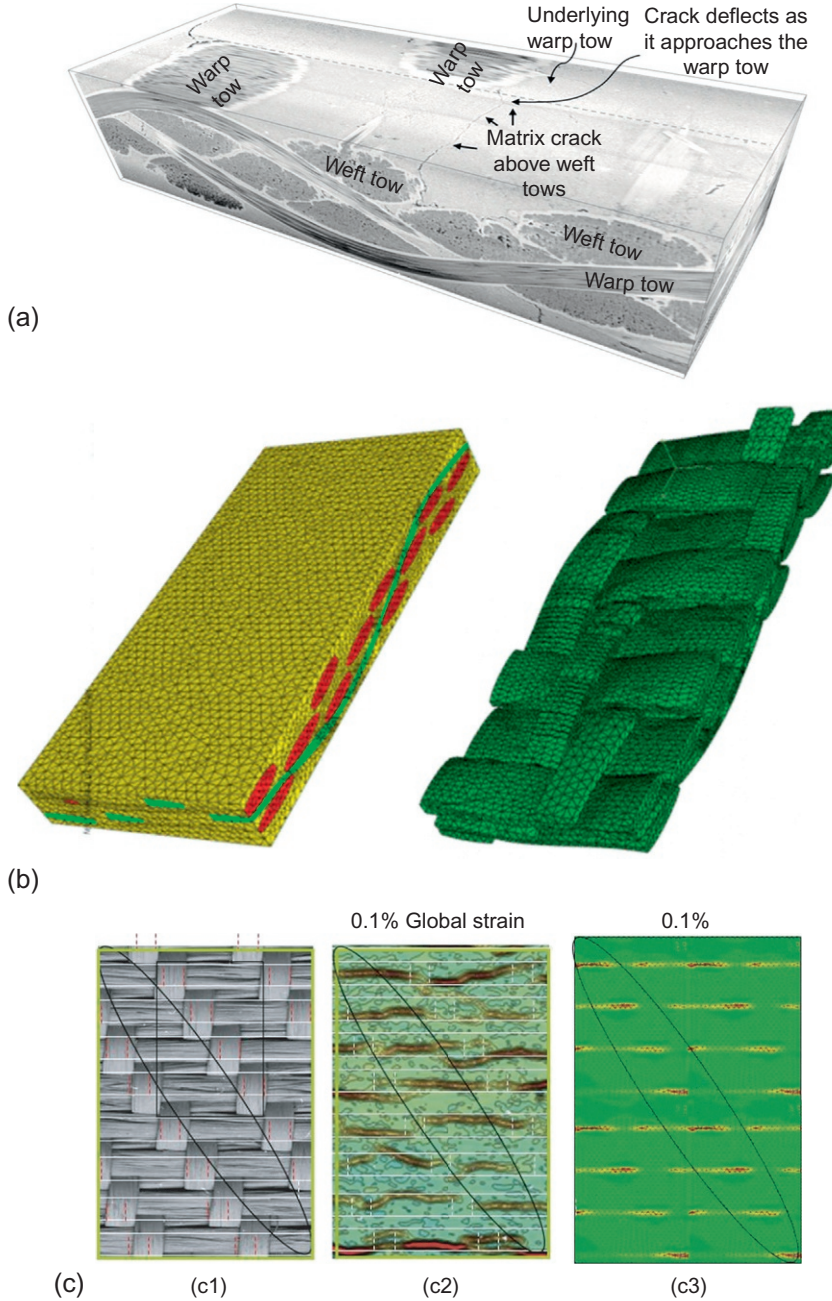

Figure 10.13 (a) 3D visualization of μCT data provides further detail of the observation in (a) that matrix cracks that have formed above a weft tow segment arrest when they approach the region where a warp tow that crosses over the weft tow. (b) Virtual specimen generated from the μCT data. The top graph shows the two architectures and the bottom graph shows the mesh for the entire model. (c1) Textile preform coated with thin layer of matrix (C/SiC angle interlock). (c2) Observations of microcracks by digital image correlation in composite formed by full infiltration of SiC matrix into preform in (a). (c3) Predicted crack pattern.

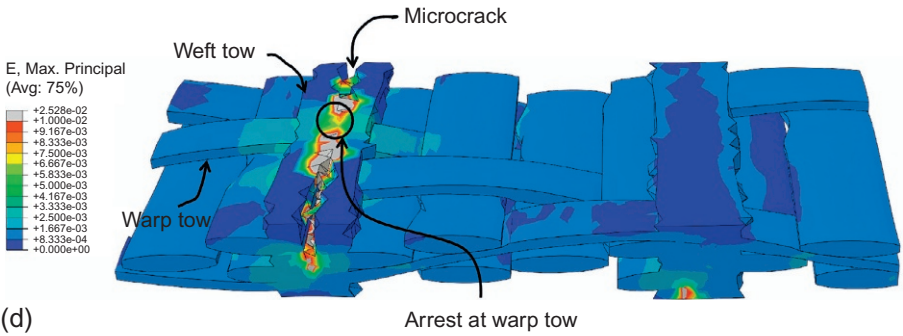

Figure 10.13 Continued. (d) Detailed rendering of a simulation shows one microcrack above a weft tow correctly predicted to arrest upon approaching the underlying warp tow.

calibrated from the same tests by matching the predicted matrix cracking stress with the experiment.

The matrix containing the crack is present in this image, but the matrix elsewhere has been stripped away in rendering the image to reveal the underlying tow architecture. All such warp tow segments are indicated by the vertical dashed lines in Figure 10.13c; they correlate consistently with crack arrest. (The right image in Figure 10.13c actually refers to a material in which the weft tow spacing was larger than in the left and center images, but is otherwise of identical architecture; it has been rescaled to facilitate comparisons. Importantly, the relation of crack position to weft tow position is the same in all three images.)

Key features of the crack pattern, including the approximate periodicity of the microcracks, which form above near-surface weft tows, and the alignment of microcracks in diagonal bands (one of which is outlined by the ellipse in Figure 10.13c), are replicated well by the virtual tests. The locations of the cracks relative to underlying weft tows are also well predicted by the 3D A-FEM simulation. One particular characteristic of the microcracking demonstrates the potential of the A-FEM for virtual tests because of its capability in predicting details. The microcracks seen in experiments form above weft tows and propagate both into the composite and across the surface of the composite, tracking the weft tow. However, the propagation across the surface is limited: when the microcrack approaches the region where the weft tow dips beneath a warp tow, propagation is arrested. Thus, the microcracks remain of finite length (Figure 10.13c). This behavior is replicated well by the 3D A-FEM simulations. The images of Figures 10.13c and d focus on a single microcrack in the matrix layer. The microcrack can be seen to have followed a weft tow and then arrested as it approached the location where the weft tow is submerged under a warp tow.

The phenomenon of crack arrest is correlated with lowering of stress in the superficial matrix by straightening of the warp tow. (Earlier evidence for tow straightening in this class of composites was reported in Berbon et al., 2002.) Both this stress heterogeneity and the critical stress for microcracking depend on geometrical details such

as the thickness of the superficial matrix layer and the orientations of tows. They will therefore be affected by stochastic variance in the tow architecture. By simulating the evolution of discrete crack systems with high fidelity, the virtual tests can directly relate variance in microstructure to variance in failure due to microcracking (a potentially fatal event in hot structures).

10.6 Concluding remarks

In this chapter, an elemental augmentation procedure has been established to derive the augmented finite elements (A-FEs) that can accurately account for arbitrary intra-element cracks and their interaction without the need for additional external DoFs as in X-FEM or extra nodes as in PNM. Although the formulation presented in this paper is specific to the bilinear elements, there is no major technical barrier to extend the augmentation procedure to other types of 2D or 3D elements. It has been demonstrated that the new formulation makes it much easier to handle the multiple crack interaction problems including crack coalescence or bifurcation, since it does not require complex numerical algorithms to track the complex crack fronts and to account for their interactions.

The new A-FEM formulation does not need to assume deformation modes for elemental displacement enrichment as in the embedded discontinuity method. Instead, it introduces internal node-pairs with normal displacements as internal nodal DoFs, which are eventually condensed at an elemental level. Thus, the crack displacements are natural outcomes of the elemental equilibrium consideration. The advantage is multifold. First, it enables a unified treatment of both weak and strong discontinuities, as demonstrated by the numerical examples in Sections 10.5.2 and 10.5.3. Second, for strong discontinuities with piecewise linear constitutive relations, the new A-FEM formulation ensures an exact solution (in the piecewise linear limit) to the condensed elemental equilibrium, which greatly improves the numerical accuracy, stability, and efficiency, as demonstrated in the four-point shear beam test simulations. Third, the unique A-FEM formulation makes it straightforward to repeat the augmentation procedure within an element to include multiple intra-element cracks, which is very powerful in dealing with multiple-crack interaction problems because such augmented elements do not need extra external DoFs or nodes.

A novel elemental condensation algorithm that can provide analytical solution to local equilibrium has also been developed. The novelty in this algorithm is that, instead of assuming trial crack displacements and iterating for elemental equilibrium such as in the Newton–Raphson method, it starts with trial cohesive segments in the cohesive laws and finds the analytical solution (in piecewise linear sense) to the elemental equilibrium through a simple consistency check. For piecewise linear cohesive laws with only a small number of possible stiffness segments, this algorithm is very efficient.

Through the numerical examples, we have demonstrated that the new A-FEM method, empowered by the new elemental condensation algorithm, achieved very significant improvements in numerical accuracy, efficiency, and stability. In

particular, through a rigorous comparison study on a four-point shear beam test, which involves a complex process of nonlinear crack propagation that is coupled with global instability (snapback), we have demonstrated that the A-FEM solution is rather insensitive to mesh sizes and mesh structures, whereas the numerical cost of the A-FEM (in CPU time) is merely twice that of the elastic, crack-free calculation with the same mesh. The A-FEM's capabilities in high-fidelity simulations of interactive cohesive cracks in heterogeneous solids have also demonstrated through the coupled debonding/kinking processes frequently observed in fiber-reinforced polymer matrix composites.

Acknowledgment

The authors thank the US ARO (grant #: W911NF-13-1-0211) and the US AFOSR (Contract #: FA9550-09-1-0477) for the support of this work.

References

Alfaiate, J., Wells, G.N., Sluys, L.J., 2002. On the use of embedded discontinuity elements with crack path continuity for mode I and mixed-mode fracture. Eng. Fract. Mech. 69, 661–686.

Areias, P.M.A., Belytschko, T., 2005. Analysis of three-dimensional crack initiation and propagation using the extended finite element method. Int. J. Numer. Methods Eng. 63 (5), 760–788.

Armero, F., Garikipati, K., 1996. An analysis of strong discontinuities in multiplicative finite strain plasticity and their relation with the numerical simulation of strain localization in solids. International Journal of Solids & Structures 33, 2863–2885.

Bale, H., et al., 2011. Characterizing three-dimensional textile ceramic composites using synchrotron X-ray micro-computed-tomography. J. Am. Ceram. Soc. 95 (1), 392–402.

Belytschko, T., Fish, J., Engelmann, B.E., 1988. A finite element with embedded localization zones. Comput. Methods Appl. Mech. Eng. 70 (1), 59–89.

Berbon, M.Z., et al., 2002. Effect of weave architecture on tensile properties and local strain heterogeneity in thin-sheet C-SiC composites. J. Am. Ceram. Soc. 85, 2039–2048.

Borden, M.J., et al., 2011. A phase-field description of dynamic brittle fracture. ICES Report, The Institute for Computational Engineering and Sciences, The University of Texas at Austin.

Bourdin, B., Francfort, G.A., Marigo, J.J., 2008. The variational approach to fracture. J. Elast. 91, 5–148.

Camanho, P.P., et al., 2006. Prediction of in situ strengths and matrix cracking in composites under transverse tension and in-plane shear. Compos. Part A: Appl. Sci. Manuf. 37, 165–176.

Carpinteri, A., et al., 1993. Is mode II fracture energy a real material property? Comput. Struct. 48 (3), 397–413.

Cavalli, M.N., Thouless, M.D., Yang, Q.D., 2004. Modeling the deformation and fracture of weld-bonded joints. Weld. J. 83, 133S–139S.

Cavalli, M.N., Thouless, M.D., Yang, Q.D., 2005. Modeling the deformation and failure of aluminum spot welded joints. Int. J. Fatigue Fract. 28, 861–874.

Cervera, M., Chiumenti, M., Codina, R., 2010. Mixed stabilized finite element methods in nonlinear solid mechanics. Part II: strain localization. Comput. Methods Appl. Mech. Eng. 199, 2571–2589.
Chang, K.Y., Liu, S., Chang, F.K., 1991. Damage tolerance of laminated composites containing an open hole and subjected to tensile loadings. J. Compos. Mater. 25, 274–301.
Cox, B.N., Yang, Q.D., 2006. In quest of virtual tests for structural composites. Science 314, 1102–1107.
Cox, B.N., et al., 1994. Failure mechanisms of 3D woven composites in tension, compression, and bending. Acta Metall. Mater. 42, 3967–3984.
Cox, B.N., Dadkah, M.S., Morris, W.L., 1996. On the tensile failure of 3D woven composites. Compos. Part A 27A, 447–458.
Cox, B.N., et al., 2014. Stochastic virtual tests for high temperature ceramic matrix composites. Ann. Rev. Mater. Sci. 44, 17.1–17.51.
Davila, C.G., Camanho, P.P., Rose, C.A., 2005. Failure criteria for FPR laminates. J. Compos. Mater. 39, 323–345.
de Borst, R., 2003. Numerical aspects of cohesive zone models. Eng. Fract. Mech. 70, 1743–1757.
de Borst, R., Remmers, J.J.C., Needleman, A., 2006. Mesh-independent discrete numerical representations of cohesive-zone models. Eng. Fract. Mech. 73 (2), 160–177.
De Borst, R., et al., 2012. Nonlinear Finite Element Analysis of Solids and Structures. John Wiley & Sons, UK.
Dias-da-Costa, D., et al., 2009. Towards a generalization of a discrete strong discontinuity approach. Computational methods in Applied Mechanics and Engineering 198, 3670–3681.
Dias-da-Costa, D., et al., 2013. An embedded formulation with conforming finite elements to capture strong discontinuities. Int. J. Numer. Meth. Eng. 93, 224–244.
Do, B.C., et al., 2013. Improved cohesive stress integration schemes for cohesive zone elements. Eng. Fract. Mech. 107, 14–28.
Dolbow, J., Moës, N., Belytschko, T., 2001. An extended finite element method for modeling crack growth with frictional contact. Comput. Methods Appl. Mech. Eng. 190, 6825–6846.
Dvorkin, E.N., Cuitiño, A.M., Gioia, G., 1990. Finite elements with displacement interpolated embedded localization lines insensitive to mesh size and distortions. Int. J. Numer. Methods Eng. 30 (3), 541–564.
Fang, X.J., et al., 2011a. High-fidelity simulations of multiple fracture processes in a laminated composites in tension. J. Mech. Phys. Solids 59, 1355–1373.
Fang, X.J., et al., 2011b. An augmented cohesive zone element for arbitrary crack coalescence and bifurcation in heterogeneous materials. Int. J. Numer. Methods Eng. 88, 841–861.
Fawcett, A., Trostle, J., Ward, S., 1997. 777empennage certification approach. In: International Conference on Composite Materials, Gold Coast, Australia.
Gasser, T.C., Holzapfel, G.A., 2006. 3D crack propagation in unreinforced concrete. A two-step algorithm for tracking 3D crack paths. Comput. Methods Appl. Mech. Eng. 195 (37–40), 5198–5219.
Goutianos, S., Sorensen, B.F., 2012. Path dependence of truss-like mixed mode cohesive laws. Eng. Fract. Mech. 91, 117–132.
Hallett, S.R., Wisnom, M.R., 2006a. Experimental investigation of progressive damage and the effect of layup in notched tensile tests. J. Compos. Mater. 40, 119–141.
Hallett, S.R., Wisnom, M.R., 2006b. Numerical investigation of progressive damage and the effect of layup in notched tensile tests. J. Compos. Mater. 40, 1229–1245.
Hutchinson, J.W., Evans, A.G., 2000. Mechanics of materials: top-down approaches to fracture. Acta Mater. 48, 125–135.

Huynh, D.B.P., Belytschko, T., 2009. The extended finite element method for fracture in composite materials. Int. J. Numer. Methods Eng. 77, 214–239.

Iarve, E.V., Mollenhauer, D., Kim, R., 2005. Theoretical and experimental investigation of stress redistribution in open-hole composite laminates due to damage accumulation. Compos. Part A 36, 163–171.

Iarve, E.V., et al., 2011. Mesh independent matrix cracking and delamination modelling in laminated composites. Int. J. Numer. Methods Eng. 88, 749–773.

Ibrahimbegovic, A., Melnyk, S., 2007. Embedded discontinuity finite element method for modeling of localized failure in heterogeneous materials with structured mesh: an alternative to extended finite element method. Comput. Mech. 40 (1), 149–155.

Jirásek, M., 2000. Comparative study on finite elements with embedded discontinuities. Comput. Methods Appl. Mech. Eng. 188, 307–330.

Kaddour, A.S., et al., 2013. Mechanical properties and details of composite laminates for the test cases used in the thrid world-wide failure exercise. J. Compos. Mater. 47, 2427–2442.

Kafkalidis, M.S., et al., 2000. Deformation and fracture of An adhesive layer constrained by plastically-deforming adherends. Int. J. Adhes. Sci. Technol. 14, 1593–1646.

Linder, C., Armero, F., 2007. Finite elements with embedded strong discontinuities for themodeling of failure in solids. International J. Numer. Meth. Engng 72, 1391–1433.

Linder, C., Armero, F., 2009. Finite elements with embedded branching. Finite Elem. Anal. Des. 45, 280–293.

Ling, D.S., Yang, Q.D., Cox, B.N., 2009. An augmented finite element method for modeling arbitrary discontinuities in composite materials. Int. J. Fract. 156, 53–73.

Ling, D.S., et al., 2011. Nonlinear fracture analysis of delamination crack jumps in laminated composites. J. Aerosp. Eng. 24, 181–188.

Ling, D.S., et al., 2014. A finite element method with mesh-separation based approximation technique and its application in modeling crack propagation with adaptive mesh refinement. Int. J. Numer. Methods Eng. 99, 487–521.

Liu, W., et al., 2013. An accurate and efficient augmented finite element method for arbitrary crack interactions. J. Appl. Mech. 80, 041033-1–041033-12.

Liu, W., et al., 2014. An efficient augmented finite element method (A-FEM) for arbitrary cracking and crack interaction in solids. Int. J. Numer. Methods Eng. 99, 438–468.

Liu, W., et al., 2015. A consistency-check based algorithm for element condensation in augmented finite element methods for fracture analysis. Eng. Fract. Mech. 139, 78–97.

LLorca, J., González, C., et al., 2011. Multiscale modeling of composite materials: a roadmap towards virtual testing. Adv. Mater. 23, 5130–5147.

Miehe, C., Hofacker, M., Welschinger, F., 2010. A phase field model for rate-independent crack propagation: robust algorithmic implementation based on operator splits. Comput. Methods Appl. Mech. Eng. 199, 2765–2778.

Moës, N., Belytschko, T., 2002. Extended finite element method for cohesive crack growth. Eng. Fract. Mech. 69, 813–833.

Mohammadizadeh, S., 2013. A novel augmented finite element method for modeling arbitrary cracking in 2D solids (Ph.D. thesis), Department of Mechanical and Aerospace Engineering, University of Miami.

Morris, W.L., Inman, R.V., Cox, B.N., 1989. Microscopic deformation in a heated unidirectional graphite/epoxy composite. J. Mater. Sci. 24, 199–204.

Mousavi, S.E., Xiao, H., Sukumar, N., 2010. Generalized gaussian quadrature rules on arbitrary polygons. Int. J. Numer. Methods Eng. 82, 99–113.

Naderi, M., Jung, J., Yang, Q.D., 2015. Augmented finite element method for arbitrary cracking in 3D solids. Int. J. Fract, submitted.

Oliver, J., Huespe, A., 2002. On strategies for tracking strong discontinuities in computational failure mechanics. In: Mang, H.A., Rammersdorfer, F.G., Erberhardsteiner, J. (Eds.), Proceedings of the Fifth World Congress on Computational Mechanics (WCCM V), Vienna, Austria.

Oliver, J., et al., 2004. Continuum approach to the numerical simulation of material failure in concrete. Int. J. Numer. Anal. Methods Geomech. 28 (7–8), 609–632.

Ortiz, M., Leroy, A., Needleman, A., 1987. A finite element method for localized failure analysis. Comput. Methods Appl. Mech. Eng. 61, 189–214.

Parmigiani, J., Thouless, M.D., 2007. The effects of cohesive strength and toughness on mixed-mode delamination of beam-like geometries. Eng. Fract. Mech. 74, 2675–2699.

Pierron, F., et al., 2007. Full-field assessment of the damage process of laminated composite open-hole tensile specimens. Part II: experimental results. Compos. Part A 38, 2321–2332.

Remmers, J.C., 2006. Discontinuities in materials and structures – a unifying computational approach. PhD Thesis, Delft University.

Rinaldi, R., et al., 2012. Generating virtual textile composite specimens using statistical data from micro-computed tomography: 3D tow representations. J. Mech. Phys. Solids 60 (8), 1561–1581.

Rudraraju, S., et al., 2010. In-plane fracture of laminated fiber reinforced composites with varying fracture resistance: experimental observations and numerical crack propagation simulations. Int. J. Solids Struct. 47, 901–911.

Simo, J.C., Hughes, T.J.R., 1986. On the variational foundations of assumed strain methods. J. Appl. Mech. 53, 51–54.

Simo, J.C., Rifai, M.S., 1990. A class of mixed assumed strain methods and the method of incompatible modes. Int. J. Numer. Methods Eng. 29, 1595–1638.

Simo, J.C., Oliver, J., Armero, F., 1993. An analysis of strong discontinuities induced by softening solutions in rate-independent solids. J. Comput. Mech. 12, 277–296.

Sluys, L.J., Berends, A.H., 1998. Discontinuous failure analysis for mode I and mode II localization problems. Int. J. Solids Struct. 35, 4257–4274.

Soden, P.D., Hinton, M.J., Kaddour, A.S., 1998. A comparison of the predictive capabilityies of current failure theories for composite laminates. Compos. Sci. Technol. 58, 1225–1254.

Sukumar, N., Moran, B., Belytschko, T., 1998. The natural element method in solid mechanics. Int. J. Numer. Methods Eng. 43, 839–887.

Thouless, M.D., Yang, Q.D., 2008. A parametric study of the peel test. Int. J. Adhes. Adhes. 28, 176–184.

Turon, A., et al., 2006. A damage model for the simulation of delamination in advanced composites under variable-mode loading. Mech. Mater. 38, 1072–1089.

Turon, A., et al., 2007. An engineering solution for mesh size effects in the simulation of delamination using cohesive zone models. Engin. Fract. Mech. 74, 1665–1682.

Van de Meer, F.P., 2012. Mesolevel modeling of failure in composite laminates: contitutive, kinematic and algorithic aspects. Arch. Comput. Method Eng. 19, 381–425.

Van de Meer, F.P., Sluys, L.J., 2009. A phantom node formulation with mixed mode cohesive law for splitting in laminates. Int. J. Fract. 158, 107–124.

Van de Meer, F.P., Oliver, C., Sluys, L.J., 2010. Computational analysis of progressive failure in a notched laminate including shear nonlinearity and fiber failure. Compos. Sci. Technol. 70, 692–700.

Wang, J.S., Suo, Z., 1990. Experimental determination of interfacial toughness using Brazil-nut-sandwich. Acta Metall. 38, 1279–1290.

Wisnom, M.R., Chang, F.-K., 2000. Modelling of splitting and delamination in notched cross-Ply laminates. Compos. Sci. Technol. 60, 2849–2856.

Wriggers, P., Korelc, J., 1996. On enhanced strain methods for small and finite deformation of solids. Comput. Mech. 18, 413–428.
Xu, X.-P., Needleman, A., 1994. Numerical simulations of fast crack growth in brittle solids. J. Mech. Phys. Solids 42, 1397–1434.
Yang, Q.D., Cox, B.N., 2005. Cohesive models for damage evolution in laminated composites. Int. J. Fract. 133 (2), 107–137.
Yang, Q.D., Thouless, M.D., 2001. Mixed mode fracture of plastically-deforming adhesive joints. Int. J. Fract. 110, 175–187.
Yang, Q.D., Thouless, M.D., Ward, S.M., 1999. Numerical simulations of adhesively-bonded beams failing with extensive plastic deformation. J. Mech. Phys. Solids 47, 1337–1353.
Yang, Q.D., et al., 2003. Failure in the junction region of T-stiffeners: 3D-braided vs. 2D tape laminate stiffeners. Int. J. Solid Struct. 40, 1653–1668.
Yang, Q.D., et al., 2005. Evaluation of macroscopic and local strains in a 3D woven C/SiC composite. J. Am. Ceram. Soc. 88, 719–725.
Yang, Q.D., et al., 2006. Fracture and length scales in human cortical bone: the necessity of nonlinear fracture models. Biomaterials 27, 2095–2113.
Yang, Q.D., et al., 2010a. A-FEM for complex multi-scale damage evolution in laminated composites. In: Proceedings of SAMPE Technical Conference, Paper #465, vol. 42, May, pp. 1–8.
Yang, Q.D., et al., 2010b. An improved cohesive element for shell delamination analyses. Int. J. Numer. Methods Eng. 83 (5), 611–641.
Yang, Q.D., et al., 2011. Virtual testing for advanced aerospace composites: advances and future needs. J. Eng. Mater. Technol. 133, 11002–11008.

Isogeometric analysis for modelling of failure in advanced composite materials

11

J.J.C. Remmers[*], *C.V. Verhoosel*[*], *R. de Borst*[†]
*Eindhoven University of Technology, Eindhoven, The Netherlands; [†]University of Glasgow, Glasgow, UK

11.1 Introduction

Isogeometric analysis (IGA) has recently received much attention in the computational mechanics community. The basic idea is to use splines, which are the functions commonly used in computer-aided design (CAD), as the basis functions for the analysis rather than the traditional Lagrange basis functions (Hughes et al., 2005; Cottrell et al., 2009). Originally, non-uniform rational B-splines (NURBS) have been used in IGA, but their inability to achieve local refinement has driven their gradual replacement by the more advanced T-splines (Sederberg et al., 2003).

An important advantage of IGA is that the functions used for the representation of the geometry in the CAD drawings are employed directly for the analysis. This avoids the need for a sometimes elaborate meshing procedure. This important feature allows for a design-through-analysis approach, which yields a significant reduction of the time needed for the preparation of the analysis model (Cottrell et al., 2009). Whereas a traditional finite-element discretisation results in the piecewise linear approximation of curved boundaries, in an isogeometric analysis, the geometry of these curved boundaries is an exact representation. This is beneficial in the numerical analysis of thin-walled shell structures, which can be very sensitive to imperfections in the geometry (Bushnell, 1981).

Another important advantage is the higher-order continuity of the isogeometric shape functions. This feature allows for a straightforward implementation of shell theories which require $\mathcal{C}^1$ continuity such as Kirchhoff–Love models (Kiendl et al., 2009; de Borst et al., 2012; Haartsen, 2012). A Reissner–Mindlin shell formulation has been developed by Benson et al. (2010) using NURBS basis functions. Although $\mathcal{C}^1$ continuity is then no requisite, good results and a high degree of robustness were reported for large deformation problems. In addition, the exact description of the geometry allows for an exact computation of the shell director (Dornisch et al., 2013). Recently, the seven-parameter shell model (Bischoff et al., 2004) was cast in an isogeometric formulation by Echter et al. (2013).

A further benefit of basis functions that possess a higher degree of continuity is that the computation of stresses is vastly improved. In shell analysis, this can be particularly important when non-linear material phenomena such as damage or delamination, which can occur in laminated structures, are included in the analysis. In the latter case, the computation of an accurate three-dimensional stress field in a specific material

Numerical modelling of failure in advanced composite materials. http://dx.doi.org/10.1016/B978-0-08-100332-9.00011-6
Copyright © 2015 Elsevier Ltd. All rights reserved.

point in the shell becomes mandatory. Solid-like shell elements are then an obvious choice (Parisch, 1995; Hashagen and de Borst, 2000). This shell element is characterised by the absence of rotational degrees of freedom, which is convenient when stacking them. Nevertheless, this element still possesses shell kinematics and is rather insensitive to shear locking and membrane locking.

An isogeometric version of a solid-like shell element has been presented in Hosseini et al. (2013) and Hosseini et al. (2014a). Here, the advantage of an accurate geometric description of the shell mid-surface is combined with the three-dimensional stress representation of conventional solid-like shell elements. The formulation adopts NURBS (or T-spline) basis functions for the discretisation of the shell mid-surface, whereas a higher-order B-spline function is used for the interpolation in the thickness direction. An important advantage of using B-spline basis functions is their ability to model weak and strong discontinuities in the displacement field by knot insertion (Verhoosel et al., 2011). Weak discontinuities are usually introduced by subdividing the shell in the thickness direction in multiple layers with each a piecewise polynomial interpolation, as demonstrated previously in Reddy (1984) and Braun et al. (1994). Strong discontinuities can be used to model delaminations. Conventionally, these delaminations are modelled using interface elements, or in a more general manner, by exploiting the partition-of-unity property of Lagrange polynomials (Remmers et al., 2003). The knot-insertion technique allows us to do this in an IGA formulation in a straightforward manner, as demonstrated by Hosseini et al. (2014b).

In this chapter, we will review the isogeometric implementation of two families of shell formulations; a Kirchhoff–Love shell model and a layered continuum shell formulation. In the next section, the basic concepts of IGA are reviewed briefly. Here, special attention is paid to the Bézier extraction technique (Scott et al., 2011), which allows us to implement the isogeometric models in a conventional finite-element code. In Section 11.3, a non-linear isogeometric Kirchhoff–Love shell model is presented. The performance of this model is demonstrated by means of a classical shell buckling example. In Section 11.4, the algorithmic and implementation aspects of a fully isogeometric continuum shell model are given. This model allows us to analyse the exact stress state in multi-layered materials. In addition, by using the knot insertion technique, the model can be used to simulate delamination growth using a cohesive zone approach. The chapter is closed with some conclusions and an outlook to future developments.

11.2 Isogeometric finite-element discretization

In this section, we briefly summarise some of the basic concepts of IGA. First, the fundamentals of NURBS and B-splines are explained. Next, the Bézier extraction technique will be outlined. For a more detailed overview of IGA and Bézier extraction, the reader is referred to Hughes et al. (2005), Cottrell et al. (2009), Sederberg et al. (2003), de Borst et al. (2012), Scott et al. (2011), and Borden et al. (2011).

11.2.1 Fundamentals of NURBS and B-splines

A univariate B-spline $C(\xi)$ is a piecewise polynomial curve in a univariate domain parametrised by coordinate ξ, composed of a linear combination of B-spline basis functions:

$$C(\xi) = \sum_{i=1}^{n} h_{i,p}(\xi) P_i \tag{11.1}$$

where p is the order and n is the number of the basis functions. The term $h_{i,p}(\xi)$ represents a B-spline basis function and the coefficients P_i are points in space, which are commonly denoted as *control points*. B-spline basis functions are defined over a knot vector, Ξ, which is a set of non-decreasing real numbers representing coordinates in the parameter domain:

$$\Xi = \left[\xi_1, \xi_2, \ldots, \xi_{n+p+1}\right] \tag{11.2}$$

The parametric coordinates ξ_i divide the B-spline into elements. If all knots are equally spaced, the knot vector is called uniform; if they are unequally spaced, they are non-uniform. Between two distinct knots (knot span), a B-spline basis function has $\mathcal{C}^{\infty}$ continuity while it reduces to $\mathcal{C}^{p-1}$ across a knot. If a knot value appears more than once, the knot is called a multiple knot. At this knot the continuity is $\mathcal{C}^{p-k}$. A B-spline is said to be open if its first and last knots are repeated $p+1$ times. The continuity of an open B-spline at the boundaries of the domain is $\mathcal{C}^{-1}$, which is denoted as a *strong discontinuity*. This is needed to describe a sharp boundary of a domain.

In one dimension, the B-spline basis functions are defined using the Cox–de Boor formulation (Cox, 1972; de Boor, 1972) starting with piecewise constants ($p=0$):

$$h_{i,0}(\xi) = \begin{cases} 1 & \xi_i \leq \xi < \xi_{i+1} \\ 0 & \text{otherwise} \end{cases} \tag{11.3}$$

from which the pth-order functions, $p \geq 1$, are derived recursively using:

$$h_{i,p}(\xi) = \frac{\xi - \xi_i}{\xi_{i+p} - \xi_i} h_{i,p-1}(\xi) + \frac{\xi_{i+p+1} - \xi}{\xi_{i+p+1} - \xi_{i+1}} h_{i+1,p-1}(\xi) \tag{11.4}$$

Figure 11.1 shows the B-spline basis functions $h_{i,3}$, defined over the knot vector $\Xi = [0, 0, 0, 0, 1, 2, 2, 3, 3, 3, 4, 4, 4, 4]$. Note that the continuity of this third-order basis function is C^{-1} at the boundaries. Due to knot insertion, the continuity of this spline at $\xi = 2$ is $\mathcal{C}^1$; at $\xi = 3$, the continuity is even reduced to $\mathcal{C}^0$.

B-spline surfaces, or multivariate B-splines, can be constructed using two knot vectors, such as $\Xi = [\xi_1, \xi_2, \ldots, \xi_{n+p+1}]$ and $\mathcal{H} = \left[\eta_1, \eta_2, \ldots, \eta_{m+q+1}\right]$ and a set of $n \times m$

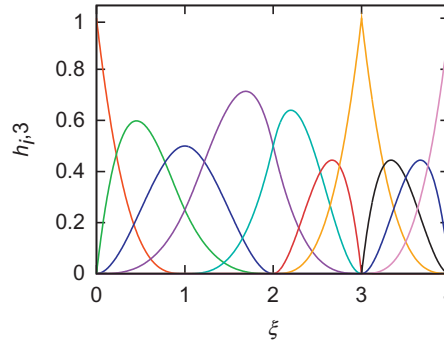

Figure 11.1 Third-order B-spline basis functions defined over a knot vector $\Xi = [0, 0, 0, 0, 1, 2, 2, 3, 3, 3, 4, 4, 4, 4]$.

control points $P_{i,j}$ known as the control net. By defining two univariate basis functions $h_{i,p}$ and $h_{j,p}$ over these two knot vectors, the B-spline surface is then constructed as

$$S(\xi, \eta) = \sum_{i=1}^{n} \sum_{j=1}^{m} h_{i,p}(\xi) h_{j,q}(\eta) P_{i,j} \tag{11.5}$$

Note that the order of the basis functions p and q, respectively, is not necessarily the same in the two directions.

B-spline basis functions satisfy the partition of unity property, which means that the sum of all basis functions $h_{i,p}(\xi)$ equals 1.0 in each point ξ in the domain, as can be seen in Figure 11.1. Also each basis function has a local support which is contained in the interval $[\xi_i, \xi_{i+p+1}]$. Generally, open B-splines are used in numerical analysis, since they are interpolatory at the boundary, which facilitates the application of Dirichlet boundary conditions.

A drawback of B-splines is their inability to exactly represent engineering objects such as cylindrical sections. For this reason, NURBS, which encapsulate B-splines and can represent such objects exactly, have become the standard in CAD. NURBS are defined by augmenting each control point with a weight W_i, which by definition is a positive number. To construct a NURBS, a control net with n control points P_i and a set of n scalar weights W_i is required. Accordingly, the NURBS basis functions are defined as

$$R_{i,p} = \frac{h_{i,p}(\xi) W_i}{\mathcal{W}(\xi)}; \quad \text{where} \quad \mathcal{W}(\xi) = \sum_{k=1}^{n} h_{k,p}(\xi) W_k \tag{11.6}$$

Note that there is no summation implied over the repeated index i. When all weights W_i are equal, a B-spline is obtained. NURBS surfaces are constructed by the weighted tensor product of B-spline functions, similar to what is done for B-spline surfaces, see Equation (11.5).

The technique to construct surface representation by using the tensor product of one-dimensional B-splines or NURBS has a number of disadvantages, such as the inability

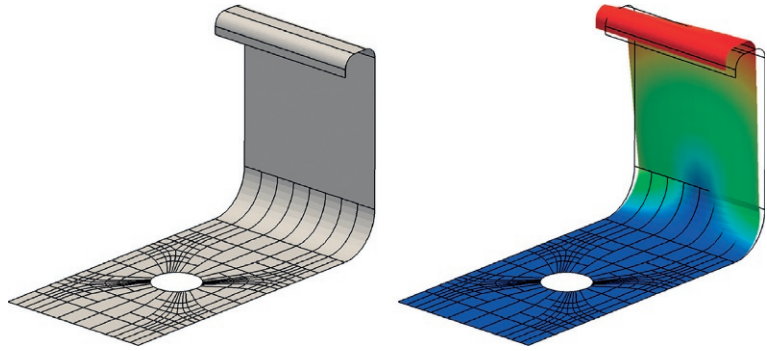

Figure 11.2 Example of a complex geometry represented by T-splines, which can be used to mesh topological features such as holes in combination with local refinements.

to refine the patch locally or represent a gap or a cutout in the domain. These difficulties have led to the development of alternative spline technologies, such as T-splines (Sederberg et al., 2003). Because they do not rely on the tensor-product structure of NURBS, T-splines are able to represent objects of arbitrary topological complexity and they can be refined locally (see Figure 11.2). Because of these properties T-splines are ideal for isogeometric finite-element analysis. As a result, current development in mesh-generation algorithms for IGA focus on the application T-splines.

11.2.2 Bézier extraction

As noted in the previous section, the parametric coordinates ξ_i in a knot vector divide the parameter domain into elements. Similar to the finite-element method, these elements, which refer to the knot intervals $\{\xi_i, \xi_{i+1}\}$ with a positive length, allow for piecewise integration using quadrature rules. Basis functions $h_{i,p}$ have a local support over a knot interval $\{\xi_i, \xi_{i+p+1}\}$, which means that each element may have different basis functions, as demonstrated in Figure 11.3. This is at variance with the finite-element method where the numerical integration is done on a single parent element, which is the basis for each element in the mesh.

To blend IGA into the data structure of existing finite-element computer codes, Bézier elements and Bézier extraction operators are used to provide a finite-element structure for B-splines, NURBS (Borden et al., 2011), and T-splines (Scott et al., 2011). In general, a Bézier curve of degree p is defined by a linear combination of $p+1$ Bernstein basis functions $\mathbf{B}(\xi)$ (Piegl and Tiller, 1997). It can be demonstrated that for each element e, there exists an extraction operator $\boldsymbol{C}_\mathrm{e}$ that maps a piecewise Bernstein polynomial basis onto the element-specific B-spline basis, according to

$$\mathbf{h}_\mathrm{e} = \boldsymbol{C}_\mathrm{e}\mathrm{B} \tag{11.7}$$

A schematic representation of this action is shown in Figure 11.4. The Bézier extraction operator for multivariate B-splines and NURBS can be computed by exploiting

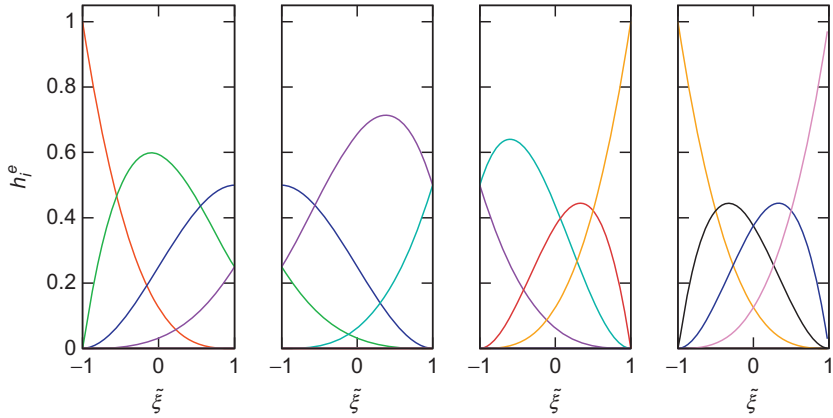

Figure 11.3 B-spline basis functions plotted over [−1,1]. The basis functions are different per element, which is in contrast with standard finite elements.

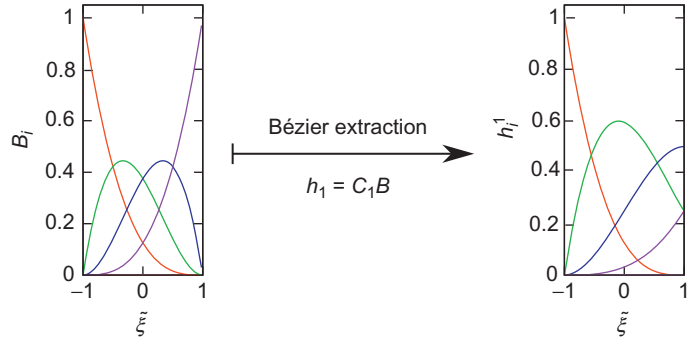

Figure 11.4 Schematic representation of the Bézier extraction operator for element 1 in Figure 11.3.

their tensor-product structure, see Borden et al. (2011) for details. For an in-depth discussion of Bézier extraction for T-splines, for which a global tensor-product structure is absent, see Scott et al. (2011).

To describe the domain for IGA using the Bézier extraction technique, the following information is needed:

- A list of control point coordinates. This is equivalent to the nodal coordinates in a regular finite-element analysis.
- An element connectivity table. This table contains the control points whose corresponding basis functions are supported on each element. Again, this is equivalent to a traditional finite-element mesh representation.
- A list of weights W_i. Each control point i can have a weight, which is a scalar value. When using B-splines, this list may be omitted.
- A list of Bézier extraction operators $\boldsymbol{C}_e$ for each element e. In most cases, the extraction operator is a relatively sparse matrix (de Borst et al., 2012).

For relatively simple geometries such as rectangular panels and cylinders, the control point coordinates and weights and the element connectivity and extraction matrices can be calculated manually, as demonstrated in Borden et al. (2011). For more complex geometries with cutouts and local refinements, the use of T-splines is recommended. In this case, external software is needed to obtain all the meshing information. Unfortunately, commercial software in this field is sparse. Currently, the T-spline add-on to the CAD programme Rhinoceros[1,2] is the only commercially available piece of software that can perform this task.

11.3 Kirchhoff–Love Shell element

11.3.1 Kinematics and implementation

In general, the strain in a shell is given by:

$$\boldsymbol{\epsilon} = \boldsymbol{\epsilon}^0 + z\boldsymbol{\chi}$$

where the array $\boldsymbol{\epsilon}^0$ contains the in-plane strains at the reference plane, z is the vertical coordinate with respect to the shell reference plane and χ is the curvature. The fundamental assumption in the Kirchhoff–Love formulation is that the director is taken equal to the unit normal vector to the shell reference plane:

$$\mathbf{d} = \frac{\mathbf{e}_1 \times \mathbf{e}_2}{\|\mathbf{e}_1 \times \mathbf{e}_2\|} \tag{11.8}$$

where

$$\mathbf{e}_1 = \frac{\partial \mathbf{x}}{\partial \xi}; \quad \mathbf{e}_2 = \frac{\partial \mathbf{x}}{\partial \eta}$$

with ξ, η the local coordinates of the mid-surface, Figure 11.5. As a consequence, the rotations θ_ξ and θ_η are constrained by

$$\theta_\xi = -\frac{\partial w}{\partial \xi} \quad \text{and} \quad \theta_\eta = -\frac{\partial w}{\partial \eta} \tag{11.9}$$

with w the out-of-plane displacement of the shell. Substitution of these constraints results in the curvatures for a Kirchhoff–Love shell theory:

$$\boldsymbol{\chi} = \begin{pmatrix} -\dfrac{\partial^2 w}{\partial \xi^2} \\ -\dfrac{\partial^2 w}{\partial \eta^2} \\ -2\dfrac{\partial^2 w}{\partial xi \partial \eta} \end{pmatrix} \tag{11.10}$$

[1] Rhinoceros. Commercially available 3D modeller that is using NURBS. www.rhino3d.com.

[2] T-spline add-on for Rhino. This commercially available add-on allows to convert NURBS geometries as drawn in Rhinocesors to T-splines. www.tsplines.com/products/tsplines-for-rhino.html.

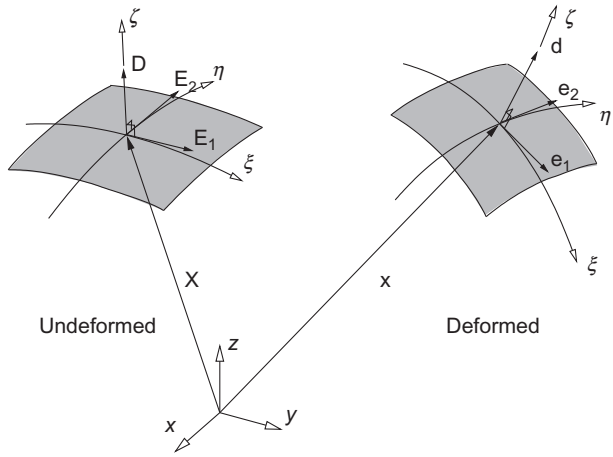

Figure 11.5 Local coordinate system of a shell element. Curvilinear coordinate system (ξ,η,ζ) of a shell element. The vectors $\mathbf{E}_1$, $\mathbf{E}_2$ and $\mathbf{D}$ are the base vectors for the undeformed shell; $\mathbf{e}_1$, $\mathbf{e}_2$ and $\mathbf{d}$ are the corresponding base vectors in the deformed configuration, where $\mathbf{d}$ is perpendicular to the shell's mid-surface by definition.

The second-order derivatives which now evolve require a $\mathcal{C}^1$ continuity, similar to the Euler–Bernoulli beam. Because $\mathcal{C}^1$-continuity is naturally obtained using splines of order two or higher, the Kirchhoff–Love shell formulation can be discretised straightforwardly in IGA. However, special attention needs to be paid at boundary conditions. With conventional shell elements, a clamped boundary condition is obtained by constraining the rotational degrees of freedom at the boundary. In the Kirchhoff–Love element formulation, these degrees of freedoms are absent. Instead, the derivative of the displacement with respect to the direction normal to the boundary must be constraint. In the isogeometric formulation, this can be done by constraining both the degree of freedom at the boundary and its neighbour, as shown in Figure 11.6.

11.3.2 Examples

The isogeometric Kirchhoff–Love formulation has been subjected to a series of numerical experiments to test its performance (Haartsen, 2012). A good example of such a test is the Scordelis-Lo roof example. Its geometry is a single-curved shell

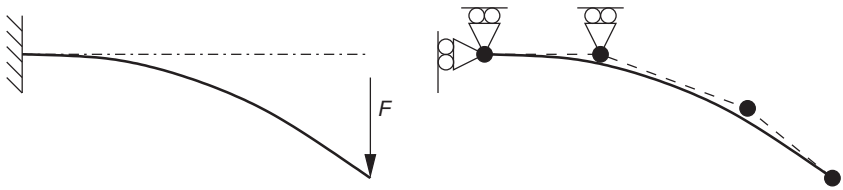

Figure 11.6 Schematic representation of the clamped horizontal plate with end load (left) and the applied boundary conditions on the isogeometric control net representing the clamped-condition in the discretised problem (right).

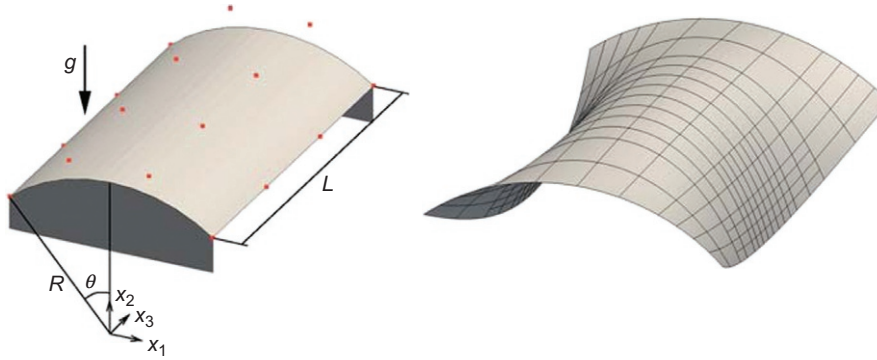

Figure 11.7 Left: Geometry and boundary conditions of the Scordelis–Lo roof example. Right: the deformed T-spline mesh (de Borst et al., 2012).

in the shape of a cylinder segment with rigid diaphragm supports ($u_x = u_y = 0$) at its ends and free side edges, see Figure 11.7. The dimensions of the roof are $L = 50$ m, $R = 25$ m, $t = 0.25$ m, and $\phi = 40°$. The roof is made of an isotropic material with Young's modulus and Poisson's ratio $E = 432$ MPa and $v = 0.0$, respectively. The roof is subjected to gravity loading $g = 90$ N/m^2.

The Scordelis–Lo roof tests the element's ability to handle complex membrane states (Belytschko et al., 1985). A substantial part of the strain energy is membrane strain energy. The representation of inextensional deformation is less important in this problem. The benchmark quantity used to test convergence is the vertical displacement u_z of the side edge midpoint, which is 0.3024 m. It should be noted that the Scordelis-Lo roof problem is executed as a linear problem. Figure 11.7 shows the deformed geometry of the Scordelis–Lo roof problem computed with a third-order T-spline mesh. The displacement converges to a value of 0.3006 m, a value that has been reported by various authors (Kiendl et al., 2009; Haartsen, 2012).

In the second example, the buckling load of a cylindrical shell is investigated (Singer et al., 2002). A cylinder with a radius $R = 100$ mm, a length $L = 200$ mm and a thickness $t = 1$ mm is subjected to a uniform compressive load. The radial displacements at the top and bottom edge are constrained. The cylinder is made of an isotropic material with Young's modulus $E = 10.0$ MPa and Poisson's ratio $v = 0.3$.

To assess the quality of the numerical results, an analytical expression for the critical buckling strain ϵ_{c1} for perfect short cylinders under axial compression is used (Singer et al., 2002):

$$\epsilon_{cl} = \frac{t}{cR}, \quad \text{where } c = \sqrt{3(1-v^2)} \tag{11.11}$$

For the given parameters, the critical buckling strain is $\epsilon_{cl} = 0.0061$. This value is used to compare the numerically calculated critical buckling strains for various mesh sizes. To this end, a linear buckling analysis is performed in which the lowest eigenvalues and corresponding modes of the global stiffness matrix are calculated.

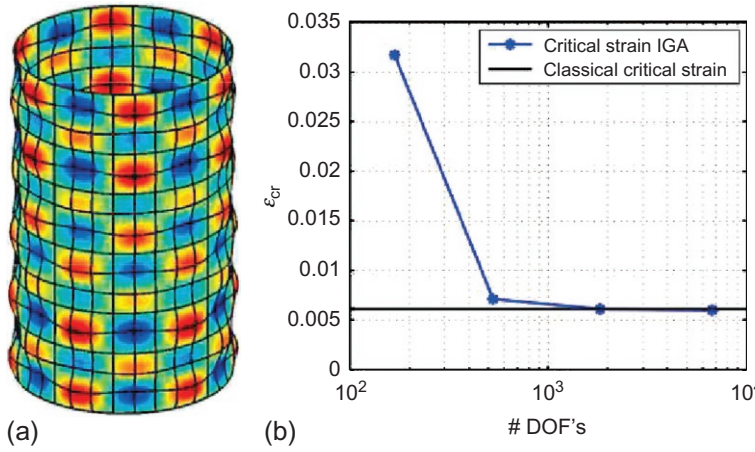

Figure 11.8 Cylindrical shell buckling example. Left: Eigenmode of the critical buckling load obtained with a model with 32×16 third-order Bézier elements (1824 degrees of freedom). Right: Convergence of the numerical solution upon mesh refinement (Haartsen, 2012).

It can be seen in Figure 11.8 that upon mesh refinement, the numerically calculated critical buckling strain of the cylinder approaches the classical critical buckling strain but converges to a value $\epsilon_{cl} = 0.00603$. The calculated critical buckling mode is shown in Figure 11.8a and is periodic in circumferential direction (8 full waves) and periodic in axial direction (10 half waves).

Considering the complexity of the deformation field, it is remarkable that the solution already converges when 32×16 third-order Bézier elements are used. The total number of degrees of freedom in this model is 1824. To obtain the same accuracy, a conventional finite-element mesh needs many more degrees of freedom.

11.4 Continuum shell formulation

Conventional zero thickness shells such as Kirchhoff–Love or Reisner–Mindlin shell formulations (and modifications thereof) are the ideal choice for the analysis of the stiffness or the structural stability of shell structures. When non-linear material behaviour such as damage, plasticity or delamination is present in the analysis, a continuum element with an accurate representation of the stresses is needed. Because of the slender nature of shell structures, special elements have been developed that can be used in thin applications. An example of such an element is the solid-like shell element (Parisch, 1995). In this element, an internal stretch term is added to obtain a quadratic term in the displacement field in the thickness direction. As a consequence, the normal strain varies linearly, which significantly reduces Poisson thickness locking. The element has been extended to be used in laminated composites, including delamination (Hashagen and de Borst, 2000; Remmers et al., 2003).

An isogeometric version of this element has been developed by Hosseini et al. (2013). In this element, NURBS or T-spline basis functions are used to construct the mid-surface of the shell. The displacement field in the through-the-thickness direction is discretised using standard linear-shape functions, including the additional stretch term to alleviate thickness locking, similar to Parisch (1995). In a later stage, the linear shape functions and the stretch term in this model were replaced by a higher-order B-spline basis function (Hosseini et al., 2014a). In this way, a B-spline volume patch is created by multiplying a bivariate and a univariate spline function using Equation (11.5). Because of the higher-order continuity of the discretisation in thickness direction, the strain field varies at least linearly over the thickness. Again, locking is hereby avoided.

In this section, we will further explore the capabilities of this version of this isogeometric continuum shell element and briefly discuss the extension toward a discontinuous continuum shell element to model delamination growth (Hosseini et al., 2014b).

11.4.1 Kinematics and equilibrium equations

Figure 11.9 shows the undeformed and the deformed configurations of a continuum shell element. The reference surface of the shell is denoted by S_0. The variables ξ and η are the local curvilinear coordinates in the two independent in-plane directions, and ζ is the local curvilinear coordinate in the thickness direction. The position of a material point within the shell body in the undeformed configuration is written as a function of the three curvilinear coordinates:

$$\mathbf{X}(\xi,\eta,\zeta) = \mathbf{X}^0(\xi,\eta) + \zeta\mathbf{D}(\xi,\eta), \quad 0 \le \zeta \le 1 \tag{11.12}$$

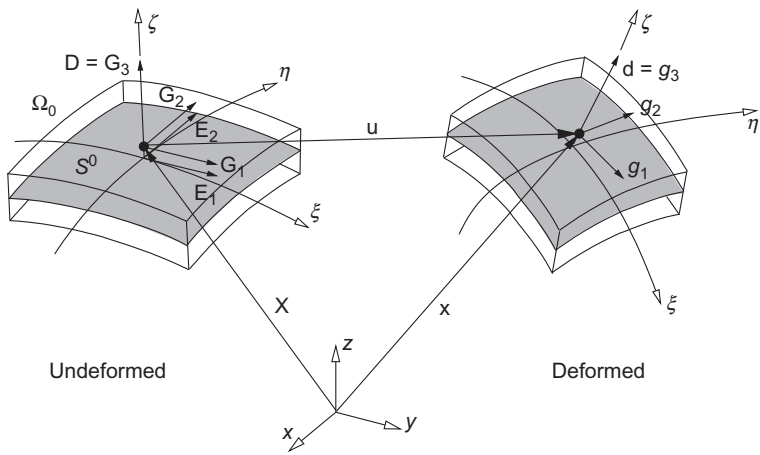

Figure 11.9 Kinematics of the continuum shell in the undeformed and in the deformed configuration. The corresponding covariant triads for any point in the shell body are denoted by $\mathbf{G}_i$ and $\mathbf{g}_i$.

where $\mathbf{X}^0(\xi, \eta)$ is the projection of the point on the reference surface of the shell and $\mathbf{D}(\xi, \eta)$ is the thickness director perpendicular to the surface S_0 at this point.

In any material point, a local reference triad can be established. The covariant base vectors are then obtained as the partial derivatives of the position vectors with respect to the curvilinear coordinates $\Theta^i = [\xi, \eta, \zeta]$. First, we define a set of basis vectors on the reference surface in the undeformed configuration as

$$\mathbf{E}_\alpha = \frac{\partial \mathbf{X}^0}{\partial \Theta^\alpha}, \quad \alpha = 1,2 \tag{11.13}$$

so that the shell director can be written as

$$\mathbf{E}_3 = \mathbf{D} = \frac{\mathbf{E}_1 \times \mathbf{E}_2}{\|\mathbf{E}_1 \times \mathbf{E}_2\|} t \tag{11.14}$$

where t is the thickness of the shell. Now, using Equation (11.12), the covariant triad for any point within the shell body is obtained as

$$\begin{aligned} \mathbf{G}_\alpha &= \frac{\partial \mathbf{X}}{\partial \Theta^\alpha} = \mathbf{E}_\alpha + \zeta \mathbf{D}_{,\alpha}, \quad \alpha = 1,2 \\ \mathbf{G}_3 &= \mathbf{D} \end{aligned} \tag{11.15}$$

where the subscript comma denotes partial differentiation.

The position of the material point in the deformed configuration $\mathbf{x}(\xi, \eta, \zeta)$ is related to $\mathbf{X}(\xi, \eta, \zeta)$ via the displacement field $\mathbf{u}(\xi, \eta, \zeta)$ as

$$\mathbf{x}(\xi, \eta, \zeta) = \mathbf{X}(\xi, \eta, \zeta) + \mathbf{u}(\xi, \eta, \zeta) \tag{11.16}$$

The displacement field $\mathbf{u}$ can be of any order that is in contrast to the standard solid-like shell formulation where an internal stretch term is added to obtain a quadratic term in the displacement field in the thickness direction. Similarly, in the deformed configuration, we can establish the covariant triad as

$$\boldsymbol{g}_i = \frac{\partial \mathbf{x}}{\partial \Theta^i} = \mathbf{G}_i + \mathbf{u}_{,i}, \quad i = 1,2,3 \tag{11.17}$$

which convention will be used in the remainder. Using Equations (11.15) and (11.17), the metric tensors $\mathbf{G}$ and $\mathbf{g}$ can be determined as

$$G_{ij} = \mathbf{G}_i \cdot \mathbf{G}_j, \quad g_{ij} = \mathrm{g}_i \cdot \mathrm{g}_j, \quad i,j = 1,2,3 \tag{11.18}$$

The contravariant basis vectors needed for the calculation of the strains can be derived as

$$\mathbf{G}^i = (\mathbf{G})^{-1} \mathbf{G}_i \tag{11.19}$$

where $(\mathbf{G})^{-1}$ is the inverse of the metric tensor with components G_{ij}. The volume of the element in the undeformed configuration is evaluated using the covariant metric tensor $\mathbf{G}$ in the following manner:

$$\mathrm{d}\Omega_0 = \sqrt{\det(\mathbf{G})}\ \mathrm{d}\xi\ \mathrm{d}\eta\ \mathrm{d}\zeta \tag{11.20}$$

The Green–Lagrange strain tensor γ is defined conventionally in terms of the deformation gradient $\mathbf{F}$:

$$\gamma = \frac{1}{2}\left(\mathbf{F}^{\mathrm{T}} \cdot \mathbf{F} - \mathbf{I}\right) \tag{11.21}$$

where $\mathbf{I}$ is the unit tensor. The deformation gradient can be written in terms of the base vectors as

$$\mathbf{F} = \mathbf{g}_i \otimes \mathbf{G}^i \tag{11.22}$$

which leads to following representation of the Green–Lagrange strain tensor:

$$\boldsymbol{\gamma} = \gamma_{ij}\mathbf{G}^i \otimes \mathbf{G}^j \quad \text{with } \gamma_{ij} = \frac{1}{2}\left(g_{ij} - G_{ij}\right) \tag{11.23}$$

where the summation convention has been used for repeated indices. Substituting Equations (11.15) and (11.17) for G_{ij} and g_{ij} into this relation yields:

$$\gamma_{ij} = \frac{1}{2}\left(\mathbf{G}_i \cdot \mathbf{u}_{,j} + \mathbf{u}_{,i} \cdot \mathbf{G}_j + \mathbf{u}_{,i} \cdot \mathbf{u}_{,j}\right) \tag{11.24}$$

Note that in this strain expression, only first-order derivatives of the shape functions are present, as opposed to the Kirchhoff–Love shell, which contains second-order derivatives. In a total Lagrangian formulation, the internal virtual work is expressed in the reference configuration Ω_0:

$$\delta W_{\mathrm{int}} = \int_{\Omega_0} \delta\boldsymbol{\gamma}^{\mathrm{T}} : \mathbf{S}\mathrm{d}\Omega_0 \tag{11.25}$$

where $\mathbf{S}$ is the second Piola Kirchhoff stress tensor.
The resulting system of non-linear equations is typically solved in an incremental, iterative manner, which requires computation of the tangential stiffness matrix. Details on the derivation of this stiffness matrix can be found in Hosseini et al. (2014a).

11.4.2 Discretisation

As we have mentioned in Section 11.2.1, B-spline and NURBS basis functions are $\mathcal{C}^{p-k}$ continuous at a knot with multiplicity k. This means that we are able to control the continuity of the basis functions at a knot by arbitrarily selecting its multiplicity.

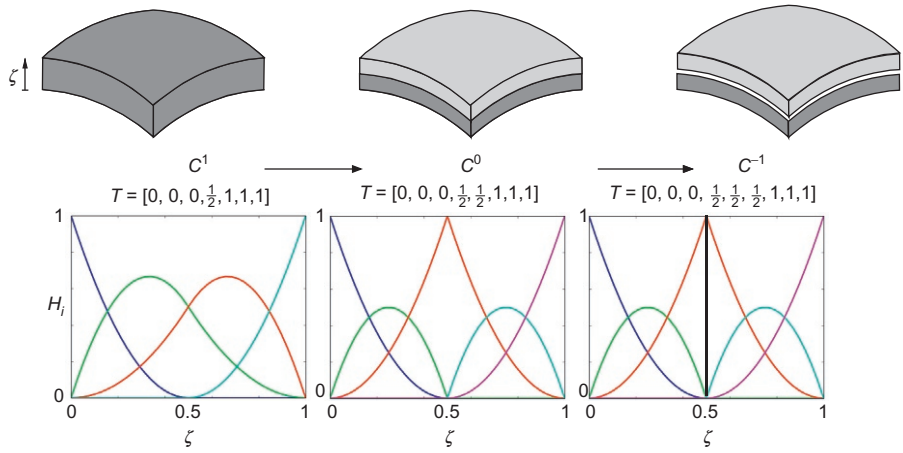

Figure 11.10 Schematic representation of introducing a discontinuity in the thickness direction of a shell. Weak and strong discontinuities between the layers of a composite shell are created by knot insertion.

This property is useful for modelling traction-free cracks and adhesive interfaces (strong discontinuity) and layered structures with C^0 continuity between the layers (weak discontinuity) (Verhoosel et al., 2011).

Figure 11.10 shows the steps needed to make a discontinuity in the thickness direction of a shell structure. Assume that a quadratic B-spline basis function h_i defined over a knot vector $\mathcal{T} = \left[0,0,0,\frac{1}{2},1,1,1\right]$ has been used in the thickness of the shell. This gives us four basis functions, which are all C^1 continuous at $\zeta = \frac{1}{2}$. In the remainder, this element will be called the *lumped* element. Now suppose that we want to have a composite shell consisting of two layers of equal thickness. The deformation of composite structures requires a unique displacement at the interfaces and different strain fields in the adjacent layers. In the example of Figure 11.10 this is simply achieved by having a displacement field which is C^0 continuous at the interface $\zeta = \frac{1}{2}$. This leads to the new knot vector $\mathcal{T} = \left[0,0,0,\frac{1}{2},\frac{1}{2},1,1,1\right]$. Henceforth, we will denote this element as the *layered* element. Subsequently, the complete separation of the layers is obtained if we insert the second knot as $\mathcal{T} = \left[0,0,0,\frac{1}{2},\frac{1}{2},\frac{1}{2},1,1,1\right]$, and this element will be denoted as the *discontinuous* element. Figure 11.10 shows the corresponding basis functions through the knot insertion process.

11.4.3 Examples

The performance of the continuum shell element is first studied in the analysis of the deflection of a multi-layer composite panel. Conventionally, these structures are simulated with a zero-thickness shell element. This is generally sufficient for calculating displacements, but it does not allow for computing the stresses and strains in the individual layers accurately.

We consider the square laminate shown in Figure 11.11. The panel has dimensions $a \times b = 0.6 \times 0.4$ m and consists of six layers of a unidirectional material, with a stacking sequence $[0, 90, 0]_s$. Each layer is 0.2 mm thick, so that the total thickness of the shell is 1.2 mm. The layers can be modelled as a transversely isotropic material with $E_1 = 130$ GPa, $E_2 = E_3 = 7$ GPa, $v_{12} = 0.33$, and $G_{12} = 5$ GPa. The panel is simply supported on all four sides and is loaded by a distributed load

$$q_z = q_0 \sin\frac{\pi x}{a} \sin\frac{\pi y}{b}$$

with $q_0 = 1$ MPa.

The panel has been simulated for three different discretizations: second-order in the thickness direction, fourth order in the thickness direction (*lumped* in Figure 11.10) and second order per layer with weak discontinuities at the boundaries between the layers (*layered* in Figure 11.10). A reference solution for the out-of-plane displacement of the midpoint is obtained from classical laminate theory. This displacement is equal to -2.62×10^{-2} mm.

Figure 11.12 shows σ_{xx} in the midpoint of the panel as a function of the thickness coordinate of the shell obtained for different discretizations. The results from one second-order and one fourth-order B-spline element lead to the same stress distribution as that of a second-order B-spline per layer (weak discontinuities at layer boundaries). All the results are in agreement with the reference solution from the classical laminated plate theory.

Next, the ability of the shell element to compute interlaminar stresses is examined. This issue is of importance when damage and failure of composite materials need to be considered in the simulations. The normal stress σ_{zz} is presented in Figure 11.13 as a function of thickness of the shell. By using second-order and third-order B-splines per layer, *layered* (2) and *layered* (3) elements, respectively, which are C^0 continuous at the interfaces, we can capture a σ_{zz} distribution in the thickness direction, which is zero through most of the thickness and equals $q_0 = 1$ MPa at the top surface. Adopting just one element of second-order and of fourth-order B-splines, *lumped* (2) and *lumped* (4), respectively, for the discretization in the thickness direction results in a fluctuation of the σ_{zz} distribution. From the results it is concluded that in order to compute σ_{zz} accurately, we need to enforce C^0-continuity of the basis functions at the interfaces.

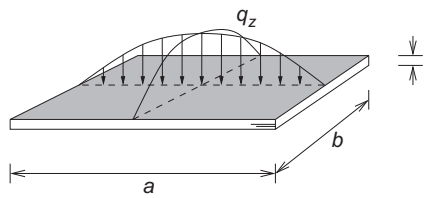

Figure 11.11 Geometry, loading of a rectangular panel. All four edges are simply supported.

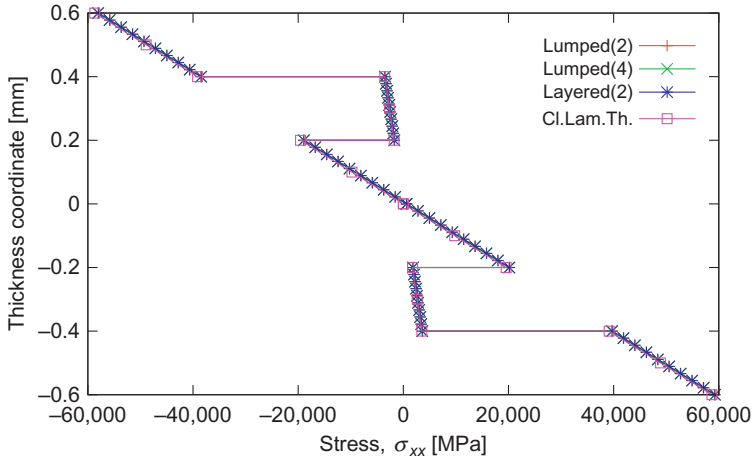

Figure 11.12 σ_{xx} at the mid-point of the panel as a function of the thickness of the panel for *lumped* and *layered* discretisations with B-splines of various orders in thickness direction. The solution obtained by the classical laminate theory is shown as a reference. The thickness of the plate is 1.2 mm. (Hosseini et al., 2014a).

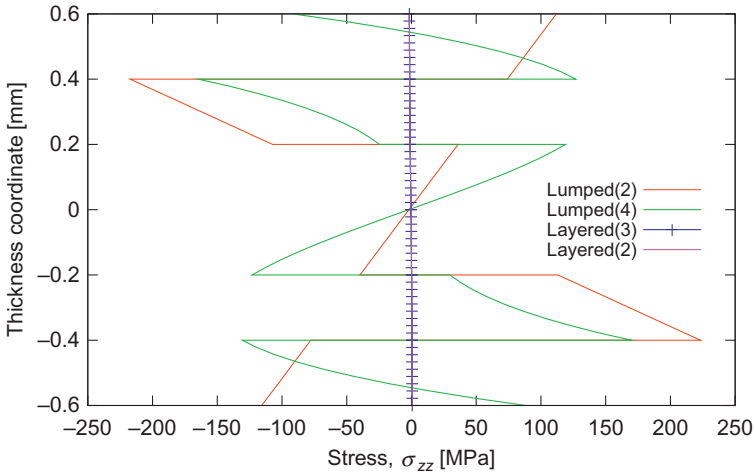

Figure 11.13 σ_{zz} at the mid-point as a function of the thickness of the panel for *lumped* and *layered* discretisations with B-splines of various orders in thickness direction. The thickness of the panel is 1.2 mm (Hosseini et al., 2014a).

The simulations are now repeated for a 10 times thicker panel with $q_0 = 100$ MPa. The results presented in Figure 11.14 show again that applying basis functions with $\mathcal{C}^0$ continuity between the layers results stress distribution that can be expected for a thick panel. The jump at $z = 0$ is caused by the fact that the displacement boundary condition $u_z = 0$ at the edges has been enforced at $z = 0$.

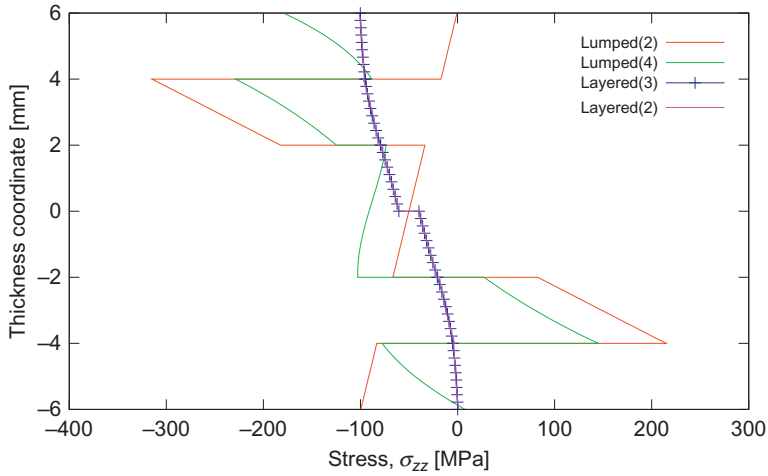

Figure 11.14 σ_{zz} at the mid-point as a function of the thickness of the panel for *lumped* and *layered* discretisations with B-splines of various orders in thickness direction. The thickness of the panel is 12 mm (Hosseini et al., 2014a).

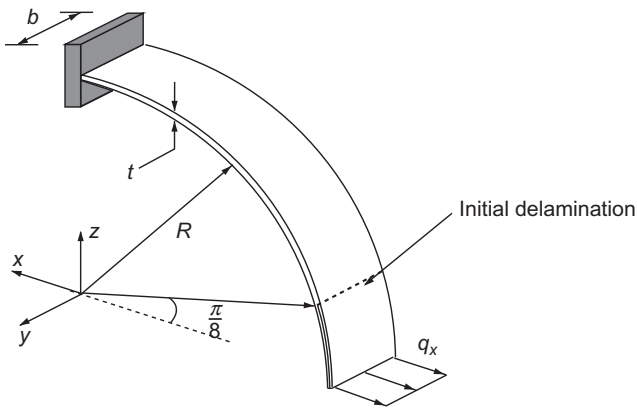

Figure 11.15 Geometry of the curved panel with two layers and an initial delamination.

In the next example, delamination propagation is simulated in a curved panel. The geometry of the panel is shown in Figure 11.15. The panel has a radius of $R=10$ m, a width of $b=1$ m, and a thickness of $t=0.1$ m. The panel is considered to have two isotropic layers with a Young's modulus $E=2\times1000$ Pa and a Poisson's ratio $v=0.3$. An initial delamination is taken over at angle $\pi/8$. The curved panel is clamped at one edge and subjected to a constant distributed load of q_x. This provides a suitable test case to investigate mixed-mode delamination propagation with large rotations at the interface.

Delamination growth can be modelled by extending the weak form of the equilibrium conditions, Equation (11.25) with a cohesive zone traction term. The opening of this interface is equal to the relative displacements of two material points on either side of the interface. A detailed description of this term can be found in Hosseini et al. (2014b). Here, we model the interface behaviour by means of a mixed-model constitutive relation (Turon et al., 2006), with fracture toughnesses $\mathcal{G}_{Ic} = 10\ \mathrm{J/m^2}$ and $\mathcal{G}_{IIc} = 10\ \mathrm{J/m^2}$ in mode I and mode II, respectively. The corresponding interface strengths are $t_3^0 = 100$ Pa and $t_s^0 = 500$ Pa. The dummy stiffness is $K = 10^6$ Pa.

The numerical simulations have been done using two different meshes of 256×1 and 512×4 discontinuous elements. The obtained load–displacement graphs are shown in Figure 11.16, which show a good agreement and confirm mesh insensitivity.

Figure 11.17 shows the deformation of the panel. First, both layers start moving in the loading direction. In this process damage at the interface starts to grow. After a certain deformation and a certain damage growth, the lower layer moves in the reverse direction while the top layer keeps moving in the loading direction. At the final stage, the lower layer has returned to its initial configuration, the interface is fully damaged

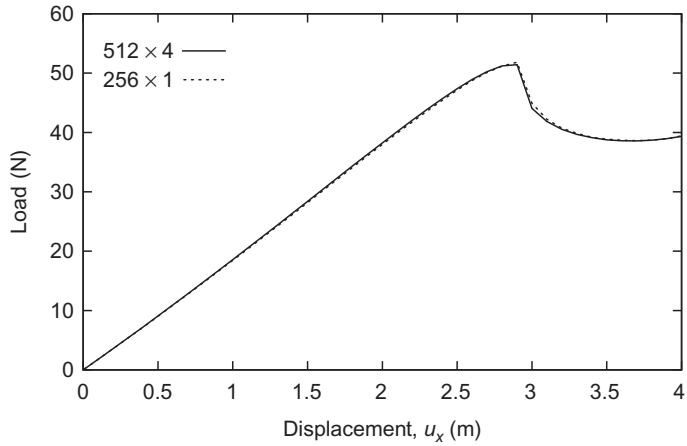

Figure 11.16 Load-displacement curve for delamination propagation in the curved panel (Hosseini et al., 2014b).

Figure 11.17 Deformation of the curved panel. Grey indicates the initial configuration, red represents the areas with damage $\omega \approx 1$ and blue shows the areas with $\omega = 0$ (Hosseini et al., 2014b).

and the upper layer remains in the new configuration. In Figure 11.17, the grey colour indicates the initial configuration, the red colour represents the areas with damage $\omega \approx 1$ and the blue colour shows the areas without damage ($\omega = 0$).

11.5 Concluding remarks

Isogeometric analysis is a promising new technique in the field of computational mechanics. One of the most interesting features, at least from an engineering point of view, is the possibility to integrate fully the CAD design of complex structures and their numerical analysis in one platform, the so-called design-through-analysis paradigm. This is especially of importance for the aerospace and automotive industry, where composites materials are used in complex geometries for lightweight design.

Surprisingly, a less known feature of isogeometric basis functions, their higher-order continuity, is even more important for the development of shell and continuum shell elements to analyse structural stability and damage in thin-walled composite structures. The higher-order shape functions enable us to implement the relatively simple but powerful Kirchhoff–Love elements, without the need for rotational degrees of freedom. In addition, because of the higher-order continuity, the shell director is uniquely defined and is initially exactly perpendicular to the shell mid-surface, even at inter-element boundaries. Finally, the undeformed geometry of the structure is represented exactly, even for conical sections. This is beneficial for the analysis of shell buckling, which is extremely sensitive to small geometric imperfections.

The higher-order continuity contributes to a better representation of stresses in continuum shell elements, in any material point, even at element boundaries. This is an important requirement for the simulation of non-linear material behaviour such as damage. Interfaces and delaminations can be modelled by reducing the order of the isogeometric shape functions by knot insertion. Combined with a cohesive zone model, this allows us to simulate delamination growth in a multi-layer composite with only one isogeometric continuum element in the thickness direction.

In recent years, a lot of progress has been made in the development of isogeometric element formulations. However, the development of commercially viable pre- and post-processing tools is not yet up to par. Most examples presented in this chapter use a rather simple geometry, so the corresponding meshes can be created manually. For more complex geometries, one has to rely on advanced meshing tools, which are sparse. At the moment, Rhinoceros is the only programme that provides access to all meshing data, including the Bézier extraction operators, for T-spline meshes. Unfortunately, this programme does not allow straightforwardly to create complex three-dimensional features such as stiffeners and joints, which are common features in composite structures. The development of dedicated analysis suitable geometry construction algorithms for IGA will undoubtedly contribute to the original promise of IGA to seamlessly merge the design and the mechanical analysis of complex structures.

References

Belytschko, T., Stolarsky, H., Liu, W.K., Carpenter, N., Ong, J.S.J., 1985. Stress projection for membrane and shear locking in shell finite elements. Comput. Methods Appl. Mech. Eng. 51, 221–258.

Benson, D.J., Bazilevs, Y., Hsu, M.C., Hughes, T.J.R., 2010. Isogeometric shell analysis: the Reissner-Mindlin shell. Comput. Methods Appl. Mech. Eng. 199, 276–289.

Bischoff, M., Wall, W., Bletzinger, K.U., Ramm, E., 2004. Models and finite elements for thin-walled structures. In: Stein, E., de Borst, R., Hughes, T.J.R. (Eds.), In: Encyclopedia of Computational Mechanics, vol. 2. Wiley, Chichester, pp. 59–137, Chapter 3.

Borden, M.J., Scott, M.A., Evans, J.A., Hughes, T.J.R., 2011. Isogeometric finite element data structures based on Bézier extraction. Int. J. Numer. Methods Eng. 87, 15–47.

Braun, M., Bischoff, M., Ramm, E., 1994. Nonlinear shell formulations for complete three-dimensional constitutive laws including composites and laminates. Comput. Mech. 15 (1), 1–18.

Bushnell, D., 1981. Buckling of shells – pitfall for designers. AIAA J. 19 (9), 1183–1226.

Cottrell, J., Hughes, T.J.R., Bazilevs, Y., 2009. Isogeometric Analysis: Toward Integration of CAD and FEA. John Wiley & Sons, Chichester.

Cox, M.G., 1972. The numerical evaluation of B-splines. IMA J. Appl. Math. 10, 134–149.

de Boor, C., 1972. On calculating with B-splines. J. Approx. Theory 6, 50–62.

de Borst, R., Crisfield, M.A., Remmers, J.J.C., Verhoosel, C.V., 2012. Nonlinear Finite Element Analysis of Solids and Structures, second ed. Wiley Series in Computational Mechanics, Chichester, UK.

Dornisch, W., Klinkel, S., Simeon, B., 2013. Isogeometric ReissnerMindlin shell analysis with exactly calculated director vectors. Comput. Methods Appl. Mech. Eng. 253, 491–504.

Echter, R., Oesterle, B., Bischoff, M., 2013. A hierarchic family of isogeometric shell finite elements. Comput. Methods Appl. Mech. Eng. 254, 170–180.

Haartsen, T.I.F., 2012. Simulation of buckling of thin-walled structures using isogeometric analysis (M.Sc. thesis), Eindhoven University of Technology, Eindhoven, The Netherlands.

Hashagen, F., de Borst, R., 2000. Numerical assessment of delamination in fibre metal laminates. Comput. Methods Appl. Mech. Eng. 185, 141–159.

Hosseini, S., Remmers, J.J.C., Verhoosel, C.V., de Borst, R., 2013. An isogeometric solid-like shell formulation for non-linear analysis. Int. J. Numer. Methods Eng. 95, 238–256.

Hosseini, S., Remmers, J.J.C., Verhoosel, C.V., de Borst, R., 2014a. An isogeometric continuum shell element for non-linear analysis. Comput. Methods Appl. Mech. Eng. 271, 1–22.

Hosseini, S., Remmers, J.J.C., Verhoosel, C.V., de Borst, R., 2014b. Propagation of delamination in composite materials with isogeometric continuum shell elements. Int. J. Numer. Methods Eng. http://dx.doi.org/10.1002/nme.4730.

Hughes, T.J.R., Cottrell, J., Bazilevs, Y., 2005. Isogeometric analysis: CAD, finite element, NURBS, exact geometry and mesh refinement. Comput. Methods Appl. Mech. Eng. 194, 4135–4195.

Kiendl, J., Bletzinger, K.U., Linhard, J., Wüchner, R., 2009. Isogeometric shell analysis with Kirchhoff-Love elements. Comput. Methods Appl. Mech. Eng. 198, 3902–3914.

Parisch, H., 1995. A continuum-based shell theory for non-linear application. Int. J. Numer. Methods Eng. 38, 1855–1883.

Piegl, L., Tiller, W., 1997. The NURBS Book, second ed. Springer-Verlag, New York.

Reddy, J.N., 1984. A simple higher-order theory for laminated composite plates. J. Appl. Mech. 51 (4), 745–752.

Remmers, J.J.C., Wells, G.N., de Borst, R., 2003. A solid-like shell element allowing for arbitrary delaminations. Int. J. Numer. Methods Eng. 58, 2013–2040.

Scott, M.A., Borden, M.J., Verhoosel, C.V., Sederberg, T.W., Hughes, T.J.R., 2011. Isogeometric finite element data structures based on Bézier extraction of T-splines. Int. J. Numer. Methods Eng. 88, 126–156.

Sederberg, T.W., Zheng, J., Bakenov, A., Nasri, A., 2003. T-splines and T-NURCCs. ACM Trans. Graph. 22, 477–484.

Singer, J., Arbocz, J., Weller, T., 2002. Buckling Experiments, Shells, Built-up Structures, Composites and Additional Topics. Vol. 2. John Wiley & Sons, New York. ISBN: 9780471974505

Turon, A., Camanho, P.P., Costa, J., 2006. A damage model for the simulation of delamination in advanced composites under variable-mode loading. Mech. Mater. 38, 1072–1089.

Verhoosel, C.V., Scott, M.A., de Borst, R., Hughes, T.J.R., 2011. An isogeometric approach to cohesive zone modeling. Int. J. Numer. Methods Eng. 87 (1–5), 336–360.

This page intentionally left blank

Peridynamics for analysis of failure in advanced composite materials

12

A. Askari*, Y. Azdoud†, F. Han†, G. Lubineau†, S. Silling‡
*Boeing Commercial Airplane, Everett, WA, USA, †King Abdullah University of Science and Engineering (KAUST), Physical Sciences and Engineering Division, COHMAS Laboratory, Thuwal, Saudi Arabia, ‡Sandia National Laboratories, Albuquerque, NM, USA

12.1 Introduction

Many mathematical models and computational methods have been proposed and developed to predict the evolution of degradation in composites (Soden et al., 1998; Hinton et al., 2002; Lubineau and Ladevèze, 2008). However, predicting the behavior up to failure of these materials using conventional continuum damage mechanics or fracture mechanics remains challenging.

On the one hand, anisotropic damage mechanics has been adapted for composite materials, and it has reached a level where it can describe every single classical mechanism in laminates (Lubineau and Ladevèze, 2008). For example, the damage mesomodel for laminates (Ladevèze and Le Dantec, 1992), coupled with micro- and mesomechanics since the last decade (Ladevèze and Lubineau, 2001, 2003; Ladevèze et al., 2006), can predict in an accurate manner the progressive evolution of transverse cracking, diffuse damage (fiber/matrix debonding), interlaminar plasticity, fiber breaking, as well as interlaminar delamination. Yet, handling the final localization (which is key because it results in macroscopic cracks and failure) is somehow challenging as specific techniques have to be used (Allix and Deu, 1997; Allix et al., 2003) to ensure mesh objectivity, which remains not yet completely understood for laminated composites. We also note that damage mechanics-based approaches do not allow (at least in their raw formulation) for discontinuous solutions. Cracks are smoothed out and globally represented by internal damage variables. This is relevant to progressive and distributed degradation, but might be questioned as relevant to the final failure that generally results from the severe localization of a macroscopic crack, which shifts the failure to a regime in which homogenization may not be possible.

On the other hand, fracture mechanics mainly addresses the extension of preexisting cracks and does not address the initiation problem that is quite complex, especially in laminated composites. Even predicting crack extension is somewhat difficult when multiple cracks with complex shapes and interactions have to be considered, as a remeshing process is often needed if the finite element framework is used. Although remeshing can be avoided with some special elements, such as cohesive elements, *a priori* knowledge of the crack path is required to place these elements (Kilic et al., 2009). Placing the elements is generally possible for a limited number of configurations, such as the

Numerical modelling of failure in advanced composite materials. http://dx.doi.org/10.1016/B978-0-08-100332-9.00012-8
Copyright © 2015 Elsevier Ltd. All rights reserved.

prediction of interlaminar delamination, in which cracks clearly appear and extend at the interface between adjacent plies (Allix and Ladevèze, 1995). Nevertheless, location of cracks is usually unknown *a priori* in complex structures. Similarly, prediction of crack propagations also requires an additional growth criterion. This criterion is *a priori* based on material properties and local loading conditions. However, it is extremely difficult to identify such a criterion for cracks propagation from experimental data, especially in composite materials.

To address these concerns, a recently developed theory of solid mechanics, known as peridynamics and proposed by Silling (2000), redefines the problem by using integral equations rather than partial differential equations. In peridynamics, the equilibrium of a material point is assumed to be attained by an integral of internal forces exerted by nonadjacent points across a finite distance. These internal forces are thus nonlocal interactions in a continuous body. The interaction between pairs of points is defined over the connection vector, called the *bond*, of these two points. A bond is permitted to break irreversibly when it is stretched beyond a critical value. As a result, two-dimensional surfaces crossing all broken bonds represent cracks in a three-dimensional body. These definitions allow crack initiation and evolution simultaneously at multiple sites, with spontaneous paths inside a material and without formulating a complex crack growth criterion (Kilic et al., 2009).

Peridynamics, however, comes with huge computational cost that pushes classical engineering problems out of reach. Furthermore, peridynamics is characterized by volume-like boundary conditions that can make its application tedious for engineers who are more used to traction-like boundary conditions. Consequently, a reasonable strategy is to reserve peridynamics for parts of the structure where key mechanisms, such as damage or fracture, strongly impact the solution, and then to use continuum mechanics for the rest of the structure for which the conventional continuum model can satisfy solution accuracy and boundary conditions and can reduce consumption of computational resources. Then, the challenge lies in how to couple the peridynamic model and the conventional continuum model together efficiently. Recently, some coupling schemes have been proposed, including the force-based coupling method (Seleson et al., 2013), the Arlequin coupling method (Han and Lubineau, 2012), and the morphing coupling method (Lubineau et al., 2012). The force-based coupling method derives a coupled force equilibrium equation, which blends the peridynamic and continuum models in a transition region by using a weighting function. In contrast, the Arlequin coupling method belongs to the energy-based coupling strategy in which the coupling is performed at the energy level by using a partition of unity concept. The morphing coupling method is inspired by the idea of homogenization. Using the equivalent energy density of both models, it constructs a balance between local stiffness and the weighted nonlocal modulus.

In the remainder of this chapter, Section 12.2 briefly introduces the fundamentals of peridynamic theory. Special peridynamic material models for composites are addressed in Section 12.3. As a very recent method to formalize continuum mechanics reference problems, peridynamics is still at its infancy when it comes to complex material behaviors such as those observed in laminated composites. Even so, we provide a few examples based on our recent work and discuss needed developments and

the potential of the approach. We then focus on the upscaling problem and on how to handle the simulation of large structures by restricting the use of peridynamics to localized areas. Because the morphing coupling method is simple and easy to use, we present a brief introduction on this method and provide a benchmark example for crack extension in Section 12.4.

12.2 Peridynamic theory

Peridynamic theory is a generalization of standard solid mechanics that is adapted to certain applications in which the standard theory either fails to apply or requires extensive modification. In particular, peridynamics applies to the modeling of defects, especially cracks, that form spontaneously and grow. To accomplish this, peridynamic equations omit the partial derivatives of the deformation with respect to the spatial coordinates, because these derivatives cannot be evaluated on points of discontinuity in the deformation. Peridynamic equations are integro-differential equations rather than partial differential equations. The resulting theory is *strongly nonlocal* in that it allows direct interaction, through a material model, of material points that are separated by a finite distance. Introductions to peridynamic theory can be found in Silling (2000), Silling and Lehoucq (2010), and Madenci and Oterkus (2014).

One way of deriving peridynamic equations is to consider the strain energy density $W(\mathbf{x})$ at a point $\mathbf{x}$ in a body $\mathcal{B}$. In the peridynamic model, the strain energy density is determined by the deformation of all the material in a neighborhood $\mathcal{H}_\mathbf{x}$ centered at $\mathbf{x}$ with radius $\delta > 0$. The maximum interaction distance δ is called the *horizon* of the material and is treated like a material property. The neighborhood $\mathcal{H}_\mathbf{x}$ is called the *family* of $\mathbf{x}$ (Figure 12.1). The key distinction between this model and the standard theory is that, in peridynamics, $W(\mathbf{x})$ is determined by the collective deformation of all the points in $\mathcal{H}_\mathbf{x}$, rather than the deformation gradient at $\mathbf{x}$.

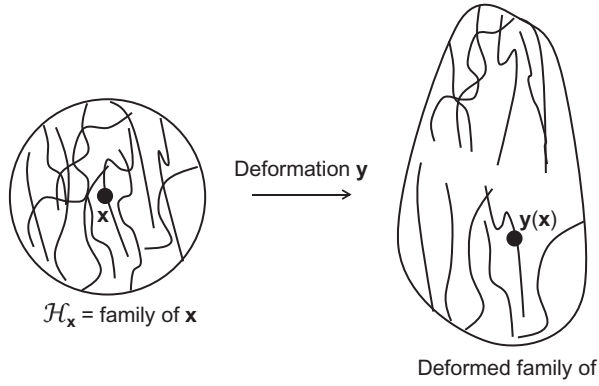

Figure 12.1 The strain energy density at a material point $\mathbf{x}$ is determined by the deformation of its family.

To represent the dependence of W on the deformation of $\mathcal{H}_{\mathbf{x}}$ requires the use of mathematical objects called *states*, which are simply mappings defined on $\mathcal{H}_{\mathbf{x}}$. The deformation within $\mathcal{H}_{\mathbf{x}}$ is represented by the *deformation state* $\underline{\mathbf{Y}}[\mathbf{x}]$ defined by

$$\underline{\mathbf{Y}}[\mathbf{x}]\langle \mathbf{q}-\mathbf{x}\rangle = \mathbf{y}(\mathbf{q})-\mathbf{y}(\mathbf{x}), \tag{12.1}$$

where $\mathbf{q}\in\mathcal{H}_{\mathbf{x}}$. The relative position vector $\mathbf{q}-\mathbf{x}$ is called the *bond* from $\mathbf{x}$ to $\mathbf{q}$, which is henceforth denoted by $\boldsymbol{\xi}$. Thus, the deformation state maps any bond onto its image under deformation $\mathbf{y}$ (Figure 12.2). In an elastic peridynamic material, the dependence of the strain energy density on the deformation of the family is represented by

$$W(\mathbf{x}) = \hat{W}(\underline{\mathbf{Y}}[\mathbf{x}]), \tag{12.2}$$

where $\hat{W}$ is the material model. The key idea is that W depends on the *mapping* of $\mathcal{H}_{\mathbf{x}}$ onto its deformed image, not just on the deformation of particular bonds.

The potential energy Φ corresponding to a deformation field $\mathbf{y}$ in a bounded elastic body subjected to external body force density field $\mathbf{b}$ is given by

$$\Phi = \int_{\mathcal{B}} (W(\mathbf{x}) - \mathbf{b}(\mathbf{x})\cdot\mathbf{y}(\mathbf{x}))\,\mathrm{d}V_{\mathbf{x}}, \tag{12.3}$$

which is formally the same as in the standard theory. To obtain the equilibrium equation, the first variation of Φ is evaluated with respect to $\mathbf{y}$. The Euler–Lagrange equation corresponding to stationary Φ is then found to be

$$\int_{\mathcal{H}_{\mathbf{x}}} (\mathbf{t}(\mathbf{q},\mathbf{x}) - \mathbf{t}(\mathbf{x},\mathbf{q}))\,\mathrm{d}V_{\mathbf{q}} + \mathbf{b}(\mathbf{x}) = \mathbf{0} \tag{12.4}$$

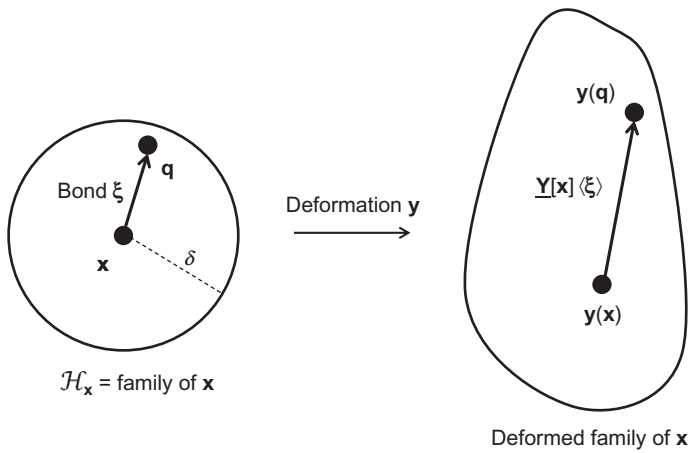

Figure 12.2 Point **x** is connected to its neighbors **q** by bonds. The deformation state maps these bonds into their images under deformation.

for all $\mathbf{x} \in \mathcal{B}$, where $\mathbf{t}(\mathbf{q},\mathbf{x})$ and $\mathbf{t}(\mathbf{x},\mathbf{q})$ are vectors called *bond force densities*. These have dimensions of force/volume^2. They are derived from the material model for strain energy density by

$$\mathbf{t}(\mathbf{q},\mathbf{x}) = \hat{W}_{\underline{\mathbf{Y}}}(\underline{\mathbf{Y}}[\mathbf{x}])\langle \mathbf{q}-\mathbf{x}\rangle, \quad \mathbf{t}(\mathbf{x},\mathbf{q}) = \hat{W}_{\underline{\mathbf{Y}}}(\underline{\mathbf{Y}}[\mathbf{q}])\langle \mathbf{x}-\mathbf{q}\rangle, \tag{12.5}$$

where the symbol $\hat{W}_{\underline{\mathbf{Y}}}$ denotes the Fréchet derivative of the strain energy density W with respect to the deformation state. The Fréchet derivative has the property that for a small change in the deformation state $d\underline{\mathbf{Y}}$, the corresponding change in the strain energy density at $\mathbf{x}$ is given by

$$\hat{W}(\underline{\mathbf{Y}} + d\underline{\mathbf{Y}}) - \hat{W}(\underline{\mathbf{Y}}) = \hat{W}_{\underline{\mathbf{Y}}} \bullet d\underline{\mathbf{Y}} \tag{12.6}$$

plus higher-order terms, where the inner product of two states is defined by

$$\underline{\mathbf{A}} \bullet \underline{\mathbf{B}} = \int_{\mathcal{H}} \underline{\mathbf{A}}\langle \boldsymbol{\xi}\rangle \cdot \underline{\mathbf{B}}\langle \boldsymbol{\xi}\rangle \, \mathrm{d}V_{\boldsymbol{\xi}}. \tag{12.7}$$

Thus, $\hat{W}_{\underline{\mathbf{Y}}}$ is the work conjugate of $\underline{\mathbf{Y}}$. For elastic and inelastic materials, the bond force vectors can be regarded as belonging to the *force state* $\underline{\mathbf{T}}$ evaluated for particular bonds, and we write

$$\mathbf{t}(\mathbf{q},\mathbf{x}) = \underline{\mathbf{T}}[\mathbf{x}]\langle \mathbf{q}-\mathbf{x}\rangle, \quad \mathbf{t}(\mathbf{x},\mathbf{q}) = \underline{\mathbf{T}}[\mathbf{q}]\langle \mathbf{x}-\mathbf{q}\rangle. \tag{12.8}$$

The material model gives the force state as a function of the deformation state and possibly other variables such as temperature θ and rate of change of the deformation state $\dot{\underline{\mathbf{Y}}}$:

$$\underline{\mathbf{T}} = \hat{\underline{\mathbf{T}}}(\underline{\mathbf{Y}}, \dot{\underline{\mathbf{Y}}}, \theta, \ldots). \tag{12.9}$$

For the special case of an elastic material, we write

$$\hat{\underline{\mathbf{T}}} = \hat{W}_{\underline{\mathbf{Y}}}. \tag{12.10}$$

An example of a peridynamic material model is given by

$$\hat{W}(\underline{\mathbf{Y}}) = \frac{kv^2}{2}, \; v = \frac{3\displaystyle\int_{\mathcal{H}} \underline{e}\langle \boldsymbol{\xi}\rangle \, \mathrm{d}V_{\boldsymbol{\xi}}}{\displaystyle\int_{\mathcal{H}} |\boldsymbol{\xi}| \, \mathrm{d}V_{\boldsymbol{\xi}}}, \quad \underline{e}\langle \boldsymbol{\xi}\rangle = |\underline{\mathbf{Y}}\langle \boldsymbol{\xi}\rangle| - |\boldsymbol{\xi}|, \tag{12.11}$$

where k is the bulk modulus, v is the nonlocal dilatation, and $\underline{e}$ is the *bond extension state*. The factor of three appears so that this expression for v gives the same value as the conventional dilatation $u_{i,i}$ for deformations that are small and isotropic. For any bond $\boldsymbol{\xi}$, the value of $\underline{e}\langle \boldsymbol{\xi}\rangle$ is the change in length of the bond due to deformation.

The nonlocal dilatation v is computed from the mean length change in the family as it deforms. The corresponding force state is found from the Fréchet derivative of $\hat{W}$ to be

$$\underline{\hat{\mathbf{T}}}\langle\boldsymbol{\xi}\rangle = \left(\frac{3kv}{\int_{\mathcal{H}}|\boldsymbol{\zeta}|\,\mathrm{d}V_{\boldsymbol{\zeta}}}\right)\underline{\mathbf{M}}\langle\boldsymbol{\xi}\rangle, \quad \underline{\mathbf{M}}\langle\boldsymbol{\xi}\rangle = \frac{\underline{\mathbf{Y}}\langle\boldsymbol{\xi}\rangle}{|\underline{\mathbf{Y}}\langle\boldsymbol{\xi}\rangle|} \tag{12.12}$$

for any bond $\boldsymbol{\xi}\in\mathcal{H}$. In this expression, $\boldsymbol{\zeta}$ is used as the dummy bond variable in the volume integral. The state $\underline{\mathbf{M}}$ contains the deformed bond directions. For this material model, which represents a linear elastic fluid, the bond forces are parallel to the deformed bond vectors. Material models with this property are called *ordinary* material models; all others are called *nonordinary*. Further discussion of this peridynamic fluid material model may be found in Silling et al. (2007).

A special case of ordinary material models is called *bond-based* materials. These have the property that the force in each bond is determined *only* by the deformation of that particular bond, independently of what happens to the other bonds in the family. An example of a bond-based material model is given by

$$\underline{\hat{\mathbf{T}}}\langle\boldsymbol{\xi}\rangle = C(\boldsymbol{\xi})\underline{e}\langle\boldsymbol{\xi}\rangle\underline{\mathbf{M}}\langle\boldsymbol{\xi}\rangle \tag{12.13}$$

for all $\boldsymbol{\xi}\in\mathcal{H}$. In this material, each bond acts like a linear elastic spring whose spring constant is the scalar-valued micromodulus function C. In *isotropic* bond-based material models (in which $C(\boldsymbol{\xi})$ is independent of the direction of $\boldsymbol{\xi}$), only one elastic modulus can be reproduced and, in three dimensions, the Poisson ratio is always 1/4. This restriction is not true for the more general *state-based* material models, such as the fluid material model discussed above, in which the Poisson ratio is 1/2. The key distinction is that in the fluid model (12.12), the bond forces depend on the collective deformation, embodied in v, of the entire family, whereas in Equation (12.13), each bond's force density depends only on its own deformation. We will see in the next section that a suitable choice of $C(\boldsymbol{\xi})$, especially through its dependence on bond direction, results in a simple way to include anisotropy in a material model.

A useful example of a nonordinary material model is found in *correspondence* materials. In these materials, a stress–strain relation from the standard theory is adapted to the peridynamic setting. Suppose that we are given such a stress–strain relation in the form

$$\boldsymbol{\sigma}(\mathbf{x}) = \hat{\boldsymbol{\sigma}}(\mathbf{F}(\mathbf{x})), \quad \mathbf{F}(\mathbf{x}) = \frac{\partial\mathbf{y}}{\partial\mathbf{x}}(\mathbf{x})$$

for any $\mathbf{x}\in\mathcal{B}$, where $\boldsymbol{\sigma}$ is the Piola stress. In the correspondence approach, a *nonlocal deformation gradient* $\bar{\mathbf{F}}(\underline{\mathbf{Y}})$ is computed from

$$\bar{\mathbf{F}} = \left(\int_{\mathcal{H}}\omega(|\boldsymbol{\xi}|)\underline{\mathbf{Y}}\langle\boldsymbol{\xi}\rangle\otimes\boldsymbol{\xi}\,\mathrm{d}V_{\boldsymbol{\xi}}\right)\mathbf{K}^{-1}, \quad \mathbf{K} = \int_{\mathcal{H}}\omega(|\boldsymbol{\xi}|)\boldsymbol{\xi}\otimes\boldsymbol{\xi}\,\mathrm{d}V_{\boldsymbol{\xi}}, \tag{12.14}$$

where ω is a weighting function called the *influence function*. As discussed in Silling et al. (2007), this nonlocal deformation gradient agrees with the conventional deformation gradient $\mathbf{F} = \partial \mathbf{y}/\partial \mathbf{x}$ whenever the deformation is uniform; that is, whenever $\mathbf{F}$ is constant. The force state is then found from

$$\underline{\hat{\mathbf{T}}}\langle \boldsymbol{\xi} \rangle = \omega(|\boldsymbol{\xi}|)\hat{\boldsymbol{\sigma}}(\bar{\mathbf{F}})\mathbf{K}^{-1}\boldsymbol{\xi} \tag{12.15}$$

for any bond $\boldsymbol{\xi} \in \mathcal{H}$. If $\hat{\boldsymbol{\sigma}}$ is elastic, then the peridynamic correspondence material model is also elastic, and the strain energy density function $\hat{W}$ agrees with the one in the standard model whenever the deformation is uniform.

Correspondence models are useful because they allow material models in the standard theory to be "recycled" without deriving a peridynamic model from scratch. However, they suffer from some practical limitations owing to the fact that in general they are noninvertible. That is, for a given $\underline{\mathbf{T}}$, there are usually an infinite number of choices of $\underline{\mathbf{Y}}$ such that $\underline{\mathbf{T}} = \underline{\hat{\mathbf{T}}}(\underline{\mathbf{Y}})$ if a correspondence model is used. This noninvertibility has implications for material stability and, unless corrective terms are introduced, results in troublesome zero-energy modes in particle type numerical discretizations. These undesirable behaviors, along with innovative approaches to controlling them, are discussed in Littlewood (2010), Tupek et al. (2013), Tupek and Radovitzky (2014), and Breitenfeld et al. (2014).

Damage is modeled by including a dependence on the *damage state* $\underline{\phi}$ in the material model:

$$\underline{\mathbf{T}} = \underline{\hat{\mathbf{T}}}(\underline{\mathbf{Y}}, \underline{\phi}). \tag{12.16}$$

The damage state is a scalar-valued state that, for each bond, varies from 0 (undamaged) to 1 (fully damaged). For each bond $\boldsymbol{\xi}$, $\underline{\phi}\langle \boldsymbol{\xi} \rangle$ is a nondecreasing function of time. Commonly, damage in a bond is treated as *bond breakage* in which $\underline{\phi}\langle \boldsymbol{\xi} \rangle$ jumps discontinuously from 0 to 1 according to some criterion. A breakage criterion that is often used in numerical simulations is *critical bond strain*. In this approach, each bond is assigned a critical value $s_*\langle \boldsymbol{\xi} \rangle$. The damage in the bond jumps irreversibly from 0 to 1 when the bond strain $s\langle \boldsymbol{\xi} \rangle$ exceeds $s_*\langle \boldsymbol{\xi} \rangle$, where the bond strain is defined by

$$s\langle \boldsymbol{\xi} \rangle = \frac{e\langle \boldsymbol{\xi} \rangle}{|\boldsymbol{\xi}|} \tag{12.17}$$

for any bond $\boldsymbol{\xi} \in \mathcal{H}$. In practice, if a peridynamic continuum is viewed as a complex network of bonds going in every direction, the breakage of an individual bond makes it more likely that its neighbors will also break, because more load is shifted to these neighbors. As more and more bonds break, a progressive process of failure occurs in the continuum. This process may be either stable or unstable, depending on the geometry and loading conditions. In three dimensions, the geometry of the failed regions usually organizes into two-dimensional surfaces, possibly curved, that we interpret as cracks. Thanks to the compatibility of the peridynamic field equations with discontinuities, cracks form spontaneously and without restriction or

supplemental kinetic relations that are needed in traditional fracture mechanics. In particular, the concept of a stress intensity factor is not needed in peridynamics.

In a model of a brittle elastic solid, the critical bond strain can be calibrated to match the critical energy release rate of the material (Silling and Askari, 2005). We will see in the next section that allowing dependence of $s_*\langle\boldsymbol{\xi}\rangle$ on the direction of $\boldsymbol{\xi}$ provides a simple way to model anisotropy in material fracture and failure.

Peridynamic equations can be linearized under the assumption of small displacement (not necessarily small displacement gradient). The resulting equilibrium equation has the following form:

$$\int_{\mathcal{N}_\mathbf{x}} \mathbf{C}(\mathbf{x},\mathbf{q})(\mathbf{u}(\mathbf{q})-\mathbf{u}(\mathbf{x}))\,dV_\mathbf{q} + \mathbf{b}(\mathbf{x}) = \mathbf{0}, \tag{12.18}$$

where $\mathbf{C}$ is the tensor-valued micromodulus field, $\mathbf{u}(\mathbf{x}) = \mathbf{y}(\mathbf{x}) - \mathbf{x}$ is the displacement field, and $\mathcal{N}_\mathbf{x}$ is a neighborhood of $\mathbf{x}$. In general, the radius of $\mathcal{N}_\mathbf{x}$ is 2δ, where δ is the horizon of the underlying nonlinear material model that is being linearized (Silling, 2010). The linearized equilibrium equation is formally the same as in Kunin's nonlocal theory (Kunin, 1983).

12.3 Peridynamic material models for composites

Here we discuss some methods for treating unidirectional reinforced laminates with peridynamics. Most published peridynamic models for composites are homogenized; that is, they involve smoothed material property fields that do not explicitly include heterogeneities. Because of its nonlocal nature, peridynamics offers opportunities for studying aspects of composite mechanics that are not easily reproduced in the standard local theory. Due to their heterogeneous composition, nonlocal interactions appear whenever composites are represented with smoothed displacement fields. This nonlocality occurs not because of physical interactions across finite distances, as in electrostatics, but because of the tendency of the material phases to readjust individually relative to each other when only their averaged value is specified. The resulting exchange of forces between the phases occurs over finite distances that can be estimated using, for example, a shear lag type of analysis. The length scale for these interactions involves not only geometrical length scales (fiber diameter, ply thickness, etc.) but also the relative material properties of the phases (Silling, 2014).

One way of modeling a unidirectionally reinforced lamina with peridynamics is to use the correspondence approach discussed in the previous section. Any stress–strain model for a lamina from standard lamination theory can be directly incorporated into a peridynamic model using correspondence. The resulting peridynamic model has the same characteristics as the standard model for reproducing the anisotropic elastic properties of a lamina. All four independent elastic moduli can be reproduced (Jones, 1999). The correspondence approach can also be applied to a three-dimensional model of a laminate, introducing a fifth elastic modulus that can be

specified independently, as in lamination theory. The correct A and D matrices are predicted by the peridynamic correspondence model for any orientation of the plies in an arbitrarily chosen layup.

Because the correspondence approach borrows a stress–strain relation from the standard theory, it is suitable for the application of failure models, such as the Hashin model, that are based on components of the stress tensor (Hashin, 1980). Such a failure model can be represented as a surface in the stress space of the form

$$\psi(\boldsymbol{\sigma}, a_1, a_2, \ldots, a_N) < \psi_0 \tag{12.19}$$

for a nonfailed material, where $\boldsymbol{\sigma}$ is the stress tensor and $\psi_0, a_1, a_2, \ldots, a_N$ are parameters for the failure model calibrated for a material. In the correspondence model, failure occurs when the condition

$$\psi(\hat{\boldsymbol{\sigma}}(\bar{\mathbf{F}}), a_1, a_2, \ldots, a_N) < \psi_0 \tag{12.20}$$

fails to hold, where $\bar{\mathbf{F}}$ is the nonlocal deformation gradient tensor discussed previously.

When failure occurs according to this condition, the next question is how to translate this event into bond damage. Many ways are possible. One approach is to break the "worst" bond, that is, the bond that should break first on the basis of physical intuition or because of some condition derived from the failure model. For example, the peridynamic bond damage model could break the bond within the family of a point $\mathbf{x}$ that has the greatest tensile bond strain, assuming that the material is failing under tension. For failure under compression, the model could break the bond with the greatest compressive strain. The difficulty here is that in the Hashin model, there are an infinite number of combinations of stress components that result in failure. These infinite combinations therefore introduce an ad hoc character to the peridynamic model in trying to identify the "worst" bond by introducing an extraneous bond failure criterion.

An alternative is to use the failure surface ψ more directly to identify bond damage. One way to do this is to evaluate the gradient of this surface, in the sense of Fréchet derivatives, with respect to the deformation state. Using the chain rule leads to

$$\psi_{\underline{\mathbf{Y}}} = \frac{\partial \psi}{\partial \boldsymbol{\sigma}} \cdot \frac{\partial \hat{\boldsymbol{\sigma}}}{\partial \mathbf{F}} \cdot \bar{\mathbf{F}}_{\underline{\mathbf{Y}}}. \tag{12.21}$$

Here, the Fréchet derivative $\bar{\mathbf{F}}_{\underline{\mathbf{Y}}}$ is computed from Equations (12.6) and (12.14). The term $\partial \hat{\boldsymbol{\sigma}} / \partial \mathbf{F}$ is the fourth-order elasticity tensor for an incremental deformation. Under the assumption that bond damage occurs preferentially in those bonds that contribute the most to $\psi_{\underline{\mathbf{Y}}}$, a possible bond damage model is then

$$\dot{\underline{\phi}}\,\langle \boldsymbol{\xi} \rangle = \lambda \psi_{\underline{\mathbf{Y}}} \langle \boldsymbol{\xi} \rangle \tag{12.22}$$

for any bond $\boldsymbol{\xi} \in \mathcal{H}$, where $\lambda > 0$ is independent of $\boldsymbol{\xi}$. Continuum damage models can be similarly adapted to peridynamics.

Most of the published peridynamic lamina models are bond-based. Among these are the models of Askari et al. (2006), Xu et al. (2007, 2008), Hu et al. (2011, 2012), Hu et al. (2014), and Liu and Jia (2012). In these models, anisotropy is introduced by giving special properties to bonds that are parallel to the fiber direction in the undeformed configuration. These bonds are called *fiber bonds*; all other bonds in the lamina model are called *matrix bonds*. Referring to the bond-based expression (12.13), and using a coordinate system in which x_1 is parallel to the fibers, the scalar micromodulus of a bond in the plane of the lamina may be written as

$$C(\boldsymbol{\xi}) = C_m(|\boldsymbol{\xi}|) + C_f(|\boldsymbol{\xi}|)\Delta(\xi_2), \tag{12.23}$$

where Δ denotes the Dirac delta function. Applying this material model in the peridynamic equilibrium equation (12.4) results in

$$\int_{\mathcal{H}} C_m(|\boldsymbol{\xi}|)\underline{e}\langle\boldsymbol{\xi}\rangle\underline{\mathbf{M}}\langle\boldsymbol{\xi}\rangle \, \mathrm{d}V_{\boldsymbol{\xi}} + \int_{\mathcal{L}} C_f(|\boldsymbol{\xi}|)\underline{e}\langle\boldsymbol{\xi}\rangle\underline{\mathbf{M}}\langle\boldsymbol{\xi}\rangle \, \mathrm{d}\ell_{\boldsymbol{\xi}} + \mathbf{b}(\mathbf{x}) = \mathbf{0}, \tag{12.24}$$

where $\mathcal{L}$ is the line segment $[-\delta,\delta]$ along the x_1-axis and $\ell_{\boldsymbol{\xi}}$ is the path length in the line integral. The second integral sums up the forces in the fiber bonds. In this form, it is easy to see the strength of the peridynamic formulation for composites: the fiber bonds need not deform continuously with the matrix bonds, allowing the exploration of deformations in which the fibers separate from the matrix.

Bond-based material models for composites are compatible with simple bond breakage models that allow interesting damage progression phenomena to be reproduced. Using a critical bond strain breakage criterion, we can allow fiber bonds to have a critical strain that is independent of the matrix bond critical strain. Laminas can be anisotropic in damage formation as well as in elastic response. Compressive failure in a lamina can be modeled using a critical bond strain criterion under compression as well as under tension.

Bond-based lamina models can be assembled into laminate models with arbitrary stacking sequences. Additional bonds, with their own elastic and failure properties, connect points within the laminas. These *interlayer* bonds can extend only between neighboring plies or over multiple plies, according to the modeling assumptions one wishes to make. A critical bond strain failure criterion for interlayer bonds can be calibrated to match the tensile and shear energy release rates, G_{Ic} or G_{IIc}, for delaminations, but not both of these constants independently. More flexibility can be obtained with alternative failure criteria for interlayer bonds. For example, interlayer bonds can be considered to fail when the shear angle between neighboring plies exceeds some critical angle (Oterkus, 2010; Oterkus et al., 2012). When applied together with a critical tensile bond strain criterion, measured energy release rates in both tensile and shear modes can be reproduced during delamination. Bond-based models for composites, coupled with conventional finite element models, have been successfully applied to the failure of large aerospace structures (Oterkus et al., 2012). Later sections in this chapter discuss the coupling of peridynamics with finite element

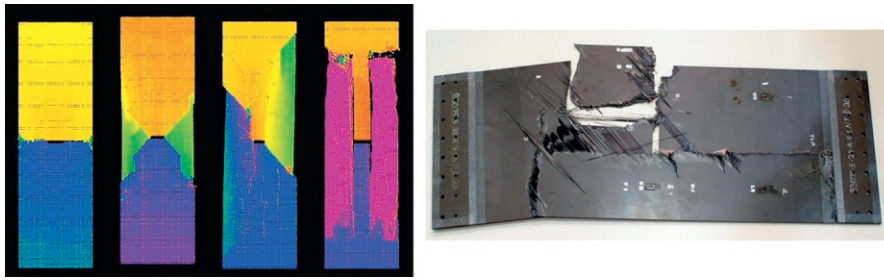

Figure 12.3 Left: Simulated damage patterns using a bond-based peridynamic model. Right: The result of a typical test.

meshes. A bond-based mechanical model has also been coupled with a peridynamic heat conduction model for composites (Oterkus and Madenci, 2014).

Bond-based laminate models with anisotropic critical bond strain breakage criteria can reproduce a surprisingly large spectrum of damage phenomena in composites. An example is shown in Figure 12.3, which shows the failure of laminates in simulated large-notch tension (LNT) tests, along with a typical experimental result. Figure 12.4 shows delaminations predicted due to impact from a rigid projectile using the shear bond approach. It also shows computed compressive failure in a model of compression after impact (CAI).

Unlike the correspondence models, bond-based material models for composites cannot match all four independent elastic moduli in laminas. Because, in effect, C_m and C_f act like independent parameters for purposes of calibrating the elastic properties of the model, only two elastic moduli can be reproduced by manipulating these two parameters. A modification of the bond-based model described above that includes a dependence of C_m on the bond angle as well as the length (that is, $C_m(\boldsymbol{\xi})$ instead of $C_m(|\boldsymbol{\xi}|)$) allows three elastic moduli to be matched.

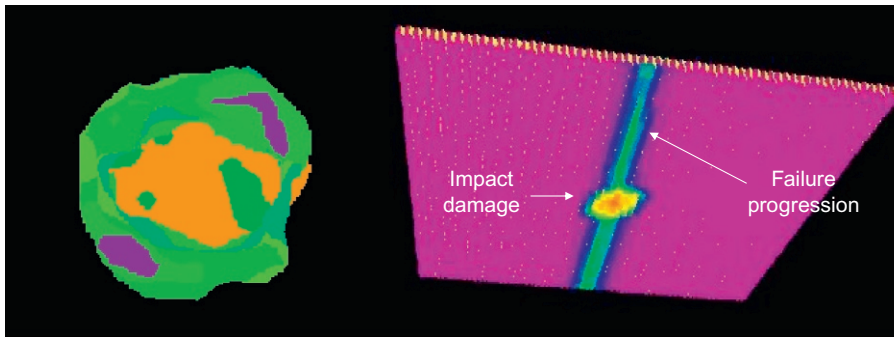

Figure 12.4 Left: Simulated delaminations caused by impact (viewed from impacted side). Right: Compression after impact.

Kilic et al. (2009) introduced a nonhomogenized bond-based lamina representation. In their approach, structures representing fibers are explicitly included in the lamina. These structures are discretized in detail in the numerical model. This approach has the advantage of reproducing some features of composite responses that are the outcome of the heterogeneity of the mesoscale. However, the price paid is the introduction of features that have a much larger size than the actual fibers they represent.

Another approach to peridynamic modeling of a lamina that allows all four elastic moduli to be matched, yet provides many of the advantages of the bond-based model, is to use an ordinary state-based model (Colavito et al., 2013; Barut et al., 2014; Madenci and Oterkus, 2014, pp. 77). Recall that in ordinary state-based models, the bond force density vector is always parallel to the deformed bond, but the force density can depend on the deformation of other bonds in the family. This allows a volume-dependent term to be included in the lamina model, as well as an angle-dependent matrix bond micromodulus. The resulting expression for bond force then typically takes the form

$$\underline{\hat{\mathbf{T}}}\langle\boldsymbol{\xi}\rangle = \left[(C_m(\boldsymbol{\xi}) + C_f(|\boldsymbol{\xi}|)\Delta(\xi_2))(\underline{e}\langle\boldsymbol{\xi}\rangle + av)\right]\underline{\mathbf{M}}\langle\boldsymbol{\xi}\rangle, \tag{12.25}$$

where a is a constant and v is the two-dimensional dilatation,

$$v = \frac{2\displaystyle\int_{\mathcal{H}} \underline{e}\langle\boldsymbol{\xi}\rangle \, \mathrm{d}V_{\boldsymbol{\xi}}}{\displaystyle\int_{\mathcal{H}} |\boldsymbol{\xi}| \, \mathrm{d}V_{\boldsymbol{\xi}}}. \tag{12.26}$$

Here, $\mathcal{H}$ refers to the family in the plane of the lamina.

12.4 Toward a novel treatment of localization

Peridynamic theory has provided promising results for simulating the failure of composites. For any point in a body, however, peridynamic models must account for all interactions exerted by other points in the neighborhood of this point. This results in a huge computational cost. The morphing coupling method is able to constrain the peridynamic model to small but critical domains, such as the damage nucleation or fracture regions, while a conventional contact-force-based continuum mechanics model is employed over the rest of the structure. Based on the work presented in Lubineau et al. (2012) and Azdoud et al. (2013, 2014), the morphing coupling method is stated as follows.

For simplicity, we focus on a bond-based peridynamic model for linearized elastic materials. The equilibrium equation of the peridynamic model has been shown in Equation (12.4). A possible bond-based constitutive model is given by

$$\mathbf{t}(\mathbf{q},\mathbf{x}) = \frac{C(\mathbf{x},|\boldsymbol{\xi}|)}{2}\{u_{\boldsymbol{\xi}}(\mathbf{q}) - u_{\boldsymbol{\xi}}(\mathbf{x})\}\boldsymbol{\gamma}_{\boldsymbol{\xi}}, \tag{12.27}$$

where the bond $\boldsymbol{\xi} = \mathbf{q} - \mathbf{x}$ is the relative position vector, $C(\mathbf{x}, |\boldsymbol{\xi}|)$ denotes the micromodulus at point $\mathbf{x}$, which is a function of the length of $\boldsymbol{\xi}$, $\boldsymbol{\gamma}_{\boldsymbol{\xi}} = \boldsymbol{\xi}/|\boldsymbol{\xi}|$ is the direction of bond $\boldsymbol{\xi}$ in the reference configuration, and $u_{\boldsymbol{\xi}}(\mathbf{q})$ denotes the projection of the displacement $\mathbf{u}(\mathbf{q})$ at point $\mathbf{q}$ to the bond $\boldsymbol{\xi}$ (i.e., $u_{\boldsymbol{\xi}}(\mathbf{q}) = \mathbf{u}(\mathbf{q}) \cdot \boldsymbol{\gamma}_{\boldsymbol{\xi}}$) (Lubineau et al., 2012).

We consider a complete domain $\mathcal{B}$. This domain $\mathcal{B}$ consists of three subdomains, $\mathcal{B}_1$, $\mathcal{B}_2$, and $\mathcal{B}_m$, that is, $\mathcal{B} = \mathcal{B}_1 \cup \mathcal{B}_2 \cup \mathcal{B}_m$, $\mathcal{B}_1 \cap \mathcal{B}_2 = \emptyset$, $\mathcal{B}_1 \cap \mathcal{B}_m = \emptyset$, and $\mathcal{B}_2 \cap \mathcal{B}_m = \emptyset$. For definiteness and without major restrictions, we assume that $\mathcal{B}_2$ is totally embedded within $\mathcal{B}_m$ and that $\mathcal{B}_m$ is totally embedded within $\mathcal{B}_1$, such that $\partial\mathcal{B}_2 \cap \partial\mathcal{B}_1 = \emptyset$ and $\partial\mathcal{B} \subset \partial\mathcal{B}_1$. Therefore, $\mathcal{B}_m$ becomes a transition domain between $\mathcal{B}_1$ and $\mathcal{B}_2$ (see Figure 12.5).

Let the subdomains $\mathcal{B}_1$ and $\mathcal{B}_2$ be treated by the conventional continuum model and the peridynamic model, respectively. We mainly focus on the finite morphing domain, $\mathcal{B}_m$, where both models coexist and work cooperatively. The displacement, $\bar{\mathbf{u}}$, is imposed on the part $\partial\mathcal{B}_{\mathbf{u}}$ of $\partial\mathcal{B}$, and the surface force $\bar{\mathbf{f}}$ is imposed on the complementary part $\partial\mathcal{B}_{\mathbf{f}}$ of $\partial\mathcal{B}$. In addition, the whole domain $\mathcal{B}$ is subjected to body forces denoted by $\mathbf{b}$.

The morphing technique is then defined as a simple evolution of the material properties characterizing each model. The morphing coupling method is proposed by the following set of equations that represent a hybrid continuum/peridynamic model:

□ **Kinematic admissibility and compatibility**

$$\boldsymbol{\epsilon}(\mathbf{x}) = \frac{1}{2}\left(\nabla\mathbf{u}(\mathbf{x}) + (\nabla\mathbf{u})^{\mathrm{T}}(\mathbf{x})\right) \qquad \forall\mathbf{x} \in \mathcal{B}\backslash\mathcal{B}_2, \tag{12.28}$$

$$\eta_{\boldsymbol{\xi}}(\mathbf{q}, \mathbf{x}) = u_{\boldsymbol{\xi}}(\mathbf{q}) - u_{\boldsymbol{\xi}}(\mathbf{x}) \qquad \forall(\mathbf{q}, \mathbf{x}) \in \mathcal{B}\backslash\mathcal{B}_1, \tag{12.29}$$

$$\mathbf{u}(\mathbf{x}) = \bar{\mathbf{u}}(\mathbf{x}) \qquad \forall\mathbf{x} \in \partial\mathcal{B}_{\mathbf{u}}. \tag{12.30}$$

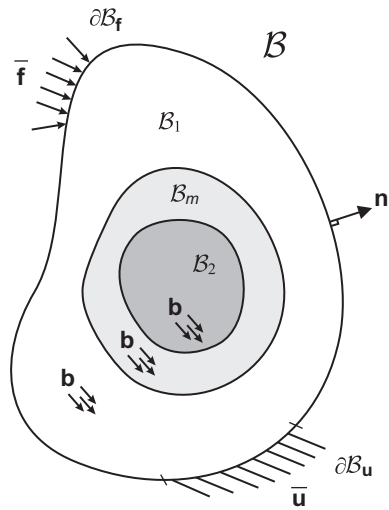

Figure 12.5 The whole domain $\mathcal{B}$ consists of $\mathcal{B}_1$, $\mathcal{B}_2$, and $\mathcal{B}_m$.

□ **Static admissibility**

$$\div \boldsymbol{\sigma}(\mathbf{x}) + \int_{\mathcal{H}_\mathbf{x}} \{\mathbf{t}(\mathbf{q},\mathbf{x}) - \mathbf{t}(\mathbf{x},\mathbf{q})\}\, \mathrm{d}V_\mathbf{q} = -\mathbf{b}(\mathbf{x}) \qquad \forall \mathbf{x} \in \mathcal{B}, \tag{12.31}$$

$$\boldsymbol{\sigma}(\mathbf{x}) \cdot \mathbf{n}(\mathbf{x}) = \bar{\mathbf{f}}(\mathbf{x}) \qquad \forall \mathbf{x} \in \partial\mathcal{B}_\mathbf{f}. \tag{12.32}$$

□ **Constitutive equations**

$$\boldsymbol{\sigma}(\mathbf{x}) = \mathbf{K}(\mathbf{x}) : \boldsymbol{\epsilon}(\mathbf{x}) \qquad \forall \mathbf{x} \in \mathcal{B} \backslash \mathcal{B}_2, \tag{12.33}$$

$$\mathbf{t}(\mathbf{q},\mathbf{x}) = \frac{C(\mathbf{x},|\boldsymbol{\xi}|)}{2} \eta_{\boldsymbol{\xi}}(\mathbf{q},\mathbf{x}) \boldsymbol{\gamma}_{\boldsymbol{\xi}} \qquad \forall \mathbf{x} \in \mathcal{B} \backslash \mathcal{B}_1. \tag{12.34}$$

In Equation (12.33), $\mathbf{K}(\mathbf{x})$ is the stiffness tensor of the conventional continuum model at the point $\mathbf{x}$. In Equation (12.34), $C(\mathbf{x},|\boldsymbol{\xi}|)$ is the peridynamic micromodulus at point $\mathbf{x}$. $C(\mathbf{x},|\boldsymbol{\xi}|)$ is defined by using *a priori* morphing function, α, such that

$$C(\mathbf{x},|\boldsymbol{\xi}|) = \alpha(\mathbf{x}) c^0(|\boldsymbol{\xi}|). \tag{12.35}$$

Based on Equation (12.31), we note that the parameters $\alpha(\mathbf{x})$ and $\mathbf{K}(\mathbf{x})$ determine the particular type of this model, that is, the continuum, peridynamic, or hybrid model, at any material point $\mathbf{x}$ in the whole region $\mathcal{B}$:

- For a point $\mathbf{x} \in \mathcal{B}$, if and only if

$$\mathbf{K}(\mathbf{x}) = \mathbf{K}^0 \quad \text{and} \quad \alpha(\mathbf{q}) \equiv 0, \quad \forall \mathbf{q} \in \mathcal{H}_\mathbf{x}, \tag{12.36}$$

  then this point $\mathbf{x}$ strictly belongs to the conventional continuum model. The strain energy density at this point can be written as

$$W(\mathbf{x}) = \frac{1}{2} \boldsymbol{\epsilon}(\mathbf{x}) : \mathbf{K}^0 : \boldsymbol{\epsilon}(\mathbf{x}). \tag{12.37}$$

- For a point $\mathbf{x} \in \mathcal{B}$, if and only if

$$\mathbf{K}(\mathbf{x}) = \mathbf{0} \quad \text{and} \quad \alpha(\mathbf{q}) \equiv 1, \quad \forall \mathbf{q} \in \mathcal{H}_\mathbf{x}, \tag{12.38}$$

  then this point $\mathbf{x}$ strictly belongs to the peridynamic model. The strain energy density at this point can be written as (see Han and Lubineau, 2012)

$$W(\mathbf{x}) = \int_{\mathcal{H}_\mathbf{x}} c^0(|\boldsymbol{\xi}|) \frac{\eta_{\boldsymbol{\xi}}^2(\mathbf{q},\mathbf{x})}{4}\, \mathrm{d}V_\mathbf{q}. \tag{12.39}$$

- For a point $\mathbf{x} \in \mathcal{B}$, if and only if

$$\mathbf{K}(\mathbf{x}) \neq \mathbf{0} \quad \text{and} \quad \exists \mathbf{q} \in \mathcal{H}_\mathbf{x}, \quad \text{such that} \quad 0 < \alpha(\mathbf{q}) < 1, \tag{12.40}$$

  then we can say this point $\mathbf{x}$ belongs to the hybrid model. The strain energy density at this point can be written as (see Lubineau et al., 2012)

$$W(\mathbf{x}) = \frac{1}{2} \boldsymbol{\epsilon}(\mathbf{x}) : \mathbf{K}(\mathbf{x}) : \boldsymbol{\epsilon}(\mathbf{x}) + \int_{\mathcal{H}_\mathbf{x}} c^0(|\boldsymbol{\xi}|) \frac{\alpha(\mathbf{x}) + \alpha(\mathbf{q})}{2} \frac{\eta_{\boldsymbol{\xi}}^2(\mathbf{q},\mathbf{x})}{4}\, \mathrm{d}V_\mathbf{q}. \tag{12.41}$$

If the material in $\mathcal{B}$ is homogeneous and the body $\mathcal{B}$ is under homogeneous deformation, the strain energy density should be independent of the morphing function α. It means that the strain energy density is the same at some point $\mathbf{x}$ whatever the model. Thus, Equation (12.37) is equal to Equation (12.39), that is,

$$\frac{1}{2}\boldsymbol{\epsilon}(\mathbf{x}):\mathbf{K}^0:\boldsymbol{\epsilon}(\mathbf{x})=\int_{\mathcal{H}_\mathbf{x}} c^0(|\boldsymbol{\xi}|)\frac{\eta_{\boldsymbol{\xi}}^2(\mathbf{q},\mathbf{x})}{4}\,\mathrm{d}V_\mathbf{q}. \tag{12.42}$$

Let us consider an infinitesimal homogeneous transformation over the small neighborhood of point $\mathbf{x}$ such that

$$\boldsymbol{\epsilon}(\mathbf{q})\simeq\boldsymbol{\epsilon}(\mathbf{x})=\overline{\boldsymbol{\epsilon}}\quad\text{and}\quad\eta_{\boldsymbol{\xi}}(\mathbf{q},\mathbf{x})=\frac{\boldsymbol{\xi}\cdot\overline{\boldsymbol{\epsilon}}\cdot\boldsymbol{\xi}}{|\boldsymbol{\xi}|}\quad\forall\mathbf{q}\in\mathcal{H}_\mathbf{x}. \tag{12.43}$$

Based on Equation (12.43), Equation (12.42) yields

$$\mathbf{K}^0=\int_{\mathcal{H}_\mathbf{x}} c^0(|\boldsymbol{\xi}|)\frac{\boldsymbol{\xi}\otimes\boldsymbol{\xi}\otimes\boldsymbol{\xi}\otimes\boldsymbol{\xi}}{2|\boldsymbol{\xi}|^2}\,\mathrm{d}V_\mathbf{q}. \tag{12.44}$$

Similarly, an equivalence exists between Equations (12.37) and (12.41), and considering Equations (12.43) and (12.44), we have

$$\mathbf{K}(\mathbf{x})=(1-\alpha(\mathbf{x}))\mathbf{K}^0+\int_{\mathcal{H}_\mathbf{x}} c^0(|\boldsymbol{\xi}|)\frac{\alpha(\mathbf{x})-\alpha(\mathbf{q})}{2}\frac{\boldsymbol{\xi}\otimes\boldsymbol{\xi}\otimes\boldsymbol{\xi}\otimes\boldsymbol{\xi}}{2|\boldsymbol{\xi}|^2}\,\mathrm{d}V_\mathbf{q}. \tag{12.45}$$

The advantage of this method is that we do the coupling only at the level of the constitutive equation. This makes it easy to define the morphing coupling and to conduct it from an algorithmic point of view. That is, for a given function α over region $\mathcal{B}$, the governing equations (12.28)–(12.34) can be directly solved based on the constitutive relations (12.44) and (12.45).

The coupling qualities have been described by using a one-dimensional example in Lubineau et al. (2012). Some two- or three-dimensional numerical examples in Lubineau et al. (2012) and Azdoud et al. (2013) illustrate the accuracy of the morphing coupling method. Figure 12.6 presents a fracture simulation (Azdoud et al., 2014) that uses an adaptive morphing coupling method. The morphing function α automatically updates itself following the crack propagation, which directly determines the scopes of the peridynamic and continuum models. A simple fracture criterion based on the critical stretch of the bond is used, which was addressed in Section 12.2. Above this critical strain, the bond is broken in an irreversible manner. In the numerical implementation, appropriate discretization schemes, such as the finite element method (FEM) and the discontinuous Galerkin finite element method (DGFEM), are employed with the conventional continuum model and the peridynamic model, respectively. Compared with the application of DGFEM to conventional continuum mechanics (Arnold et al., 2002), it is easier to apply DGFEM to peridynamics without the flux constraint over the boundary of the elements (Chen and Gunzburger, 2011).

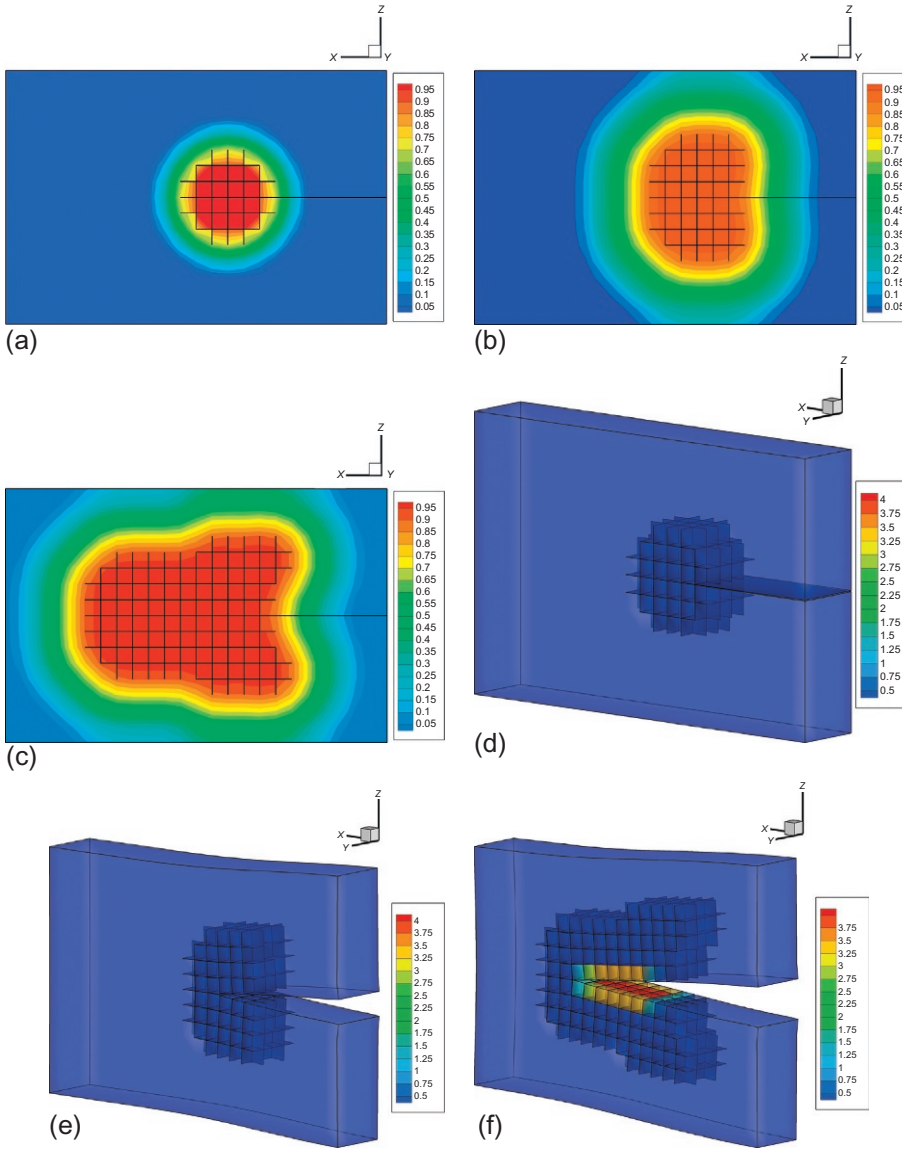

Figure 12.6 The evolution of morphing function α on the cross section perpendicular to the y-axis ((a)–(c)) and the dissipated energy in a deformed body ((d)–(f)) under displacement increments (1 increment in (a) and (d), 30 increments in (b) and (e), 50 increments in (c) and (f)). We note that the evolution of the morphing function follows the propagation of the crack. DGFEM, represented by the square element in (a)–(c), is embedded in the peridynamic zone (red) of the cross sections.

12.5 Summary

Peridynamic theory is a recent but powerful and promising solid mechanics framework that can be used for failure analysis of composites materials. Peridynamic models fall into the category of nonlocal mechanics, which allows direct interactions between nonadjacent material points by using integral equations. The connection vector between two points is named a *bond*. Peridynamic damage is modeled by defining a breakage criterion at each bond. The failure process in peridynamics is captured as more and more bonds break in a continuum.

Here, we considered three peridynamic models for composites: the correspondence model, the bond-based lamina model, and the ordinary state-based lamina model. Both the peridynamic correspondence model and the state-based lamina model can reproduce all four independent elastic moduli in lamina, whereas only two elastic moduli can be matched by the bond-based lamina model. Furthermore, a modification of the bond-based model can reproduce three moduli at the most. In addition, the peridynamic correspondence models, which translate stress–strain models from standard lamination theory into bond damage, can be employed for the simulation of failure in composites. The bond-based laminate models with anisotropic bond breakage criteria have been applied to simulate the failure of laminates under LNTs and under CAI. Compared with the bond-based models, the ordinary state-based material model provides more advantages including a volume-dependent term as well as an angle-dependent term.

An efficient coupling strategy, called the morphing method, is proposed to glue the bond-based peridynamic model to the conventional continuum model. The morphing method couples both models at the level of constitutive parameters in terms of the conservation of strain energy. This capability makes it possible to apply the coupled model to complex structures. And it is possible to extend this strategy to the state-based peridynamic model. Some adaptive fracture simulations have been successfully conducted so far. Future work is required to apply the morphing coupling to nonlinear problems, such as damage or plasticity.

In sum, it is clear that peridynamics is currently in its infancy in describing the full complexity of the degradation mechanisms that can initiate and develop in laminated composites. Much progress is needed on how to control anisotropic failure and on how to introduce plasticity and time-dependent behaviors that will be crucial in describing impact-induced damage in composites. Yet, it seems clear that peridynamics will be able to overcome some recurrent limitations of classical continuum mechanics, because its raw mathematical formulation allows for the development of discontinuities. Future work is needed to make this theoretical tool fully applicable.

Acknowledgments

We acknowledge KAUST for funding part of this research and for providing the necessary technical support. Sandia National Laboratories is a multiprogram laboratory managed and operated by Sandia Corporation, a wholly owned subsidiary of

Lockheed Martin Corporation, for the U.S. Department of Energy's National Nuclear Security Administration under Contract DE-AC04-94AL85000.

References

Allix, O., Deu, J.F., 1997. Delayed-damage modelling for fracture prediction of laminated composites under dynamic loading. Eng. Trans. 45, 29–46.

Allix, O., Feissel, P., Thévenet, P., 2003. A delay damage mesomodel of laminates under dynamic loading: basic aspects and identification issues. Comput. Struct. 81, 1177–1191.

Allix, O., Ladevèze, P., 1995. Damage analysis of interlaminar fracture specimens. Compos. Struct. 31, 61–74.

Arnold, D.N., Brezzi, F., Cockburn, B., Marini, L.D., 2002. Unified analysis of discontinuous Galerkin methods for elliptic problems. SIAM J. Numer. Anal. 39, 1749–1779.

Askari, E., Xu, J., Silling, S.A., 2006. Peridynamic analysis of damage and failure in composites. In: 44th AIAA Aerospace Sciences Meeting and Exhibit, AIAA 2006-88.

Azdoud, Y., Han, F., Lubineau, G., 2013. A morphing framework to couple non-local to local anisotropic continua. Int. J. Solids Struct. 50, 1332–1341.

Azdoud, Y., Han, F., Lubineau, G., 2014. The morphing method as a flexible tool for adaptive local/non-local simulation of static fracture. Comput. Mech. 54, 711–722.

Barut, A., Madenci, E., Phan, N., 2014. Peridynamics damage prediction in composites due to compression after impact. In: 55th AIAA/ASMe/ASCE/AHS/SC Structures, Structural Dynamics, and Materials Conference, AIAA 2014-1525.

Breitenfeld, M.S., Geubelle, P.H., Weckner, O., Silling, S.A., 2014. Non-ordinary state-based peridynamic analysis of stationary crack problems. Comput. Methods Appl. Mech. Eng. 272, 233–250.

Chen, X., Gunzburger, M., 2011. Continuous and discontinuous finite element methods for a peridynamics model of mechanics. Comput. Methods Appl. Mech. Eng. 200, 1237–1250.

Colavito, K.W., Barut, A., Madenci, E., Phan, N., 2013. Residual strength of composite laminates with a hole by using peridynamic theory. In: 54th AIAA/ASME/ASCE/AHS/ASC Structures, Structural Dynamics, and Materials Conference, AIAA 2013-1761.

Han, F., Lubineau, G., 2012. Coupling of nonlocal and local continuum models by the Arlequin approach. Int. J. Numer. Methods Eng. 89, 671–685.

Hashin, Z., 1980. Failure criteria for unidirectional fiber composites. J. Appl. Mech. 47, 329–334.

Hinton, M.J., Kaddour, A.S., Soden, P.D., 2002. A comparison of the predictive capabilities of current failure theories for composite laminates, judged against experimental evidence. Compos. Sci. Technol. 62, 1725–1797.

Hu, W., Ha, Y.D., Bobaru, F., 2011. Modeling dynamic fracture and damage in a fiber-reinforced composite lamina with peridynamics. Int. J. Multiscale Comput. Eng. 9, 707–726.

Hu, W., Ha, Y.D., Bobaru, F., 2012. Peridynamic model for dynamic fracture in unidirectional fiber-reinforced composites. Comput. Methods Appl. Mech. Eng. 217, 247–261.

Hu, Y.L., Yu, Y., Wang, H., 2014. Peridynamic analytical method for progressive damage in notched composite laminates. Compos. Struct. 108, 801–810.

Jones, R.M., 1999. Mechanics of Composite Materials, second ed Brunner-Routledge, New York.

Kilic, B., Agwai, A., Madenci, E., 2009. Peridynamic theory for progressive damage prediction in center-cracked composite laminates. Compos. Struct. 90, 141–151.
Kunin, I.A., 1983. Elastic Media with Microstructure II: Three-Dimensional Models. Springer-Verlag, Berlin.
Ladevèze, P., Le Dantec, E., 1992. Damage modeling of the elementary ply for laminated composites. Compos. Sci. Technol. 43, 257–267.
Ladevèze, P., Lubineau, G., 2001. On a damage mesomodel for laminates: micro-meso relationships, possibilities and limits. Compos. Sci. Technol. 61, 2149–2158.
Ladevèze, P., Lubineau, G., 2003. On a damage mesomodel for laminates: micromechanics basis and improvement. Mech. Mater. 35 (8), 763–775.
Ladevèze, P., Lubineau, G., Marsal, D., 2006. Towards a bridge between the micro- and the mesomechanics of delamination for laminated composites. Compos. Sci. Technol. 66 (6), 698–712.
Littlewood, D.J., 2010. Simulation of dynamic fracture using peridynamics, finite element modeling, and contact. In: ASME 2010 International Mechanical Engineering Congress and Exposition, pp. 209–217.
Liu, D., Jia, T., 2012. Peridynamic applications for orthotropic materials. Michigan State University, Final report.
Lubineau, G., Azdoud, Y., Han, F., Rey, C., Askari, A., 2012. A morphing strategy to couple non-local to local continuum mechanics. J. Mech. Phys. Solids 60, 1088–1102.
Lubineau, G., Ladevèze, P., 2008. Construction of a micromechanics-based intralaminar mesomodel, and illustrations in ABAQUS/standard. Comput. Mater. Sci. 43, 137–145.
Madenci, E., Oterkus, E., 2014. Peridynamic Theory and its Applications. Springer, New York.
Oterkus, E., 2010. Peridynamic theory for modeling three-dimensional damage growth in metallic and composite structures. Ph.D. thesis. University of Arizona.
Oterkus, E., Madenci, E., Weckner, O., Silling, S., Bogert, P., Tessler, A., 2012. Combined finite element and peridynamic analyses for predicting failure in a stiffened composite curved panel with a central slot. Compos. Struct. 94, 839–850.
Oterkus, S., Madenci, E., 2014. Fully coupled thermomechanical analysis of fiber reinforced composites using peridynamics. In: 55th AIAA/ASMe/ASCE/AHS/SC Structures, Structural Dynamics, and Materials Conference, AIAA 2014-0694.
Seleson, P., Beneddine, S., Prudhomme, S., 2013. A force-based coupling scheme for peridynamics and classical elasticity. Comput. Mater. Sci. 66, 34–49.
Silling, S.A., 2000. Reformulation of elasticity theory for discontinuities and long-range forces. J. Mech. Phys. Solids 48, 175–209.
Silling, S.A., 2010. Linearized theory of peridynamic states. J. Elast. 99, 85–111.
Silling, S.A., 2014. Origin and effect of nonlocality in a composite. J. Mech. Mater. Struct. 9, 245–258.
Silling, S.A., Askari, E., 2005. A meshfree method based on the peridynamic model of solid mechanics. Comput. Struct. 83, 1526–1535.
Silling, S.A., Lehoucq, R.B., 2010. Peridynamic theory of solid mechanics. Adv. Appl. Mech. 44, 73–168.
Silling, S.A., Epton, M., Weckner, O., Xu, J., Askari, E., 2007. Peridynamic states and constitutive modeling. J. Elast. 88, 151–184.
Soden, P.D., Hinton, M.J., Kaddour, A.S., 1998. A comparison of the predictive capabilities of current failure theories for composite laminates. Compos. Sci. Technol. 58, 1225–1254.
Tupek, M.R., Radovitzky, R., 2014. An extended constitutive correspondence formulation of peridynamics based on nonlinear bond-strain measures. J. Mech. Phys. Solids 65, 82–92.

Tupek, M.R., Rimoli, J.J., Radovitzky, R., 2013. An approach for incorporating classical continuum damage models in state-based peridynamics. Comput. Methods Appl. Mech. Eng. 263, 20–26.

Xu, J., Askari, A., Weckner, O., Razi, H., Silling, S., 2007. Damage and failure analysis of composite laminates under biaxial loads. In: 48th AIAA Structures, Structural Dynamics, and Materials Conference, AIAA 2007-2315.

Xu, J., Askari, A., Weckner, O., Silling, S., 2008. Peridynamic analysis of impact damage in composite laminates. J. Aerosp. Eng. 21, 187–194.

Multiscale modeling of the response and life prediction of composite materials

13

*C. Oskay**
*Vanderbilt University, Nashville, TN, USA

13.1 Introduction

Multiscale computational modeling and simulation is a promising paradigm for predicting the failure and life of composite materials and structures. Multiscale modeling of composite materials and application of these models to predict the behavior under various loading and environmental conditions have been active areas of research in the past couple of decades. Despite significant progress, a number of outstanding challenges have so far limited the impact of this approach on the composites industry and the state of the practice. First is the issue of computational complexity: multiscale modeling requires performing (coupled or uncoupled) simulations at multiple time and length scales. Significant computational resources are typically needed to predict the response using multiscale approaches. Second, multiscale models require calibration of model parameters that operate at multiple time and length scales. This implies that high-fidelity experiments at each scale need to be conducted to reliably calibrate these model parameters. Therefore, multiscale modeling approaches also require the development of multiscale experimental approaches and protocols for model calibration and validation.

Figure 13.1 illustrates the map of the relevant length and time scales that affect the mechanical performance of a composite structure or component. The continuum scales, in which the theory of continuum mechanics is valid, span the length scales from the composite structure to the representative cell (e.g., unit cell, representative volume element, etc.) of the material microstructure. Below the scale of the representative cell, the next relevant finer scales resolve the atomic structure of the constituent materials (e.g., matrix, reinforcement). The resolution of the constituent materials is performed using discrete mechanics (e.g., molecular dynamics), which also requires resolution of the finer time scales (Tadmor et al., 2011). Analysis and understanding at the discrete scales is very important for characterization of material properties and deformation behavior inaccessible to experimental approaches (e.g., interfacial properties), but the length and time scale disparity between the discrete and continuum scales prohibit strong coupling between them for problems of practical relevance (coupon size and up). This chapter focuses on multiscale modeling at the continuum scales only.

Multiscale modeling of failure in composites has progressed in two fronts: sequential and concurrent approaches. Although both approaches take the hierarchical

Numerical modelling of failure in advanced composite materials. http://dx.doi.org/10.1016/B978-0-08-100332-9.00013-X
Copyright © 2015 Elsevier Ltd. All rights reserved.

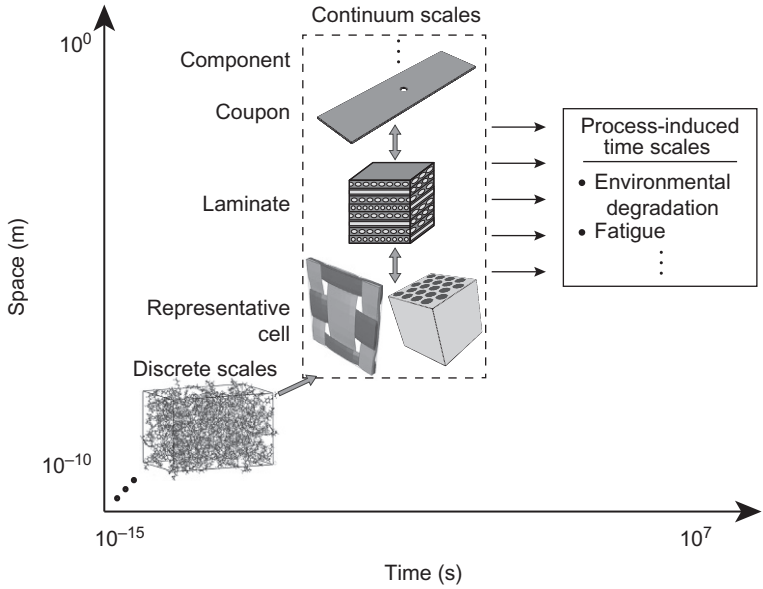

Figure 13.1 Map of the relevant multiple length and time scales in response and life prediction of composite materials.
(Discrete scales figure reprinted from Zhu et al., 2007 with permission from Elsevier.)

perspective to multiscale modeling, the difference is in the coupling of the fine and coarse scale models. In the sequential approach, which is performed in a *bottom-up* fashion, the response at the fine scale informs the coarse scale simulation through constitutive response matching (Llorca et al., 2011). The constitutive behavior on a large scale is typically expressed in terms of a known phenomenological form. The coarse scale model parameters are identified using optimization or homogenization (e.g., Ladeveze et al., 2006; Feld et al., 2012; Yvonnet et al., 2013) based on response surfaces produced by simulations conducted at the fine scale. The constitutive behavior at the fine scale is either assumed or identified through a similar strategy from the next fine scale. An approach to concurrent modeling of composites is the computational homogenization (Guedes and Kikuchi, 1990; Terada and Kikuchi, 1995; Feyel and Chaboche, 2000), rooted in the mathematical homogenization theory pioneered by Babuska (1975), Benssousan et al. (1978), Suquet (1987), and Sanchez-Palencia (1980). A significant number of additional concurrent modeling approaches exist, including the variational multiscale enrichment (Oskay, 2012, 2013), heterogeneous multiscale method (Engquist and Huang, 2003), multiscale finite element method (Hou and Wu, 1997), multilevel Voronoi cell finite element method (Ghosh et al., 2001), among many others. The key common characteristics of the concurrent models are that (1) the response at the fine and coarse scales are strongly coupled to each other and concurrently evaluated; and (2) the response at the coarse and fine scales are solved numerically. The methods primarily differ in their approach to bridging

information across scales such as through local enrichment (e.g., Babuska and Melenk, 1997) or averaging (e.g., Babuska, 1975; Benssousan et al., 1978; Nemat-Nasser and Hori, 1999) procedures. Concurrent multiscale models are attractive because materials with arbitrarily complex microstructures can be modeled within the same computational framework. Also a phenomenological modeling exercise does not need to be performed because the coarse scale response is implicitly computed using the bridging operation. One important drawback of the concurrent modeling is that computational cost and memory requirements are typically very high and need to be coupled with reduced order modeling to maintain computational tractability.

At the continuum level, the presence of multiple time scales could be induced by loading and environmental processes. For instance, the prediction of the long-term behavior under cyclic loading or long-term degradation in composites when subjected to aggressive environmental agents (e.g., thermal fluctuations, water, etc.) requires tracking the response at multiple time scales ranging from seconds to years. Modeling progressive damage accumulation and failure in composite materials subjected to cyclic loading is associated with solving a highly nonlinear problem that includes a very large number of time steps required to resolve each load cycle in a structure's load trajectory. This intractability could be addressed using multiple time scale strategies, including the cycle jump method (Chaboche, 1988; Chow and Wei, 1991; Paas et al., 1993), manifold-based multitemporal modeling (Acharya and Sawant, 2006), wavelet transformation (Joseph et al., 2010; Chakraborty and Ghosh, 2013), and the multiple time scale homogenization (Oskay and Fish, 2004a,b). The common idea in these computational approaches is to approximate the evolution of a structure using the response from a small number of resolved cycles within the load trajectory of the structure and interpolating the response evolution between the resolved cycles. In the context of failure analysis of composite materials and structures, applications of multiple time scale modeling strategies have been relatively recent and many issues in this area remain outstanding. A key challenge is the simultaneous treatment of multiple time and length scales for evaluation of the long-term degradation and failure response of composite materials.

This chapter provides an overview of a multiscale space–time computational homogenization framework for predicting the failure response of composite materials under monotonic and cyclic loading conditions. The framework that we propose is tuned for computational efficiency through the use of reduced order modeling procedures in space and time. We contend that the widespread use of advanced multiscale modeling and simulation methods is possible in the near future if mathematically robust multiscaling procedures are combined with physically based reduced modeling approaches.

The remainder is organized as follows: In Section 13.2, we review the formulation and implementation of a unified multiscale modeling framework for composite materials that encompasses multiple time and length scales for response and life prediction. In Section 13.3, results from recent investigations on carbon fiber-reinforced polymer (CFRP) composites are provided. In Section 13.4, we draw specific conclusions projecting from the proposal multiscale computational framework and provide a perspective of future trends in multiscale modeling of composites.

13.2 Multiscale modeling in space–time

The state of the practice in the prediction of the long-term performance degradation of composites typically uses weakly coupled *response* and *lifing* models. Response models idealize mechanical response to (e.g., cyclic) loading, whereas *lifing* models predict long-term performance (see, e.g., Liu and Lessard, 1994; Mao and Mahadevan, 2002; Subramanian et al., 1995; Ye, 1989, among many other works). The response models compute life prediction metrics such as stress range, strain range, intensity factors, stress or strain invariants, or others, which are then employed in the lifing model to phenomenologically determine life. An alternative paradigm is the application of the progressive damage accumulation models directly to long-term loading and environmental conditions. In this paradigm, the response and lifing models are one and the same. The life prediction is performed by subjecting the model to a long-term load spectrum. We note that this paradigm is computationally demanding and requires efficient multiscaling algorithms and models to realize the analysis in an acceptable time frame and resources. Herein, we present such a computational modeling framework that allows the prediction of the long-term damage accumulation and the failure of composite structures.

13.2.1 Multiscale space–time homogenization setting

The multiscale framework employs the computational homogenization method with multiple time and length scales (Crouch et al., 2013b). Figure 13.2 illustrates the decomposition of the problem into two spatial and two temporal scales. The generalization of the approach to three or more length and time scales is conceptually straightforward. Ω denotes the body of the composite structure, component, or a specimen. The domain of the composite body is parameterized by the macroscopic position vector, $\mathbf{x}$. Let θ denote the body of the representative cell (e.g., representative volume element, unit cell), which resolves the microscopic heterogeneity in the

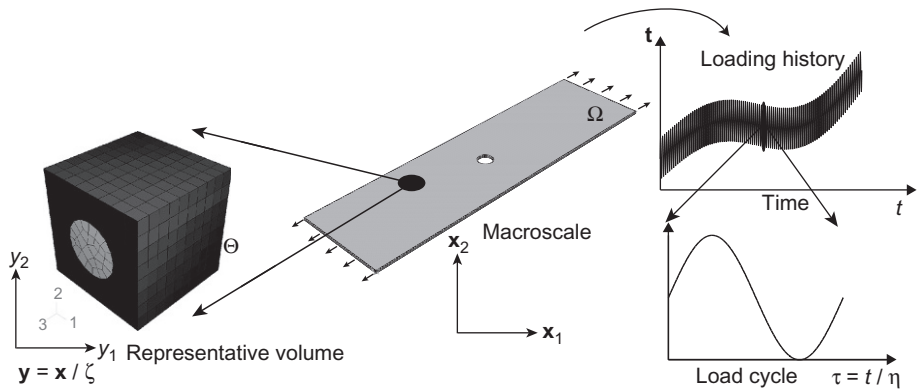

Figure 13.2 The multiscale setting of the life prediction approach.

composite material. θ is parameterized by the microscopic position vector, $\mathbf{y}$. Because the treatment of the microstructure is numerical, the morphology of the representative cell is arbitrary; that is, unidirectionally reinforced, textile, three dimensional (3D) woven, and other composite geometries are treated similarly. The composite body is subjected to loading and environmental conditions that consist of the repetition of a characteristic load cell (e.g., a representative spectrum or load cycle) and loads that vary slowly during the observation period.

Consider an arbitrary response function (e.g., stress, strain) denoted as $\phi^{\zeta\eta}$, defined over the domain of the composite. The response function fluctuates in space and time. The spatial oscillations, which have a periodicity of approximately the size of the representative cell, are due to the heterogeneity of the composite material. Temporal oscillations are due to fluctuating loading (or environmental) conditions. The gradual accumulation of damage due to the repeated load cycles and the response to the slowly varying loads results in the gradual variation of the response fields observed at a *macrochronological* time scale. This time scale is parameterized using the time parameter $t \in [0, t_l]$, where t_l denotes the observation period (i.e., life). The response of the composite domain to the representative load cell occurs at a much shorter time scale, which is parameterized by the *microchronological* time coordinate $\tau \in [0, \tau_0]$. τ_0 denotes the size of the representative load cell. The micro- and macro-coordinates in space and time are related to each other by the following scaling relationships:

$$\mathbf{y} = \frac{\mathbf{x}}{\zeta}; \quad \tau = \frac{t}{\eta}, \tag{13.1}$$

in which $0 < \zeta \ll 1$ and $0 < \eta \ll 1$ are scaling parameters in space and time, respectively. The physical significance of the scaling parameters is that they represent the characteristic size ratios between the fine and coarse scales in space or time. The original response fields that are functions of a single time and length scale are expressed in terms of the two length and two time scales introduced above, that is,

$$\phi^{\zeta\eta} = \phi(\mathbf{x}, \mathbf{y}(\mathbf{x}), t, \tau(t)). \tag{13.2}$$

The derivatives with respect to space and time are, respectively, obtained through the chain rule:

$$\nabla\phi^{\zeta\eta}(\mathbf{x}, t) = \nabla_{\mathbf{x}}\phi(\mathbf{x}, \mathbf{y}, t, \tau) + \frac{1}{\zeta}\nabla_{\mathbf{y}}\phi(\mathbf{x}, \mathbf{y}, t, \tau) \tag{13.3}$$

$$\dot{\phi}^{\zeta\eta}(\mathbf{x}, t) = \phi_{,t}(\mathbf{x}, \mathbf{y}, t, \tau) + \frac{1}{\eta}\phi_{,\tau}(\mathbf{x}, \mathbf{y}, t, \tau), \tag{13.4}$$

in which $\nabla_{\mathbf{x}}(\cdot)$ and $\nabla_{\mathbf{y}}(\cdot)$ are gradient operators with respect to the macroscopic and microscopic coordinates, respectively; a comma followed by a subscript variable t and τ denotes the partial time derivative with respect to the macrochronological and microchronological coordinates, respectively.

The formulation of the concurrent multiscale homogenization model relies on the asymptotic expansion of the displacement field, $\mathbf{u}$, with respect to the spatial scaling parameter, ζ:

$$\mathbf{u}(\mathbf{x},\mathbf{y},t,\tau) = \bar{\mathbf{u}}(\mathbf{x},t,\tau) + \sum_{i=1}^{n} \zeta^i \mathbf{u}^i(\mathbf{x},\mathbf{y},t,\tau) + O(\zeta^{n+1}). \tag{13.5}$$

Equation (13.5) decomposes the displacement field into a macroscopic displacement field ($\bar{\mathbf{u}}$) and a series of microscopic fields ($\mathbf{u}^i$) whose effect on the overall displacement reduces with each order (through multiplication with ζ^i). The temporal scales do not admit a useful expansion because the displacement response within the microchronological cell could be of the same order of magnitude as the macrochronological (i.e., temporally homogenized) displacements.

The procedure for the homogenization analysis consists of decomposing the original governing equations defining the failure process (i.e., equilibrium, kinematical, constitutive, and boundary conditions), and asymptotic matching to identify governing equations at each scale at the scale separation limit ($\zeta \to 0$). The homogenization procedure is explained in detail in a number of texts such as Benssousan et al. (1978) and Cioranescu and Donato (1999).

13.2.2 Temporal scales versus spatial scales

The aforementioned homogenization procedure requires explicit definition of two conditions, which cannot be derived from the asymptotic analysis: (1) the boundary conditions of the representative cell; and (2) the definition of the homogenization operator, which relates the macroscopic quantities to their microscopic counterparts.

Periodicity in space–time

A number of boundary conditions have been proposed for evaluating the composite response at the scale of the microstructure including static uniform, kinematic uniform, periodic as well as more advanced boundary conditions that better capture the local postfailure behavior (see, e.g., Coenen et al., 2012; Fish and Fan, 2008; Huet, 1999; Mesarovic and Padbidri, 2005). Perhaps the most commonly used condition is the locally periodic boundary conditions, which assumes that all response fields (e.g., displacement, stress, strain, etc.) are taken to be locally periodic with respect to the representative cell throughout the deformation process:

$$\phi(\mathbf{x},\mathbf{y},t,\tau) = \phi(\mathbf{x},\mathbf{y}+\mathbf{k}\hat{\mathbf{y}},t,\tau), \tag{13.6}$$

where $\hat{\mathbf{y}}$ denotes the periods of the microstructure and $\mathbf{k}$ is a $d \times d$ diagonal matrix with integer components.

The generalization of the local periodicity condition to time domain is not possible in problems that involve damage accumulation and failure. This is because the damage accumulation process in the composite materials is modeled using internal state

variables (e.g., the damage variables), which are postulated to be irreversible (for non-healing materials) to obey thermodynamic constraints. The magnitude of these damage fields at the end of a microchronological cell will therefore be higher than at the beginning, clearly violating periodicity with respect to time. Strictly speaking, the evolution of the response fields is an initial value problem in the time domain, not a boundary value problem. Therefore, it is not necessary to prescribe the end values of the response fields within a microchronological cell to correctly pose the problem. However, the transition of the response fields from microchronological scale to the macrochronological scale imposes a constraint on the end values. The concept of *almost periodicity*, previously proposed in Oskay and Fish (2004a), resolves this difficulty by allowing small changes in the values of the response function at the boundaries of the microchronological cell. Almost periodicity assumes that at neighboring points in a temporal domain homologous by the load period, the change in the value of a response function is of the order of the scaling parameter $O(\eta)$ and does not vanish (Oskay and Fish, 2004b; Fish and Oskay, 2005). We denote the temporal averaging operator as:

$$\langle \phi \rangle_{\tau}(\mathbf{x},\mathbf{y},t) := \frac{1}{\tau_0}\int_0^{\tau_0} \phi(\mathbf{x},\mathbf{y},t,\tau)\,\mathrm{d}\tau. \tag{13.7}$$

The almost periodic temporal homogenization operator in the rate form is expressed as (Oskay and Fish, 2004a):

$$\dot{\tilde{\phi}}\,(t) \equiv \mathcal{M}(\phi)_{,t} = \tilde{\phi}_{,t}(t) + \dot{\phi}_{\mathrm{ap}}(t) \tag{13.8}$$

$$\dot{\phi}_{\mathrm{ap}} = \frac{1}{\eta}\left\langle \frac{\partial \phi}{\partial \tau} \right\rangle_{\tau}, \tag{13.9}$$

in which $\tilde{(\cdot)}$ is a time homogenization operator (discussed in the following), and $\dot{\phi}_{\mathrm{ap}}$ denotes the almost periodic component of the time rate of evolution of the temporally homogenized response field. Equation (13.8) implies that the time differentiation and the time homogenization operators do not commute.

Homogenization operators in space–time

The homogenization operator in space typically is considered to be the averaging operation over the representative cell. The homogenized field $\bar{\phi}$ of the pertinent field ϕ is expressed as

$$\bar{\phi} \equiv \langle \phi \rangle_{\mathbf{y}} = \frac{1}{|\Theta|}\int_{\Theta} \phi\,\mathrm{d}\mathbf{y}, \tag{13.10}$$

where $|\Theta|$ denotes the volume of the representative cell and $\langle \cdot \rangle_{\mathbf{y}}$ the spatial averaging operation. A constraint that is imposed on the choice of the boundary conditions as

well as the homogenization operator is the energy compatibility between the micro- and macroscopic scales, known as the Hill–Mandel condition:

$$\langle \boldsymbol{\sigma} : \boldsymbol{\epsilon} \rangle_{\mathbf{y}} = \langle \boldsymbol{\sigma} \rangle_{\mathbf{y}} : \langle \boldsymbol{\epsilon} \rangle_{\mathbf{y}}, \tag{13.11}$$

in which $\boldsymbol{\sigma}$ and $\boldsymbol{\epsilon}$ are the strain and stress tensors, respectively. By the definition of the homogenization operator, the right-hand side of Equation (13.11) is defined in terms of the macroscopic stress and strain. Local periodicity condition and the spatial homogenization operator together automatically satisfy the Hill–Mandel condition in the context of computational homogenization.

It is natural to consider the temporal averaging equation (Equation 13.7) as the temporal homogenization operator, which is also consistent with spatial homogenization (Oskay and Fish, 2004a). Even though this choice is possible, a more computationally convenient homogenization operator, the *fixed point operator* was recently proposed in Crouch et al. (2013b):

$$\widetilde{\phi}(t) = \phi(t, \tau^*), \tag{13.12}$$

in which $\tau^* \in [0, \tau_0]$ is an arbitrary but fixed point within the microchronological cell. This operator implies that it is possible to accurately track the evolution of damage and failure in the composite by tracking a fixed point within the microchronological cell, rather than the average. One attractive property of the fixed point operator compared to the averaging operator is its distributive property, which allows simple decomposition of the nonlinear fields (i.e., $\phi = \psi\xi \rightarrow \widetilde{\phi} = \widetilde{\psi}\widetilde{\xi}$).

Crouch and Oskay (2015) demonstrated that the micro–macro transition is also accurate (but not exact) using an arbitrary choice of the fixed point. Consider the micro–macro transition of the rate of strain energy defined using the almost periodic homogenization operation:

$$\Phi := \mathcal{M}(\boldsymbol{\sigma} : \dot{\varepsilon}) - \widetilde{\boldsymbol{\sigma}} : \dot{\widetilde{\varepsilon}} \approx 0. \tag{13.13}$$

The left term of Equation (13.13) is the time-homogenized strain energy rate at the microchronological scale and the right term is the energy rate computed using the time-homogenized stress and strain, respectively. Equation (13.13) is analogous to the Hill–Mandel condition used in spatial homogenization, but applied in the time domain and in rate form. Application of the fixed point and almost periodicity operators yield (Crouch and Oskay, 2015):

$$\Phi = \frac{\tau_0 - 2\tau^*}{\eta} \widetilde{\boldsymbol{\sigma}} : \frac{\partial^2 \varepsilon(t, \tau^*)}{\partial \tau^2}, \tag{13.14}$$

which implies that the micro–macro transition is satisfied up to the third-order (with respect to time derivatives of strain) term when the fixed-point operator is chosen to be the midpoint (i.e., $\tau^* = \tau_0/2$). Despite a slightly larger error, the choice of $\tau^* = 0$ is

computationally more convenient, since the fixed-point coincides with the initial state of the microchronological cell. Provided that the evolution of the response fields is relatively smooth, the fixed-point operator homogenizes the microchronological scale response with reasonable accuracy.

13.2.3 Governing equations and multiscale system

The starting point of the multiscale model formulation is the governing equations of the composite body that defines the progressive accumulation of damage and deformation. The governing equations are posed at the level of the constituents throughout the domain of the structure. Neglecting the inertial terms (i.e., under quasi-static loading conditions), the equilibrium in the composite body is expressed as ($\mathbf{x} \in \Omega$ and $t \in [0, t_l]$):

$$\nabla \cdot \boldsymbol{\sigma}^{\zeta\eta}(\mathbf{x},t) + \mathbf{b}^{\zeta}(\mathbf{x}) = 0, \tag{13.15}$$

where $\boldsymbol{\sigma}^{\zeta\eta}$ denotes the Cauchy stress, $\mathbf{b}^{\zeta}$ the body force, and $\nabla\cdot\,(\cdot)$ the divergence operator. In the context of damage-visco-plasticity, the constitutive response of a composite constituent is expressed as:

$$\boldsymbol{\sigma}^{\zeta\eta} = \left(\mathbf{I} - \mathbf{D}^{\zeta\eta}\left(\mathbf{x},t;\boldsymbol{\omega}^{\zeta\eta},\mathbf{s}^{\zeta\eta}\right)\right) : \mathbf{L}^{\zeta}(\mathbf{x}) : \left(\boldsymbol{\epsilon}^{\zeta\eta}(\mathbf{x},t) - \boldsymbol{\epsilon}_{\mathrm{vp}}^{\zeta\eta}\left(\mathbf{x},t;\mathbf{h}^{\zeta\eta}\right)\right), \tag{13.16}$$

in which $\mathbf{I}$ denotes the fourth-order identity tensor; $\mathbf{D}^{\zeta\eta}$ is a fourth-order damage tensor built as a function of the damage variable vector, $\boldsymbol{\omega}^{\zeta\eta}$; $\mathbf{L}^{\zeta}$ the tensors of elastic moduli of the constituents; $\boldsymbol{\epsilon}^{\zeta\eta}$ the total strain; and $\boldsymbol{\epsilon}_{\mathrm{vp}}^{\zeta\eta}$ the viscoplastic strain. The evolution of the damage variable vector and the viscoplastic strains at a material point of a constituent is often nonlinear, history-dependent functions that are described in terms of internal state variables, $\mathbf{s}^{\zeta\eta}$ and $\mathbf{h}^{\zeta\eta}$, respectively. It is worth emphasizing that the damage-visco-plastic constitutive models idealize the behavior of the composite constituents (e.g., polymer matrix, carbon fiber, etc.), and not the composite. The tensorial expression of damage allows the possible anisotropic damage evolution within the constituent.

The boundary conditions prescribed on the body consist of slowly varying and oscillating components as illustrated in Figure 13.2:

$$\mathbf{u}_i^{\zeta\eta}(\mathbf{x},t) \;\; = \hat{\mathbf{u}}^{\eta}(\mathbf{x},t); \;\; \mathbf{x} \in \Gamma_u; \;\; t \in [0,t_l], \tag{13.17}$$

$$\boldsymbol{\sigma}^{\zeta\eta} \cdot \mathbf{n} \;\; = \hat{\mathbf{t}}^{\eta}(\mathbf{x},t); \;\; \mathbf{x} \in \Gamma_t; \;\; t \in [0,t_l], \tag{13.18}$$

where $\hat{\mathbf{u}}$ and $\hat{\mathbf{t}}$ are the prescribed displacements and tractions on the boundaries Γ_u and Γ_t, respectively ($\Gamma = \Gamma_u \cup \Gamma_t$ and $\Gamma_u \cap \Gamma_t = \varnothing$), and $\mathbf{n}$ is the unit normal to Γ_t. The period of oscillations is taken to be slow enough that inertial forces are insignificant and the response remains quasi-static.

The boundary value problem defined by Equations (13.15)–(13.18) along with the evolution equations for the damage variables, internal state variables, and the viscoplastic strains is analyzed using the asymptotic expansion method described previously. The displacement field decomposition (Equation 13.5) is substituted into the governing equations which, along with the pertinent homogenization operators discussed, leads to the decomposition of the boundary value problem into coupled micro- and macroscale problems in time and space. The details of the asymptotic analysis applied to space, time, and space–time in the context of composite damage modeling are provided in Oskay and Fish (2007), Crouch et al. (2013b), and Crouch and Oskay (2015) and will be skipped here for brevity. Figure 13.3 summarizes the resulting coupled system of multiscale equations for a composite, in which elasto-damage constitutive equations with scalar damage variables are used to idealize the constituent response. The system consists of the *macrochronological-macroscopic* (denoted as [t-**x**]), the *microchronological-microscopic* (denoted as [τ-**y**]), the *macrochronological-microscopic* (denoted as [t-**y**]), and the *microchronological-macroscopic* (denoted as [τ-**x**]) problems. The [t-**x**] problem provides the response of the long-term behavior of the spatially homogenized response of the composite under the slow varying loads and under the cumulative effect of the short-term loads. The spatio-temporally homogenized response is tracked to answer the life prediction problem of the composite structure. [τ-**y**] problem defines the evolution of a single characteristic volume subjected to a representative load cell. In the context of computational homogenization, the

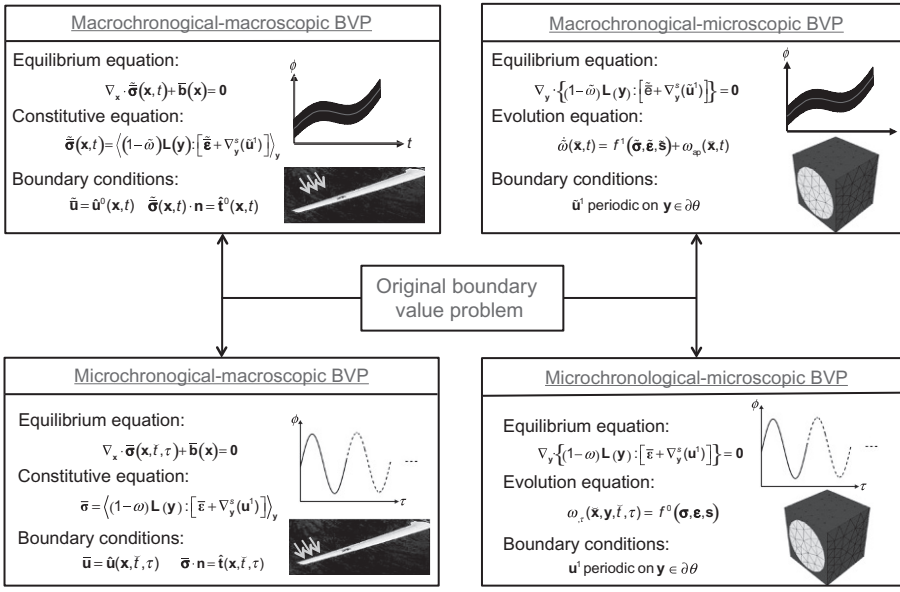

Figure 13.3 Multiple spatio-temporal boundary value problems obtained through asymptotic analysis.

solution of the [τ-**y**] problem constitutes the stress-update at a macroscopic material point. The [τ-**x**] problem defines long-term behavior of the representative cell. This problem computes the accumulated damage fields due to each representative load cell as well as the slow loading components. The [τ-**x**] problems also allow computation of adaptive macrochronological time step sizes that control the accuracy characteristics of the multiscale model. The [t-**y**] problem evaluates the cyclic behavior of the homogenized domain, by which the macroscopic equilibrium is maintained at each microchronological time step. The [τ-**y**] problem is also coupled to the [t-**x**] problem in that it provides the initial state of the homogenized problem at each macrochronological time step.

The computational approach shown in Figure 13.3 provides a rigorous framework for response and life prediction of composites. Yet, the straightforward implementation of this framework is computationally expensive. The expense stems from the need to evaluate highly nonlinear and fully coupled four-boundary value problems. Bringing the proposed framework out of the academic sphere and to the industry requires bringing down the computational complexity of the proposed framework to the order of the phenomenological modeling approach, without significantly compromising on its accuracy and predictive capabilities. This calls for carefully designed reduced-order modeling approaches in both space and time.

13.2.4 Reduced-order modeling

The computational complexity problem associated with concurrent (spatial) multiscale modeling approaches has been an active research area in the past couple of decades. One of the oldest idea for reduced-order modeling is the Taylor's hypothesis, which assumes that each constituent within the representative cell is subjected to uniform and equal deformation. This approach satisfies kinematical compatibility, but the equilibrium at the microscale is not satisfied. More elaborate reduced-order models have been recently proposed including (but not limited to) those based on proper orthogonal decompositions (Yvonnet and He, 2007), the boundary element method (Gosz et al., 1992), the Voronoi cell method (Ghosh and Moorthy, 1995), the spectral method (Aboudi, 1982), the transformation field analysis (TFA) (Dvorak, 1992; Bahei-El-Din et al., 2004), the fast Fourier transforms (Moulinec and Suquet, 1994, 1998), the network approximation method (Berlyand and Kolpakov, 2001), and the TFA-based homogenization with eigenstrains (Chaboche et al., 2001; Michel and Suquet, 2004; Fish et al., 1997). Recently, the eigendeformation-based homogenization method (EHM) was proposed (Oskay and Fish, 2007; Crouch and Oskay, 2010; Yuan and Fish, 2009) to efficiently evaluate the RVE level response. This method is derived based on a generalization of the TFA, and extends the eigenstrain formulations to account for the interfacial debonding effects, in addition to nonlinear and failure processes within the constituent materials of the heterogeneous microstructure. In what follows, we provide an overview of the EHM approach, as well as the model order reduction performed to increase the computational efficiency of the time scale computations.

13.2.4.1 Spatial model reduction

The premise of EHM is to devise a low-cost approximation to the nonlinear microscale boundary value problem defined over the representative cells based on the idea of precomputing certain microstructural information (e.g., concentration tensors, localization operators, influence functions) through linear elastic simulations prior to the analysis of the macroscale structure. To this end, the microscale displacement field is expressed as

$$\mathbf{u}^1(\mathbf{x},\mathbf{y},t,\tau) = \mathbf{H}(\mathbf{y}) : \bar{\boldsymbol{\epsilon}}(\mathbf{x},t,\tau) + \int_{\Theta} \mathbf{h}(\mathbf{y},\hat{\mathbf{y}}) : \boldsymbol{\mu}(\mathbf{x},\hat{\mathbf{y}},t,\tau)\, \mathrm{d}\hat{\mathbf{y}}, \tag{13.19}$$

in which $\mathbf{H}$ and $\mathbf{h}$ respectively denote the elastic and inelastic influence functions, $\bar{\boldsymbol{\epsilon}}$ denotes the macroscopic strains computed as the symmetric gradient of the macroscopic displacement, $\bar{\mathbf{u}}$.; and $\boldsymbol{\mu}$ denotes the inelastic strain. In the presence of viscoplastic and damage processes (considering major symmetry in the constituent elastic moduli tensors):

$$\boldsymbol{\mu} = \mathbf{L}^{-1} : \left[(\mathbf{I} - \mathbf{D}) : \boldsymbol{\epsilon}_{\mathrm{vp}} + \mathbf{D} : \boldsymbol{\epsilon} \right] : \mathbf{L}. \tag{13.20}$$

The elastic influence functions represent the linear elastic response of the representative cell to uniform unit strains, whereas the inelastic influence functions are computed as numerical approximations to Green's functions of the representative cell problem. It is also possible to extend Equation (13.20) to account for the progressive debonding process between constituents (Oskay and Fish, 2007). The reduction of the model order is achieved through the following discretization of the inelastic strain field, $\boldsymbol{\mu}$:

$$\boldsymbol{\mu}(\mathbf{x},\mathbf{y},t) = \sum_{\gamma=1}^{n} N_{\mathrm{ph}}^{(\gamma)}(\mathbf{y}) \boldsymbol{\mu}^{(\gamma)}(\mathbf{x},t,\tau), \tag{13.21}$$

in which $N_{\mathrm{ph}}^{(\gamma)}$ are the phase shape functions; $\boldsymbol{\mu}^{(\gamma)}$ are phase inelastic strain coefficients, and n the order of the discretization. All other state variables are also assumed to follow the same discretization as in Equation (13.22). The discretization of the inelastic strain field has a geometric character defined by the partitioning of the domain of the representative cell into n subdomains (also referred to as *parts*). The simplest choice for the phase shape functions is to take $N_{\mathrm{ph}}^{(\gamma)}$ to be piecewise constant with nonzero values on the subdomain $\theta^{(\gamma)} \in \theta$, only. It is also possible to choose the shape functions to be nonuniform as proposed in Michel and Suquet (2003, 2004). Considering isotropic damage-elasticity models to describe the constitutive behavior of the composite constituents, the governing equations of the representative cell problem reduce to the following algebraic form:

$$\sum_{\gamma=1}^{n} \left[\delta_{\eta\gamma} \mathbf{I} - \mathbf{P}^{(\eta\gamma)} \omega^{(\eta)}(\mathbf{x},t,\tau) \right] : \boldsymbol{\mu}^{(\gamma)}(\mathbf{x},t,\tau) = \omega^{(\eta)}(\mathbf{x},t,\tau) \mathbf{A}^{(\eta)} : \bar{\boldsymbol{\epsilon}}(\mathbf{x},t,\tau), \tag{13.22}$$

in which $\omega^{(\gamma)}$ denotes the scalar phase damage coefficient; $\boldsymbol{\delta}$ denotes the Kronecker delta; and $\mathbf{P}^{(\eta\gamma)}$ and $\mathbf{A}^{(\eta)}$ are coefficient tensors computed as a function of the influence functions $\mathbf{H}$ and $\mathbf{h}$, as well as the elastic properties $\mathbf{L}$. Evaluation of Equation (13.23) along with the constitutive equations particularized for each part is an approximation to the microscale boundary value problem. Because of the definition of the elastic and inelastic influence functions, the microscale equilibrium is automatically satisfied for all inelastic strain coefficient tensors that satisfy Equation (13.23). The macroscopic stress tensor is expressed in terms of the phase inelastic strain coefficients as

$$\bar{\boldsymbol{\sigma}}(\mathbf{x},t,\tau) = \bar{\mathbf{L}} : \bar{\boldsymbol{\epsilon}}(\mathbf{x},t,\tau) + \sum_{\gamma=1}^{n} \bar{\mathbf{M}}^{(\gamma)} : \boldsymbol{\mu}^{(\gamma)}(\mathbf{x},t,\tau), \tag{13.23}$$

in which $\bar{\mathbf{L}}$ and $\bar{\mathbf{M}}^{(\gamma)}$ are coefficient tensors, which are also functions of the influence functions and the elastic constituent properties, only.

In the above formulation, the reduced-order model solves for n inelastic strain coefficient tensors at each load step of a representative cell analysis. This is in contrast to the nonlinear finite element analysis of the problem, where the unknowns are n_u nodal displacement vectors within the finite element discretization of the representative cell. The idea is that n is sufficiently small compared to n_u making the reduced model much faster than the finite element evaluation of the microscale problem. The efficiency and accuracy of the EHM approach is directly linked to the choice of the phase shape functions, the partitioning of the representative cell, and the order of the partitioning, n. A number of ideas have been proposed in reduced model identification strategy including adaptively selecting the partitioning as a function of damage state within the representative cell (Oskay and Fish, 2007), partitioning based on the constituents only (Yuan and Fish, 2009), identification of the optimal reduced model through optimization (Sparks and Oskay, 2013), and the method of failure paths (Crouch and Oskay, 2010). An example of the partitioning strategy based on the method of failure paths in the context of a unidirectional fiber-reinforced matrix composite unit cell is illustrated in Figure 13.4. The unit cell is partitioned into four parts. Part 1 constitutes the entire fiber domain and models fiber cracking. Parts 2, 3, and 4 constitute subdomains of the matrix and respectively model transverse cracking, delamination, and the interaction between the two failure mechanisms. In this example, the underlying finite element discretization of the unit cell contains 1204 elements ($n_u = 416$). The degrees of freedom of the unit cell problem are therefore reduced from approximately 1200 to 24.

13.2.4.2 Temporal model reduction

The reduced-order modeling applied in space has a very significant impact on the efficiency of the life prediction system shown in Figure 13.3. However, life prediction of a large-scale composite structure even with the reduced-order modeling previously described remains computationally too expensive. A temporal model order reduction along with adaptive macrochronological time-stepping algorithms provides a path toward bringing this system to efficiency levels needed for solving practical composite life prediction problems.

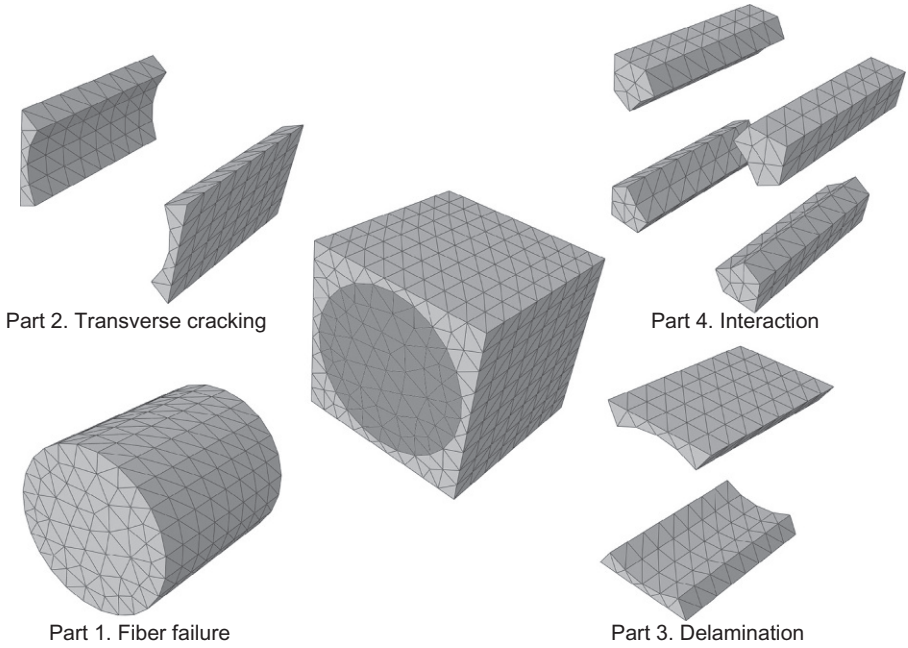

Figure 13.4 Partitioning of the unidirectionally reinforced unit cell based on the method of failure paths.
Reproduced from Figure 1 in Bogdanor et al. (2013b).

The temporal model order reduction approximates the microchronological-macroscopic ([τ-**x**]) problem as a linear process, eliminating the computationally costly nonlinear equilibrium iterations otherwise needed (Crouch and Oskay, 2015). The approximation is based on two observations. First is that the change in the response fields between the beginning and the end of a representative microchronological cell is small. This is particularly apparent in high-cycle fatigue response of composites where the cyclic response displays insignificant variations from a load cycle to the next, until the very end of life. This observation is also consistent with the almost periodicity assumption previously discussed. The second is that the minute changes in the response fields and state variables within a representative microchronological cell have negligible effect on the equilibrium process. By these two considerations, the equilibrium state over the microchronological cell is established based on the stress state at the fixed point:

$$\bar{\boldsymbol{\sigma}}^m(\mathbf{x},\tau) \approx \bar{\mathbf{L}} : \bar{\boldsymbol{\epsilon}}^m(\mathbf{x},\tau) + \sum_{\gamma=1}^{n} \bar{\mathbf{M}}^{(\gamma)} : \boldsymbol{\mu}^{m(\gamma)}(\mathbf{x},\tau^*), \tag{13.24}$$

in which $\bar{\boldsymbol{\sigma}}^m$, $\bar{\boldsymbol{\epsilon}}^m$, and $\boldsymbol{\mu}^{m(\gamma)}$ denote the macroscopic stress, strain, and phase inelastic strains at a fixed but arbitrary macrochronological time instant, respectively.

The consideration of Equation (13.25) in the approximation of the microchronological equilibrium results in two simplifications. Under the condition of proportional loading, the evaluation of the microchronological equilibrium reduces to obtaining the linear elastic responses subjected to unit loads along the direction of the prescribed boundary loads, and employing superposition to compute the displacement, strain, and stress response. Next, the nonlinear microchronological-microscopic [τ-$\mathbf{y}$] problems are decoupled from the [t-$\mathbf{x}$] problem and can be evaluated independently of each other at each integration point throughout the domain. Parallelization of the microchronological damage evolution computation is therefore trivial and completely scalable. We note that nonlocal models employed to address spurious mesh dependence and limit damage localization may complicate the parallelization process.

The computational efficiency and accuracy of the life prediction system is optimized by considering an adaptive time-stepping strategy for the macrochronological problems. The macrochronological time step size is typically chosen such that the damage increment due to the almost periodic damage accumulation does not exceed a prescribed tolerance. The selection of the time step size, therefore, requires estimation of the damage state in the next macrochronological time step. The damage state estimation strategies based on linear and quadratic approximations were previously suggested in Oskay and Fish (2004a) and Crouch et al. (2013b). When the quadratic damage estimation is employed, the thermodynamic constraints impose additional requirements on the macrochronological time step size in order to ensure thermodynamic consistency (Crouch and Oskay, 2015).

13.3 Investigation of CFRP composites

The proposed multiscale computational life prediction framework was applied to investigate the performance of CFRP composites subjected to monotonic and cyclic loading conditions. Here, we review and summarize the results of investigations performed on IM7/977-3 graphite-epoxy composite specimens originally presented in Crouch et al. (2012, 2013a,b). A suite of experiments conducted in collaboration and at the US Air Force Research Laboratory (AFRL) was employed to calibrate and validate the multiscale life prediction framework. A more comprehensive model performance assessment study to fully characterize the capabilities of the current framework and compare its predictions to those of a number of commercially available and university codes is currently underway. This study, funded by the AFRL, involves the blind prediction of the monotonic, cyclic strength predictions as well as the residual strength after fatigue for various specimen and layup configurations. The results of this study will be reported in future publications upon completion. Such comparative investigations are critical to identifying the advantages and challenges associated with using multiscale codes for practical applications.

13.3.1 Experiments

Two separate sets of experiments were performed. The first set of experiments was employed to calibrate the parameters of the multiscale model (i.e., calibration experiments), whereas the second set was used in the validation of the model (i.e., validation experiments). In some of the specimens, progressive damage accumulation was tracked using acoustic emission monitoring, X-ray radiography, and X-ray computed tomography techniques. The acoustic emission system detects the stress waves that are produced by the strain energy release caused by a local failure event within the composite. This acoustic energy is recorded as a *hit*. The acoustic emission hit count is correlated to the density of local failure events as a function of load amplitude (for monotonic loading) and load cycles (for fatigue loading). X-ray radiography and computed tomography provides the visualization of the extent and types of damage within the specimen as 2D or 3D images, respectively. Because all characterization techniques employed are nondestructive, the quantity and location of damage as a function of load or load cycles can be tracked.

The calibration experiments were conducted on 0° and 90° layups subjected to monotonic and cyclic loading conditions. The 90° specimens were loaded in three-point bending monotonically, and under unidirectional tension cyclically (R-ratio = 0.1). The 0° specimens were subjected to unidirectional tension under monotonic and cyclic loading conditions. The validation experiments were performed on specimens with quasi-isotropic ($[+45,0,-45,90]_{2s}$) layup. The specimens were subjected to uniaxial monotonic tension and cyclic tension (R-ratio = 0.1) loads. The number of plies in the 0°, 90°, and quasi-isotropic specimens were 8, 16, and 16, respectively. Under monotonic loads, the typical failure patterns observed in the 0°, 90°, and quasi-isotropic specimens are shown in Figure 13.5. The critical failure

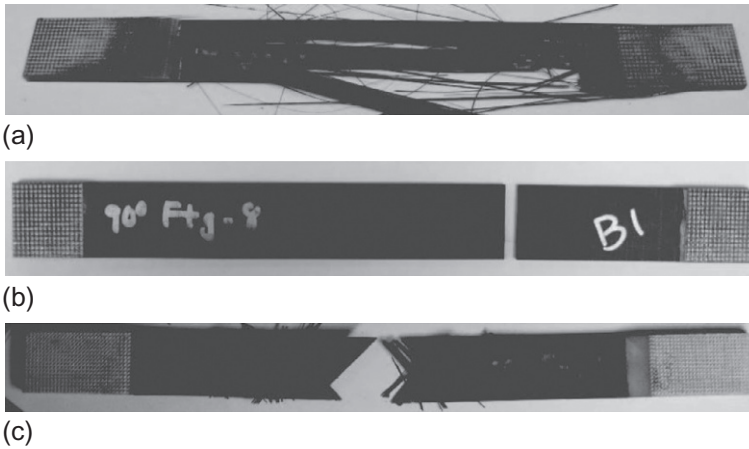

Figure 13.5 Failure profiles when subjected to monotonic loading. (a) 0° specimens; (b) 90° specimens; and (c) quasi-isotropic specimens.
(Figure from Crouch et al., 2012; reprinted by permission of the American Institute of Aeronautics and Astronautics, Inc.)

mechanisms for the 90° and 0° specimens were matrix and fiber cracking, respectively. In quasi-isotropic specimens, a combination of delamination, transverse matrix cracking, and fiber failure was observed.

13.3.2 Calibration

The calibration of the multiscale models against experimental measurements typically involves multiparameter optimization. The difficulty associated with the calibration of a multiscale model is that many traditional experiments provide information at the coupon or specimen levels, which are dictated by the properties of the composite. In contrast, the multiscale model parameters are defined at the scale of the constituents. It is well known that particularly for resins, the bulk material properties often differ significantly from the *in situ* properties. Fiber properties are often characterized better and used in the calibration process.

In its general form, the multiscale model parameter identification is posed as an optimization problem using the following expression:

$$\boldsymbol{\phi}_{\text{opt}} = \underset{\boldsymbol{\phi}\in\mathcal{V}}{\arg\min}\ \psi(\boldsymbol{\phi}). \tag{13.25}$$

In this equation, $\boldsymbol{\phi}$ denotes the vector of all model parameters in the multiscale model (i.e., fiber and matrix material parameters); $\mathcal{V}$ denotes the space of physically admissible material parameters (modeled as a constraint to the search space); $\boldsymbol{\phi}_{\text{opt}}$ indicates the parameter vector that leads to the best match between the simulated and experimental observables; and ψ denotes the objective function expressed as:

$$\psi(\boldsymbol{\phi}) = \sum_{i=1}^{n_{\text{data}}} \| \mathbf{f}^i_{\text{sim}} - \mathbf{f}^i_{\text{exp}} \|_{Lp}. \tag{13.26}$$

Here n_{data} is the number of experimental datasets available for the calibration process ($n_{\text{data}} \geq n_{\text{exp}}$); $\mathbf{f}^i_{\text{sim}}$ and $\mathbf{f}^i_{\text{exp}}$ the observables computed using the multiscale simulations and obtained from the calibration experiments, respectively; and $\| \cdot \|_{L^p}$ denotes the L^p norm (typically set to the Euclidian norm $p = 2$).

The constrained optimization problem defined in Equation (13.26) can be evaluated using gradient-based or evolutionary optimization algorithms (Oskay and Fish, 2008). Unfortunately, neither gradient-based nor evolutionary approaches are satisfactory when the optimization is posed in a very general form. The gradient-based optimization methods often converge to local minima of the objective function that may not correspond to the true optimal parameter vector. The evolutionary approaches do find the global minima, but they are computationally exhaustive when the size of the parameter vector is relatively large. The decomposition of the optimization problem into separate sets by observing the weak coupling or decoupling between some of the parameters significantly simplifies the identification process. In this approach, a subset of material parameters are identified based on a corresponding subset of observables. The form of the optimization problem defined in Equations (13.26) and (13.27) remain the same but are applied to identify

a smaller set of parameters. In the current context, we divide the optimization problem into four steps:

1. Selection of the microstructure morphology.
2. Calibration of the elastic properties and selection of the reduced-order model.
3. Calibration of the inelastic properties for monotonic loading.
4. Calibration of the cyclic failure properties.

The reduced order multiscale computational model predictions are clearly affected by the composite microstructure morphology. The fiber volume fraction, and at some cases, limited number of scanning electron microscopy (SEM) images, provide the necessary information used to digitally construct a microstructure morphology. A unit cell (i.e., smallest element of an ordered microstructure) is employed when only the fiber volume fraction information is available. If sufficient SEM images are available that characterize higher order statistics of the material morphology, it is possible to construct a statistically representative volume element. In the current investigations, a cubic unit cell is employed (Figure 13.4) since only the fiber volume fraction was available. In step (2), the tensor of elastic moduli of the fiber and matrix are calibrated. The elastic response from the calibration experiments as well as the manufacturer data on stiffness (employed as initial conditions to the optimizations) is employed to identify the in situ matrix and fiber elastic properties. In the current study, the EHM approach with the method of failure paths is employed to determine the reduced order model. The model employed is described in Figure 13.4 and Section 13.2.4.1. The coefficient tensors of the reduced order model only depend on the elastic constituent properties and the microstructure and are computed following the selection of the reduced order model.

The inelastic material parameters of the composite constituents are separated into two sets. The first set contains the parameters that characterize the evolution of the inelastic processes under monotonic loading or a single load cycle (i.e., short-term response). The second set of parameters characterizes the sensitivity of the damage evolution to the long-term processes. Steps (3) and (4) identify the parameters based on the optimization procedure defined by Equations (13.26) and (13.27). Figure 13.6 displays the comparison of the calibrated model response and the experimental data under monotonic and cyclic loading. The calibrated multiscale model describes failure in the 0° and 90° specimens with high accuracy.

13.3.3 Validation

The capabilities of the calibrated multiscale model in predicting the failure behavior under monotonic and cyclic loading are assessed using the experimental data on the quasi-isotropic specimens. The monotonic failure response under tension is compared in Figure 13.7a. The behavior of the composite specimens is primarily brittle. The strength and strain-to-failure is captured very accurately with the calibrated model (the comparisons made to the experimental means). Figure 13.7b,c provides the comparison of damage accumulation as a function of cycles. The maximum amplitude of loading applied in the experiments was 17% of the ultimate monotonic strength.

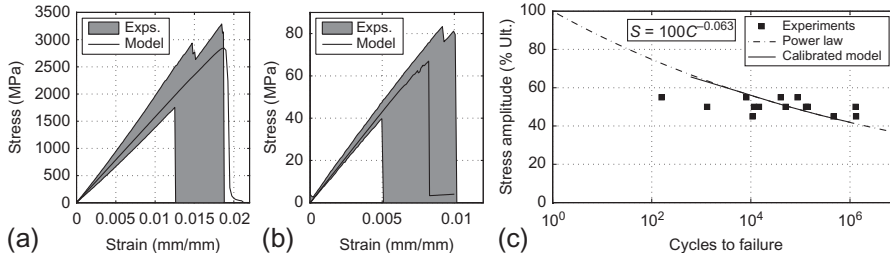

Figure 13.6 Comparison of the experimental data and calibrated model results: (a) monotonic uniaxial tension response of 0° specimens; (b) monotonic uniaxial tension response of 90° specimens; and (c) stress-life curves of 90° specimens under tensile cyclic loading.
(a) and (b) from Crouch et al. (2012); reprinted by permission of the American Institute of Aeronautics and Astronautics, Inc. and (c) reprinted from Crouch et al. (2013b) with the permission of Springer.

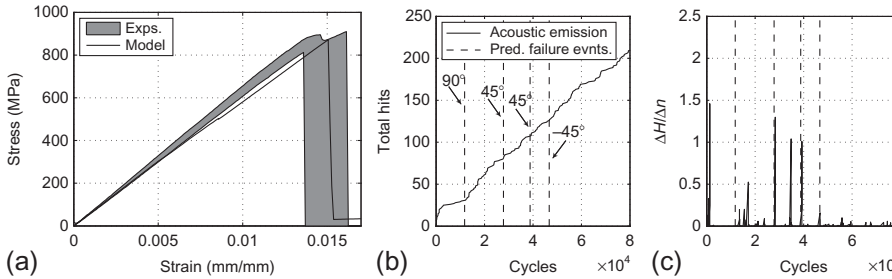

Figure 13.7 Comparison of the experimental data and calibrated model predictions for quasi-isotropic specimens: (a) monotonic uniaxial tension response; (b) acoustic emission data as a function of cycles; and (c) acoustic emission hit rate as a function of cycles.
(a) and (b) from Crouch et al. (2012); reprinted by permission of the American Institute of Aeronautics and Astronautics, Inc. and (c) reprinted from Crouch et al. (2012) with the permission of Springer.

We seek to study subcritical damage initiation only since the applied loading is well below the fatigue limit. The experimental data is from the acoustic emission recordings. The main damage initiation events are interpreted as spikes in the rate of acoustic emission hits. The spikes in the rates are in very good agreement with the simulation predictions. The predictions show the onset of transverse matrix cracking in different plies (identified as ply orientations in the figure). We note that the correlation of the acoustic emission data with specific damage events is not yet well understood. Despite close agreement, the match between the specific failure events and their predictions by the multiscale model is to be interpreted from the qualitative perspective.

The extent of the capability of the proposed model in capturing the spatial distribution of damage is illustrated in Figure 13.8. The comparison is from the uniaxial loading of the quasi-isotropic specimen. The damage distributions correspond to

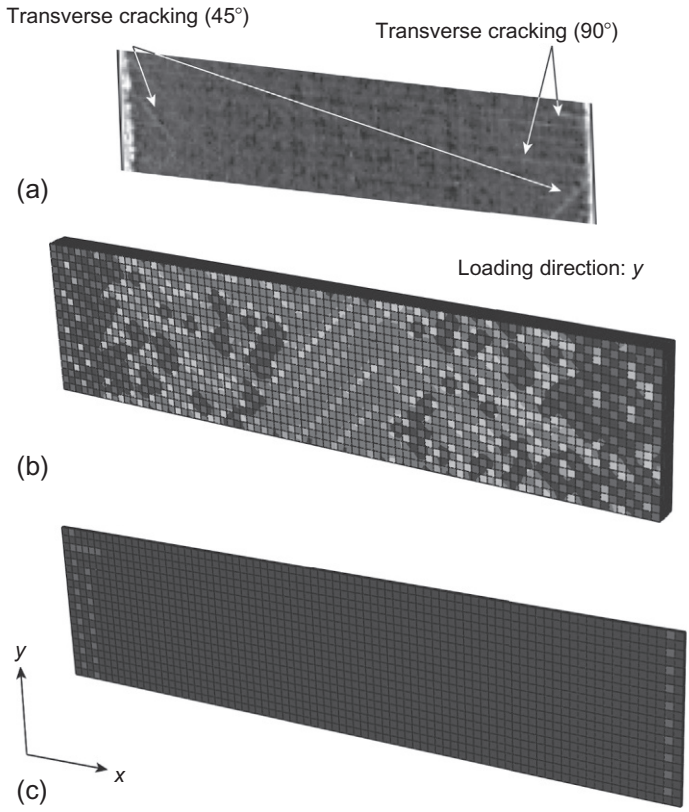

Figure 13.8 Damage profiles at 71% of the ultimate load: (a) experimental, (b) top (45) ply (simulated), (c) the center (90) ply of the specimen (simulated).
(Figure reprinted from Crouch et al. (2013a) with the permission of Elsevier.)

71% of the ultimate monotonic strength. The simulations predictions are compared to the X-ray tomography image, which shows that there is a reasonable match between the predicted and observed damage distributions.

The example as described provides a partial validation of the multiscale modeling framework. Further validation of the approach is needed to properly assess the validity of the underlying constitutive models and the overall computational framework. Thorough validation studies are currently underway.

13.4 Conclusions and future trends

Multiscale modeling holds great promise in achieving the capability to predict the response of composite materials and structures. The computational framework discussed in this chapter provides a foundation and a framework for gaining such a capability. This chapter demonstrated that multiscale modeling, along with model

reduction approaches that retain the underlying physics of damage and failure processes, can predict the complex failure mechanisms and interactions in composites with complex layups. Computational multiscaling based on hierarchical approach remains computationally costly. The reduced order modeling in space–time is therefore an indispensable component of the multiscale framework. A number of challenges and opportunities remain that will require significant attention from the computational mechanics and composites communities in the near future. We briefly touch on four of these challenges below: (1) capturing failure mechanisms for high-fidelity predictions; (2) quantification of uncertainty in response and life; (3) linking to the molecular scales; and (4) connecting to the manufacturing processes.

The investigations on CFRP composites discussed in Section 13.3 shows that the tensile failure in the layups considered are captured with high accuracy. The primary mechanisms of failure were transverse matrix cracking, fiber fracture, and delamination. For other layups, material and loading configurations, other mechanisms may contribute to or dominate ultimate failure. For instance, fiber kinking and shear under compressive loadings, fatigue failure under tension-compression loading may not have been investigated to the same degree as failure under tension using multiscale approaches yet. We note that thorough theoretical, single-scale numerical and experimental investigations do exist and would guide the multiscale modeling efforts. One key issue is to devise appropriate constituent scale constitutive models and reduced order models that can reproduce composite level failure mechanisms.

The spatial variability in the morphology, internal stress state, and damage state within the microstructure naturally leads to the uncertainty in the failure response and life of composites, which can be substantial even for carefully prepared laboratory specimens as illustrated in Figure 13.9. Multiscale modeling provides a unique capability to directly link the variability in the material microstructure to structural performance. The uncertainty in composite materials has primarily been addressed at the laminate level (Sriramula and Chryssanthopoulos, 2009), with fewer studies

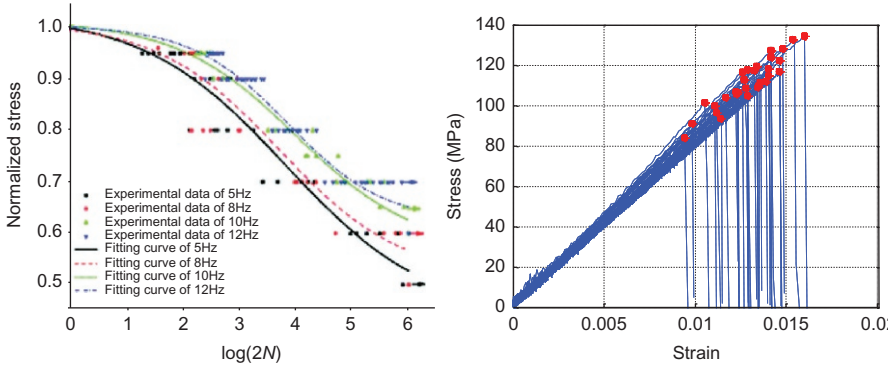

Figure 13.9 Variability in composite specimens (a) when subjected to cyclic loading. Reprinted from Chen et al. (2006) with permission from Wiley; (b) when subjected to monotonic loading.

(Chamis, 2004; Shiao and Chamis, 1999) dedicated to quantifying ply-level uncertainty, and even fewer studies on the effect of uncertainties in the constituent materials. Bayesian statistical approaches could serve as a powerful basis for modeling uncertainty in composite materials (Bogdanor et al., 2013a).

The calibration of the constituent material properties is an indirect procedure as discussed above. The properties are back-calculated from the results of the standardized experiments performed on composite specimens. Establishing the link between the constituent properties, or more generally the constituent model, and the molecular structure of the constituents provides an alternative paradigm. Molecular dynamics simulations performed at the scale of the composite constituents provide the behavior of the material based on the interatomic potentials associated with the constituent's molecular structure. The sequential multiscale modeling could then be employed to fit a phenomenological constitutive law offline to the predictions of the molecular dynamics simulations. We note that molecular dynamics modeling for complex polymers is still limited and simulations with realistic microstructures remain very much an open research topic with connections to multiscale modeling (e.g., coarse graining).

Because multiscale modeling relies on the resolution of the material microstructure, accurate characterization of the initial state of residual stress, density, and statistical configuration of defects directly affect model predictions. The natural connection between the microstructure and performance therefore calls for establishing the link between processing and microstructure. Significant investments are already being made in this regard in the United States and elsewhere, such as the National Network for Manufacturing Initiative as a part of the Advanced Manufacturing Partnership. Such investments are likely to provide the means to obtain this critical information. Establishing the representative microstructures with correct defect distributions and stress states would also allow linking the uncertainty in the composite behavior to the microstructure state. This knowledge will ultimately help narrowing the uncertainty bounds in the predictions. Multiscale modeling could play a critical role in linking manufacturing to composite properties and ultimately composite performance and life.

References

Aboudi, J., 1982. A continuum theory for fiber-reinforced elastic-viscoplastic composites. J. Eng. Sci. 20 (55), 605–621.

Acharya, A., Sawant, A., 2006. On a computational approach for the approximate dynamics of average variables in nonlinear ode systems: toward the derivation of constitutive laws of the rate type. J. Mech. Phys. Solids 54, 2183–2213.

Babuska, I., 1975. Homogenization and application. Mathematical and computational problems. In: Hubbard, B. (Ed.), Numerical Solution of Partial Differential Equations—III, SYNSPADE. Academic Press, New York.

Babuska, I., Melenk, J.M., 1997. The partition of unity method. Int. J. Numer. Methods Eng. 40, 727–758.

Bahei-El-Din, Y.A., Rajendran, A.M., Zikry, M.A., 2004. Micromechanical model for damage progression in woven composite systems. Int. J. Solids Struct. 41, 2307–2330.

Benssousan, A., Lions, J.L., Papanicolaou, G., 1978. Asymptotic Analysis for Periodic Structures. North-Holland, Amsterdam.

Berlyand, L., Kolpakov, A.G., 2001. Network approximation in the limit of small interparticle distance of the effective properties of a high-contrast random dispersed composite. Arch. Ration. Mech. Anal. 159, 179–227.

Bogdanor, M., Mahadevan, S., Oskay, C., 2013a. Uncertainty quantification in damage modeling of heterogeneous materials. Int. J. Multiscale Comput. Eng. 11, 289–307.

Bogdanor, M., Crouch, R.D., Clay, S.B., Oskay, C., 2013b. Modeling Rate Dependent Damage Evolution in Composite Structures, vol. 1763. American Institute of Aeronautics and Astronautics, Reston, VA.

Chaboche, J., 1988. Continuum damage mechanics I: general concepts & II: damage growth, crack initiation and crack growth. J. Appl. Mech. 55, 59–72.

Chaboche, J., Kruch, S., Maire, J., Pottier, T., 2001. Towards a micromechanics based inelastic and damage modeling of composites. Int. J. Plasticity 17, 411–439.

Chakraborty, P., Ghosh, S., 2013. Accelerating cyclic plasticity simulations using an adaptive wavelet transformation based multitime scaling method. Int. J. Numer. Methods Eng. 93, 1425–1454.

Chamis, C.C., 2004. Probabilistic simulation of multi-scale composite behavior. Theor. Appl. Fract. Mech. 41, 51–61.

Chen, H., Hwang, S., Chen, H.S., 2006. Accelerated fatigue properties of unidirectional carbon/epoxy composite materials. Polym. Comp. 27, 138–146.

Chow, C., Wei, Y., 1991. A model of continuum damage mechanics for fatigue failure. Int. J. Fatigue 50, 301–306.

Cioranescu, D., Donato, P., 1999. An introduction to homogenization. Oxford Lecture Series in Mathematics and its Applications, 17 Oxford Univ. Press, Oxford, UK.

Coenen, E., Kouznetsova, V., Geers, M.G.D., 2012. Novel boundary conditions for strain localization analyses in microstructural volume elements. Int. J. Numer. Methods Eng. 90, 1–21.

Crouch, R., Clay, S., Oskay, C., 2013a. Experimental and computational investigation of progressive damage accumulation in CFRP composites. Compos. Part B: Eng. 48, 59–67.

Crouch, R., Oskay, C., 2010. Symmetric meso-mechanical model for failure analysis of heterogeneous materials. Int. J. Multiscale Comput. Eng. 8, 447–461.

Crouch, R., Oskay, C., 2015. Accelerated time integrator for multiple time scale homogenization. Int. J. Numer. Methods Eng. doi:10.1002/nme.4863.

Crouch, R., Oskay, C., Clay, S., 2013b. Multiple spatio-temporal scale modeling of composites subjected to cyclic loading. Comput. Mech. 51, 93–107.

Crouch, R.D., Oskay, C., Clay, S.B., 2012. Multiscale modeling of damage accumulation in carbon fiber reinforced polymers subjected to fatigue. In: 54th AIAA/ASME/ASCE/AHS/ASC Structures, Structural Dynamics, and Materials Conference, 1615 American Institute of Aeronautics and Astronautics, Reston, VA.

Dvorak, G.J., 1992. Transformation field analysis of inelastic composite materials. Proc. R. Soc. Lond. A 437, 311–327.

Engquist, W.B.E., Huang, Z., 2003. Heterogeneous multiscale method: a general methodology for multi-scale modeling. Phys. Rev. B 67 (9), 92–101.

Feld, N., Allix, O., Baranger, E., Guimard, J.M., 2012. A micromechanics-based mesomodel for unidirectional laminates in compression up to failure. J. Compos. Mater. 46, 2893–2909.

Feyel, F., Chaboche, J.L., 2000. Fe^2 multiscale approach for modelling the elastoviscoplastic behavior of long fiber SiC/Ti composite materials. Comput. Methods Appl. Mech. Eng. 183, 309–330.

Fish, J., Fan, R., 2008. Mathematical homogenization of nonperiodic heterogeneous media subjected to large deformation transient loading. Int. J. Numer. Methods Eng. 76, 1044–1064.
Fish, J., Oskay, C., 2005. A nonlocal multiscale fatigue model. Mech. Adv. Mater. Struct. 12, 485–500.
Fish, J., Shek, K., Pandheeradi, M., Shephard, M.S., 1997. Computational plasticity for composite structures based on mathematical homogenization theory and practice. Comput. Methods Appl. Mech. Eng. 148, 53–73.
Ghosh, S., Lee, K., Raghavan, P., 2001. A multi-level computational model for multi-scale damage analysis in composite and porous materials. Int. J. Solids Struct. 38, 2335–2385.
Ghosh, S., Moorthy, S., 1995. Elastic-plastic analysis of arbitrary heterogeneous materials with the Voronoi cell finite element method. Comput. Methods Appl. Mech. Eng. 121 (1–4), 373–409.
Gosz, M., Moran, B., Achenbach, J., 1992. Matrix cracking in transversely loaded fiber composites with compliant interphases. In: Damage Mechanics in Composites, AMD-150/AD-32. ASME, New York.
Guedes, J., Kikuchi, N., 1990. Preprocessing and postprocessing for materials based on the homogenization method with adaptive finite element methods. Comput. Methods Appl. Mech. Eng. 83, 143–198.
Hou, T., Wu, X., 1997. A multiscale finite element method for elliptic problems in composite materials and porous media. J. Comput. Phys. 134, 169–189.
Huet, C., 1999. Coupled size and boundary-condition effects in viscoelastic heterogeneous and composite bodies. Mech. Mater. 31, 787–829.
Joseph, D., Chakraborty, P., Ghosh, S., 2010. Wavelet transformation based multi-level scaling for crystal plasticity FE simulations under cyclic loading. Comput. Methods Appl. Mech. Eng. 199, 2177–2194.
Ladeveze, P., Lubineau, G., Marsal, D., 2006. Towards a bridge between the micro- and mesomechanics of delamination for laminated composites. Compos. Sci. Technol. 66, 698–712.
Liu, B., Lessard, L.B., 1994. Fatigue and damage-tolerance analysis of composite laminates stiffness loss, damage-modeling, and life prediction. Compos. Sci. Technol. 51, 43–51.
Llorca, J., Gonzalez, C., Molina-Aldareguia, J., Segurado, J., Seltzer, R., Sket, F., Rodriguez, M., Sadaba, S., Munoz, R., Canal, L.P., 2011. Multiscale modeling of composite materials: a roadmap towards virtual testing. Adv. Mater. 23, 5130–5147.
Mao, H., Mahadevan, S., 2002. Fatigue damage modelling of composite materials. Compos. Struct. 58, 405–410.
Mesarovic, S., Padbidri, J., 2005. Minimal kinematic boundary conditions for simulations of disordered microstructures. Philos. Mag. 85, 65–78.
Michel, J., Suquet, P., 2003. Nonuniform transformation field analysis. Int. J. Solids Struct. 40, 6937–6955.
Michel, J., Suquet, P., 2004. Computational analysis of nonlinear composite structures using the nonuniform transformation field analysis. Comput. Methods Appl. Mech. Eng. 193, 5477–5502.
Moulinec, H., Suquet, P., 1994. A fast numerical method for computing the linear and nonlinear properties of composites. C. R. Acad. Sci. Paris II 318, 1417–1423.
Moulinec, H., Suquet, P., 1998. A numerical method for computing the overall response of nonlinear composites with complex microstructure. Comput. Methods Appl. Mech. Eng. 157, 69–94.
Nemat-Nasser, S., Hori, M., 1999. Micromechanics: Overall Properties of Heterogeneous Materials. North-Holland, Amsterdam.

Oskay, C., 2012. Variational multiscale enrichment for modeling coupled mechano-diffusion problems. Int. J. Numer. Methods Eng. 89, 686–705.
Oskay, C., 2013. Variational multiscale enrichment method with mixed boundary conditions for modeling diffusion and deformation problems. Comput. Methods Appl. Mech. Eng. 264, 178–190.
Oskay, C., Fish, J., 2004a. Fatigue life prediction using 2-scale temporal asymptotic homogenization. Int. J. Numer. Methods Eng. 61, 329–359.
Oskay, C., Fish, J., 2004b. Multiscale modeling of fatigue for ductile materials. Int. J. Comp. Multiscale Eng., 2.
Oskay, C., Fish, J., 2007. Eigendeformation-based reduced order homogenization for failure analysis of heterogeneous materials. Comput. Methods Appl. Mech. Eng. 196, 1216–1243.
Oskay, C., Fish, J., 2008. On calibration and validation of eigendeformation-based multiscale models for failure analysis of heterogeneous systems. Comput. Mech. 42, 181–195.
Paas, M., Schreurs, P., Brekelmans, W.A.M., 1993. A continuum approach to brittle and fatigue damage theory and numerical procedures. Int. J. Solids. Struct. 30, 579–599.
Sanchez-Palencia, E., 1980. Non-homogeneous media and vibration theory. Lecture Notes in Physics, 127 springer-Verlag, Berlin.
Shiao, M., Chamis, C.C., 1999. Probabilistic evaluation of fuselage-type composite structures. Prob. Eng. Mech. 14, 179–187.
Sparks, P., Oskay, C., 2013. Identification of optimal reduced order computational models for failure of heterogeneous materials. Int. J. Multiscale Comput. Eng. 11, 185–200.
Sriramula, S., Chryssanthopoulos, M.K., 2009. Quantification of uncertainty modelling in stochastic analysis of FRP composites. Compos. A: Appl. Sci. Manuf. 40, 1673–1684.
Subramanian, S., Reifsnider, K., Stinchcomb, W.W., 1995. Residual strength and life prediction of composite laminates. Technical Report PL-TR-95-3006. Phillips Laboratory.
Suquet, P., 1987. Elements of homogenization for inelastic solid mechanics. In: Sanchez-Palencia, E., Zaoui, A. (Eds.), Homogenization Techniques for Composite Media. Springer-Verlag, Berlin.
Tadmor, E., Materials, R., Miller, E., 2011. Modeling Continuum, Atomistic and Multiscale Techniques. Cambridge University Press, UK.
Terada, K., Kikuchi, N., 1995. Nonlinear homogenization method for practical applications. In: Ghosh, S., Ostoja-Starzewski, M. (Eds.), Computational Methods in Micromechanics, AMD-212/MD-62. ASME, New York, pp. 1–16.
Ye, L., 1989. On fatigue damage accumulation and material degradation in composite materials. Compos. Sci. Technol. 36, 339–350.
Yuan, Z., Fish, J., 2009. Multiple scale eigendeformation-based reduced order homogenization. Comput. Methods Appl. Mech. Eng. 198, 2016–2038.
Yvonnet, J., He, Q., 2007. The reduced model multiscale method (R3M) for the non-linear homogenization of hyperelastic media at finite strains. J. Comput. Phys. 223, 341–368. doi:10.1016/j.jcp.2006.09.019.
Yvonnet, J., Monteiro, E., He, Q.C., 2013. Computational homogenization method and reduced database model for hyperelastic heterogeneous structures. Int. J. Multiscale Comput. Eng. 11, 201–225.
Zhu, R., Pan, E., Roy, A.K., 2007. Molecular dynamics study of the stress–strain behavior of carbon-nanotube reinforced Epon 862 composites. Mater. Sci. Eng. A 447, 51–57.

This page intentionally left blank

Part Four

Engineering and scientific applications of numerical modelling for analysis of failure in advanced composite materials

This page intentionally left blank

Micromechanical failure analysis of advanced composite materials

14

C. McCarthy*, T. Vaughan†
*University of Limerick, Ireland; †National University of Ireland, Galway, Ireland

14.1 Introduction

14.1.1 Background

Advanced composite materials are strong, lightweight, engineered materials consisting of high-performance reinforcing fibres embedded in a toughened polymeric matrix, to form a *ply* or *lamina*. A suitable number of lamina are then stacked at various orientations relative to each other according to a predefined stacking sequence to form a laminate, as illustrated in Figure 14.1. The laminate is then formed or reworked to become a structural member for use in high-performance systems, such as air and land transport vehicles and renewable energy structures, to name but a few. However, much of their development has been driven by the rapid expansion of the commercial aviation sector, with a new generation of efficient aircraft realising composite material usage accounting for upwards of 50% of the airframe structure (by weight). Realising such large composite structures presents a number of challenges, as accurate predictive tools and extensive physical testing are needed in both the design and certification phases of production. Also, the fabrication of such large composite assemblies requires advanced large-scale manufacturing and processing techniques.

However, despite the fact that composite materials are being used in primary load-bearing aircraft structures, current design practices and strength predictions are not fully mature and, surprisingly, there is a lack of supporting evidence that many of the ply-level failure criteria developed *thus far* could provide meaningful and accurate predictions for composite materials beyond a limited range of circumstances (Hinton and Soden, 1998). Failure in composite materials is a consequence of phenomena taking place at (or below) the microscopic scale and the difficulties associated with accurately predicting material failure is due to the inherent heterogeneity at this scale, that is, the existence of two phases in the material microstructure with vastly different constitutive behaviour. Local microscopic damage mechanisms, including fibre fracture, fibre–matrix debonding, and matrix micro-cracking contribute to gradual ply degradation. These local phenomena are rarely independent events as, through the process of damage accumulation, these local failures coalesce and traverse higher length scales until ultimately leading to macroscopic failure.

Thus, failure in an advanced composite is a multiscale process involving the interaction of a multitude of simultaneously occurring local damage mechanisms. This multiscale nature of damage is shown schematically in Figure 14.1, where damage initiates at the 'intra-ply level' through a number of local intra-ply failure

Numerical modelling of failure in advanced composite materials. http://dx.doi.org/10.1016/B978-0-08-100332-9.00014-1
Copyright © 2015 Elsevier Ltd. All rights reserved.

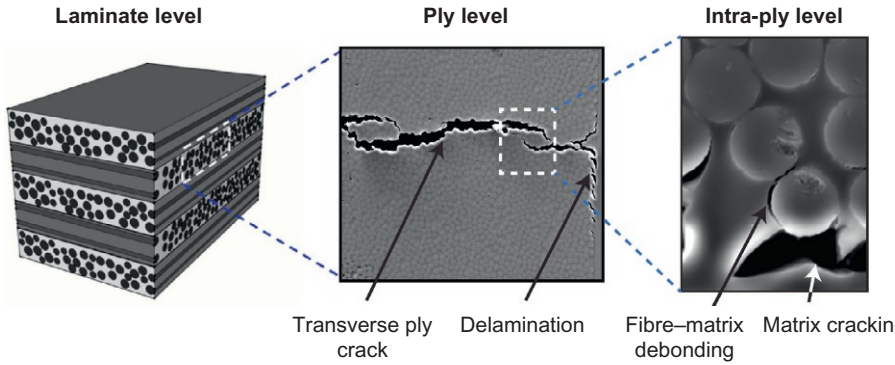

Figure 14.1 Hierarchical nature of damage in a composite from intra-ply-level damage at the microscale to delamination at the macroscale.
Redrawn using authors' own images following Hobbiebrunken et al. (2006) and Lafarie-Frenot et al. (2001).

mechanisms. At this level, fibre–matrix debonding occurs at the interface and, due to stress redistribution, matrix yielding/cracking occurs in adjoining matrix regions which, in turn, forms a transverse crack at the 'ply level'. From the ply level, the stress concentration at the tip of the transverse crack causes delamination at the ply boundary, as shown, and also results in stress redistribution to neighbouring plies, which can bring about earlier failure through fibre fracture, thus affecting the composite on the 'laminate level'.

Central to the prediction of any multiscale failure analysis of advanced composite materials and/or structures is the creation and validation of a suitable micromechanical model, and this chapter details the development, validation, and utilisation of one such micromechanics model developed by the authors over the past 5 years (Vaughan and McCarthy, 2010, 2011a, 2011b; McCarthy and Vaughan, 2012; Vaughan et al., 2012; O'Dwyer et al., 2012, 2013, 2014; Hardiman et al., 2012).

14.1.2 Rational

Previously, commercial design practices relied heavily on costly experimental tests on coupons and structural elements, as well as generous safety margins to accommodate material uncertainty. To advance the use of composite materials and maximise their application, predictive capabilities are advancing as an effective means to reduce certification costs as the industry moves towards certification by analysis supported by test and demonstration. The current state of the art in finite element (FE) modelling of damage and failure in composite structures uses continuum damage mechanics to predict ply degradation, where various internal damage mechanisms are generalised to create a damage tensor, upon which the mechanical properties depend. While these models allow for an adequate prediction of experimental non-linear behaviour, they still rely on non-physical material parameters, such as plasticity/damage coupling

factors, to account for non-linear behaviour (O'Higgins et al., 2011). Moreover, these models do not consider the microscopic development of failure and, consequently, offer little insight into *why* composites fail.

Hence, in order to predict microscopic damage accumulation and its effect on the macroscopic structure, multiscale modelling approaches have begun to appear in the literature. In particular, *computational micromechanics* has been shown to provide a suitable framework to present detailed predictions of local deformation mechanisms in heterogeneous materials (González & Llorca, 2007a,b). At a fundamental level, any loading situation on composite materials results in an interaction between the constituents, and so representing the fibre and matrix phases discretely in micromechanical simulations facilitates a better understanding of their influence on macroscopic and structural behaviour for both material scientists and engineers. Early computational micromechanics models resolved local stress and strain fields to analyse the effect of particle size, shape and distribution (Brockenbrough et al., 1991), thus establishing quantitative relations between the microstructure morphology and physical properties at higher length scales. Recent advances in fracture modelling means discrete micro-scale damage processes can be simulated through, for example, the use of cohesive zone models at particle interfaces. Llorca, González and co-workers (González & Llorca, 2007a,b; Totry et al., 2008; Canal et al., 2009) have combined these with non-linear constitutive models to describe the behaviour of individual phases, providing a computational framework that enables the prediction of diffuse and complex fracture patterns. The work from our group further develops this approach to better understand the failure behaviour of a carbon fibre/epoxy composite under a range of loading scenarios at both a material and a structural level. This chapter outlines the development of a micromechanics damage model that examines the failure behaviour of a carbon fibre/epoxy composite under a range of loading scenarios at both a material and a structural level.

14.1.3 Current state of the art

The field of micromechanics is extensive, and a wide range of strategies are available to predict material behaviour at multiple length scales, including periodic homogenisation models, mean field methods, bounding methods or embedding approaches. Extensive reviews that outline these methods have been carried out by Bohm (1998), Trias (2005) and more recently by Pindera et al. (2009). In the context of computational micromechanics, the method most widely used is the periodic homogenisation approach.

The accuracy of micromechanics-based failure predictions relies heavily on the definition of a suitable representative volume element (RVE). An RVE normally takes a form similar to that shown in Figure 14.2, where the fibres of diameter, d_f, are distributed within a square epoxy matrix domain, A, having a side of length, L. The distribution of fibres within the RVE should be statistically equivalent to the actual experimental microstructure (Grufman and Ellyin, 2008). A significant number of numerical and experimental strategies have been proposed to define suitable fibre arrangements in the RVE, including the authors' nearest neighbour algorithm

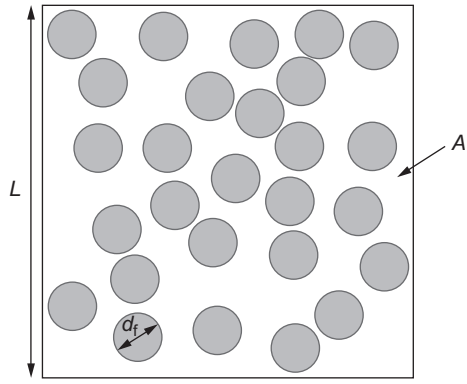

Figure 14.2 Idealised square RVE.

(NNA) (Vaughan and McCarthy, 2010), which will be used extensively in this chapter.

Indeed, the field of multiscale modelling, and more specifically, its implementation using commercial FE codes, is receiving much attention from academic researchers (Ghosh et al., 2007), aircraft manufacturers (de Boer and Poort, 2010) and commercial software developers (Firehole Technologies, 2009). The development of such tools can provide widespread access to novel multiscale computational approaches and, consequently, now has commercialisation potential. Indeed, the authors' NNA has also been streamlined into a software tool, and is available for download (McCarthy and Vaughan, 2012).

14.1.4 Chapter outline

This chapter begins by examining microstructure generation and characterisation, where we present real carbon fibre reinforced plastic (CFRP) microstructures. We present statistical characterisation of these microstructures, where a number of important statistical descriptors are defined and then used to create the NNA. The NNA is then used to create statistically equivalent microstructure geometries for input into the FE models. In Section 14.3, we describe FE model development. RVEs are defined and described along with periodic boundary conditions (PBCs) and non-linear material property modelling. Section 14.4 describes the prediction of mechanical properties for the composite, including macroscale modulus and strength predictions. Section 14.5 is dedicated to micromechanical analysis applications of macroscopic materials and structures, which includes the analysis of bonded composite joints. Micromechanical experimental calibrations and validation techniques are described in Section 14.6, with some applications. Finally, we close the chapter with conclusions and ways forward, future research topics and some information on related journals.

14.2 Microstructural characterisation and generation

14.2.1 Experimental characterisation of composite microstructures

This section considers the spatial arrangement of fibres in HTA/6376, a high-strength CFRP used extensively in the aerospace industry. Transverse sections were prepared for microscopy from a 2-mm thick, 16-ply unidirectional composite laminate using standard grinding and polishing techniques, which used a final particle size of 0.05 μm. The analysis considered 40 images from the transverse cross-sections, each measuring 320 μm × 240 μm and one of these is shown in Figure 14.3a. Digital image analysis was used to extract fibre diameters and x,y coordinates of each fibre centre by using a colour threshold in each image, as shown in Figure 14.3b.

14.2.2 Statistical characterisation of composite microstructure

The data extracted from the digital image analysis was used to generate statistical functions that characterise the morphology of the CFRP microstructure. Figure 14.4a shows the distribution of fibre diameters, which conformed to a lognormal distribution, as shown. The mean fibre diameter was 6.6 μm and the fibre volume fraction (V_f) was computed as 59.2%. To characterise the spatial arrangement fibres, nearest neighbour distribution, second-order intensity and radial distribution functions are considered to describe both short- and long-range interactions of fibres, which are discussed below.

14.2.2.1 Nearest neighbour distribution functions

Nearest neighbour distribution functions can detail the short-range interaction of fibres by analysing the distance between each fibre and their nth closest neighbour (Diggle, 2003). Shown respectively in Figure 14.4b and c are the first- and second-nearest neighbour distributions of fibres. These distributions exhibit narrow ranges, and high peaks

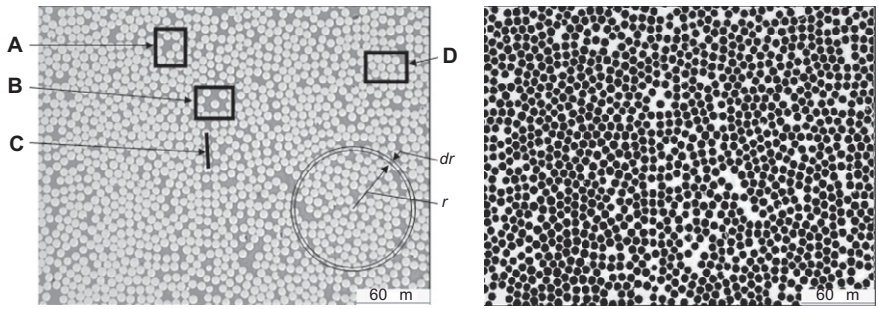

Figure 14.3 (a) Micrograph of HTA/6376 and (b) computed microstructure obtained using digital image analysis.

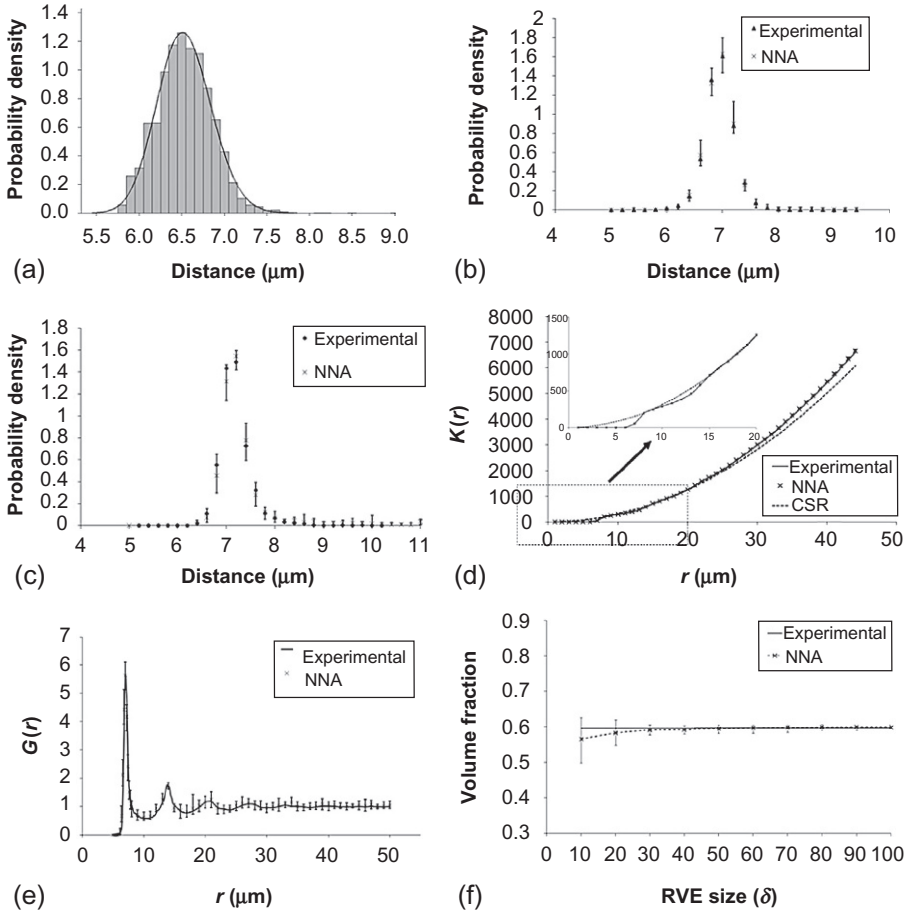

Figure 14.4 Statistical functions used to characterise both short- and long-range interactions of fibres within experimental microstructure and numerically generated microstructures (NNA). (a) Fibre diameter distribution fit to a lognormal distribution curve, (b) first nearest neighbour distribution function, (c) second-nearest neighbour distribution function, (d) second-order intensity function, (e) radial distribution function, and (f) effect of RVE size on fibre volume fraction.

occur at distances of 7 μm and 7.2 μm, respectively. From Figure 14.4a, the mean of the diameter distribution was found to be 6.6 μm, which implies that, for neighbouring fibres, the average inter-fibre spacing is in the region of 0.4–0.6 μm.

14.2.2.2 Second-order intensity functions

The second-order intensity function, $K(r)$, may be used to distinguish between different types of point patterns and is defined as the number of further points expected to lie within a radial distance, r, of an arbitrary point (see Figure 14.3a), divided by the number of points per unit area. The boundary of the domain has a significant effect when

calculating this function and an estimator which accounts for edge-correction has been established by Ripley (1977) as

$$K(r) = \frac{A}{N^2} \sum_{k=1}^{N} w_k^{-1} I_k(r) \tag{14.1}$$

where N is the total number of points in the area, A. $I_k(r)$ is the number of points lying within a radial distance, r, of a given fibre and w_k is the ratio of the circumference lying within the area, A, to the whole circumference of the circle. Shown in Figure 14.4d are the second-order intensity functions for the CFRP composite and a distribution that exhibits complete spatial randomness (CSR), described by $K(r) = \pi r^2$. It can be seen that the experimental curve is initially below the CSR curve and shows evidence of a slight stair shape, which is indicative of a certain amount of regularity in the fibre arrangement at shorter distances (i.e. $r \leq 15$ μm). However, at larger distances (i.e. $r > 15$ μm), the curve is above and diverging away from the CSR pattern, which is a result of long-range clustering.

14.2.2.3 Radial distribution functions

The radial distribution function can describe how the average fibre density varies as a function of distance from a given fibre centre. It is found by determining the number of fibres lying within an annular region of inner radius, r, and outer radius, $r + \mathrm{d}r$ (see Figure 14.3a) and dividing this by the average number of fibres per unit area. It is closely related to the derivative of the second-order intensity function and is mathematically defined as

$$G(r) = \frac{1}{N_a(2\pi r)} \cdot \frac{\mathrm{d}K(r)}{\mathrm{d}r} \tag{14.2}$$

where $\mathrm{d}K(r)$ is the average number of fibre centres lying within an annulus of inner radius, r, and outer radius, $r + \mathrm{d}r$, and N_a is the number of fibres per unit area. The measured radial distribution function of the CFRP microstructure, shown in Figure 14.4e, exhibits a large peak at a distance of 7 μm, which coincides with the peak seen in the first nearest neighbour distribution function (shown in Figure 14.4b). For the medium range (i.e. 10 μm $\leq r \leq$ 25 μm), the function exhibits some fluctuations, typical of a high-volume fraction composite, due to the physical area taken up by the fibres. At the long range (i.e. $r \geq 25$ μm), the function approaches unity as the value of r becomes large enough to be representative of the overall region, indicating that the microstructure is statistically homogeneous.

14.2.3 Numerical microstructure generation

14.2.3.1 Nearest neighbour algorithm

The NNA was developed to generate high-volume fraction fibre distributions that are statistically equivalent to the CFRP microstructure, characterised above. The importance of the short-range interaction of fibres has already been highlighted and so, to

accurately reproduce this, the NNA uses a bottom-up approach that populates a region using an *'adjusted'* measure of first- and second-nearest neighbour distribution functions (Vaughan and Mccarthy, 2010).

1. A random point is created having coordinates (x_1, y_1), lying in a sample square area, A. The diameter, d_1, of the surrounding fibre is drawn from a lognormal distribution fitting the experimentally measured diameter distribution, as shown in Figure 14.4a.
2. A second point is created (x_2, y_2), which is the centre of the first nearest neighbour of the previous fibre. The distance from (x_1, y_1) to (x_2, y_2) is assigned from the adjusted first nearest neighbour distribution function and the new point is oriented at a random angle θ_1, as shown in Figure 14.5a. The fibre diameter is assigned from the experimentally measured diameter distribution, as before.
3. A third point is created (x_3, y_3), which is the centre of the second-nearest neighbour of the first fibre. The distance from (x_1, y_1) to (x_3, y_3) is assigned from the adjusted second-nearest neighbour distribution function and the new point is oriented at a random angle θ_2, as shown in Figure 14.5b, while the fibre diameter is assigned from the experimentally measured diameter distribution.
4. The process is repeated for each fibre thereafter (see Figure 14.5c) until the sample area is filled, as shown in Figure 14.5d. The NNA ensures that none of the fibres overlap with one another and the fibres lie within the sample area chosen. If overlaps occur or a fibre is placed outside the sample area, orientation angles or inter-fibre distances are reassigned until a suitable configuration is found. If no suitable configuration can be found (i.e. near a boundary or in a region saturated with fibres), the algorithm will then move on to the next fibre and continue as before. For any fibre crossing a boundary, a corresponding fibre is placed on the opposing boundary to maintain geometric periodicity.

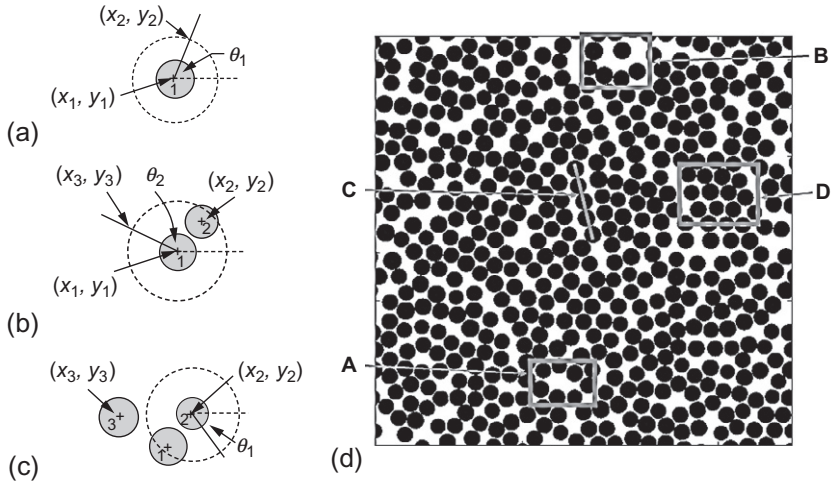

Figure 14.5 (a) Assigning a fibre's nearest neighbour, (b) assigning a fibre's second-nearest neighbour, (c) nearest neighbour being assigned for a subsequent fibre, and (d) generated distribution using nearest neighbour algorithm.

14.2.3.2 Statistical characterisation of numerical microstructures

A resulting microstructure measuring 165 μm × 165 μm is shown in Figure 14.5d, where the NNA is seen to reproduce short-range regularity, matrix-rich regions and 'lines' of fibres much the same as in the original micrograph (compare Figure 14.3a with Figure 14.5d). Four regions (A, B, C and D) have been identified in both images to highlight these similarities. A statistical analysis of 20 microstructures generated by the NNA has shown excellent correlation between nearest neighbour, radial and second-order intensity function when compared to the experimentally measured statistical functions, as shown in Figure 14.4b–e. This shows that the NNA re-creates both short- and long-range interactions of fibres of the original CFRP microstructure.

The effect of RVE size and resulting fibre volume fraction of a series of microstructures generated by the NNA is shown in Figure 14.4f, where there is a large variance in resulting V_f for the smallest models, i.e. $\delta = 10$, where δ is defined as the length of the side of the RVE (L) divided by the fibre radius (r_f). This is due to the relative size of the fibres compared to the overall RVE window size and the conditions the NNA uses when placing fibres near a boundary. For smaller models, the influence of the boundary is relatively large compared to the overall area of the RVE. The larger models (i.e. $\delta \geq 20$) are seen to converge close to the experimental fibre volume fraction of 59.2% showing very little variance in the fibre volume fractions being produced.

14.3 Finite element framework

14.3.1 Model description

14.3.1.1 Microstructural geometries

For micromechanical analyses, the NNA allows a range of RVEs to be generated that are statistically similar but topologically different. Figure 14.6a and b shows two-dimensional representations generated by the NNA that measured 66 × 66 μm ($\delta = 20$) and each containing approximately 80 fibres. These geometries were exported to the ABAQUS FE code using Python scripts to create two- and three-dimensional FE models. For the two-dimensional case, fibre and matrix regions were discretised using a quad-dominated mesh, consisting of predominantly four-noded (CPEG4) and a relatively small number of three-noded (CPEG3) full integration generalised plane strain elements. A layer of four-noded cohesive elements (COH2D4) was introduced between the fibre and the matrix to predict the onset of fibre–matrix debonding. In three dimensions, fibre and matrix regions were discretised using six-noded wedge elements (C3D6), whereas eight-noded cohesive elements (COH3D8) were introduced between fibre and matrix regions to predict fibre–matrix debonding. To ensure accurate prediction of shear bands in the matrix, sufficiently dense meshes consisting of approximately 85,000 elements were used. It was found that any increased mesh refinement provided no further accuracy to the solutions obtained (Vaughan, 2011).

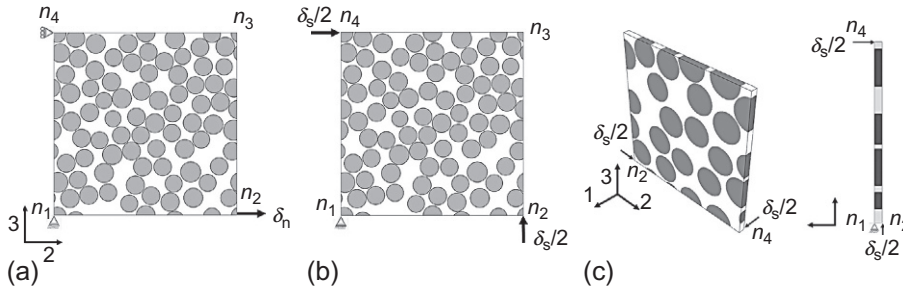

Figure 14.6 (a) Two-dimensional plane strain analysis of transverse tensile loading, (b) two-dimensional plane strain analysis of transverse shear loading, and (c) three-dimensional analysis of in-plane shear loading.

14.3.1.2 PBCs and mechanical loading

The micromechanical analyses used PBCs to ensure a macroscopically homogeneous stress/displacement field exists across the boundaries of the RVE (Van der Sluis et al., 2000; Terada et al., 2000). PBCs consist of a series of kinematic boundary ties to ensure that, in deformed configurations, there are both stress and displacement continuity on opposing RVE boundaries, which maintains spatial periodicity and allows the micro to macro transition. In three dimensions, the PBCs may be expressed as

$$\begin{aligned}
&\mathbf{u}(0, x_2, x_3) - \mathbf{u}(t, x_2, x_3) = \mathbf{u}_1 \\
&\mathbf{u}(x_1, 0, x_3) - \mathbf{u}(x_1, l, x_3) = \mathbf{u}_2 \\
&\mathbf{u}(x_1, x_2, 0) - \mathbf{u}(x_1, x_2, h) = \mathbf{u}_3
\end{aligned} \tag{14.3}$$

where $\mathbf{u_1}$, $\mathbf{u_2}$ and $\mathbf{u_3}$ are the displacement vectors that relate the displacements on opposite faces of the RVE shown in Figure 14.6c, while t, l and h correspond to the RVE dimensions in the 1, 2 and 3 directions, respectively. These conditions are used to impose a range of deformation modes on RVE models to characterise material behaviour.

The micromechanical analysis considers both two- and three-dimensional models. In the case of two-dimensional plane strain models, it is assumed that loading occurs in the 2–3 plane and kinematic ties are therefore only active in the 2 and 3 directions. For transverse tensile loading, a relative displacement is applied in the 2 direction (δ_t) through the control node n_2, such that $\mathbf{u}_2 = (0, \delta_n, 0)$, as shown in Figure 14.6a. In a similar fashion, transverse shear loading may be induced by applying a relative displacement in the 2 and 3 directions (δ_s) through the control nodes n_2 and n_4, such that $\mathbf{u}_2 = (0, 0, \delta_s/2)$ and $\mathbf{u}_3 = (0, \delta_s/2, 0)$, as shown in Figure 14.6b. Similarly, in three dimensions (see Figure 14.6c), in-plane shear may be applied using a relative displacement in the 1 and 2 directions through the control nodes n_2 and n_4, such that $\mathbf{u}_1 = (0, \delta_s/2, 0)$ and $\mathbf{u}_2 = (\delta_s/2, 0, 0)$, as shown in Figure 14.6c. The control node, n_1, remains fully constrained throughout to prevent rigid body motion during deformation. Note that throughout this chapter, these loading regimes, which do not include thermal residual stresses, are referred to as the mechanical loading (ML) cases.

14.3.1.3 Thermal loading

The effect of thermal residual stresses has also been considered in a number of micromechanical models presented. These are formed during cooling of the material from cure temperature (448 K) to room temperature (298 K). To characterise the effect of thermal residual stress on the macroscopic behaviour of the material, an initial thermal load, $\Delta T = -150$ K, was applied globally to each node in the RVE, and this was subsequently followed by a mechanical load, as described above. Note that throughout this chapter, this loading regime is referred to as the thermo-mechanical loading (TML) case.

14.3.1.4 Volume-based homogenisation

The homogenisation procedure relates the microscopic state variables, in this case the local stress and strain fields, to the macroscopic averaged quantities. To evaluate the average stresses ($\overline{\sigma}_{ij}$) and strains ($\overline{\varepsilon}_{ij}$) over the RVE, the following relations may be used:

$$\overline{\sigma}_{ij} = \frac{1}{V}\sum_{k=1}^{n}\left(\sigma_{ij_k}V_k\right) \tag{14.4}$$

$$\overline{\varepsilon}_{ij} = \frac{1}{V}\sum_{k=1}^{n}\left(\varepsilon_{ij_k}V_k\right) \tag{14.5}$$

where V is the total volume of the RVE, k is the element number, V_k is the volume of element k in the FE mesh, n is the total number of elements and σ_{ij} and ε_{ij} are the ij stresses and strains, respectively, in the element k. The effective properties can be determined from the relevant stress–strain ratio for a given loading condition, that is,

$$E_{ij} = \frac{\overline{\sigma}_{ij}}{\overline{\varepsilon}_{ij}} \tag{14.6}$$

14.3.1.5 Surface-based homogenisation

A surface-based homogenisation scheme may be more conveniently used to determine the average stresses ($\overline{\sigma}_{ij}$) and strains ($\overline{\varepsilon}_{ij}$) of an RVE undergoing microscopic damage processes. This involves computing the average stresses from surface tractions acting on edges (two dimensional) or faces (three dimensional) of an RVE.

14.3.2 Constituent material behaviours

14.3.2.1 Fibres

The HTA fibres were assumed here to be orthotropic linear elastic, and their mechanical properties were taken from Fiedler et al. (2005a) and are listed in Table 14.1.

Table 14.1 Constituents' thermomechanical properties (Fiedler et al., 2005a)

Elastic properties	Fibre (HTA)	Matrix (6376)
E_{11} (GPa)	238	3.63
E_{22} (GPa)	28	0.34
E_{33} (GPa)	28	
ν_{12}	0.23	
ν_{23}	0.33	
ν_{31}	0.03	
G_{12} (GPa)	24	
G_{23} (GPa)	7.2	
G_{31} (GPa)	24	
Coefficients of thermal expansion		
α_{11} (K^{-1})	-0.1×10^{-6}	10×10^{-6}
α_{22} (K^{-1})	10×10^{-6}	
α_{33} (K^{-1})	10×10^{-6}	

14.3.2.2 Matrix

The 6376 epoxy matrix was assumed to be an elastic–plastic solid whose thermoelastic constants are summarised in Table 14.1. The yielding behaviour of the polymer matrix is sensitive to hydrostatic stress, and as a result, the Mohr–Coulomb yield criterion was employed. The Mohr–Coulomb criterion states that yielding will occur on a given plane when the shear stress (τ) exceeds the cohesive stress of the material plus the frictional force acting along the failure plane, such that

$$\tau = c - \sigma_{\mathrm{n}} \tan\phi \tag{14.7}$$

where c is the cohesion yield stress, σ_{n} is the normal stress acting on the failure plane and ϕ is the angle of internal friction. In Mohr's stress plane (see Figure 14.7a), the yield surface of the Mohr–Coulomb model can be expressed in terms of the maximum and minimum principal stresses such that,

$$f(\sigma_1, \sigma_3) = (\sigma_1 - \sigma_3) + (\sigma_1 + \sigma_3)\sin\phi - 2c\cos\phi = 0 \tag{14.8}$$

where σ_1 and σ_3 are the maximum and minimum principal stresses, respectively. For the Mohr–Coulomb model, the cohesion stress and the angle of internal friction can be related to the tensile (σ_{T}) and compressive (σ_{C}) strengths of the material by the following expressions,

$$\sigma_{\mathrm{T}} = 2c\frac{\cos\phi}{1+\sin\phi} \tag{14.9}$$

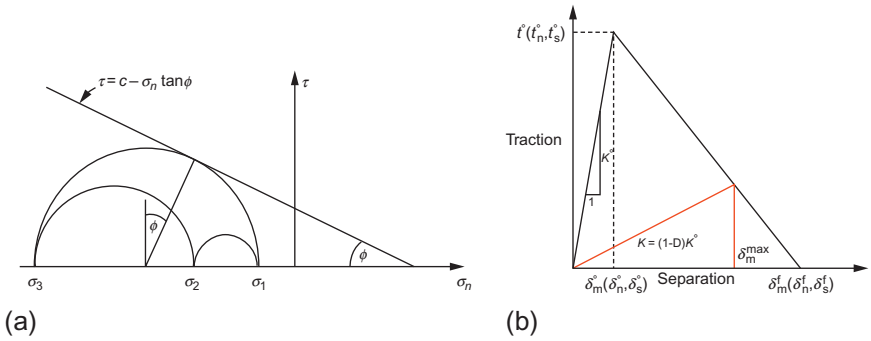

Figure 14.7 (a) Mohr–Coulomb yield locus in the Mohr stress space and (b) traction-separation law governing behaviour of cohesive elements.

$$\sigma_C = 2c\frac{\cos\phi}{1-\sin\phi} \tag{14.10}$$

Based on the tensile and compressive strengths of the 6376 matrix ($\sigma_T = 103$ MPa and $\sigma_C = 264$ MPa; Fiedler et al., 2005b), the internal friction angle and cohesion stress for the 6376 epoxy matrix were found to be $\phi = 26°$ and $c = 82$ MPa, respectively. A non-associative flow rule was used to compute the direction of plastic flow in which the dilatant angle is assumed to be zero.

14.3.2.3 Fibre–matrix interface

The behaviour of the fibre–matrix interface was modelled using cohesive elements available in ABAQUS, which introduce a displacement discontinuity at the fibre–matrix interface when the local stress satisfies a critical condition. Their constitutive response is defined in terms of a traction-separation law which relates the separation displacement between the top and bottom faces of the element to the traction vector acting upon it. Figure 14.7b shows that the initial response of the traction-separation model is assumed to be linear elastic. An initial elastic stiffness of $K = 10^5$ GPa/m was used to ensure the displacement continuity at the interface in the absence of damage. The initial linear response is followed by the initiation of damage, based on the maximum stress criterion, which is followed by linear softening. Failure of the interface initiates when either the normal stress (t_n) or the shear stress (t_s) exceed the predefined normal (t_n^o) or shear (t_s^o) strengths. The evolution of damage at the interface is controlled by a linear softening curve, meaning that once the failure stress is exceeded, the element stiffness reduces linearly until complete failure at a specified normal (δ_n^f) or shear (δ_s^f) displacement. This effective displacement at failure (δ^f) determines the rate of damage in the element, and this was defined in terms of the fracture energy, Γ, which corresponds to the area under the traction-separation curve. For simplicity, it was assumed that the interfacial normal strength was equal to the interfacial shear strength, that is, $t_n^o = t_s^o$, and the fracture energies were the same for mode I

and mode II type failure. Different normal and interfacial shear strengths and mode mixity have also been implemented, and the reader is referred to O'Dwyer et al. (2014) for more details.

14.4 Prediction of mechanical behaviour

14.4.1 Homogenised effective properties

Within the linear regime, effective properties were calculated for numerically generated microstructures of increasing size using a volume-averaged homogenisation procedure. Twenty microstructures were generated using the NNA at each value of δ and Figure 14.8a and b shows the mean values of the homogenised effective properties. Error bars have been included indicating the maximum and minimum values calculated at each value of δ, with a large variance evident at low values of δ as a result of the wide range of fibre volume fractions, caused by boundary effects. It was determined that the effective properties converged to a constant value when $\delta = 20$, where it was found that the maximum and minimum values of all 20 generated microstructures fell within 10% of the mean values and showed good correlation to experimental results.

14.4.2 Interfacial stress state under transverse loading

Radial plots of the stress distribution within the interface, following the approach outlined in Hojo et al. (2009), are shown in Figures 14.9 and 14.10. The plots have been arranged such that the highlighted fibre in Figure 14.10a has been isolated and compared to the single fibre case in Figure 14.9a. The normal (t_n) and shear (t_s) tractions in the interface of the fibre have been plotted radially. The edge of the fibre represents the zero axis for t_n and t_s. The absolute value of t_n has been plotted for clarity (as positive and negative shear generally contribute equally to the damage initiation criteria). In

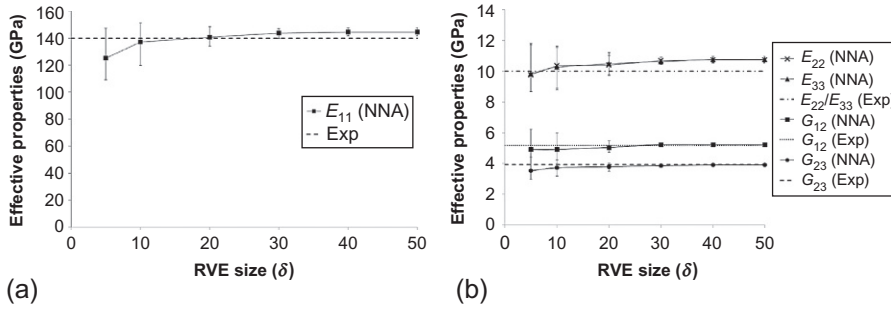

Figure 14.8 Effective properties of the numerically generated microstructures in (a) the longitudinal direction and (b) the transverse and in-plane directions.
Experimental values (denoted by 'Exp') are taken from O'Higgins et al. (2008).

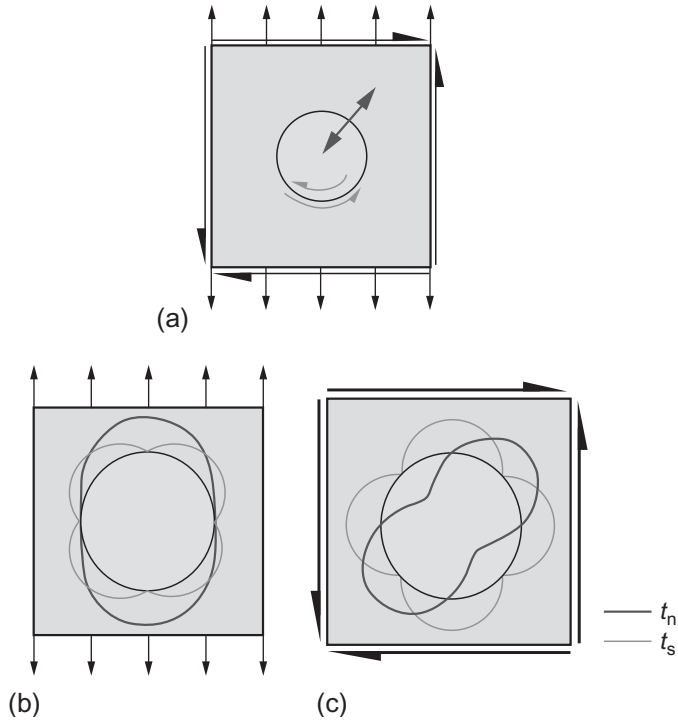

Figure 14.9 (a) Single-fibre RVE; normal and shear interfacial tractions under (b) transverse tension and (c) transverse shear.

addition, negative values of t_n (although shown) are generally not considered in the failure initiation criteria.

14.4.2.1 Single fibre RVE

A number of important interfacial stress distribution characteristics are visible in Figure 14.9 for the single fibre case. The most important, with relation to this study, is the relative magnitude of t_n and t_s, shown in Figure 14.9b and c, respectively. Under transverse tension, t_n is twice the magnitude of t_s and no compressive interfacial stress was observed. An analytical solution for this case has been presented previously (Lesne et al., 1995) which produces distributions of t_n and t_s, which are almost indistinguishable from those shown here. Under transverse shear, the magnitude of t_n and t_s are equal, with a large compressive t_n stress.

14.4.2.2 Multifibre RVE

Figure 14.10b and c shows distributions of t_n and t_s for the fibre in Figure 14.10a marked 'A', in a multifibre RVE, generated using the NNA. Under transverse tension and shear, the effect of the neighbouring fibres on the distribution of t_n around the fibre

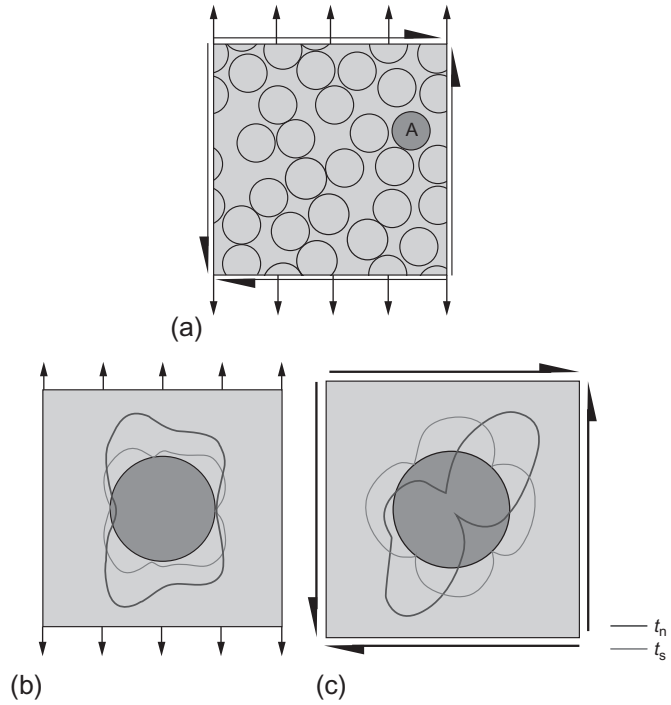

Figure 14.10 (a) Multifibre RVE; normal and shear interfacial tractions under (b) transverse tension and (c) under transverse shear.

is illustrated by the irregular shape of t_n. Local maxima of t_n are found to be located along lines connecting the centres of the nearest adjacent fibres, and an amplification of t_n relative to t_s was found in comparison to the single fibre case (shown in Figure 14.9b). It can be seen that the shape of the distribution of t_s is not as strongly influenced by the presence of the neighbouring fibres. It can also be seen that t_n is now larger than t_s in both transverse tension and shear, where the magnitude of both were equal in the single fibre case under transverse shear.

14.4.3 Micromechanical damage models

14.4.3.1 Effect of fibre–matrix interface strength

Figure 14.11a shows the transverse tensile behaviour of an RVE having a range of interfacial strengths under both mechanical (ML) and thermo-mechanical loading (TML). The strength of the fibre–matrix interface largely dictated the macroscopic response of the RVE, with a higher transverse strength being seen for increasing fibre–matrix interfacial strength for the ML and TML cases. Under transverse tensile loading, a weak interface ($t^o_{n/s} = 15\,\text{MPa}$) results in the lowest transverse strength, with non-linear

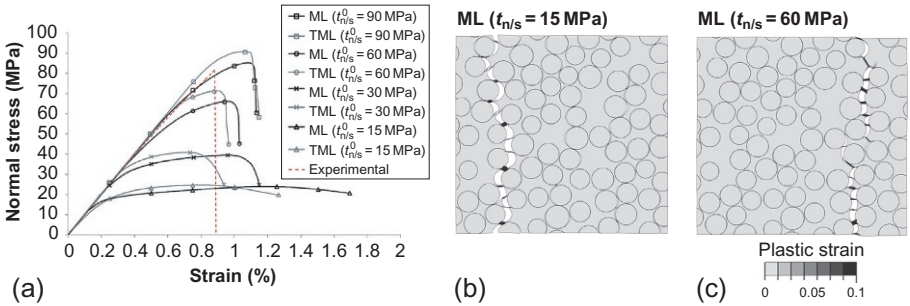

Figure 14.11 (a) Transverse tensile behaviour of an RVE generated by the NNA for a range of various interfacial strengths under both ML and TML loading, compared to experimental results obtained from O'Higgins et al. (2011). Damage progression during transverse tensile loading through an RVE that had a fibre–matrix interface strength of (b) $t_{n/s} = 15$ MPa and (c) $t_{n/s} = 60$ MPa.

behaviour observed at a relatively low strain level. Due to the relatively low interfacial strength (compared to the yield stress of the matrix), failure was dominated by fibre–matrix debonding and very little matrix yielding was evident, as shown in Figure 14.11b. For a stronger fibre–matrix interface ($t^o_{n/s} = 60$MPa), matrix yielding becomes more prevalent as the interface strength begins to approach the cohesion stress of the matrix ($c = 82$ MPa) and this interaction between both damage modes was effective in changing the final fracture path of the RVE, as shown in Figure 14.11c, when compared to an interface strength of $t^o_{n/s} = 15$MPa (see Figure 14.11b).

Shown in Figure 14.12a is the transverse shear behaviour of an RVE having a range of interfacial strengths under both ML and TML. Again, the fibre–matrix interface strength governs the macroscopic response and ultimate strength of the material. For an interfacial strength of $t^o_{n/s} = 60$MPa, the transverse shear strength is lowest and non-linear behaviour occurs very early in the loading history. Final fracture of the material is manifested as a dominant band of interface cracks orientated approximately perpendicular to the main

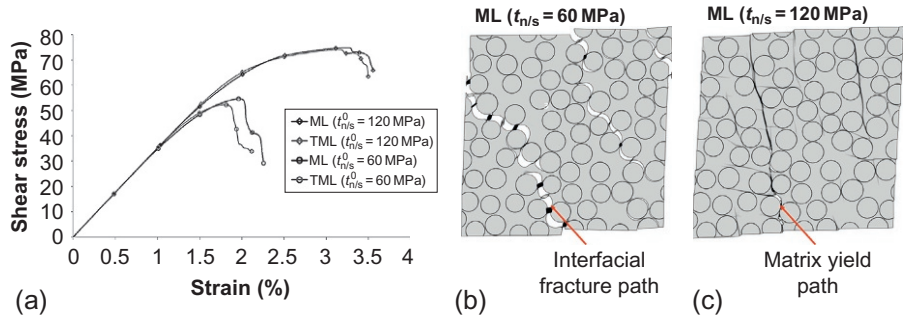

Figure 14.12 (a) Transverse shear behaviour of an RVE generated by the NNA for a range of various interfacial strengths under both ML and TML loading; (b) fracture path of the RVE under ML for (b) $t^o_{n/s} = 60$ MPa and (c) $t^o_{n/s} = 120$ MPa.

principal tensile loading axis, as shown in Figure 14.12b. For an interfacial strength of $t^o_{n/s} = 120$ MPa, failure of the material is governed by the matrix behaviour as the interface strength is larger than the matrix yield stress (i.e. $c = 82$ MPa) and the final fracture path is made up of a combination of heavily yielded matrix regions, oriented almost parallel to both the horizontal and vertical shear loading axes, together with a number of interfacial cracks brought about by high shear stresses that resulted from extensive matrix yielding, as shown in Figure 14.12c.

14.4.3.2 Effect of interface fracture energy

Figure 14.13a shows the transverse shear response of an RVE that had an interfacial strength of $t^o_{n/s} = 60$ MPa for the range of interfacial fracture energies. Increasing the interfacial fracture energy improved both the transverse shear strength and strain-to-failure of the material. It is interesting to compare fracture paths through an RVE for the lowest ($\Gamma = 2.5$ J/m^2) and highest ($\Gamma = 100$ J/m^2) fracture energies considered, as shown in Figure 14.13b and c, respectively. For the lowest interface fracture energy ($\Gamma = 2.5$ J/m^2), damage was limited to the fibre–matrix interfaces and yielding of intermediate matrix bridges between neighbouring debonding fibres. Meanwhile, for the highest fracture energy considered ($\Gamma = 100$ J/m^2), fibre–matrix debonding was widespread across the RVE and the slow rate of softening at the interface promoted extensive yielding in matrix regions adjoining interfacial cracks, as shown in Figure 14.13c. The slow rate of softening leads to a higher transverse shear strength and means that damage is more effectively dissipated over the entire RVE, producing favourable response characteristics, such as increased strength and higher strain to failure.

14.4.4 Damage accumulation under cyclic loading

Composite materials exhibit a sequential accumulation of a multitude of hierarchical dissipative mechanisms, whose initiation and subsequent propagation depends heavily on the loading history. Micromechanics may be used to illustrate this complex damage accumulation process by subjecting an RVE ($t^o_{n/s} = 90$ MPa, $\Gamma = 10$ J/m^2) to a

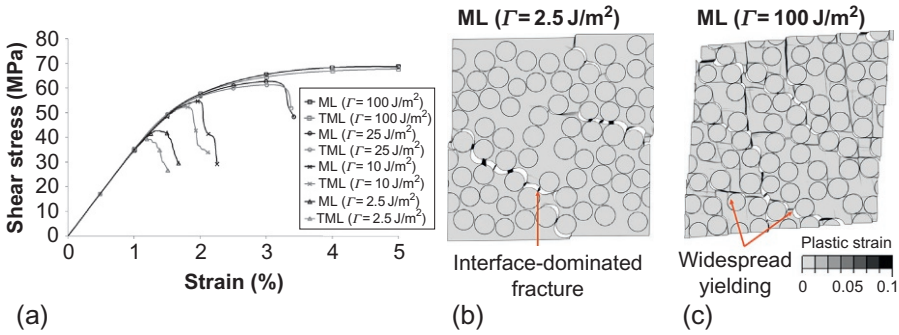

Figure 14.13 (a) Effect of fracture energy on transverse shear behaviour; progression of damage through an RVE with interfacial fracture energies of (b) $\Gamma = 2.5$ J/m^2 and (c) $\Gamma = 100$ J/m^2.

regime of successive transverse tensile ($\varepsilon_{22} = 1\%$) and compressive ($\varepsilon_{22} = -2\%$) loadings, followed by a subsequent transverse tensile load to failure ($\varepsilon_{22} = \varepsilon_f$). Figure 14.14 shows that the initial transverse tensile load (Path O-A) causes non-linear behaviour as a result of fibre–matrix debonding and yielding in the matrix, which are shown for the Load Point A in the RVE insert to Figure 14.14a. The unloading path of the material (Path A–B) shows a reduced slope denoting a loss in material stiffness caused by crack opening at fibre–matrix interfaces. Also, unloading does not take place through the origin (O) as some permanent plastic strain remains in the material. However, crack closure does occur at debonded interfaces during the unloading phase, as shown by the final configuration of the RVE at the Load Point B in the RVE insert to Figure 14.14b. Upon subsequent compressive loading (Path B–C), the compressive modulus is recovered to almost that of the undamaged material as a result of crack closure and compressive load take up between the newly formed crack faces. Further non-linear behaviour in the compressive loading phase is seen as a result of more fibre–matrix debonding and matrix yielding occurring, as shown at the Load Point C in the RVE insert to Figure 14.14c. A reduction in the compressive modulus is seen during the next unloading phase (Path C–D) as a result of damage occurring during compressive loading. Again, unloading does not take place through the origin as a new permanent

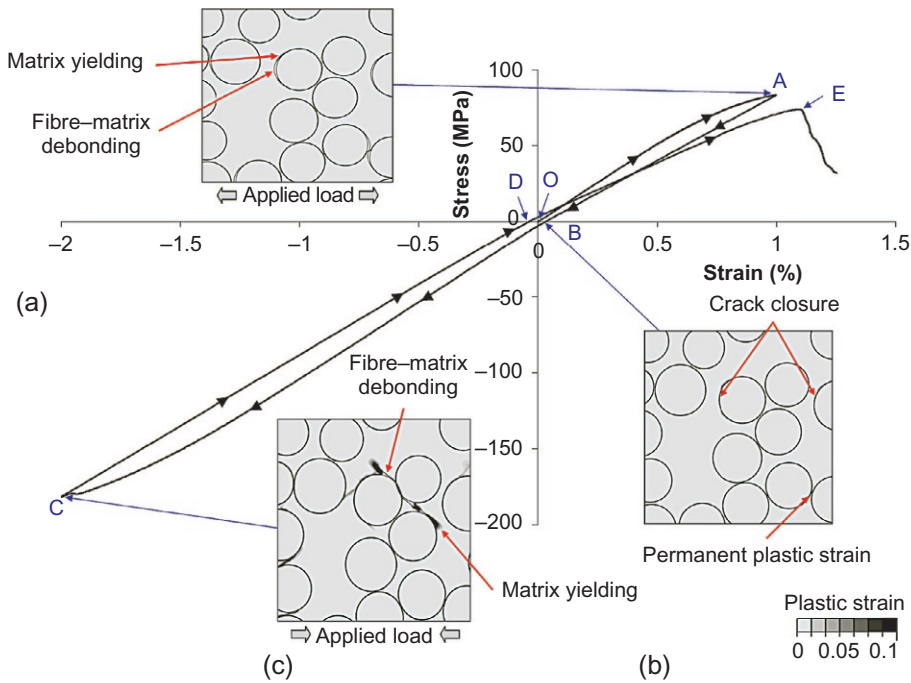

Figure 14.14 The response of an RVE subject to successive tensile and compressive loading and microscopic damage accumulation observed, (a) following initial tensile loading (Load Point A); (b) following unloading from tensile stress state (Load Point B) and; (c) following subsequent compressive loading (Load Point C). (*Note:* a deformation scale factor of five has been used in the above images.)

plastic strain exists in the material as a result of the previous loading cycles. Upon subsequent tensile loading (Path D–E), a further reduction in the tensile modulus is also seen (compared to the unloading phase in Path A–B) as a result of cracks developed during the previous compressive loading phase. It is also noticeable that the tensile strength for this cycle has reduced, which indicates that the material was at the cusp of its ultimate tensile strength at Load Point A. The compression damage sustained during the previous load cycle was enough to actually trigger ultimate failure (i.e. Load Point E) in the composite at a lower stress than at Load Point A.

14.5 Applications to failure surfaces and structural load cases

In this section, we develop further the micromechanical model to reproduce the well-known interactive failure criteria of Hashin (1980). In addition, the model is further extended to a structural load case where an adhesive bond-line is added to the RVE to form a micromechanical model of a bonded composite joint.

14.5.1 Generation of failure surfaces

14.5.1.1 Effect of thermal residual stress on transverse failure surface

Failure of the material was predicted under a combination of transverse shear and transverse normal loads to examine the effect of thermal residual stress on the failure surface in the transverse plane. By varying the ratio of the applied transverse shear/normal displacements (δ_s/δ_n), a failure envelope for the material was constructed for both the ML and TML cases. Figure 14.15 shows the failure envelope generated for both the ML and TML cases in the $\sigma_{22} - \tau_{23}$ stress space, where an interface strength of $t^o_{n/s} = 60\text{MPa}$ and a fracture energy of $\Gamma = 10\ \text{J/m}^2$ was assumed, meaning that failure was dominated by interface cracking. The inclusion of thermal residual stress has meant that the TML case has been shifted and slightly contracted compared to the ML case. This shift in the fracture surface occurs as, for tension-dominated loading, thermal residual stress has a beneficial effect on the failure strength. This is due to the large compressive stresses that exist at the interface following thermal cool-down from cure temperature, which effectively delay the onset of debonding. As the loading begins to become shear dominated, the presence of thermal residual stress begins to affect the fracture surface negatively, as increased interfacial shear stress following the thermal loading phase contributes to earlier failure of the material. For compression-dominated loading, thermal residual stress shows slightly negative effects as failure at the interface must occur due to shear failure (*note*: a compressive stress at the interface cannot cause debonding to occur). The largest difference between the ML and TML failure surfaces occurs for a loading ratio of $\delta_s/\delta_n = -4$. Interestingly, the fracture path for this loading ratio comprises a series

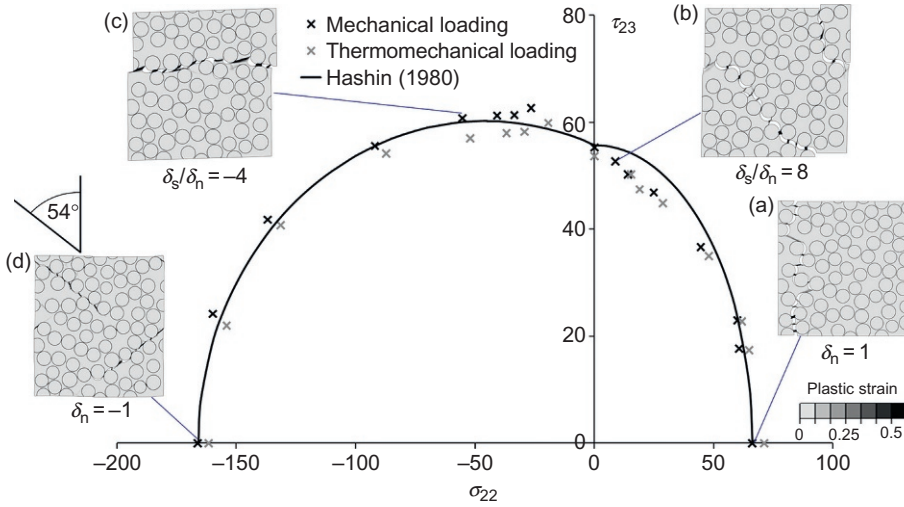

Figure 14.15 Failure surface generated by micromechanical models using combined transverse normal and shear loading regime.

of interfacial cracks orientated parallel to the horizontal shear loading axis, as shown in Figure 14.15c, indicating that the failure at these interfaces was shear dominated.

14.5.1.2 *Effect of local fibre volume fraction on transverse failure surface*

To consider the effect of fibre volume fraction (V_f) on the transverse behaviour, a series of RVEs were generated with fibre volume fractions of $V_f = 20\%$, $V_f = 40\%$ and $V_f = 59\%$. The NNA was used to generate the microstructures for $V_f = 59\%$, while a hard-core model was used to generate microstructures for both $V_f = 20\%$ and $V_f = 40\%$, as shown in Figure 14.16a–c. Figure 14.16d shows the effect of fibre volume fraction on the transverse failure surface when a fibre–matrix interface strength of $t^o_{n/s} = 60\,\text{MPa}$ and a fracture energy of $\Gamma = 10\ \text{J/m}^2$ were assumed. For this interface-dominated failure, it was found that reducing the fibre volume fraction actually results in a slight expansion of the transverse failure surface. Figure 14.16d shows only a slight difference between the failure surfaces of 40% and 59% fibre volume fraction; however, the 20% fibre volume fraction shows much higher failure strengths for all loading ratios. This higher transverse strength for lower fibre volume fractions can be attributed to the larger inter-fibre spacing between neighbouring fibres (however, it should be noted that the longitudinal strength would decrease with decreasing fibre volume fraction). Thus, in lower fibre volume fraction arrangements, the larger inter-fibre spacing effectively delays the onset of debonding, resulting in higher strengths for each loading ratio. Figure 14.16e shows the effect of fibre volume fraction on the transverse failure surface for a perfect fibre–matrix interface, such that failure was matrix dominated. In contrast to interface-dominated failure, reducing the fibre volume fraction in the case of matrix-dominated failure

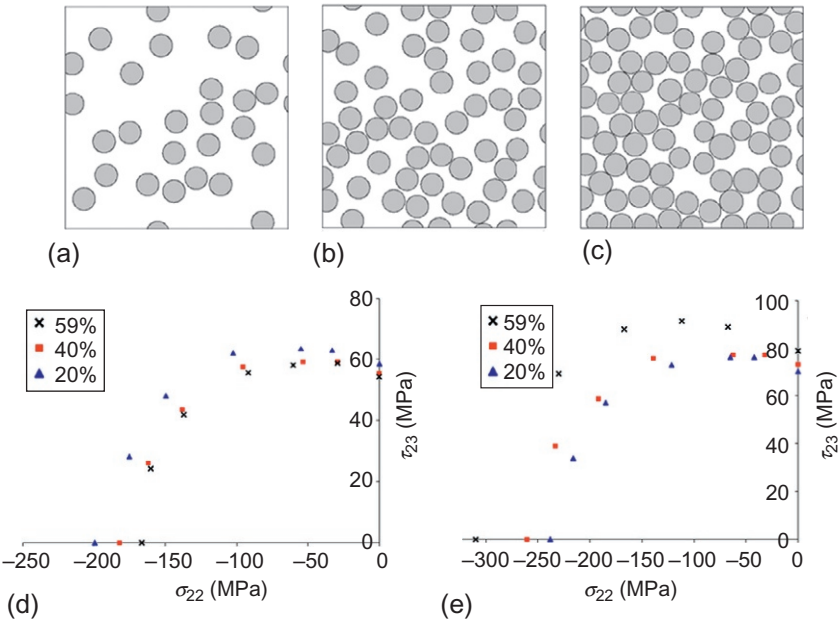

Figure 14.16 Fibre distributions generated at (a) $V_f = 20\%$, (b) $V_f = 40\%$ and (c) $V_f = 59\%$; effect of fibre volume fraction on transverse failure surface for (d) interface-dominated failure and (e) matrix-dominated failure.

resulted in a contraction of the transverse failure surface, as shown in Figure 14.16e. This is caused by the lack of reinforcement in low fibre volume fraction configurations, which allows matrix yield paths to propagate more easily.

14.5.2 Micromechanical modelling of bonded composite joints

A novel application of RVEs is to extend and augment them to model subsections of composite structures. In this case, we extend the RVE developed earlier in this chapter to model composite bonded joints. The proposed FE model consists of a microscale RVE of the interface between a composite ply and an adhesive layer, away from the edges of an adhesive joint. The two sections are separated by a damageable interface referred to here as the bond-line. The model is shown in terms of an adhesive single-lap joint with composite adherands in Figure 14.17, where the axial load, F, on the joint induces Mode *I* and Mode *II* deformations on the composite–adhesive interface. The material models used here are similar to those shown in Figure 14.7, more details are listed in O'Dwyer et al. (2013).

14.5.2.1 Bond-line strength effects

A key advantage of modelling subsections of bonded joints with micromechanical models is that design variables, such as bond-line strength, can be varied to examine '*what-if*' scenarios. In Figure 14.18a, the strength of the composite joint is plotted

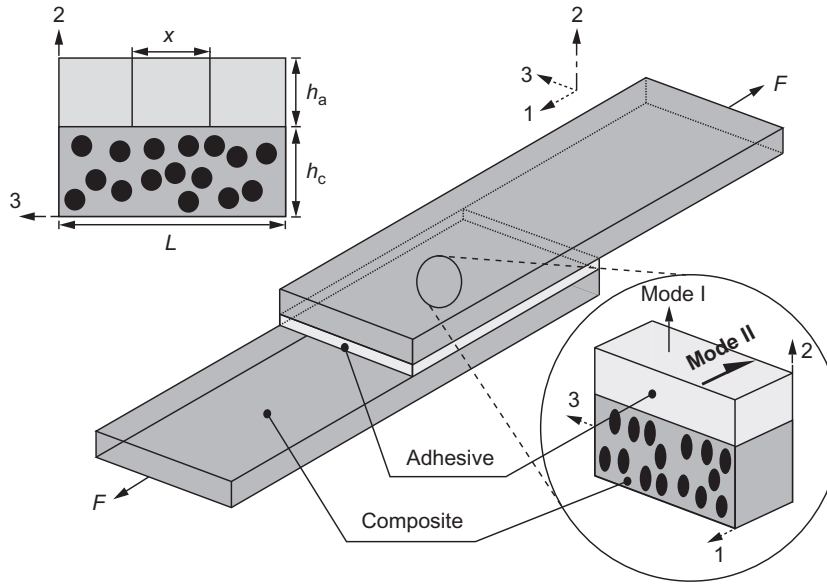

Figure 14.17 Adhesive layer model as applied to a composite bonded joint, including local reinforcement orientations. The dimensions L and x are the width of the RVE and the weakened central region of the bond-line, respectively.

against the bond-line strength (i.e. the composite–adhesive interface strength). It can be seen in Figure 14.18a that under mode I loading, joint strength increases linearly with respect to bond-line strength until a maximum is reached at a bond-line strength (t_n^c) of approximately 77 MPa. Any further increase in bond-line strength produces no increase in joint model strength. This corresponds to the condition where the damage

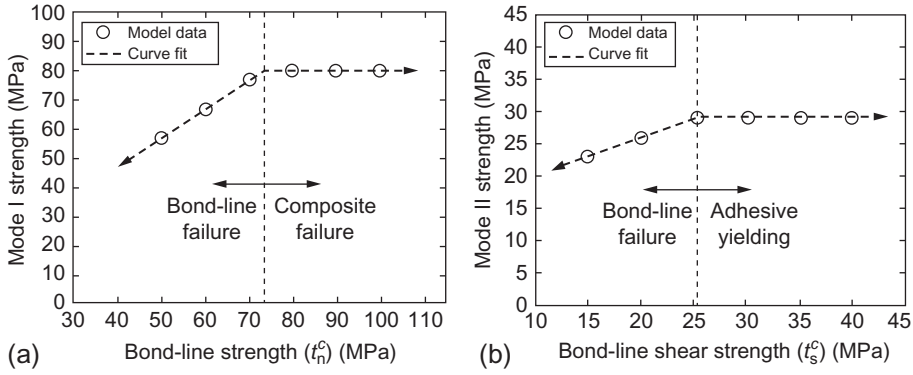

Figure 14.18 Bond strength variation, (a) bond-line model strength variation under mode I; (b) bond shear strength variation under mode II.

processes transfers from the bond-line to the composite region, as the bond-line strength exceeds that of the composite. Similar trends are found in Figure 14.18b, where a plateau is reached once the shear strength of the bond-line (t_s^c) exceeds 25 MPa. This corresponds to the point where the damage process transfers to the adhesive. The critical bond-line strength is slightly lower than the yield point, under shear, of the adhesive, which can be attributed to stress concentrations (caused by the fibres) propagating into the adhesive and initiating adhesive yielding.

14.5.2.2 Failure modes and modelling first-ply failure

Failure at the bond-line and within the composite region has been reported from adhesive bonding tests and a mix of the two failure modes on a single failure surface is also a common result (e.g. Feih and Shercliff, 2005; Kim et al., 2006). It has been shown that under mode I conditions, the current models are capable of producing failure in the composite and the bond-line separately, depending on the bond-line strength. Hence, in this section a variation in bond-line strength is considered where a central section of the bond-line is weakened. The strong region is assigned a strength of $t_n^c = 78$ MPa (i.e., just exceeding the strength at which failure was entirely within the composite, see Figure 14.18a). A parameter W is introduced as the strength of the weakened region, normalised by the strength of the strong region. The length of the weakened region is varied with relation to the overall bond-line RVE length, L (x and L are shown in Figure 14.17). Another parameter w is introduced to characterise the length of the weakened region as $w = x/L$. Six different lengths of weakened regions were investigated, corresponding to $w = 0$, 0.2, 0.4, 0.6, 0.8, 1. Three RVEs were analysed at each value of w to investigate if fibre distribution influenced the tendency for mixed failure to occur.

Investigations carried out corresponding to $W = 0.8$, 0.9 resulted in failure of the bond-line, as failure initiated and propagated in the bond-line without debonding occurring in the composite. A central region weakened to $W = 0.95$ ($t_n^c = 74$ MPa) produced mixed failure in some cases; the failure pattern is shown in Figure 14.19. It can be seen that the debonded fibres are predominantly located beneath the section of bond-line that remained intact. The fibres that debonded form the weak point in the loading path in this region, as the bond-line directly above remained intact. In the central region of the RVE, damage initiated at the weakened region of bond-line, preventing debonding of the adjacent fibres. This was common across all mixed failure models; however, some slight overlapping of debonding and bond-line damage was found to occur.

14.6 Micromechanical experimental calibration and validation techniques

This section outlines some very useful and novel experimental techniques that can be used to both calibrate and validate micromechanical FE models at and/or below the microscale. The list of techniques and equipment is not exhaustive, but does give some insight to what is currently being used by many research institutions concerned with micromechanical characterisation of composites.

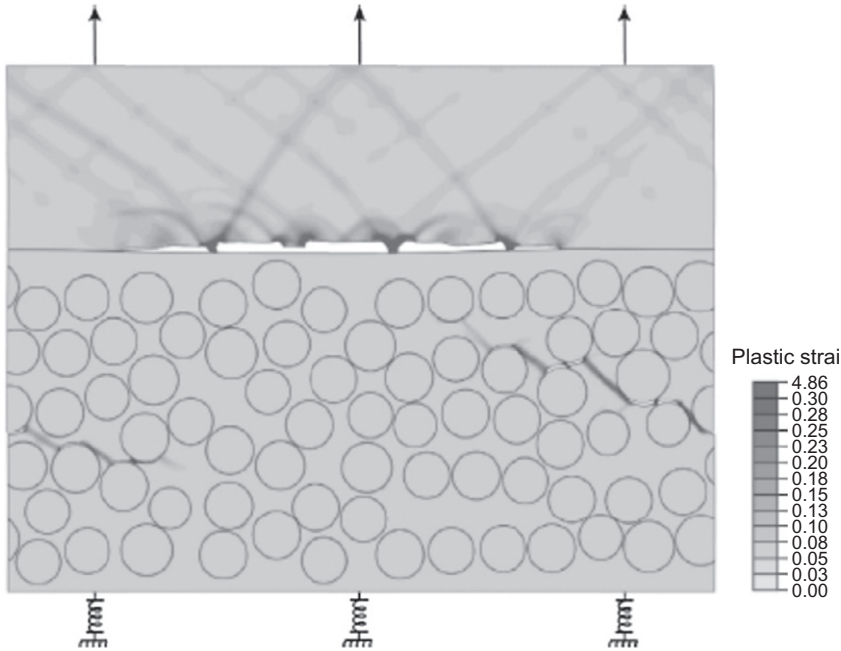

Figure 14.19 Mixed failure under mode I loading.

14.6.1 In situ *scanning electron microscope micro-testing*

Micro-testing miniature composite specimens, and indeed composite bonded joints, in the chamber of a scanning electron microscope (SEM) is a relatively new technique and can be used to understand the failure mechanisms in composites in real time at, and below, the microscale. Figure 14.20a shows a picture of the microtest system based at the University of Limerick in a tensile/compression testing configuration, where a miniature single-lap bonded composite joint is *in situ* prior to testing. Figure 14.20b shows an image of the microscale fracture in this joint during testing. Figure 14.20c demonstrates the resolution that can be achieved, in real time, with this technique, where cracks down to the fibre-level scale can be resolved, with clarity, and with local macroscopic load-displacement information superimposed.

14.6.2 *Nano-indentation to determine fibre, matrix and fibre–matrix interphase properties*

Nano-indentation using a continuous stiffness mode, which can determine the hardness and modulus of a surface as a function of depth into the surface, is a very useful technique to locally determine the mechanical properties of the fibres, matrix and fibre–matrix interphase (Hodzic et al., 2001a) at and below the microscale for input into micromechanical models, where material property homogeneity cannot be assumed. Figure 14.21a shows a nano-indent into a resin-rich pocket of a

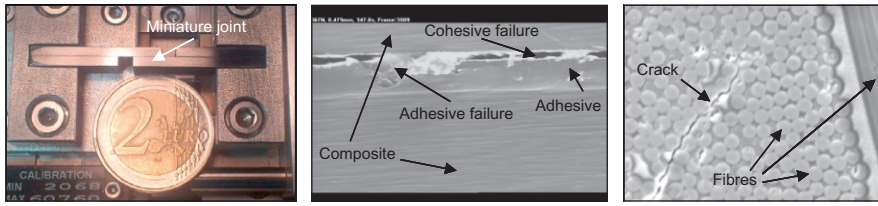

Figure 14.20 Microscale testing of a miniature bonded joint: (a) joint *in situ* before testing, (b) cohesive and adhesive failure, and (c) fibre-level scale crack growth observable.

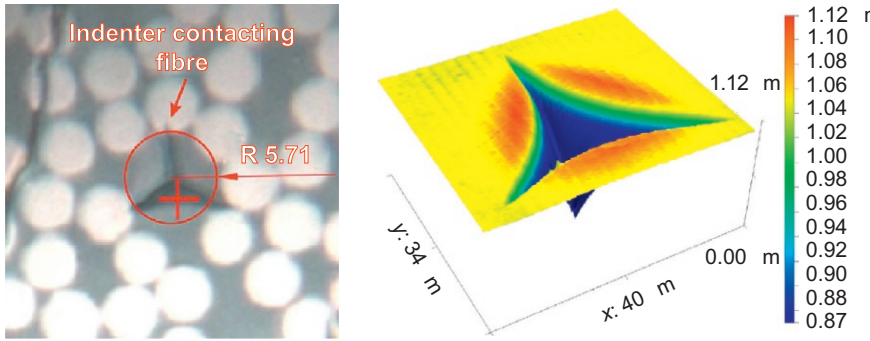

Figure 14.21 (a) Nano-indentation into a resin pocket in a carbon fibre composite and (b) a nano-scan showing matrix pile-up around the residual indentation impression.

unidirectional composite carried out recently by the authors. In addition, nano-scratch is another useful technique to determine the change in material properties across a surface, and a combination of both techniques can yield a surface field measure of mechanical properties (Hodzic et al., 2001b). State-of-the-art nano-indentation facilities can also scan the surface of the indentation or scratch using the indenter tip (just like an atomic force microscope) to yield important pile-up information around the indenter tip, which can be used to determine other physical properties of composites, such as plasticity in the matrix. Figure 14.21b shows one such scan on a composite carried out for a pending publication by the authors, where it can be clearly seen that significant pile-up occurred around the matrix.

14.6.3 3D micro-CT for NDI evaluation

Three-dimensional micro-CT is a very powerful non-destructive technique to examine the surface and subsurface material composition and integrity of composites. Figure 14.22 shows a scan of a carbon-fibre-PEEK epoxy composite, where it can be clearly seen that relatively large volumes of composite can be scanned in three dimensions down to the fibre-level scale. Also, what makes this approach particularly attractive is the ability to isolate fibres from the matrix, as shown in Figure 14.22a, and

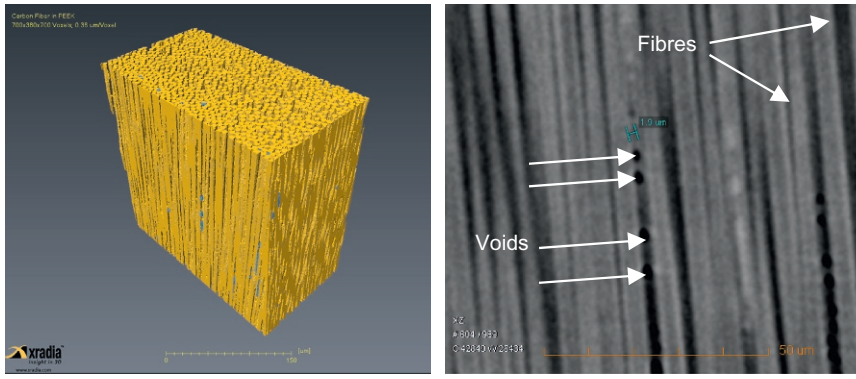

Figure 14.22 Micro-CT images of a carbon-fibre composite sample: (a) carbon fibres isolated from the matrix, (b) cross-section showing the voids in the composite.

the ability to isolate and examine voids in the matrix, as shown in Figure 14.22b. For fibre-level detail scanning, ultra-high resolution detectors are normally required, and sample volumes tend to be very small (≈ 1 mm^3).

14.7 Conclusions and ways forward

14.7.1 Conclusions of the chapter

This chapter sets out to introduce the reader the important area of micromechanical modelling for the analysis of failure in advanced composite materials. The previous sections have demonstrated the details of how such models are formed and then used to solve complex problems in composites at both material and structural levels. Although the micromechanical models require a solid understanding of composites, geometric topology, FE analysis and non-linear material modelling, once they are created they can be used for extensive and cost-efficient parameter studies for both materials and structural design. Automated tools that shield the user from this extensive *know-how* are now available on the market (e.g., see McCarthy and Vaughan, 2012). Experimental techniques described herein are used to both calibrate and validate the micromechanical models. However, at and below the microscale great care is needed to interoperate results from these experiments and to extract useful material property information for input to the micromechanical models.

14.7.2 Future research topics

The most immediate area for further research is the development of a damage model for the epoxy matrix (and the adhesive materials for joint micromechanical models). Micro-cracking of both the matrix (and the adhesive materials) can increase the

energy-absorbing capacity during crack growth in the composite (at the composite–adhesive interface) and the inclusion of such energy-absorbing mechanisms would improve the correlation between the modelling and experiments. Extended FE approaches, where matrix cracks could be modelled discretely, may be a useful numerical technique to solve this problem.

Delamination of composite plies is an underdeveloped area of micromechanical analyses. Such a case was investigated by Ye and Chen (2011) for single fibres at different orientations; however, the case of randomly distributed fibres has not been investigated. Interactions of the stress fields in plies orientated at different angles open the possibility for premature yielding of the matrix and interfacial damage to occur. Three-dimensional stress gradients would be induced during loading, and RVEs would be required to be sufficiently large to capture the gradients in their entirety. This model would therefore suffer from high computational costs, but would provide new insight into the causes of delamination of composite materials and damage progression during delamination. In addition, the model could be adapted to investigate the stress distributions related to different ply orientations within a laminate, and such a study could reveal whether stress distributions between certain ply orientations in a laminate cause more critical stress concentrations, and could aid in the optimisation of ply orientations for different boundary value problems.

True multiscale analysis of damage to composites is another area for potential future development. With this approach, micromechanical models would be linked to macroscopic models of composite materials and/or structures, and a real-time link, with feedback, would be provided between both scales. Hence once damage was predicted to initiate at the macroscale, a micromechanical model of the failing region would be formed (with appropriate boundary conditions). The micromechanical model would then predict the 'true' damage response at the microscale and feed the effects of this damage back to the macroscale model, which would then need to be updated. This would be an iterative process as the damage develops, and so would require extensive computational power.

With reference to experiments, digital image correlation techniques, in tandem with *in situ* SEM testing provide an opportunity to validate the crack path prediction of micromechanical models. A possible approach is to extract exact fibre positions at the start of an *in situ* SEM video, and export these positions to a microscale FEA model. Validation of the crack path prediction of the microscale models could then be achieved through application of appropriate boundary conditions to the model, to correspond to the conditions applied in the test. Direct comparison of the experimental crack path and the path predicted at the microscale could be made, and the method could be used to further refine and tune the parameters of micromechanical models.

14.7.3 Related journals, conferences

Many scientific and engineering journals publish papers on micromechanical modelling of composite materials, and the reader is referred to the reference section of this chapter for a comprehensive list of relevant papers.

14.8 Acknowledgements

This publication has emanated from research conducted with the financial support of Science Foundation Ireland under Grant Number SFI 13/IA/1833. The authors would also like to thank Noel O'Dowd, Donal O'Dwyer, Mark Hardiman, Andrew Keane and Daniel Mortell for their many useful contributions to this work over the past number of years.

References

Bohm, H.J., 1998. A short introduction to the basic aspects of continuum micromechanics, Institute of Lightweight Design and Structural Biomechanics (ILSB), Vienna University of Technology.

Brockenbrough, J.R., Suresh, S., Wienecke, H.A., 1991. Deformation of metal-matrix composites with continuous fibers: geometrical effects of fiber distribution and shape. Acta Metall. Mater. 39 (5), 735–752.

Canal, L.P., Segurado, J., Llorca, J., 2009. Failure surface of epoxy-modified fiber-reinforced composites under transverse tension and out-of-plane shear. Int. J. Solids Struct. 46 (11–12), 2265–2274.

de Boer, H., Poort, G., 2010. Multiscale damage modelling in Abaqus. In: IV European Conference on Computational Mechanics, Paris.

Diggle, P., 2003. Statistical Analysis of Spatial Point Patterns. Arnold, London.

Feih, S., Shercliff, H.R., 2005. Adhesive and composite failure prediction of single-L joint structures under tensile loading. Int. J. Adhes. Adhes. 25 (1), 47–59.

Fiedler, B., Gagel, A., Hobbiebrunken, T., Schulte, K., Hojo, M., Ochiai, S., 2005a. Modelling of the transverse strength of fibre reinforced epoxy composite at low and high temperature. Compos. Inter. 12 (3/4), 379–394.

Fiedler, B., Hobbiebrunken, T., Hojo, M., Schulte, K., 2005b. Influence of stress state and temperature on the strength of epoxy resins. In: 11th International Conference on Fracture (ICF 11), Turin, Italy, on CD.

Firehole Technologies Inc., 2009. Helius: MCT. Laramie, WY.

Ghosh, S., Bai, J., Raghavan, P., 2007. Concurrent multi-level model for damage evolution in microstructurally debonding composites. Mech. Mater. 39 (3), 241–266.

González, C., Llorca, J., 2007a. Virtual fracture testing of composites: a computational micromechanics approach. Eng. Fract. Mech. 74 (7), 1126–1138.

González, C., Llorca, J., 2007b. Mechanical behavior of unidirectional fiber-reinforced polymers under transverse compression: microscopic mechanisms and modeling. Compos. Sci. Technol. 67 (13), 2795–2806.

Grufman, C., Ellyin, F., 2008. Numerical modelling of damage susceptibility of an inhomogeneous representative material volume element of polymer composites. Compos. Sci. Technol. 68 (3–4), 650–657.

Hardiman, M., Vaughan, T.J., McCarthy, C.T., 2012. The effect of fibre constraint in the nanoindentation of fibrous composite microstructures: a finite element investigation. Comp. Mater. Sci. 64, 162–167.

Hashin, Z., 1980. Failure criteria for unidirectional composites. J. Appl. Mech. 47, 329–335.

Hinton, M.J., Soden, P.D., 1998. Predicting failure in composite laminates: the background to the exercise. Compos. Sci. Technol. 58 (7), 1001–1010.

Hobbiebrunken, T., Hojo, M., Adachi, T., De Jong, C., Fiedler, B., 2006. Evaluation of interfacial strength in CF/epoxies using FEM and in-situ experiments. Compos. Part A Appl. Sci. Manuf. 37 (12), 2248–2256.

Hodzic, A., Stachurski, Z.H., Kim, J.K., 2001a. Nano-indentation of polymer-glass interfaces. Part I. Experimental and mechanical analysis. Polymer 41 (18), 6895–6905.

Hodzic, A., Kalyanasundaram, S., Kim, J.K., Lowe, A.E., Stachurski, Z.H., 2001b. Application of nano-indentation, nano-scratch and single fibre tests in investigation of interphases in composite materials. Micron 32 (8), 765–775.

Hojo, M., Mizuno, M., Hobbiebrunken, T., Adachi, T., Tanaka, M., Ha, S.K., 2009. Effect of fiber array irregularities on microscopic interfacial normal stress states of transversely loaded UD-CFRP from viewpoint of failure initiation. Compos. Sci. Technol. 69 (11–12), 1726–1734.

Kim, K.S., Yoo, J.S., Yi, Y.M., Kim, C.G., 2006. Failure mode and strength of uni-directional composite single lap bonded joints with different bonding methods. Compos. Struct. 72 (4), 477–485, 70.

Lafarie-Frenot, M.C., Hénaff-Gardin, C., Gamby, D., 2001. Matrix cracking induced by cyclic ply stresses in composite laminates. Compos. Sci. Technol. 61 (15), 2327–2336.

Lesne, P.M., Allio, N., Valle, R., 1995. Combined effects of the fibre distribution and of the fibre matrix or interphase matrix transverse modulus ratio on the possible fracture modes of unidirectional composites submitted to a transverse loading. Acta Metall. Mater. 43 (12), 4247–4266.

McCarthy, C.T., Vaughan, T.J., 2012. COMM Toolbox: a MATLAB toolbox for micromechanical analysis of composite materials. J. Compos. Mater. 46 (14), 1715–1729.

O'Dwyer, D.J., O'Dowd, N.P., McCarthy, C.T., 2013. Micromechanical investigation of damage processes at composite-adhesive interfaces. Compos. Sci. Technol. 86, 61–69.

O'Dwyer, D.J., O'Dowd, N.P., McCarthy, C.T., 2014. Numerical micromechanical investigation of interfacial strength parameters in a carbon fibre composite material. J. Compos. Mater. 48 (6), 749–760.

O'Dwyer, D.J., O'Dowd, N.P., McCarthy, C.T., 2012. Investigation of strain hardening effects under in-plane shear of unidirectional composite materials. Comp. Mater. Sci. 64, 179–182.

O'Higgins, R.M., McCarthy, M.A., McCarthy, C.T., 2008. Comparison of open hole tension characteristics of high strength glass and carbon fibre-reinforced composite materials. Compos. Sci. Technol. 68 (13), 2770–2778.

O'Higgins, R.M., McCarthy, C.T., McCarthy, M.A., 2011. Identification of damage and plasticity parameters for continuum damage mechanics modelling of carbon and glass fibre-reinforced composite materials. Strain 47 (1), 105–115.

Pindera, M.-J., Khatam, H., Drago, A.S., Bansal, Y., 2009. Micromechanics of spatially uniform heterogeneous media: a critical review and emerging approaches. Compos. Part B Eng. 40 (5), 349–378.

Ripley, B.D., 1977. Modelling spatial patterns. J. R. Stat. Soc. Ser. B 39 (2), 172–212.

Terada, K., Hori, M., Kyoya, T., Kikuchi, N., 2000. Simulation of the multiscale convergence in computational homogenization approaches. Int. J. Solids Struct. 37 (16), 2285–2311.

Totry, E., González, C., Llorca, J., 2008. Failure locus of fiber-reinforced composites under transverse compression and out-of-plane shear. Compos. Sci. Technol. 68 (3–4), 829–839.

Trias, D., 2005. Analysis and simulation of transverse rando fracture of long fibre reinforced composites (Ph.D. thesis), Dep. dEnginyeria Mecanica i de la Construccio Industrial, Girona, University of Girona.

Van der Sluis, O., Schreurs, P.J.G., Brekelmans, W.A.M., Meijer, H.E.H., 2000. Overall behaviour of heterogeneous elastoviscoplastic materials: effect of microstructural modelling. Mech. Mater. 32 (8), 449–462.

Vaughan, T., 2011. Micromechanical modelling of damage and failure in fibre reinforced composites under loading in the transverse plane (Ph.D. thesis). University of Limerick, Limerick.

Vaughan, T.J., McCarthy, C.T., 2010. A combined experimental-numerical approach for generating statistically equivalent fibre distributions for high strength laminated composite materials. Compos. Sci. Technol. 70 (2), 291–297.

Vaughan, T.J., McCarthy, C.T., 2011a. Micromechanical modelling of the transverse damage behaviour in fibre reinforced composites. Compos. Sci. Technol. 71 (3), 388–396.

Vaughan, T.J., McCarthy, C.T., 2011b. A micromechanical study on the effect of intra-ply properties on transverse shear fracture in fibre reinforced composites. Compos. Part A Appl. Sci. Manuf. 42 (9), 1217–1228.

Vaughan, T.J., McCarthy, C.T., McNamara, L.M., 2012. A three-scale finite element investigation into the effects of tissue mineralisation and lamellar organisation in human cortical and trabecular bone. J. Mech. Behav. Biomed. 12, 50–62.

Ye, Q., Chen, P., 2011. Prediction of the cohesive strength for numerically simulating composite delamination via CZM-based FEM. Compos. Part B Eng. 42 (5), 1076–1083.

This page intentionally left blank

Computational micromechanics strategies for the analysis of failure in unidirectional composites

15

F. Naya[*], *C.S. Lopes*[*], *C. González*[*,†], *J. LLorca*[*,†]
*IMDEA Materials Institute, Madrid, Spain; †Polytechnic University of Madrid, Madrid, Spain

15.1 Introduction

It is well established that the mechanical properties of composite materials are controlled by the properties and spatial distribution of the different phases and interphases at the scale of μm. This circumstance leads naturally to a bottom-up strategy to determine the macroscopic properties starting from the mechanisms of deformation at the microscale, and micromechanical models have always been considered superior to purely phenomenological ones both in terms of accuracy and predictive capabilities. Nevertheless, the actual development of robust micromechanical models has been hindered by two facts, namely the lack of accurate data about the mechanical properties of phases and interphases at the nm–μm scale and the complexity of the three-dimensional (3D) microstructure, which precludes the use of simple analytical approximations in most cases.

The exponential growth of computational power in the last decades as well as the development of experimental techniques to characterise the mechanical behaviour of materials at the nm–μm scale (mainly instrumented nanoindentation) have overcome these limitations. Models based on computational micromechanics are very popular to understand the deformation and fracture mechanisms of engineering materials and to optimise the microstructure. In the case of unidirectional fibre-reinforced composites, they have demonstrated their accuracy to predict the mechanical behaviour as well as the fracture mechanisms under different loading conditions (González and LLorca, 2007a; Totry et al., 2009, 2010; Vaughan and McCarthy, 2011a,b; Canal et al., 2012a), to determine the failure surface under multiaxial loading (Totry et al., 2008a–c; Canal et al., 2009; Romanowicz, 2012; Melro et al., 2013) or in the presence of porosity (Vajari et al., 2014), and as key elements within multiscale modelling strategies to carry out virtual testing of composite structures (LLorca et al., 2011, 2013).

Unidirectional polymer–matrix composite plies are the building blocks of the multidirectional laminates used in the majority of structural applications. Unidirectional plies are highly anisotropic and undergo either fibre- or matrix-dominated damage upon loading. Computational micromechanics is able to capture the onset and propagation of damage and to provide the magnitudes of strength and toughness associated

Numerical modelling of failure in advanced composite materials. http://dx.doi.org/10.1016/B978-0-08-100332-9.00015-3
Copyright © 2015 Elsevier Ltd. All rights reserved.

to each failure mode that can be used for the structural design of laminates. This chapter summarises the current state of the art on the application of computational micromechanics to study the mechanical behaviour of unidirectional plies. The overall computational micromechanics strategies to determine the strength and toughness of unidirectional plies are outlined in Section 15.2. The experimental techniques to determine the properties of the constituents (matrix, fibres and interfaces) are presented in Section 15.3 and several examples of application of computational micromechanics in unidirectional plies are shown in Section 15.4. Finally, the conclusions and the future developments in this area are briefly summarised in Section 15.5.

15.2 Computational micromechanics strategies for unidirectional plies

Unidirectional plies are transversally isotropic solids, whose elastic behaviour is determined by five elastic constants: the elastic modulus in the fibre direction, E_1, the elastic modulus perpendicular to the fibres, E_2, the in-plane Poisson's ratio, v_{12}, and the in-plane and out-of-plane shear moduli, G_{12} and G_{23}, respectively. They can be easily obtained from the elastic properties of the matrix and the fibres by means of simple micromechanical or analytical homogenisation models (Böhm, 2014). Upon loading, unidirectional plies present a linear behaviour (except in the case of in-plane shear) until a critical stress is reached, leading to the onset of damage. Damage progresses rapidly afterwards and failure takes place at low strains (of a few percent).

Five different physical failure mechanisms can be identified in unidirectional plies depending on the loading direction (Figure 15.1). The tensile strength of the ply loaded parallel to the fibres, X_T, is controlled by the brittle fracture of the fibres, whereas the compressive strength along the same orientation, X_C, is dictated by the development of fibre kinking (Budiansky and Fleck, 1994). If the ply is subjected to tensile stresses perpendicular to the fibres, the tensile strength Y_T is governed by matrix and interface failure, which leads to the formation of a crack perpendicular to the tensile axis (Canal et al., 2012a,b), and the compressive strength perpendicular to the fibres, Y_C,

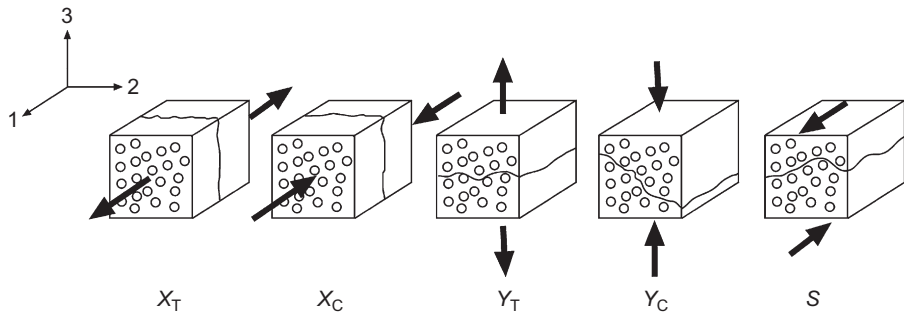

Figure 15.1 Schematic of the different failure micromechanisms in unidirectional plies as a function of the loading conditions.

is dominated by the formation of a shear band of localised plastic deformation in the matrix across the ply (González and LLorca, 2007a). Finally, the shear strength parallel to the fibres, S_L, is controlled by the matrix and interface shear strength.

Note that these failure mechanisms are linked to each other, i.e., the compressive strength parallel to the fibres is severely reduced in the presence of shear stresses that facilitate the formation of kink bands (Vogler and Kyriakides, 2001). Thus, the maximum load-bearing capability of the ply under any stress state is dictated by a failure locus in the stress space. This failure locus (or failure criterion) is made up of the intersection of the various smooth surfaces, which correspond to the different physical failure modes depicted in Figure 15.1. So far, the failure locus was obtained by means of phenomenological or physically based models, whose accuracy has to be verified through costly and time-consuming experimental campaigns (Puck and Schürmann, 2002; Dávila et al., 2005; Kaddour et al., 2004). In addition, results obtained for a unidirectional ply could not be extrapolated to materials with different fibre volume fraction or constituent properties. Finally, the failure of unidirectional plies also depends on the energy dissipated by each damage mode, which has to be measured by means of complex mechanical tests or estimated by comparison with experiments (Pinho et al., 2006; Camanho et al., 2014a,b).

Computational micromechanics offers a novel approach to determine the failure locus and the toughness associated with the different failure modes of unidirectional plies. The former can be obtained by means of computational homogenisation of a representative volume element (RVE) of the ply microstructure, whereas the latter can be determined by means of embedded cell models. The main features of both strategies are presented below.

15.2.1 Computational homogenisation

The failure locus of a unidirectional composite ply can be obtained by computational homogenisation, in which the mechanical behaviour of an RVE of the ply microstructure is determined under different loading conditions by means of a numerical method (usually the finite element method). In contrast to standard homogenisation techniques based on the mean-field approximation (Mori-Tanaka, self-consistent, etc.) (Nemat-Nasser and Hori, 1999), computational homogenisation can account for complex non-linear behaviours (geometrical and material). In addition, the details of the stress and strain microfields are resolved, and thus it is possible to track the nucleation and growth of damage during the simulation, a key aspect to model the localisation of damage and fracture.

The first step in the computational homogenisation strategy is the creation of an RVE of the unidirectional composite lamina, which is made up by random and homogeneous distribution of circular fibres in a square domain. Several strategies can be used to this end (Trias et al., 2006; Vaughan and McCarthy, 2010) but the most popular one is the random sequential absorption algorithm (Segurado and LLorca, 2002; González and LLorca, 2007a). Fibre centres are generated randomly and sequentially, and each new fibre is accepted if the distance between neighbouring fibre surfaces is higher than a minimum distance (of the order of $0.1R$, where R stands for the fibre radius) to ensure

an adequate finite element discretisation of this region. In addition, the distance between the fibre surface and the RVE edges should be higher than the same critical distance to avoid distorted finite elements during meshing. The process finishes once the desired fibre volume fraction within the RVE is reached. The 3D RVE is obtained by extruding the two-dimensional (2D) microstructure along the fibre direction.

An important issue in computational homogenisation is the minimum size of the RVE, which should contain all the necessary information about the statistical description of the microstructure. In addition, the RVE should be large enough so that the average properties of this volume element are independent of its size and position within the material. The critical size of the RVE regarding this second criterion depends on the phase and interface properties and spatial distribution, the failure modes and also on the boundary conditions applied to the RVE. It has been demonstrated that, for a given size of the RVE, periodic boundary conditions always provide a better approximation to the effective properties of the inhomogeneous material than those obtained under imposed forces or displacements (Hazanov and Huet, 1994). Thus, computational homogenisation of unidirectional plies is carried out by imposing periodic boundary conditions on a periodic RVE. To this end, fibres intersecting the RVE edges were split into an appropriate number of parts and copied to the opposite sides of the RVE to create a periodic microstructure (Figure 15.2).

The periodic boundary conditions can be expressed in terms of the displacement vectors $\vec{U}_1$, $\vec{U}_2$ and $\vec{U}_3$ which relate the displacements between opposite faces according to the following equations

$$\begin{aligned}\vec{U}_1 &= \vec{u}\,(0, x_2, x_3) - \vec{u}\,(L_1, x_2, x_3)\\ \vec{U}_2 &= \vec{u}\,(x_1, 0, x_3) - \vec{u}\,(x_1, L_2, x_3)\\ \vec{U}_3 &= \vec{u}\,(x_1, x_2, 0) - \vec{u}\,(x_1, x_2, L_3)\end{aligned} \tag{15.1}$$

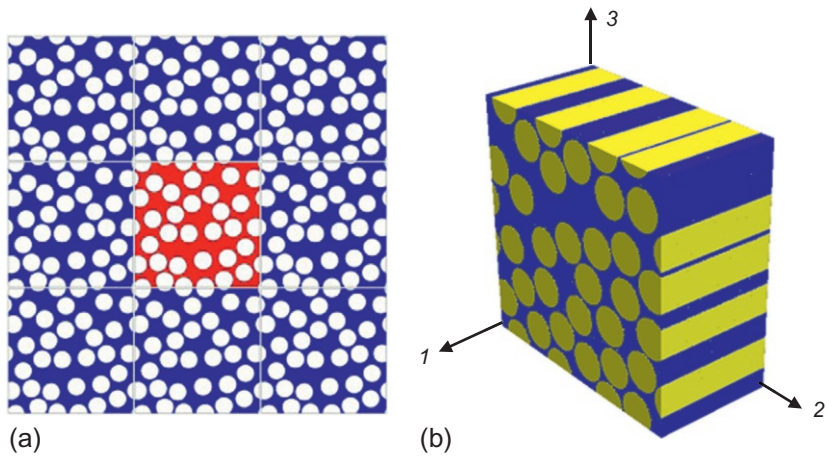

Figure 15.2 (a) Schematic of the microstructure model of a unidirectional composite ply obtained with periodic boundary conditions. (b) Periodic RVE containing a random and homogeneous dispersion of 30 circular fibres.

where L_1 and $L_2 = L_3$ stand for the dimensions of the RVE. Different loading conditions (including uniaxial and multiaxial stress states) can be obtained with different combinations of $\vec{U}_1$, $\vec{U}_2$ and $\vec{U}_3$ (Totry et al., 2010).

In the case of matrix-dominated properties of unidirectional plies (transverse tension and compression as well as shear), it was found that accurate predictions of the strength could be obtained with RVE containing a few dozens of fibres (in the range 30–50) under periodic boundary conditions (González and LLorca, 2007a). Moreover, these predictions can be refined if the final strength is obtained by averaging the results obtained with various fibre realisations are averaged (Hine et al., 2002). Finally, information about the dispersion in the mechanical properties due to the statistical variations in the fibre spatial distribution or in the constituent properties can also be obtained.

To predict the failure locus of the unidirectional ply, the fracture mechanisms of the constituents have to be introduced in the model through the constitutive equations of fibres, matrix and interface. Fibres are modelled as linear elastic, isotropic (glass) or transversally isotropic solids (carbon), whose behaviour is dictated by their elastic constants. Fibres fail in a brittle fashion in tension and fibre fracture can be taken into account by means of interface elements inserted perpendicular to the fibre axis at different locations along the fibre (González and LLorca, 2006, 2007b). The interface elements are initially closed and open up once the longitudinal stress in the fibre reaches a critical value. This value may change for fibre to fibre and from location to location within one fibre following the experimental fibre strength given by the Weibull model.

Interface decohesion at the fibre/matrix interface is also included in the computational homogenisation framework through interface elements and crack propagation along the interface is taken into account by means of a cohesive crack model. The initial mechanical behaviour of these elements is very stiff to ensure the displacement continuity between fibre and matrix. This regime end at critical stress which depends on the normal, N, and tangential, S, interface strengths. The stress transferred through the interface decreases progressively until zero as the cohesive crack opens and this regime is controlled by the interface fracture toughness, Γ_{int}. More details about the numerical implementation of interface decohesion can be found in González and LLorca (2007a) and Totry et al. (2008c).

Finally, the mechanical behaviour of the epoxy matrix has to be accounted for. Epoxy matrices fail at a very low strains in a brittle fashion under uniaxial tension while they undergo considerable plastic deformation under compression and shear and the flow stress is pressure dependent (Kinloch and Young, 1983; Quinson et al., 1997). These features have been taken into account by means of different modifications of the Drucker–Prager model to include the different behaviour in tension and compression (González and LLorca, 2007a; Canal et al., 2009; Vaughan and McCarthy, 2011a; Vajari et al., 2014; Melro et al., 2013). The epoxy matrix was modelled as an isotropic, elastoplastic solid. Plastic deformation and fracture was included by means of a continuum plasticity-damage model developed by Lubliner et al. (1989) and modified by Lee and Fenves (1998). The yield surface of the epoxy is expressed by a modification of the Drucker–Prager yield function according to

$$\phi(I_1, J_2, \sigma_1, \beta, \alpha) = \frac{1}{1-\alpha}\left(\sqrt{\frac{3J_2}{2}} + \frac{I_1}{3}\alpha + \beta\langle\sigma_1\rangle\right) - \sigma_m^{yc} = 0 \tag{15.2}$$

where I_1 stands for the first invariant of the stress tensor, J_2 is the second invariant of the deviatoric stress tensor, α is the pressure-sensitivity parameter of the Drucker–Prager yield criterion, σ_1 is the maximum principal stress, $\langle\rangle$ is the Macaulay brackets (which return the argument if positive and zero otherwise) and β is a parameter function of the tensile σ_{yt} and compressive σ_{yc} yield stress according to

$$\beta = \frac{\sigma_m^{yc}}{\sigma_m^{yt}}(1-\alpha) - (1+\alpha) \tag{15.3}$$

The corresponding yield surface under plane stress conditions is plotted in Figure 15.3(a) in the stress space of the principal stresses. Under compression, the

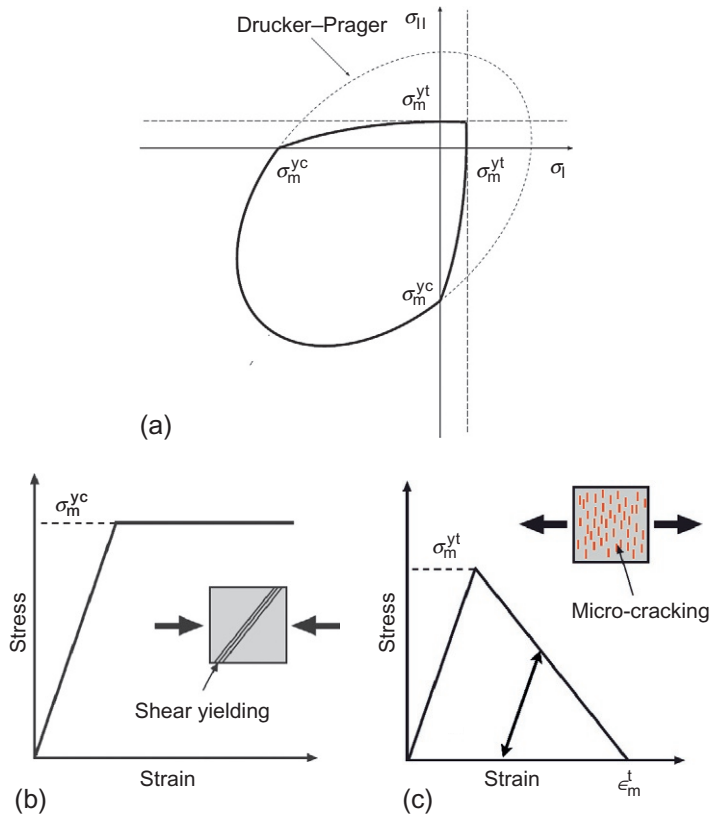

Figure 15.3 (a) Yield surface of the epoxy matrix under plane stress conditions. (b) Postyield behaviour in compression and shear. (c) Post-yield behaviour in tension.

matrix follows the standard Drucker–Prager yield criterion. In tension, however, yielding is mainly controlled by the maximum principal stress. In addition, the post-yielding behaviour was different in compression and tension, in agreement with the experimental behaviour of epoxy resins. Plastic deformation at constant flow stress occurred in compression and shear after yielding, leading to final failure by the formation of a shear band (Figure 15.3b). Conversely, the brittle behaviour in tension due to microcracking was accounted for by a linear softening law. The energy dissipated by unit volume during tensile cracking was controlled by the failure strain, $\varepsilon_m^{\mathrm{t}}$ (Figure 15.3c). To avoid mesh-sensitivity problems associated with continuum damage models and softening, mesh regularisation was carried out by means of the crack band model (Bazant and Oh, 1983) from the matrix fracture energy, Γ_{m}, which is related to the stress–strain relationship in tension according to

$$\Gamma_{\mathrm{m}} = \frac{1}{2}\sigma_{\mathrm{m}}^{\mathrm{yt}}\varepsilon_{\mathrm{m}}^{\mathrm{t}} l_{\mathrm{ch}} \tag{15.4}$$

where l_{ch} is the characteristic length of the finite element. More details about the finite element implementation can be found in Canal et al. (2012a,b).

Finally, note that the results provided by computational homogenisation are valid up to the maximum in the stress–strain curve. Afterwards, damage localisation leads to the formation of a crack and/or a shear band throughout the RVE and the post-peak behaviour depends on the actual orientation of the crack/shear band, whereas the amount of energy dissipated during fracture is influenced by the periodic boundary conditions. Thus, while computational homogenisation stands as a powerful strategy to predict the failure locus of unidirectional plies, it cannot be used to determine the fracture energy associated with each failure mode.

15.2.2 Embedded cell models

Final fracture of unidirectional plies always takes place by the localisation of damage in one plane. The fracture plane is parallel to the fibres in the case of matrix-dominated failure (transverse tension and compression as well as shear), while it is perpendicular to them under tension parallel to the fibres. Fracture in compression parallel to the fibres occurs by the formation of a kink band due to fibre microbuckling. The width of the kink band is $\approx$30R–50R, and the kink band is oriented at 10° to 20° with respect to the plane perpendicular to the fibres (Fleck, 1997; Vogler and Kyriakides, 2001).

The energy dissipated during the propagation of a crack along the failure plane divided by the crack surface is the toughness associated with the failure mode and can be obtained by computational micromechanics using embedded cell models (González and LLorca, 2007b). In this approach, full details of the composite microstructure (including the spatial distribution of the fibres) are resolved in the fracture region, and simple constitutive equations (based on any suitable homogenisation approximation) and coarser discretisations are used in the rest of the model to save computer time (Figure 15.4). The region in which the microstructure is resolved should include all the area in which damage occurs during the propagation of the

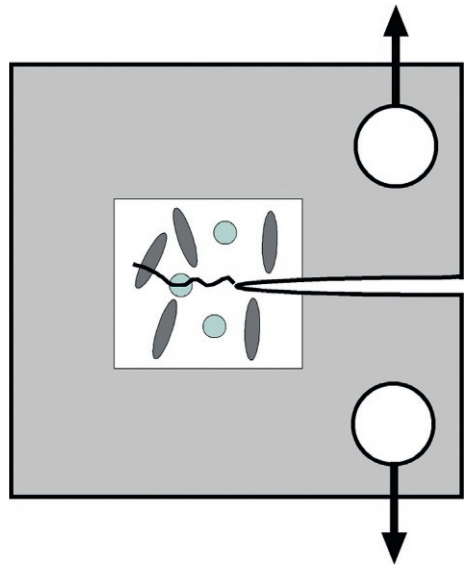

Figure 15.4 Schematic of an embedded cell simulation of fracture. The details of the composite microstructure (matrix, reinforcements and interfaces) are included in front of the notch tip, whereas the remaining material (in grey) is represented as a homogeneous material whose constitutive equation is provided by a suitable homogenisation model.

crack, so the energy spent by the different failure micromechanisms (fibre and interface fracture, matrix plastic deformation, etc.) is accounted for. This methodology was originally developed to determine the toughness associated with tensile fracture parallel to the fibres in Ti/SiC composites as a function of temperature (González and LLorca, 2006, 2007b,c), and it was recently applied to determine the intraply toughness of glass/epoxy fibre-reinforced composites (Canal et al., 2012a)

15.3 Experimental Micromechanics

The accuracy of the determination of ply properties in unidirectional composites by means of computational micromechanics relies on the actual properties of the fibre, matrix and fibre/matrix interface. In a first approximation, they could be obtained by means of tests carried out in either fibres or matrix specimens or in specific coupons for the interface. For instance, tensile tests on individual fibre filaments or yarns can be used to determine the elastic modulus and strength of the fibre, and neat resin specimens can be used to measure the stiffness and the strength in tension, compression and shear as well as the fracture toughness of the matrix. The determination of the fibre/matrix interface properties requires manufacturing additional *ad hoc* specimens. This is the case of a single fibre embedded in a resin coupon for the pull-out test (Desarmot and Favre, 1991) or the resin drop cured on a single fibre for the microbond

test (Miller et al., 1987). However, matrix properties extracted from neat resin specimens or interface properties obtained from pull-out or microbond tests could not be representative of the actual properties within the unidirectional ply because of the differences in the manufacturing process, the curing conditions and the residual stresses. For instance, the matrix and interface properties depend on the local thermal history during curing that could be modified due to the large fibre volume fraction in the ply. Therefore, the optimum solution relies on the use of nanomechanical testing techniques to measure the *in situ* matrix and interface properties within the actual composite ply.

15.3.1 Matrix characterisation

Instrumented nanoindentation is based on the continuous recording of applied load P and the tip displacement δ (Figure 15.5a and c) during an indentation process. This information is used to extract relevant mechanical properties of the material, such as the yield stress and elastic modulus, from the load–displacement curve (Figure 15.5b). Although the nanoindentation test is very straightforward, the inverse

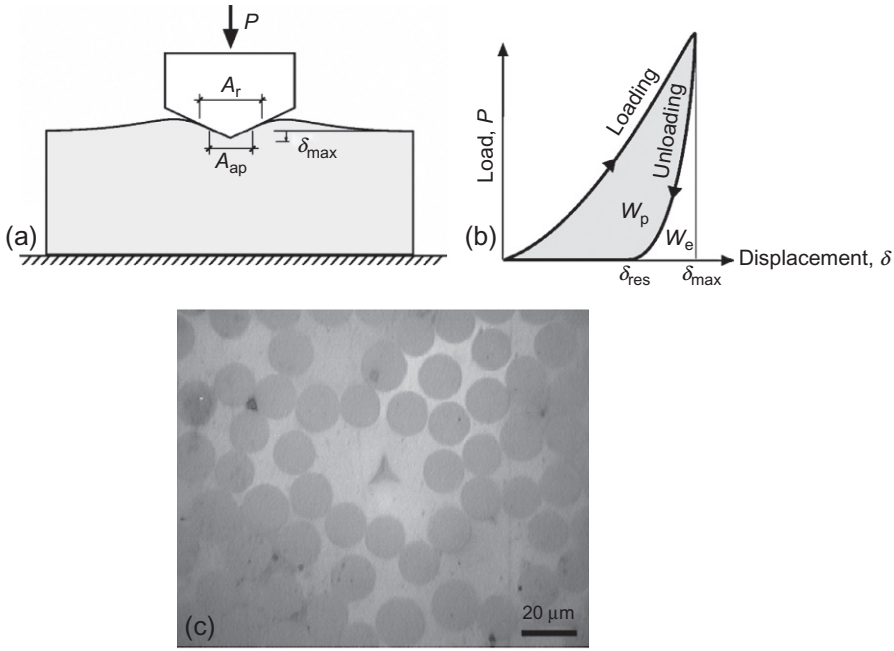

Figure 15.5 (a) Sketch of an indentation process. Notice the differences between the apparent and real material hardness obtained with the different contact areas. (b) Typical load–displacement curve. (c) Berkovich indentation carried out in a matrix-rich region in an epoxy/glass fibre composite.

process to obtain the material properties from the indentation load–displacement curve could be very challenging because there is not a unique correspondence between both. This is the case, for instance, of amorphous polymers whose flow stress is dependent on pressure and which experience finite deformations below the indenter tip, leading to important geometrical effects due to the accommodation of the surrounding material (pile-up and sink-in phenomena). As a result, the real current contact area between the tip and the material, A_r, is not known and differs from the apparent one, A_{ap}, (Figure 15.5a) and specific assumptions should be formulated to determine the modulus and strength of the material. Rodríguez et al. (2012a) have developed a novel methodology based on instrumented indentation to determine the mechanical properties of amorphous materials which present cohesive-frictional behaviour, as is the case of most thermoset and thermoplastic polymers. The approach is based on the concept of a universal hardness equation, which results from the assumption of a characteristic indentation pressure proportional to the hardness. The actual universal hardness equation is obtained from a detailed finite element analysis of the process of sharp indentation for a very wide range of material properties, and the inverse problem (i.e., how to extract the elastic modulus, the compressive yield stress σ_{yc} and the pressure-sensitivity parameter α used in Equation 15.4 from nanoindentation tests) is solved. In the case of amorphous polymers, these properties can be obtained from unloading stiffness, and the apparent indentation hardness (P/A_{ap} in Figure 15.5a) can be obtained from the geometry of the indenter tip and the applied load and the ratio between the elastic energy stored in the specimen and the total energy spent during indentation.

This methodology can be used to measure *in situ* the matrix properties in fibre-reinforced composites by means of instrumented nanoindentation into resin pockets on a polished cross-section of the composite. Nanoindentations should be placed sufficiently far away from the stiff fibres to avoid their constraining effect. In general, it is not difficult to find resin locations that are far enough from any fibre because of the inhomogeneous fibre arrangement at the microscopic level (Figure 15.5c) even in the case of plies with a very high-fibre volume fraction (60–70%).

15.3.2 Interface characterisation

In the case of the fibre–matrix interface, the most suitable *in situ* techniques to measure the strength are the push-in and the push-out tests. The push-out test requires the preparation of a thin slice perpendicular to the fibres with a thickness of the order of the fibre diameter. Individual fibres can be pushed out from the composite using a nanoindenter with a flat tip and the shear strength of the interface can be obtained from the load–displacement curve. Although the procedure seems to be rather simple, with the exception of the sample preparation, the analysis of the test is difficult due to the uncertainties in assessing the localisation of the onset of debonding. Moreover, the slicing process leads to a significant relaxation of the residual stresses that could modify the mechanical response of the matrix–fibre interface.

In the push-in test, a single fibre is pushed by means of a nanoindenter on a cross-section of a bulk specimen until interface debonding occurs, as illustrated in

Figure 15.6a. The load–displacement curve deviates from the initial linear and elastic behaviour due to the progressive and stable propagation of the interface crack along the fibre–matrix interface, Figure 15.6b. The main advantage of this technique is that it does not require any laborious sample preparation, but interpretation is somehow difficult because the length of the debonded interface below the surface is not known.

Rodríguez et al. (2012b) developed a strategy to extract the interface shear strength of fibre-reinforced polymers (glass and carbon) from push-in tests. The strategy is based on performing a fibre push-in tests at the central fibre of a highly packed fibre cluster with hexagonal symmetry, which is often found in unidirectional composites with a high-fibre volume fraction (Figure 15.6c). The mechanics of this test was analysed in detail by means of 3Dfinite element simulations to establish the influence of different parameters (interface shear strength, toughness and friction as well as fibre longitudinal elastic modulus and curing stresses) on the critical load at the onset of debonding. From the results of the numerical simulations, a simple relationship between the indentation critical load (point at which non-linearity of the load–displacement curve is observed) and the interface shear strength S was proposed and validated. It should be noticed that neither push-in or push-out tests provide

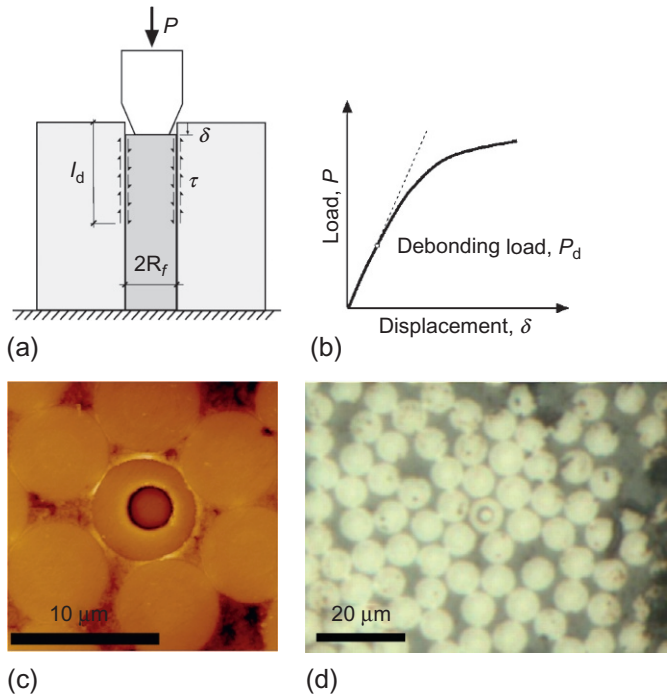

Figure 15.6 (a) Sketch of an indentation process. Notice the debonded area below the indentor progressing through the indentation. (b) Typical load–displacement curve. (c) Atomic force micrograph for a push-in test carried out in a carbon/epoxy composite in a highly packed area and (d) optical image of the indented fibre.

the actual value of the normal interface strength, N, that may differ from the shear strength. Ogihara and Koyanagi (2010) studied the interface failure under combined shear and normal stress states in a glass fibre/epoxy composite and concluded that the shear strength of the interface was higher than the normal strength ($N = 1.5S$) and proposed a quadratic stress criteria to estimate the interface strength under multiaxial stress states.

15.3.3 Characterisation based on full-field measurements

Although *in situ* tests based on instrumented nanoindentation provide valuable information regarding the mechanical parameters governing the material behaviour at the microscale, they still rely on the extensive use of finite element simulations to extract the information from a single load–displacement curve. Complementary information about the deformation and fracture processes at the micron scale can be obtained by means of *in situ* mechanical tests within a scanning electron microscope in combination with the application of optical full-field measurement methods, e.g., digital image correlation (DIC). DIC is widely used in the field of experimental mechanics to obtain the full displacement field from optical images taken at different stages of deformation. Its popularity among the optical methods comes from the availability of commercial packages, the low cost of high-resolution digital cameras and the general simplicity of sample preparation and optical set-up. Surface preparation of the specimens is crucial to obtain good results using DIC. The microstructure of the material has first to be revealed by polishing with diamond slurry a section perpendicular to the fibres. A speckle pattern has to be created on the surface by depositing submicron alumina particles from a suspension in propanol using iodine as a dispersant. A typical pattern is found in the scanning electron micrograph of Figure 15.7(a), showing the homogeneous dispersion of submicron alumina particles on the specimen surface, (Canal et al., 2012b).

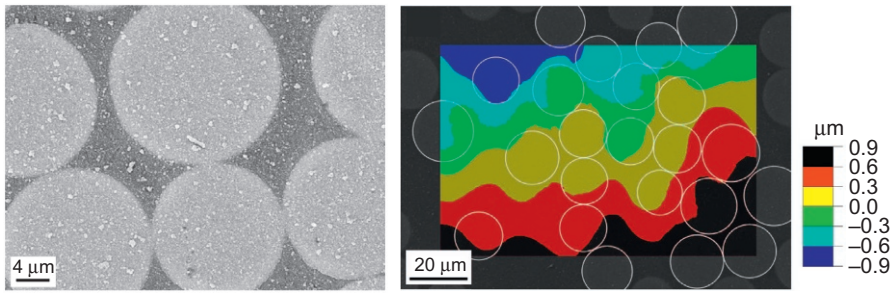

Figure 15.7 (a) SEM micrograph of a glass fibre/epoxy composite showing the Al_2O_3 particles used for digital image correlation speckle. (b) Vertical displacement field obtained by digital image correlation during a transverse to the fibre compression test.

Canal et al. (2012b) exploited both techniques to obtain very detailed information about the onset and progression of damage during transverse compression as a function of the applied strain at the microscale. The failure pattern was clearly shown by the high-resolution scanning electron micrographs (Figure 15.8), whereas the displacement field at the specimen surface was obtained by DIC (Figure 15.7b) and compared with finite element simulations of the actual microstructure of the material. The results showed good agreement in terms of average strains at the constituent level, although the DIC technique was not able to capture the sharp strain gradients (derivatives of the displacement field) arising from the fibre/matrix interface due to the high elastic contrast between the constituents.

In summary, the most relevant mechanical properties of the matrix (σ_{yc} and α) and the interface (S and N) can be obtained by means of *in situ* micromechanical tests carried out on the cross-sections of the composite plies. These techniques are also useful to assess the degradation of the constituent properties due to environmental effects (water uptake, ageing, etc.) during the service life of the material.

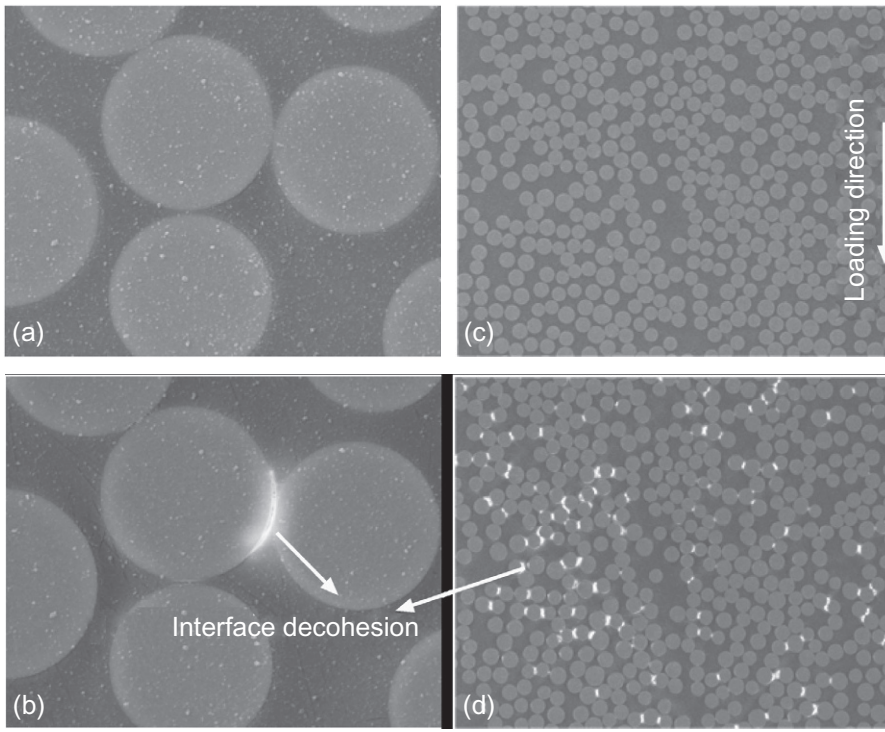

Figure 15.8 *In situ* SEM micrographs during transverse-to-the-fibre compression obtained at 250 and 6000 magnification level: (a and b) initial unloaded state, (c and d) after 1.8% compressive strain.

15.4 Applications: Matrix-dominated Failure

The computational micromechanics strategy we have described can be used to predict the ply strength and the failure locus under multiaxial stress states of unidirectional composites (by means of computational homogenisation) and the fracture toughness associated with a given failure mode (through embedded cell simulations). Examples of both types of analyses are presented in the following together with new applications of computational micromechanics that try to bridge the gap between micromechanics and mesomechanics analysis.

15.4.1 Transverse compressive strength and failure locus

Failure of a unidirectional composite ply under compression perpendicular to the fibres takes place by the development of a macroscopic shear band at an angle of 56° with the direction perpendicular to the compression axis (Figure 15.9a). Micrographs at higher magnification (Figure 15.9b) demonstrated that plastic strain localisation in the matrix and decohesion at the fibre–matrix interface were the dominant fracture mechanisms at the microscopic level. The ply strength under compression perpendicular to the fibres can be obtained by the finite element analysis of a periodic RVE of the composite (González and LLorca, 2007a). The numerical simulations were able to predict not only the compressive strength of the unidirectional composites but the microscopic failure mechanisms, as shown in the contour plots of the accumulated plastic strain in the matrix in Figure 15.9c, including the orientation of the shear band.

The same strategy can be easily extended to simulate the mechanical behaviour under multiaxial stress states that are extremely difficult to achieve experimentally. These results were used to assess the accuracy of physically based failure theories (Puck and Schürmann, 2002; Dávila et al., 2005) in Totry et al. (2008a,b) or Camanho et al. (2014a,b). For instance, Totry et al. (2008c) carried out simulations under the combined action of transverse compression and in-plane shear and determined the failure envelope in the σ_2–τ_{12} space for a PEEK matrix reinforced with 60 vol. % of AS4 carbon fibres (Vogler and Kyriakides, 2001). The correlation between experiments and computational micromechanics was excellent not only in the ply strength but also on the shape of the failure locus (Figure 15.10). The numerical model captured accurately the transition from shear failure by splitting along the fibres for low compressive stresses to compressive failure along an inclined surface parallel to the fibres. The former was characterised by a linear increase of the shear strength with the applied compressive stress as a result of the pressure-sensitivity behaviour of the polymeric matrix. The end of this regime was accompanied by a change in the failure mode to compressive failure, leading to a gentle reduction in the maximum shear strength at failure.

15.4.2 In-plane shear deformation

The computational micromechanics strategy is also very useful to ascertain the influence of the constituent properties on the macroscopic properties of the composite. For instance, Totry et al. (2010) studied the effect of fibre, matrix and interface properties

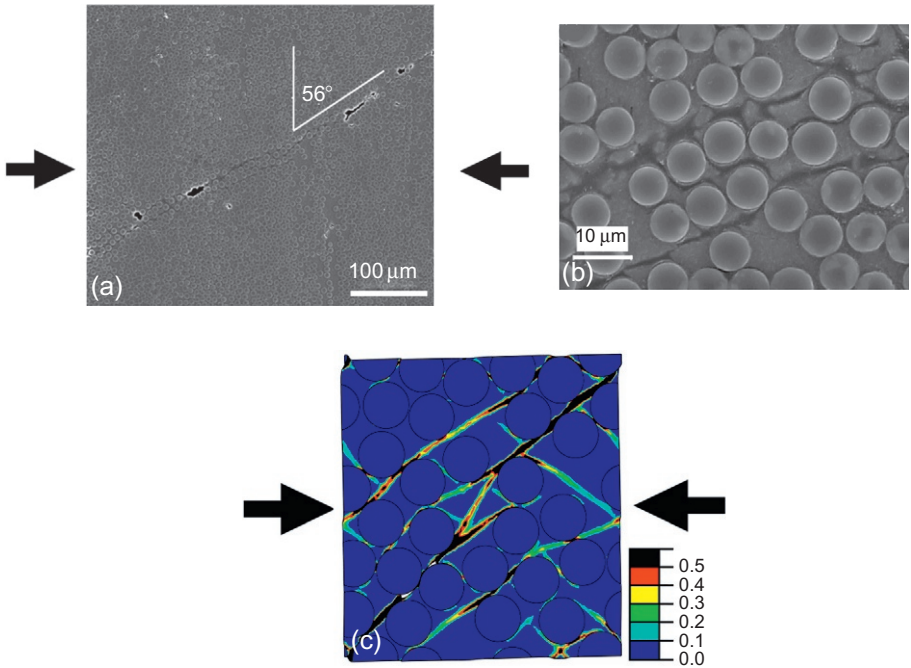

Figure 15.9 Failure micromechanisms under compression perpendicular to the fibres of an 8552 epoxy matrix reinforced with 60 vol. % of AS4 C fibres. (a) Scanning electron micrograph showing that failure occurred by the formation of a shear band in the matrix. (b) Detail of (a) showing strain localisation in the matrix and interface decohesion around the shear band. (c) Contour plot of the accumulated plastic strain in the matrix obtained from the FE simulation of an RVE of the composite microstructure. Strain localisation in the matrix and interface decohesion around the shear band are clearly visible.

on the in-plane shear deformation of carbon laminates by a detailed combination of experiments and simulations. They carried out V-notch in-plane shear tests in cross-ply epoxy laminates reinforced with high strength (HS) and high modulus (HM) carbon fibres and followed the development of damage by means of optical microscopy up to different strains. The tests were simulated through the finite element analysis of periodic RVEs of the composite lamina deformed by shear parallel and perpendicular to the fibres. The simulations demonstrated that the development of interface fracture significantly modified the in-plane shear behaviour as it hindered the load transfer between matrix and fibres and precipitated fracture by the coalescence of interply cracks.

15.4.3 Influence of manufacturing defects

Computational micromechanics simulations of an RVE can also be used to address the effect of manufacturing defects in the material at the micro level. For instance, small air entrapments generated during resin infiltration in liquid moulding led to a

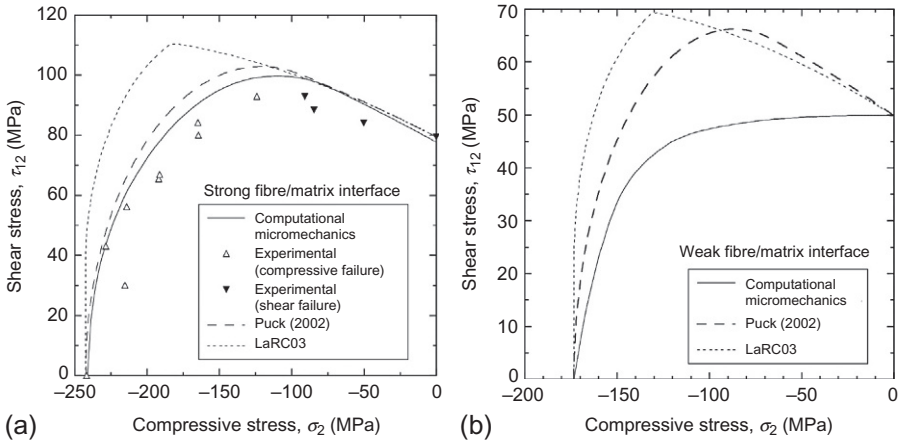

Figure 15.10 (a) Computational micromechanics predictions of the $\sigma_2 - \tau_{12}$ failure locus and experimental results (Vogler and Kyriakides, 2001). The predictions from physically based models (Puck and LaRC03) are also included for comparison. (b) Effect of the fibre/matrix interface on the failure locus.
From Totry et al. (2008c).

reduction on the matrix-controlled mechanical properties (e.g. transverse tension and compression, interlaminar shear strength, longitudinal compression, etc.). Vajari et al. (2014) introduced 1–5 vol.% porosity at the interfibre space and within the matrix in an RVE of a unidirectional composite and studied the effect of porosity on the strength under transverse tension, transverse compression and out-of-plane shear. It was found that, in agreement with experimental data in the literature, porosity reduced markedly the strength of composite under all loading conditions although it did not modify the dominant failure mechanisms. Failure under tension was controlled by interface decohesion, whereas failure in compression was dominated by the localisation of a plastic shear band in the matrix. Interfibre voids acted as stress concentrators, which triggered the onset of failure at lower stresses.

15.4.4 Fracture toughness

The embedded cell approach presented above can analyse the propagation of a single crack in the ply and compute the fracture toughness associated to the different failure modes. Canal et al. (2012a) applied this methodology to determine the intraply toughness of a unidirectional E-glass/epoxy ply. The crack propagated parallel to the fibres from the notch of a beam loaded in three-point bending (Figure 15.13a). The numerical model was validated against *in situ* experiments carried out within a scanning electron microscope. The formation and progression of the damage process zone was observed during the test and showed that interface decohesion controlled the onset of fracture (Figure 15.13b). Interface cracks started at the equator of the fibres and

propagated towards theirs pole. The final physical crack was formed by the growth of voids in the debonded fibres and the shear failure of the matrix ligaments between adjacent fibres.

The three-point bending tests were simulated using the embedded cell method. The microstructure (including matrix, fibres and the interface) was represented in the fracture process zone around the notch region and the remaining beam was assumed to behave as a homogeneous and elastic anisotropic solid. The numerical simulations predicted very accurately the macroscopic response of the composite in terms of load–displacement curve, as well as the damage development and crack growth in front of the notch tip (Figure 15.13c), demonstrating the ability of the embedded cell approach to simulate the fracture behaviour of heterogeneous materials.

15.4.5 Transverse ply cracking in cross-ply laminates

Computational micromechanics has been limited so far to the analysis of RVEs containing several dozens of fibres. This scenario is changing rapidly because of the ever-increasing power of digital computers and to the development of more efficient simulation tools. Now it is becoming possible to bridge the gap between microscale and mesoscale models by the direct expansion of the computational micromechanics models presented above. This is the case, for instance, of the work carried out by Herráez et al. (2015) regarding the onset and propagation of transverse cracking in cross-ply glass–epoxy laminates with $[0_2/90_n]_s$ stacking sequence ($n = 1$, 2, 4 and 8). In this work, the supporting plies of the laminate at 0° plies were modelled as homogeneous, anisotropic linear elastic solids while the actual microstructure of the unidirectional composites was included in the central layers at 90° (Figure 15.11). Failure by interface decohesion and matrix cracking was introduced

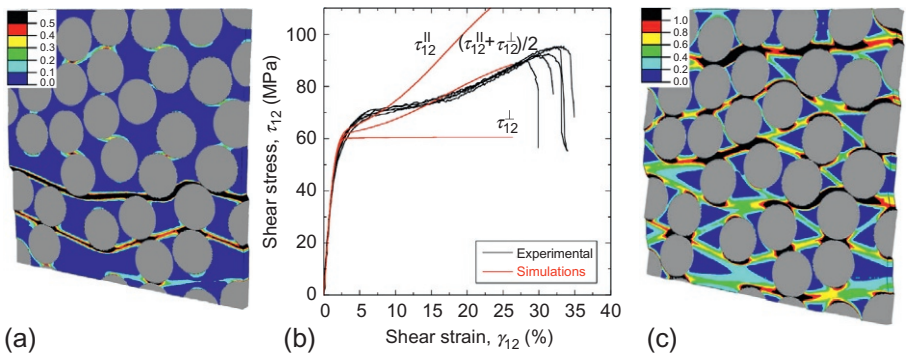

Figure 15.11 Representative volume element of an unidirectional carbon/epoxy composite ply subjected to in-plane shear. (a) Contour plot of the effective plastic strain under in-plane shear loading parallel to the fibres, $\tau_{12}^{\parallel}$. (b) Prediction of the in-plane stress–strain curve $\tau_2 - \gamma_{12}$ of the cross-ply laminate and comparison with experimental results. (c) Contour plot of the effective plastic strain under in-plane shear loading perpendicular to the fibres, $\tau_{12}^{\perp}$.

in the constitutive equation of interfaces and matrix in the central 90° ply and perfect bonding between plies was assumed in the model. The length of the laminate (≈10 mm in this work) was large enough to allow the development of multiple matrix cracking so the transverse crack density (number of cracks per unit length) can be determined. The matrix and interface properties were obtained from *in situ* micromechanical tests, as described in Section 15.3 (Canal et al., 2012a).

In-plane tensile stress along the 0° plies were applied to the laminate, including the effects of thermal residual stress developed upon processing. Deformation led to cracking of the transverse 90° plies. The transverse cracks were formed by the coalescence and growth of fibre/matrix interface decohesions and the subsequent shear failure of the matrix ligaments between adjacent fibres at a given section of the ply (Figure 15.12a). These results are in good agreement with the experimental observations of the transverse failure micromechanisms of glass/epoxy laminates described in Canal et al. (2012a). The transverse crack path depended not only on the actual fibre spatial distribution within the RVE but also on the thickness of the 90° plies. In particular, crack branching and meandering towards the 0°/90° interface was more prone to occur in thicker 90° plies (Figure 15.12b). In addition, when the crack reached 0° ply, damage was spread along the interface between 0°and 90° plies, and this phenomenon was also more noticeable in laminates with thicker 90° plies.

In agreement with the experimental results in the literature, the strain-to-failure increased as the thickness of the 90° plies decreased (Nairn, 2000; Parvizi et al., 1978). In addition, the critical strain for first matrix cracking seemed to reach a steady-state value, independent of the ply thickness for thick 90° plies (>300 μm). Parvizi et al. (1978) measured the critical strain for first matrix cracking in cross-ply E-glass/epoxy cross-ply laminates and found that the size effects that disappeared with the thickness of the 90° ply was approximately 400–500 μm. In addition, the critical matrix strain increased from 0.6% to 1.6% when the 90° ply thickness decreased

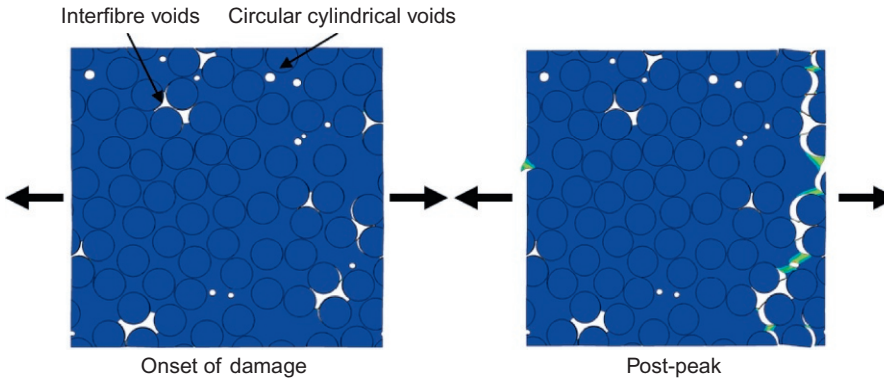

Figure 15.12 RVE of a porous unidirectional ply subjected to transverse tension showing cylindrical voids in the matrix and interfibre porosity. Damage by interface decohesion is triggered at the interfibre voids and propagates by the formation of a crack perpendicular to the tensile stress that links the interfibre voids in the microstructure.

from 400 to 100 μm and these experimental results were in good agreement with the numerical simulations carried out by Herráez et al. (2015). Finally, the simulations showed that the crack density increased linearly with the applied strain, leading to a very high density of thin cracks, whereas thick plies presented a lower density of thicker cracks, in agreement with the trends predicted by the shear lag model (Figure 15.12b).

15.5 Conclusions and future developments

The results presented in this chapter show that computational micromechanics has become a powerful tool to link the microstructural features of unidirectional fibre-reinforced composites with the macroscopic ply properties (Figures 15.13 and 15.14). These capabilities have been put together in a computational tool kit for Abaqus, VIPPER (VIrtual Ply PropERty) (Naya et al., 2014), which allows us to carry out virtual design of unidirectional plies by computing the macroscopic properties (stiffness, strength) from the mechanical properties of fibres, matrix and interface and the volume fraction, shape and spatial distribution of the fibres. This tool is very useful from the industrial viewpoint to select new material configurations with optimised properties for specific applications and also to provide the input data for the structural analysis of laminates within the framework of computational mesomechanics (LLorca et al., 2011).

Further developments in the area of computational micromechanics are expected in various directions. Multifunctional properties (thermal and electrical conductivity, electromagnetic shielding, damping, acoustic behaviour) can be included in the current strategy insofar as the governing equations of these phenomena can be solved using the finite element method. In addition, complex RVE corresponding to different

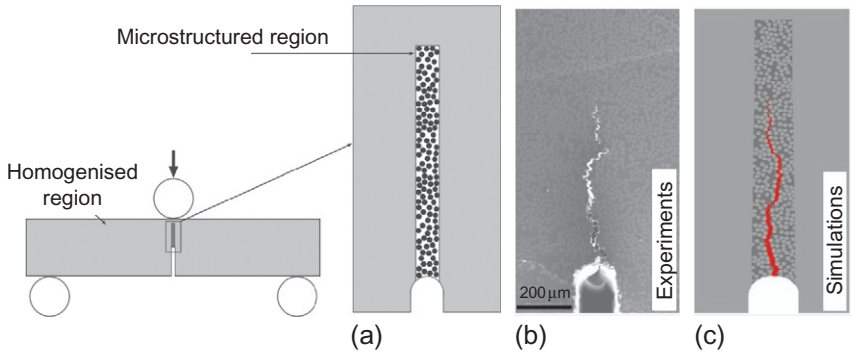

Figure 15.13 (a) Embedded cell strategy to determine the intraply toughness of a unidirectional composite ply. The details of the microstructure (fibres and matrix) are resolved in front of the notch, whereas the remaining material is represented by a homogeneous, transversally isotropic solid. (b) Scanning electron microscopy micrograph of the crack emanating from the notch root. (c) Simulated crack path for the applied load and displacement in (b).

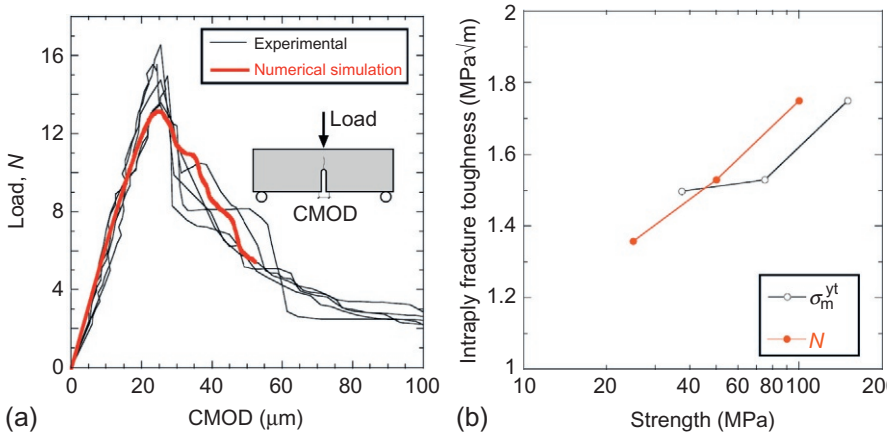

Figure 15.14 (a) Load-CMOD (crack mouth opening displacement) of the three-point bending embedded model and comparison with experimental results. (b) Effect of interface tensile strength, N, and of the matrix tensile strength, σ_m^{yt}, on the apparent interply toughness computed with the embedded cell strategy shown in Figure 15.13.

fibre architectures (woven, braided, stitched, etc.) can be simulated owing to the increased power of digital computers, so the strength, toughness and failure locus under multiaxial stress states can be accurately predicted by means of computational micromechanics. Finally, current models for matrix and interface fracture are purely phenomenological and the model parameters are fitted with experimental data obtained through nanomechanics. Although this strategy is very useful, the development of physically based fracture models of polymers and interfaces (coming from molecular dynamics simulations) will bring chemistry into the design strategy of fibre-reinforced polymers, laying the foundations for a true multiscale model strategy that goes from atoms to structures.

Acknowledgements

This paper summarises the results obtained in a number of research projects and fellowships supported by the Spanish Ministry of Economy and Competitiveness, the Seventh Framework Program of the European Union and Airbus. We gratefully acknowledge their support. In addition, we acknowledge the contributions of Dr. J. M. Molina-Aldareguía, and Dr. J. Segurado as well as from the graduate students and postdoctoral associates from our research groups.

References

Bazant, Z.P., Oh, B.H., 1983. Crack band theory for fracture of concrete. Mater. Struct. 16, 155–177.

Böhm, H.J., 2014. A Short Introduction to Basic Aspects of Continuum Micromechanics. Vienna University of Technology, Vienna, Austria.

Budiansky, B., Fleck, N.A., 1994. Compressive kinking of fibre composites: a topical review. Appl. Mech. Rev. 47, S246–S270.
Camanho, P.P., Catalanotti, G., Xavier, J., 2014a. Measurement of the compressive crack resistance curve of composites using the size effect law. Compos. Part A 56, 300–307.
Camanho, P.P., Arteiro, A., Melro, A.R., Cantalanotti, G., Vogler, M., 2014b. Three-dimensional invariant-based failure criteria for fibre-reinforced composites. Int. J. Solids Struct. 55, 92–107.
Canal, L.P., Segurado, J., LLorca, J., 2009. Failure surface of epoxy-modified fiber-reinforced composites under transverse tension and shear. Int. J. Solids Struct. 46, 2265–2274.
Canal, L.P., González, C., Segurado, J., LLorca, J., 2012a. Intraply fracture of fiber-reinforced composites: microscopic mechanisms and modeling. Comp. Sci. Technol. 72, 1223–1232.
Canal, L.P., González, C., Molina-Aldareguía, J.M., Segurado, J., LLorca, J., 2012b. Application of digital image correlation at the microscale in fiber-reinforced composites. Compos. Part A 43, 1630–1638.
Dávila, C., Camanho, P.P., Rose, C.A., 2005. Failure criteria for FRP laminates. J. Comp. Mater. 39, 323–345.
Desarmot, G., Favre, J.P., 1991. Advance in pull-out testing and data analysis. Comp. Sci. Technol. 42, 151–187.
Fleck, N.A., 1997. Compressive failure of fiber composites. Adv. Appl. Mech. 33, 43–117.
González, C., LLorca, J., 2006. Multiscale modeling of fracture in fiber-reinforced composites. Acta Mater. 54, 4171–4181.
González, C., LLorca, J., 2007a. Mechanical behavior of unidirectional fiber-reinforced polymers under transverse compression: microscopic mechanisms and modeling. Comp. Sci. Technol. 67, 2795–2806.
González, C., LLorca, J., 2007b. Virtual fracture testing of composites: a computational micromechanics approach. Eng. Fract. Mech. 74, 1126–1138.
González, C., LLorca, J., 2007c. Numerical simulation of the fracture behavior of Ti/SiC composites between 20°C and 400°C. Metall. Mater. Trans. A 38, 169–179.
Hazanov, S., Huet, C., 1994. Order relationships for boundary condition effects in heterogeneous bodies smaller than the representative volume. J. Mech. Phys. Solids 42, 1995–2011.
Herráez, M., Mora, D., Naya, F., Lopes, C.S., González, C., LLorca, J., 2015. Transverse cracking of cross-ply laminates: A computational micromechanics perspective. Compos. Sci. Technol. 110, 196–204.
Hine, P.J., Lusti, H.R., Gusev, A.A., 2002. Numerical simulation of the effects of volume fraction, aspect ratio and fibre length distribution on the elastic and thermoelastic properties of short fibre composites. Comp. Sci. Technol. 62, 1445–1453.
Kaddour, A.S., Hinton, M.J., Soden, P.D., 2004. Failure Criteria in Fiber-Reinforced Polymer Composites: The World Wide Failure Exercise. Elsevier, Oxford, UK.
Kinloch, A.J., Young, R.J., 1983. Fracture Behaviour of Polymers. Applied Science Publishers, London and New York.
Lee, J., Fenves, G.L., 1998. Plastic-damage for cyclic loading of concrete structures. J. Eng. Mech. 124, 892–900.
LLorca, J., et al., 2011. Multiscale modeling of composite materials: a roadmap towards virtual testing. Adv. Mater. 23, 5130–5147.
LLorca, J., González, C., Molina-Aldareguía, J.M., Lópes, C.S., 2013. Multiscale modeling of composites. Towards virtual testing … and beyond. JOM 65, 215–225.
Lubliner, J., Oliver, J., Oller, S., Oñate, E., 1989. A plastic-damage model for concrete. Int. J. Solids Struct. 25, 299–329.
Melro, A.R., Camanho, P.P., Andrade, Pires F.M., Pinho, S.T., 2013. Micromechanical analysis of polymer composites reinforced by unidirectional fibres: part II—micromechanical analyses. Int. J. Solids Struct. 50, 1906–1915.

Miller, B., Muri, P., Rebenfeld, L., 1987. A microbond method for determination of the shear strength of a fiber/resin interface. Comp. Sci. Technol. 28, 17–32.

Nairn, J., 2000. Matrix microcracking in composites. In: Talreja, R., Manson, J.A. (Eds.), In: Comprehensive Composite Materials, vol. 2. Elsevier Science.

Naya, F., Herraez, M., Lopes, C.S., Segurado, J., González, C., LLorca, J., 2014. VIPPER (VIrtual Ply PropERty) Simulator. IMDEA Materials Institute, Getafe, Madrid.

Nemat-Nasser, S., Hori, M., 1999. Micromechanics. Overall Properties of Heterogeneous Materials. Elsevier, Amsterdam, North-Holland.

Ogihara, S., Koyanagi, J., 2010. Investigation of combined stress state failure criterion for glass fiber/epoxy interface by the cruciform specimen method. Compos. Sci. Technol. 70, 143–150.

Parvizi, A., Garret, K.W., Bailey, J.E., 1978. Constrained cracking in glass fibre-reinforced epoxy cross-ply laminates. J. Mater. Sci. 13, 195–201.

Pinho, S.T., Robinson, P., Iannucci, L., 2006. Fracture toughness of the tensile and compressive fibre failure modes in laminated composites. Comp. Sci. Technol. 66, 2069–2079.

Puck, A., Schürmann, H., 2002. Failure analysis of FRP laminates by means of physically-based phenomenological models. Comp. Sci. Technol. 62, 1633–1662.

Quinson, R., Perez, J., Rink, M., Pavan, A., 1997. Yield criteria for amorphous glassy polymers. J. Mater. Sci. 32, 1371–1379.

Rodríguez, M., Molina-Aldareguía, J.M., González, C., LLorca, J., 2012a. Determination of the mechanical properties of amorphous materials through instrumented nanoindentation. Acta Mater. 60, 3953–3964.

Rodríguez, M., Molina-Aldareguía, J.M., González, C., LLorca, J., 2012b. A methodology to measure the interface shear strength by means of the fiber push-in test. Comp. Sci. Technol. 72, 1924–1932.

Romanowicz, M., 2012. A numerical approach for predicting the failure locus of fiber reinforced composites under combined transverse compression and axial tension. Comput. Mater. Sci. 51, 7–12.

Segurado, J., LLorca, J., 2002. A numerical approximation to the elastic properties of sphere-reinforced composites. J. Mech. Phys. Solids 50, 2107–2121.

Totry, E., González, C., LLorca, J., 2008a. Failure locus of fiber-reinforced composites under transverse compression and out-of-plane shear. Comp. Sci. Technol. 68, 829–839.

Totry, E., González, C., LLorca, J., 2008b. Influence of the loading path on the strength of fiber-reinforced composites subjected to transverse compression and shear. Int. J. Solids Struct. 45, 1663–1675.

Totry, E., González, C., LLorca, J., 2008c. Prediction of the failure locus of C/PEEK composites under transverse compression and longitudinal shear through computational micromechanics. Comp. Sci. Technol. 68, 3128–3136.

Totry, E., González, C., LLorca, J., Molina-Aldareguía, J.M., 2009. Mechanisms of shear deformation in fiber-reinforced polymers: experiments and simulations. Int. J. Fracture 158, 197–209.

Totry, E., Molina-Aldareguía, J.M., González, C., LLorca, J., 2010. Effect of fiber, matrix and interface properties on the in-plane shear deformation of carbon-fiber reinforced composites. Comp. Sci. Technol. 70, 970–980.

Trias, D., Costa, J., Turón, A., Hurtado, J., 2006. Determination of the critical size of a statistical representative volume element (SRVE) for carbon reinforced polymers. Acta Mater. 54, 3471–3484.

Vajari, D.A., González, C., LLorca, J., Legarth, B.N., 2014. A numerical study of the influence of microvoids in the transverse mechanical response of unidirectional composites. Comp. Sci. Technol. 97 (46–54), 2014.

Vaughan, T.J., McCarthy, C.T., 2010. A combined experimental–numerical approach for generating statistically equivalent fibre distributions for high strength laminated composite materials. Comp. Sci. Technol. 70, 291–297.

Vaughan, T.J., McCarthy, C.T., 2011a. Micromechanical modelling of the transverse damage behaviour in fibre reinforced composites. Comp. Sci. Technol. 71, 388–396.

Vaughan, T.J., McCarthy, C.T., 2011b. A micromechanical study on the effect of intra-ply properties on transverse shear fracture in fibre reinforced composites. Compos. Part A 42, 1217–1228.

Vogler, T.J., Kyriakides, S., 2001. On the initiation and growth of kink bands in fiber composites: part I experiments. Int. J. Solids Struct. 38, 2639–2651.

This page intentionally left blank

Numerical modelling for predicting failure in textile composites

16

M.Y. Matveev, A.C. Long
University of Nottingham, Nottingham, UK

16.1 Introduction

Textile composites, which are a combination of polymer matrix and textile reinforcements, provide an attractive alternative to unidirectional (UD) composites as they enable easier and automated manufacturing of complex component shapes. Ease of draping results in lower overall manufacturing costs. The large variety of available textile reinforcements, which includes woven, braided and knitted fabrics, offers a large choice of engineering solutions. Components made of textile composites are extensively used in aerospace, marine and other industries including some primary, load-bearing structures (Long, 2006). Amongst the more advanced technologies, braiding can be employed for manufacturing a textile reinforcement shaped around a foam core, which then can be moulded by RTM to produce a component with multi-axial reinforcement. Three-dimensional (3D) woven reinforcements are applied in the manufacturing of structures where a higher delamination resistance is required (Long, 2006). However, the inherent structure of textile reinforcements adds complexity to the performance analysis of composite materials.

An extensive review of analytical models published by Crookston et al. (2005) concluded that analytical models can provide an efficient first estimation of elastic properties but compromise the precision of strength analysis due to simplification of geometry and yarn–yarn and yarn–matrix interaction. Although new analytical models are still of interest for the research community, the majority of analyses are performed numerically. This approach provides more flexibility in defining reinforcement geometry and allows more complex mechanics to be added since it relies on available finite element (FE) solvers.

Most of the approaches for both analytical and numerical modelling of textile composites are based on multi-scale concepts which separates modelling problem as several consequent tasks. Typically, a textile composite component consists of several layers of textile with many interwoven yarns. In turn each yarn consists of thousands of single fibres. This complexity leads to limitations that make it impractical to create a theoretical or numerical model which takes account of all of these details at once. At the same time, a composite can be considered as a hierarchy of structures on different scale levels: individual fibres in matrix at the micro-scale, textile reinforcement in matrix at the meso-scale and a whole component at the macro-scale. Next, all the scales starting from the micro-scale are progressively homogenised by representing

Numerical modelling of failure in advanced composite materials. http://dx.doi.org/10.1016/B978-0-08-100332-9.00016-5
Copyright © 2015 Elsevier Ltd. All rights reserved.

a heterogeneous medium as a homogeneous medium with equivalent effective stiffness and strength. A domain of a geometry required to calculate the effective properties is usually referred to as a representative volume element (RVE). Extracting and modelling of individual geometrical scale levels of the composite structure by RVE is the key problem of the multi-scale approach, as described, for example, by Ghosh (2008) or Lomov et al. (2001).

Analysis of textile composites is mainly a problem at the meso-scale because the elastic properties of the yarns are calculated at the micro-scale with numerical or analytical models or obtained by mechanical testing. A general roadmap for textile composite modelling (create geometry, create FE mesh, apply boundary conditions (BCs) and damage model) has already become a standard procedure except for the last step of damage modelling. This chapter will be focused on practical issues of meso-scale modelling of textile composites. It includes a review of methods for geometrical modelling of textile reinforcements, the problem of meshing the geometry and finally damage modelling. Examples of successful modelling of damage initiation and propagation in textile composites are presented. Finally, the chapter will give an overview for current trends in research and possible future breakthroughs in this area of research.

16.2 Unit cell modelling

16.2.1 Geometry modelling

At the meso-scale, yarns are interwoven together in textile structures and form textile composites together with a matrix material. Following the multi-scale approach, yarns are assumed to be homogeneous and transversely isotropic with the effective properties of fibre bundles, i.e., UD composites. The geometry of the textile composite is defined by the reinforcement, in particular, the weave style and weave parameters (e.g., number of ends/picks per cm, yarn linear density). The repetitive patterns of common weave styles are shown in Figure 16.1. It is often assumed that geometry of the RVE at a chosen scale can be idealised as a periodic structure, e.g., hexagonal arrangement of fibres at the micro-scale instead of a random arrangement.

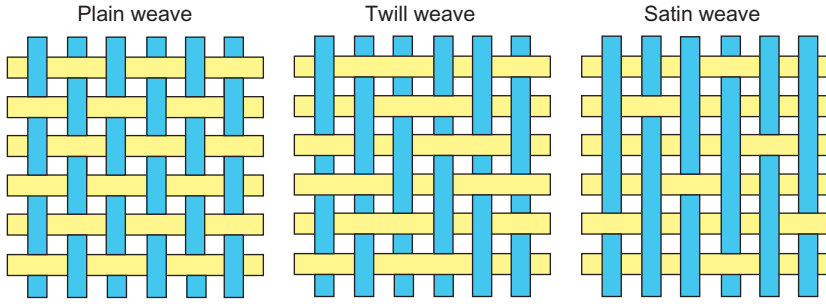

Figure 16.1 Examples of textile weave patterns.

The periodicity of the weave pattern is usually used to reduce the RVE of the textile composite to a periodic unit cell. Obviously, a unit cell of a textile composite is an idealisation similar to the assumption of a regular fibre arrangement in a UD composite, whereas real samples exhibit some variations from this pattern. However, use of the averaged unit cell geometry has proven to be an effective way to study properties of composites. The unit cell geometry can be defined by parameters measured directly from a reinforcement or a textile composite (width of yarn, thickness of a yarn and layer, length of a unit cell) as shown in Figure 16.2.

According to the review published by Crookston et al. (2005), effective methods include an orientation averaging approach for 3D woven composites as suggested by Cox and Dadkhah (1995), a range of models based on classical laminate theory was developed by Ishikawa and Chou (1982) for the prediction of elastic properties and Eshelby's inclusion theory as applied by Huysmans et al. (1998). Numerical modelling makes it possible to analyse geometries with yarns following arbitrary paths, having arbitrary cross-section shapes and complex mechanical interaction of yarns and matrix.

Geometrical models for numerical analysis can be as simple as yarn paths following sine waves (Ito and Chou, 1998) or circular arcs (Dasgupta et al., 1996) with constant cross-section, which can be chosen for convenience of construction of the model (often designed such that yarns are in perfect contact with each other where they cross over). An artificial yarn path and constant yarn cross-section can lead to inadequate representation of the actual geometry. A more refined geometry can be created with one of the textile pre-processors, the two most well-known of which are TexGen (Long and Brown, 2011) and WiseTex (Lomov et al., 2000). TexGen software is based on representation of yarns in a textile as periodic cubic splines. Automatic geometry refinement of yarn cross-sections ensures the absence of yarn interpenetrations. Despite the fact that there is no physical basis behind these procedures, built-in refinements of the geometry based on extensive experimental measurements provide good results when compared to micro-computed tomography (μ-CT) scans of a textile unit cell. WiseTex software is based on a mechanical approach using the principle of

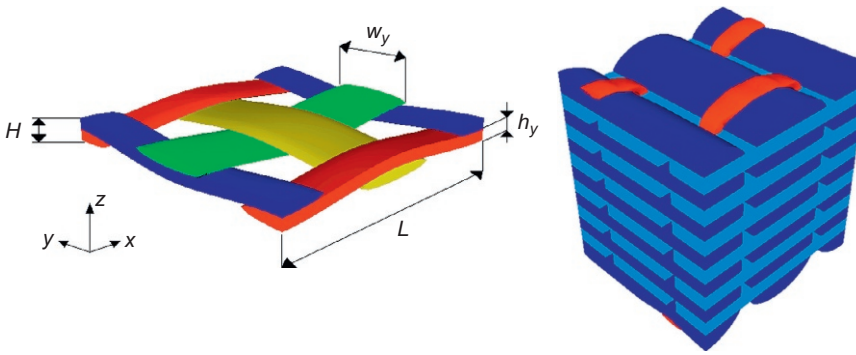

Figure 16.2 The unit cell of a plain weave textile composite and its parameters (matrix removed) (left) and the unit cell of an orthogonal 3D woven composite (matrix removed) (right).

minimum mechanical energy (Lomov et al., 2000). Using the data about a weaving pattern and mechanical behaviour of dry yarns, WiseTex software can accurately predict yarn paths. However, experimental determination of mechanical behaviour of dry yarns requires additional studies and can be a challenging problem.

A completely different way to create geometry is based on textile mechanics and modelling of mechanical loading during compaction and forming. Initial research by Wang and Sun (2001) relied on representing yarns in a textile in the form of chains of one-dimensional (1D) rods connected by frictionless pins. The chains are then put into contact to predict textile geometry. This approach, called the digital chain element method, was further developed by Zhou et al. (2004) by representing yarns as multi-chain bundles. It allowed the shape of the yarns along with the textile geometry to be predicted. The digital chain element method can be useful in prediction of complex geometries when a textile pre-processor fails to predict the correct geometry (Green et al., 2014a).

Many successful attempts have been made to numerically estimate the elastic properties of textile composites using the pre-processors mentioned previously; e.g., a geometry created in WiseTex was used for FE analysis of a plain weave by Kurashiki et al. (2007a)), a braided composite by Ivanov et al. (2009) and a satin weave by Daggumati et al. (2010). TexGen was used for analysis of a 3D textile composite by Zeng et al. (2014), and for 2D textiles and a braided textile composite by Schultz and Garnich (2013). Prediction of correct elastic properties is relatively straightforward and requires only a geometrical model with correct fibre volume fraction and local fibre orientations.

16.2.2 Boundary conditions

Choice of BCs, which should be applied to a unit cell, is essential for correct prediction of the stress–strain state of the unit cell. Obviously, the choice of a unit cell is never unique, but it does not affect the results of analysis when correct BCs are applied. In some cases the size of a unit cell can be quite large, e.g., the length (L) of the plain weave unit cell in Figure 16.2 can be at least an order of magnitude smaller than that of the 3D composite unit cell, which will result in higher computational time. A possible way to deal with this problem will be discussed later in this section.

A periodic representation of a composite requires correctly formulated BCs. Von Neumann and Dirichlet BCs both satisfy the Hill–Mandel principle of homogeneity (Hazanov and Amieur, 1995). However, von Neumann and Dirichlet BCs do not provide a purely periodic solution in the case of a periodic unit cell; moreover, they provide elastic properties that are lower and upper bounds for elastic properties for a periodic arrangement, respectively. For periodic unit cells, periodic BCs are required to satisfy both periodicity of the stress–strain field and the Hill–Mandel condition. The periodic BCs schematically illustrated in Figure 16.3 for an arbitrary pair of corresponding points A and B can be written as:

$$\mathbf{u}^{\mathrm{A}} = \mathbf{u}^{\mathrm{B}} + \langle \boldsymbol{\varepsilon} \rangle \cdot \mathbf{d} \tag{16.1}$$

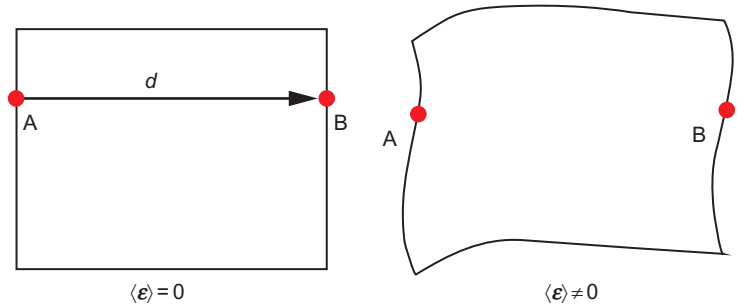

Figure 16.3 Unit cell with applied periodic BCs: no load (left), load (right).

where $\mathbf{u}^{A}$ and $\mathbf{u}^{B}$ are displacements at corresponding points A and B, $\langle \boldsymbol{\varepsilon} \rangle$ is the average applied strain and $\mathbf{d}$ is the translational vector for the pair A–B (for a different pair vector $\mathbf{d}$ will be different as well, depending on the location of points on the boundary).

An overview of the application of periodic BCs in Abaqus software was presented by Li (2001). Periodic BCs for unit cells of plain and satin weave textile composites and their reduced unit cells were presented, e.g., by Whitcomb et al. (2000). Later this method was extended by De Carvalho et al. (2011) for an arbitrary case of internal symmetries including shift, reflection and rotation. The algorithm is based on transformation of canonical periodic BCs (16.1) into a new form:

$$\mathbf{u}^{A} = \gamma \boldsymbol{T} \cdot \mathbf{u}^{\hat{A}} - \langle \boldsymbol{\varepsilon} \rangle \cdot \boldsymbol{T} \cdot \mathbf{d} \tag{16.2}$$

where $\boldsymbol{T}$ is a transformation matrix between sub-domains (reduced unit cell) of the full unit cell and $\gamma = \pm 1$ is the load reversal factor which ensures load compatibility between sub-domains.

This algorithm can be extremely useful when analysing a large unit cell, such as the volume of the 3D composite unit cell in Figure 16.2. A process for unit cell reduction is shown in Figure 16.4.

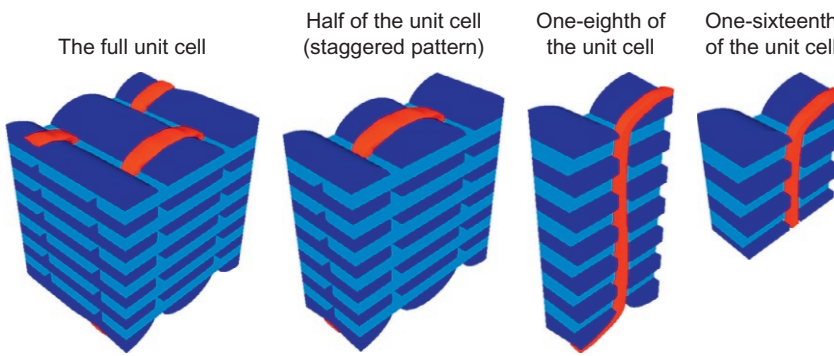

Figure 16.4 Reduced unit cells of orthogonal 3D woven composite.

An objection may be raised that periodic BCs in the through thickness direction are incorrect when compared to composite laminates with a finite number of layers. Still further, through thickness periodic BCs mean that each layer is placed and oriented exactly in the same way as adjacent layers while in real life it can be shifted or rotated in plane. Ivanov et al. (2010) studied stress distributions in inner and outer layers of a textile composite laminate. A full FE solution for the composite under tensile loading was compared with a solution obtained using a one-layer model with applied periodic BCs. It was shown that the relative error for the inner layers is relatively small (below 10%) while for the outer layers the error can be up to 50% in certain areas, as shown in Figure 16.5. The relative error was shown to decrease with an increase in the number of layers in the laminate. Special BCs for a single layer model were proposed to approximate the behaviour of the outer layers. This method was later developed for application to laminates with arbitrary shift between layers (Ivanov et al., 2011).

16.2.3 Meshing techniques

A major problem in FE analysis of textile composites is posed by the generation of an FE model (mesh) of the internal geometry. An FE mesh created by any meshing processor has to be checked for mesh quality, which governs precision of the FE solution. The mesh quality of a conformal tetrahedral mesh, expressed in terms of solution error, can be estimated *a priori* in terms of mesh parameters or *a posteriori* in terms of solution parameters. Krizek (1992) derived *a priori* estimation of the solution error, which was found to be in direct proportion with maximal dimension of elements and the inverse ratio of the sine of the maximum angle between faces in an element. The reference manual of Abaqus/Standard™ defines mesh quality *a priori* in terms of aspect ratio, which is the ratio between the longest and shortest edges of an element (ABAQUS 6.9 Documentation, 2010) and recommends that this should not exceed 10. In other words, distorted elements with high-aspect ratio and internal angles close to

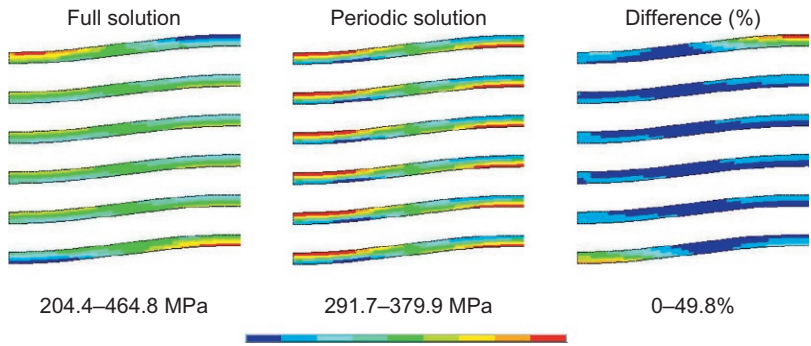

Figure 16.5 Stress distributions in longitudinal yarns under longitudinal tension obtained by full FE analysis and a periodic analysis.
Adapted from Ivanov et al. (2010) with permission from Elsevier.

180° are highly undesirable because they increase solution error. It has been pointed out by several researchers, e.g., Kim and Swan (2003a) and Potter et al. (2012), that for textile composite unit cells conformal FE meshes usually contain distorted elements in regions between the yarns. The problem is worsened when periodic BCs need to be applied due to the requirement of matching nodes on opposite faces of the unit cell. The meshing problem is often solved by introducing an artificial gap between yarns. This helps to allow better quality meshes to be generated, although a clearance between yarns is not usually observed in real textile composites. Also, the fibre volume fraction within the yarns, which needs to be increased to maintain the required global fibre volume fraction, can become unrealistically high. While a good-quality mesh can be constructed for some 2D textile composites, this remains a significant problem for more complex reinforcements (e.g., 3D textile composites).

The mesh superposition technique (Kurashiki et al., 2007b; Zako et al., 2003) and domain superposition technique (Jiang et al., 2008) suggest that the textile structure and matrix boundary domain be meshed separately and then linked during FE analysis. This approach allows easy meshing of any complex geometry without any poorly shaped elements. This technique has shown promising results in predicting elastic and strength properties of woven composites (Kurashiki et al., 2007b; Zako et al., 2003; Jiang et al., 2008). However, a discontinuity of stresses and strains at the interface of yarns and matrix appears in solutions obtained using superposition techniques. This is likely to cause difficulties if used in conjunction with a damage model.

Meshing problems discussed above can be avoided using a voxel mesh technique (Kim and Swan, 2003a). A voxel mesh consists of rectangular cuboidal elements and the element attributes are defined by those present at the voxel centroid. The quality of the voxel mesh is known *a priori*, the mesh can be generated for any geometry without any artificial changes in textile geometry and periodic BCs can be easily applied. On the other hand, the high resolution of a voxel mesh (large number of elements), which is required to achieve a good quality representation of the textile geometry, is limited by computational costs. Comparison between voxel and conformal meshes has shown that for a good prediction the number of voxel elements should be at least two times higher than the number of tetrahedral elements in the converged solution. This is related to additional stress concentrations at the interface between geometrical features introduced by the voxel mesh. To decrease this effect, a voxel mesh can be locally refined (Kim and Swan, 2003a,b) or a smoothing algorithm can be used to improve the interface surface (Potter et al., 2012).

Another solution to the meshing problem can be provided by recent developments in the form of the X-FEM technique (Moes et al., 1999), which provides an opportunity to model arbitrary discontinuities (inclusions and cracks) without remeshing a model. In contrast with conventional meshing techniques, X-FEM is a modification of a common FE method that approximates discontinuity behaviour (inclusions and cracks) with additional terms for the displacement field:

$$u_{x-fem}(x) = \sum_{i \in I} N_i u_i(x) + \sum_{j \in J} N_j H(x) a_j(x) + \sum_{k \in K} N_k \left(\sum_{\alpha=1}^{4} F_\alpha(x) b_{k\alpha} \right) \tag{16.3}$$

where I is the set of all nodes in the mesh, $N_i(x)$ is the nodal shape function, u_i is the standard degrees of freedom (DOF) of node i, a_j and $b_{k\alpha}$ are the DOF of nodes from node sets J and K enriched with the Heaviside function $H(x)$ and crack tip function $F_\alpha(x)$, respectively. A detailed discussion of X-FEM implementation can be found in Moes et al. (1999).

This method proposes enrichment of a conventional mesh with specially constructed nodal functions to accommodate the heterogeneity of material without constructing a conformal mesh. This approach was used by Ling et al. (2009) to compute the stress distribution in a textile composite as shown in Figure 16.6. However, current implementation of X-FEM in commercial codes (e.g. Abaqus) still has some limitations, such as no automatic facility to mesh inclusions, the FE domain can contain only a single crack or non-interacting cracks and no parallel processing is available.

16.3 Damage modelling

Non-linear behaviour in textile composites is more complex than that of UD laminates. First of all, the stress–strain state in textile composites is more complex due to their internal structure. Second, the damage in textile composites includes all possible types of damage just within one unit cell, namely matrix failure, intra-laminar failure of yarns, inter-laminar failure at the yarn–yarn interface and yarn–matrix interface. Two major approaches to model damage in textile composites are continuum damage mechanics (CDM), where failure of a material leads to a degradation of elastic properties of the corresponding FE, and the cohesive element technique, which makes it possible to simulate cracks in a discontinuous way.

16.3.1 Continuum damage mechanics

Damage modelling at the meso-scale assumes yarns in textile composites to be homogeneous and transversely isotropic with properties and behaviour equal to those of UD composites. Since UD composites are not isotropic it is crucial to distinguish the mode of failure, which is usually classified as shown in Figure 16.7. In a CDM, each element is assigned several damage variables which dictate the reduction of the effective properties of the element. The number of variables can vary depending on the approach,

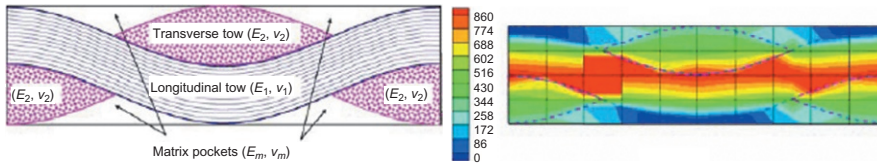

Figure 16.6 Material domains (left); longitudinal stress distribution predicted with X-FEM (right).
Adapted from Ling et al. (2009).

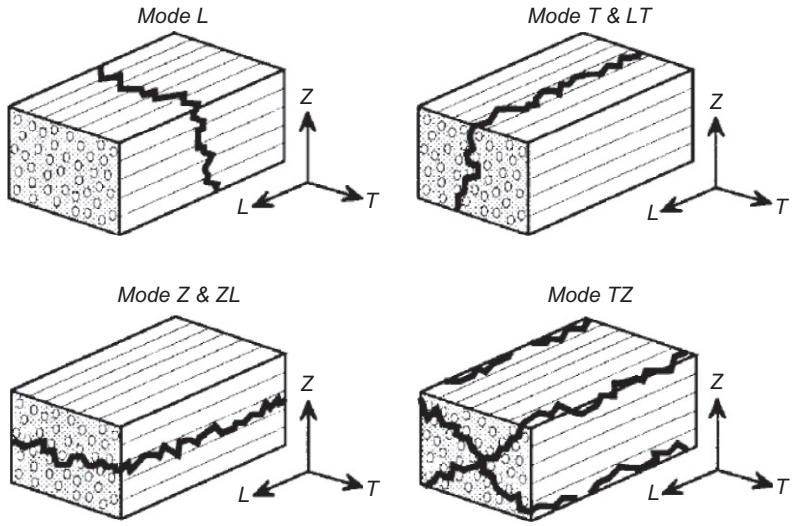

Figure 16.7 Possible modes of failure.
Adapted from Lomov et al. (2007).

but the minimum number is three, which corresponds to the reduction of longitudinal, transverse and shear moduli due to failure. At the initial state, the variables are zero and then increase after the onset of failure.

The simplest criteria for yarn failure as a homogeneous medium are the maximum stress and strain criteria, which can show the mode of failure. Once strengths in all the directions are predicted with one of the micro-scale methods (e.g. numerical, Ernst et al., 2010; or empirical Chamis micromechanical formulae, Chamis, 1984), it can be stated that damage initiates when stresses exceed limiting values of the tensile or compressive strength in the corresponding direction (Blackketter et al., 1993). A range of failure criteria such as polynomial Tsai-Hill (Azzi and Tsai, 1965) and Hoffman (Zako et al., 2003) criteria and the Puck criterion are also sometimes used for predicting the onset of failure in yarns. Onset of failure in matrix pockets should be predicted with a criterion that takes into account hydrostatic pressure, e.g., the Raghava (modified von Mises) criterion (Caddell et al., 1974).

The damage propagation in UD composites or yarns in a textile composite is often modelled with the use of CDM based on a phenomenological or a theoretical model. One of the early applications was shown by Blackketter et al. (1993), who performed numerical studies of a composite reinforced with a plain weave textile. The maximum stress and maximum principal stress criteria were applied to predict damage initiation in yarns and matrix, respectively. Three damage variables governed instantaneous reduction of the elastic modulus due to longitudinal, transverse and shear load. Damage initiation in the longitudinal direction was assumed to degrade all elastic properties to 1% of their initial value and damage in the transverse direction was assumed to degrade properties to 1% of initial value for Young's moduli and 20% of initial value for shear moduli. The strength of the composite under tensile loading was

over-predicted by 20%, while predicted non-linear behaviour and ultimate strength under shear loading was in relatively good agreement with experimental data.

Zako et al. (2003) used a phenomenological damage model based on CDM together with the Hoffman criterion for prediction of non-linear behaviour of a plain weave textile composite. The stress–strain relationship was assumed to be as follows:

$$\begin{pmatrix}\sigma_{11}\\ \sigma_{22}\\ \sigma_{33}\\ \sigma_{12}\\ \sigma_{13}\\ \sigma_{23}\end{pmatrix} = \begin{pmatrix} d_L^2C_{11} & d_Ld_TC_{12} & d_Zd_TC_{13} & 0 & 0 & 0\\ & d_T^2C_{11} & d_Zd_TC_{23} & 0 & 0 & 0\\ & & d_Z^2C_{11} & 0 & 0 & 0\\ & & & d_{TZ}C_{44} & 0 & 0\\ & \text{sym.} & & & d_{ZL}C_{55} & 0\\ & & & & & d_{LT}C_{66}\end{pmatrix}\begin{pmatrix}\varepsilon_{11}\\ \varepsilon_{22}\\ \varepsilon_{33}\\ \varepsilon_{12}\\ \varepsilon_{13}\\ \varepsilon_{23}\end{pmatrix} \tag{16.4}$$

where

$$d_L = 1 - D_L,\quad d_Z = 1 - D_Z,\quad d_T = 1 - D_T$$

$$d_{TZ} = \left(\frac{2d_Td_Z}{d_T + d_Z}\right)^2,\ d_{ZL} = \left(\frac{2d_Ld_Z}{d_L + d_Z}\right)^2,\quad d_{LT} = \left(\frac{2d_Td_L}{d_T + d_L}\right)^2$$

where D_L, D_Z, D_T are components of the damage tensor (damage variables), which is defined with respect to the modes of failure shown in Figure 16.7. The damage variables were allowed to have binary values of 0 or 1 when undamaged and damaged, respectively. The analysis predicted damage initiation near the edges of transverse yarns as shown in Figure 16.8 and their further propagation into matrix material, which was similar to experimental observations. This feature of damage in textile composites was then observed in other studies (Daggumati et al., 2010; Melro et al., 2012). However, the predicted stiffness degradation with the abrupt degradation

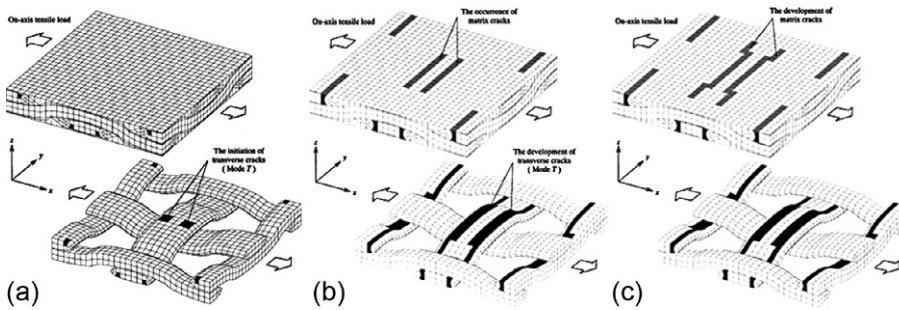

Figure 16.8 Damage patterns in plain weave composite.
Adapted from Zako et al. (2003). Reprinted from Zako et al. (2003) with permission from Elsevier.

model was overestimated compared to experimental data by Zako et al. (2003). Moreover, it can be said that this type of "abrupt element discount" model does not reflect the progressive nature of damage within an element.

Many damage models assume that damage initiation and damage evolution in an element could be described by the same equation. A natural development of these approaches is a model with a phenomenological or physical evolutional law. A large group of approaches employ a rigorous basis of fracture mechanics, e.g., those developed by Ladeveze and Lubineau (2002) or Maimi et al. (2008) for UD composites. All of them are based on expressing a free energy ψ of the medium as a function of effective stress and damage variables in one way or another. The thermodynamic driving forces, Y, can then be found as a derivate of the free energy considering a damage variable d_i as a "crack length":

$$Y = \frac{\partial \psi}{\partial d_i} \tag{16.5}$$

Positive values of the driving force in a certain direction correspond to crack growth, i.e., an increase of the damage variable governed by an evolutionary law. The form of the law can vary as there is no consensus on this. In theory, all the parameters of the evolutional law can be extracted from experiments on UD laminates, but in practice there is usually a lack of data for these models.

These CDM models were initially developed for UD laminates and have been validated against experimental data. Later this type of model was implemented for modelling of textile composites. Ivanov et al. (2009) used the Puck criterion and the Zako damage model (Zako et al., 2003) coupled with a thermodynamic evolution law for predicting the damage development of a triaxial braided composite. The parameters of the degradation law were defined by the inverse experimental FEA modelling of the stress–strain state of a UD composite. The developed approach showed good agreement with experiments for the braided composite.

Melro et al. (2012) conducted studies of the non-linear response of a five-harness satin weave composite under tensile, shear and mixed loadings using Maimi's model (Maimi et al., 2008) as the damage model for the yarn material. The matrix damage model was also based on the same free energy concept as a damage model for yarns. The predicted stress curves were in a good qualitative agreement with the experimental data, but no quantitative comparisons were presented.

In FE implementation, all the CDM models are often named 'element discount methods' due to stiffness degradation of the damaged elements. A large number of published papers show that this method can be usefully applied in a range of modelling problems. However, Gorbatikh et al. (2007) indicated that some of these models may be inadequate under shear loading causing widening of the zones with transverse damage in the direction perpendicular to fibres instead of increasing the crack length in the transverse direction. It was proposed that this happens not due to 'discounting' elements but due to the application of the CDM approach to modelling of meso-cracks while initially it was developed to model "diffused" damage (i.e. micro-cracks) before any substantial large cracks (meso-cracks) had occurred.

One of the possible solutions is to reduce locality of the CDM application (also called volume averaging), i.e., consider damage variables to describe not a single element but a group of elements. Ivanov et al. (2009) used such an approach to model a triaxial braided composite which consisted of yarns subdivided into segments that can be considered as series of UD composites. These segments were analysed via a CDM framework as described above.

The choice of the damage model is still debatable for 3D numerical models such as textile composites. The extensive studies undertaken within "The World-Wide Failure Exercise" (WWFE) (Hinton et al., 2004) reviewed and benchmarked more than 10 damage theories for various loading cases of various UD laminates. Further studies of failure under a 3D stress state (Kaddour and Hinton, 2013) found that even for the better theories, failure was predicted between 10% and 50% from experimental results in 45% of the cases. Additionally, a reliable prediction required an extensive experimental data set (~20–70 parameters). Theories that performed best were identified: Carrere et al. (2012), Cuntze (2012), Pinho et al. (2012) and Deuschle and Kroplin (2012).

16.3.2 "Cohesive element" damage models

An alternative to the CDM approach is to model cracks as discontinuities; this method was reviewed by Wisnom (2010). The key idea is to introduce damageable surfaces (sometimes fictitious), i.e., cohesive elements, the behaviour of which is defined in terms of linear elastic fracture mechanics, into a numerical model of a composite. The constitutive equation for traction-displacement for a cohesive element with linear softening shown in Figure 16.9 can be written as

$$\tau = (1 - d)K\Delta \tag{16.6}$$

where τ is traction, Δ is displacement, K is stiffness and d is damage variable.

An integrated non-linear behaviour of the opening cracks will govern the non-linear response of the composite. This allows the interaction between intralayer and interlayer cracks to be taken into account, and at the same time avoids non-physical effects of CDM as discussed above. In addition, it allows the link of strain energy release rate to damage propagation in cohesive elements.

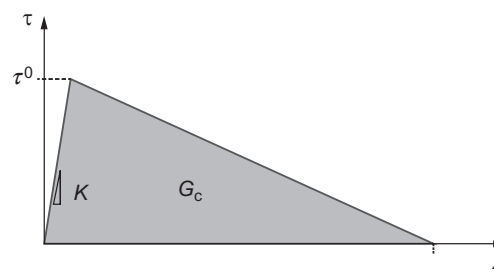

Figure 16.9 Linear softening law for a cohesive element.
Reprinted from Turon et al. (2007) with permission from Elsevier.

This method has proved to be adequate for various UD laminates (e.g. Hallett et al., 2008) and was used to model damage in a textile composite by McLendon and Whitcomb (2013). However, it required *a priori* knowledge about crack orientation which is not always possible for some loading cases, especially in the matrix. A possible way to extend this approach is via X-FEM techniques as discussed earlier.

16.3.3 Comparison with experiments

Comparison of numerical results with experiments is the most important part of the validation of a numerical model. Most of the published studies perform comparisons for a small number of loading scenarios (usually UD tension) and to the authors' knowledge none of the studies has carried out exhaustive validations comparable to the WWFE for UD composites.

Blackketter et al. (1993) used the simplest element discount CDM model to predict behaviour of a plain weave composite. A comparison of stress–strain curves for UD tensile loading is shown in Figure 16.10. The predicted stress–strain curve captured the initial Young's modulus and the kink in the stress–strain curve. The final strength was overpredicted by about 20%.

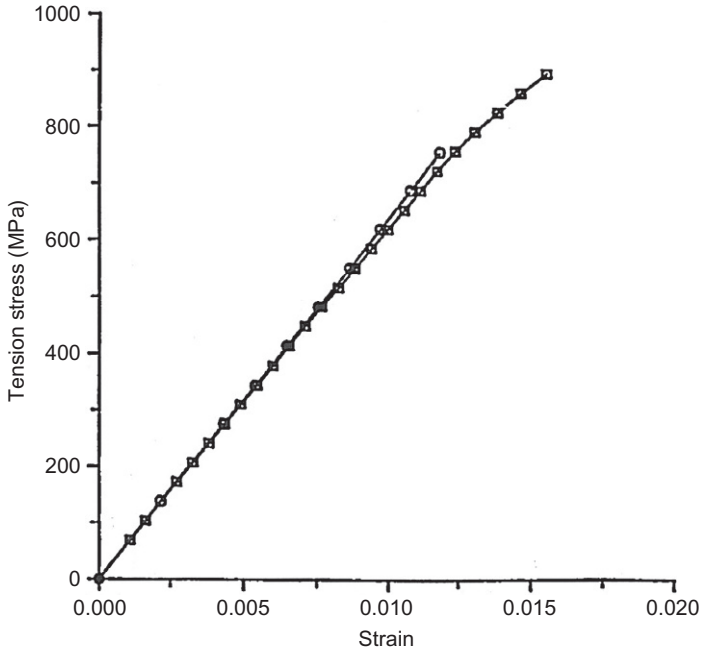

Figure 16.10 Comparison of predicted (□) and experimental (○) stress–strain curves for carbon fibre plain weave composite.
Reprinted, with permission, from Blackketter et al. (1993), copyright ASTM International, 100 Barr Harbor Drive, West Conshohocken, PA 19428.

A similar CDM model proposed by Zako et al. (2003) predicted some unnatural discontinuities in stress–strain curves (Figure 16.11) where a continuous curve was expected. However, comparison of the Young's modulus reduction showed good correlation with experimental results. The main difference was again a sudden drop in predicted modulus while a smooth degradation was expected.

A CDM model with phenomenological gradual degradation law employed by Matveev et al. (2014) was able to capture gradual degradation of the Young's modulus of a textile composite based on a TexGen model. Numerical analysis captured the kink in the stress–strain curve as shown in Figure 16.12. The kink was explained by

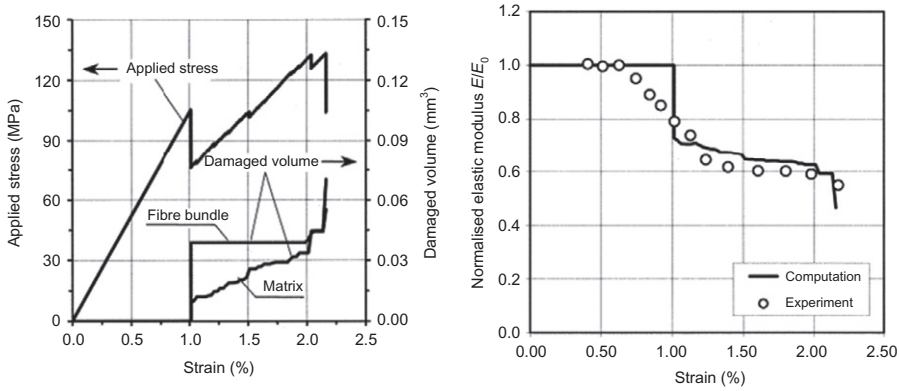

Figure 16.11 Predicted stress–strain curve for glass fibre plain weave composite and volume of damaged material (left) (Zako et al., 2003); predicted and experimental modulus reduction (right) (Zako et al., 2003).
Reprinted from Zako et al. (2003) with permission from Elsevier.

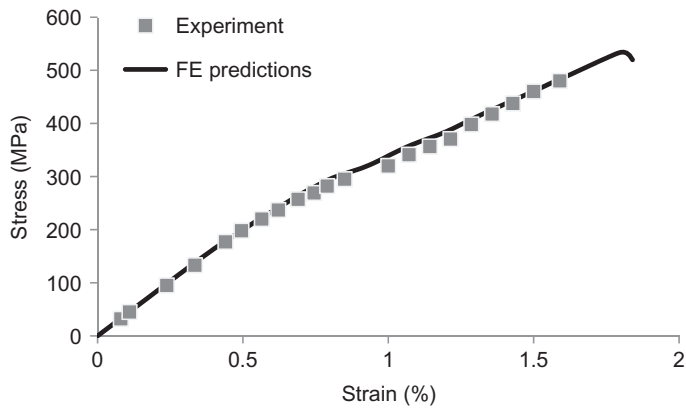

Figure 16.12 Predicted and experimental stress–strain curves for carbon fibre plain weave composite.
Reprinted from Matveev et al. (2014) with permission from Elsevier.

straightening of the yarns and transverse damage within them. However, the final strength was overpredicted by about 10%. The three examples considered here show that even simple CDM models can give adequate results in the case of simple loading scenarios.

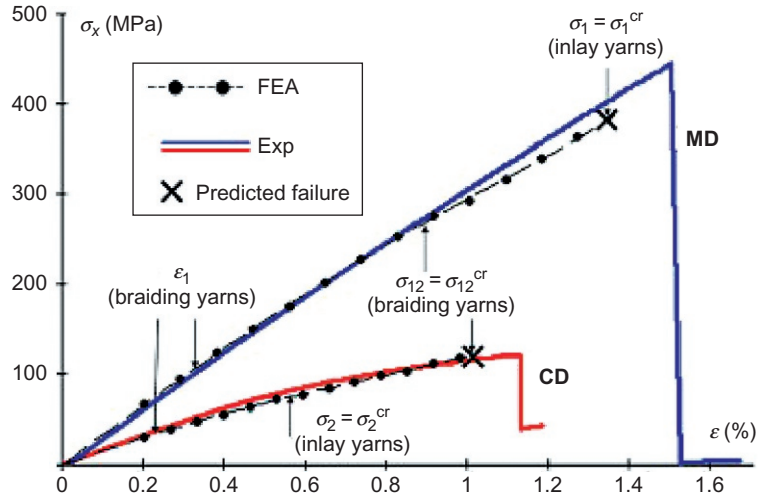

Figure 16.13 Predicted and experimental stress–strain curves for carbon fibre-braided composite. MD – load in machine direction, CD – load in cross direction. Reprinted from Ivanov et al. (2009) with permission from Elsevier.

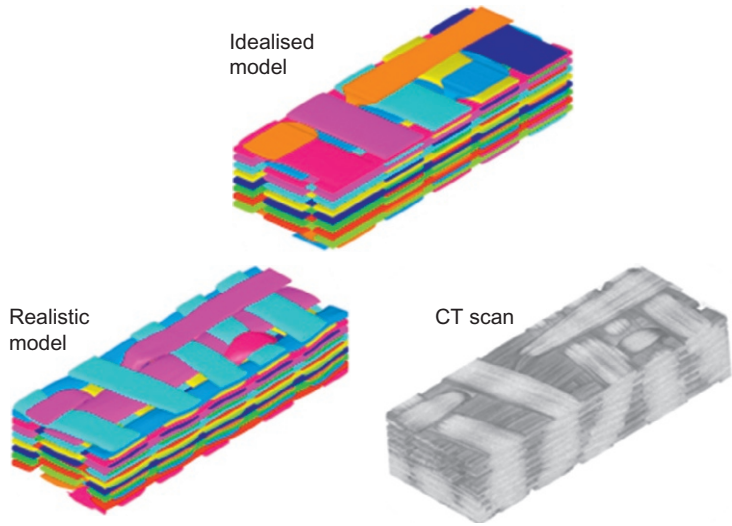

Figure 16.14 Idealised and realistic models of 3D woven composite, and CT scan of the composite (Green et al., 2014b).

A CDM model based on a thermodynamic evolution law was utilised by Ivanov et al. (2009) for numerical analysis of non-linear behaviour of a braided composite. The analysis predicted lower final strength for the machine direction (parallel to the axis of the braider) and higher for the cross direction (transverse to the axis of the braider) than in experiments. Stress–strain curves are shown in Figure 16.13.

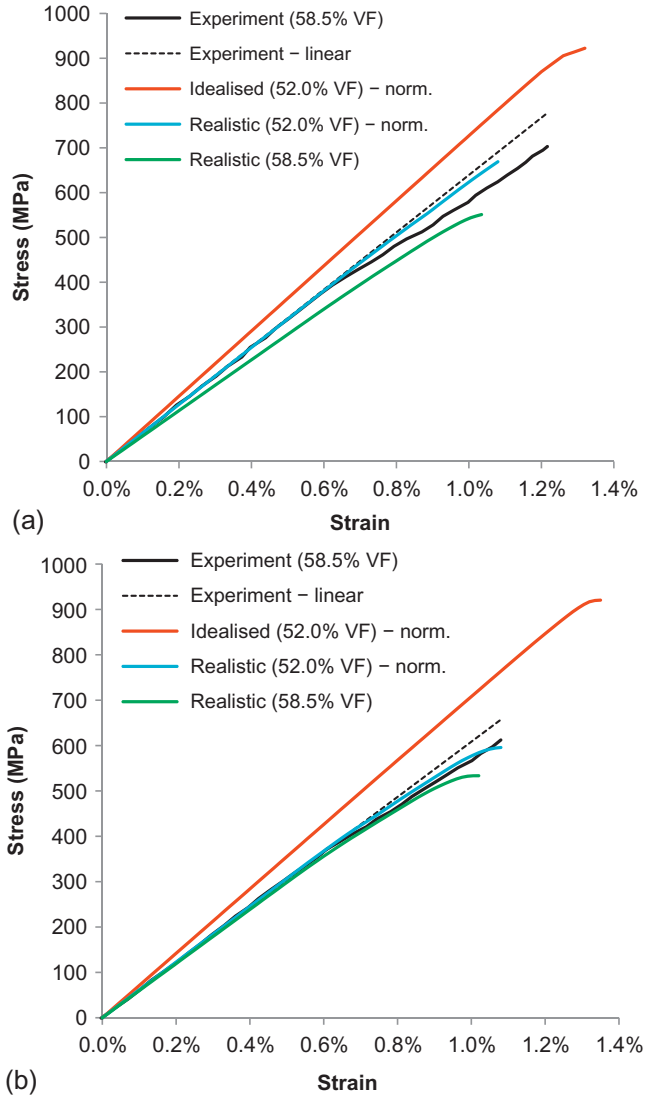

Figure 16.15 Comparison of experimental and predicted stress–strain curves for textile models shown in Figure 16.14 for loading in warp direction (a) and weft direction (b) (Green et al., 2014b).

All of the cases above relied on highly idealised models of textile reinforcement, usually created with a textile geometry pre-processor. However, in some cases, a geometry created with a geometry pre-processor may have insufficient accuracy for correctly predicting composite behaviour. In this case, as mentioned, the digital chain element method makes it possible to generate a more realistic geometry (Green et al., 2014a), shown in Figure 16.14 alongside an idealised geometry created with a textile pre-processor and a computer tomography (CT) scan. The main difference between the models is the presence of high in-plane and out-of-plane waviness in the realistic model, while the idealised model had almost straight warp and weft yarns. Comparison of the idealised and realistic models performed by Green et al. (2014b) showed that the idealised model overestimates both the Young's modulus and strength by up to 17% and 47%, respectively. In contrast, the realistic model predicted conservative results underestimating both Young's modulus and strength and captured a kink in the stress–strain curves. Figure 16.15a and b compares the stress–strain curves. This study clearly showed a need for accuracy in textile geometry and its effect on mechanical properties of composites.

16.4 Conclusions

Research in the area of damage modelling of textile composites has been active for more than 20 years. However, only several questions have been completely resolved. One of the problems with a definite answer is construction of the meso-scale geometry of the textile reinforcement. Many researchers have shown that textile pre-processors are capable of providing models that are realistic enough to predict elastic properties of textile composites very close to experimental values. In rare cases, especially when the textile deviates from the nominal design due to some distortions, textile pre-processors cannot predict the geometry of the reinforcement. In these cases, it is recommended to use a more sophisticated approach such as the digital chain element approach which yields realistic results even for the case of complex 3D weaves. A feature of a "good" meso-scale model is that it accurately predicts the global fibre volume fraction and the fibre volume fraction within yarns.

The next issue considered in this chapter was the generation of the FE mesh for unit cells. In the absence of an automated meshing technique that can yield a conformal mesh for an arbitrary complex geometry with no distorted elements, the voxel meshing technique seems to be an appropriate compromise between meshing efforts and computational costs. However, this can become a limitation for models of textile composites with large unit cells due to the mesh density required for an accurate solution.

A major issue with numerical analysis is the choice of the damage model. A large number of available theories prevent any standardisation of the procedure, and many models do not include all the possible mechanisms of failure. In addition, application of some of the advanced theories is limited by available experimental data required to extract model parameters. However, in the case of a simple loading such as UD tension or shear even simple degradation models can yield relatively accurate predictions.

16.5 Current trends

Most of the work on the modelling of textile composites focuses on efficient representation of non-linear behaviour and implementation of as many failure mechanisms as possible. These attempts may stimulate research into a combination of the CDM technique with cohesive element models because delamination between yarn and matrix or between layers is impossible to predict with CDM. One of the promising steps towards the realistic modelling of failure in textile composites seems to be the application of the X-FEM approach, which makes it possible to simulate arbitrarily oriented intra- and inter-yarn failure zones.

Recently, the idea of linking manufacturing defects and geometrical variability has attracted attention of the research community. It has been proposed that some of the discrepancies between experiments and numerical simulations may stem from various defects and unaccounted deviations from the idealised composite structure. Stochastic simulations at both micro- and meso-scales have shown that elastic properties and strength of composites are distributed around their mean values. Validation of such approaches may lead to greater confidence in the use of predictive modelling techniques within the design process for textile composites.

References

ABAQUS 6.9 Documentation. 2010. Abaqus Analysis User's Manual, Online Documentation, Dassault Systemes.

Azzi, V., Tsai, S., 1965. Anisotropic strength of composites. Exp. Mech. 5 (9), 283–288.

Blackketter, D.M., Walrath, D.E., Hansen, A.C., 1993. Modeling damage in a plain weave fabric-reinforced composite-material. J. Compos. Technol. Res. 15 (2), 136–142.

Caddell, R.M., Raghava, R.S., Atkins, A.G., 1974. Pressure dependent yield criteria for polymers. Mater. Sci. Eng. 13 (2), 113–120.

Carrere, N., Laurin, F., Maire, J.F., 2012. Micromechanical-based hybrid mesoscopic 3D approach for non-linear progressive failure analysis of composite structures. J. Compos. Mater. 46 (19–20), 2389–2415.

Chamis, C.C., 1984. Simplified composite micromechanics equations for strength, fracture-toughness and environmental-effects. SAMPE Quart. 15 (4), 41–55.

Cox, B.N., Dadkhah, M.S., 1995. The macroscopic elasticity of 3D woven composites. J. Compos. Mater. 29 (6), 785–819.

Crookston, J.J., Long, A.C., Jones, I.A., 2005. A summary review of mechanical properties prediction methods for textile reinforced polymer composites. Proc. Inst. Mech. Eng. L J. Mat. 219 (L2), 91–109.

Cuntze, R., 2012. The predictive capability of failure mode concept-based strength conditions for laminates composed of unidirectional laminae under static triaxial stress states. J. Compos. Mater. 46 (19–20), 2563–2594.

Daggumati, S., Van Paepegem, W., Degrieck, J., Xu, J., Lomov, S.V., Verpoest, I., 2010. Local damage in a 5-harness satin weave composite under static tension: part II – meso-FE modelling. Compos. Sci. Technol. 70 (13), 1934–1941.

Dasgupta, A., Agarwal, R.K., Bhandarkar, S.M., 1996. Three-dimensional modeling of woven-fabric composites for effective thermo-mechanical and thermal properties. Compos. Sci. Technol. 56 (3), 209–223.

De Carvalho, N.V., Pinho, S.T., Robinson, P., 2011. Reducing the domain in the mechanical analysis of periodic structures, with application to woven composites. Compos. Sci. Technol. 71 (7), 969–979.

Deuschle, H.M., Kroplin, B.H., 2012. Finite element implementation of Puck's failure theory for fibre-reinforced composites under three-dimensional stress. J. Compos. Mater. 46 (19–20), 2485–2513.

Ernst, G., Vogler, M., Huhne, C., Rolfes, R., 2010. Multiscale progressive failure analysis of textile composites. Compos. Sci. Technol. 70 (1), 61–72.

Ghosh, S., 2008. Adaptive concurrent multilevel model for multiscale analysis of composite materials including damage. In: Kwon DHA, Y.W., Talreja, R.R. (Eds.), Multiscale Modeling and Simulation of Composite Materials and Structures. Springer, New York, pp. 83–164.

Gorbatikh, L., Ivanov, D., Lomov, S., Verpoest, I., 2007. On modelling of damage evolution in textile composites on meso-level via property degradation approach. Compos. A Appl. Sci. Manuf. 38 (12), 2433–2442.

Green, S.D., Matveev, M.Y., Long, A.C., Ivanov, D., Hallett, S.R., 2014b. Mechanical modelling of 3D woven composites considering realistic unit cell geometry. Compos. Struct. 118, 284–293.

Green, S.D., Long, A.C., El Said, B.S.F., Hallett, S.R., 2014a. Numerical modelling of 3D woven preform deformations. Compos. Struct. 108, 747–756.

Hallett, S.R., Jiang, W.G., Khan, B., Wisnom, M.R., 2008. Modelling the interaction between matrix cracks and delamination damage in scaled quasi-isotropic specimens. Compos. Sci. Technol. 68 (1), 80–89.

Hazanov, S., Amieur, M., 1995. On overall properties of elastic heterogeneous bodies smaller than the representative volume. Int. J. Eng. Sci. 33 (9), 1289–1301.

Hinton, M., Soden, P., Kaddour, A.S., 2004. Failure criteria in fibre-reinforced-polymer composites. The World-Wide Failure Exercise. Elsevier Science, Oxford, UK.

Huysmans, G., Verpoest, I., Van Houtte, P., 1998. A poly-inclusion approach for the elastic modelling of knitted fabric composites. Acta Mater. 46 (9), 3003–3013.

Ishikawa, T., Chou, T.W., 1982. Stiffness and strength behavior of woven fabric composites. J. Mater. Sci. 17 (11), 3211–3220.

Ito, M., Chou, T.W., 1998. An analytical and experimental study of strength and failure behavior of plain weave composites. J. Compos. Mater. 32 (1), 2–30.

Ivanov, D.S., Baudry, F., Van Den Broucke, B., Lomov, S.V., Xie, H., Verpoest, I., 2009. Failure analysis of triaxial braided composite. Compos. Sci. Technol. 69 (9), 1372–1380.

Ivanov, D.S., Lomov, S.V., Ivanov, S.G., Verpoest, I., 2010. Stress distribution in outer and inner plies of textile laminates and novel boundary conditions for unit cell analysis. Compos. A Appl. Sci. Manuf. 41 (4), 571–580.

Ivanov, D.S., Ivanov, S.G., Lomov, S.V., Verpoest, I., 2011. Unit cell modelling of textile laminates with arbitrary inter-ply shifts. Compos. Sci. Technol. 72 (1), 14–20.

Jiang, W.G., Hallett, S.R., Wisnom, M.R., 2008. Development of domain superposition technique for the modelling of woven fabric composites. Comput. Methods Appl. Sci. 10, 281–291.

Kaddour, A.S., Hinton, M.J., 2013. Maturity of 3D failure criteria for fibre-reinforced composites: comparison between theories and experiments: part B of WWFE-II. J. Compos. Mater. 47 (6–7), 925–966.

Kim, H.J., Swan, C.C., 2003a. Voxel-based meshing and unit-cell analysis of textile composites. Int. J. Numer. Methods Eng. 56 (7), 977–1006.

Kim, H.J., Swan, C.C., 2003b. Algorithms for automated meshing and unit cell analysis of periodic composites with hierarchical tri-quadratic tetrahedral elements. Int. J. Numer. Methods Eng. 58 (11), 1683–1711.

Krizek, M., 1992. On the maximum angle condition for linear tetrahedral elements. SIAM J. Numer. Anal. 29 (2), 513–520.

Kurashiki, T., Nakai, H., Hirosawa, S., Imura, M., Zako, M., Verpoest, I., et al., 2007a. Mechanical behaviors for textile composites by FEM based on damage mechanics. Key Eng. Mater. 334–335, 257–260.

Kurashiki, T., Zako, M., Nakai, H., Imura, M., Hirosawa, S., 2007b. Damage development of woven composites based on multiscale analysis. In: 16th International Conference on Composite Materials, Kyoto, Japan.

Ladeveze, P., Lubineau, G., 2002. An enhanced mesomodel for laminates based on micromechanics. Compos. Sci. Technol. 62 (4), 533–541.

Li, S., 2001. General unit cells for micromechanical analyses of unidirectional composites. Compos. A Appl. Sci. Manuf. 32 (6), 815–826.

Ling, D.S., Yang, Q.D., Cox, B., 2009. An augmented finite element method for modeling arbitrary discontinuities in composite materials. Int. J. Fract. 156 (1), 53–73.

Lomov, S.V., Gusakov, A.V., Huysmans, G., Prodromou, A., Verpoest, I., 2000. Textile geometry preprocessor for meso-mechanical models of woven composites. Compos. Sci. Technol. 60 (11), 2083–2095.

Lomov, S.V., Huysmans, G., Luo, Y., Parnas, R.S., Prodromou, A., Verpoest, I., et al., 2001. Textile composites: modelling strategies. Compos. A Appl. Sci. Manuf. 32 (10), 1379–1394.

Lomov, S.V., Ivanov, D.S., Verpoest, I., Zako, M., Kurashiki, T., Nakai, H., et al., 2007. Meso-FE modelling of textile composites: road map, data flow and algorithms. Compos. Sci. Technol. 67 (9), 1870–1891.

Long, A.C., 2006. Design and Manufacture of Textile Composites. Taylor & Francis, Cambridge.

Long, A.C., Brown, L.P., 2011. Modelling the geometry of textile reinforcements for composites: TexGen. In: Boisse, P. (Ed.), Composite Reinforcements for Optimum Performance. Woodhead Publishing Ltd, Cambridge, pp. 239–264.

Maimi, P., Mayugo, J.A., Camanho, P.P., 2008. A three-dimensional damage model for transversely isotropic composite laminates. J. Compos. Mater. 42 (25), 2717–2745.

Matveev, M.Y., Long, A.C., Jones, I.A., 2014. Modelling of textile composites with fibre strength variability. Compos. Sci. Technol. 105, 44–50.

McLendon, W.R., Whitcomb, J.D., 2013. Random fibre-matrix model for predicting damage in multiscale analysis of textile composites under thermomechanical loads. In: 19th International Conference on Composite Materials, Montreal, Canada.

Melro, A.R., Camanho, P.P., Pires, F.M.A., Pinho, S.T., 2012. Numerical simulation of the nonlinear deformation of 5-harness satin weaves. Comput. Mater. Sci. 61, 116–126.

Moes, N., Dolbow, J., Belytschko, T., 1999. A finite element method for crack growth without remeshing. Int. J. Numer. Methods Eng. 46 (1), 131–150.

Pinho, S.T., Darvizeh, R., Robinson, P., Schuecker, C., Camanho, P.P., 2012. Material and structural response of polymer-matrix fibre-reinforced composites. J. Compos. Mater. 46 (19–20), 2313–2341.

Potter, E., Pinho, S.T., Robinson, P., Iannucci, L., McMillan, A.J., 2012. Mesh generation and geometrical modelling of 3D woven composites with variable tow cross-sections. Comput. Mater. Sci. 51 (1), 103–111.

Schultz, J.A., Garnich, M.R., 2013. Meso-scale and multicontinuum modeling of a triaxial braided textile composite. J. Compos. Mater. 47 (3), 303–314.

Turon, A., Davila, C.G., Camanho, P.P., Costa, J., 2007. An engineering solution for mesh size effects in the simulation of delamination using cohesive zone models. Eng. Fract. Mech. 74 (10), 1665–1682.

Wang, Y.Q., Sun, X.K., 2001. Digital-element simulation of textile processes. Compos. Sci. Technol. 61 (2), 311–319.

Whitcomb, J.D., Chapman, C.D., Tang, X.D., 2000. Derivation of boundary conditions for micromechanics analyses of plain and satin weave composites. J. Compos. Mater. 34 (9), 724–747.

Wisnom, M.R., 2010. Modelling discrete failures in composites with interface elements. Compos. A Appl. Sci. Manuf. 41 (7), 795–805.

Zako, M., Uetsuji, Y., Kurashiki, T., 2003. Finite element analysis of damaged woven fabric composite materials. Compos. Sci. Technol. 63 (3–4), 507–516.

Zeng, X.S., Brown, L.P., Endruweit, A., Matveev, M., Long, A.C., 2014. Geometrical modelling of 3D woven reinforcements for polymer composites: prediction of fabric permeability and composite mechanical properties. Compos. A Appl. Sci. Manuf. 56, 150–160.

Zhou, G.M., Sun, X.J., Wang, Y.Q., 2004. Multi-chain digital element analysis in textile mechanics. Compos. Sci. Technol. 64 (2), 239–244.

This page intentionally left blank

Multi-scale modelling for predicting fracture behaviour in through-thickness reinforced laminates

17

G. Allegri[1], *G. Mohamed*[2], *S.R. Hallett*[2]
[1]Imperial College London, London, UK; [2]University of Bristol, Bristol, UK

17.1 Introduction

17.1.1 Preliminary considerations

Several experimental and numerical techniques have been presented in the literature for addressing the design of through-thickness reinforced composite structures. Regardless of the specific nature of the through-thickness reinforcement (stitch, Z-pin or tuft), a common 'multi-level' (or multi-scale) modelling strategy can be identified when considering the bulk of the existing literature:

1. First of all it is necessary to characterise and predict the bridging actions exerted by a single reinforcing entity (Z-pins in the case considered here) embedded into a delaminated composite. We will denote this element of the overall modelling strategy as level-1 meso-scale analysis (meso-1).
2. The second level of the modelling approaches requires identifying the bridging response of multiple reinforcements (Z-pin array) bridging delaminations. This represents a level-2 meso-scale analysis (meso-2), whereby homogenisation is introduced into the models to appropriately 'smear' the mechanical response of multiple interacting Z-pins.
3. Finally it is necessary to consider full structures, i.e., macro-scale models, where reinforcements are selectively applied in regions prone to delamination damage. This usually requires a further homogenisation step with respect to the meso-2 level, because equivalent through-thickness properties will have to be introduced to reduce the computational cost of the simulations.

Depending on the overall approach taken, there may be some overlap between the modelling levels mentioned above. Moreover, different modelling techniques may be required at the different scales. A most important point to note in this type of analysis is that fracture mechanics is not valid in the presence of large-scale delamination bridging, so extreme care needs to be taken when scaling up from coupon test results to full-scale (macro) structural components. However, it is in principle possible to translate the results of single Z-pin testing into an *apparent* fracture toughness or a set of mode-mixity-dependent bridging forces (meso-1), which can then be employed to predict the response of Z-pin arrays (meso-2). Similarly, the macro-scale

Numerical modelling of failure in advanced composite materials. http://dx.doi.org/10.1016/B978-0-08-100332-9.00017-7
Copyright © 2015 Elsevier Ltd. All rights reserved.

structural response can be predicted by considering the interaction of multiple reinforcement arrays in a component.

17.1.2 Overview of meso-1-level modelling

Focusing on the meso-1 level, both semi-analytical models and detailed finite element models have been employed to predict the mechanical response of single Z-pins. Cox (Cox and Sridhar, 2002; Cox, 2005) described the traction-displacement response of an angled tow bridging to be a delamination by assuming that the through-thickness reinforcement carries an axial force, but it is perfectly plastic in terms of shear behaviour. The interaction between the two and the embedding composite laminate is modelled as the indentation of a rigid punch in a perfectly plastic half space. The equilibrium during progressive pullout of the tow from the laminate is ensured by frictional forces, which comprise both residual and enhancement terms. The former are due to thermal residual stresses between the tow and the laminate, whereas the latter are caused by 'snubbing'. Snubbing refers to the localised increase of frictional force due to contact pressure in the neighbourhood of the delamination plane, which is analogous to that experienced by pulling a rope wrapped around a drum. Because the laminate is assumed to be perfectly plastic under punch indentation, the through-thickness reinforcement can 'plough' across the laminate. Plain and Tong (2009) developed a model conceptually similar to that proposed by Cox and applied it to the analysis of stitches. Both the aforementioned models assume a rope-like behaviour for the through-thickness reinforcement, in other words, the stitch does not carry an axial bending moment. However, depending on the specific nature of the through-thickness reinforcement, the 'rope' assumption may not be appropriate, in that the through-thickness reinforcement may tend to behave as a beam when its bending stiffness is sufficiently large.

Tong and Sun (2004, 2007) developed a model for metallic through-thickness reinforcement whereby Z-pins are assumed to behave as Euler–Bernoulli beams embedded into an elasto-plastic foundation. Bianchi and Zhang (2012) adopted a similar approach for describing the effect of T300/BMI Z-pins bridging a mode II delamination. The expected bending stiffness for small diameter rods made either of metal or unidirectional composite is much larger than that expected for stitches, which typically comprise twisted yarns. Allegri and Zhang (2007) considered the limit of rigid through-thickness reinforcement inserted in an orthotropic elastic foundation to model the behaviour of unidirectional composite Z-pins. Moreover it is important to observe that in multi-directional laminates (i.e. for stacking sequences other than unidirectional), the Z-pin ploughing may be prevented from the ply fibres bridging the resin pockets surrounding the Z-pin. Because the fibres are linear elastic until failure and they are much stronger than the matrix, one may expect that the laminate will provide an elastic foundation for the through-thickness reinforcement.

As an alternative to the semi-analytical models described above, detailed finite element simulations of the progressive pullout of Z-pins from composite laminates have been presented in the literature. Meo et al. (2005) simulated the mode I Z-pin pullout by meshing both the Z-pin and a laminate unit cell with solid elements. They included

thermal residual stress in their analyses, as well as cohesive elements at the interface between the Z-pin and the embedding laminate. The friction during pullout was described by the superposition of a residual term plus a Coulomb enhancement factor, with a limit value of the frictional shear stress introduced to match the experimental results. Cui et al. (2011) developed a plane strain finite element model for mixed-mode Z-pin pullout, whereby they also considered the presence of splits within the Z-pin. Splitting occurs because of the large shear stresses that are typically attained within the Z-pin matrix, especially in a mode II dominate regime. Cui et al. (2011) employed cohesive elements to model the splitting behaviour, as well as the fibre failure mode that represents the ultimate rupture condition for unidirectional through-thickness reinforcement. The splits tend to appear in the unsupported region of the Z-pin, i.e., the segment that has already been pulled out from the laminate, but may also partially extend within the embedded portions of the through-thickness reinforcement. The main effect of the splits is to reduce the bending stiffness of the Z-pin, but this does not constitute final failure, because independent strands can still withstand an axial pulling force. The actual position of the splits is a function of the stress field. Cui et al. (2011) seeded candidate splitting-planes within the Z-pin to divide it into a sufficiently large number of strands sliding with respect to each other. Although this approach is correct from a qualitative point of view, the final results depend on the assumed splitting density and relative positioning, i.e., there is an element of mesh dependency in the analysis. Finite element simulations at the meso-1 level have the potential of capturing the complex behaviour governing the Z-pin pullout and failure, as they can account for cohesive/frictional behaviour at interfaces, internal splitting, matrix/laminate plasticity as well as fibre failure. However, the computational cost associated with these models is much larger than that for semi-analytical approaches. This makes it clear there is a trade-off between physical consistency/accuracy and the computational resources available. This trade-off is particularly important if one considers the fact that meso-1 modelling is just a prerequisite for meso-2 and macro-scale analysis. For a multi-scale approach to be feasible, the computational cost of the meso-1 models must be kept at a reasonable level. Nonetheless, meso-1 finite element analysis is extremely useful in assessing the relative influence of different mechanisms on the overall Z-pin response. This complements experimental observations and may also inform the development of robust and computationally efficient semi-analytical models, which can be considered as ‘reduced-order’ approaches to deal with delamination bridging due to through-thickness reinforcement.

17.1.3 Overview of meso-2-level modelling

Several analytical and numerical techniques have been developed to simulate the response of multiple Z-pins bridging delaminated interfaces (meso-2 level). Ratcliffe and O’brien (2004) introduced a semi-analytical model of double cantilever beam (DCB) coupons, whereby Z-pins were represented using discrete springs connecting the coupon arms. The Z-pin pullout response was modelled by introducing a progressive stiffness degradation of the springs. The energy release rate associated with the delamination growth in the coupons was computed from the elastic potential

energy change associated with a sufficiently small increment of the interlaminar crack length. Byrd and Birman (2005) also developed an analytical model for Z-pinned DCB coupons, whereby the through-thickness reinforcement is described as a continuous (i.e. homogenized) elastic foundation. Robinson and Das (2004) and Song et al. (2012) followed a similar approach, assuming that the elastic foundation between the DCB arms experienced a linear displacement-dependent softening, as a consequence of the progressive Z-pin pullout. These (semi)-analytical models are quite instructive for understanding the physics of delamination bridging, and they also provide suitable data-reduction schemes for experimental testing.

Finite element analysis provides a more general and flexible framework for assessing the performance of through-thickness reinforced composite structures. Note that the experimental evidence (Cartié, 2000; Partridge and Cartié, 2005; Cartié et al, 2006a) shows the presence of Z-pins, which does not influence the onset of delamination in composite laminates. Hence, any modelling attempt must be based on correctly representing the sequence of damage development in through-thickness reinforced composites. This consists in the fracture of ply interfaces, unaffected by the presence of the Z-pins, which is then followed by a large-scale bridging that progressively develops as the interlaminar crack advances. Large-scale bridging does not obey the similitude and superposition principles that govern linear elastic fracture mechanics. Therefore, trying to simulate the effect of through-thickness reinforcement just by increasing the interlaminar fracture toughness values leads to erroneous results. The dissipation mechanism associated with the progressive pullout of Z-pins need to be adequately represented within the modelling framework adopted.

Cartié (2000) carried out a finite element analysis of Z-pinned ASTM-standard coupon, modelling the Z-pins as nonlinear springs undergoing progressive softening during pullout. The nonlinear spring response was based on experimental pullout tests performed on single Z-pin coupons (Cartié, 2000; Partridge and Cartié, 2005; Cartié et al, 2006a). The energy release rate at the delamination tip was calculated employing the J-integral, thus linking the experimental meso-1 results with meso-2 analysis. Cartié et al. (2006b) also demonstrated the possibility of modelling the bridging action exerted by Z-pins on the delamination surfaces by applying nodal forces, i.e., without the need of introducing nonlinear elements to represent the through-thickness reinforcement. Grassi and Zhang (2003) addressed the finite element modelling of Z-pinned DCB coupons using the virtual crack closure technique. They too employed nonlinear springs to represent the bridging action exerted by Z-pins, applying the Cox and Shridar model to predict the response of individual through-thickness composite rods. Allegri and Zhang (2007) took a similar approach for analysing Z-pinned T and 'cross' joints, the latter cases involving the analysis of mode II bridging. Yan et al. (2003, 2004) employed spring elements with bi-linear response to represent the constraining action exerted by Z-pins on delamination surfaces and calculated the resulting energy release rate via the J-integral.

Dantuluri et al. (2007) employed bi-linear cohesive elements (Camanho and Dávila, 2002) to model the fracture of interfaces superposed to bi-linear springs that represented the discrete bridging forces exerted by the Z-pins. Kravchenko et al. (2013) applied the same approach to the analysis of DCB coupons using a tri-linear

bridging model for the Z-pin response. Bianchi and Zhang (2011, 2012) employed two different bi-linear cohesive element properties to predict the response of DCB and end-notch flexure (ENF) coupons. The cohesive elements coincident with Z-pin strips were given enhanced toughness to represent the bridging meso-mechanics, whereas the others had the standard properties of the unreinforced material. Cui et al. (2013) adopted a similar modelling strategy, employing the mixed-mode response obtained from their meso-1 models (Cui et al., 2011) for the cohesive elements representing individual Z-pins within interfaces.

Summarising the modelling approaches presented so far, it is worth remarking that the level of homogenisation that can be introduced at the meso-2 level is inherently limited by the representation of the fracture process. In more detail, the mesh must be refined enough to provide an accurate estimation of the energy release rate if the virtual crack closure technique or the J-integral method are employed. For cohesive element models, the mesh must be fine enough for damage to initiate beyond the elastic branch of the traction-displacement law. If Z-pins are modelled using spring elements, it is in principle possible to 'smear' the bridging forces, having elements comprising multiple Z-pins, provided that the associated stages of the pull-out response are sufficiently similar. However, if the Z-pins are represented with cohesive elements, it is necessary to selectively apply the enhancement of interface properties to elements that are geometrically coincident with individual through-thickness rods, or Z-pin strips.

17.2 Modelling single Z-pin behaviour

Following on from the separation of scales into meso-1 and meso-2, which was introduced in Section 17.1, a more detailed presentation of a particular implementation of such a multi-scale modelling approach is given here, first for meso-1, and then for meso-2 in Section 17.3.

17.2.1 Model formulation

Consider a Z-pin having a total length L_T embedded into a composite laminate (Figure 17.1). A delamination intersects the Z-pin at a given depth. Let the two sub-laminates separated by the interlaminar crack have the same elastic properties.

The thickness of the sub-laminates is denoted as L^- and L^+. Upon delamination opening/sliding, the Z-pin exerts bridging forces that constrain the interlaminar crack displacements. The Z-pin pullout displacement is denoted as W, and U is the delamination sliding displacement. The Z-pin is described here as an axially inextensible Euler–Bernoulli beam embedded in a Winkler's (i.e., linear) elastic foundation. The foundation supports the Z-pin by a distributed normal force. The frictional forces acting on the Z-pin are described as an equivalent axial load per unit length. Considering small but finite rotations of the Z-pin cross-section, the following differential equations govern the deformation of the through-thickness reinforcement

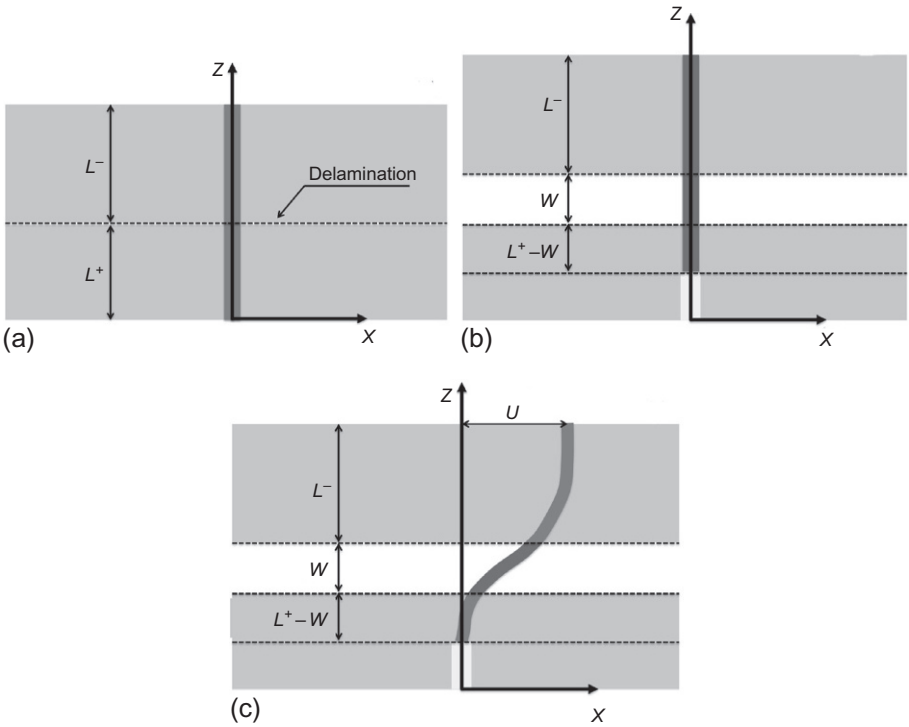

Figure 17.1 Z-pin bridging a delamination: (a) reference configuration; (b) opening mode; (c) sliding mode.

$$\mathrm{EI}\frac{\mathrm{d}^4u}{\mathrm{d}z^4} - N\frac{\mathrm{d}^2u}{\mathrm{d}z^2} + q = 0 \tag{17.1}$$

$$\frac{\mathrm{d}N}{\mathrm{d}z} = -\mathrm{EI}\frac{\mathrm{d}^3u}{\mathrm{d}z^3}\frac{\mathrm{d}^2u}{\mathrm{d}z^2} - p \tag{17.2}$$

where EI is the Z-pin bending stiffness, u is the transversal displacement, N is the axial force carried by the Z-pin; p and q are, respectively, the distributed tangential and normal load along the Z-pin axis. When pullout occurs, the Z-pin can be considered divided into three segments: the first is embedded in the lower sub-laminate, the second is unsupported, and the third sits within the upper sub-laminate. Equations (17.1) and (17.2) are valid for any of the three segments, with $p = q = 0$ in the unsupported region. In the following discussion, $[\ldots]^-$ and $[\ldots]^+$, respectively, indicate quantities evaluated within the lower and the upper embedded segments.

The expression of the normal foundation force is given as follows:

$$q^- = k^- u, \quad q^+ = k^+(u - U) \tag{17.3}$$

where

$$k_x^- = k_x^+ = \bar{k}_x \tag{17.4}$$

and $\bar{k}_x$ is the foundation stiffness provided by the embedding sub-laminates. For the tangential forces, the following expression is postulated:

$$p^- = -p_0 - (p_1 - p_0)\mathrm{e}^{-fW} - \mu k_x^- |u|, \quad p^+ = p_1 + \mu k_x^+ |U - u| \tag{17.5}$$

In Equation (17.5), p_0 and p_1 are residual frictional forces. The actual amount of residual frictional force attained in the lower sub-laminate is assumed to be a function of the pullout displacement via the exponential function in the first of Equation (17.5); f is a residual friction scaling constant. Equation (17.5) comprise a Coulomb friction terms, with characteristic coefficient μ, that accounts for the 'snubbing' effect described above. The Z-pin is assumed to be able to translate freely in the vertical (z) direction from the lower sub-laminate. This implies that the axial force at the tip of the lower embedded segment is set to zero. However, at the same position, the transversal displacement is restrained and the curvature is set to zero. For the upper tip of the Z-pin, the transversal displacement is set to be equal to U, whereas the associated rotation is set to zero.

Continuity conditions for the displacements, rotation, axial force, shear force and bending moment are enforced at the interfaces between the Z-pin segments. The tip transversal displacement of the Z-pin is expressed as follows:

$$U = \frac{\phi}{\sqrt{1-\phi^2}} W \tag{17.6}$$

where ϕ is the local mode-mixity at the Z-pin location. It is worth stressing the fact that the aforementioned 'local' mode-mixity differs from that attained at the actual tip of the interlaminar crack. The relative mode-mixity depends on the relative opening/sliding displacements along the delamination surfaces in the wake of the interlaminar crack tip. In single Z-pin testing, the mode-mixity can be adjusted by changing the ratio of the sliding to opening displacements, for example, by means of the loading jig developed by Yasaee et al. (2014). However, when Z-pin arrays are considered, the mode-mixity needs to be extracted from finite element simulations at meso-2 level.

A variety of numerical techniques are available for solving the nonlinear differential Equations (17.1) and (17.2) with the boundary conditions described above. The results that will be presented in the remainder of this section have been obtained using the adaptive collocation routine 'bvp4c' available in MATLAB. The equations are solved for incremental pullout displacements at a fixed mode-mixity. The solution proceeds until either complete pullout occurs or the Z-pin fails. Thus, establishing which failure mode affects composite Z-pins is crucial for the success of any modelling attempt. The experimental evidence that has been gathered demonstrates that the ultimate rupture

of the Z-pins is essentially governed by a fibre tensile failure mode. This is best described using Weibull's failure criterion, which can be expressed in the following compact form:

$$\overline{\sigma}_{\max} = X_{\mathrm{T}} \left[\frac{V_0}{V_{\mathrm{eff}}} \right]^{1/m} \tag{17.7}$$

where X_{T} is the axial tensile strength obtained from a constant strain test carried out on the volume of material V_0; m is the Weibull exponent, V_{eff} is an effective volume and $\overline{\sigma}_{\max}$ is an average peak tensile stress along the Z-pin axis. In the analysis that follows, we consider the typical longitudinal strength X_{T} obtained from the ASTM standard test on unidirectional T300/BMI coupons. The strength value is obtained applying Equation (17.7), which involves the calculation of the effective volume V_{eff} by means of an integral of the actual stress distribution over all the entire volume of the Z-pin. The stress distribution is obtained from the axial force and bending moment resultants along the Z-pin axis that are yielded by the solution of Equations (17.1) and (17.2). The cross-sectional axial and shear forces calculated at the mid-delamination plane represent the bridging tractions that the Z-pin exerts on the delamination edges. These bridging tractions have been denoted as $\bar{X}$ and $\bar{Z}$ in Figure 17.2. In principle, there may be a bending moment at the mid-delamination plane. This is, however, negligible, because the delamination mid-plane is usually very close to the Z-pin inflection point. We therefore denote as 'bridging maps' the loci of the bridging forces expressed as functions of the pullout displacement and mode-mixity, i.e.

$$\bar{X} = \bar{X}(W, \phi), \quad \bar{Z} = \bar{Z}(W, \phi) \tag{17.8}$$

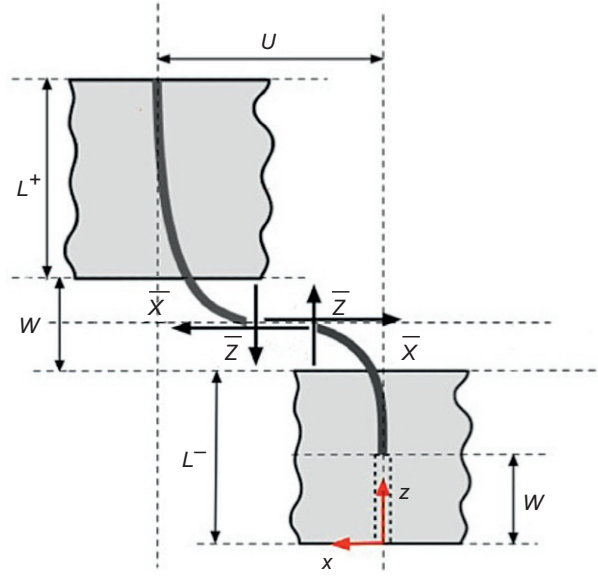

Figure 17.2 Bridging forces during Z-pin pullout.

The bridging maps in Equation (17.8) are implicit functions of the pullout displacement and mode-mixity. This represents an additional complication for the implementation of the Z-pin response in finite element analysis at the meso-2 level, as will be discussed in Section 17.3. However, this issue can be easily dealt with, for example, by storing the bridging maps into lookup tables that are suitably interpolated during a progressive damage analysis.

The amount of energy dissipated during the pullout of a single Z-pin is expressed as follows:

$$\Psi(\phi) = \int_0^{W^*(\phi)} \bar{Z}(s, \phi)\mathrm{d}s + \frac{\pi}{4} G_{\mathrm{IC}}^{\mathrm{f}} D^2 H[L^- - W^*(\phi)] \tag{17.9}$$

where $W^*(\phi)$ is the pullout displacement corresponding to the failure of the Z-pin, H is the Heaviside function, D is the Z-pin diameter and $G_{\mathrm{IC}}^{\mathrm{f}}$ is the fracture toughness associated with the tensile fibre failure of the Z-pin. Therefore, the energy dissipated due to bridging comprises two terms: the first represents the work done by the frictional forces, while the second represents the energy spent to fracture the Z-pin. The latter contributes to the energy dissipated only if Z-pin rupture occurs before the pullout is complete (i.e., for $W^* < L^-$).

Multiplying the energy dissipated by the Z-pin bridging yielded by Equation (17.9) with the Z-pin aerial density ρ, it is straightforward to obtain the apparent fracture toughness $G^*(\phi)$ associated with the pullout of Z-pin arrays taking place at constant mode-mixity. The apparent fracture toughness is expressed as follows:

$$G^*(\phi) = \frac{4\rho}{\pi D^2} \Psi(\phi) \tag{17.10}$$

The fracture toughness in Equation (17.10) is 'apparent', because it is not a material property, but a structural property at the meso-1 level. The assembly of the laminate with the through-thickness reinforcement array constitutes the structure. Albeit here only quasi-static loading is considered, one can envisage an extension of Equation (17.9) to arbitrary pullout histories; in this case, there is a path dependency of the dissipated energy on the pullout displacement. It is also important that, when mode II is considered, the pullout displacement for an orthogonally inserted Z-pin is zero. Thus Equations (17.9) and (17.10) yield:

$$G^*(1) = \rho G_{\mathrm{IC}}^{\mathrm{f}} \tag{17.11}$$

Equation (17.11) proves that the mode II ($\phi = 1$) apparent fracture toughness of a Z-pinned composite is proportional to the fracture toughness for the tensile fibre failure of a single Z-pin.

17.2.2 Model validation

The semi-analytical approach described in Section 17.2.1 has been applied to the prediction of the mixed-mode response of single T300/BMI pins inserted in a

quasi-isotropic laminate, reported by Yasaee et al. (2014). The model includes six parameters that must be estimated by means of experimental tests. These are the foundation stiffness in Equations (17.3) and (17.4); the residual friction coefficients p_0 and p_1 together with the pullout scaling factor f in Equation (17.5). Finally the Weibull exponent m and the Z-pin fracture toughness for fibre failure G_{IC}^{f} are also included in the model parameters to be identified. It is worth stressing that the last two parameters could in principle be estimated by strength and fracture tests carried out on the T300/BMI material that constitutes the Z-pin, leaving a total of four unknowns to be identified to predict the response of the through-thickness reinforcement. The unknown parameters were calibrated considering the experimental trend of the apparent fracture toughness shown in Figure 17.3, as well as the load–displacement response for coupons tested in mode I ($\phi = 0.189$) and mode II ($\phi = 0.983$) dominated conditions, which are shown in Figure 17.4. For the Z-pin Young's modulus, characteristic strength and Coulomb friction coefficient, the data from the literature given in Table 17.1 have been considered. The calibration process has been performed by means of a multi-objective minimisation of the error between the model predictions and the experimental data for the mode I/II response and the overall apparent toughness trend. Genetic algorithms have been employed to solve the minimisation problem that yields the calibrated parameters given in Table 17.2.

In Figure 17.3, the apparent toughness trend yielded by the calibrated model is shown with by the continuous line. One can observe a steady increase of $G^*(\phi)$ from pure mode I to a mode-mixity of approximately 0.4. Beyond the latter, the model predicts that the Z-pin will fail before experiencing complete pullout. This causes a reduction of the apparent fracture toughness. The decreasing trend continues monotonically as the mode-mixity increases. The minimum value of the apparent fracture toughness is attained in pure mode II, where no frictional pullout takes place. From

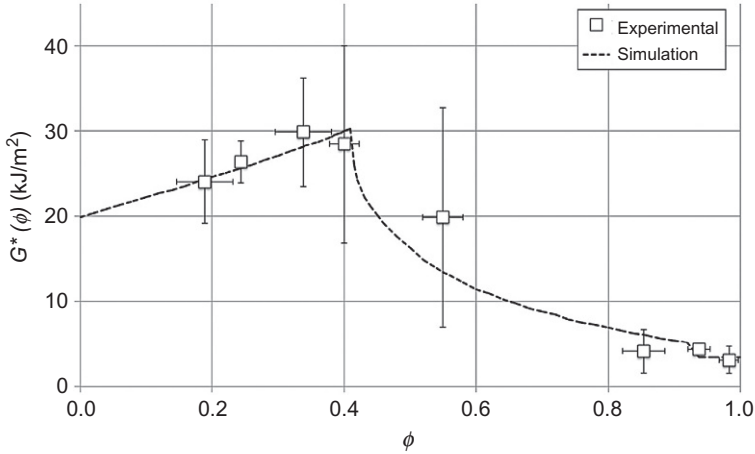

Figure 17.3 Apparent fracture toughness of single Z-pin coupons normalised for a 2% aerial density versus mode-mixity and model prediction (solid line).

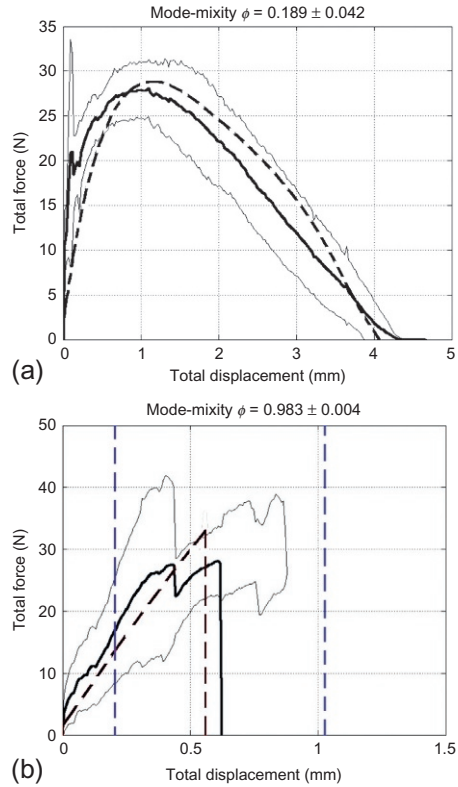

Figure 17.4 Comparison of load–displacement plots for calibration; average experimental values in thick black continuous lines; results from the calibrated model in thick black dashed lines. The thin black lines represent plus/minus one standard deviation from the mean experimental load. The dashed vertical lines in (b) represent the bounds of plus/minus one standard deviation from the average displacement to failure.

Table 17.1 Assumed stiffness, strength and friction properties for the Z-pin

E (GPa)	X_T (MPa)	V_0 (mm^3)	μ
115	1860	2250	0.7

From Allegri et al. (2014).

Table 17.2 Calibrated model parameters

$\bar{k}_x$(N/mm^2)	p_0 (N/mm)	p_1 (N/mm)	f (1/mm)	m	G_{IC}^f (kJ/m^2)
165	10.500	0.375	1.5	27	170

From Allegri et al. (2014).

Figure 17.4, one can observe that the calibrated model yields load–displacement curves that are in good agreement with the coupon test results, i.e., typically within one standard deviation from the mean experimental response. Regarding the apparent toughness trend, a large scatter of the energy data affects the transition region. However, as discussed by Yasaee et al. (2014), this appears to be an inherent feature of the Z-pin response at mode-mixities between 0.4 and 0.7. In this range, no clear preference towards complete pullout or premature failure emerges from the experimental tests and the Z-pin behaviour cannot be considered deterministic.

As a validation case for the model presented in Section 17.2.1, we consider the load–displacement curves for the mode mixity values 0.243, 0.338, 0.400, 0.550, 0.854 and 0.938. These curves were not included in the aforementioned calibration process. The results of this validation study are presented in Figure 17.5. The agreement between the model prediction is excellent for the mode-mixities ranging from 0.243 to 0.400. At $\phi = 0.550$, i.e., in the transition region, the experimental load-displacement curves are widely scattered, due to the fact that some Z-pins fail, whereas others experience complete pullout. The deterministic model presented here cannot capture this random behaviour, which clearly cannot be ascribed only to the Z-pin misalignment. This is because the latter has been included in the calculation of the actual mode-mixity for each of the coupons tested. However, the model predictions are still within one standard deviation from the experimental data in terms of energy dissipation and, consequently, apparent fracture toughness. For the last two values of the mode-mixity considered (i.e. 0.854 and 0.938), the model predictions are close to the average load–displacement traces. However, a significant experimental scatter still affects the Z-pin response. Again this appears to be an intrinsic feature of the mechanical behaviour of Z-pins. The source of this randomness is most possibly due to the effect of the residual curvature that affects the Z-pins following insertion and cure and that can be clearly appreciated in some of the X-ray computed tomography (CT) scan images of the tested coupons, as shown in Figure 17.6. The residual curvature induces stresses in the through-thickness reinforcement that may lead either to premature failure or complete pullout depending on the relative shearing direction.

17.3 Modelling the behaviour of multiple Z-pins

17.3.1 Cohesive element implementation

The meso-2 level implementation of the meso-1 constitutive bridging law described in Section 17.2 is achieved via means of continuum-based cohesive elements written in a user-element subroutine (VUEL) in ABAQUS\Explicit. The user-defined cohesive elements are implemented as sets of continuum elements that represent the unpinned and pinned regions. A schematic of the element arrangement is presented in Figure 17.7.

An explicit code was chosen to overcome some of the inherent convergence difficulties that can be encountered during material softening. For cases when failure and material degradation can occur, an explicit scheme is more favourable because it can handle large changes in the stiffness matrix compared to an implicit analysis.

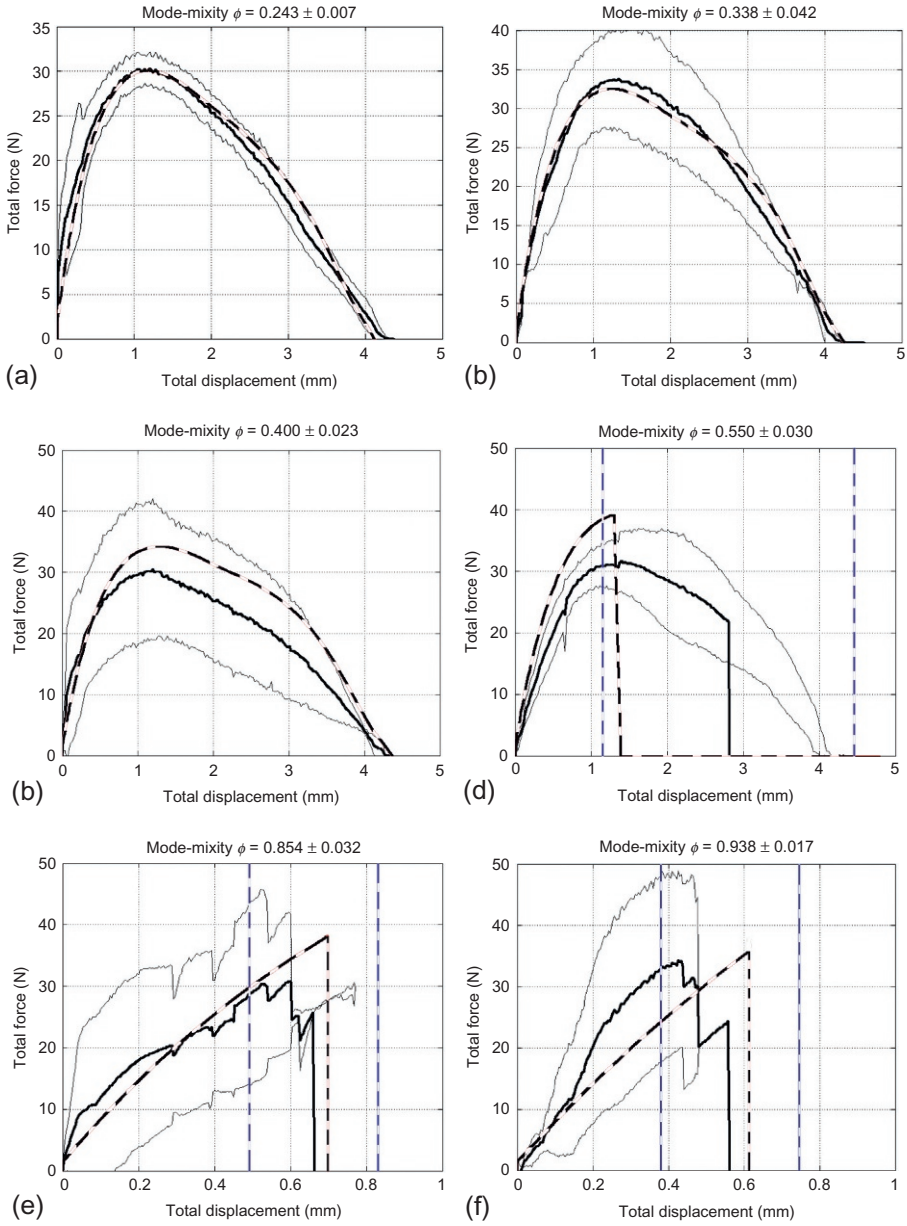

Figure 17.5 Model validation; average response in thick black lines; model predictions in thick **red lines. One standard deviation scatter bands on mean load in thin black lines. The dashed vertical lines in (e–f) represent the bounds of plus/minus one standard deviation from the average displacement to failure.

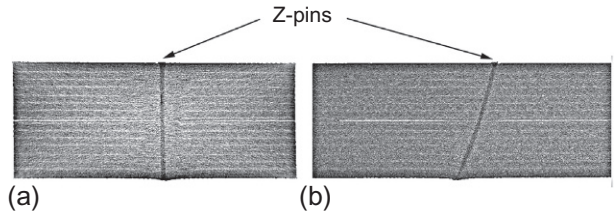

Figure 17.6 CT scan images of Z-pins: (a) a straight Z-pin; (b) a misaligned Z-pin. Note the residual curvature of the misaligned Z-pin in (b).

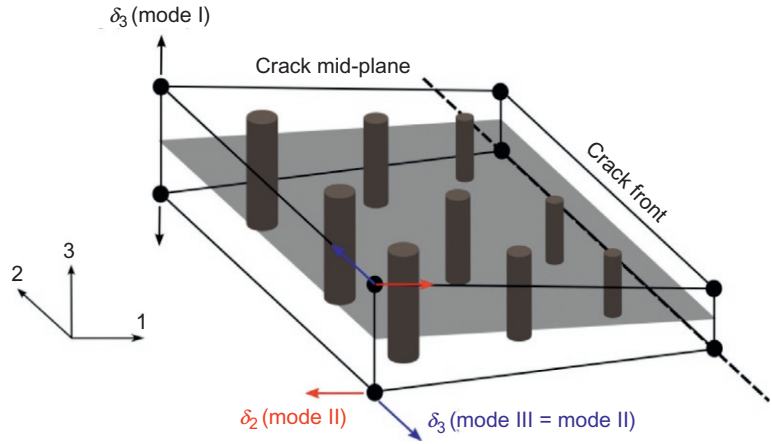

Figure 17.7 Schematic of cohesive element formulation with cohesive and Z-pin interface features (all shear displacements are mode II, i.e. $\delta_2 = U$, $\delta_3 = 0$).

The unpinned cohesive zone model is governed by the laminate intrinsic toughness and behaves according to a mixed-mode bi-linear traction-separation law as implemented by Jiang et al. (2007). The energy dissipated during the crack opening is controlled via a constitutive formulation that uses a simple damage variable combined with a simple bilinear softening cohesive/de-cohesive law that relates the interfacial traction components (σ) and the relative displacement components (δ). The Z-pin bridging map, as derived from the meso-1 semi-analytical mode and shown in Figure 17.8, is stored as an array of facets and points. At each time increment, the bridging stresses are interpolated from the 'nodal' (points) values of the facet on which the mixed-mode relative displacement δ_m can be projected, as illustrated in Figure 17.9. These stresses are then added to the unpinned stresses (which govern the underlying material interface behaviour) in locations that are modelled as having been reinforced by Z-pins.

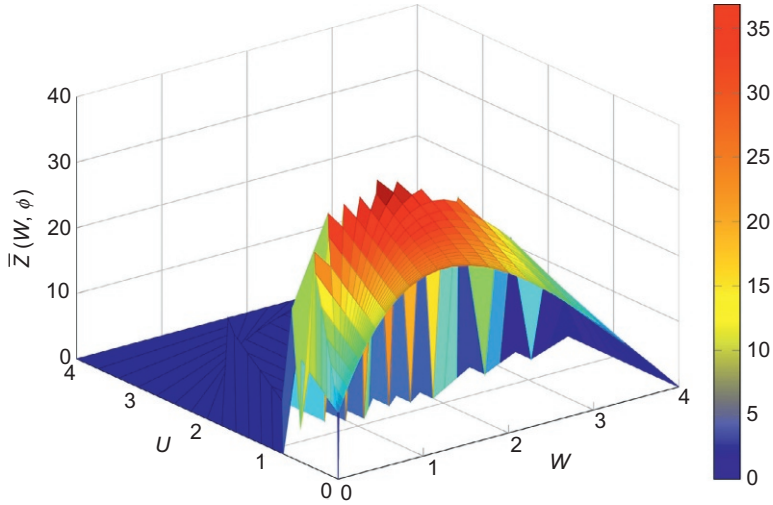

Figure 17.8 3D Z-pin bridging map of axial force ($\bar{Z}$) as a function of delamination opening (W) and sliding (U) displacements.

17.3.2 Quasi-static experimental tests

The efficacy of the modelling strategy described above is evaluated by simulating DCB and mixed-mode bending (MMB) specimens, both pinned and unpinned, using finite element (FE) analysis. Sixty-four plies of carbon-reinforced IM7/8552 were manufactured in which the stacking sequences for the full laminate were $[(0/-45/90/45)_{4s}]_s$. Mechanical properties are given in Table 17.3. The Z-pins are made from the same pultruded T300/BMI as those considered for the single Z-pin tests. The specimens have an initial crack a_0 long, formed by inserting a thin polytetrafluoroethylene (PTFE) film in the mid-plane of the specimen in the pre-crack region before curing. In the pinned laminate configuration, the Z-pinned region covers 22.75 mm in length and spans the entire width of the specimen. Having an unreinforced region as well as reinforced region gives a clear indication of the bridging effect of the pins once a crack has initiated and propagated during testing.

MMB tests are popular mixed-mode fracture toughness tests in that they easily facilitate the setup of different loading conditions using the same geometry of specimens. The loading conditions are defined by the linear relationship of three different displacement points of the specimen (ASTM D6671/D6671M – 13, 2013):

$$\Delta_{\mathrm{LP}} = \left(\frac{c}{L}\right)\Delta_I + \left(\frac{c+L}{L}\right)\Delta_{\mathrm{M}} \tag{17.12}$$

In Equation (17.12), L refers to half the specimen length and c is the length from the point of load application to the mid-point of the specimen. Different

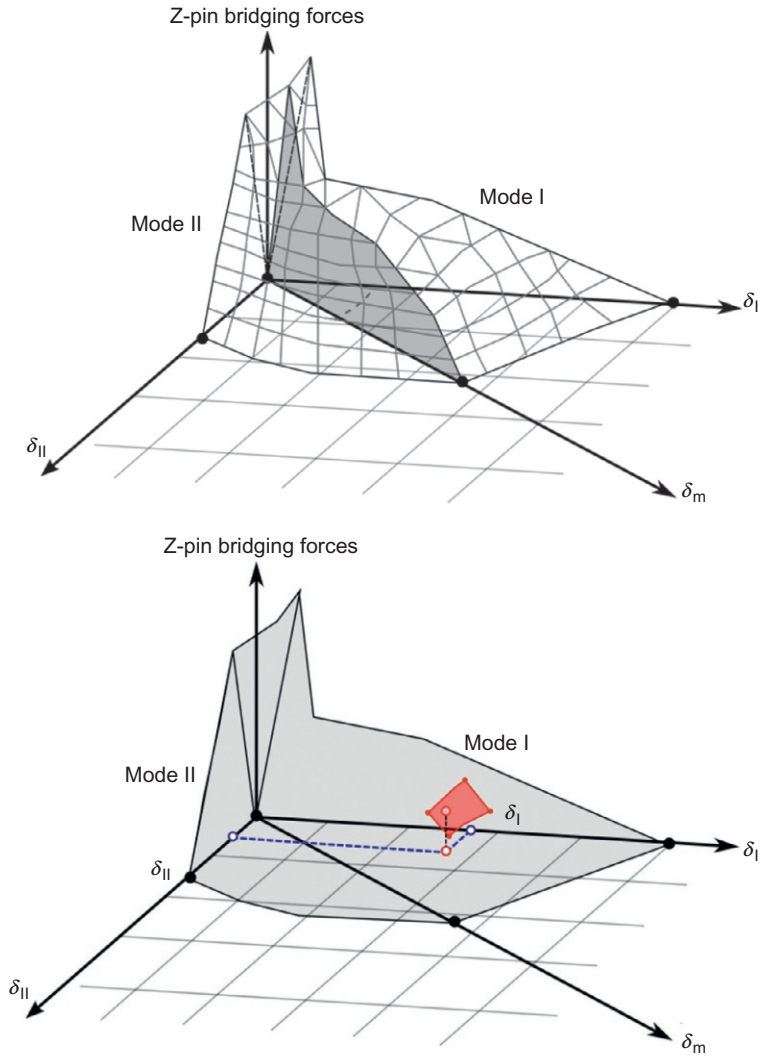

Figure 17.9 Mixed-mode Z-pin bridging law. The bridging stresses are interpolated from the 'nodal' (points) values of the facet on which the mixed-mode relative displacement δ_m can be projected.

Table 17.3 Elastic properties for the IM/8552 pre-preg

E_1 (GPa)	E_2 (GPa)	E_3 (GPa)	ν_{12} (–)	ν_{13} (–)	ν_{23} (–)	G_{12} (GPa)	G_{13} (GPa)	G_{23} (GPa)
161	11.38	11.38	0.3	0.3	0.45	5.17	5.17	3.92

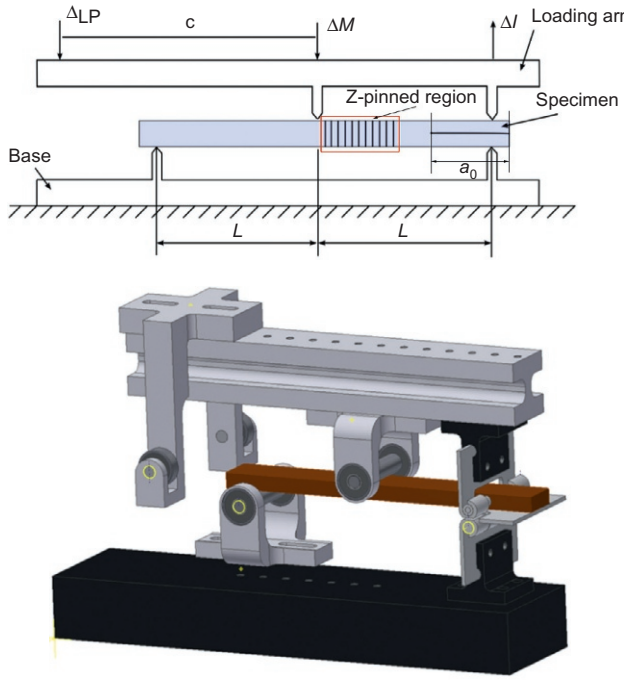

Figure 17.10 MMB test configuration.

mixed-mode conditions can be obtained by varying the length c, based on the following relationship:

$$c = \frac{L\left(\frac{1}{2}\sqrt{3\frac{1-\phi}{\phi}}+1\right)}{3-\frac{1}{2}\sqrt{3\frac{1-\phi}{\phi}}} \tag{17.13}$$

The MMB test apparatus is illustrated in Figure 17.10; the initial crack length a_0 is 25 mm and the first unpinned length is 10 mm followed by a pinned region of 22.75 mm. The mixed-mode (ϕ) loading cases considered are $\phi = 22, 43$ and 66% corresponding to a lever length c of 101, 57.5 and 41 mm, respectively.

These tests allow the validation of the meso-2 model for a configuration in which the damage mechanism is predominantly large-scale bridging without any other interaction with intra-laminar damage mechanisms.

17.3.3 Finite element model

Figure 17.11 shows various possible arrangements of finite element models (FEMs) for DCB/MMB specimens. Because the composite is unidirectional and the delamination

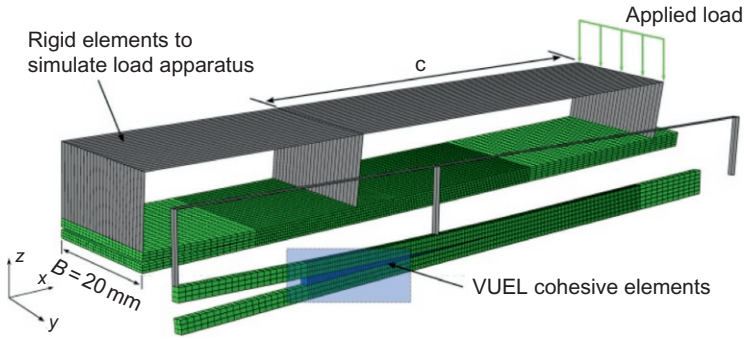

Figure 17.11 Three-dimensional FEM of an MMB specimen.

front is straight, consistent results can be obtained without resorting to full three-dimensional simulations, provided that the Z-pin bridging forces are scaled according to the specimen width. Therefore, to reduce the computational running time, a simplified 'strip' mesh was developed, which represents the specimen with two elements across its width under generalised plain strain boundary conditions. This gives a single row of approximately seven Z-pins along its length. The cohesive element formulation effectively 'smears' the periodic pin arrangement across the elemental area, hence individual modelling of the pins is not required. The unpinned and pinned regions are modelled using the same cohesive element formulation (VUEL) simply by activating (or deactivating) the appropriate resin/pin feature. Eight-node continuum shell elements SC8R with reduced integration and hourglass control are used to model the composite laminate beams, which accurately capture the laminate rotations. The in-plane cohesive element size is determined such that there are four or five elements within the fracture process zone. The cohesive element length used is 0.5 mm for all simulations, the upper bound of acceptable simulation results for the cohesive properties given in Table 17.4. Only two elements per unit width were defined in the model since the crack propagation is orthogonal to this direction.

The loading velocity defined in all solutions is approximately 1 mm/s (defined initially by a smooth ramp rate followed by a constant velocity), which produced satisfactory results with insignificant dynamic effects. Furthermore, mass scaling was used to accelerate the solution time and no damping was used in the models.

Element deletion was not active in these models since the cohesive elements have an in-built penalty algorithm to resist interpenetration of crack faces once an element has failed. These pseudo-failed elements do not have the ability to carry stress or

Table 17.4 Assumed cohesive properties of unpinned IM7/8552.

G_{IC} (N/mm)	G_{IIC} (N/mm)	σ_{Imax} (MPa)	σ_{IImax} (MPa)	E_I (N/mm^3)	E_{II} (N/mm^3)
0.21	1.0	30	60	1×10^5	1×10^5

contribute to the stiffness matrix; however, they allow the visualisation of state-dependent variables and negate the need for surface-to-surface contact algorithms.

17.3.4 Simulation results

A comparison of the numerically calculated force versus applied displacement with the tests results for a pin aerial density of 2% and pin diameter $d = 0.28$ mm is presented in Figure 17.12. An initial linear elastic response is observed for both pinned and unpinned specimens. The onset of delamination growth is similar for both cases, regardless of the presence of the pins, indicating that the initial fracture toughness (an intrinsic material property) is controlled by the resin-rich interfacial properties. For the unpinned specimens, a monotonic, continuous load drop characterizes the propagation of the delamination crack, which continues to grow until it has reached the full length of the specimen. For the pinned specimens, following a small load drop as the crack tip propagates through the unpinned region, the crack reaches the first row of Z-pins. Here, the pins begin to exert traction forces that bridge (or partially suppress) further crack opening displacement, characterized by a gradual increase in the global force response. Because the pins are discrete entities embedded in the composite laminate, it is appropriate to refer to this phenomenon as 'apparent toughness' because it cannot be attributed to any intrinsic material properties. The numerical results are in excellent agreement with those obtained from the experimental tests.

The results of several MMB simulations, using the same set of input parameters and bridging map, are shown in Figure 17.13. Again very good agreement is reached, giving

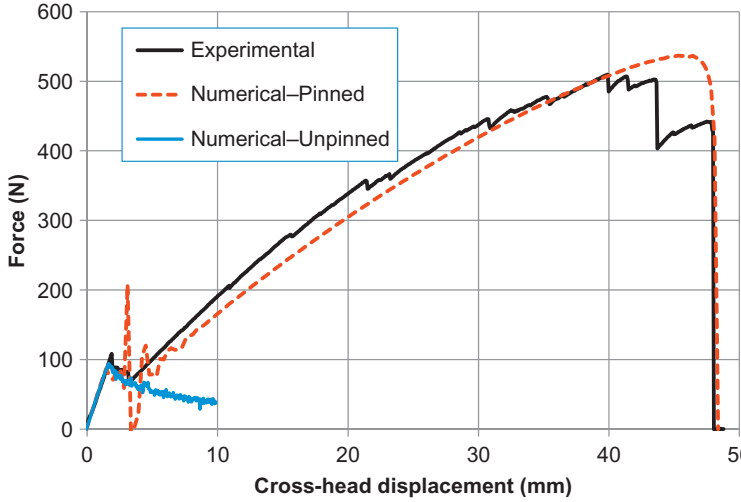

Figure 17.12 Comparison between DCB experimental tests and numerical prediction (Z-pin configuration: 2% aerial density and $D = 0.28$ mm).

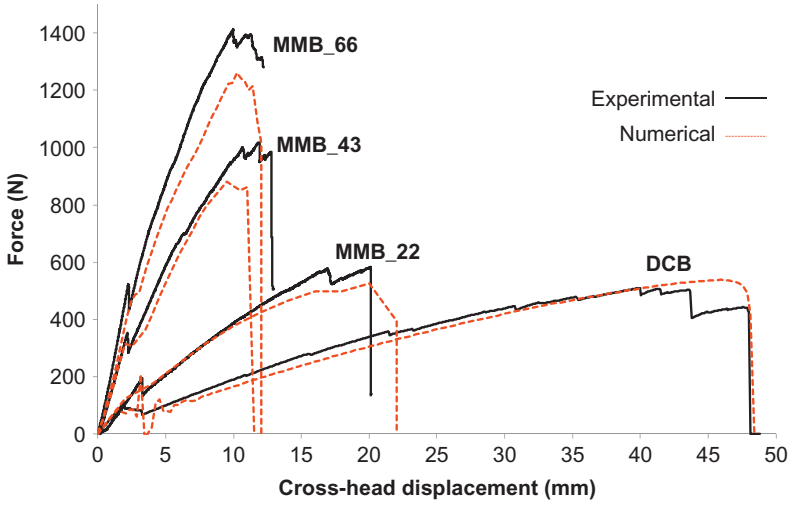

Figure 17.13 Comparison between MMB experimental tests and numerical prediction (Z-pin configuration: 2% aerial density and $D = 0.28$ mm).

confidence that the meso-2 level Z-pin cohesive element tool is capable of modelling mixed-mode response of pinned composite laminates without any additional calibration.

17.4 Conclusions

A modelling framework for predicting the apparent fracture toughness enhancement in Z-pinned laminates has been presented and validated by means of experimental data. The modelling approach is based on linking the fracture behaviour of ply interfaces bridged by Z-pins (meso-2 level) to the mixed-mode pullout response of single Z-pins (meso-1 scale). The Z-pins meso-1-mechanics is described via a reduced-order model, whereby the Z-pin is considered as an Euler–Bernoulli beam embedded into an elastic foundation. The meso-2-mechanics is represented by 'bridging maps', obtained from the meso-1 model and implemented into finite element analysis by means of a 'smeared force' cohesive zone formulation. The 'bridging maps' are essentially lookup tables that are suitably interpolated during the analysis to yield the bridging tractions as functions of the delamination opening/sliding displacements. The meso-2 analyses have been carried out using an explicit finite element solver to avoid convergence issues associated with large-scale bridging. The modelling approach proposed requires the identification of six parameters governing the Z-pin response on a subset of experimental tests performed at the meso-1 level. The aforementioned parameters comprise the elastic foundation stiffness, the frictional properties of the Z-pin/laminate interface and Weibull's statistics associated with tensile fibre failure of the Z-pin. Once these parameters have been estimated, the fracture behaviour of

Z-pinned laminates can be predicted. No additional experimental inputs or calibration factors need to be introduced in the meso-2 level FEMs and the results obtained are in excellent agreement with the experiments for the full mode-mixity range (from pure mode I to 66% mode II).

Acknowledgement

The authors would like to acknowledge the support of Rolls-Royce plc for their support of this research through the Composites University Technology Centre (UTC) at the University of Bristol, UK.

References

Allegri, G., Zhang, X., 2007. On the delamination and debond suppression in structural joints by Z-fibre pinning. Compos. Part A: Appl. Sci. Manuf. 38 (4), 1107–1115.

Allegri, G., Yasaee, M., Partridge, I.K., Hallett, S.R., 2014. A novel model of delamination bridging via Z-pins in composite. Int. J. Solids Struct. 51 (19–20), 3314–3332.

ASTM D6671/D6671M – 13, 2013. Standard test method for mixed mode I-mode II interlaminar fracture toughness of unidirectional fiber reinforced polymer matrix composites. Book of Standards, vol. 15.03. ASTM International.

Bianchi, F., Zhang, X., 2011. A cohesive zone model for predicting delamination suppression in Z-pinned laminates. Compos. Sci. Technol. 71 (16), 1898–1907.

Bianchi, F., Zhang, X., 2012. Predicting mode-II delamination suppression in Z-pinned laminates. Compos. Sci. Technol. 72 (8), 924–932.

Byrd, L.W., Birman, V., 2005. The estimate of the effect of Z-pins on the strain release rate, fracture and fatigue in a composite co-cured Z-pinned double cantilever beam. Compos. Struct. 68, 53–63.

Camanho, P.P., Dávila, C.G., 2002. Mixed-mode decohesion finite elements for the simulation of delamination in composite materials. NASA-Technical Paper, 211737(1), 33.

Cartié, D.D.R., 2000. Effect of Z-fibresTM on the delamination behaviour of carbon fibre/epoxy laminates (PhD thesis). Cranfield University.

Cartié, D.D.R., Dell'Anno, G., Poulin, E., Partridge, I.K., 2006a. 3D reinforcement of stiffener-to-skin T-joints by Z-pinning and tufting. Eng. Fract. Mech. 73 (16), 2532–2540.

Cartié, D.D.R., Troulis, M., Partridge, I.K., 2006b. Delamination of Z-pinned carbon fibre reinforced laminates. Compos. Sci. Technol. 66 (6), 855–861.

Cox, B.N., 2005. Snubbing effects in the pullout of a fibrous rod from a laminate. Mech. Adv. Mater. Struct. 12, 85–98.

Cox, B.N., Sridhar, N., 2002. A traction law for inclined tows bridging mixed-mode cracks. Mech. Compos. Mater. Struct. 9, 299–331.

Cui, H., Lia, Y., Koussiosb, S., Zub, L., Beukersb, A., 2011. Bridging micromechanisms of Z-pin in mixed mode delamination. Compos. Struct. 93 (11), 2685–2695.

Cui, H., Li, Y., Koussios, S., Beukers, A., 2013. Mixed mode cohesive law for Z-pinned composite analyses. Comput. Mater. Sci. 75, 60–68.

Dantuluri, V., Maiti, S., Geubelle, P.H., Patel, R., Kilic, H., 2007. Cohesive modeling of delamination in Z-pin reinforced composite laminates. Compos. Sci. Technol. 67 (3–4), 616–631.

Grassi, M., Zhang, X., 2003. Finite element analyses of mode I interlaminar delamination in z-fibre reinforced composite laminates. Compos. Sci. Technol. 63 (13), 1815–1832.

Jiang, W.G., Hallett, S.R., Green, B.G., Wisnom, M.R., 2007. A concise interface constitutive law for analysis of delamination and splitting in composite materials and its application to scaled notched tensile specimens. Int. J. Numer. Methods Eng. 69 (9), 1982–1995.

Kravchenko, S., Kravchenko, O., Wortmann, M., Pietrek, M., Horst, P., Byron, P.R., 2013. Composite toughness enhancement with interlaminar reinforcement. Compos. A: Appl. Sci. Manuf. 54, 98–106.

Meo, M., Achard, F., Grassi, M., 2005. Finite element modelling of bridging micromechanics in through-thickness reinforced composite laminates. Compos. Struct. 71 (3–4), 383–387.

Partridge, I.K., Cartié, D.D.R., 2005. Delamination resistant laminates by Z-Fiber^{tm} Pinning. Part I: manufacture and fracture performance. Compos. A: Appl. Sci. Manuf. 36 (1), 55–64.

Plain, K.P., Tong, L., 2009. Traction law for inclined through-thickness reinforcement using a geometrical approach. Compos. Struct. 88 (4), 558–569.

Ratcliffe, J.G., O'brien, T.K., 2004. Discrete spring model for predicting delamination growth in z-fiber reinforced DCB specimens, NASA/TM-2004-213019, ARL-TR-3190.

Robinson, P., Das, S., 2004. Mode I DCB testing of composite laminates reinforced with z-direction pins: a simple model for the investigation of data reduction strategies. Eng. Fract. Mech. 71, 345–364.

Song, M.C., Sankar, B.V., Subhash, G., Yen, C.F., 2012. Analysis of mode I delamination of Z-pinned composites using a non-dimensional analytical model. Compos. Part B 43 (4), 1776–1784.

Tong, L., Sun, X., 2004. Bending effect of through-thickness reinforcement rods on mode I delamination toughness of DCB specimen. I. Linearly elastic and rigid-perfectly plastic models. Int. J. Solids Struct. 41 (24–25), 6831–6852.

Tong, L., Sun, X., 2007. Bending effect of through-thickness reinforcement rods on mode II delamination toughness of ENF specimen: Elastic and rigid-perfectly plastic analyses. Compos. A: Appl. Sci. Manuf. 38 (2), 323–336.

Yan, W., Liu, H.Y., Mai, Y.W., 2003. Numerical study on the mode I delamination toughness of Z-pinned laminates. Compos. Sci. Technol. 63, 1481–1493.

Yan, W., Liu, H.Y., Mai, Y.W., 2004. Mode II delamination toughness of Z-pinned laminates. Compos. Sci. Technol. 64, 1937–1945.

Yasaee, M., Lander, J.K., Allegri, G., Hallett, S.R., 2014. Experimental characterisation of mixed mode traction–displacement relationships for a single carbon composite Z-pin. Compos. Sci. Technol. 94 (9), 123–131.

Numerical modelling of impact and damage tolerance in aerospace composite structures

18

A.F. Johnson[*], *N. Toso-Pentecôte*[†], *D. Schueler*[†]
*Consultant, Stuttgart, Germany; [†]German Aerospace Center (DLR), Institute of Structures and Design, Stuttgart, Germany

18.1 Introduction

Aircraft structures are vulnerable to impact damage resulting from impact by hard or soft bodies, such as steel fragments, birds, burst tyre rubber or hail. With the increasing use of polymer composite materials in aircraft structures, the impact response of such materials has been a subject of extensive research that has led to the development of theoretical models able to capture the impact mechanics of materials and structures, required for the derivation of reliable design rules needed by the aircraft industry (Abrate, 1998; Davies and Olsson, 2004). The use of polymer composite materials in commercial aircraft was first limited to secondary structures such as inspection panels, spoilers or air brakes that do not reduce aircraft structural integrity on failure. Improvements in manufacturing technology, the development of innovative material systems and a better understanding of their mechanical behaviour have now led to the use of composites for primary aircraft structures that carry flight, pressurisation or ground loads, which are critical for structural integrity. For primary load-bearing structures, such as the fuselage or wing skin with related safety regulations (FAA AC 23-13A, 2005), validated numerical methods are required to determine impact behaviour. These enable cost savings through 'right-first-time' design and reduction of experimental tests in the certification process by use of computational analysis, which was a major objective of the industry-led EU project MAAXIMUS (2013).

Impact incidents are commonly classified according to impact velocity: low velocity, high velocity and ballistic impact (Davies and Zhang, 1995; Olsson, 2000). Under low-velocity impact (LVI), an impacted plate deforms according to plate theory as the impact duration is longer than the time needed for flexural waves to reach the boundaries. For shorter impact durations under high-velocity impact (HVI), the target response is governed by flexural waves. Ballistic impact is characterised by a local impact response from through-thickness dilatational stress waves. Typical scenarios for LVI are 'tool drop' where the impactor hits the target accelerated by gravity from up to a few metres in height and the impact of ground equipment, such as stairs or deicing equipment. HVI scenarios usually occur in flight or on take-off and include bird strikes or impact by hail, tyre rubber, engine fragments or runway debris. Ballistic impact cases are low mass with often supersonic impact velocities arising from weapons with application to security protection systems.

Numerical modelling of failure in advanced composite materials. http://dx.doi.org/10.1016/B978-0-08-100332-9.00018-9
Copyright © 2015 Elsevier Ltd. All rights reserved.

In this chapter, the focus is on carbon fibre composite aircraft structures under HVI that are commonly classified further into soft body impact (hail, birds, tyre rubber) and hard body impact (runway debris, engine parts). Soft bodies may disintegrate on impact exhibiting a fluid-like flow behaviour or be highly deformable (rubber), whereas hard bodies usually remain intact after impact. For aircraft structures, the impact scenarios for different categories of projectiles are specified in safety regulations, or are derived from test programmes. Bird strike regulations require the airplane to safely continue its flight after impact with a 4-lb bird (8 lb on the empennage) at design cruising speed V_C (EASA CS25, FAA 14 CFR 25: §§ 25.571 and 25.631). For hailstones diameters range from 5 to 100 mm with velocities for hail on ground 10–50 m/s and in flight at V_C, see Field et al. (2009). In the case of uncontained engine failure, metal fragments can impact the fuselage or wing with velocities in the range 61–295 m/s and masses ranging from 22 g to 20.4 kg (DOT/FAA/AR-04/16, 2004). Foreign object debris (FOD) such as runway debris, stones or metal fragments could impact aircraft when launched by a tyre or by jet blast from another aircraft, as discussed in Chadwick et al. (2001). Burst tyre fragments may impact the lower wing skin or fuselage with impact velocities dependent on the tangential tyre speed and typically about 100 m/s, impactor mass can be up to several kg (Mines et al., 2007; Toso-Pentecôte et al., 2010).

The FAA route to certification adopted by civil aircraft manufacturers is based on the well-known test pyramid for aircraft structures, as set out for composite aircraft in FAA AC 20-107B (2010), which foresees five levels of tests from material characterisation test specimens, through structural elements of increasing complexity up to full aircraft structures. It is clear from the range of impact threats and the size of the regulation test programmes that certification of composite structures subjected to impact loads is no longer feasible by extensive test campaigns alone. The way forward as discussed by Hachenberg (2002) is to use design analysis to support a limited number of tests at each level of the test pyramid. This requires the development and validation of computational methods to support the design of a composite aircraft under the full range of flight and service loads defined in the airworthiness specifications. This is a 'building block' approach, as each level strongly relies on the validity of design analysis results obtained on simpler structures at the levels below. For the structural impact behaviour, improved composites damage and failure models with appropriate finite element (FE) codes are needed and should be validated by structural impact tests at each level of the test pyramid.

This chapter presents HVI test data from gas gun impact tests on advanced composite structures and discusses numerical methods to predict observed impact damage at the structural element level of the test pyramid, which are validated by the tests. Section 18.2 presents meso-scale composite ply damage and failure models and energy-based delamination models suitable for use in explicit FE codes for prediction of impact damage. The application of the FE models in Section 18.3 is used to predict tyre rubber impact damage on a rib-stiffened composite panel structure. Section 18.4 discusses a test programme on the influence of tensile and compressive pre-stress on HVI damage in composite plate structures, followed by the extension of the FE modelling procedures to pre-stressed panels under impact and prediction of residual strengths and damage tolerance (DT). Concluding remarks in Section 18.5 are followed by future trends, sources of further information and references.

18.2 Composites damage and failure models

Impact damage in composite laminates usually is a combination of several damage modes. The typical failure mechanisms are fibre breakage, matrix cracking, fibre/matrix debonding and delamination at the ply interfaces (Liu, 1988). Matrix cracking is driven by stiffness mismatch and debonding between fibre and matrix that leads to failure of the weaker matrix, especially under tensile and shear loading (Liu and Malvern, 1987). Delamination damage is the separation of laminated plies due to the failure of the interfaces between plies of different orientation, often initiated by transverse ply matrix cracks. In delaminated regions the transfer of loads between adjacent plies is inhibited, which can lead to severe reductions in strength and stiffness of the laminate. Since this type of damage is internal and not detectable by visual inspection, it is a major concern in the application of composite materials in aircraft structures (Garg, 1988). The challenge in modelling composite materials is the formulation of realistic damage and failure models and their corresponding energy absorption mechanisms. Whilst damage is initiated at the microscale, models are required suitable for use with sufficient accuracy at length scales appropriate to engineering structures.

18.2.1 Meso-scale ply damage models

For structural analyses, composite laminates are usually assumed to be composed of homogeneous orthotropic elastic plies, with ply failure determined by specifying failure boundaries under in-plane loads, based on a number of failure conditions (Tsai and Wu, 1971; Chang and Chang, 1987; Hashin, 1980; Puck and Schürmann, 1998). Depending on the parameters chosen, these failure envelopes may allow the prediction of failure initiation or ply ultimate failure. They do not consider stiffness reductions in the ply due to microdamage in the fibres or matrix and energy dissipation during the damage evolution process, which are important for understanding impact damage in laminates. In continuum damage mechanics (CDM), internal state variables are introduced to describe the stiffness reductions and damage progression as a basis for advanced laminate models. Ladevèze and co-workers (Ladevèze and Le Dantec, 1992; Allix and Ladevèze, 1992) developed a CDM mesoscale model in which the laminate is represented by the two basic constituents: ply and interface. The CDM ply model captures intra-laminar damage and failure, whilst the interface model describes the debonding of adjacent plies.

Within the CDM framework, Ladevèze and Le Dantec (1992) developed a plane stress ply damage model that captures the internal degradation and rupture behaviour of uni-directional (UD) fibre composite plies. Stiffness degradation by matrix microcracking, fibre/matrix debonding and fibre failure is introduced through additional damage parameters and damage evolution laws. The elementary ply is assumed to be homogenous and orthotropic with an elastic or elastic-plastic constitutive law. Micro-damage is considered by degrading the ply stiffness properties with increasing load until ultimate failure is reached. The ply damage elastic law can then be written in a plane stress formulation suitable for shell elements as:

$$\boldsymbol{\varepsilon}_{\mathrm{el}} = \mathbf{K}^{-1}\boldsymbol{\sigma} \Leftrightarrow \begin{cases} \varepsilon_{11}^{\mathrm{e}} = \dfrac{\sigma_{11}}{E_1^0\left(1+\gamma\langle\sigma_{11}\rangle_-\right)(1-d_1)} - \dfrac{v_{21}}{E_2^0}\sigma_{22} \\ \varepsilon_{22}^{\mathrm{e}} = -\dfrac{v_{12}}{E_1^0}\sigma_{11} + \dfrac{\langle\sigma_{22}\rangle_+}{E_2^0(1-d_2)} + \dfrac{\langle\sigma_{22}\rangle_-}{E_2^0} \\ \varepsilon_{12}^{\mathrm{e}} = \dfrac{\sigma_{12}}{2G_{12}^0(1-d_{12})} \end{cases} \tag{18.1}$$

$$\text{with} \begin{cases} \langle a\rangle_+ = a \ \text{ if } a \geq 0;\ \text{else } \langle a\rangle_+ = 0 \\ \langle a\rangle_- = a \ \text{ if } a < 0;\ \text{else } \langle a\rangle_- = 0 \end{cases}.$$

Here $\boldsymbol{\sigma}$ and $\boldsymbol{\varepsilon}_{\mathrm{el}}$ are vectors of stress and elastic strain components, and $\mathbf{K}$ is the elastic stiffness matrix. Subscripts 11, 22 and 12 denote the fibre, transverse fibre and in-plane shear directions, respectively. E_1^0, E_2^0 and G_{12}^0 are the initial undamaged elastic moduli. The damage parameters d_1 (fibre damage), d_2 (matrix damage transverse to the fibres), d_{12} (in-plane shear damage) have values $0 \leq d_i \leq 1$ and represent stiffness reductions due to micro-damage in the ply.

For the elastic fibres assumed here, $d_1 = 0$ so that damage evolution is governed by two 'conjugate forces' or energy release rate functions Y_2 and Y_{12} obtained from the partial derivatives of the strain energy function with respect to d_2 and d_{12} respectively:

$$Y_2 = \frac{\langle\sigma_{22}\rangle_+^2}{2E_2^0(1-d_2)^2}, \quad Y_{12} = \frac{\sigma_{12}^2}{2G_{12}^0(1-d_{12})^2}. \tag{18.2}$$

Based on experimental results, Ladevèze and Le Dantec (1992) introduce the quantities:

$$\underline{Y} = \sup_{\tau\leq t}\left(\sqrt{Y_{12}(\tau) + bY_2(\tau)}\right), \quad \underline{Y_2} = \sup_{\tau\leq t}\left(\sqrt{Y_2(\tau)}\right), \tag{18.3}$$

which are used to define the damage evolution laws:

$$d_2 = \frac{\left\langle \underline{Y} - Y_{20}\right\rangle_+}{Y_{2\mathrm{c}}} \quad \text{if } d_2 < 1,\ \underline{Y_2} < Y_{2\mathrm{s}} \text{ and } \underline{Y} < Y_{12\mathrm{s}};\ \text{else } d_2 = 1 \tag{18.4}$$

$$d_{12} = \frac{\left\langle \underline{Y} - Y_{120}\right\rangle_+}{Y_{12\mathrm{c}}} \quad \text{if } d_{12} < 1,\ \underline{Y_2} < Y_{2\mathrm{s}} \text{ and } \underline{Y} < Y_{12\mathrm{s}};\ \text{else } d_{12} = 1. \tag{18.5}$$

The failure threshold values $Y_{2\mathrm{s}}$, $Y_{12\mathrm{s}}$ control, respectively, the brittle failure of the fibre/matrix interface and shear failure, whereas the progressive damage evolution is governed by the parametersY_{20}, $Y_{2\mathrm{c}}$, Y_{120}, $Y_{12\mathrm{c}}$ and the coupling parameter b.

To model the influence of microcracks and internal friction that may lead to permanent plastic strains, a plasticity law is introduced with the elastic domain function f and the hardening law $R(p)$:

$$f = \sqrt{\tilde{\sigma}_{12}^2 + a^2\tilde{\sigma}_{22}^2} - R(p) - R_0, \quad R(p) = \beta p^{\mathrm{m}} \tag{18.6}$$

with p being the effective plastic strain, R_0 the yield stress, a a material dependent coupling parameter and

$$\widetilde{\boldsymbol{\sigma}} = \left(\sigma_{11}, \frac{\langle \sigma_{22} \rangle_+}{(1-d_2)} + \langle \sigma_{22} \rangle_-, \frac{\sqrt{2}\sigma_{12}}{(1-d_{12})} \right)^{\mathrm{T}} \tag{18.7}$$

the 'effective' stress.

The material input parameters are obtained from a set of characterisation tests under both monotonic and cyclic loads with coupons of different layups as described in detail by Ladevèze and Le Dantec (1992) and Pickett and Fouinneteau (2006). Maximum ply damage is controlled by threshold energy values for the conjugate forces Y_{2s}, Y_{12s}. From the definitions in Equations (18.4) and (18.5), these ultimate damage conditions may be related to ply failure stresses or strains in transverse tension and in-plane shear. At this point, the ply is fully damaged with the damage parameters set to $d_2 = d_{12} = 1$, as defined in Equations (18.4) and (18.5). In the FE code implementation, it is more usual to set the damage parameters to a maximum damage limit $d_{\mathrm{m}} < 1$, allowing the fully damaged ply to sustain low stresses. Ultimate failure in the damaged plies or the laminate may then be achieved by applying other established multiaxial ply failure criteria such as maximum strain, modified Puck, etc. In this way, the CDM model is used to describe ply degradation such as matrix cracking, while ply ultimate failure may be controlled by fibre fracture.

18.2.2 Cohesive interface delamination models

Whereas ply damage is modelled as homogenised diffuse microdamage, delamination damage in composites is characterised by sharp inter-ply cracks that are controlled by fracture mechanics. To model possible delamination zones between plies, interface elements or contact interfaces are commonly introduced that transfer inter-laminar loads according to a cohesive interface traction–separation law that includes material softening and absorbs the fracture energy at failure. This approach, which combines fracture mechanics and CDM, was first introduced by Cui and Wisnom (1993), Schellekens and de Borst (1994) and Allix et al. (1995). The inter-laminar fracture toughness energies, also referred to as critical energy-release rates, govern crack propagation and are determined from quasi-static coupon tests with double cantilever beam (DCB) specimens for mode I opening and end notched flexure (ENF) specimens for mode II shear (Davies, 2008). The frequently used bilinear traction–separation law for the cohesive interface, see for example Greve and Pickett (2006), is linear elastic up to a strength-based damage initiation condition with an energy-based crack propagation criterion based on the area under the traction–displacement curve. The damage initiation criterion is linked to the matrix strength and the crack propagation criterion to the inter-laminar fracture toughness energies G_{IC} and G_{IIC} for mode I opening and mode II shear, respectively.

Delamination in real structures occurs under combined mode I crack opening and mode II shear. Several failure criterions for mixed-mode interface crack propagation

have been formulated, as reviewed in Reeder (1992). The criterion most commonly applied is a power law condition where the crack energy release rates of each mode are normalised by their critical values:

$$\left(\frac{G_{\mathrm{I}}}{G_{\mathrm{IC}}}\right)^{\alpha}+\left(\frac{G_{\mathrm{II}}}{G_{\mathrm{IIC}}}\right)^{\alpha}=1 \tag{18.8}$$

Wu and Reuter (1965) were the first to introduce the criterion with a linear interaction ($\alpha=1$) which is a conservative assumption for most materials. Test results from mixed-mode bending experiments indicate that α takes values between 1 and 2 depending on the material system (Allix et al., 1998; Reeder, 1992).

18.2.3 Code implementation for panel impact

The ply damage and failure models discussed here were implemented in the commercial explicit crash and impact code PAM-CRASH^{TM} in collaboration with the software company Engineering Systems International. The code uses a bilinear four-node quadrilateral isoparametric shell element due to Belytschko with uniform reduced integration in bending and shear. A Mindlin–Reissner shell formulation is used with a layered shell description to model a composite ply, a sublaminate or the complete laminate. For modelling delamination, the composite laminate is treated as a stack of shell elements. Each ply or sublaminate ply group is represented by layered shell elements, and individual sublaminate shells are connected using cohesive interfaces with an interface traction–displacement law. Interface contact is broken when the interface energy dissipated reaches the mixed-mode delamination energy criteria as discussed in Greve and Pickett (2006). The 'stacked shell' approach is an efficient way of modelling delamination in composite shell structures, with the advantage that the critical integration time step is relatively large as it depends on the area size of shell elements not on the inter-ply thickness. The cohesive interface delamination model was validated in PAM-CRASH^{TM} by Greve and Pickett (2006) who showed good agreement with test results from DCB, ENF and mixed-mode delamination tests. Further validation studies on the ply damage model with shear plasticity on composite test specimens and plates under impact loads are given in Johnson et al. (2001) and Johnson (2005). PAM-CRASH^{TM} is used in Section 18.3 for impact simulations on stiffened composite plates.

The composite ply and interface models were also implemented in material user-subroutines within the framework of Abaqus FEA (Schueler and Toso-Pentecôte, 2012). Here the 'stacked shell' approach is used with eight-node reduced integration continuum shell elements representing single plies or sublaminates that are connected to layers of cohesive elements that model delamination crack propagation. Continuum shell elements unlike conventional four-node shell elements discretize a three-dimensional region similar to solid elements and have displacement degrees of freedom at the nodes only. They use a plane stress formulation enhanced with a formulation for transverse shear and thickness stresses (Abaqus, 2010). Cohesive

elements are usually used with small or zero thickness and track the displacement jumps between shell element layers. Interface tractions are then computed following the traction-displacement law described in Turon et al. (2006), which is similar to the one implemented in PAM-CRASH^{TM}. The ply and interface models were implemented for the application with implicit (Abaqus/Standard) and explicit solvers (Abaqus/Explicit). The modelling of fracture processes with cohesive zone models usually requires a fine mesh for a proper discretisation of the crack process zone. Here the maximum interface strengths were adjusted following the approach described in Turon et al. (2007) such that the same element size could be used for cohesive and ply layers. This procedure was validated in the current work by simulating DCB and ENF test specimens. In Section 18.4, coupled implicit–explicit simulation schemes are used for modelling impact on pre-loaded composite plates. Static pre-loads are introduced with the implicit solver with simplified versions of the mesomodels omitting plasticity and failure since the pre-loads of interest are within the elastic regime. The results are then transferred into the explicit environment to simulate the transient impact event including damage, plasticity and failure.

Studies in the literature show that carbon/epoxy composites exhibit strain rate dependence in stiffness, strength and failure behaviour, which is more significant in resin dominated shear and compression properties. Gilat et al. (2002) reported only small increases in tensile stiffness and transverse strength properties at high rates. Tests by Daniel et al. (2011) were not highly significant, with compression and shear stiffness and strength properties increasing linearly with log strain rate. Koerber and Camanho (2011) measured longitudinal UD carbon/epoxy compression properties at strain rates up to 118 s^{-1}, showing small changes in modulus, but compression strength increases of 40% over quasi-static values. Under combined transverse compression/shear loads, Koerber et al. (2010) also found 40% increases in the multiaxial failure strengths and larger increases in yield stresses. The available test data on G_{IC} and G_{IIC} is inconclusive as to the effect of rate, due to the difficulty of performing dynamic interface crack propagation tests. Tsai et al. (2001) performed dynamic mode II crack propagation tests and found that the dynamic G_{IIC} in carbon/epoxy laminates is principally equal to the quasi-static value and insensitive to the crack speed up to 1100 m/s. Cairns (1992) also found that G_{IC} was insensitive to strain rate, but G_{IIC} increased by an average 30% with rate for toughened resin systems. However Kusaka et al. (1998) found 30% reductions in G_{IC} with rate.

Note that the composites damage and failure models developed here and implemented in commercial FE codes are based on an assumption of rate-independent behaviour, with materials properties used for the validation studies based on quasi-static tests. This is currently standard industry practice for LVI and HVI impact simulations of composite structures, which is an important assumption made in the chapter. Reasons for this are the lack of international dynamic test standards for measuring rate-dependent composites properties, so established test procedures are missing. Dynamic failure models for composites are not well understood nor implemented in current commercial FE codes. In justification it should be pointed out that carbon fibres are highly elastic in tension, thus fibre-dominated properties that control laminate tensile strengths should not be significantly rate dependent.

The increased fibre compression strengths and transverse compression/shear strengths reported here suggest that the quasi-static failure models will be conservative for design of structures under HVI loads: alternatively failure envelopes in the models could be modified where high rate properties are known. The available test data on G_{IC} and G_{IIC} is inconclusive as to the effect of rate. However, rate effects are expected to be more significant in ballistic impacts, where penetration and failure are determined by through-thickness dilatational stress waves and combined compression/shear behaviour.

18.3 Impact damage in composite panel structures

There have been several studies of impact damage mechanisms in composite plate structures under HVI loads, see for example Williams et al. (1979), Takeda et al. (1981, 1982), Garg (1988), Davies and Olsson (2004). The basic mechanisms for blunt, hard body projectiles are a through-thickness compressive stress wave initiating in the contact region that is reflected as a tensile wave from the back face, causing back face damage and inter-ply delamination. This takes place within a few microseconds after impact, followed by out-of-plane bending and propagation of flexural waves in the plate causing the damage to propagate away from the contact point through microcracks and delamination. Because damage propagation is dependent on ply orientation and position through the laminate thickness, impacted specimens often exhibit a characteristic 'peanut'-shaped damage and delamination zone centred on the impact point, Liu (1988), Guynn and O'Brien (1985). For hard projectiles with increasing impact velocity and kinetic energy, the initial contact damage will cause fibre fracture and penetration of the plate by the projectile, with insufficient time for the delamination zones to develop.

These failure mechanisms were observed in gas gun tests on a typical 2.1-mm thick composite aircraft panel, see Johnson et al. (2014), where a 12-mm steel cube would penetrate the panel for impact velocities above 95 m/s (60 J), while a Ø25-mm glass ball at 70 m/s (50 J) rebounded causing delamination damage. This shows that for hard bodies the critical impact damage thresholds are highly dependent on size and shape of the impactor, as well as panel material and dimensions. Impact tests from soft bodies such as gelatine (synthetic bird) (Kermanides et al., 2006; Kindervater et al., 2010) and ice (Kim and Kedward, 2000) show the impactor flows on contact, causing delamination damage in composite structures, and at sufficiently high-impact energies visible damage and fracture may also occur. High-energy impact tests with tyre rubber projectiles on aluminium aircraft panels reported by Mines et al. (2007) showed that impact energy was converted to large deformation strain energy in the rubber, which rebounded causing some indentation damage but no fracture.

It is apparent from the wide range of impact threats for composite aircraft structures and the size of the regulation test programmes required in the structural test pyramid FAA AC20-107B (2010) that certification under impact loads is no longer feasible by testing alone and should be supported by validated FE simulation methods

(Hachenberg, 2002). DT, maintenance and related safety issues of aircraft structures were discussed in DOT/FAA/AR-99/49 (1999) and by Ilcewicz (2006). Damage threats were categorised according to severity, visibility and their impact on the structural strength of the damaged component. A key element is the definition of five categories of damage severity. Category 1 (barely visible impact damage, BVID) is based on a *no-growth* concept, meaning that damage up to the boundary of visible detectability, will not grow under operational loads and will not cause a loss of residual strength below design ultimate load (DUL) level. Categories 2 and 3 are visible impact damage (VID) seen in routine and visual inspections. Here the residual strength may not fall below design limit load (DLL) level, corresponding to maximum operational loads. Category 4 is high-energy discrete source damage where the aircraft has a 'get you home' requirement with limited flight manoeuvres at below DLL, and Category 5 damage is more severe discrete source damage due to abnormal events, which reduces residual strength below the structural integrity limit and normally grounds the aircraft.

To support compliance with the impact DT requirements for aircraft structures, it is seen that impact models are required for prediction of the damage state of composite structures from a range of hard and soft body projectiles and related impact scenarios. Critical here is to predict whether there will be BVID, such as delamination damage through the laminate thickness, or VID which may range from surface ply damage, indentations and complete penetration of the structure. The ply damage and delamination models discussed in Section 18.2 and implemented into stacked shell elements with cohesive interfaces in PAM-CRASH™ have been successfully applied to predict damage in a number of impact scenarios. Johnson et al. (2013) show test data and numerical simulation of impact damage from steel cube projectiles impacting stringer stiffened carbon/epoxy panel structures and also sandwich panels with folded aramid composite cores. With impact velocities in the range 55–100 m/s, the FE simulations successfully predicted both rebound and penetration in the stringer stiffened panels, and skin fracture with core penetration in the sandwich panels. For use in bird impact simulations of aircraft structures a fluid model for gelatine flow under impact has been developed (Johnson and Holzapfel, 2003) and applied to several bird impact simulations on composite wing leading edges, wing pods and fuselage structures, see Kermanides et al. (2006), Kindervater et al. (2010). Good agreement with bird flow over these structures and reasonable prediction of structural damage under HVI give confidence in the gelatine and composites damage models used here and the suitability of PAM-CRASH™ for structural impact simulation. As a further example, the code is applied here to simulate damage in a composite aircraft panel structure under tyre rubber impact.

18.3.1 FE Simulation of tyre rubber impact in stiffened composite panels

A design study was carried out within ALCAS (2009) of tyre rubber fragments impacting prototype aircraft wheel bay panels with bonded and riveted C-frames, one manufactured using a thermoplastic resin (C/PEEK) and one using a thermoset

resin (C/RTM6). Figure 18.1 shows the geometry of the rib-stiffened panel with rectangular rubber fragment impactor. FE analyses were made to predict impact damage for tyre rubber fragment mass 0.85 kg impacting at a velocity of 93 m/s with impact angle 70° and impactor kinetic energy 3.7 kJ, which represents the typical impact scenario of a burst tyre fragment on a lower fuselage panel during start or landing. The panel structure is composed of a 1690 × 1000 mm composite panel stiffened by six C-frames, 1300 mm in length, 120 mm in height, flange width 41 mm, which are bonded and connected by riveted fasteners to the panel, with frame spacing 330 mm. For the impact analysis, the panel is assumed to be clamped at the edges of the long sides and at the ends of the C-frames. Table 18.1 gives some details of the two-panel structures.

Panel 1 is composed of 22 UD carbon/epoxy plies with RTM6 resin and a quasi-isotropic layup with thickness about 6.0 mm: Panel 2 has 44 C/PEEK plies and similar thickness. Impact simulations were performed with the commercial explicit code PAM-CRASH^{TM}. A stacked shell laminate model was used with 22 plies for the thermoset panel and 44 plies for the thermoplastic panel and after preliminary studies with different configurations, the laminate was idealised by four sublaminates of layered shells connected by three cohesive interfaces. This approximation limits the role of delamination damage to three interfaces, but keeps the model size within bounds.

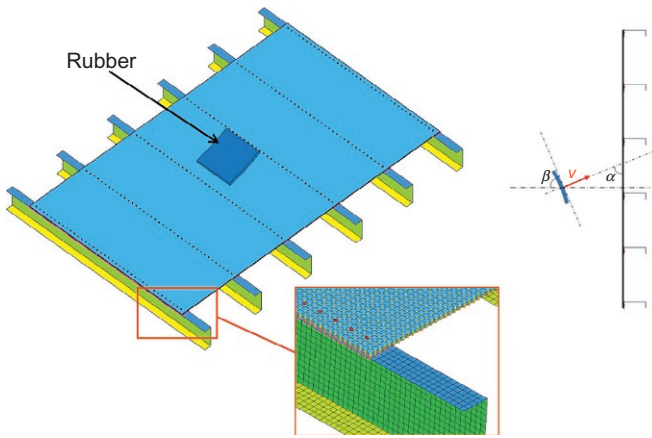

Figure 18.1 Overview of the FE model and orientation of the rubber fragment at impact.

Table 18.1 Description of the panel materials

	Panel 1 (thermoset resin)		Panel 2 (thermoplastic resin)	
	Skin	**C-frame**	**Skin**	**C-frame**
Material	G1157/RTM6	G1157/RTM6	C/PEEK	G1157/RTM6
thickness	6.03 mm (22 plies)	4.11 mm (15 plies)	6.16 mm (44 plies)	4.11 mm (15 plies)

The C-frames consisted of 15 plies giving 4.1 mm thickness and were modelled as single layered composite shells. The bonding of the C-frames to the skin was modelled by a cohesive interface, to allow possible debonding. The riveted fasteners are modelled using mesh-independent link elements, with all degrees of freedom are tied, which fail at given tensile and shear loads. The final structure model consists of 130,450 shells with a typical element edge length of 8 mm. In the PAM-CRASH^{TM} stacked shell model, the cohesive interfaces are contact constraints between adjacent shells and do not influence the time step, which is governed by shell element size. For the large panel structure modelled here, mesh refinement studies with 5-mm shell elements did not lead to significant changes in damage behaviour, so that 8-mm elements were used for the main study. Materials parameters for the meso-scale ply models were obtained from an extensive test programme on both materials systems carried out in ALCAS (2009), including monotonic and cyclic tests in tension and compression for determining ply damage parameters and fracture toughness tests for delamination failure energies G_{IC} and G_{IIC}.

The tyre rubber projectile represents tyre tread, without fibre reinforcements, and was ca. $210 \times 210 \times 16.5$ mm in size, with slight curvature and mass 0.85 kg. Rubber may be modelled using a hyperelastic Mooney–Rivlin material model, as discussed in Boyce and Arruda (2000), Karagiozova and Mines (2007). A large strain tensile test programme was carried out at the DLR to determine the Mooney–Rivlin parameters of aircraft tyre rubber and the model was verified for tensile strains up to about 50%. The rubber projectile was modelled by solid elements, with mesh size ca. 2.7 mm, giving 35,500 elements.

Typical numerical predictions of damage are shown in Figures 18.2 and 18.3 for both RTM and PEEK structures for the case of tyre rubber fragment with orientation angles defined in Figure 18.1, $\alpha = \beta = 70°$. The angle α determines the impact angle to the panel face, while β controls the orientation of the projectile to the flight direction. The impact point is chosen midway between two C-frames which is considered to be the worst case for impact damage in this structure. With such deformable projectiles, skin penetration is not usually important and simulations show that the rubber

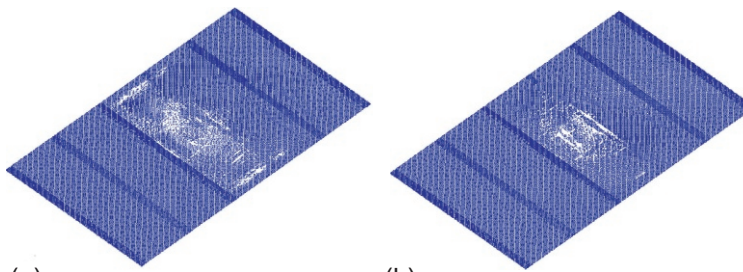

Figure 18.2 Predicted delamination areas in the (a) thermoset and (b) thermoplastic panels after a rubber impact with 0.85 kg at 93 m/s and $\alpha = \beta = 70°$ (white areas mean full delamination).

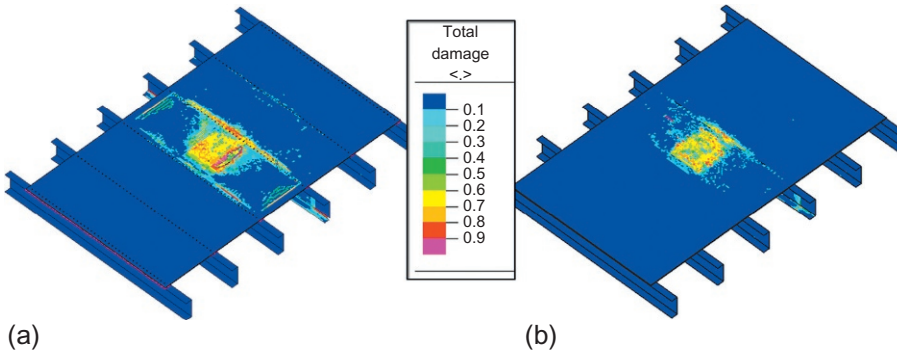

Figure 18.3 Predicted total damage in the (a) thermoset and (b) thermoplastic panels after a rubber impact with 0.85 kg at 93 m/s and $\alpha = \beta = 70°$ (0: no damage, 1: full damage).

projectile rebounds causing ply damage without fracture in the contact zone and delamination damage over a wider region due to wave effects.

Figure 18.2a and b shows delamination damage at the upper cohesive interface for the RTM and PEEK panels, respectively. The white regions represent delamination failures which extend to the bay panel between frames. The extent of the delaminated areas is larger in the thermoset panel compared to the thermoplastic panel. The failure of the adhesive bond between the C-frame ahead of the impact point and the skin is also predicted, whereas the fasteners do not fail and keep the C-frame attached to the skin. In addition, delamination areas are observed at the clamped edges due to wave propagation in the thermoset panel, which is not the case for the thermoplastic structure. Concerning the ply damage, Figure 18.3a and b shows ply damage contours on the upper face of the two panels. Ply damage propagates beyond the impact point to the adjacent C-frame interfaces. Damage is more widespread in the thermoset panels, in which local failures are predicted, confirming the well-known brittle behaviour of thermoset compared to the thermoplastic structures. Tyre rubber impact tests on the panels were carried out within ALCAS (2009) and the simulation results here are in good qualitative agreement with damage observed for similar impact test conditions on the two prototype structures.

More detailed results of parameter studies with this model, in which the impact angles are varied can be found in Toso-Pentecôte et al. (2009), and a study of tyre rubber impact on a composite wing lower cover is given in Johnson et al. (2009).

The FE simulations shown here demonstrate the use of the dynamic FE code PAM-CRASH™ with composite ply damage models and cohesive interfaces for simulating damage in large composite structures under HVI. It showed that the rubber projectile rebounds and causes local ply damage and delamination or stiffener debonding, which may be away from the impact position due to wave effects. Nevertheless, full separation of the frames near the impact position is not observed as the frames are also riveted. In the simulation studies, the impact kinetic energies were high 3.7 kJ. However, for rubber projectiles a large part of this impact energy is stored as elastic strain energy in the rubber due to the large deformations, which reduces damage in the composite structures. The work emphasises the importance of efficient delamination

models for soft body impact damage in composite structures and demonstrates the application of FE codes as a design tool for prediction of impact damage in composite structures.

18.4 DT of pre-stressed composite panels under impact loads

This section extends the discussion of composite structures under impact to consider the residual strengths of impact-damaged composite structures to establish their DT to impact loads. This is a major requirement imposed by the safety authorities for certification of primary composite structures in transport aircraft. Experimental results are first presented in Section 18.4.1 from a test programme to study the influence of tensile and compressive pre-stress on HVI damage in composite plate structures and the residual strengths after impact. This is followed in Section 18.4.2 by the extension of the FE modelling procedures to predict damage in pre-stressed panels under impact and compute residual strengths of impact-damaged panels to establish their DT.

18.4.1 Impact tests on pre-stressed panels

There have been a number of experimental studies on the influence of pre-load on impact response of composite plates and structural elements. Tension pre-loaded plates under low-velocity, low-energy 10 J impacts had no significant influence of pre-load (Whittingham et al., 2004), but tensile pre-loads on larger plates subjected to high-energy 350 J impacts (Pickett et al., 2009) showed that failure modes were influenced by the pre-load. Under compression pre-loads on larger panels, it was found for low-velocity drop tower impact tests (Heimbs et al., 2009) and higher-velocity gas gun impacts (Zhang et al., 1999) that pre-loads causing panel buckling had a significant influence on impact damage. Irving et al. (2004) carried out synthetic bird impact tests at 80 m/s on a composite spar structure pre-loaded in bending which showed that pre-loads led to reduced visible impact damage, but reductions in beam residual strength after impact. This previous work shows interaction effects between pre-load and impact damage, but is often based on low velocity drop tower impact tests relevant to BVID damage, rather than Categories 3 and 4 discrete source impact damage from bird strike, metal fragments, etc. This led to an experimental DT study for EASA on the 'Significance of Load upon Impact Behaviour of Composite Structure' (LIBCOS), as reported in Toso-Pentecôte and Johnson (2011), which is briefly summarised here. Gas gun impact tests were carried out on composite plates, representative of an idealised fuselage bay or wing panel and pre-loaded in either tension or compression at strain levels typical of aircraft DLL. Two impact scenarios were considered: notch damage from 12-mm steel cube projectiles, and blunt impact damage from Ø25-mm glass balls. The influence of pre-loads and impact damage on panel residual strengths and DT were studied.

The UD carbon/epoxy prepreg Cycom 977-2-35-12KHTS-134-300, a typical industry-standard composite material from civil transport aircraft, was used to manufacture the composite panels. Two generic laminate layups were selected: Lam. A, a

17-ply lay-up with nominal thickness 2.125 mm for the tension-loaded panels; Lam. B a 25-ply lay-up with thickness 3.125 mm for the compression-loaded panels, see Johnson et al. (2014) for more information on laminate layup and design of test specimens. For the impact test programme, plate geometry of 750 mm × 200 mm was selected as standard. A portable hydraulic pre-stressing test fixture was developed at the DLR which can apply uniaxial compression or tensile loads up to 1000 kN on plate specimens situated in the target chamber for impact tests with the 60-mm gas gun. The composite test plates have aluminium end tabs 200 × 125 × 20 mm in size for clamping in the fixture and for load introduction. The long sides are supported by two pairs of rails built into the loading frame with knife edge contact at the plate edges. The supports are 15 mm inside the plate edges and with the tab lengths of 125 mm, it follows that test plates in the fixture have an effective size 500 × 170 mm for transverse impact loading.

Axial tensile pre-loads are applied to the test plates up to 0.25% strain, monitored by two pairs of back-to-back strain gauges attached to the plates. For compression pre-loads in these thin composite plates buckling takes place below 0.25% compression strain. Quasi-static tests on undamaged plates were used to define a compression buckling load Pb for composite plates with the same end clamping conditions and lateral rail supports. Maximum compression pre-loads in the post-buckle range of 1.4 Pb were applied for the composite plates tested. Impact conditions were selected to provide plate penetration from a 12 mm steel cubes, referred to as 'notch damage', and rebound with delamination damage from Ø25-mm glass balls, referred to as 'blunt impact'. Depending on the impact load scenario impact velocities normal to the plate were in the range 64–136 m/s. After each impact test, panels were inspected for visible damage and by lock-in thermography for delamination. The damaged plate specimens were subsequently loaded through the tabs to ultimate failure in tension or compression, as appropriate, to determine residual strengths. For the tensile tests, the long sides of the plate were free, whilst in the compression tests the long sides were supported in the rails used for compression pre-loading, so that plate boundary conditions are the same for the HVI tests and the residual strength tests. A table summarising all tests, with impact conditions, pre-loads and measured residual strengths is provided in Johnson et al. (2014). To make a rapid assessment of the effect of impact damage and pre-loads on panel residual strengths and DT, a *residual strength factor (RSF)* was defined as:

RSF = failure load in damaged plate/failure load in baseline (undamaged) plate.

18.4.1.1 Impact damage with tension pre-loads

Notch damage tests on stress-free panels and those pre-loaded up to 0.25% strain had impact velocities in the range 93.4–103.7 m/s, with kinetic energies 58.4–71.2 J. Figure 18.4a shows typical impact damage and final tensile failure mode from a notch impact test without pre-strain, and Figure 18.5a showing comparative damage on a panel with 0.25% tensile pre-strain, at a similar impact velocity. In both cases, the steel cube projectile passed through the plate with a small entry hole, and extensive fibre splitting at the back face. In the residual strength tests, the impacted plates exhibited

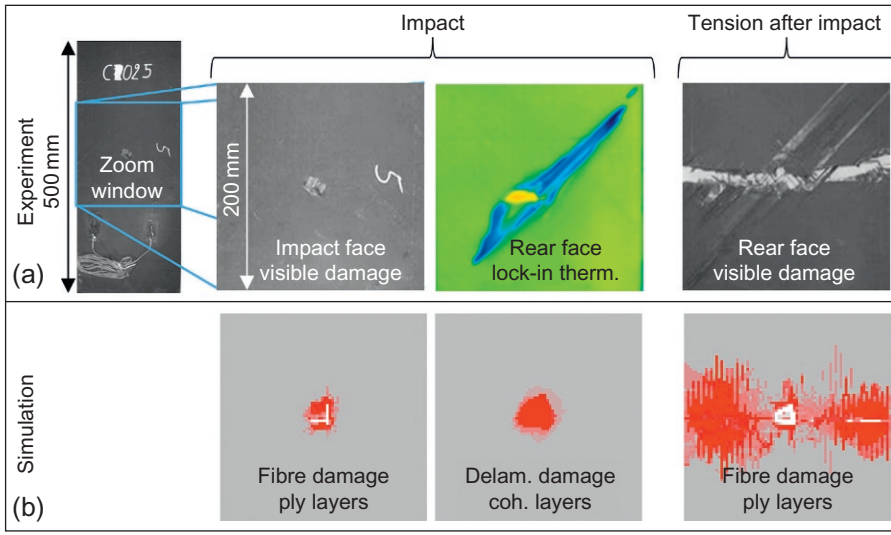

Figure 18.4 Notch impact test on plate without pre-load ($v = 100.6$ m/s, $E = 67.8$ J) and residual strength test. (a) Observed impact damage and tensile failure mode; (b) FE simulation of damage and failure.

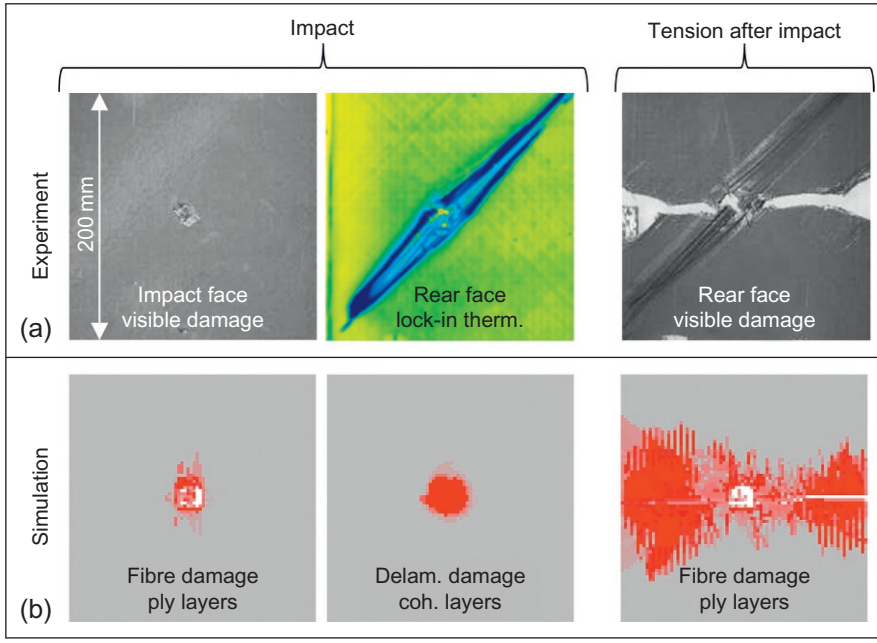

Figure 18.5 Notch impact test on plate with 0.25% pre-strain ($v = 97.8$ m/s, $E = 64.1$ J) and residual strength test. (a) Observed impact damage and tensile failure mode; (b) FE simulation of damage and failure.

almost linear behaviour up to brittle fracture from large transverse crack initiated from the central notch. The pre-strained plates generally showed more extensive rear face damage than the stress-free plates, with small reductions in residual strengths. The notch damage is severe and led to failure loads equal to about half the baseline strengths, with RSF factors in the range 0.48–0.61. The blunt impact tests with the glass balls had impact velocities in the range 63.8–69.7 m/s, with kinetic energies 36.6–51.0 J, see Johnson et al. (2014) for more information. The blunt projectiles rebounded from the plates showing a small round contact mark on the impact face, with delamination and more extensive damage near the back face. In the residual strength tests, final failure surfaces were brittle with extensive fibre and ply pull-out over the complete plate width. The delamination damage caused reduction in tensile failure loads, with RSF factors in the range 0.63–0.76 which are above values seen in notch damage tests.

DT for aerospace composites is defined as the capability of the composite structure to sustain an impact event and retain appropriate residual strength. Studies by Soutis and Curtis (1996) on small impacted test specimens showed that the residual strength is critically dependant on impact damage, which is characterised most simply by the impact energy. For the 2.1-mm composites plates under tensile loads tested here, the residual strength data from both blunt and notch impacts with and without tensile pre-loads are plotted against impact energy on a single graph, Figure 18.6. Multiple plate tests were carried out for each load scenario, so that the figure indicates the scatter found in residual strength measurements on the impact-damaged plates. For composite fuselage bay panels typical values for DLL, expressed as an equivalent strain are DLL = 0.25% strain, with DUL = 0.4% strain, which are marked on the figure as representative values based on the test plate properties. For the notch impact tests with energies above 60 J, there is penetration and residual strengths are fairly constant with RSF ~0.5, and are

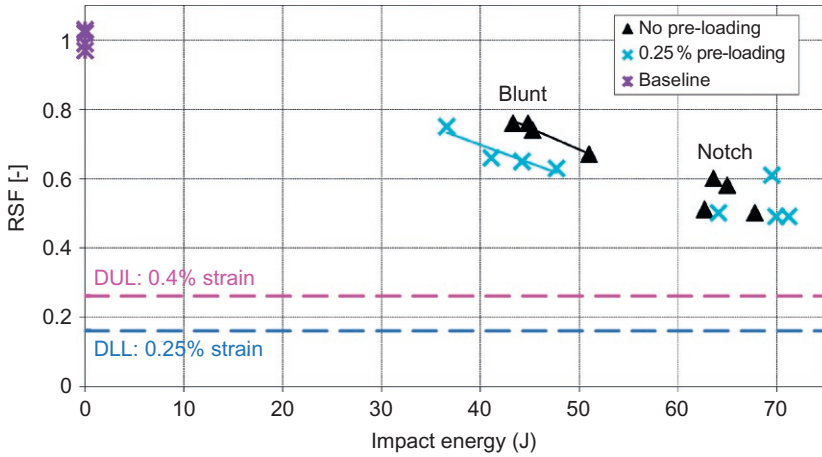

Figure 18.6 Residual tensile strength–impact energy curve for 2.1-mm composite plates (Toso-Pentecôte and Johnson, 2011).

expected to remain at this value at higher impact velocities with the same size projectiles. The blunt impact data are at energy levels below 60 J in the BVID region, where they are sensitive to small increases in impact energy and are reduced by tensile pre-loads, but with RSF values above 0.6. It is concluded that for the composite plates tested there are significant reductions in residual strengths for both blunt and notch impacts, which may be reduced further by tensile pre-loads. However, this is not significant for DT in typical aircraft panels under small object impacts (FOD) studied here, since residual strengths of damaged panels remain well above DUL.

18.4.1.2 Impact damage with compression pre-loads

Compressive strengths were measured from Q/S baseline tests on four undamaged plates, with mean value 125.8 kN. The onset of buckling was observed close to 38 kN, showing a three-cell buckle mode with three cells along the length including a larger central buckle. Brittle failure was initiated at the long plate edges at positions between the central and outer buckles. The notch damage tests impact velocities were in the range of 126.6–136.4 m/s, with impactor kinetic energies of 107.4–124.7 J and impacts targeted on the convex face of the buckled plate. There was visible damage where the steel cube passed through the plate, with extensive damage and delamination at the back face, which shows up clearly in the lock-in thermography images, see Johnson et al. (2014). In the subsequent Q/S compression tests after impact the plates with notch damage had the same initial stiffness and buckled at about the same point as the baseline plates, with the final collapse load not significantly reduced by notch damage. The RSF values of all plates were in the range of 0.89–1.02 showing that the notch damage which caused visible damage to the plates does not influence significantly the buckling failure strength of the plates. In the blunt impact tests with Ø25 mm glass balls velocities were 77.6–85.7 m/s, with kinetic energies of 58.4–70.9 J. Impact tests on the compression-loaded plates with pre-load 1.4 Pb were performed with impacts targeted on the convex (CV) or concave (CC) face of the central buckle. Figure 18.7a shows impact damage observed in blunt impact tests with pre-load 1.4 Pb, for impacts on the convex face (left side) and concave face (right side). There is little or no visible damage on the front face, with some light splitting of the rear 45° plies and extensive delamination damage on the back face. The figure shows that the concave impact test plates had more visible back face damage with smaller delamination area than the convex impact test plates. In residual strength tests, these plates fail earlier than compression tests with notch damage, with a wide range of RSF values from 0.64–0.92, indicating a more significant residual strength reduction and a wider range of behaviour for blunt impact. The delamination damage initiated buckling at lower loads around 20 kN compared with 38 kN in the baseline tests. A detailed analysis of the RSF values showed a significant reduction in residual strength with compression pre-load in the post-buckle region, which was more severe for impacts on the convex face.

Figure 18.8 shows the compilation plot of the residual compression strength data plotted against impact energy for the 3.1-mm composites plates, from both blunt and notch impacts with and without compression pre-loads up to 1.4Pb. In this case, DLL was nominally chosen to be 1.4 Pb for the 3.1-mm thick composite panels, hence

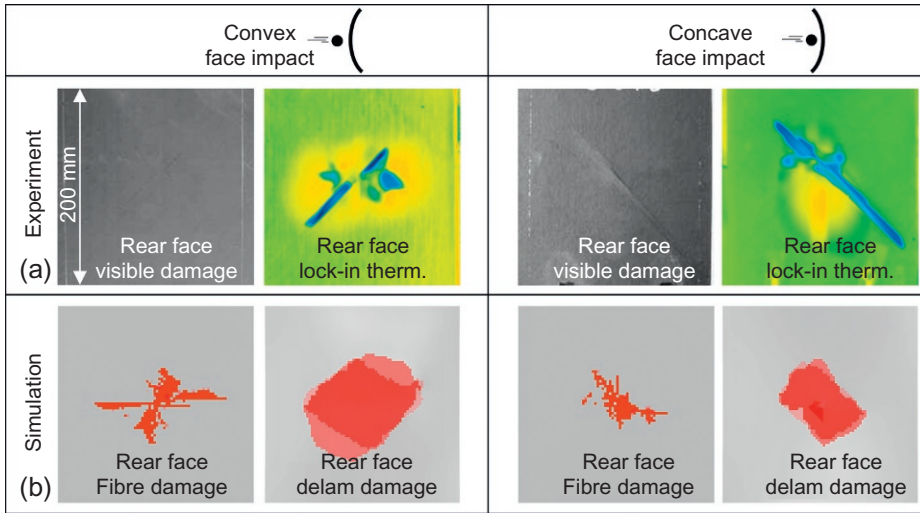

Figure 18.7 Blunt impact test on plates with compression pre-loads 1.4 Pb with impact on convex face (left, $v = 82.2$ m/s, $E = 65.2$ J) and concave face (right, $v = 82.4$ m/s, $E = 60.8$ J): (a) Observed impact damage; (b) FE simulation of damage.

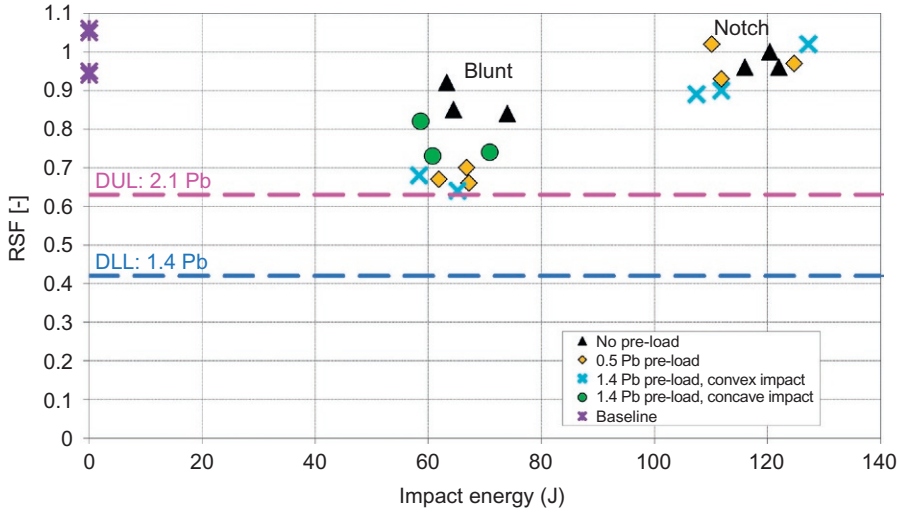

Figure 18.8 Residual compression strength–impact energy curve for 3.1-mm composite plates (Toso-Pentecôte and Johnson, 2011).

DUL = 2.1 Pb, which are marked on the figure. It is estimated that the critical impact energy for fracture and penetration of these 3.1-mm composite panels from these small projectiles is $E_F \sim 90$ J. For the notch impact tests with energies above 100 J, there is penetration and the residual strength is in the range 0.9–1.1, showing that notch damage with high-compression pre-loads has no significant influence on residual compression buckling strength of the panels. The blunt impact data are at energy levels below 80 J and the projectiles rebound causing extensive delamination damage in the plates. In the residual compression strength tests, the delaminations grow with RSF values in the range 0.62–0.9. The scatter in RSF values for blunt impact is influenced partly by impact energy, but it is more strongly dependent on the buckled state at impact, being lower for impact on the convex face of the buckled plate. The influence on DT is seen in the figure where the blunt impact RSF data with compression pre-loads are lower than the unloaded values and are reduced to DUL for pre-loads of 1.4 Pb. Because these blunt impacts may be in the BVID category, they have reached the allowable damage limit FAA AC20-107B where the RSF should not fall below DUL. This appears therefore to be a critical load case for DT. By contrast the notch damage RSF data are close to unity, and well above DUL even for the high-compression pre-load ratio, indicating excellent DT under small object FOD.

18.4.2 FE modelling of DT in pre-stressed panels after impact

DT compliance after impact has to show that the damaged structure retains its residual strength under flight loads, which should be above DUL or DLL depending on the impact damage category. To reduce the dependence on expensive test programmes, such as the LIBCOS tests discussed here, FE simulation methods are required which can perform the coupled analysis of impact damage simulations, followed by the quasi-static loading of the damaged structure to ultimate failure. Progress made will be demonstrated in this section using the composite damage models discussed in Section 18.2 and implemented into the Abaqus implicit and explicit codes. Validation studies will use impact test data presented in Section 18.4.1 on composite panel structures subjected to notch or blunt impact damage from HVI tests, before being loaded to ultimate failure to determine residual strengths.

18.4.2.1 FE simulation of impact damage in pre-stressed plates

There have been a number of numerical studies to investigate the influence of static pre-loads on the impact behaviour of composite plates, see for example Pickett et al. (2009) for LVI and Heimbs et al. (2014) for HVI. In this work, the methodology to simulate impact on pre-loaded plates developed in Schueler et al. (2013), Heimbs et al. (2014) and Schueler (2015) is adopted. The pre-loaded material state is simulated using the implicit solver. Compressive pre-loads in the post-buckling regime are treated in a Riks analysis (Riks, 1979), whereas for tensile pre-loads the standard implicit scheme is applied. The pre-loaded material state is then transferred into Abaqus/Explicit to carry out the transient impact simulation.

The flat composite plates with free test length of 500 mm and width of 200 mm were modelled using a stack of five continuum shell element layers with four cohesive interfaces. In a preliminary study, this through-thickness discretisation was found suitable for capturing the main delaminations observed in the impacted plates. For shell and cohesive elements, an in-plane edge length of 2.5 mm was selected with a regular mesh throughout the plate. For the cohesive elements, a thickness of zero was specified to avoid an artificial increase in the laminate thickness which could influence the bending stiffness. Note that in preliminary validation studies, the in-plane element length and the maximum tractions were adjusted such that the crack process zone (softening portion of the traction–separation law) extends over several elements in DCB and ENF simulations. The clamping at the short edges was modelled by fully constraining the boundary nodes, whereas the knife edge supports along the long edges were represented by rigid shell elements as supports. The impactors were modelled with eight-node solid elements, assigning linear elastic material behaviour for the steel cube causing notch damage and the glass ball representing blunt impact.

Figure 18.4b shows numerical results for notch impact without pre-load and subsequent tensile ultimate failure, for comparison with observed damage states and final tensile failure mode in Figure 18.4a. In the test perforation occurred leading to notch damage with a hole about the size of the 12-mm steel cube projectile at the front face and more severe damage at the rear face with splits and the separation of fibre bundles in the 45° surface ply. No significant delamination cracks propagated beyond the boundaries of the visible damage. In the simulation, the laminate is perforated leading to extensive local fibre damage in the shell element layers and delamination damage in the cohesive elements at the contact zone. The extensive damage propagating along the rear face 45° ply fibres is not captured in the simulation, since in the model the surface ply is one of three plies in a multi-layered shell element and therefore cannot split off.

Steel cube impact on plates pre-loaded with 0.25% tension pre-strains gave similar results with the same damage mechanisms present as in the stress-free plate, see Figure 18.5b. The detailed numerical results with tensile pre-loads differ slightly: the local fibre damage in the plies is not more extensive than without pre-load, but more severe in the contact zone with more failed elements eliminated leaving a clear-cut hole. Without pre-load, the hole partially closes after perforation due to elastic spring back. Related to this the extent of delaminations is smaller with tensile pre-loads. Due to the stress stiffening effect of the in-plane tensile load, the out-of-plane plate response is stiffer leading to increased ply failure rather than delamination damage due to bending. The simulation of the subsequent tensile tests on the damaged plates for determination of residual strengths after impact are discussed in the next subsection.

Figure 18.7b shows impact simulations carried out on the plates with 1.4Pb compression pre-loads and impacted by blunt glass ball projectiles on either the convex or concave face. Here it is seen that the damage mechanisms are quite different to those seen in the tension-loaded plates. At an impact speed of 82 m/s, the impactor rebounds for both convex and concave face impact. In both cases, a small dent is visible at the front with some splits in the 45° rear surface ply. Phase images from lock-in

thermography reveal extensive internal delamination damage that is significantly larger in size for convex than for concave face impacts. This is well captured by the model that predicts larger delamination areas for the convex face impacts compared with the concave impacts. From the simulations, it can be concluded that the more severe damage for convex face impact results from the large deformations and shock waves that occur when the convex buckle is forced into a concave shape by the impactor at contact. This then leads to an increased delamination damage area which in subsequent Q/S compression tests causes the lower residual compression strengths in the convex plate impacts noted in the test data.

18.4.2.2 FE simulation of plate residual strengths after impact

The prediction of ultimate failure behaviour in plates after impact without pre-loads has been investigated analytically and numerically, see the review by Wang et al. (2010) which also includes FE results for plates loaded in tension after LVI. Davies et al. (2004) and González et al. (2012) performed FE simulations for compression after impact test specimens, which is a widely used test procedure to assess DT of composite structures (ASTM D7136, 2007). In this subsection, the residual tensile strength reduction due to notch impact damage is investigated numerically. To simulate quasi-static post-impact failure, the numerical methodology is extended by an additional step in which Abaqus/Explicit is used to introduce the quasi-static loads up to tensile failure. A loading rate of 1 m/s is chosen such that the kinetic energy is small compared to the internal energy and inertia effects may be neglected. Figures 18.9 and 18.10 show predicted tensile load-deflection curves to ultimate

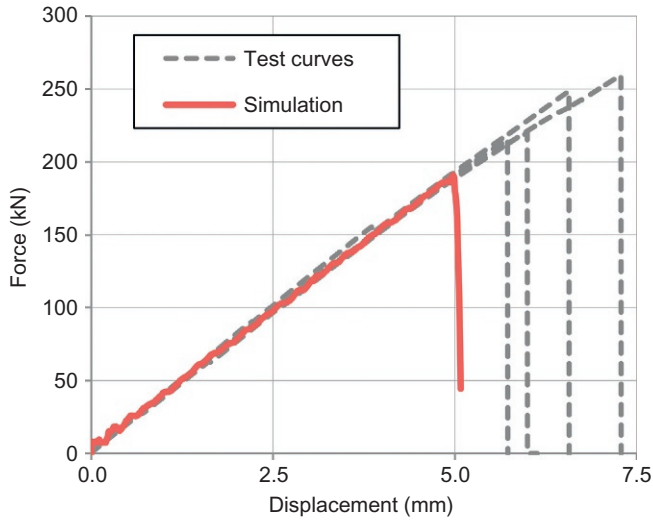

Figure 18.9 FE simulation of Q/S plate residual tensile strength test after notch impact without pre-load ($v = 100.6$ m/s, $E = 67.8$ J) and comparison with measured curves.

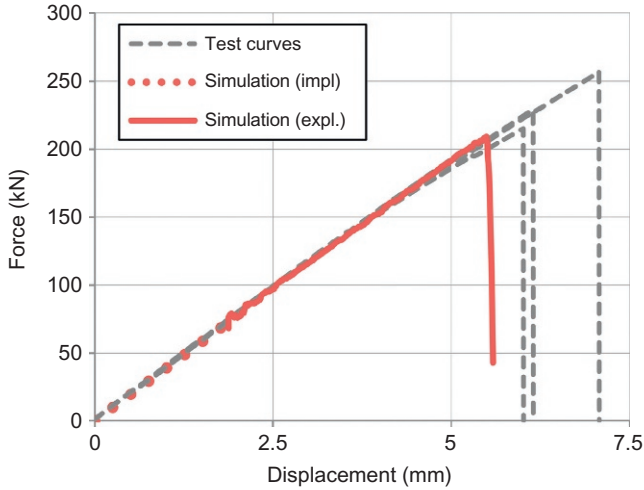

Figure 18.10 FE simulation of Q/S plate residual tensile strength test after notch impact with 0.25% pre-strain ($v = 97.8$ m/s, $E = 64.1$ J) and comparison with measured curves.

failure on plates with notch impact damage with and without tensile pre-loads. Dashed lines represent measured curves from several repeat tests in the LIBCOS programme revealing scatter in the failure displacement and failure loads for each load case; see Toso-Pentecôte and Johnson (2011). The figures show that the simulated load-deflection curves follow the test curves closely, but fail at lower loads than the tests. For notch impact without pre-load the predicted residual tensile strength is 19% lower, and for impact with 0.25% tension pre-strain it is 8% lower than the mean measured failure strengths. Prediction of the tensile failure mode is good, as seen in the right-hand column in Figures 18.4 and 18.5. Both test and simulation reveal a transverse crack in the plate centre initiating from the notch damage, which is well captured in the simulated fibre damage.

The influence of pre-load on the residual strength in the numerical results is controlled by two mechanisms. For impact with tensile pre-load, a larger clear-cut notch is obtained causing a load re-distribution in subsequent tensile loading. Impact without pre-load leads to the elimination of fewer elements in the impact zone, giving a smaller 'sharper' notch which initiates earlier failure under quasi-static loads. Second, there is larger delamination area for impact without pre-load which grows with load constraining the re-distribution of loads around the notch, increasing total damage area which causes earlier failure and reduced residual strength. The difference in residual strengths between the two cases indicates that the post-impact quasi-static response is highly sensitive to small changes in the impact damage state. It is suspected that this is the reason for the model being conservative. With an element edge length of 2.5 mm and an edge length of 12 mm for the cube projectile, the notch size cannot be captured exactly and is rather over-predicted, which leads to lower residual strength values compared to the test. A high sensitivity of residual strength to small

changes in the impact damage can also be concluded from the scatter observed in the repeated experimental tests.

Simulation of residual compressive strength of plates with blunt impact damage is ongoing research and not considered further here. Delamination damage in the plates caused by impact influences the post-impact buckling behaviour then continues to grow slowly during further compressive loading which may change the buckling modes in the damaged plate. Thus residual compression strength modelling is more complex than determination of damaged plate tensile strengths and a challenge for the damage mechanics models under development.

18.5 Conclusions and outlook

The chapter has discussed the numerical methods used for predicting impact damage in advanced composite structures to support design and certification of composite aircraft structures. A key element is the development of reliable composites damage models for implementation in commercial FE codes, which are then validated at test specimen and substructure level within the aircraft industry certification test pyramid. DLR experience on modelling damage progression and failure in composite structures under impact was reviewed based on meso-scale composites ply damage models and an energy-based delamination failure criteria in explicit FE codes. Along with other industry and research partners, these damage models have been implemented in the commercial FE codes PAM-CRASH^{TM} and Abaqus/Standard and Abaqus/Explicit. The chapter reviews progress made in predicting impact damage and DT of stiffened composite aircraft panels subjected to hard and soft body impacts. For deformable impactors such as ice, birds, tyre rubber, etc., valid models are required for projectile materials under impact. In a design case study, FE models for large deformations in rubber were successfully applied to simulate HVI damage from tyre rubber fragments impacting carbon/epoxy aircraft panels stiffened with C-frames. The work emphasises the importance of efficient delamination models for soft body impact damage in composite structures. Full solid element models are not appropriate for predicting damage in large aircraft shell structures, and it was shown that reasonably good results could be obtained at significantly lower computer cost using stacked shell laminate models in PAM-CRASH^{TM} with cohesive interface elements.

The second part of the chapter considered the DT of composite aircraft structures under impact loads. This is a major requirement imposed by the safety authorities for certification of primary composite structures in transport aircraft. Here it is necessary to demonstrate that an impact-damaged structure has sufficient residual strength to sustain design loads during flight without failure. Results of a DLR test programme were summarised in which composite aircraft panels were subjected to FOD impacts from gas gun tests by steel cubes and blunt glass projectiles causing notch and delamination damage. These damaged plates were then tested under Q/S loads to determine residual tensile and compression strengths. The tests produced some unexpected results, showing that residual compression strengths were not much reduced for plates

with notch perforation damage, but were significantly lowered by delamination damage from blunt impacts. The impact damage states in tension and compression were simulated with the composites damage and delamination models implemented in the Abaqus FE code, showing good agreement with damage modes and extent of delamination and ply damage. The FE methodology was then extended to allow the impact-damaged plates to be loaded quasi-statically to predict damage growth and residual tensile strength at ultimate fracture. FE simulation of notch impact-damaged plates with and without tensile pre-loads gave promising results but underestimated the measured residual tensile strengths. Future work will consider blunt impact damage and compression strengths in buckled plates. These are challenging load scenarios for the FE codes and the composites damage models being developed here.

Important current and future activities are to develop improved dynamic test methods for composite materials, especially for damage propagation, dynamic failure behaviour and fracture toughness properties. High rate composites damage and failure models are required for implementation into FE codes for use in dynamically loaded composite structures. Discrete element methods and element splitting techniques require further development for modelling fragmentation and delamination damage observed in crash and impact failures in composite structures. To support certification by analysis for aircraft structures, improved multiscale computational strategies are required to predict impact damage in larger aircraft structures, which is often localised at impactor contact and at critical joints and boundaries. Efficient stochastic analysis methods are required for use with explicit FE codes since impact events are stochastic in nature. A certification strategy could use stochastic analysis with variation in the impact load conditions to determine failure envelopes for specific impact scenarios. This would allow DT compliance procedures to be based on critical failure modes, rather than considering multiple load cases in deterministic analyses.

18.6 Further reading

The chapter has focused on mesoscale ply damage and delamination models as a basis for prediction of impact damage composite structures under impact conditions relevant to transport aircraft structures. Space did not allow the review of alternative approaches for composites damage and impact behaviour. A good recent source on composites damage and failure is Robinson et al. (2012), which includes a chapter by Olsson (2012) on low- and medium-velocity impact. For more comprehensive information on impact in composites and sandwich structures see the books by Abrate (1998) and Abrate et al. (2013). DT of composites is reviewed in Sierakowski and Newaz (1995). Major sources of information in the field of impact in structures are *Int. J of Impact Engineering* and *Int. J of Crashworthiness*, with current research on composites damage modelling and impact behaviour well covered in the composites journals: *Composites Science and Technology*, *Composites Part A*, *Composite Structures*, *J of Composite Materials* and *Applied Composite Materials*.

Acknowledgements

Some of the work presented here was carried out and partly funded in the EU ALCAS and MAAXIMUS projects. The authors acknowledge the EC funding of the research activities and discussions with project partners. The impact tests on pre-stressed panels presented in Section 18.4.1 were funded by the European Aviation Safety Agency (EASA), and the authors wish to acknowledge EASA for permitting figures from the LIBCOS Final Report to be used in the chapter. Particular thanks go to Simon Waite of EASA for his guidance and constructive criticism of this work. The authors also wish to thank their DLR colleagues H. Kraft, A. Reiter and H. Abu El-Hija for assistance with mechanical testing and R. Aoki for NDT tests.

References

Abaqus, 2010. Abaqus Analysis User's Manual. Dassault Systèmes Simulia Corp, Providence, RI.

Abrate, S., 1998. Impact on Composite Structures. Cambridge University Press.

Abrate, S., Castanié, B., Rahapakse, Y.D.S. (Eds.), 2013. Dynamic Failure of Composite and Sandwich Structures. Springer, Dordrecht.

ALCAS, 2009. Advanced low cost aircraft structures. EU Research Project, FP6-516092.

Allix, O., Ladevèze, P., 1992. Interlaminar interface modelling for the prediction of delamination. Compos. Struct. 22 (4), 235–242.

Allix, O., Ladevèze, P., Corigliano, A., 1995. Damage analysis of interlaminar fracture specimens. Compos. Struct. 31 (1), 61–74.

Allix, O., Lévêque, D., Perret, L., 1998. Identification and forecast of delamination in composite laminates by an interlaminar interface model. Compos. Sci. Technol. 58 (5), 671–678.

ASTM D7136, 2007. Standard Test Method for Measuring the Damage Resistance of a Fiber-Reinforced Polymer Matrix Composite to a Drop-Weight Impact Event. ASTM International, West Conshohocken, PA.

Boyce, M.C., Arruda, E.M., 2000. Constitutive models of rubber elasticity: a review. Rubber Chem. Technol. 73, 504–523.

Cairns, D.S., 1992. Static and dynamic strain energy release rates in toughened thermosetting composite laminates. Technical report NASA-CR-196613, NASA.

Chadwick, A., Evans, R., Findlay, D., Rickett, B., Spriggs, J., 2001. Airport runway debris detection study report no: 72/01/R/146/U. Technical report, Roke Manor Research Limited.

Chang, F.-K., Chang, K.-Y., 1987. A progressive damage model for laminated composites containing stress concentrations. J. Compos. Mater. 21 (9), 834–855.

Cui, W., Wisnom, M.R., 1993. A combined stress-based and fracture-mechanics-based model for predicting delamination in composites. Composites 24 (6), 467–474.

Daniel, I.M., Werner, B.T., Fenner, J.S., 2011. Strain-rate-dependent failure criteria for composites. Compos. Sci. Technol. 71 (3), 357–364.

Davies, P., 2008. Review of standard procedures for delamination resistance testing. In: Sridharan, S. (Ed.), Delamination Behaviour of Composites. Woodhead, Cambridge, UK, pp. 65–81.

Davies, G.A.O., Olsson, R., 2004. Impact on composite structures. Aeronaut. J. 108 (1089).

Davies, G.A.O., Zhang, X., 1995. Impact damage prediction in carbon composite structures. Int. J. Impact Eng. 16 (1), 149–170.

Davies, G.A.O., Hitchings, D., Besant, T., Clarke, A., Morgan, C., 2004. Compression after impact strength of composite sandwich panels. Compos. Struct. 63 (1), 1–9.

DOT/FAA/AR-04/16, 2004. Uncontained Engine Debris Analysis Using the Uncontained Engine Debris Damage Assessment Model. Federal Aviation Administration. National Technical Information Service (NTIS), Springfield, Virginia 22161.

DOT/FAA/AR-99/49, 1999. Review of Damage Tolerance for Composite Sandwich Airframe Structures. Federal Aviation Administration. National Technical Information Service (NTIS), Springfield, Virginia 22161.

EASA CS 25. Certification specifications: large aeroplanes. European Aviation Safety Agency, www.easa.europa.eu.

FAA 14 CFR 25. Airworthiness standards: part 25 Transport category airplanes. Federal Aviation Administration, www.airweb.faa.gov.

FAA AC 23-13A, 2005. Fatigue, Fail-Safe, and Damage Tolerance Evaluation of Metallic Structure for Normal, Utility, Acrobatic, and Commuter Category Airplanes. Federal Aviation Administration, www.airweb.faa.gov.

FAA AC 20-107B, 2010. Advisory Circular on Composite Aircraft Structure. Federal Aviation Administration, www.airweb.faa.gov.

Field, P.R., Hand, W., Cappelluti, G., McMillan, A., Foreman, A., Stubbs, D., Willows, M., 2009. Hail Threat Standardisation. European Aviation Safety Agency, www.easa.europa.eu.

Garg, A.C., 1988. Delamination-a damage mode in composite structures. Eng. Fract. Mech. 29 (5), 557–584.

Gilat, A., Goldberg, R.K., Roberts, G.D., 2002. Experimental study of strain-rate-dependent behavior of carbon/epoxy composite. Compos. Sci. Technol. 62 (10–11), 1469–1476.

González, E.V., Maimí, P., Camanho, P.P., Turon, A., Mayugo, J.A., 2012. Simulation of drop-weight impact and compression after impact tests on composite laminates. Compos. Struct. 94 (11), 3364–3378.

Greve, L., Pickett, A.K., 2006. Delamination testing and modelling for composite crash simulation. Compos. Sci. Technol. 66 (6), 816–826.

Guynn, E.G., O'Brien, T.K., 1985. The influence of layup and thickness on composite impact damage and compression strength. In: Proceedings of 26th Structures, Structural Dynamics, Materials Conference, Orlando, FL, pp. 187–196.

Hachenberg, D., 2002. The role of advanced numerical methods in the design and certification of future composite aircraft structures. In: World Congress on Computational Mechanics, WCCM V, Vienna, July.

Hashin, Z., 1980. Failure criteria for unidirectional fiber composites. J. Appl. Mech. 47 (2), 329–334.

Heimbs, S., Heller, S., Middendorf, P., Hähnel, H., Weiße, J., 2009. Low velocity impact on CFRP plates with compressive preload: test and modelling. Int. J. Impact Eng. 36, 1182–1193.

Heimbs, S., Bergmann, T., Schueler, D., Toso-Pentecôte, N., 2014. High velocity impact on preloaded composite plates. Compos. Struct. 111, 158–168.

Ilcewicz, L., 2006. Composite damage tolerance and maintenance safety issues. In: FAA Composite Damage Tolerance and Maintenance Workshop.

Irving, P.E., et al., 2004. Effect of preload on bird strike damage in carbon fibre polymer composite beas. CAA report, Cranfield University, CU/WA9/W30814E/62.

Johnson, A.F., 2005. Modelling impact damage in composite structural elements. In: Beaumont, P., Soutis, C. (Eds.), Multiscale Modelling of Composite Materials and Systems. Woodhead, Cambridge, UK, pp. 401–429.

Johnson, A.F., Holzapfel, M., 2003. Modelling soft body impact on composite structures. Compos. Struct. 61, 103–113.

Johnson, A.F., Pickett, A.K., Rozycki, P., 2001. Computational methods for predicting impact damage in composite structures. Compos. Sci. Technol. 61, 2183–2192.

Johnson, A.F., Toso-Pentecôte, N., Schwinn, D., 2009. Modelling damage in composite aircraft panels under tyre rubber impact. In: 17th International Conference on Composite Materials ICCM17, Edinburgh.

Johnson, A.F., Toso-Pentecôte, N., Kilchert, S., 2013. Validation of damage modeling in composite fuselage structures under high velocity impact. CEAS Aeronaut. J. 4 (3), 253–264.

Johnson, A.F., Toso-Pentecôte, N., Schueler, D., 2014. Damage tolerance of pre-stressed composite panels under impact loads. Appl. Compos. Mater. 21, 123–147.

Karagiozova, D., Mines, R.A.W., 2007. Impact of aircraft rubber tyre fragments on aluminium alloy plates: II-Numerical simulation using LS-DYNA. Int. J. Impact Eng. 34 (4), 647–667.

Kermanides, T., Labeas, G., Sunaric, M., Johnson, A.F., Holzapfel, M., 2006. Bird strike simulation on a novel composite leading edge design. Int. J. Crashworthiness 11 (3), 189–201.

Kim, H., Kedward, K.T., 2000. Modeling hail ice impacts and predicting impact damage initiation in composite structures. AIAA J. 38 (7), 1278–1288.

Kindervater, C.M., Schwinn, D., Reiter, A., 2010. Bird strike qualification of the external stores of the new DLR research aircraft HALO. In: 47th ICAS Congress, Berlin.

Koerber, H., Camanho, P.P., 2011. High strain rate characterisation of unidirectional carbon-epoxy IM7-8552 in longitudinal compression. Compos. Part A 42, 462–470.

Koerber, H., Xavier, J., Camanho, P.P., 2010. High strain rate characterisation of unidirectional carbon-epoxy IM7-8552 in transverse compression and in-plane shear using digital image correlation. Mech. Mater. 42, 1004–1019.

Kusaka, T., Hojo, M., Mai, Y.-W., Kurokawa, T., Nojima, T., Ochiai, S., 1998. Rate dependence of mode 1 fracture behaviour in carbon-fibre/epoxy composite laminates. Compos. Sci. Technol. 58 (3–4), 591–602.

Ladevèze, P., Le Dantec, E., 1992. Damage modelling of the elementary ply for laminated composites. Compos. Sci. Technol. 43 (3), 257–267.

Liu, D., 1988. Impact-induced delamination – a view of bending stiffness mismatching. J. Compos. Mater. 22 (7), 674–692.

Liu, D., Malvern, L.E., 1987. Matrix cracking in impacted glass/epoxy plates. J. Compos. Mater. 21 (7), 594–609.

MAAXIMUS, 2013. More affordable aircraft through extended, integrated and mature numerical sizing. EU Research project FP7-213371.

Mines, R.A.W., McKeown, S., Birch, R.S., 2007. Impact of aircraft rubber tyre fragments on aluminium alloy plates: I – experimental. Int. J Impact Eng. 34 (4), 637–646.

Olsson, R., 2000. Mass criterion for wave controlled impact response of composite plates. Compos. A: Appl. Sci. Manuf. 31 (8), 879–887.

Olsson, R., 2012. Low- and medium-velocity impact as a cause of failure in polymer matrix composites. In: Robinson, P. (Ed.), Failure Mechanisms in Polymer Matrix Composites. Woodhead, Cambridge, UK, pp. 53–78.

PAM-CRASH^{TM} FE Code, Engineering Systems International, F-94513 Rungis Cedex, France.

Pickett, A.K., Fouinneteau, M.R.C., 2006. Material characterisation and calibration of a meso-mechanical damage model for braid reinforced composites. Compos. Part A 37, 368–377.

Pickett, A.K., Fouinneteau, M.R.C., Middendorf, P., 2009. Test and modelling of impact on preloaded composite panels. Appl. Comp. Mat. 16, 225–244.

Puck, A., Schürmann, H., 1998. Failure analysis of FRP laminates by means of physically based phenomenological models. Compos. Sci. Technol. 58 (7), 1045–1067.

Reeder, J.R., 1992. An evaluation of mixed-mode delamination failure criteria. Technical memorandum 104210, NASA.

Riks, E., 1979. An incremental approach to the solution of snapping and buckling problems. Int. J. Solids Struct. 15 (7), 529–551.

Robinson, P., Greenhalgh, E., Pinho, S. (Eds.), 2012. Failure Mechanisms in Polymer Matrix Composites. Woodhead, Cambridge, UK.

Schellekens, J.C.J., De Borst, R., 1994. Free edge delamination in carbon-epoxy laminates: a novel numerical/experimental approach. Compos. Struct. 28 (4), 357–373.

Schueler, D., 2015. High velocity impact on preloaded composite structures (PhD Dissertation), in process, University of Stuttgart.

Schueler, D., Toso-Pentecôte, N., 2012. MAAXIMUS D3.5.3 – Task 3.5.1 Implementation of advanced ply and interface damage models. DLR-IB 435-2012/21, 36S.

Schueler, D., Toso-Pentecôte, N., Voggenreiter, H., 2013. Impact on buckled composite panels. In: 17th International Conference on Composite Structures, 17–21 June 2013, Porto, Portugal.

Sierakowski, R.L., Newaz, G.M., 1995. Damage tolerance in advanced composites. Technomic, Lancaster, PA.

Soutis, C., Curtis, P.T., 1996. Prediction of post-impact compressive strength of CFRP laminated composites. Compos. Sci. Technol. 56, 677–684.

Takeda, N., Sierakowski, R.L., Malvern, L.E., 1981. Wave propagation experiments on ballistically impacted composite laminates. J. Compos. Mater. 15 (2), 157–174.

Takeda, N., Sierakowski, R.L., Ross, C.A., Malvern, L.E., 1982. Delamination-crack propagation in ballistically impacted glass/epoxy composite laminates. Exp. Mech. 22 (1), 19–25.

Toso-Pentecôte, N., Johnson, A.F., 2011. LIBCOS – significance of load upon impact behaviour of composite structure, EASA.2009.OP.24, Final report. European Aviation Safety Agency, Cologne, Germany, 08/11/2011.

Toso-Pentecôte, N., Johnson, A.F., Chabrier, G., 2009. Modelling and simulation of tyre impacts on stiffened composite panels, composites 2009. In: 2nd ECCOMAS Conf. on Mechanical Response of Composites, Imperial College, London.

Toso-Pentecôte, N., Schwinn, D., Johnson, A.F., 2010. Modelling and simulation of tyre impacts on stiffened composite panels. In: SEICO 2010. SAMPE Europe, Paris, France.

Tsai, J.L., Guo, C., Sun, C.T., 2001. Dynamic delamination fracture toughness in unidirectional polymeric composites. Compos. Sci. Technol. 61 (1), 87–94.

Tsai, S.W., Wu, E.M., 1971. A general theory of strength for anisotropic materials. J. Compos. Mater. 5 (1), 58–80.

Turon, A., Camanho, P.P., Costa, J., Dávila, C.G., 2006. A damage model for the simulation of delamination in advanced composites under variable-mode loading. Mech. Mater. 38 (11), 1072–1089.

Turon, A., Davila, C.G., Camanho, P.P., Costa, J., 2007. An engineering solution for mesh size effects in the simulation of delamination using cohesive zone models. Eng. Fract. Mech. 74 (10), 1665–1682.

Wang, S.X., Wu, L.Z., Ma, L., 2010. Low-velocity impact and residual tensile strength analysis to carbon fiber composite laminates. Mater. Des. 31 (1), 118–125.

Whittingham, B., Marshall, I.H., Mitrevski, T., Jones, R., 2004. The response of composite structures with pre-stress subject to low velocity impact damage. Compos. Struct. 66, 685–698.

Williams, J.G., Anderson, M.S., Rhodes, M.D., Starnes, J.H., Stroud, W.J., 1979. Recent developments in the design, testing and impact-damage tolerance of stiffened composite panels. Technical memorandum 80077, NASA.

Wu, E.M., Reuter Jr., R.C., 1965. Crack extension in fiberglass reinforced plastics, vol. 275. Illinois Univ. Dept. of Theoretical and Applied Mechanics.

Zhang, Z., Davies, G.A.O., Hitchings, D., 1999. Impact damage with compressive preload and post-impact compression of carbon composite plates. Int. J. Impact Eng. 22, 485–509.

Strength prediction methods for composite structures: Ensuring aeronautical design office requirements

19

F. Laurin[*], *N. Carrere*[†], *J.-F. Maire*[*]
*ONERA, Châtillon Cedex, France; †ENSTA Bretagne and Laboratoire Brestois de Mécanique et des Systèmes, Brest Cedex, France

19.1 Introduction

Because of their high specific properties, the use of fibre-reinforced polymer composites has increased over the past few years, for the design of primary structures, such as the centre wing box, the wings or the fuselage. Composite materials satisfy the need of aeronautical companies for lighter, safer and less polluting civil aircrafts. The recently developed multi-scale damage and failure approaches (Hinton et al., 2002; Kaddour and Hinton, 2013) permit us to predict accurately the final failure of current parts of composite structures (i.e. parts with a moderate stress gradient) subjected to complex multi-axial loadings. However, composite structures can be considerably weakened by the introduction of geometrical singularities (Sutherland et al., 1999a,b) such as holes, notches or cutouts. Consequently, the strength analysis of high-stress gradient parts of the structures still remains a key problem in the design of engineering structures.

From an academic point of view, many advanced strength analysis methods for perforated composite plates can be found in the literature. Some methods are based on (i) continuum damage modelling to predict the intralaminar damage (i.e. transverse cracks) and the fibre failures and (ii) cohesive zone modelling to predict interlaminar damage (i.e. delamination between the different plies) (Camanho et al., 2007; Abisset et al., 2011; Laurin et al., 2013; Martin-Santos et al., 2014; Pinho et al., 2013). Other methods use only cohesive zone elements to model the experimentally observed cracks (Hallett et al., 2008; Wisnom and Hallett, 2009; Achard et al., 2014) (both intra- and interlaminar damage) to establish/understand the damage and failure scenarios for complex configurations of perforation (Green et al., 2007) (different diameters of hole, different thicknesses of the plies, etc.). Furthermore, other authors explicitly mesh all the possible cracks (Violeau et al., 2009; Daghia and Ladeveze, 2012) and manage crack nucleation and propagation through linear fracture mechanics associated with advanced numerical strategies. As an alternative, some authors used extended finite element (FE) methods to model the damage and failure mechanisms (Jaśkowiec and van der Meer, 2014; Cahill et al., 2014; Ahmad et al., 2014), thus avoiding the mesh dependence problems. Although such methods can be found in some commercial FE codes (ABAQUS Inc., 2013), their applications to composite materials remain

Numerical modelling of failure in advanced composite materials. http://dx.doi.org/10.1016/B978-0-08-100332-9.00019-0
Copyright © 2015 Elsevier Ltd. All rights reserved.

recent and these complex approaches have to be evaluated on different industrial test cases before being introduced to the existing industrial standards. These recent damage and failure approaches, physically based, offer a fine description of the different damage and failure mechanisms observed in a laminated open-hole plate subjected to tensile loading and present interesting predictive capabilities. However, these advanced failure approaches are currently too complex to be used in a design office, and the associated computational times remain prohibitive to design aeronautical structures.

From an industrial point of view, some fast computational strength analysis methods, specific to the prediction of failure for perforated plates such as the point stress method (Whitney and Nuismer, 1974; Nuismer, 1976; Wang et al., 2004) or the average stress method (Nuismer and Labor, 1978, 1979), are widely used owing to their simplicity (easy to identify, implement and analyse) and because they could be used to predict failure for large aeronautical structures. However, the semi-empirical aspect of these current open-hole failure approaches requires fitting the allowables systematically against large test campaigns. Moreover, the use of these semi-empirical methods in design offices, available only for the already tested configurations, impedes breakthroughs in the design of composite structures and, for instance, the determination of the optimal stacking sequences for the different considered loading cases.

The aim of the present study is to propose alternative fast computational methods matching the different requirements of design offices, that is, a fast computational method easy to identify, to be used by stress engineers and available for a large number of configurations.

To accurately predict the final failure of composite structures, it is first necessary to predict the stress and strain within the different constitutive plies. The different sources of non-linearities usually observed in carbon/epoxy uni-directional (UD) plies will be summarised as well as the mesoscopic damageable non-linear behaviour. To predict the strength of open-hole plates subjected to tensile loading, two different fast computational methods are considered in this study. First, the fracture characteristic volume (FCV) method, based on the approach proposed by Hochard et al. (2007, 2009) on two-dimensional (2D) woven composites, is used in this study as an alternative to the point stress method. Second, a coupled-based criterion, based on the concept of finite fracture mechanics that was originally introduced by Leguillon (2002), is proposed and applied to the prediction of open-hole plate rupture due to fibre failure. Then, the predictive capabilities of these two strength analysis methods are evaluated through comparisons with many test cases representative of the aeronautical industries. Finally, we discuss the complementarity between these fast computational methods and the existing advanced damage and failure approaches and suggest some perspectives.

19.2 Presentation of the material progressive failure approach

The prediction of the non-linear mesoscopic behaviour up to the specimen failure is performed with the progressive failure approach proposed in Laurin et al. (2007) and briefly summarised in this section. The present multi-scale failure approach considers

the UD ply as the elementary entity of modelling and is predictive for different stacking sequences. The progressive failure approach is based on (i) the definition of the mesoscopic behaviour, (ii) the choice of a mesoscopic failure criterion and (iii) the degradation of the properties of the failed plies in the laminate.

First, to accurately predict the failure of a ply in a laminate, it is necessary to estimate correctly the mesoscopic stresses and strains. A non-linear thermo-viscoelastic behaviour is proposed in Equation (19.1).

$$\underline{\sigma} = \underline{\underline{\widetilde{C}}} : \left(\underline{\varepsilon} - \underline{\varepsilon}^{\text{th}} - \underline{\varepsilon}^{\text{nl}} - \underline{\varepsilon}^{\text{ve}}\right) \tag{19.1}$$

where $\underline{\sigma}$ is the mesoscopic stress, $\underline{\underline{\widetilde{C}}}$ is the effective rigidity, $\underline{\varepsilon}$ is the total strain and $\underline{\varepsilon}^{\text{th}}$ is the thermal strain (in order to take into account the thermal residual stresses, which are essential to predict accurately the first ply failure in a laminate). $\underline{\varepsilon}^{\text{nl}}$ is the non-linear elastic strain (Huchette, 2005) (in order to describe the hardening observed experimentally (Ishikawa et al., 1985) in UD plies subjected to longitudinal tensile loadings and especially in new generations of composite materials such as T700GC/M21 (Huchette, 2005) reported in Figure 19.1a). $\underline{\varepsilon}^{\text{ve}}$ is the viscoelastic strain (Laurin et al., 2007) (in order to consider the non-linearity observed in UD plies subjected to shear loading which is essential to accurately predict the behaviour and final failure of $[\pm 45°]_s$ laminates subjected to tensile loading as reported in Figure 19.1b, or of highly disoriented laminates containing many $\pm 45°$ plies also subjected to tensile loading).

Second, the prediction of the ply failure within the laminate is obtained using a failure criterion, based on Hashin's hypotheses (Hashin, 1980), distinguishing the fibre (Equation 19.2) and in-plane interfibre (Equation 19.3) failure modes and modelling separately the failure mechanisms in tension and in compression for each failure mode.

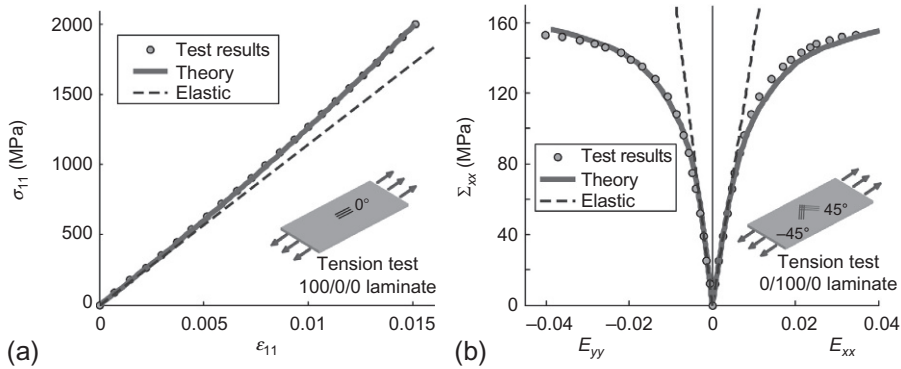

Figure 19.1 Comparison between predicted and measured (Huchette, 2005) macroscopic failure behaviour of T700GC/M21 (a) 100/0/0 and (b) 0/100/0 laminated unnotched specimens subjected to uni-axial tensile loading.

$$\begin{cases} f_1^+ = \left(\dfrac{\sigma_{11}}{X_t}\right)^2 = 1 & \text{if } \sigma_{11} \geq 0 \\ f_1^- = \left(\dfrac{\sigma_{11}}{X_c}\right)^2 + \left(\dfrac{\tau_{12}}{S_c^f(1-p\sigma_{22})}\right)^2 = 1 & \text{if } \sigma_{11} < 0 \end{cases} \tag{19.2}$$

$$\begin{cases} f_2^+ = \left(\dfrac{\sigma_{22}}{Y_t}\right)^2 + \left(\dfrac{\tau_{12}}{S_c(1-p\sigma_{22})}\right)^2 = 1 & \text{if } \sigma_{22} \geq 0 \\ f_2^- = \left(\dfrac{\sigma_{22}}{Y_c}\right)^2 + \left(\dfrac{\tau_{12}}{S_c(1-p\sigma_{22})}\right)^2 = 1 & \text{if } \sigma_{22} < 0 \end{cases} \tag{19.3}$$

where X_t and X_c are, respectively. the longitudinal tensile and compressive strengths, Y_t and Y_c are the transverse tensile and compressive strengths, S_c is the in-plane shear strength and S_c^f is the in-plane shear strength for fibre mode.

The two main improvements in the fibre failure criterion, as compared to Hashin's criterion, are (i) the introduction of coupling between the intralaminar damage and the longitudinal tensile strength (allowing to obtain conservative predictions for complex multi-axial loadings) and (ii) to take into account the influence of the in-plane shear on the ply failure in compression. The main improvement in the interfibre failure criterion is a better description of the reinforcement of the apparent strength of the material for combined in-plane shear and transverse compressive loadings (due to the introduction of the p parameter).

Third, when a ply within the laminate is broken in interfibre mode (i.e. when transverse cracks are present in the ply), its mechanical properties are progressively degraded using a thermodynamical degradation approach based on damage modelling already developed at Onera (Maire and Chaboche, 1997). The initial elastic compliance $\underline{\underline{S}}^0$ is increased (Equation 19.4) by the degradation of the ply failed in in-plane interfibre mode ($d_2\underline{\underline{H}}_2$). The kinetics of degradation (scalar variable noted d_2) is distinguished from the effects of the ply failure (effect tensor $\underline{\underline{H}}_2$).

$$\underline{\underline{\widetilde{S}}} = \underline{\underline{S}}^0 + d_2\underline{\underline{H}}_2 \quad \text{with} \quad d_2 = \beta\left\langle \sqrt{f_2^+} - 1 \right\rangle_+ \quad \text{and} \quad \dot{d}_2 \geq 0 \tag{19.4}$$

where β is a material coefficient correlated to the kinetics of degradation due to ply failure in interfibre mode. The effect tensor $\underline{\underline{H}}_2$ can be determined only through the knowledge of the elastic properties (Dvorak et al., 1985).

Finally, for a laminated unnotched coupon, the final rupture is assumed to be due to the first ply failure in fibre mode or in transverse compression. For the stacking sequences used in this study, containing only 0°, ±45° and 90° plies, the final failure is always due to ply failure in fibre mode. This multi-scale failure approach can be easily identified through the normalised tests currently performed in aeronautical industries (Laurin et al., 2007). To summarise, the identification tests are: (i) tensile and compressive tests on 0° plies (to identify the elastic moduli, Poisson's ratios and strengths in the longitudinal and transverse directions), a tensile test on a $[\pm 45°]_s$ laminate (to identify the in-plane shear modulus, viscosity and strength) and one test on a multi-layered laminate (to identify the kinetics of degradation of the mechanical properties due to a ply

failure in interfibre mode (material coefficient in Equation 19.4). The present approach has thus been identified using characterisation tests on the T700GC/M21 and IM7/8552 composite materials. The predicted macroscopic stress at failure on T700GC/M21 unnotched plates (Huchette, 2005) with different aeronautical stacking sequences (noted *X*/*Y*/*Z* with *X*% of 0° plies, *Y*% of ±45° plies and *Z*% of 90° plies) subjected to uni-axial tensile loading have been compared successfully with the available proprietary test results. (Note that only the normalised values of the experimental data are reported in Figure 19.2.) The tested laminates present a total thickness evolving, as a function of the stacking sequence, from 4.2 mm (16 plies) to 5.2 mm (20 plies).

Nevertheless, the definition of the final rupture of high-stress gradient parts of composite structures, and especially for open-hole plates, cannot be reduced to the first ply failure in fibre mode (which could lead one to underestimate the failure strength by a factor of two or three, mainly due to the stress gradient around the hole) or to the first failure of a multi-layered element (i.e. failure of a laminate) inside the structure. To predict accurately the final failure, it is necessary to take into account the sudden and huge degradation of the mechanical properties due to the fibre failure, as explained in Section 19.1. However, introducing the softening behaviour into the modelling and avoiding the mesh dependence increase drastically the complexity of modelling and the computational time. Consequently, it is necessary to re-define the final failure of such a structure. In aeronautical industries, the strength method most often used is dedicated to the prediction of failure of open-hole plates, namely the point stress method (Whitney and Nuismer, 1974; Nuismer, 1976; Wang et al., 2004). The point stress method consists of applying the failure criterion at a distance d_0 from the hole, which is outside the high-stress gradient area. However, it is well known that the semi-empirical aspect of the point stress method requires the critical distance to be fitted against large test campaigns on open-hole plates with different stacking sequences and different perforation diameters. Therefore, in the present study, two alternative strength analysis methods are proposed and described in the following sections.

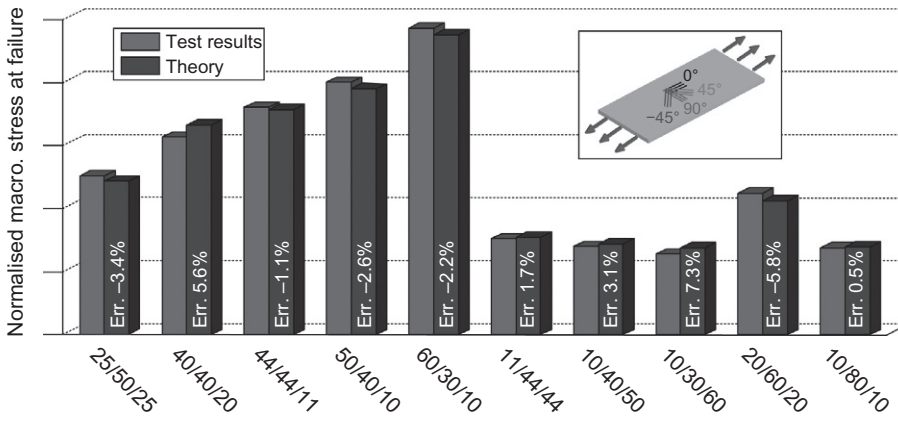

Figure 19.2 Comparison between predicted and measured macroscopic stress at failure for different T700GC/M21 laminated un-notched coupons subjected to uni-axial tensile loading.

19.3 FCV method

19.3.1 Principle of the FCV method

An FCV method, based on the approach proposed by Hochard et al. (2007, 2009) on 2D woven composites, is used in this study as an alternative to the point stress method to predict the strength of laminated open-hole plates. The FCV method assumes that the structure is considered broken when one of the two fibre failure criteria (f_1^+ or f_1^- expressed in Equation 19.2) is reached at one point in the specimen, these fibre failure criteria being however computed using the stress tensor averaged over a given volume Ω, as reported in Figure 19.3a. This characteristic volume is a cylinder defined by its radius l_0 and its height, which is equal to the thickness of the ply. This internal length l_0 is independent of the considered stacking sequence but should be defined as a function of the radius (r) of perforation as proposed in Whitney and Nuismer (1974) and written in Equation (19.5). Thus, only one tensile test on a perforated plate is required to identify the parameter ρ.

$$l_0 = \rho\sqrt{r} \tag{19.5}$$

Concerning the identification procedure, the internal length ρ is different for tensile or compressive loading on open-hole plates because the involved failure mechanisms are also different. It is recommended to identify the internal length ρ in tension on a 50/40/10 laminated perforated plate subjected to uni-axial tensile loading with a hole diameter equal to 6.35 mm and a w/d ratio equal to 5 because (i) this configuration of test is usually available in the characterisation test campaigns performed in aeronautical industries, (ii) the rupture of the open-hole specimen is clearly due to fibre failure and (iii) the scattering in the test results remains rather small. The internal length ρ in compression has to be identified using a uni-axial compression test on a 50/40/10 laminated perforated plate presenting the same configuration of perforation.

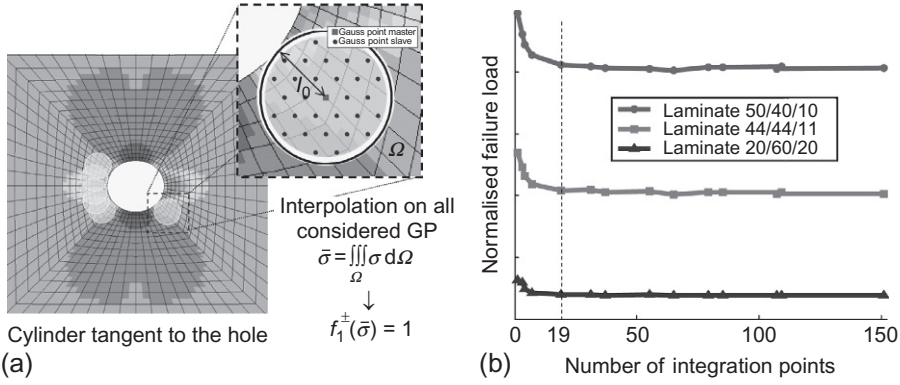

Figure 19.3 (a) Principle of the fracture characteristic volume (FCV) method and (b) influence of the number of integration points on the predicted failure loads for different laminates.

The computational strategy associated with the proposed alternative method for the strength analysis of perforated plates, which is detailed in Laurin et al. (2014), can be decomposed into three main steps: (i) the estimation of the membrane loadings within the perforated structures, which can be computed using the analytical method proposed by Tan (1994) for large specimens (with a plate width-to-hole diameter ratio superior to 3); otherwise, for narrow specimens, using elastic FE simulations performed with the commercial FE code Samcef© on shell elements, (ii) the determination, as a post-treatment, of the non-linear fracture behaviour of the different plies constituting the laminate using the progressive multi-scale failure approach presented in Section 19.2 and, finally, (iii) the prediction of the ultimate rupture of the composite structure using the FCV method. Moreover, to reduce the computational time, the failure criterion using the averaged stress tensor is computed only in the cylinders tangent to the hole where the stress gradient is the strongest, as illustrated in Figure 19.3a, instead of being calculated at each Gauss point. This strategy remains relevant for multi-perforated plates. Indeed, each perforation has to be considered separately and the rupture of the specimen is assumed to occur around the hole, which leads to failure for the lowest applied loading. A convergence study has been performed to demonstrate that, from 19 integration points, the predicted failure load becomes independent of the choice of the number of integration points in the volume (see Figure 19.3b). In the following, all the simulations are performed with the minimum number of integration points to obtain a robust computation with a reduced calculation time.

19.3.2 Interest and limitations of the FCV method

The proposed alternative strength analysis method has been developed to predict the strength of laminated open-hole plates, which rupture results from tensile fibre failures. Therefore, the present approach is relevant for thin specimens but also for thick specimens, provided that thin plies are used and the ply sequence is repeated in blocks. This application domain corresponds to the current problematics of many industries.

Nevertheless, some particular test cases cannot be treated with the present approach. Indeed, it is assumed that the final failure of the open-hole plate is due to ply failure in tensile fibre mode. However, it has been demonstrated experimentally and numerically (Hallett et al., 2008; Wisnom and Hallett, 2009) that the final failure of laminated open-hole plates can be due to delamination if thick plies (i.e. blocks of same orientation plies stacked together) are used. The analytical method, based on Tan's approach (Tan, 1994), is not able to predict accurately the out-of-plane stresses in the vicinity of the perforation. Therefore, the FCV strength analysis method is not able to predict the final failure of open-hole plates if the critical failure mode is delamination (e.g. for open-hole plates constituted from thick plies, Hallett et al., 2008).

In the present computational strategy, the mesoscopic non-linearities (viscosity, intraply damages, etc.) are assumed to present a limited influence on the macroscopic rigidity but are essential to predict accurately the final failure due to loading report from a damaged ply to a sane one. This assumption is relevant for most of the stacking sequences, consisting of 0°, ±45° and 90° plies. To demonstrate this point, the failure loads of open-hole plates with different lay-ups, predicted with the post-treated

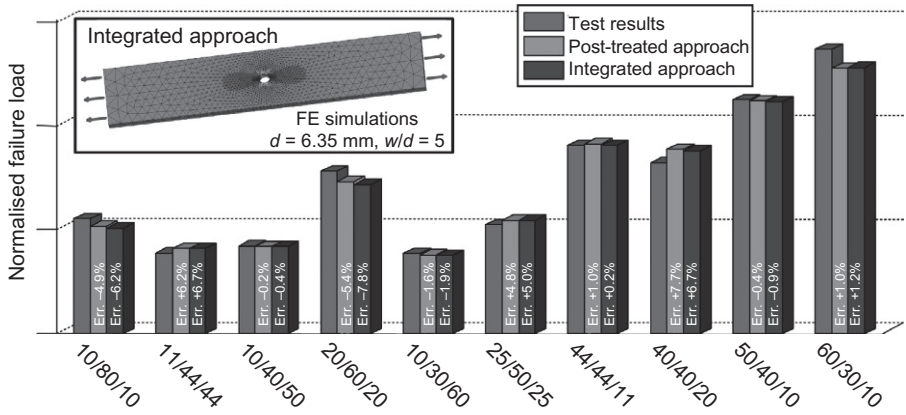

Figure 19.4 Comparison of the failure loads predicted with the post-treated and the integrated approaches on different T700GC/M21 laminated open-hole plates ($d = 6.35$ mm and $w/d = 5$).

strategy, have been compared with those predicted with an integrated strategy. The present approach associated with the FCV method has thus been implemented into an FE code as a non-linear material behaviour. The integrated strategy thus manages all the possible loading reports, but the time of the non-linear FE computation, using multi-layered solid shell elements, is much longer than that of the post-treated strategy (about 1 hour instead of less than 2 min). For the selected lay-ups, the predicted failure loads are very similar with the two strategies (see Figure 19.4) and close to the available test results. Nevertheless, the present strength analysis method is not suitable (non-conservative predictions) for laminated open-hole plates that present a highly macroscopic non-linear behaviour up to failure as observed in $[\pm 45°]_s$ laminates.

To conclude, the proposed strength analysis method is relevant for classical stacking sequences using thin plies or consisting in composite materials presenting a high toughness, such as most recent carbon/epoxy materials. The whole strength analysis method dedicated to laminated perforated plates, including the analytical method to determine the membrane loadings, the present approach to predict the non-linear behaviour and the ply failures and, finally, the FCV method to predict the final failure of the specimen, have been implemented in Matlab. The computational time on a notebook computer is about 2 min. Therefore, this simplified strength analysis method provides a short computational time and matches the different requirements of a design office.

19.4 The coupled criterion approach

19.4.1 Principle of the method

Leguillon (2002) demonstrates that it is necessary to use a criterion which combines energy and stress conditions to describe a crack nucleation mechanism in the vicinity of a stress concentration. This approach has already been used to describe different

failure mechanisms encountered in specimens with stress concentrations, such as the delamination initiated from the edges in laminated composites (Zubillaga et al., 2014). The aim of this chapter is to apply this coupled criterion (CC) to predict the failure of notched specimens and especially open-hole plates subjected to tensile loading. The diameter of the hole is d, the width is w, the thickness of the plate is h and the length is L. When the load reaches the failure load (noted σ^*), two symmetric cracks of length a^* are initiated from the hole.

The energetic condition compares the change in the potential energy ΔW and in the toughness G^c of the laminate. ΔW is expressed as a variation between the final state (with a crack of length a) and the initial state (without a crack) at a fixed macroscopic loading (imposed displacement ΔL). This criterion is defined in Equation (19.6).

$$G^{inc}(a) = -\frac{\Delta W}{\Delta S} = -\frac{W(a) - W(0)}{\Delta S} = A(a)\varepsilon^2 E^{eq} d \geq G^c \tag{19.6}$$

where $G^{\text{inc}}(a)$ is the incremental energy release rate in which the infinitesimal energy rates of the classical Griffith approach are replaced by finite energy increments. Under the assumption of plane elasticity, the area is $\Delta S = a \cdot h$. $A(a)$ is a dimensionless parameter depending only on the geometry. ε is the global strain of the open-hole specimen ($\varepsilon = \Delta L/L$). E^{eq}, reported in Equation (19.7), has been defined in Kageyama (1989) as a function of the Young's moduli of the laminate (noted respectively E_x and E_y), of the shear modulus of the laminate G_{xy} and of the Poisson's ratio v_{xy} expressed in the (x,y) axes.

$$E^{\text{eq}} = \frac{\sqrt{2E_y E_x}}{\sqrt{\sqrt{\frac{E_y}{E_x}} + \frac{E_y}{2G_{xy}} - \upsilon_{yx}}} \tag{19.7}$$

ΔW is a decreasing function of the crack length a. The coefficient $A(a)$ is null for $a = 0$ and increases as a function of a. The energetic balance, reported in Equation (19.6), thus provides a lower bound of the crack increment (a) for a given value of the applied loading (ΔL).

The stress condition, reported in Equation (19.8), assumes that the tensile normal stress $\sigma_{yy}(x)$ reaches the tensile strength σ^{c} along a distance at least equal to the nucleation length.

$$\sigma_{yy}(x) = k_{yy}(x) E^{\text{eq}} \varepsilon \geq \sigma^{\text{c}} \quad \text{for} \quad R \leq x \leq R + a \tag{19.8}$$

where $k_{yy}(x)$ is a dimensionless coefficient. Because of the stress concentration near the hole, k_{yy} is obviously a decreasing function of x. Thus, the stress condition, reported in Equation (19.8), provides an upper bound of the crack increment (a) for a given value of the applied loading.

The energetic condition (Equation 19.6) provides a lower bound of the crack increment, whereas the stress criterion (Equation 19.8) provides an upper bound. Increasing

the loading reduces the lower bound but increases the upper bound. Finally, for a monotonic and increasing applied loading, the increment of crack nucleation at a^* corresponds to the increment of crack length for which both conditions, given by Equations (19.6) and (19.8), are fulfilled for the same applied loading. a^* is thus defined by solving Equation (19.9).

$$\frac{A(a^*)}{k_{yy}^2(a^*)} = \frac{L^c}{d} \quad \text{with} \quad L^c = E^{eq}\frac{G^c}{\sigma^{c2}} \tag{19.9}$$

L^c is a characteristic fracture length of the material. Note that the previous equation always admits a solution because $A(a^*)/k_{yy}^2(a^*)$ is an increasing function of a^* and is equal to 0 for $a^* = 0$. Once the initiation length a^* is determined, the initiation strain ε^c is given in Equation (19.10), using Equation (19.6).

$$\varepsilon^c = \sqrt{\frac{G^c}{E^{eq} dA(a^*)}} \tag{19.10}$$

ε^c could be determined using Equation (19.8) and leads to the same result. The increment of crack nucleation a^* could be correlated to the internal length ρ introduced in Equation (19.5) of the FVC approach.

19.4.2 Practical applications of the CC

To apply the CC presented in Section 19.4.1, it is necessary (i) to calculate the dimensionless parameters $A(a^*)$ and $k_{yy}(x)$ and (ii) the fracture properties of the laminate (strength and toughness).

The dimensionless parameters involved in the CC (see Equations 19.6 and 19.8) are computed using FE computation. For an open-hole plate with a central perforation subjected to a uni-axial loading, some approximate analytical solutions exist (Camanho et al., 2012; Tan, 1988). These analytical approximations, however, are valid only for quasi-isotropic laminates. Consequently, an FE model (that is more general than the analytical models) has been chosen. A 2D FE model (with linear triangular elements) is used to model the laminate with plane stress assumptions. The symmetry of the problem (geometry, loading and homogenised orthotropic behaviour) allows to consider only a quarter of the plate. The mesh and the boundary conditions are given in Figure 19.5. It should be mentioned that a particular attention has been paid to the size of the mesh near the hole in order to capture the stress gradient.

The plate is subjected to an applied displacement ΔL ($\varepsilon = \Delta L/L$). In a first step, the plate is modelled without any crack, as reported in Figure 19.5. It permits to calculate the stress in the ligament ($k_{yy}(x)$ in Equation 19.8) and the energy at the initial state ($W(0)$ in Equation 19.6). In a second step, a crack of length (a) is incrementally inserted in the mesh by releasing the boundary condition on the ligament as reported in Figure 19.6. The FE solution gives the energy $W(a)$ as a function of the length of the crack length (a).

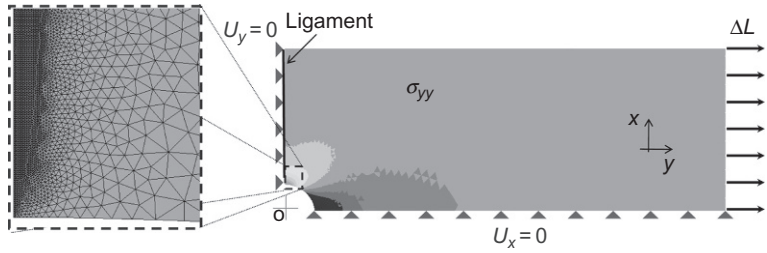

Figure 19.5 Geometry and boundary conditions of an open-hole specimen and detail of the mesh near the hole.

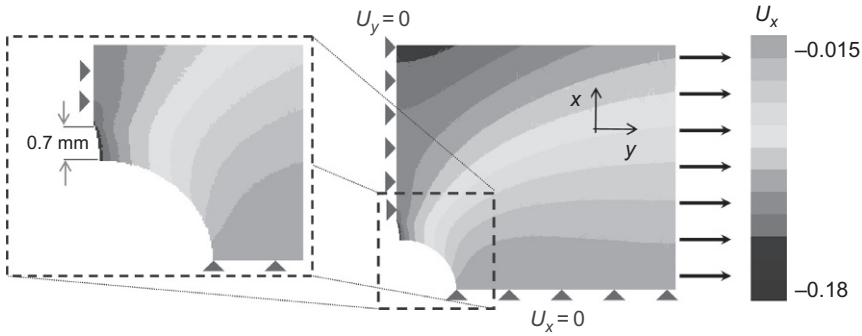

Figure 19.6 Result of the FE calculation with a crack length of 0.7 mm. The symmetry boundary conditions are released on the length of the crack (BC applied for $x > R + 0.7$ mm).

Using Equations (19.6) and (19.8), the dimensionless parameters are given in Equation (19.11).

$$A(a) = -\frac{1}{\varepsilon^2 E^{\text{eq}} d}\frac{W(a) - W(0)}{\Delta S}$$
$$k_{yy}(x) = \frac{\sigma_{yy}(x)}{E^{\text{eq}}\varepsilon} \tag{19.11}$$

Finally, these dimensionless parameters are used to calculate the crack nucleation length a^* (see Equation 19.9) and the initiation strain ε^c (see Equation 19.10). The failure load is calculated by $\sigma^c = E^{\text{lam}}\varepsilon^c$ where E^{lam} is the equivalent to Young's modulus of the laminate in the loading direction. The flowchart in Figure 19.7 summarises the different steps involved in the CC approach.

All the material properties (i.e. the homogenised elastic properties and the fracture properties of the laminate) involved in L^c could be determined from the properties of the elementary ply. Indeed, knowledge of the elastic properties of the ply allows the determination of the homogenised elastic properties of the laminate, using the classical laminate theory. The tensile strength in the direction y is determined using the progressive failure approach proposed in Section 19.2. Finally, the toughness of

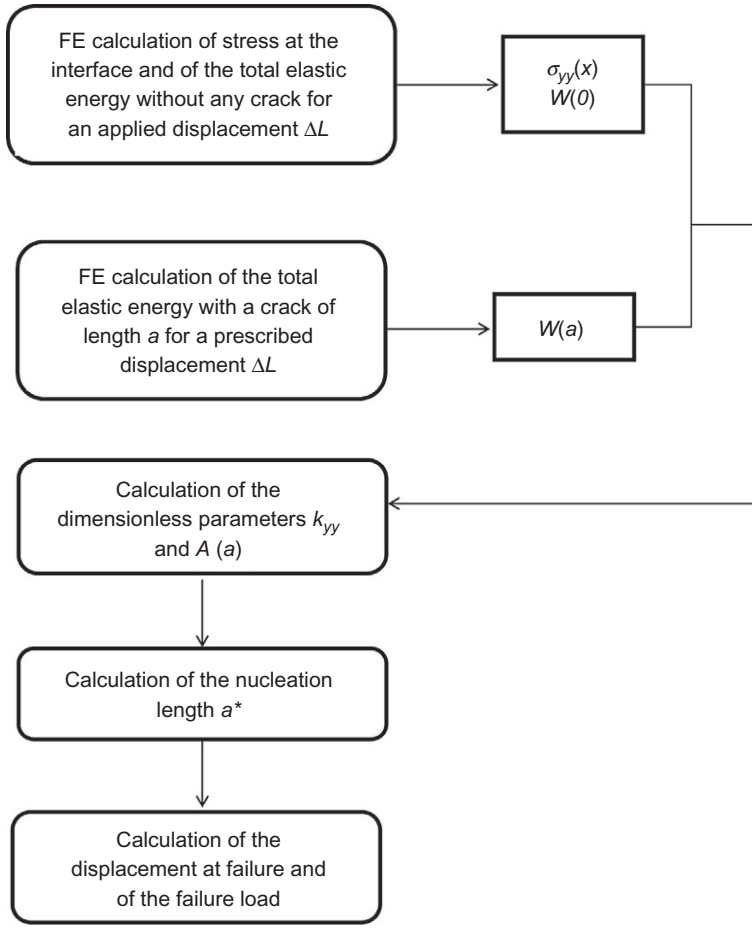

Figure 19.7 Flowchart summarising the different steps involved in the coupled criterion approach.

the laminate is calculated from the toughness of the 0° ply and of the [±45°] sub-laminate, using the approach described in Camanho and Catalanotti (2011). The elastic properties of the ply and the strength could be measured using standardised tests. The fracture toughness could be determined using compact tension tests as proposed in Pinho et al. (2006). Only six tests, performed on the ply, are required to identify all the material parameters necessary for application of the model.

For the reported cases concerning the T700GC/M21 material, the compact tension tests are not available. Consequently, the toughness of the 0° ply and of the [±45°] sub-laminate has been determined by an inverse identification approach using the failure loads experimentally determined during a tensile test on open-hole specimens on a highly oriented laminate (50/40/10) and on a highly disoriented laminate (10/80/10).

19.5 Comparisons of these strength analysis methods with available test results

Although the design of aeronautical structures necessitates the use of allowables taking into account the material dispersion (A and B values) to ensure the required level of confidence, the average values of the stiffness and strengths are used in the present study. Indeed, this study deals with the evaluation of the predictive capabilities of alternative strength analysis methods through comparisons with available test data.

19.5.1 Open-hole plates with different stacking sequences

Tensile tests on T700GC/M21 open-hole plates with 10 different stacking sequences have been performed. For all the specimens, the hole diameter is equal to 6.35 mm and the plate width-to-hole diameter ratio is fixed at five. Each test configuration has been repeated and only the average failure load is reported in this paper.

For the FCV method, the internal length ρ in tension has been identified on the 50/40/10 laminated perforated plate as explained in the Section 19.3.1. For the CC, the toughness of the 0° ply and of the [±45°] sub-laminate have been identified on the 50/40/10 and 10/80/10 laminated perforated plates as explained in Section 19.4.2.

Figure 19.8 presents the comparison between the predicted ultimate failure loads, obtained with the two proposed alternative methods, on T700GC/M21 perforated plates with different stacking sequences subjected to uni-axial tensile loading and the available test results. The predictions of the FCV method agree with the experimental data on the other nine stacking sequences even for highly oriented (60/30/10) and disoriented (10/80/10) laminates because the different material non-linearities, especially the elastic non-linearity and the viscoelasticity, are taken into account.

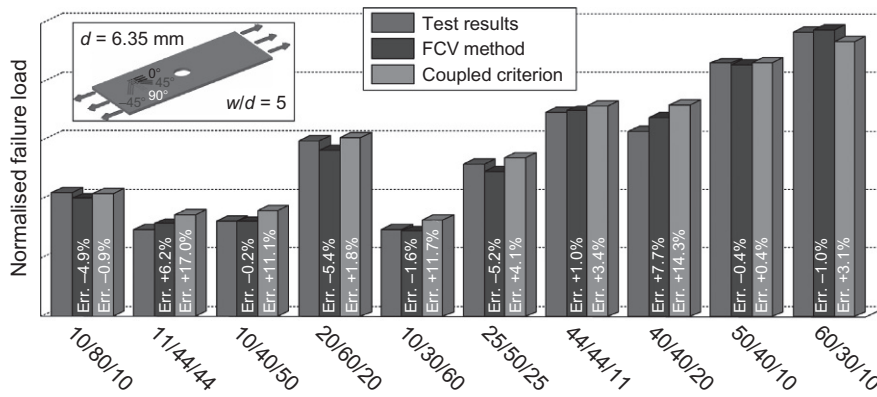

Figure 19.8 Comparison between predicted (FCV and CC methods) and measured normalised failure loads of T700GC/M21 laminated perforated plates, with different stacking sequences, subjected to uni-axial tensile loading ($d = 6.35$ mm and $w/d = 5$).

The predictions obtained with the CC method also agree with the experimental data for the oriented laminates. Nevertheless, the error increases for the disoriented laminates (higher than +10%) because the material non-linearities, which are influent on the macroscopic behaviour for such disoriented stacking sequences, are neglected with the CC approach. Contrary to the FVC method, in which the internal length is constant, the nucleation length a^* that is determined by the CC, varies as a function of the stacking sequence. Indeed, this length is a function of L^c (see Equation 19.9). It means that a^* is large for low strength (in the case of the disoriented materials) and small for high strength (in the case of the oriented materials).

19.5.2 Open-hole plates with different hole diameters

In this section, we look at the influence of the hole diameter on the strength of open-hole plates subjected to uni-axial tensile loading, the total thickness of the coupon remaining constant and the w/d ratio is fixed at 5. The variation of the hole diameter induces a modification of the stress gradient in the vicinity of the perforation. This test case is thus relevant to estimate the predictive capabilities of the proposed strength analysis methods.

From the experimental point of view, four different hole diameters have been tested for six different T700GC/M21 lay-ups (three oriented and three disoriented laminates). Each test has been repeated, and only the average failure loads are reported in Figure 19.9. For the two considered methods, the predicted macroscopic stress at failure, defined by the ultimate load at failure divided by the real section, are in good agreement with the available test results on oriented and disoriented open-hole plates with different hole diameters as illustrated in Figure 19.9.

The predictions obtained with the two different simplified approaches are rather similar for the oriented laminates (Figure 19.9a and b) but become different for the disoriented laminates (Figure 19.9c and d), especially for the small diameters of hole, for the reasons mentioned in the previous section.

For the FCV method, the introduction of the dependence of the internal length to the radius of perforation (defined in Equation 19.5) allows obtaining accurate or reasonably conservative predictions, especially for 60/30/10 perforated laminates. It should be noted that the dependence of the internal length to the hole diameter, defined in Equation (19.9), is taken into account automatically with the CC approach, contrary to the FCV method.

Moreover, some experimental data on similar configurations can be found in the literature. Indeed, Camanho et al. (2007) have performed tests on IM7/8552 quasi-isotropic open-hole plates subjected to uni-axial tensile loading. Six different hole diameters have been considered (from 2 to 10 mm), whereas the w/d ratio remains constant at five.

For the FCV method, the internal length has been identified from tests performed on the open-hole plates with a hole diameter equal to 6 mm (closest configuration to that encountered in the aeronautical industry). For the CC approach, the fracture toughness has been determined using the compact tension test available in Camanho et al. (2012) and Tan (1988).

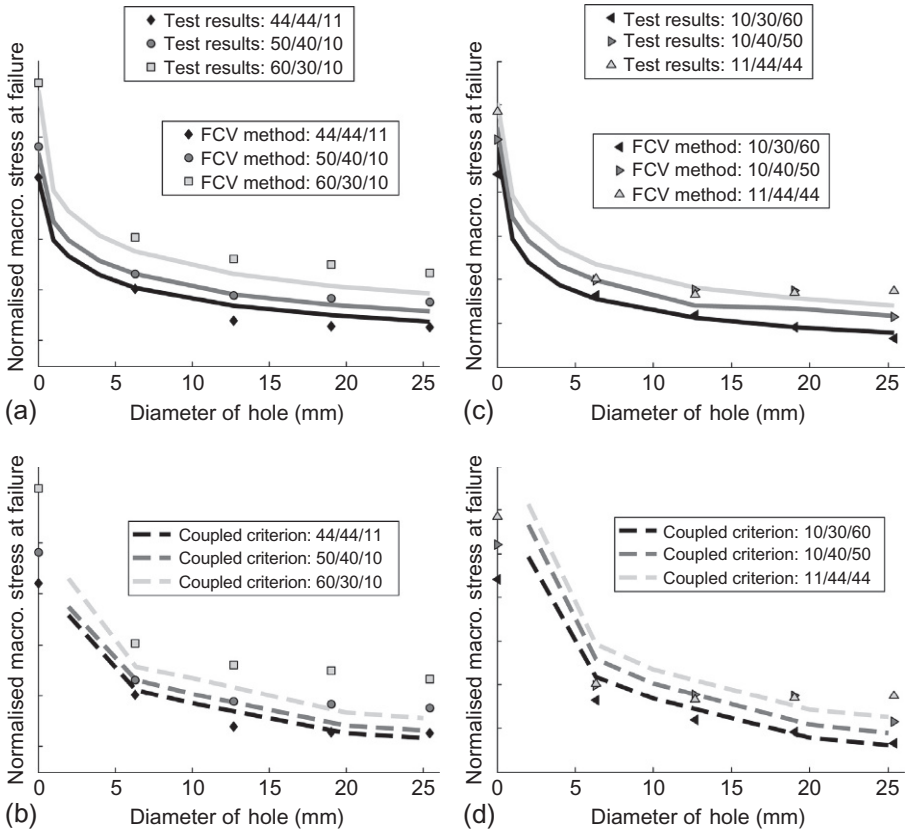

Figure 19.9 Comparison between predicted (FCV and CC methods) and measured normalised macroscopic stress at failure of T700GC/M21 laminated oriented (a, b) and disoriented (c, d) perforated plates, with different hole diameters, subjected to uni-axial tensile loading ($w/d = 5$).

Figure 19.10 presents the comparisons between the predicted macroscopic stress at failure and test results on IM7/8552 quasi-isotropic open-hole plates with different hole diameters subjected to uni-axial tensile loadings. The predictions obtained with the two methods are in good agreement with experimental data and are rather similar, except for small diameters of hole (inferior to 3 mm). The CC approach seems to better match the experimental results than the FCV method, because the influence of the hole diameter on the internal length is not *a priori* fixed with the CC approach. The CC approach and the FCV method can thus be complementary. Indeed, the influence of the stress gradient on the internal length can be determined using the CC approach. The CC approach permits us to show that the internal length is not exactly a function of $\sqrt{r}$. Finally, the FCV method could use the evolution of ρ as a function of r determined by the CC to predict the final failure of the open-hole plates for different configurations of perforation.

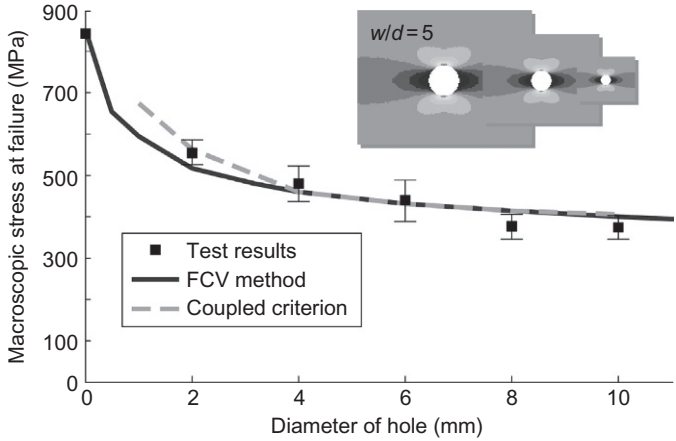

Figure 19.10 Comparison between predicted (FCV and CC methods) and measured (Camanho et al., 2007) macroscopic stress at failure of IM7/8552 quasi-isotropic perforated plates, with different hole diameters, subjected to uni-axial tensile loading ($w/d = 5$).

19.5.3 Open-hole plates with different w/d ratios

In this test case, the perforation diameter in the T700GC/M21 laminated open-hole plates remains constant at 6.35 mm, whereas the w/d ratio evolves from three to six. Figure 19.11 presents the comparison between the predicted macroscopic stresses at failure and the tensile test results. Six different stacking sequences have been investigated and each test configuration has been repeated. The predicted failure loads are consistent with the experimental data. Indeed, since the hole diameter is constant, the stress gradient near the hole remains unchanged. Therefore, the macroscopic stress at failure for large w/d ratios (superior to five) remains quasi-constant. Nevertheless, for small w/d ratios (less than four), the specimens are narrow and the influence of the free edges on the stress gradient around the hole can no more be neglected and induces a decrease in the macroscopic stress at failure. For small w/d ratios, the FCV method slightly overestimates the final failure because the edge effects are neglected by the analytical method, as reported in Figure 19.11a. This difficulty can be overcome by using the FE simulation to estimate the membrane loadings within the open-hole plate.

The results obtained with the CC approach, reported in Figure 19.11b, are similar but tend to overestimate the failure stress in the case of disoriented laminates, for the reasons mentioned previously.

19.5.4 Open-hole plates with off-axis tensile tests

Figure 19.12 presents the comparison between the predicted ultimate failure loads, obtained with the FCV method, on T700GC/M21 perforated plates with three different stacking sequences and subjected to off-axis tensile loading and the test results. For all

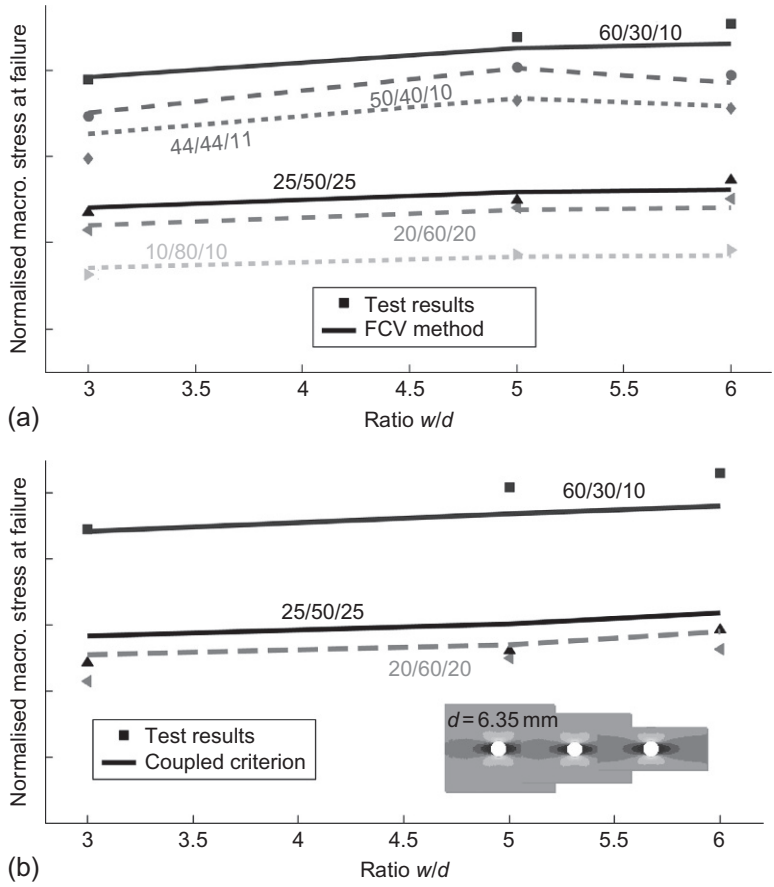

Figure 19.11 Comparison between predicted (FCV and CC methods) and measured normalised macroscopic stress at failure of T700GC/M21 laminated perforated plates, with different w/d ratios, subjected to uni-axial tensile loading ($d = 6.35$ mm).

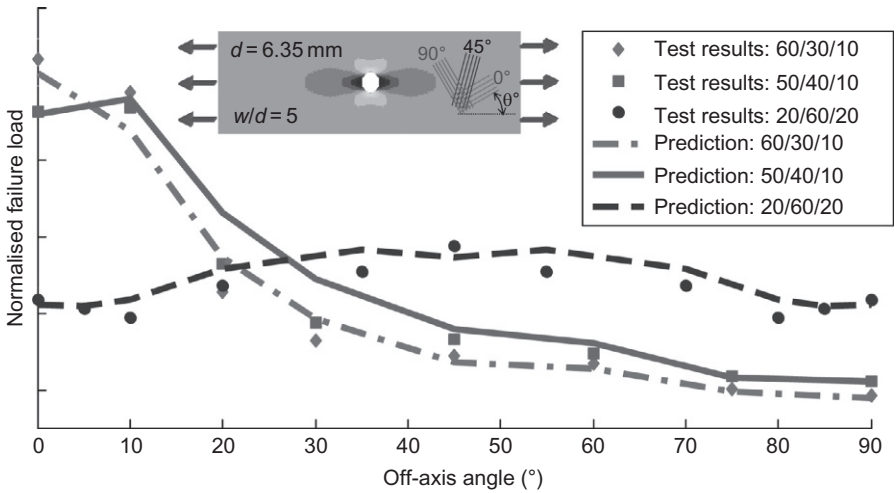

Figure 19.12 Comparison between predicted (FCV method) and measured normalised failure loads of T700GC/M21 laminated perforated plates, with different stacking sequences, subjected to off-axis tensile loading ($d = 6.35$ mm and $w/d = 5$).

the perforated tested plates, the hole diameter is 6.35 mm and the w/d ratio is fixed at five. This kind of off-axis tensile tests permit us to obtain a more complex multi-axial stress field in the vicinity of the hole, whereas the experimental device remains the same. The predicted failure loads have been successfully compared with the experimental data, such as the failure pattern which evolves as a function of the off-axis angle. The maximal error is observed in the tensile test on oriented laminates with an off-axis angle evolving between 15° and 35°, where the in-plane shear stresses, in the most loaded plies in the fibre direction, attain high values. This point should be studied in further works. The present test case has not been treated with the CC approach because of meshing issues for this particular configuration of tests on open-hole plates. This test case will be considered in further works, because no fundamental limitation is encountered here with the CC approach.

19.5.5 Multi-perforated plates

Finally, the proposed alternative strength analysis methods have been applied to T700GC/M21 open-hole plates subjected to uni-axial tensile loading with complex configurations of perforation and with unconventional stacking sequences, in order to determine its predictive capabilities. The width of the plates is $w = 38$ mm and the hole diameters are, respectively, $d = 7.8$ mm for the plates with two holes and $d = 3.9$ mm for the plates with four holes. For this test case, the membrane loadings have been determined with FE simulations for the FCV method because of the interaction between the stress gradient due to the free edges and the holes. Figure 19.13 presents the comparison between the predicted failure loads and the available test results. The tests have been performed at Onera, and only one sample for each configuration has been tested (Laurin et al., 2011). The observed failure mode is the fibre failure mode in tension for all the tested samples.

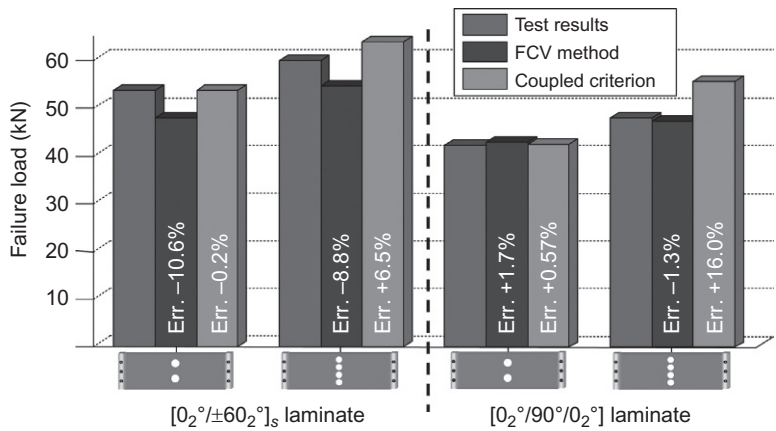

Figure 19.13 Comparison between predicted (FCV and CC methods) and measured failure loads of T700GC/M21 multi-perforated plates subjected to uni-axial tensile loading.

This test case is essential because it demonstrates that the proposed approach is able to predict accurately the final failure load of perforated plates with unconventional stacking sequences and complex configurations of perforation. Therefore, the present simplified methods could be used in an optimisation process or to generate a 'virtual' test database, contrary to the strength analysis methods used currently in design offices, such as the point stress method.

19.6 Complementarity between advanced failure approaches and fast calculation methods

The previous approaches, which do not take into account the effect on the behaviour of the catastrophic modes (such as fibre failure or delamination) leading to the final failure, permit one to limit the computational time for some specific configurations of tests, representative of aeronautical industrial problematics. However, it necessitates introducing some specific approaches to dealing with the stress concentrations as presented in Sections 19.3 and 19.4. These kinds of approaches present some limitations, as explained previously.

To overcome these limitations and extend the domain of validity of the FE predictions, it is possible to develop approaches that take into account the effect of the most significant physical phenomena experimentally observed, that is, the non-linear behaviour of the matrix, the matrix rupture, the fibre failure and the delamination (Camanho et al., 2007; Hallett et al., 2008; Violeau et al., 2009). As proposed initially by Ladevèze et al. (Allix et al., 1995), two intrinsic constituents can be defined for the meso-modelling: the ply and the interface as illustrated in Figure 19.14. Many models can be found in the literature to describe the damage and the failure of the ply based on damage mechanics (see Kaddour et al., 2013; Soden et al., 2004 for an extensive comparison between damage models or progressive failure approaches).

The present work is focused on this last type of models. The main idea of this approach consists in taking into account the effect of the failure mechanisms on the elastic properties of the ply. This damage and failure approach is close to that presented in Section 19.2. However, to predict quantitatively the progressive aspect of fibre failures in the structure and their effects (complete degradation of the mechanical

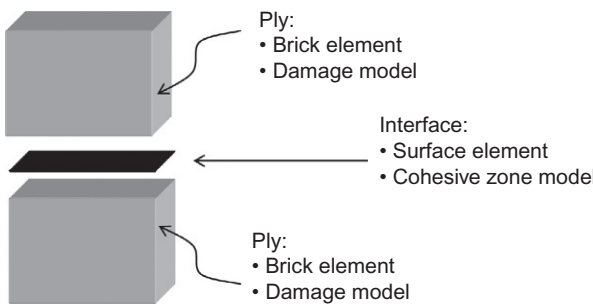

Figure 19.14 Principle of the meso-modelling: the plies and the interfaces are the two intrinsic constituents.

properties in the fibre direction), an attractive procedure consists of reformulating the multi-scale failure approach in a 'softening' framework for the fibre mode as proposed in Laurin et al. (2013) and Carrere et al. (2010). Nevertheless, numerical problems are associated with this type of modelling. Indeed, the global response of the structure becomes dependent on the used mesh (type, size and orientation of the elements of the mesh), inducing a loss of relevance in the performed FE simulations. To overcome this problem, among the existing approaches found in the literature, we have decided to mix two different regularisation techniques: (i) the reformulation of the problem in a non-local framework (Pijaudier-Cabot and Bazant, 1987; Geers et al., 1998; Germain et al., 2007) and (ii) the introduction of a delay effect in the damage (Allix, 2001; Suffis et al., 2006). Indeed, coupling these two approaches allows one to overcome some inherent limitations of each method used separately as detailed in Laurin et al. (2013). Finally, the multi-scale progressive failure approach has been rewritten in the non-local framework with delayed approach to describe accurately the softening behaviour of a ply failed in a fibre mode and has been implemented in the in-house FE code ZeBuLoN. The delamination is modelled by cohesive zone elements (Alfano and Crisfield, 2001; Vandellos et al., 2013; Ladeveze and Lubineau, 2002; Tvergaard, 1990) that permit one to describe the progressive degradation of the elastic properties of the interface based on the strength criterion (for the damage threshold) and the toughness (for the damage kinetics).

This enhanced approach has been identified on the T700GC/M21 material using data provided in the literature or available at Onera. The parameters of the evolution law of the fibre failure have been assumed to have high values to describe a violent sudden local rupture but to avoid localisation of the fibre failure. Second, the classical tests specific to fracture mechanics are required to identify the toughness of the interface between the plies and have been determined using the experimental data available at Onera (Vandellos, 2011).

Figure 19.15 summarises the comparisons between the predictions obtained by the advanced damage and failure approach and the experimental data on some test cases already presented in Section 19.5. Figure 19.15a presents the comparison between the predicted ultimate failure loads on T700GC/M21 perforated plates with three different stacking sequences (an oriented laminate, a quasi-isotropic laminate and a disoriented laminate) subjected to uni-axial tensile loading and the available test results already described in Section 19.5.1. Figure 19.15b presents the comparisons between the predicted macroscopic stress at failure and test results on T700GC/M21 50/40/10 open-hole plates with different hole diameters subjected to uni-axial tensile loadings as detailed in Section 19.5.2. Figure 19.15c presents the comparison between the predicted macroscopic stresses at failure and the tensile test results on T700GC/M21 50/40/10 open-hole plates with different w/d ratios subjected to uni-axial tensile loadings as detailed in Section 19.5.3. Finally, Figure 19.15d presents the comparison between the predicted ultimate failure loads on T700GC/M21 50/40/10 perforated plates subjected to off-axis tensile loading and the test results. For all the considered test cases, the predictions, obtained by the advanced damage and failure approach, are in as good an agreement with the experimental data as those obtained with the simplified strength analysis methods presented in Sections 19.3 and 19.4.

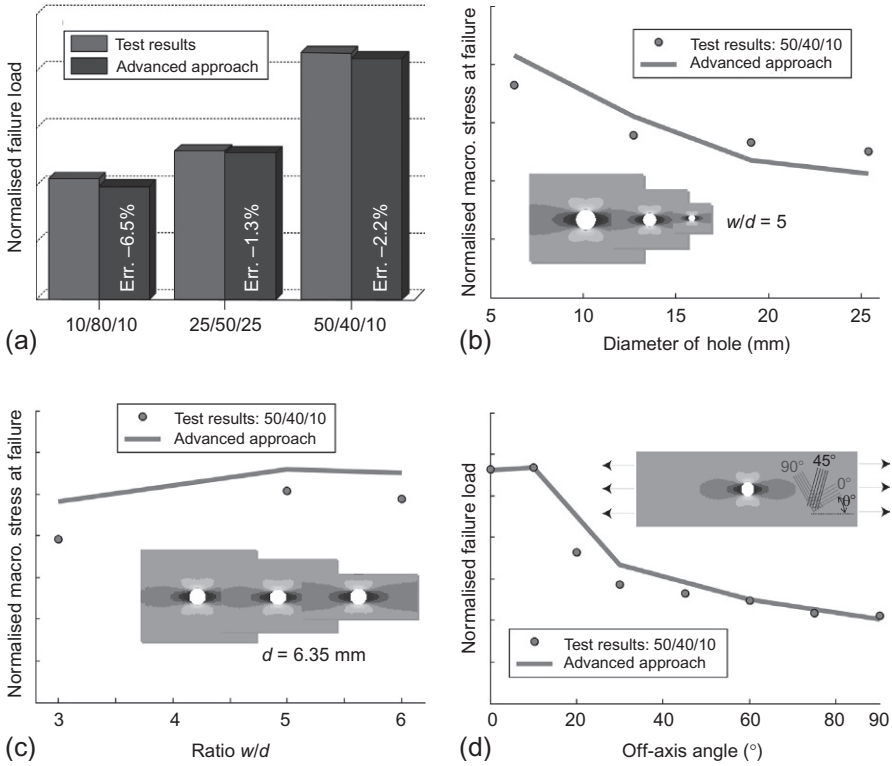

Figure 19.15 Comparison between the predicted (advanced method) and measured normalised failure loads of T700GC/M21 laminated perforated plates subjected to uni-axial tensile loading with (a) different stacking sequences, (b) different hole diameters, (c) different *w*/*d* ratios and (d) different off-axis angles.

Nevertheless, the advanced damage and failure approach being physically based, its validity domain is larger than those of the fast computational methods previously mentioned. Indeed, such an approach can be applied to test cases in which the description of the intralaminar damages (i.e. transverse cracks) and interlaminar damages (i.e. delamination) are essential to predict the final failure. As proposed in Hallett et al. (2008), the description of the damage mechanisms is critical in the case of open-hole plates manufactured from thick plies. The predictions of the damage patterns and of the failure loads of IM7/8552 quasi-isotropic $[45_4°/90_4°/-45_4°/0_4°]_s$ open-hole plates with different hole diameters have also been studied. Figure 19.16 presents the damage pattern (transverse cracks and delamination) just prior to the failure of the open-hole plate with a hole diameter equal to 3.15 mm and subjected to uni-axial tension loading. The predicted damage pattern is in good agreement with the observations available in the literature (Hallett et al., 2009). It is worth mentioning that the evolution of the ultimate failure load as a function of the hole diameter for this

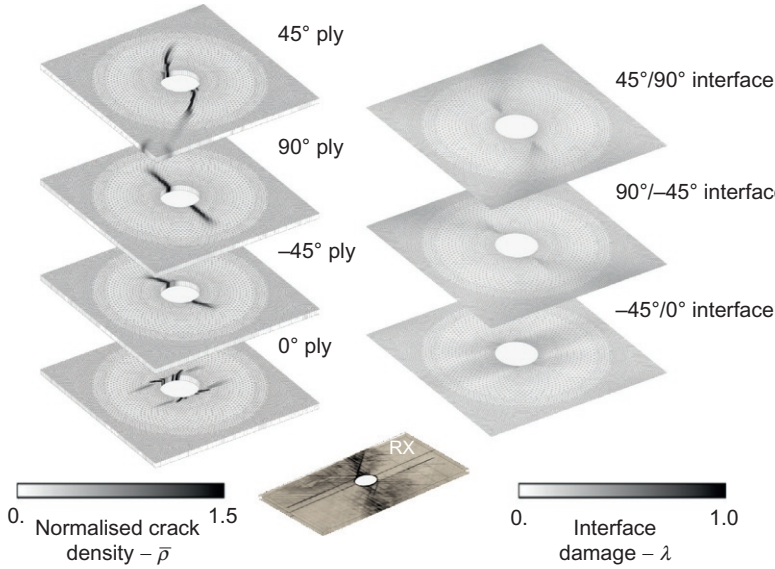

Figure 19.16 Patterns at failure load of in-plane mesoscopic damage in each ply and delamination at each interface in the $[45_4°/90_4°/-45_4°/0_4°]_s$ IM7/8552 open-hole plate subjected to tensile loading and comparison with the available experimental observation (Hallett et al., 2009).

complex test case is also reproduced accurately by the present advanced damage and failure approach.

The advanced damage and failure approach can also be used to predict the strength of complex test cases containing geometrical singularities contrary to the fast computational methods as mentioned previously, because it is physically based. Nevertheless, it can be noted that, obviously, the computational time associated with the advanced approach, describing finely the different physical mechanisms, is markedly longer (a few days) and does not match the current requirements of design offices. A computational strategy, using both advanced and simplified strength analysis methods, has still to be developed to adapt the complexity of the chosen modelling to the considered test case.

19.7 Conclusion/perspectives

Two alternative strength analysis methods dedicated to the failure predictions of open-hole plates, consisting of aeronautical stacking sequences, have been proposed. First, the FCV method, which consists of using, in the fibre failure criterion, the stress tensor averaged over a given volume, has been used in this study as an alternative to the point stress method. Second, a coupled-based criterion, based on the concept of finite fracture mechanics, has been proposed and applied to the prediction of open-hole plate rupture due to fibre failure.

These fast computational strength analysis methods (less than 2 min using a notebook computer) match the different requirements of a design office. The determination of the predictive capabilities of the proposed approaches has been performed through comparisons on a wide range of aeronautical test cases with open-hole plates (different lay-ups, hole diameters, *w/d* ratios, off-axis tensile tests and multi-perforated plates) manufactured from different carbon/epoxy materials.

Nevertheless, the present approaches assumed that the final failure of the open-hole plate is due to ply failure in tensile fibre mode, delamination is thus neglected. Moreover, for some specific stacking sequences, the global response of structures containing high-stress gradients can become highly non-linear; consequently, the proposed simplified methods are not relevant for such cases. Advanced damage and failure approaches, using cohesive zone elements to predict the onset and the propagation of delamination and a fine description of the transverse cracks and of the effects of fibre failure, are suitable in the case of open-hole plates using thick plies, the failure of which is due to inter- and intradamage and not to fibre failure.

A computational strategy, using both advanced and simplified strength analysis methods, still has to be developed to adapt the complexity of the chosen modelling to the considered test case. Moreover, further work should consist of applying the proposed strength analysis methods to open-hole plates subjected to other loadings such as compressive, multi-axial or even bending loadings.

Acknowledgement

The authors would like to express their sincere gratitude to Dr. R. Valle for valuable and helpful discussions. The authors also wish to thank Prs. E. Martin and D. Leguillon for valuable discussions and assistance in the coupled criterion.

References

ABAQUS Inc., 2013. ABAQUS 6.13 User's Manual, 2013. ABAQUS Inc, Pawtucket, RI.

Abisset, E., Daghia, F., Ladeveze, P., 2011. On the validation of a damage mesomodel for laminated composites by means of open-hole tensile tests on quasi-isotropic laminates. Compos. A: Appl. Sci. Manuf. 42, 1515–1524.

Achard, V., Bouvet, C., Castanié, B., Chirol, C., 2014. Discrete ply modelling of open hole tensile tests. Compos. Struct. 113, 369–381.

Ahmad, H., Crocombe, A.D., Smith, P.A., 2014. Strength prediction in CFRP woven laminate bolted double-lap joints under quasi-static loading using XFEM. Compos. A: Appl. Sci. Manuf. 56, 192–202.

Alfano, G., Crisfield, M.A., 2001. Finite element interface models for the delamination analysis of laminated composites: mechanical and computational issues. Int. J. Numer. Methods Eng. 50, 1701–1736.

Allix, O., 2001. A composite damage meso-model for impact problems. Compos. Sci. Technol. 61, 2193–2205.

Allix, O., Ladeveze, P., Corigliano, A., 1995. Damage analysis of interlaminar fracture specimens. Compos. Struct. 31, 61–74.

Cahill, L.M.A., Natarajan, S., Bordas, S.P.A., O'Higgins, R.M., McCarthy, C.T., 2014. An experimental/numerical investigation into the main driving force for crack propagation in uni-directional fibre-reinforced composite laminae. Compos. Struct. 107, 119–130.

Camanho, P.P., Catalanotti, G., 2011. On the relation between the mode I fracture toughness of a composite laminate and that of a the 0° ply: analytical model and experimental validation. Eng. Fract. Mech. 78, 2535–2546.

Camanho, P.P., Maimi, P., Davila, C.G., 2007. Prediction of size effects in notched laminates using continuum damage mechanics. Compos. Sci. Technol. 67, 2715–2727.

Camanho, P.P., Erçin, G.H., Catalanotti, G., Mahdi, S., Linde, P., 2012. A finite fracture mechanics model for the prediction of the open-hole strength of composite laminates. Compos. A: Appl. Sci. Manuf. 43, 1219–1225.

Carrere, N., Laurin, F., Marcin, L., Maire, J.-F., 2010. A progressive multiscale failure approach applied to high gradient structures: numerical issues and validation. In: 14th European Conference on Composite Materials (ECCM14), Budapest, Hungary, 7–10 June 2010, Paper ID: 241, pp. 1–10.

Daghia, F., Ladeveze, P., 2012. A micro-meso computational strategy for the prediction of the damage and failure of laminates. Compos. Struct. 94, 3644–3653.

Dvorak, G.J., Laws, N., Hejazi, M., 1985. Analysis of progressive matrix cracking in composite laminates I. Thermoelastic properties of a ply with cracks. J. Compos. Mater. 19, 216–234.

Geers, M.G.D., De Borst, R., Brekelmans, W.A.M., Peerlings, R.H.J., 1998. Strain-based transient-gradient damage model for failure analyses. Comput. Methods Appl. Mech. Eng. 160, 133–153.

Germain, N., Besson, J., Feyel, F., 2007. Composite layered materials: anisotropic nonlocal damage models. Comput. Methods Appl. Mech. Eng. 196, 4272–4282.

Green, B.G., Wisnom, M.R., Hallett, S.R., 2007. An experimental investigation into the tensile strength scaling of notched composites. Compos. A: Appl. Sci. Manuf. 38, 867–878.

Hallett, S.R., Jiang, W.G., Khan, B., Wisnom, M.R., 2008. Modelling the interaction between matrix cracks and delamination damage in scaled quasi-isotropic specimens. Compos. Sci. Technol. 68, 80–89.

Hallett, S.R., Green, B.G., Jiang, W.G., Wisnom, M., 2009. An experimental and numerical investigation into the damage mechanisms in notched composites. Compos. A: Appl. Sci. Manuf. 40, 613–624.

Hashin, Z., 1980. Failure criteria for unidirectional fiber composites. J. Appl. Mech. 47, 329–334.

Hinton, M.J., Kaddour, A.S., Soden, P.D., 2002. Evaluation of failure prediction in composite laminates: background to 'part B' of the exercise. Compos. Sci. Technol. 62, 1481–1488.

Hochard, C., Lahellec, N., Bordreuil, C., 2007. A ply scale non-local fibre rupture criterion for CFRP woven ply laminated structures. Compos. Struct. 80, 321–326.

Hochard, C., Miot, S., Lahellec, N., Mazerolle, F., Herman, M., Charles, J.-P., 2009. Behaviour up to rupture of woven ply laminate structures under static loading conditions. Compos. A: Appl. Sci. Manuf. 40, 1017–1023.

Huchette, C., 2005. Analyse multiéchelle des interactions entre fissurations intralaminaire et interlaminaire dans les matériaux composites stratifiés (Doctorate thesis). University of Paris VI.

Ishikawa, T., Matsushima, M., Hayashi, Y., 1985. Hardening non linear behaviour in longitudinal tension of unidirectional carbon composites. J. Mater. Sci. 20, 4075–4083.

Jaśkowiec, J., van der Meer, F.P., 2014. A consistent iterative scheme for 2D and 3D cohesive crack analysis in XFEM. Comput. Struct. 136, 98–107.

Kaddour, A.S., Hinton, M.J., 2013. Maturity of 3D failure criteria for fibre-reinforced composites: comparison between theories and experiments: part B of WWFE-II. J. Compos. Mater. 47, 925–966.

Kaddour, A.S., Hinton, M.J., Smith, P.A., Li, S., 2013. A comparison between the predictive capability of matrix cracking, damage and failure criteria for fibre reinforced composite laminates: part A of the third world-wide failure exercise. J. Compos. Mater. 47, 2749–2779.

Kageyama, K., 1989. Fracture mechanics of notched Carbon/Epoxy laminates in applications of fracture mechanics to composite materials. Eng. Fract. Mech. 327–396.

Ladeveze, P., Lubineau, G., 2002. An enhanced mesomodel for laminates based on micromechanics. Compos. Sci. Technol. 62, 533–541.

Laurin, F., Carrere, N., Maire, J.F., 2007. A multiscale progressive failure approach for composite laminates based on thermodynamical viscoelastic and damage models. Compos. A: Appl. Sci. Manuf. 38, 198–209.

Laurin, F., Carrere, N., Maire, J.-F., 2011. Strength analysis methods for high stress gradient parts in composite structures ensuring design office requirements. Proc. Inst. Mech. Eng. G J. Aerosp. Eng. 225, 291–301.

Laurin, F., Carrere, N., Huchette, C., Maire, J.F., 2013. A multiscale hybrid approach for damage and final failure predictions of composite structures. J. Compos. Mater. 47, 2713–2747.

Laurin, F., Carrere, N., Maire, J.F., Mahdi, S., 2014. Enhanced strength analysis method for composite open-hole plates ensuring design office requirements. Compos. Part B 62, 5–11.

Leguillon, D., 2002. Strength or toughness? A criterion for crack onset at a notch. Eur. J. Mech. A Solids 21, 61–72.

Maire, J.F., Chaboche, J.L., 1997. A new formulation of continuum damage mechanics (CDM) for composite materials. Aerosp. Sci. Technol. 1, 247–257.

Martin-Santos, E., Maimi, P., Gonzalez, E.V., Cruz, P., 2014. A continuum constitutive model for the simulation of fabric-reinforced composites. Compos. Struct. 111, 122–129.

Nuismer, R.J., 1976. Modeling of damage and failure in notched composite laminates. Eng. Fract. Mech. 8, 755–756.

Nuismer, R.J., Labor, J.D., 1978. Applications of the average stress failure criterion: part I – tension. J. Compos. Mater. 12, 238–249.

Nuismer, R.J., Labor, J.D., 1979. Applications of the average stress failure criterion: part II – compression. J. Compos. Mater. 13, 49–60.

Pijaudier-Cabot, G., Bazant, Z.P., 1987. Nonlocal damage theory. J. Eng. Mech. 113, 1512–1533.

Pinho, S.T., Robinson, P., Iannucci, L., 2006. Fracture toughness of the tensile and compressive fibre failure modes in laminated composites. Compos. Sci. Technol. 66, 2069–2079.

Pinho, S.T., Vyas, G.M., Robinson, P., 2013. Response and damage propagation of polymer-matrix fibre-reinforced composites: predictions for WWFE-III Part A. J. Compos. Mater. 47, 2595–2612.

Soden, P.D., Kaddour, A.S., Hinton, M.J., 2004. Recommendations for designers and researchers resulting from the world-wide failure exercise. Compos. Sci. Technol. 64, 589–604.

Suffis, A., Lubrecht, T.A.A., Combescure, A., 2006. Damage model with delay effect: analytical and numerical studies of the evolution of the characteristic damage length. Int. J. Solids Struct. 40, 3463–3476.

Sutherland, L.S., Shenoi, R.A., Lewis, S.M., 1999a. Size and scale effects in composites: I. Literature review. Compos. Sci. Technol. 59, 209–220.

Sutherland, L.S., Shenoi, R.A., Lewis, S.M., 1999b. Size and scale effects in composites: II. Unidirectional laminates. Compos. Sci. Technol. 59, 221–233.

Tan, S.C., 1988. Finite-width correction factors for anisotropic plate containing a central opening. J. Compos. Mater. 22, 1080–1097.

Tan, S.C., 1994. Stress concentrations in laminated composites. Technomic Publishing Company Inc., Lancaster, Pennsylvania, USA.

Tvergaard, V., 1990. Effect of fibre debonding in a whisker-reinforced metal. Mater. Sci. Eng. A 125, 203–213.

Vandellos, T., 2011. Développement d'une stratégie de modélisation du délaminage dans les structures composites stratifiées (Doctorate thesis). University of Bordeaux I.

Vandellos, T., Huchette, C., Carrere, N., 2013. Proposition of a framework for the development of a cohesive zone model adapted to Carbon-Fiber Reinforced Plastic laminated composites. Compos. Struct. 105, 199–206.

Violeau, D., Ladevèze, P., Lubineau, G., 2009. Micromodel-based simulations for laminated composites. Compos. Sci. Technol. 69, 1364–1371.

Wang, J., Callus, P.J., Bannister, M.K., 2004. Experimental and numerical investigation of the tension and compression strength of un-notched and notched quasi-isotropic laminates. Compos. Struct. 64, 297–306.

Whitney, J.M., Nuismer, R.J., 1974. Stress fracture criteria for laminated composites containing stress concentrations. J. Compos. Mater. 8, 253–265.

Wisnom, M.R., Hallett, S.R., 2009. The role of delamination in strength, failure mechanism and hole size effect in open hole tensile tests on quasi-isotropic laminates. Compos. A: Appl. Sci. Manuf. 40, 335–342.

Zubillaga, L., Carrere, N., Turon, A., Guillamet, G., Linde, P., 2014. Experimental and numerical analysis of free-edge delamination by means of a two-fold criterion and a cohesive zone model. Compos. A: Appl. Sci. Manuf.

Index

Note: Page numbers followed by *f* indicate figures and *t* indicate tables.

A

Aerospace composite structures
  'building block' approach, 480
  code implementation, panel impact, 484–486
  cohesive interface delamination models, 483–484
  damage tolerance, 480
  foreign object debris, 480
  high-velocity impact, 479
  impact damage, 486–491
  impact loads, 491–501
  low-velocity impact, 479
  meso-scale ply damage models, 481–483
  PAM-CRASH™, 501
  primary load-bearing structures, 479
A-FEM. *See* Augmented finite element method (A-FEM)
Aircraft fuselage and wing components, 12–14
Apparent fracture toughness, 465
AS4/55A carbon–epoxy, 135*f*
AS4/3501-6 carbon–epoxy, 135–136*f*
Augmented finite element method (A-FEM)
  composite engineering, 265
  condensation algorithm, 269–270
  continuous fiber-reinforced composite laminates, 266
  coupled fiber–matrix interface debonding and kinking, 297–299
  crack merging and crack bifurcation, 268–269
  3D formulation, 289–292
  double-notched tension specimen, 266, 267*f*
  3D textile composite, 300–303
  2D textile composite simulation, 299
  elemental condensation algorithm, 285–288
  embedded discontinuity method, 269
  four-point shear beam test, 292–296
  microscopic flaws and imperfections, 265
  noncritical intraply cracks, 265–266
  numerical implementation, 288–289
  orthotropic continuum theory, 266–267
  phase field method, 269
  piecewise linear cohesive laws, 272–275
  randomly distributed matrix-rich pockets, 267–268
  single intra-elemental crack, 275–281
  strong and weak form, 270–272
  textile composites, 267–268
  two interactive cracks, 281–285
Automated crack/delamination propagation, 15, 16*f*, 38–39

B

Ballistic impact, 479
Bézier extraction, 313–315
Bimaterial interface crack problems, 21–24
Bi-modal Weibull distribution, 195
B-K mixed-mode fracture criterion, 26, 27*f*
Bond-based laminate models, 341
Bond-based materials, 336
Bonded composite joints
  bond-line strength effects, 400–402
  failure modes, 402
Boundary value problem, 360–361
B-splines, 311–313

C

Carbon–epoxy composite material properties, 63–64
Carbon fiber-reinforced polymer (CFRP) composites
  calibration, 367–368
  experiments, 366–367
  IM7/977-3 graphite-epoxy composite specimen, 365
  validation, 368–370
CDM. *See* Continuum damage mechanics (CDM)

Ceramic matrix composites (CMCs), 299
Classical fibre-bundle models
  global load-sharing models, 201–204
  local load-sharing models, 204–205
Classical laminate theory, 323
"Cohesive element" damage models, 446–447
Cohesive element implementation, 468–470
Cohesive interface delamination models, 483–484
Cohesive interface elements
  delamination–matrix crack interaction, 68–69
  element formulations, 58–62
  finite element analysis, 55
  history and background, 55–58
  mixed-mode application example, 64–67
  properties and mesh size, 62–64
Cohesive zone model (CZM)
  envelope load damage model, 75
  fatigue models, 75
  high-cycle fatigue simulation, 82–83
  load envelope fatigue model, 76–79
  model parameters, 79–82
  quasi-static cohesive law, 75
  quasi-static model, 76
Combined field-superposition and fibre-bundle simulation, 207–208
Compact compression (CC) test, 165
Compact tension (CT) test, 165
Composite panel structures, 486–491
Computational micromechanics, 133–145, 381
  experimental micromechanics, 418–423
  matrix-dominated failure, 424–429
  multiaxial loading, 411
  multifunctional properties, 429–430
  physically based fracture models, 429–430
  three-dimensional microstructure, 411
  unidirectional plies, 412–418
  VIPPER, 429
Computer-aided design (CAD), 309
Constituent material behaviours
  fibre–matrix interface, 391–392
  fibres, 389
  matrix, 390–391
Continuum damage mechanics (CDM), 227–228, 442–446, 481
  crack opening displacements, 166–167
  damage-tolerant design, 151
  fracture process zone, 151
  intralaminar damage simulation, 157–164
  laminated composites, 152–153
  LEFM, 151
  macroscale models, 156
  mesoscale modelling, 155
  microscale modelling, 154–155
  multiscale models, 156–157
  NASA/Boeing-lead programme, 152
  size effect, composite structures, 153
  smeared cracking model, 166
  strain-softening-based formulations, 152
Continuum shell formulation
  discretisation, 321–322
  examples, 322–327
  kinematics and equilibrium equations, 319–321
Coulomb enhancement factor, 458–459
Coupled criterion approach
  practical applications, 516–518
  principle, 514–516
Coupled fiber–matrix interface debonding and kinking, 297–299
Crack bridging tractions, 55, 56*f*
Crack distribution, 185–187
Cracked laminate model
  basic element formulation, 95–96
  embedded crack front, 96–97
  level set field, 94–95
Crack growth model
  energy release rate computation, 98–100
  weak form, 100–101
Crack kinking and delamination/matrix interaction, 42–43
Crack propagation analysis, 15, 16*f*
Critical failure volume (CFV) method, 237–238
Cross-ply laminates, 184, 185*t*
Curved delamination front contours, 17–18
CZM. *See* Cohesive zone model (CZM)

D

2D A-FEM formulation
  single intra-elemental crack, 275–281
  two interactive cracks, 281–285
Damage evolution laws, 161, 482
Damage-visco-plasticity, 359

DDM. *See* Discrete damage modeling (DDM)
Delamination
  cyclic loading, 30
  fatigue loading, 84–86
  interaction with MIC, 246–247
  matrix cracking, 188–189
  Paris law, 30–33
  sharp corners, 18, 18*f*
  skin-stiffener substructure, 87–88
Delamination–matrix crack interaction, 68–69
Discrete cohesive crack approach, 161–162
Discrete damage modeling (DDM)
  critical failure volume method, 237–238
  flowchart, 237–238, 237*f*
  laminated composite, 236, 236*f*
  mesh independent crack, 236–237
  regularized x-FEM, 238–244
  unidirectional composite plate, 241–242
3D kinking model, 127–128
Domain superposition technique, 441
Double cantilever beam (DCB), 28, 102–105
2D textile composite simulation, 299
3D textile composite simulation, 300–303

E

E-Glass/LY556/HT907/DY063 fibreglass–epoxy, 136*f*
E-Glass/MY750/HY917/DY063 fibreglass–epoxy, 137*f*
Eigendeformation-based homogenization method (EHM), 361
Elastic properties, unidirectional plies, 184, 184*t*
Elemental condensation algorithm
  single intra-elemental crack, 286–287
  two intra-elemental cracks, 287–288
Element discount methods, 445
End-notched flexure (ENF) test, 82
Energy release rate (ERR), 183–185
Epoxy matrix, 141*t*
Euler–Bernoulli beams, 458
Experimental micromechanics
  full-field measurements, 422–423
  interface characterisation, 420–422
  matrix characterisation, 419–420
Extended finite element method (XFEM), 42

F

Fatigue-driven delaminations
  categories, 73–74
  CZMs, 75–83
  delamination onset simulation, 84–86
  initiation, 73
  interlaminar damage, 73
  linear elastic fracture mechanics, 73–74
  load envelope methods, 74
  mode I, mode II, and mixed-mode delamination propagation, 83–84
  onset, 73
  quasi-static loading, 74
  skin-stiffener substructure, 87–88
Fiber bridging, 25
Fiber failure, 247–248
Fibre-dominated tensile failure, 193
Fibre failure modelling
  classical fibre-bundle models, 200–205
  deterministic rule of mixtures, 200
  fibre-dominated tensile failure, 193
  hierarchical scaling law, 209–211
  high-fidelity models, 220
  high-performance fibres, 193–195
  longitudinal tensile failure, 220
  macroscopic notched specimens, 217–219
  matrix role, 197–198
  micromechanical features, 198–199
  Monte Carlo simulation, 205–208
  size effects, 196–197
  stochastic quasi-fractal fracture surfaces, 213–217
  toughening mechanisms and analytical models, 212–213
  Weibull distribution, 219
Fibre kinking, 127–128
Fibre tensile failure, 133
First order deformable laminate theory, 96
First-ply failure
  crack tunneling, 178–181
  thin and thick plies, 176–178
Floating node method, 231
Four-point shear beam test
  crack initiation, 292
  loading parameters, 293
  maximum principal stress criterion, 292
  numerical accuracy and mesh sensitivity, 293–295
  numerical efficiency and stability, 295–296

Fracture characteristic volume (FCV) method
interest and limitations, 513–514
principle, 512–513
Fracture mechanics analyses, 21–24
Fracture modes, 3, 4*f*
Fracture plane, 116–119
Fracture toughness
macroscopic notched specimens, 217–219
stochastic quasi-fractal fracture surfaces, 213–217
toughening mechanisms and analytical models, 212–213

G

Glass fibre, 141*t*
Global load-sharing models, 201–204
Green–Lagrange strain tensor, 321

H

Hardening law, 482–483
Hashin's failure criteria, 142–145
Hexcel's IM7/8552 carbon–epoxy pre-preg system, 59–60
High-cycle fatigue simulation, 82–83
High-energy impact tests, 486
High-performance fibres, 193–195
HTA/6376C carbon/epoxy laminate, 83–84, 84*t*
HTA/637C carbon/epoxy laminates, 83–84, 84*t*

I

IGA. *See* Isogeometric analysis (IGA)
IM7/8552 carbon-epoxy pre-preg, 250–251
IM7/8552 carbon/epoxy tape, 43
IM7/8552 lamina, 254*t*
IM7/8552 material properties, 123, 125*t*
IM7/8552 quasi-isotropic open-hole plates, 521
In situ scanning electron microscope micro-testing, 403
Interfacial stress state, 392–394
Intralaminar damage simulation
damage evolution laws, 161
discrete cohesive crack approach, 161–162
experimental work, 164–166
stiffness, 160–161
strain-softening materials, 163–164
UBC composite damage model, 162–163
Isogeometric analysis (IGA)
Bézier extraction, 313–315
B-spline function, 310
computer-aided design, 309
continuum shell formulation, 318–327
design-through-analysis approach, 309
interfaces and delaminations, 327
Kirchhoff–Love shell element, 315–318
non-linear material phenomena, 309–310
NURBS and B-splines, 311–313
Reissner–Mindlin shell formulation, 309
Rhinoceros programme, 327
shell buckling analysis, 327
solid-like shell elements, 309–310
Isotropic bond-based material models, 336

K

Kinking plane angle, 128–129
Kirchhoff–Love shell element
examples, 316–318
kinematics and implementation, 315–316

L

Laminated shell theory, 106
Laminate load–displacement response, 187
Laminate stiffness, 183–185
Large-notch tension (LNT) tests, 341
Level set model
buckling, 93
cracked laminate model, 94–97
crack growth model, 97–101
double cantilever beam, 102–105
solution algorithm, 101–102
virtual crack closure technique, 93–94
zero-thickness elements, 93
Linear-elastic fracture-mechanics (LEFM), 73–74, 274
Linear mixed-mode fracture criterion, 26, 27*f*
Linear shear response, 129–131
Load–displacement analyses, 66, 67*f*
Load envelope fatigue model, 76–79
Local fibre volume fraction, 399–400
Localization problem, 163–164
Local load-sharing models, 204–205
Longitudinal tensile failure, 193

M

Macroscopic notched specimens, 217–219
Material progressive failure approach
  fibre failure criterion, 510
  Hashin's hypotheses, 509–510
  multi-scale failure approach, 510–511
  non-linear mesoscopic behaviour, 508–509
  non-linear thermo-viscoelastic behaviour, 509
  softening behaviour, 511
  thermodynamical degradation approach, 510
Matrix cracking and intralaminar failure
  crack density evolution, 181–187
  crack patterns, 175, 176*f*
  delamination, 188–189
  first-ply failure, 176–181
  mechanical loads, 175
  transverse cracks, 175
Matrix-dominated failure
  fracture toughness, 426–427
  in-plane shear deformation, 424–425
  manufacturing defects, 425–426
  transverse compressive strength and failure locus, 424
  transverse ply cracking, 427–429
Mesh-independent matrix cracking
  augmented FEM, 230
  cohesive zone models, 229
  continuum damage mechanics, 227–228
  discrete damage modeling, 236–244
  energy release rate, 229
  extensive transverse ply cracking and delamination, 232, 232*f*
  floating node method, 231
  high-fidelity mechanism-based simulation tools, 227
  interlaminar failure simulation, 228–229
  load direction strains, 233, 233*f*
  local displacement discontinuity, 229
  Moiré interferometry, 232, 233*f*
  open-hole IM7/5250-4 tensile specimen, 232
  overheight compact tension specimens, 249–257
  phantom node method, 229–230
  plain weave textile, 257–260
  ply-level analysis, 228
  ply level stiffness, 260
  progressive damage modeling, 244–248
  property degradation, 227–228, 234
  regularized extended finite element method, 231
  stress–strain behavior, 234, 235*f*
  subcritical matrix damage, 233–234, 234*f*
  tensile-loaded open hole laminates, 230
  transverse cracking, 227
  two-crack double cantilever beam, 248–249
  virtual crack closure techniques, 231
Mesh superposition technique, 441
Meso-1-level modelling, 458–459
Meso-2-level modelling, 459–461
Mesoscale damage model, 155
Meso-scale ply damage models, 481–483
Micromechanical failure analysis
  bond-line strength effects, 400–402
  classification, 205–206
  combined field-superposition and fibre-bundle simulations, 207–208
  current state of the art, 381–382
  damage accumulation, 396–398
  delamination, 406
  3D micro-CT, 404–405
  experimental characterisation, 383
  failure modes, 402
  fibre–matrix interface strength, 394–396
  finite element framework, 387–392
  homogenised effective properties, 392
  interface fracture energy, 396
  interfacial stress state, 392–394
  intra-ply-level damage, 379–380, 380*f*
  local fibre volume fraction, 399–400
  local microscopic damage mechanism, 379
  microstructure generation and characterisation, 382
  nano-indentation, 403–404
  numerical microstructure generation, 385–387
  rational, 380–381
  single-step spring-based models, 206–207
  in situ scanning electron microscope micro-testing, 403
  statistical characterisation, 383–385
  thermal residual stress, 398–399
  two-scales FE models, 208

Microscale damage model, 154–155
Mindlin–Reissner shell formulation, 484
Mixed-mode bending (MMB) test, 28, 64–66, 471
Mixed-mode fracture criteria, 26–28
Mixed-mode fracture toughness testing, 28–30
Mixed-mode Z-pin bridging law, 472*f*
Mode I free-edge delamination, 58
Morphing technique, 343–344
Moving mesh technique, 20, 20*f*
Multifibre RVE, 393–394
Multi-perforated plates, 524–525
Multiple spatio-temporal boundary value problems, 360*f*
Multiple Z-pins behaviour
  cohesive element implementation, 468–470
  finite element model, 473–475
  quasi-static experimental tests, 471–473
  simulation results, 475–476
Multiscale damage modeling, 156–157
  carbon fiber-reinforced polymer, 353
  composite level failure mechanism, 371
  cyclic loading, 353
  governing equations and multiscale system, 359–361
  mathematical homogenization theory, 351–353
  mechanical performance, 351
  molecular dynamics modeling, 372
  multiscale space–time homogenization setting, 354–356
  reduced-order modeling, 361–365
  space–time computational homogenization framework, 353
  spatial variability, 371–372
  temporal scales *vs*. spatial scales, 356–359
Multiscale space–time homogenization setting, 354–356

N

Nano-indentation, 403–404
Nearest neighbour algorithm (NNA), 385–386
Nearest neighbour distribution functions, 383–384
Nondimensional crack density, 184, 184*f*
Nonlinear fracture laws, 300–302
Nonlinear shear response, 132
Non-uniform rational B-splines (NURBS), 311–313

O

Open-hole plates
  different hole diameters, 520–521
  different stacking sequences, 519–520
  different w/d ratios, 522
  off-axis tensile tests, 522–524
Overheight compact tension (OCT)
  specimens, 249–257
  test, 166

P

Paris law, 30–33, 81–82
Peridynamics
  adaptive fracture simulations, 347
  anisotropic damage mechanics, 331
  bond-based materials, 336
  bond force densities, 334–335
  brittle elastic solid model, 338
  bulk modulus, 335–336
  composites, 338–342
  crack initiation and evolution, 332
  critical bond strain, 337–338
  damage mechanics-based approach, 331
  elastic and inelastic materials, 335
  elastic peridynamic material, 334
  external body force density field, 334–335
  field equations, 337–338
  force-based coupling method, 332
  fracture mechanics, 331–332
  integro-differential equations, 333
  linear elastic fluid, 335–336
  localization treatment, 342–346
  nonlocal deformation gradient, 336–337
  plasticity, 347
  strain energy density, 333, 333*f*
  stress–strain relation, 336–337
  tensor-valued micromodulus field, 338
Phase inelastic strain coefficients, 362–363
Phase-scalar damage coefficient, 362–363
Piecewise linear cohesive laws, 272–275
Plain weave textile, 257–260
Plasticity law, 482–483
Ply damage elastic law, 481–482

Ply drop model, 66, 67*f*
16-ply laminate, 62
Polytetrafluoroethylene (PTFE), 471
Pre-stressed composite panels
  FE modelling, 497–501
  impact tests, 491–497
Pre-stressed plates, 497–499
Progressive damage modeling
  cohesive energy, 244–245
  crack propagation characteristics, 245
  delaminations, 246–247
  fiber failure, 247–248
  MIC propagation, 245–246
  mixed-mode cohesive zone interface fracture model, 244
Progressive fiber failure (PFF) methodology, 237–238
Puck's failure criterion, 112

Q

Quasi-static delamination propagation, 25–34

R

Radial distribution functions, 385
Reciprocal theorem of elasticity, 183–184
Reduced-order modeling, 361–365
Regularized x-FEM, 238–244
Representative volume element (RVE), 381–382

S

Scotch-ply type 1002 fibreglass–epoxy, 137*f*
Second-order intensity functions, 384–385
Shell-to-solid submodeling technique, 11–12
Short beam shear tests, 59
Single fibre RVE, 393
Single intra-elemental crack
  2D A-FEM formulation, 275–281
  elemental condensation algorithm, 286–287
Single leg bending (SLB) test, 28
Single-step spring-based model, 206–207
Single Z-pin behaviour
  model formulation, 461–465
  model validation, 465–468
Skin-stiffener substructure, 87–88
Snubbing, 458
Spatial model reduction, 362–363
Stacked shell approach, 484
Stacked shell laminate model, 488–489
State-based material models, 336
Stick–slip behaviour, 62, 62*f*
Stiffened composite panels, 43, 44*f*, 487–491
Stochastic quasi-fractal fracture surfaces, 213–217
Strain energy-release rate, 9–11
Strain-softening materials, 163–164
Strength prediction methods
  advanced failure approaches *vs.* fast calculation methods, 525–528
  coupled criterion approach, 514–518
  fracture characteristic volume method, 512–514
  high-stress gradient parts, 507
  material progressive failure approach, 508–511
  multi-perforated plates, 524–525
  open-hole plates, different hole diameters, 520–521
  open-hole plates, different stacking sequences, 519–520
  open-hole plates, different w/d ratios, 522
  open-hole plates, off-axis tensile tests, 522–524
  point stress method, 508
Surface-based homogenisation, 389

T

T300/BMI Z-pins, 458
T800/3900-2 carbon–epoxy, 138*f*
T300/914C carbon–epoxy, 137*f*
Temporal model reduction, 363–365
Tensile strength, 196–197
TexGen software, 437–438
Textile composites
  "cohesive element" damage models, 446–447
  continuum damage mechanics, 442–446
  3D woven reinforcements, 435
  experiments, 447–451
  meso-scale model, 451
  representative volume element, 435–436
  unit cell modelling, 436–442
  yarn–matrix interaction, 435
Textile weave patterns, 436, 436*f*

T700GC/M21 laminated open-hole plates, 522
Thermal loading, 389
Thermal residual stress, 398–399
Thermodynamic evolution law, 450
Three-dimensional invariant-based failure criteria
  aero-structures, 111
  alternative determination of kinking angle, 132
  anisotropy, 113
  computational micro-mechanics, 133–145
  3D stress states, 112
  failure criteria, 111–112, 114–116
  fibre kinking, 127–128
  fibre-reinforced polymers, 111
  fibre tensile failure, 133
  fracture plane orientation, 116–119
  kinking plane angle, 128–129
  linear shear response, 129–131
  matrix-dominated failure, 113
  micro-level failure events, 112
  nonlinear shear response, 132
  preliminary results, 122–127
  Puck's failure criterion, 112
  shear stress, 112–113
  in situ properties, 120–122
Three-dimensional micro-CT, 404–405
Three-dimensional solid, plate, and shell elements, 9–14
Through-thickness reinforced laminates
  fracture behaviour, 476–477
  meso-1-level modelling, 458–459
  meso-2-level modelling, 459–461
  multiple Z-pins, 468–476
  preliminary considerations, 457–458
  single Z-pin behaviour, 461–468
  'smeared force' cohesive zone formulation, 476–477
Traction–displacement curve, 56–57
Transformation field analysis (TFA), 361
Translaminar failure, 193
Translaminar toughening mechanisms, 212
Two-crack double cantilever beam, 248–249
Two-dimensional planar elements, 6–8
Two interactive cracks
  2D A-FEM formulation, 281–285
  elemental condensation algorithm, 287–288
Two-scales FE models, 208

U

UBC composite damage model, 162–163
UD carbon/epoxy prepreg Cycom 977-2-35-12KHTS-134-300, 491–492
Unidirectional composite plate, 241–242
Unidirectional (UD) composites
  classical fibre-bundle models, 200–205
  deterministic rule of mixtures, 200
  hierarchical scaling law, 209–211
  micromechanical features, 198–199
  Monte Carlo simulations, 205–208
  tensile failure, 197–198
Unidirectional plies
  computational homogenisation, 413–417
  embedded cell models, 417–418
Unit cell modelling, textile composites
  boundary conditions, 438–440
  geometry modelling, 436–438
  meshing techniques, 440–442
Unpinned cohesive zone model, 470

V

Virtual crack closure technique (VCCT), 93–94, 231
  application, 43–44
  crack kinking and delamination/matrix interaction, 42–43
  crack tip element length and mesh size, 39
  crack tip lengths, 8–9
  curved delamination front contours, 17–18
  DCB specimen, 34–39
  delamination front, 14–15, 20–21
  delamination growth under cyclic loading, 33–34
  delamination onset under cyclic loading, 30
  fracture mechanics analyses, 21–24
  fracture modes, 3, 4*f*
  historical overview, 4–5
  mesh normality, 19–20
  mixed-mode fracture criteria, 26–28
  mixed-mode fracture toughness testing, 28–30
  modeling, 15–16
  Paris law, 30–33
  recent developments and improvements, 40–41
  recommendations, 45–46

sawtooth behavior, 39
three-dimensional solid, plate, and shell elements, 9–14
two-dimensional planar elements, 6–8
Volume-based homogenisation, 389

W

Weakest link theory (WLT), 194
Weft-tow matrix cracks, 259–260
Weibull's failure criterion, 463–465
WiseTex software, 437–438

Y

Young modulus, 183

Z

Zako damage model, 445